APOLLO

Final Report

CASE FILE COPY

N-97842

ER 12003 JUNE 1961

Trajectory Anal

(NASA-CR-133669) APOLLO: TRAJECTORY ANALYSIS Final Report (Martin Marietta Corp.) 356 p

N73-73534

Unclas
00/99 10721

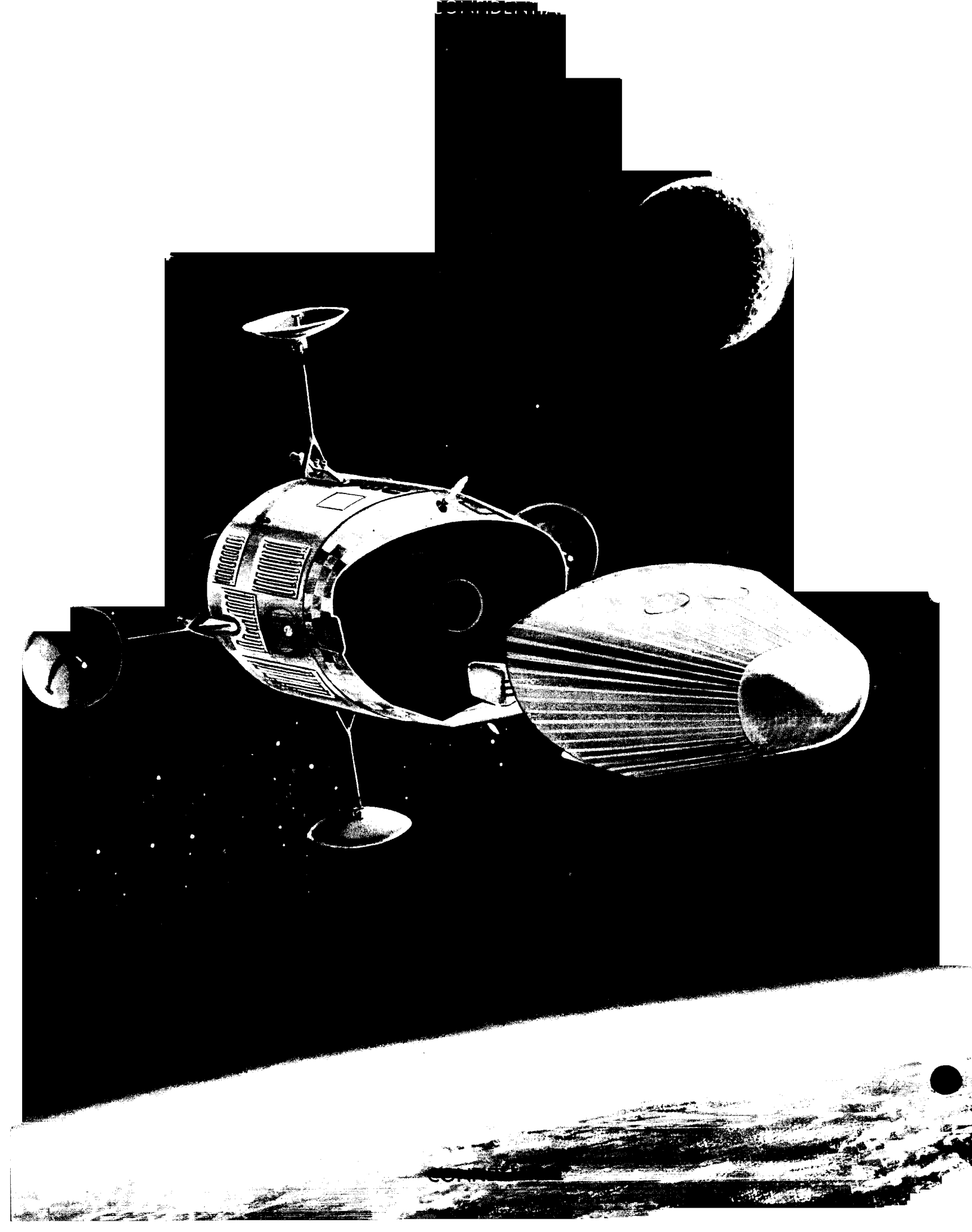

[redacted]

APOLLO

Final Report

Trajectory Analysis

ER 12003 JUNE 1961

Submitted to: NASA Space Task Group,
Contract NAS 5-303, Exhibit A, Item 1.2

CLASSIFICATION CHANGE

TO = UNCLASSIFIED [redacted]

By authority of E.O. No. 11652

Changed by D. H. Gerkensen Date 8/10/73

MARTIN

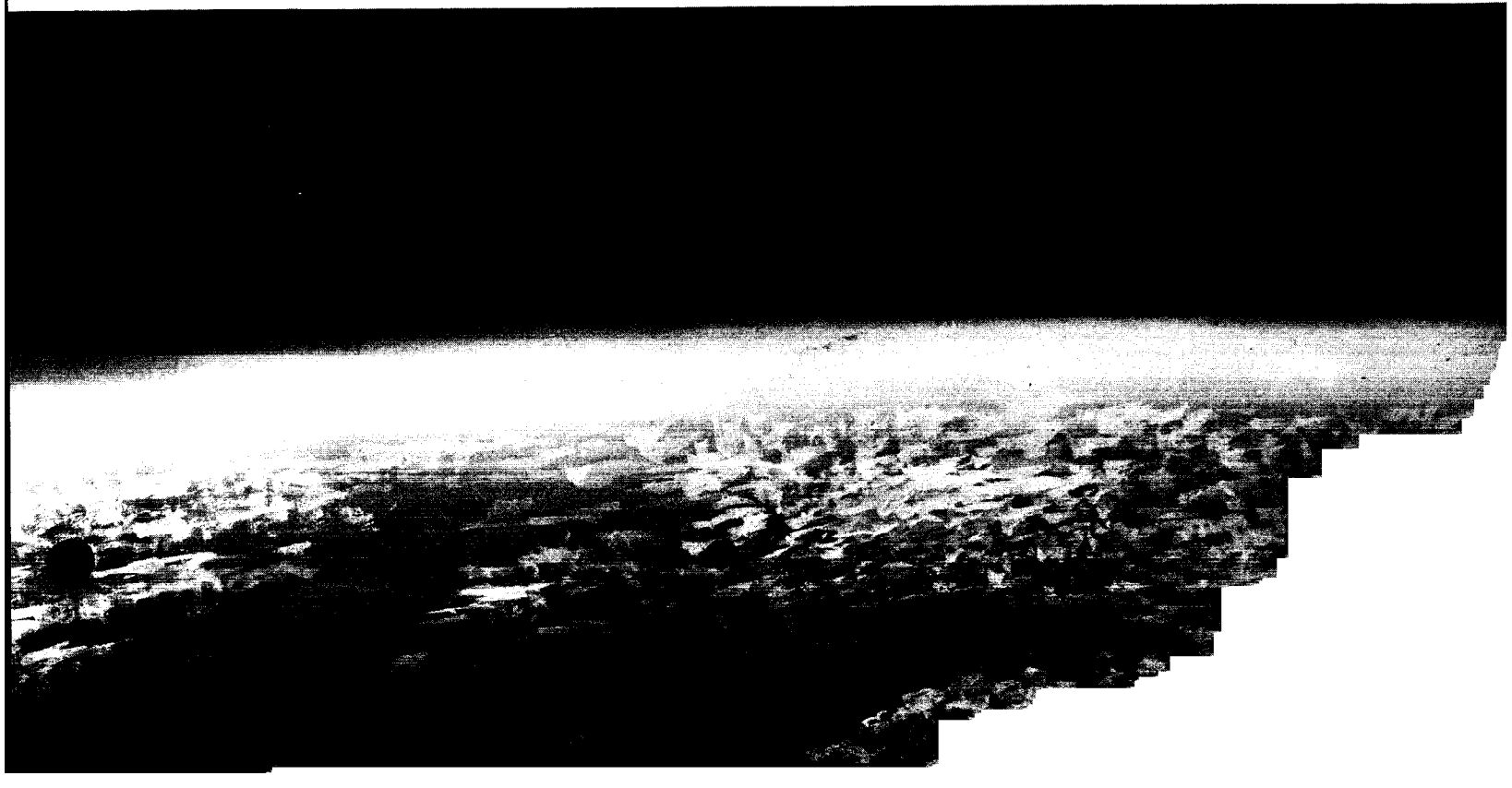

MODEL 410 — THE SYSTEM AND ITS OPERATION

*A BRIEF DESCRIPTION**

Model 410 is the spacecraft system recommended by Martin for the Apollo mission. Its design satisfies the guidelines stated in NASA RFP–302, as well as a more detailed set of guidelines developed by Martin during the Apollo design feasibility study.

We conceive the ultimate Apollo mission to be a manned journey to the lunar surface, arrived at by the preliminary steps of earth orbit, circumlunar and lunar orbit flights. Operational procedures proved out in the early steps will be carried over into the advanced steps, thus establishing a high level of confidence in the success of the lunar flights. With the recommended system, manned lunar orbit missions can be made as early as 1966.

Operational Features

For a circumlunar flight when the moon is at its most southerly declination (Fig. p–1) the launch operation proceeds southeast from Cape Canaveral and down the Atlantic Missile Range. The Saturn C–2 third stage shuts down when orbital velocity is reached at an altitude of 650,000 feet. What follows is a coasting orbit passing over the southern tip of Africa, the Indian Ocean and up the Pacific Missile Range. In this interval the crew checks out all onboard equipment, which has just passed through the accelerations, noise and vibration of the boost phase. If the pilot-commander is satisfied that all systems are working properly, the third stage is restarted and the spacecraft is injected at parabolic velocity northwest of Hawaii. If the pilot-commander is dissatisfied with the condition of the vehicle or crew, he separates from the Saturn S–IV, starts the mission abort engine, re-enters at the point shown in Fig. p–1 and lands at Edwards AFB.

Continuing translunar flight from the point of injection, the trajectory trace swings down over the Caribbean and then west over South America. This particular trajectory passes within 240 naut mi of the moon, then turns back for a direct re-entry some six days after launch. Re-entry occurs southwest of Hawaii some 3300 naut mi from the Edwards AFB landing site.

Tracking. The range coverage provided by present and planned facilities is shown in Fig. p–1 for this trajectory and for a second return trace representing the case when the moon is at the most northerly declination. This second trajectory establishes the 10000-naut mi re-entry range requirement for Apollo to meet the guidelines of operation on every day of the lunar month and of operation into a single landing site.

*For more complete descriptions, see ER 12000 or ER 12001.

Abort. During the critical launch and checkout phase, abort will be possible at any time : at the crew's discretion, automatically or by ground command. Up to nine minutes after launch (from Canaveral), the abort landing is restricted to the AMR for a circumlunar flight. Beyond this point the pilot has the option of continuing to any point along the AMR, PMR or into Edwards AFB through the use of the mission abort propulsion system and the inherent downrange maneuverability of the Model–410.

The Selected Spacecraft

The Apollo space vehicle (Model 410 spacecraft plus launching vehicle) is shown in Fig. p–2. The spacecraft—that portion of the space vehicle which makes the flight to the moon—consists of these three modules:

(1) Command module, housing the three crew members during all thrusting periods, e.g., launch from earth, any corrections to the flight path during flight in space, during re-entry and, ultimately, during landing and launch from the moon. It is the operating center from which all control of the flight is made.

(2) Propulsion and equipment module, containing all the propulsion units which operate between the point of final booster separation and re-entry after the lunar flight. It is separated from the command module at 200 naut mi from the earth on the return trip. It is designed with tankage for lunar takeoff and will be offloaded for less ambitious missions.

(3) Mission module—contained within the outer frame of the propulsion and equipment module—providing space during the lunar voyage for scientific observations and crew living functions.

Command Module

With its lifting capability, the Apollo command module represents a step forward in technology over ballistic vehicles, Mercury and (to the best of our knowledge the *Boctók* (*Vostok*). The lift results from the capsule's shape—a blunted cone flattened on the top (see Fig. p–3).

Heating and radiation protection. The Model 410 is shaped conservatively for aerodynamic heating in addition to its relatively high L/D (0.77). By accepting the large convective heat load of a nose radius smaller than that of the Mercury type, the Model 410 shape tends to minimize radiative heat transfer which is less well understood and harder to protect against. The thermal protection system provides excellent protection for the crew from the large aerodynamic heat loads, from space radiation (including solar flares) and from meteorites.

The normal mission radiation dose will not exceed the five rem limit defined by NASA. If the crew should encounter a solar event as severe as that following the May 10, 1959 flare, they would receive a dose of only 67 rem—well within the 100 rem dose limit set by Martin as tolerable during an emergency.

Thermal protection for re-entry is provided by a composite shield of deep charring ablator (nylon phenolic) bonded to superalloy honeycomb panels which are set off and insulated from the water-cooled pressure shell. The control flaps are protected from the high initial heat rate by an ablator bonded directly to the flap. The long-time, lower heating rates are handled by re-radiation from the backside. The aft bulkhead is protected by a fiberglas phenolic honeycomb panel with a foamed polyurethane insulation.

Crew provisions. The crew has access to all electronic and electrical equipment in the command module for maintenance and replacement. Both pilots have two-axis sidestick and foot controllers as well as a manual guidance mode used with the computers inoperative for deep space and re-entry operations.

Cabin pressure is maintained at the equivalent of 5000 feet altitude ("shirt sleeve" environment). Protective suiting is donned only for launching and landing, but need not be inflated except in emergency.

Guidance. The guidance system consists of both automatic and manual star tracking equipment, as well as two inertial platforms and two general purpose digital computers. Two windows, with ablative heat shield covers, are provided for use with tracking instruments.

Flight control. Pitch and yaw attitude control within the atmosphere is provided by flaps driven by hot gas servos. Outside the atmosphere dual reaction controls are used. Roll is controlled at all times by a dual reaction system.

Communications. Communications equipment includes a K_u band for re-entry, a C-band for the pre-reentry and both HF and VHF rescue beacons for landing and recovery.

Landing system. The landing system consists of a steerable parachute, retrorocket combination, enabling the M–410 to avoid local obstacles, trim out wind drift and reduce sinking speed to a nominal three feet per second—low enough for safe landing on any kind of terrain or in very rough seas. In the event of retrorocket failure, accelerations on the crew will not exceed 20 G.

Launch escape propulsion system (LEPS). LEPS is a thrust-vector-controlled, solid rocket system which separates the command module from the rest of the space vehicle in the event of an emergency during launch pad operations or during boost through the atmosphere. In an off-the-pad abort, it lifts the command module to an altitude of more than 4000 feet. During a normal boost trajectory, LEPS is jettisoned at 300,000 feet.

Propulsion and Equipment Module

The propulsion and equipment module (shown in Fig. p–3) contains propulsion devices and equipment which are not necessary for re-entry. Its outer skin serves both as a load carrying structure and as a meteorite shield for the propellant tanks, mission module and other equipment.

Propulsion devices. The mission engine, used for trajectory correction and abort, is a high preformance, modified LR–115 (Pratt & Whitney), developing 15,600 pounds of thrust. A total of 10,450 pounds of liquid hydrogen and liquid oxygen propellants may be carried, sufficient for lunar takeoff.

Four vernier engines, with 300 pounds of thrust each, are used for midcourse correction, ullage impulse to settle the mission engine propellants and for thrust vector control during operation of the mission engine. In addition there are two sets of six control jets which provide 30 pounds of thrust for roll, pitch and yaw control.

Power sources. Spacecraft equipment is powered by fuel cells (2 kw) which under normal conditions, use the boiloff from the mission propulsion system. A supply of independent reactants is provided for emergencies. Battery power is used during re-entry.

Communications. Four large antennas fold out to provide S-band communications and X-band radar altimeter information. VHF communications gear is also provided.

Mission Module

The mission module provides 400 cubic feet of living space during the lunar voyage. It serves as a midcourse work-rest area, providing freedom of movement and privacy. For operations on the lunar surface it will be a base of scientific investigations, and will serve as an airlock. The same "shirt sleeve" environment at 12.2 psi is maintained as in the command module.

The mission module provides the space and flexibility required for effective lunar reconnaissance and scientific experimentation. An Eastman-Kodak camera-telescope has been selected, for example, which has one-meter resolution at lunar orbit altitude of 50 naut mi.

MODEL 410 WEIGHT SUMMARY

Mission	Circumlunar	Lunar Orbit	Lunar Takeoff
Command Module	6954	6954	6954
Propulsion and Equipment Module	7372	13,192	15,618
Launch Escape Propulsion System	185	185	0
Adapter	489	489	0
Effective Launch Weight	15,000	20,820	22,572

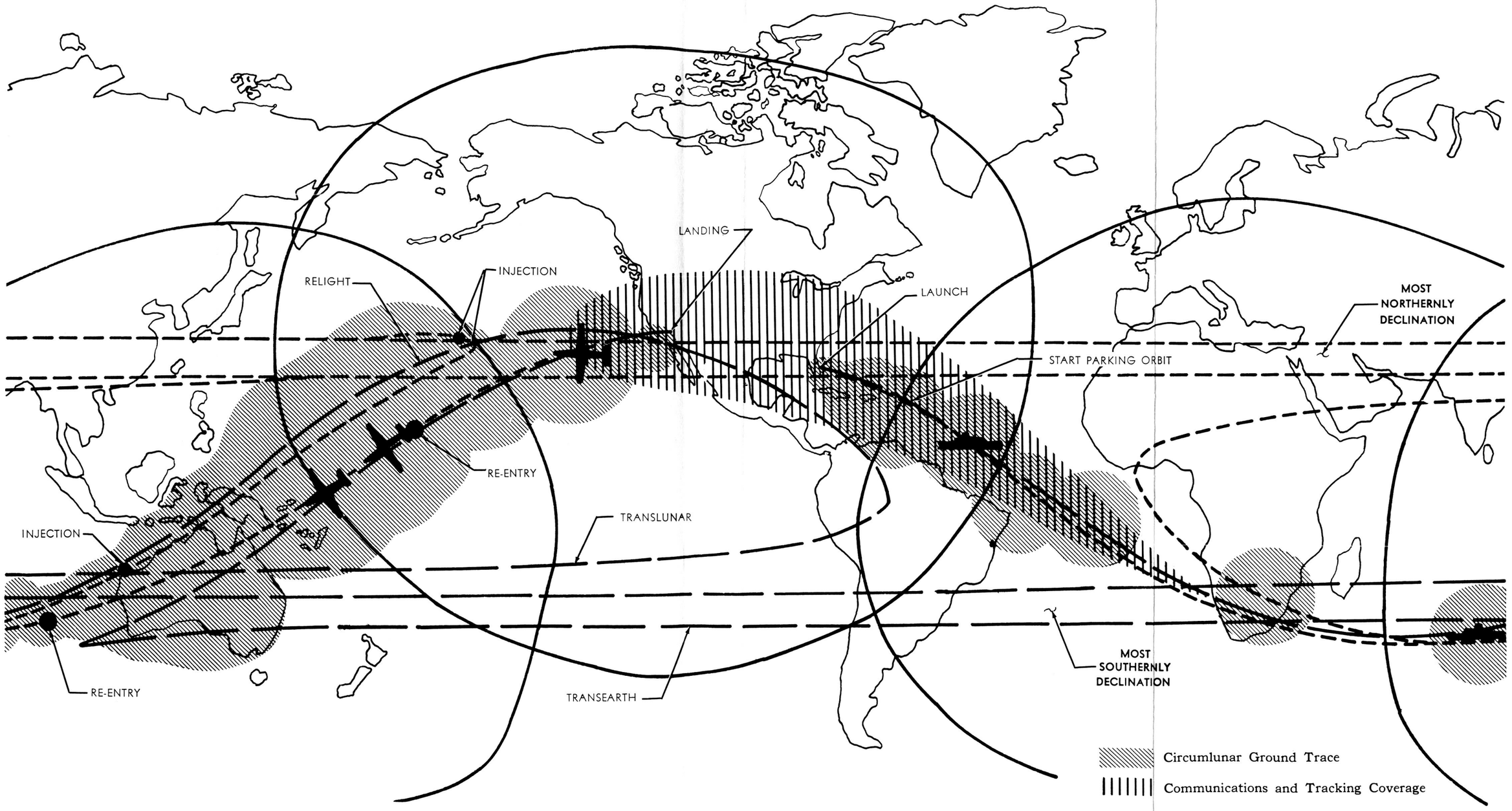

Fig. p–1 Model 410 Circumlunar Trajectory and Range Coverage

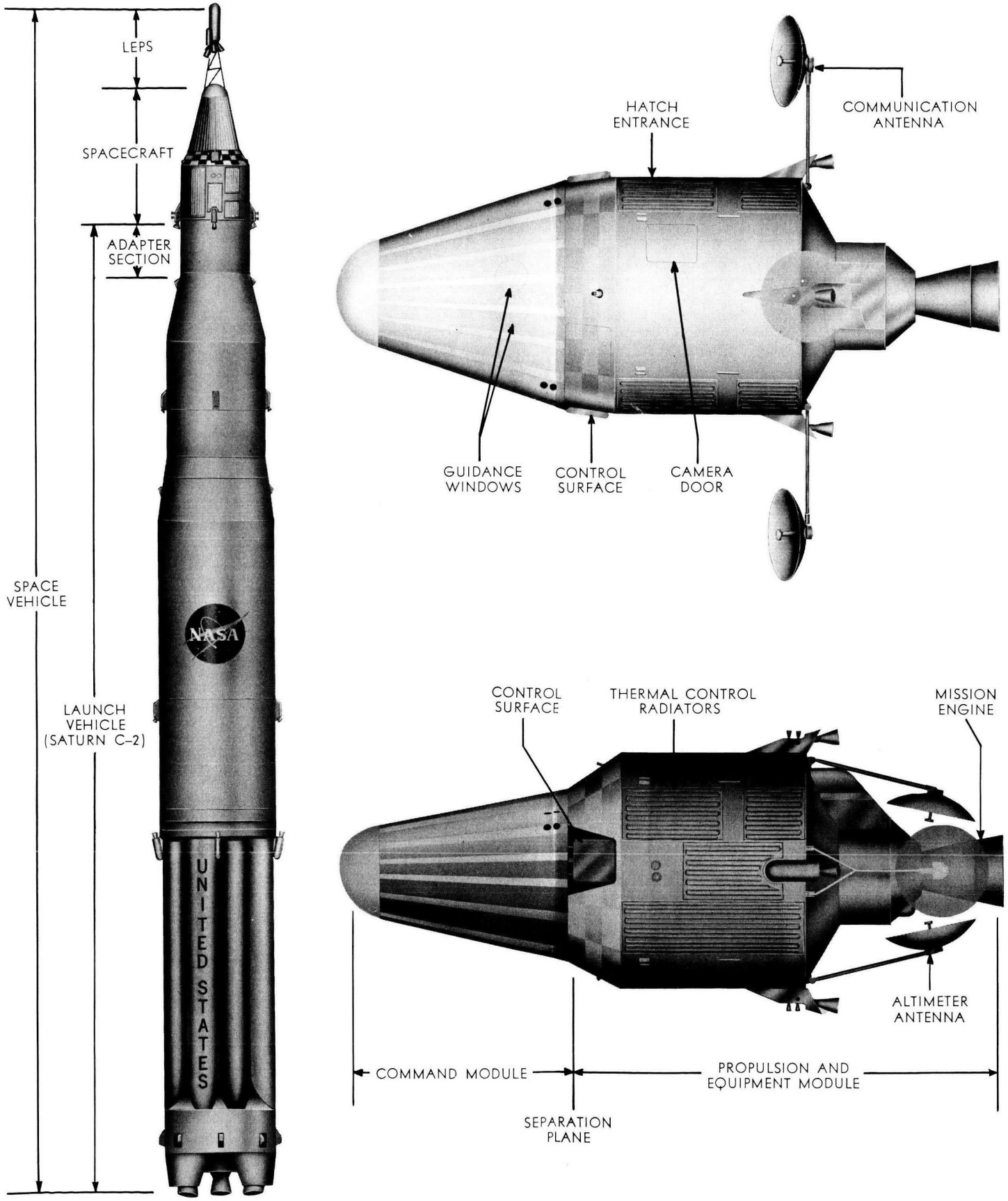

Fig. p-2. Model 410 Apollo Space Vehicle

MISSION	EFFECTIVE GROSS WEIGHT (lb)	PROPULSION ΔV CAPABILITY (fps)	
		MISSION	VERNIER
CIRCUMLUNAR	15000	1830	525
LUNAR ORBIT	20820	6100	525
LUNAR TAKEOFF	22572	8600	200

VOLUMES (cu ft)	
COMMAND MODULE	350
MISSION MODULE	400
MISSION H_2 TANK	400
MISSION O_2 TANK	122

PROPULSION SYSTEM DATA

PURPOSE	TYPE	ISP. (sec)	THRUST (lb)
MISSION (1)	H_2—O_2 (ADV. LR115)	427	15600
VERNIER (4)	N_2H_4/UDMH–N_2O_4	315	300 EACH
ATTITUDE CONTROL (14+BACKUP)	N_2H_4/UDMH–N_2O_4	250–315	15 TO 50

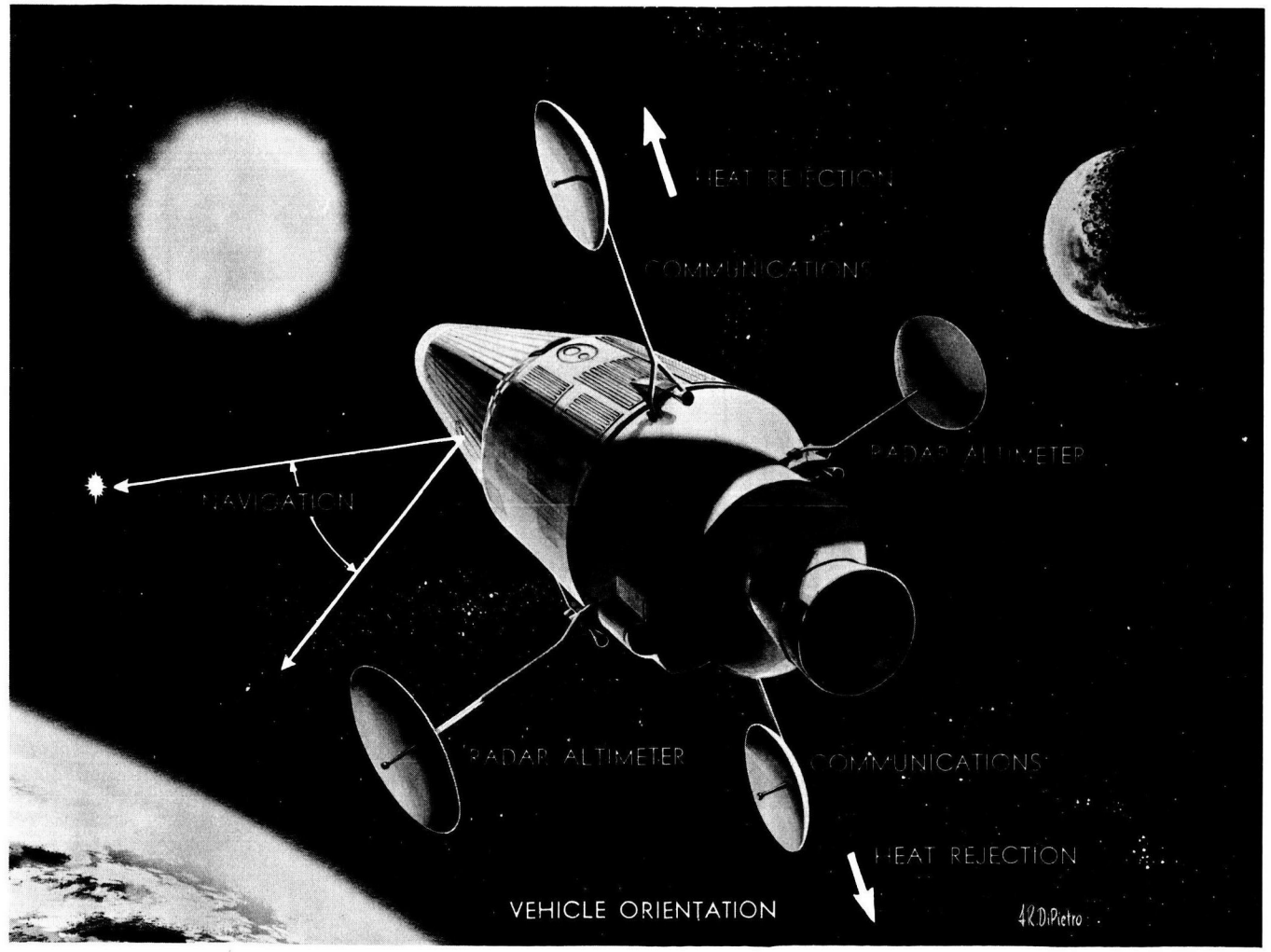

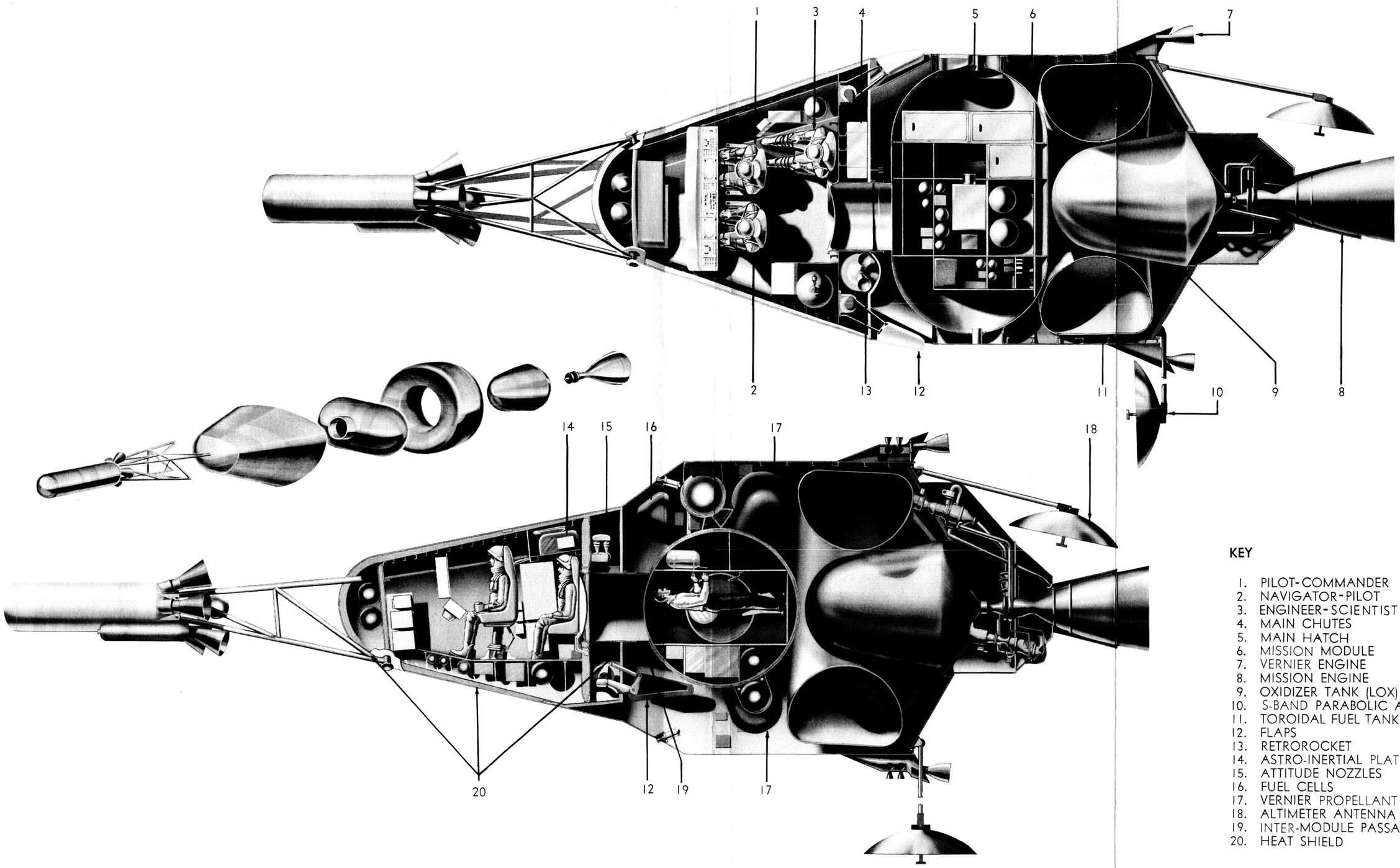

KEY

1. PILOT-COMMANDER
2. NAVIGATOR-PILOT
3. ENGINEER-SCIENTIST
4. MAIN CHUTES
5. MAIN HATCH
6. MISSION MODULE
7. VERNIER ENGINE
8. MISSION ENGINE
9. OXIDIZER TANK (LOX)
10. S-BAND PARABOLIC ANTENNA
11. TOROIDAL FUEL TANK (LH)
12. FLAPS
13. RETROROCKET
14. ASTRO-INERTIAL PLATFORM
15. ATTITUDE NOZZLES
16. FUEL CELLS
17. VERNIER PROPELLANT TANK
18. ALTIMETER ANTENNA
19. INTER-MODULE PASSAGE
20. HEAT SHIELD

Fig. p-3. Model 410 Apollo Inboard Profile

CONTENTS

		Page
	Summary	iii
I.	Introduction	I-1
II.	Ascent Phase	II-1
	A. Trajectories	II-1
	B. Escape Abort Techniques Within the Atmosphere	II-4
	C. Abort Techniques Beyond Atmosphere	II-21
III.	Lunar Trajectory Phase	III-1
	A. General Lunar Trajectory Analysis	III-1
	B. Translunar Midcourse Guidance Fuel Requirements	III-15
	C. Transearth Midcourse Guidance Fuel Requirements	III-21
	D. Translunar Abort	III-23
	E. Transearth Abort	III-32
IV.	Re-Entry Phase	IV-1
	A. Corridor Width Parametric Studies	IV-4
	B. Maneuver Requirements Parametric Studies	IV-6
	C. Maneuver Capability Parametric Study	IV-9
	D. Re-entry Vehicle Studies	IV-16
	E. Maneuverability Studies	IV-25
V.	Operational Concept	V-1
VI.	References	VI-1
VII.	Illustrations	VII-1

CONTENTS

CONTENTS (continued)

		Page
Appendix A.	Equations for Volume of Influence to Approximate Lunar Trajectory	A-1
Appendix B.	The Motion of a Satellite to the Moon	B-1
Appendix C.	Volume of Influence to Integrated Trajectory	C-1
Appendix D.	Optimum Trajectory Program	D-1

SUMMARY

The Apollo ascent trajectory, parking orbit characteristics and test program trajectories are analyzed, with emphasis on abort considerations and techniques for abort off-the-pad, at maximum dynamic pressure, after leaving the atmosphere and during injection into the translunar orbit.

A general lunar trajectory analysis yields all of the practical translunar and transearth trajectories. Trajectories not in the earth-moon plane are given particular attention. Velocity requirements for going into lunar orbit are presented as is a study of ejection from lunar orbit, including effects of remaining in lunar orbit for extended periods. Midcourse guidance fuel requirements are given for typical translunar and transearth trajectories, showing effects of velocity errors at injection into translunar orbit and variations in earth and moon mass. Also treated are abort considerations and trajectories during the translunar and transearth trajectories.

The trajectory aspects of the re-entry problem are analyzed, including parametric studies of re-entry corridor and maneuverability and several particular re-entry vehicles. The significant improvements in re-entry characteristics to be realized through the use of lifting vehicles are shown. The resulting longitudinal and lateral range maneuverability for these vehicles and the practicality of re-entry corridors of 30 naut mi with a maximum load factor of 6 g are presented. The need for a re-entry trajectory optimization program is discussed and such a program is outlined in Appendix D.

An operational concept is developed in accordance with the above studies and other factors, including ground tracking, reliability and uncertainties during the lunar journey. Since the early flights will be man's first attempt at prolonged space travel, many new problem areas will be broached in which little if any practical experience will have been accrued. Therefore, every effort must be made to insure that the Apollo vehicle used in early flights will have the flexibility to cope with the unknowns. Good ground tracking during the critical phases of injection into translunar orbit and re-entry is a necessity. Adequate launch time tolerances must be provided. Well equipped launching facilities and return base are needed.

Briefly, the operational concept uses one launch facility, Cape Canaveral, and a parking orbit nominally inclined 34.2° to the equatorial plane, which always traverses the existing Atlantic and Pacific Missile Ranges' ground tracking facilities. Parking orbit times vary from 38.7 to 66.2 minutes, allowing sufficient time for major system checkout after the high-g launch into parking orbit. Mission abort during this time uses Edwards AFB as the terminal base unless immediate re-entry is demanded. Injection into lunar orbit takes place over the PMR (position dependent on day of lunar month) and returns to earth on an orbit passing up the PMR and inclined to the equatorial plane at 35°. Landing always occurs at Edwards AFB.

The command module chosen, the Model 410 configuration, has a performance surplus adequate to cope with any expected uncertainties, and can easily meet the re-entry requirements needed for the operational concept.

I. INTRODUCTION

A manned lunar vehicle design requires trajectory information over a broad spectrum from subsonic abort trajectories through the range of space orbital trajectories to hypervelocity re-entry trajectories.

This report describes The Martin Company's Apollo trajectory studies in all major areas of the manned lunar flight from launch point to touchdown. The studies are presented in the order of their occurrence during flight, with supplemental studies covering abort techniques, control and guidance system requirements and characteristics and test program trajectories.

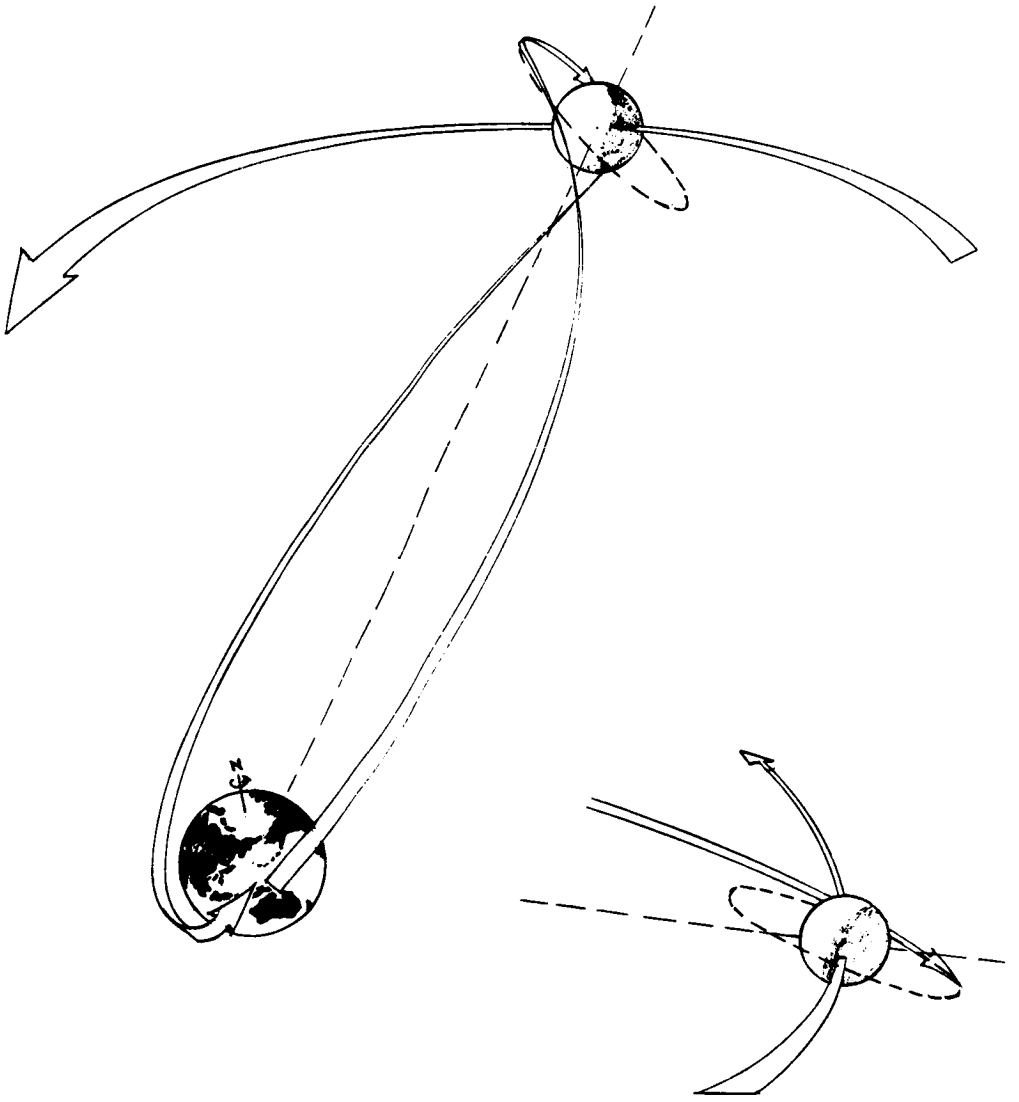

II. ASCENT PHASE

A. TRAJECTORIES

1. Ascent Trajectory

The ascent phase of the Apollo trajectory is defined as the launch, or boost, into parking orbit, the parking orbit interval, and the injection into translunar orbit.

Detailed launch trajectory studies using the Saturn C-1 or C-2 vehicles must still be made to optimize the ascent phase techniques and to obtain maximum launch time tolerances. Such studies will be more pertinent, however, when the boost vehicle is more closely defined and when the lunar flight requirements are better established.

This report employs the Saturn C-2 booster as the launch vehicle. The Case III trajectory (Ref.1) is used as the basis for the studies because it has the natural characteristic of attaining orbital velocity at an altitude of 650,000 ft while at a flight path angle of zero degree. If the third-stage motor is stopped at this altitude and angle, a nominally circular parking orbit is attained. Since the operational concept (described in Chapter V) requires the use of a parking orbit, the third-stage (S-IV) motor must therefore have restart capability. Figure II-1 presents the Saturn C-2 Case III boost trajectory from Ref. 1.

In addition to possessing motor restart capability, the third stage will also incorporate an attitude control system to facilitate equipment checkout, abort and injection procedures. From detailed studies of the general lunar trajectory (Chapter III), the time spent in parking orbit for trajectories which satisfy the operational concept has been determined as a function of day of the lunar month. This parking interval is presented in Fig. II-2, along with range from Cape Canaveral to injection. The parking orbit will vary from 35 to 71% of an orbit over the lunar month, allowing the crew sufficient time to check out major sub-systems and to perform initial star tracking measurements to realign the inertial guidance system before injection into the translunar orbit.

When injection is desired, the third-stage motor is restarted and the spacecraft is accelerated from circular orbit velocity at 650,000 ft of 25,543 ft/sec to a velocity of approximately 35,850 ft/sec at third-stage burnout. This portion of the ascent phase is also presented on Fig. II-1.

The launching of the Apollo spacecraft will take place at Cape Canaveral along a nominal azimuth of 110° (measured clockwise from the north from the geographical meridian). This azimuth is within current range safety limits and results in a parking orbit nominally inclined 34.2° to the equator.

From a performance viewpoint, any deviation from a due east launch (azimuth of 90°) results in less efficient utilization of the earth's rotational velocity, which can be related to a decrement in payload capability by the following expression for the Saturn C-2 launched from Cape Canaveral.

$$\Delta \text{Payload (in lb)} = 2.75 \left(\Delta V_{earth}\right) \text{ (in ft/sec)} - 1339$$

Where ΔV_{earth} is the incremental velocity due to the earth's rotation.

A plot of payload and ΔV_{earth} versus launch azimuth is presented in Fig. II-3. This figure shows that the payload penalty for a 110° launch is 210 lb. This reduces the payload capability of the Saturn C-2 from 20,250 lb to 20,040 lb (Case III, Ref. 1). This figure also shows a loss of 80 ft/sec in the earth rotation component, ΔV_{earth}, of the total velocity for a Cape Canaveral launch at a 110° azimuth.

A further loss of approximately 200 ft/sec will be incurred during the injection into the translunar orbit to simplify the problems associated with a possible immediate return to earth during this portion of the ascent phase. These abort considerations are discussed more fully later in this Chapter. The ΔV losses required to have the burnout angle consistent with abort requirements are presented in Fig. II-4.

The problem of the impact areas of the expended C-2 first, second, and third stages has been investigated. It is felt that stages one and two will break up well before impact and therefore impact over a wide area. However, an indication of the impact area can be obtained if the breakups are ignored and the impact trajectories computed assuming intact stages. It was found in this manner that the expended first stage would water impact about 66 naut mi downrange at latitude 28.12°N and longitude 79.33°W (a point with open water radius of 60 naut mi) and that the expended second stage would water impact about 1200 naut mi downrange, at latitude 20.2 N and longitude 60.6 W (open water radius of 170 naut mi).

The expended third stage of the C-2 booster is expected to be completely disintegrated when it re-enters. Therefore, no impact point was predicted.

2. Flight Test Trajectory

An extensive flight test program must be conducted on the full scale Apollo vehicle to proof test the abort system and determine re-entry performance under various critical conditions. A brief investigation was conducted to obtain a preliminary insight as to the ability of the various available test vehicles to duplicate the critical portions of the Apollo boost and re-entry trajectory. It appears that a satisfactory program can be developed

using Saturn C-1 and Little Joe I & II, with the Titan II used as a backup for certain of the C-1 missions.

Little Joe I. Little Joe I can be used to test the abort system at maximum dynamic pressure. Maximum q for the Saturn C-1 will be about 800 psf, and occurs at a velocity of 1500 fps (see Ref. 1). This flight condition can be obtained near burnout of the Little Joe. Figure II-5 shows that Little Joe may reach a q of 850 psf at a velocity at 1250 to 1500 psf depending upon the launch angle and time after launch. Note that the allowable weight is several thousand pounds above that of a Little Joe I vehicle with a 10,000 pound payload. This will permit the addition of heavier structure (or larger fins if required to maintain adequate stability).

Little Joe II. Because of the ground rule that the main booster engines will be shut down prior to escape, no requirement exists for escape at maximum q. If, however, the shutdown reliability of the first stage is such that it appears impossible to adhere to this ground rule, it will be necessary to test abort characteristics at the maximum acceleration which exists during C-1 first-stage burning. This acceleration is approximately 6.5 g.

By completely loading the Little Joe to obtain a Type configuration, it appears that an acceleration of about 6.5 g occurs at burnout of stage two. Preliminary calculations indicate that the high burnout altitude will produce relatively low dynamic pressure effects although the velocity will be on the order of 5000 fps.

The C-1 and C-2 trajectories clearly show more stringent abort requirements for the C-1. Therefore, no further consideration will be given to C-2.

C-I R & D vehicle. Two types of mission were examined for the C-I: boosting the Apollo into a 150-naut mi orbit, and simulation of re-entry at escape speeds. Due to lack of precise information on the S-IV second stage, the propellant loading and thrust were assumed to be 100,000 lb and 90,000 lb, respectively.

(1) 150-naut mi orbit--The S-I/S-IV combination is capable of boosting the entire Apollo vehicle into orbit without using the Apollo propulsion system.

(2) Re-entry at escape speed--Two methods of attaining the desired flight conditions (36000 fps at 400,000 ft and flight path angle of -7.4^{o}) were considered.

The first method was based on the assumption that the complete 22,000-lb Apollo vehicle had been previously put into a 150-naut mi orbit by a C-1 booster. Upon command the Apollo engine ignites and, by maintaining a predetermined pitch program, the vehicle is driven downward to simulate

re-entry from a lunar mission. It was determined that an angle of attack maintained throughout the flight of about -40° is required to obtain the desired flight path angle at 400,000-ft altitude. However, the burnout velocity is only about 32,000 fps when this technique is used.

A second, and better, method considers only the command module boosted by C-1. If the module is assumed to weigh 7500 lb, the resulting velocity at S-IV burnout is about 34,000 fps. The initial tilt angle and pitch program were chosen such that S-IV burnout occurs at 400,000 ft at the proper flight path angle.

The ability of the Saturn C-1 to duplicate re-entry conditions may be seen in Fig. II-6.

Neither of these two methods permits testing of the Apollo at true re-entry speeds, and the actual re-entry tests of the heat shield must await development of the C-2.

Titan II. In the event that the C-I vehicle is not fully developed and qualified for manned flights in time for preliminary testing of the Apollo space vehicle, the Titan II may be used to perform the earth orbit mission. The configuration selected for this mission is the Titan Dyna-Soar version, which incorporates fins in both the pitch and yaw planes on the first stage. The only change made to this Titan configuration for Apollo is the deletion of the second-stage guidance system and half of the second-stage telemetering equipment. These items (about 750 lb) are located in the Apollo vehicle itself.

Since the Titan alone is not capable of orbiting the fully-loaded Apollo, the space vehicle propulsion system is utilized as a third stage. Maximum Apollo fuel capacity results in a takeoff weight of 22,500 lb. In addition, the escape tower and adapter add about 3500 lb. The tower, however, is jettisoned at first-stage burnout. This configuration will orbit the Apollo space vehicle (with fuel tanks then empty) at altitudes from 75 to 200 naut mi, depending on the technique used (direct injection or orbit transfer). Slightly better performance may be obtained by removing the first-stage booster fins.

B. ESCAPE ABORT TECHNIQUES WITHIN THE ATMOSPHERE

1. Definition of Abort Phases

In order to return the crew unharmed, the Apollo system must have the capability to cut short an intended mission; the objective is to achieve as close to 100% safety as practicable through all phases of the mission profile. This profile consists of the prelaunch (on the pad), ascent, parking orbit and the post-injection phases as depicted in the following sketch.

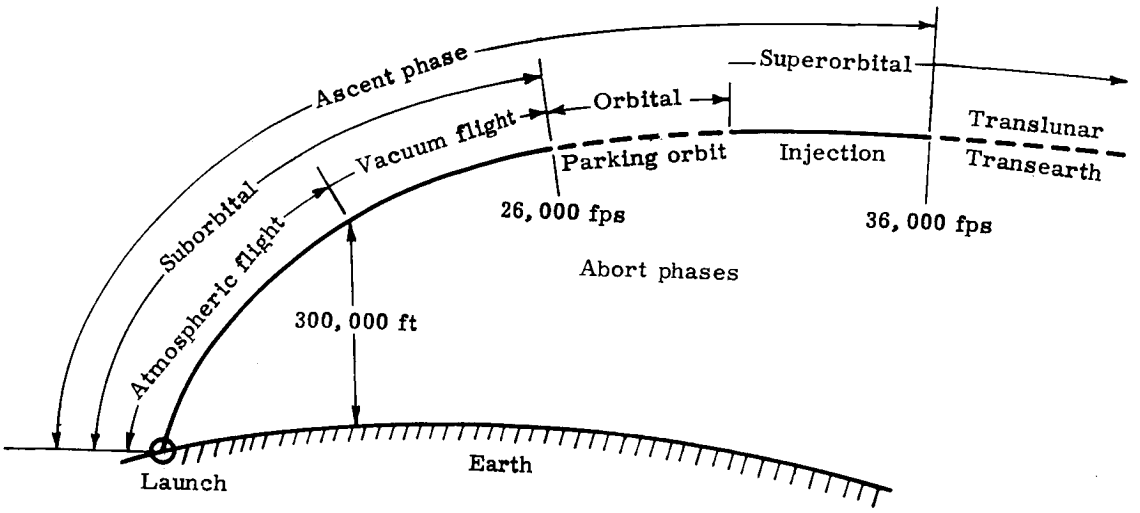

The suborbital phase includes ascent from the ground through the atmosphere and acceleration up to orbital speeds. Subsequent to this phase is the parking orbit, wherein the space vehicle is positioned relative to the moon. Then, the spacecraft is accelerated to a speed approaching that of escape. This injection phase establishes a free flight trajectory with sufficient energy to perform lunar missions. The remaining phases are the translunar (outbound trajectory to moon), lunar-orbit and transearth (inbound trajectory to earth) which complete a typical mission.

2. Abort Scheme

A subdivision is made in the suborbital phase because special systems are provided for abort within the atmosphere. The atmosphere is considered to extend to approximately 300, 000 ft, the altitude at which dynamic pressure becomes zero during ascent.

Should an emergency present itself, the decision to initiate abort is made by the crew onboard the Apollo. However, ground control backup is provided in the event that the crew should elect to have the assistance of ground control, or should give positive evidence of having become incapacitated during the emergency.

The escape technique is first to shut down booster engines, then to provide adequate thrust in the proper direction so that, at the end of burning, the escape vehicle's trajectory is adequate for survival. The necessary

thrust is provided by means of a special escape rocket motor. This motor is mounted atop a tower-like structure attached to the escape vehicle. For an abort within the atmosphere, the escape vehicle is the command module with the modular design concept.

This scheme involves the monitoring of several important variables such as pitch and rotational rates, velocity, angle of attack, and the spatial position of the longitudinal axis of the launch vehicle. Knowledge of the status of these variables permits the definition of the abort plane at any time during atmospheric flight. The abort plane is established by the velocity vector and the vector representing the longitudinal axis of the launch vehicle. This plane then becomes the flight plane of the aborting command module. Therefore, the abort maneuver is not restricted to any particular plane.

The scheme is illustrated in this sketch:

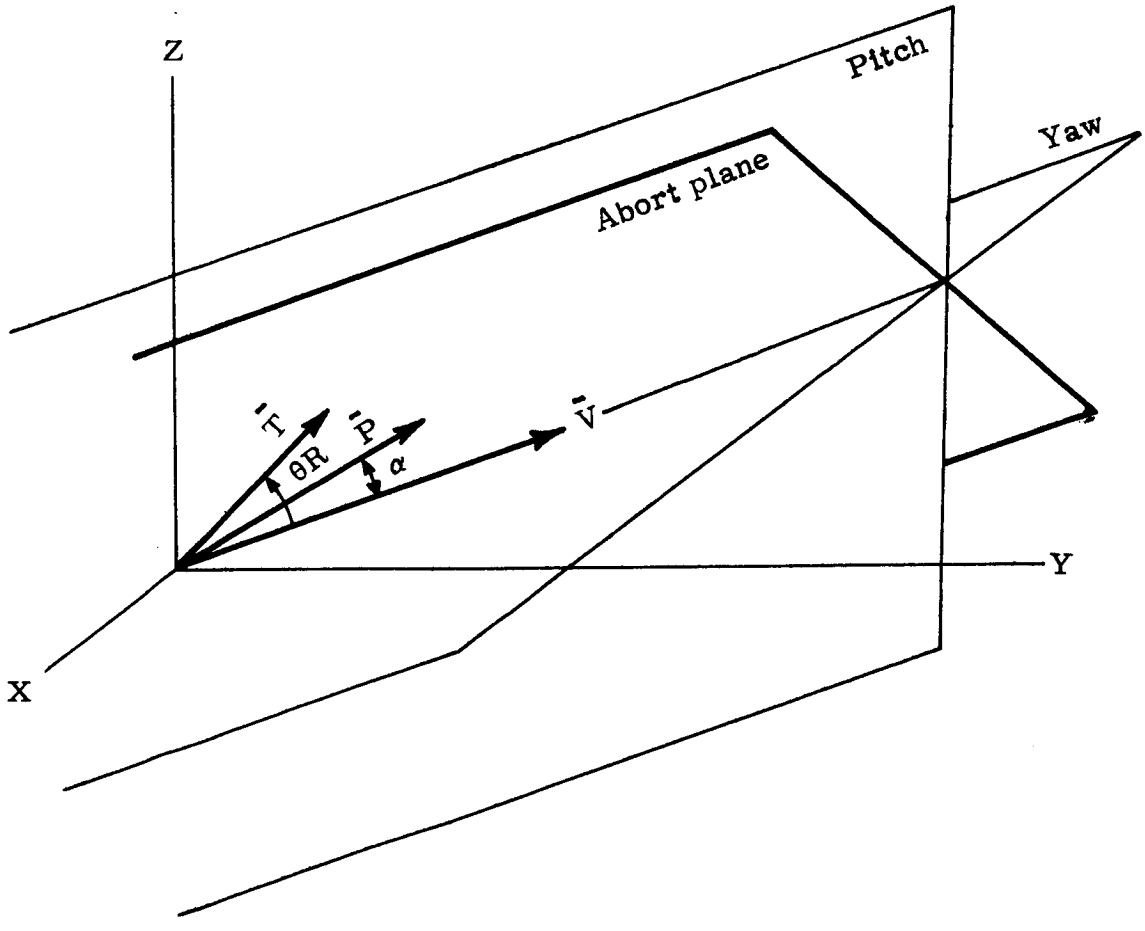

The velocity vector $\overline{V}$, along with the local vertical, defines the pitch (vertical) and yaw (horizontal) planes. The position of the booster longitudinal axis is designated by the vector $\overline{P}$. These two vectors then define the abort plane whose axis of rotation is $\overline{V}$. The included angle between $\overline{V}$ and $\overline{P}$ is the angle of attack (α) which may be introduced intentionally (as in the case of programmed flight) or may be the result of ascent guidance or booster failure. If certain prescribed pitch or rotational rates or angles of attack are exceeded, an abort maneuver is initiated.

Thus far, the plane of the maneuver has been established. It remains to define the maneuver path or direction by which adequate crew safety in abort is realized. The maneuver path is dependent upon the orientation of the escape system thrust (T). It has been found that if the thrust is directed at a specific angle (Θ_R) relative to the initial velocity vector $\overline{V}$ in the abort plane, such a maneuver path is realized. Furthermore, this required angle (Θ_R) is constant and is suitable for the entire flight regime within the atmosphere as will be shown presently. Thus by continually calculating an abort plane, the amount of pitching ($\Delta\Theta$) necessary to achieve Θ_R is known. Another way of stating this is that for any instant of flight, a direction ($\overline{T}$) in space is defined whereby the escape vehicle attitude is "driven" to alignment. Once this alignment is attained, the spatial attitude of the command module is invariant until thrust cessation.

Another desirable feature of this type abort maneuver is that the angle of attack remains in the stability region automatically. This is because the required pitch angle Θ_R is 15°, and the onset of instability occurs at an angle of attack of 20 to 25°. The maximum angle of attack will always be below 20° and occurs at abort initiation. As the abort maneuver progresses, the angle of attack decreases until escape rocket burnout. Figure II-7 illustrates this feature for an abort maneuver at the maximum dynamic pressure condition during ascent. It can be seen that the initial angle of attack is 15° and diminishes to 5° at burnout for a Θ_R of 15°. This is well within the stability margin.

The above discussion describes the scheme while the escape rocket is burning. After burning and below a burnout Mach number of 2.2, the command module continues coasting with the escape tower attached. Upon reaching a dynamic pressure of magnitude approximately equal to 200 lb/ft^2, a stabilization chute is deployed and the escape tower is jettisoned. A normal recovery follows. The coast period after thrust cessation to chute deployment is approximately three seconds and is relatively invariant.

For burnout Mach numbers greater than 2.2, the escape tower is jettisoned and control is maintained either by the aerodynamic flaps or the reaction controls. A normal recovery sequence follows.

3. Abort Performance

Abort performance is chiefly concerned with relative separation distances, load factors and dynamic pressures. There are three main areas of interest during the atmospheric flight, namely, launch (off the pad), maximum dynamic pressure (q_{max}), and atmospheric exit.

Launch (off the pad). For the escape concept on the launch pad, the escape vehicle is the command module and is accelerated away from the booster by the launch escape rocket. After rocket burnout the command module coasts for three seconds and the drogue chute is deployed. When the chute is fully effective (approximately 0.5 sec after deployment), the tower is jettisoned. The vehicle continues to coast until the main chute is opened; then a normal recovery is made.

Figure II-8 shows the altitude versus range performance of the Model 410 configuration for controlled aborts. A thrust level of 123,000 lb is applied for three seconds with a 0.5-sec tail-off. The main chute becomes fully effective 13 sec after abort initiation, but is not reflected in Fig. II-8. However, Fig. II-9 shows this effect. The altitude realized for pad emergencies is approximately 5000 ft. The ground range traversed during this time is 1800 ft. Such performance allows adequate time for sensing of a main chute failure and the deployment of a backup chute plus ample time to conduct limited maneuvers. A minimum altitude required to accomplish this has been estimated to be 3000 ft. This particular consideration is discussed in detail in Ref. 2. Figure II-10 is a time history of dynamic pressure (q) and load factor during a launch abort. Initially, the load factor is 12 g, decreasing to seven g at burnout. The direction of the load factor is from chest-to-back. An acceleration of nine g is experienced, but very rapidly decreases to five g one-half second later. This is acceptable as reported in Ref. 3. The maximum dynamic pressure is 900 lb/ft^2, occurring at the beginning of thrust tailoff. Upon nearing the peak altitude the q diminishes to 10 lb/ft^2.

As a matter of general interest, a time history of velocity, Mach number and altitude is presented in Fig. II-11 for a typical pad escape trajectory.

Effect of wind conditions was also analyzed for the Model 410 launch escape trajectory. Investigations were made regarding both a 40-fps headwind and tailwind. Results, shown in Figs. II-12 and II-13, indicate that the nominal trajectory (zero wind) is not markedly affected by these disturbances. There is no reversal in ground speed for the headwind case, nor is there any appreciable loss in altitude due to these winds. Below, in tabular form, wind effects are shown at t = 13 sec (deployment time of main chute) for a required pitch angle (θ_R) of 15 deg.

	Altitude (ft)	Range (ft)
Head wind (40 fps)	4880	1540
Zero wind (0 fps)	4900	1830
Tail wind (40 fps)	4920	2120

In order to attain comparable escape performance with the L-2C vehicle, it was necessary to increase the thrust level due to the increase in drag characteristics of the vehicle. Figure II-14 gives an altitude-range plot for the L-2C configuration having a thrust level of 147,000 lb for three seconds with a 0.7 second tailoff. Below is another table showing a comparison of the two vehicles for a zero wind and $\Theta_R = 15^o$ conditions.

	Alt. (ft)	Range (ft)	+n (g)	-n (g)	q_{max} (lb/ft^2)
Model 410	4900	1830	12.1	9	930
L-2C	3870	1300	14.6	8.2	800

+ n signifies chest-to-back acceleration

-n signifies back-to-chest acceleration

Escape at maximum dynamic pressure (q_{max}). The maximum dynamic pressure point of the ascent phase occurs approximately 70 sec. after launch

The main problem at this time is avoiding recontact with the launch vehicle. The drag-to-weight (D/W) ratio of the booster at this time is 0.386 and the D/W of the escape vehicle (Model 410 command module plus escape tower) $\approx$ 7.0. Thus it is evident that the escape vehicle decelerates much more rapidly than the launch vehicle. Relatively speaking, after escape thrust cessation, the launch vehicle "catches up" with the escape vehicle. Therefore it becomes mandatory to "sidestep" the booster as described in Section B.2 of this chapter, by altering flight path of the escape vehicle relative to the booster by flying a constant Θ_R of 15 deg. Of course, sufficient thrust must be provided to cancel the D/W deficiency and also to accelerate the escape vehicle from the booster.

For the Model 410 configuration, a thrust level of 135,000 lb for three seconds with a half second tailoff was applied for the q_{max} condition. The altitude at which q_{max} is encountered is about 33,000 ft for the Saturn C-2 launch vehicle. The increase in thrust level from that applied for pad aborts is due to the increase in specific impulse at altitude.

Figure II-15 illustrates escape performance of the Model 410 configuration at the maximum dynamic pressure condition of the Saturn C-2 booster. The initial conditions for the trajectory analysis are:

Altitude = 32,810 ft

Velocity = 1257 fps

Local Flt. Path = 62.8^{o}

Max q = 633 lb/ft^2

Abort separation distances relative to the launch vehicle are shown in the following sketch.

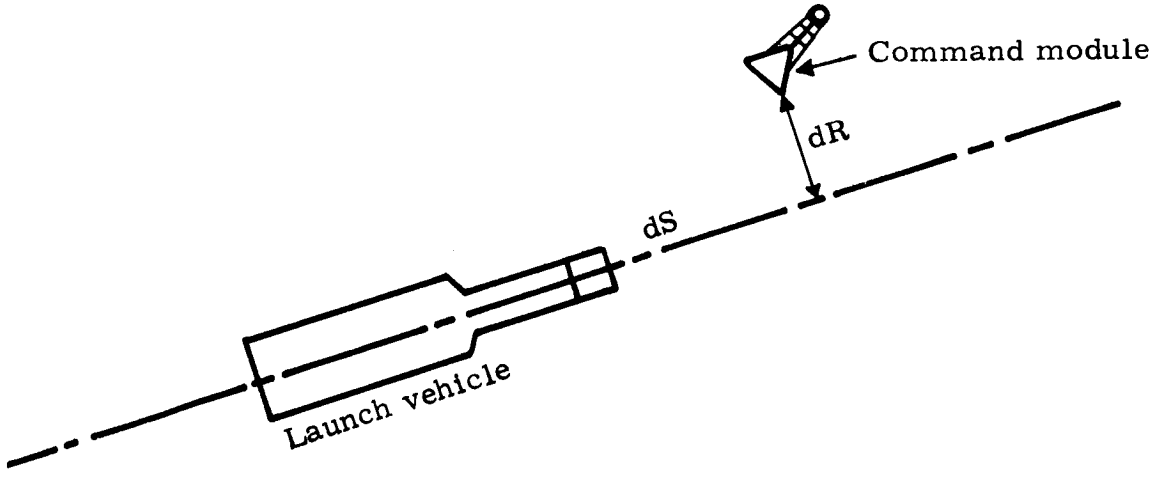

As can be seen, excellent performance is realized. The nearest approach to a normally coasting launch vehicle is 4300 ft for $\Theta_R = 15^{o}$. In event of the presence of a hazard volume, the minimum approach is approximately 3300 ft. Although the performance shown in Fig. II-15 denotes maneuvering in the pitch plane, it is, however, indicative of performance in any abort plane.

Figure II-16 gives a time history of load factor and its direction plus dynamic pressure for a typical (q_{max}) abort for the Model 410 configuration. The load factor for the thrust portion, because of the abort plane possibilities, may form a directional cone of 30^{o} as indicated in the figure. This "directional" cone angle represents a conservative range since Θ_R is 20^{o} for this case, higher than the desired 15^{o}.

A maximum acceleration of 9.5 g is felt at abort initiation and decreases to 6 g at burnout. The maximum deceleration (back-to-chest) is nine g and decreases quite rapidly to five g one second later.

Relative separation distances determined for the C-1 launch vehicle have also proven adequate. Figure II-17 presents this performance for the initial conditions quoted. Below in tabular form is a comparison of separation distances of the escape vehicle from the C-2 and C-1 boosters immediately after abort initiation.

	Separation Distance (ft)	
	t = 1 sec	2 sec
Saturn C-2	130	530
Saturn C-1	120	450

Low-q abort. Low-q abort occurs in that portion of the ascent trajectory near exit from the atmosphere. It is that flight regime in which an increase in velocity does not produce an appreciable change in dynamic pressure. For the C-2 launch trajectories, this flight regime is reached during second-stage burning and terminates when q reaches zero at an altitude of approximately 300,000 ft (midway through second-stage burning). Actually, because of the low q values, re-entries will follow the abort maneuver.

The possibility exists of having to perform abort re-entries with a lift-to-drag ratio (L/D) of zero. If the reaction roll controls experience a double failure, the vehicle may be trimmed to zero lift aerodynamically, thereby making the re-entry independent of roll control. An investigation was made to determine the peak load factor of the Model 410 (L/D = 0) for re-entries performed during the low q region. The results are plotted in Fig. II-18 for a typical C-2 ascent trajectory. Exit from the atmosphere occurs at a velocity of 9600 fps and from this point the resulting re-entry produces the highest load factor (12.7 g). A time history of this trajectory is shown in Fig. II-19. The duration of time spent in the 12-g region is 10 sec and the maximum dynamic pressure encountered is 3400 lb/ft^2. Such high q's may exceed design values.

If the aerodynamic controls fail but roll control is present, the vehicle may be manually trimmed to an L/D = 0.5. For this situation, the maximum load factor (n_{max}) occurs at the same point (9600 fps) but is reduced to eight g. The variance of n_{max} together with ascent dynamic pressure also is shown in Fig. II-18.

4. Thrust Levels and Burning Times

The thrust level (T) required is dictated by the maximum dynamic pressure condition. Near this point in the ascent trajectory, the drag loading on the escape vehicle is the greatest. Therefore, in order to accelerate the vehicle, the aerodynamic drag must first be overcome. The excess thrust (T available - drag - W sin γ) is then the accelerating force. The thrust levels were sized for off-nominal q max. conditions of a minimum of 900 lb/ft^2. This allows the use of the same launch escape tower for missions conducted with both the C-1 and C-2 boosters.

For the Model 410 configuration, having a C_DS = 75 ft^2 (Mach = 1.4), a thrust level of approximately 135,000 lb at 35,000 ft has been used to describe abort performance in the previous discussion. Performance wise, this thrust level has been proved more than adequate. It was purposely selected high to provide upper bounds on accelerations and design conditions. If actual aerodynamics, weights and rocket blast effects prove reasonably close to the estimated data, this thrust level may be reduced if desired. Thrust levels of 100,000 lb (SL) and 110,000 lb (alt) were investigated to ascertain the resulting effects on performance. For the maximum dynamic pressure condition, the performance for T = 110,000 lb applied for three seconds is noted in the form of a dashed curve on Fig. II-15. Reducing the thrust level by 20% reduces the performance by 50%, i.e., the nearest approach to the booster is reduced by one-half.

With 100,000 lb of thrust for a launch pad abort, the peak altitude is reduced by 700 ft to 4200 ft.

Even with these performance reductions, all abort requirements are met. Therefore, the selection of thrust level will await the final analysis with aerodynamic test and weight data, but will be of the order of magnitude indicated here.

An interesting phenomenon is the effect of small increases in tailoff time in lessening load factor. Figure II-20 illustrates this for a pad abort with the L-2C configuration. The load factor was reduced from 12 to eight g with an increment in tailoff time of 0.3 sec.

Burning time is chiefly dependent upon the impulse required to achieve ample altitude off the pad, and autopilot requirements. It was found that for the aforementioned thrust levels a burning time of three seconds with 0.5 sec. tailoff would provide sufficient impulse to reach altitudes over 4000 ft. In addition, the demands upon the computer and autopilot for this time interval are within its functional capabilities. A complete discussion of the abort autopilot is given in Ref. 4.

5. Hazard Volumes

For one measure of evaluating abort performance, "hazard volumes" are established which describe a volume of space that could be very dangerous to the crew.

The first consideration is given the maximum dynamic pressure condition. The assumption is that the launch booster is not exploding, but instead is continuing flight in some erratic fashion. If an explosion does occur at or immediately after abort initiation, very little can be done in avoiding shrapnel. Therefore the main concern is to avoid re-contact with any major portion of the launch vehicle. This can be accomplished by describing all possible locations of the launch vehicle after abort initiation as a function of time and avoiding them. The procedure follows:

First, the launch vehicle is allowed to coast at nominal angles of attack of +10 and -10 degrees without power and without payload. For reasons of conservatism, an additional constant lift component of 300,000 lb is assumed generated by the angle of attack. The amount of actual lift generated by the C-2 launch vehicle is obtained from Fig. II-21. This figure shows the lift curve slope C_{L_α} of the launch vehicle with and without a nose cone as a function of Mach number. The drag of the launch vehicle (Fig. II-22) is also a function of Mach number. The initial conditions for abort at q_{max} are:

γ (Local Flight Path Angle) = 62.8^{o}

V (Velocity) = 1257 fps

h (Altitude) = 32810 ft

Because the C-2 launch vehicle is inherently unstable, it will have a tendency to tumble. Therefore, after various coast intervals, the booster was deliberately rotated about its center of gravity in all directions. At each instant from initiation of abort hazard volumes are yielded by the distance of the vehicle from the booster generated by the two lift conditions and the zero-lift coast.

Assuming symmetry in the yaw plane, Fig. II-23 shows the volume radius as a function of time. The volume is a cylinder whose length is approximately 220 to 300 ft and the maximum radius of which is 960 ft at 10 sec. It was also assumed that the booster would have broken apart or exploded after ten seconds from abort initiation. Figure II-15 shows that the nearest approach to the hazard volume at q_{max} is 3300 ft.

Another approach to avoiding hazard volumes during flight would be to destroy the booster at the time of burnout of the launch escape rocket. Essentially, the resulting fireball and debris would be braked very effectively by high drag-to-weight ratios. From Fig. II-24, it is seen that the escape

vehicle descends through the initial abort altitude 60 sec after abort, during which time the vehicle has covered a lateral range of approximately two naut. mi. Thus, sufficient time elapses for the danger to subside and the nearest approach to the danger area would be 12,000 ft.

Another hazard volume may exist when an abort is performed from the launch pad. In this case the volume is the size of a fireball generated by an explosion or very rapid burning of propellants. Here again, shrapnel "patterns" and magnitudes of over-pressure also can be lethal, depending on separation distance at the time of an explosion. Because of the difficulty in predicting such distance, escape performance will be limited to avoiding the fireball.

The following estimate has been made regarding fireball size. From Ref. 5 the explosive potential can be obtained in equivalent TNT weight of RP-1 and liquid oxygen mixtures. This variation of potential is plotted as a function of propellant mixture in Fig. II-25. The total first-stage propellant weight of the C-2 launch vehicle is 650,000 lb. This amounts to 270,000 lb of LOX and 380,000 lb of RP-1. The probable minimum losses will be 10% of the propellants, and the amount of LOX to cool RP-1 is approximately 66%. The remaining LOX is 86,000 lb, giving a total mixture weight of 428,000 lb. The ratio of LOX to RP-1 = 86/348 = 25%. From Fig. II-25, the equivalent TNT weight to total propellant weight is 57%. Therefore the equivalent TNT weight is 246,000 lb. Reference 6 records a fireball size of 175 ft and a 25% yield for the Atlas launch vehicle. Reference 6 gives the following scaling equation for fireball size.

$$\frac{R}{R_o} = \left(\frac{W}{W_o}\right)^{0.4}$$

R = radius of fireball

W = equivalent TNT

$$R = 175 \left(\frac{246,000}{60,000}\right)^{0.4} = 300 \text{ ft}$$

Therefore, the hazard volume encloses a sphere whose radius is 300 ft. Its vertical velocity is 20.0 fps.

Below is a table giving the closest approach to a fireball of 300-ft radius for the launch escape presented in Fig. II-8.

Time (sec)	Hazard Miss-Distance (ft)
2	550
5	2850
10	4550
20	4700

As can be seen, the escape vehicle avoids the rising fireball by a large margin at all times.

6. Aerodynamic Considerations

For abort within the atmosphere, aerodynamic characteristics play a major role in final design and concept. Reference 7 presents the estimated aerodynamic characteristics of the Model 410 and L-2C escape configurations.

Flight with the Model 410 escape vehicle in the subsonic regime with no ballast is unstable. Since there is a short interval (three seconds) of coast flight after the launch propulsion system burnout, the escape vehicle must be inherently stable. It has been estimated (Fig. II-26) that approximately 1150 lb of inert weight is required to provide a pitching derivative (C_{M_α}) of -0.002 per degree.

At the end of the coast interval an eight-foot diameter drogue chute is deployed for stability, and the escape tower is jettisoned. Figure II-27 illustrates the stabilizing torque parameter as a function of chute diameter. With a 3.5-ft diameter chute, the stabilizing torque has essentially the same value for the chute and escape vehicle as the chute and vehicle and tower. A greater diameter than 3.5 ft provides greater stabilizing action. Thus it is evident from Fig. II-27 that for an eight ft chute, the stabilizing effect of the chute and escape vehicle is greater than the chute and vehicle and tower.

However, if there should be a need to retain the tower in order to keep the drag-to-weight ratio maximum, sufficient stability would still be maintained.

In addition, by deploying the drogue chute at this time the instability onset due to dynamic pressure decay for any disturbance would be negated.

At supersonic Mach numbers, the command module is stable with or without the tower. However, Mercury data has verified that tower blast effects significantly affect the aerodynamic characteristics of the vehicle. In fact, any stability or lifting properties may be reduced or completely nullified. The supersonic $C_D S_{ref}$ (power off) is 75 ft^2 for Model 410 and 150 ft^2 for the L-2C. Subsonically the respective $C_D S$'s are 60 and 100 ft^2. These values were used for the trajectory analyses.

During hypersonic flight the lift-to-drag (L/D) ratio corresponding to the maximum lift coefficient is 0.5 and the maximum L/D is 0.7. These values, for all practical purposes, are representative of both the Model 410 and L-2C configurations.

7. Design Concept

The concept of the Apollo abort system within the atmosphere is to provide positive control of the abort maneuver to insure a successful recovery. This is accomplished by providing guidance and thrust vectoring equipment in the abort system. The problem of the outcome of the abort maneuver in case of a failure in the special equipment has been answered in the present system by its being designed to minimize tumbling in case of complete computer autopilot or thrust vector control failure. It thereby affords a second chance for a successful escape.

Besides lending "power off" aerodynamic stability to the escape vehicle, the inert weight added to the launch escape tower also increases the moment of inertia in the pitch and yaw planes. This increase in moment of inertia helps reduce tumbling rates (due to thrust eccentricities).

Figure II-28 shows the tumbling rates at escape thrust cessation as a function of thrust eccentricity. Thrust eccentricity is defined as the perpendicular distance between the thrust vector and the center of gravity. The tumbling rates are shown for a 3.5-sec burning time for two thrust levels and two representative moment of inertia values. These rates were determined in absence of aerodynamic stability for reasons stated in Section B.6 of this chapter.

In conjunction with Fig. II-28, the angle-of-attack (α) at burnout of the escape rocket is shown versus thrust eccentricity in Fig. II-29. It was assumed that an angle-of-attack greater than 20° would result in a tumbling motion. As can be seen, the thrust offset must be smaller than 0.2 in. if tumbling is to be prevented.

The anticipated uncertainty in cg position is on the order of 0.13 in. Uncertainty in manufacturing tolerances and thrust alinement amount also to 0.1 in. Therefore thrust eccentricities as high as 0.26 in. may be realized when attempting to align the thrust vector through the design cg. Assuming that 0.26 in. is equivalent to a three-sigma error and that eccentricities larger than 0.175 in. produce tumbling, it becomes evident that 95% of the time tumbling will not occur (see sketch) after guidance system failure.

Figure II-30 shows the effect of thrust eccentricity for pad escape. In the no-tumbling region, performance is not impaired and is essentially the same as a controlled maneuver. For eccentricities greater than 0.3 in. performance deteriorates quite rapidly and the tumbling rates increase to over 40°/sec.

Restraint from rotation due to thrust or aerodynamic asymmetries would have to be provided by a rail or track. As soon as the vehicle traverses half the booster diameter, the aerodynamic load must be reacted by a force couple on the tracks. Theoretically, if the tracks extend to the extreme edge of the booster, the couple load would be infinite just before disengagement. By cutting off the top of the track some distance in from the end of the booster, loads on the booster may be held to a predetermined value.

A full analysis of the resulting motion has not been made; however, this approach from a mechanical motion and load standpoint does not offer an attractive solution.

One significant detriment for the L-2C configuration is that the track attachments to the re-entry body must be made through the heat shield. This rail would have to be removed prior to re-entry in the normal sequence, but would still leave local attachment points to provide hot spots in the heat shield which must be cooled. For both the Model 410 and L-2C lateral separation of the "tunnel", connecting the mission module with the command module would seem to present more mechanical detail design problems than a system which separates in the longitudinal axis.

Because of the curved shape of the heat shield on the L-2C vehicle and the extended flaps for the Model 410 vehicle, use of rail restrained lateral separation motion requires that the fairing between the mission and command module must be removed prior to escape rocket firing.

Since the loads and motion during separation would be dependent on the values of friction coefficient on the rails, a certain amount of trial and error testing would be required in order to establish applicable design criteria.

Another method to achieve lateral separation displacements is to allow the command module to pivot about one edge to a point where the escape rocket thrust is orientated to a desired angle. When this angle is reached, complete separation takes place.

If the launch escape rocket is used to pivot the vehicle, then the vehicle will have received a rotational velocity which is undesirable at this stage in the escape sequence. The use of a restraining snubbing actuator to absorb the rotational energy before final separation would theoretically provide a solution. The unit could then be arranged to disconnect after reaching the end of its required stroke, but it would be heavy.

This method would allow the thrust vector to be aligned through the cg for abort on the pad as well as in flight. Again mechanical and load problems appear to offset the other possible advantages.

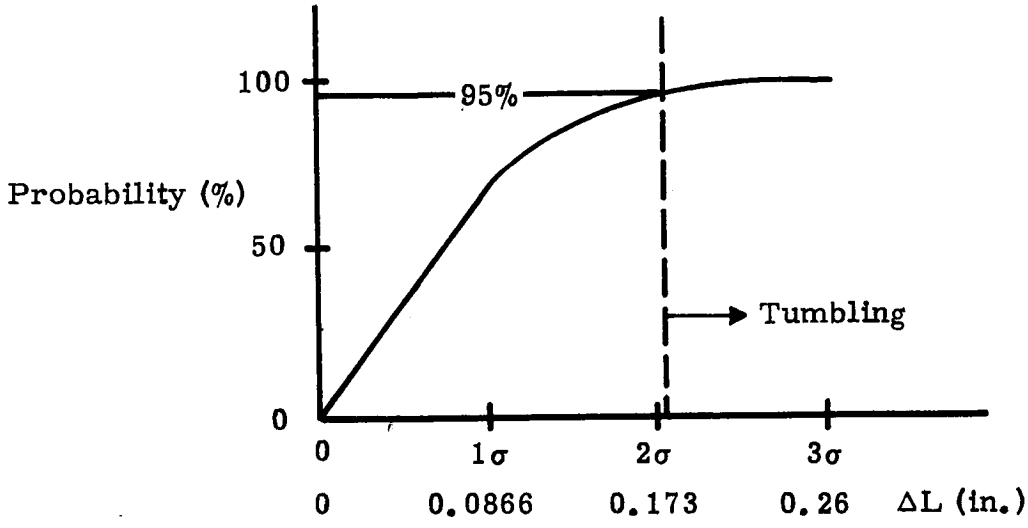

Included in Fig. II-31 are abort trajectories at q_{max}. They are presented relative to the C-2 launch vehicle for various thrust off-sets. Because the escape vehicle may penetrate the hazard volume, the performance must be classified as marginal for small thrust off-sets. Here again, the situation might be greatly improved by deliberate destruction of the booster as pointed out in the previous discussion.

8. Other Methods

If the abort system is to employ thrust eccentricity alone as the means of attaining lateral separation, then deliberate offsets must be chosen to provide "positive" lateral separation. This means that the aim point of the thrust vector must be outside the sphere of cg uncertainty. By doing this, the probability of tumbling increases even for small offsets. To circumvent tumbling, the total impulse can be reduced, but this reduces the overall performance. The vehicle may be ballasted to increase moments of inertia, but this reduces T/W and consequently the vehicle performance. Therefore it does not seem feasible to incorporate deliberate offsets, hoping to achieve the performance presented previously, and at the same time keep tumbling probabilities low.

Another escape method was briefly examined, whereby the escape vehicle is ejected similar to jet aircraft pilot seat ejections. The idea is to provide three rockets mounted to the escape vehicle. Two rockets would direct thrust in the forward direction for launch pad escapes. Normally, when the booster reaches an altitude of 5000 ft these rockets would be jettisoned and the one remaining rocket then would be fired transverse to the launch vehicle's longitudinal axis.

Various means of providing thrust vector control such as secondary injection, thrust vanes, gimbaled nozzles, etc., are discussed in Ref. 8.

Thrust direction control by means of aerodynamic surfaces (canards) appears less attractive than methods discussed in Ref. 8. A "free floating" system must be provided in case of failure. This in turn might require servo tabs on the surfaces themselves. In addition they must be capable of providing adequate control over wide ranges of flight conditions. This involves designing for nonlinear aerodynamics and completely variable aerodynamics as well.

9. Control System

The abort control system consists of an inertial guidance platform, computer, autopilot and thrust vectoring system. Only the latter two are needed just for the abort maneuvers. These systems are fully discussed in Refs. 4 and 8. A simple block diagram is presented here to show the major events during the abort sequence.

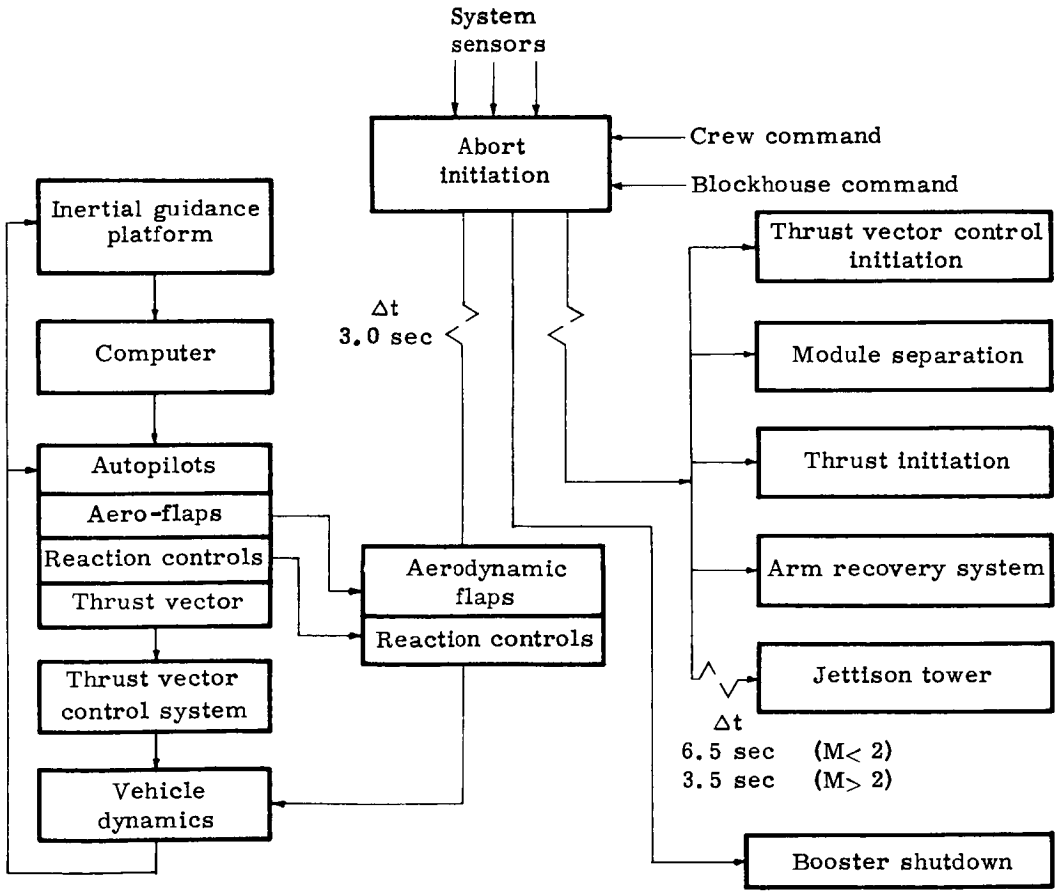

Abort can be initiated by the crew, critical system component sensors or by ground control. Prior to the abort signal all auto-pilots will be kept in continuous readiness.

Once the signal is given for abort, the main engines of the booster are shut down. After thrust decay, signals are relayed to activate the thrust vectoring system. Immediately upon sensing the module separation signal, ignition of the launch escape rocket occurs. At the same time the recovery system is armed, and a delayed signal to jettison the escape tower is generated. Another delayed signal is generated to activate the aerodynamic flap or reaction controls. Meanwhile the vehicle is being controlled by the abort autopilot and thrust control loop. After thrust tailoff, the re-entry autopilot-aero-flaps or reaction controls loops are then utilized for vehicle recovery.

Included in Fig. II-32 is a typical response to an autopilot command to reorient the vehicle's longitudinal axis by 15°. Within one second the vehicle's attitude reaches the desired value and in the remaining two seconds becomes damped out at this value.

10. Launch Escape Tower Payload Penalty

For a normal Apollo mission, the launch escape tower is jettisoned at 300,000 ft. This operation makes the overall ascent trajectory more efficient than carrying the tower to injection. The tower is dropped during second-stage burning and therefore gives rise to a certain amount of ambiguity in quoting booster payloads.

Figure II-33 resolves the problems by presenting the effect on booster payload when "jetsam" weight is carried to various points during second-stage burning.

For example, if the launch escape tower weighs 2800 lb and is jettisoned 228 seconds after launch (311,000 ft), its effective weight on booster performance ($\frac{\delta W_{PAYLOAD}}{\delta W_{ABORT}}$) is 6%. In other words, if the payload at launch is 19,000 lb without the abort tower, the effective payload for the ascent phase would be 19,168 lb (19,000 lb + 0.06 (2800) lb). Figure II-33, based on a typical Saturn C-2 trajectory, includes a time history of dynamic pressure, altitude and local flight path angle.

11. Jettison Rocket

A jettison rocket is incorporated to propel the launch escape tower away from the command module after an abort or at 300,000 ft for a normal mission. The thrust level of this motor is 27,000 lb (one-second burning time) and the rocket is positioned to provide a 100-ft clearance after one second for all conditions.

Certain problems arise in mounting this special rocket so that adequate performance is always obtained. With such a thrust level, the thrust vector must pass fairly close to the launch escape tower cg to prevent excessive tumbling.

Mounting the jettison motor on the side with a canted nozzle necessitates that the cg of the loaded escape rocket and tower must be close to the cg of the empty escape rocket and tower. To accomplish this would require some ballast.

Mounting the jettison motor atop the launch escape tower requires no ballast, but it does help to deteriorate the stability of the escape configuration. The actual mounting location is pending receipt of aerodynamic test and weight data.

C. ABORT TECHNIQUES BEYOND ATMOSPHERE

1. Suborbital Abort

The second portion of the suborbital phase takes place beyond the atmosphere. In this flight regime, essentially the same abort philosophy is followed as used in atmospheric flight. Primary abort decisions are made by the crew. The booster engines are shut down, and the required impulse is applied in the proper direction to establish safe abort trajectories.

Because of the absence of atmosphere, the launch vehicle will be in "free fall". Therefore, the problem of the booster over-running the escape vehicle is not present. The escape vehicle for this portion of flight is the command module plus the propulsion and equipment modules. The necessary impulse thrust is provided by the mission engine which is located in the aft end of the propulsion and equipment module. Its thrust rating is 15,600 lb; propellants are LOX-hydrogen.

The flight regime under discussion begins at approximately 10,000 fps and extends to orbital speeds (25,575 fps). Since this flight regime is entirely out of the atmosphere, any abort necessarily means re-entry. Heating problems are not of concern here because the re-entry speeds are well below the design speed (36,000 fps). Instead, the main interest is the resulting load factor and dynamic pressure which the manned capsule might experience. Just prior to re-entry, the propulsion and equipment module is separated from the re-entry vehicle (command module).

Figure II-34 presents a summary of an investigation conducted on the typical Saturn C-2 trajectories tabulated in Ref. 1.

The maximum load factor encountered (n) is plotted versus the velocity at which abort occurs. The load factor (n) is shown for two Cases -- I and IV

(Ref. 1., C-2 trajectories)--with no additional maneuvers other than separation ($\Delta V = 0$). Case IV proves the most critical with 10.5 g at 15,000 fps.

The aerodynamic characteristics of the re-entry vehicle are an $L/D_{max} = 0.73$ and $W/C_DA = 100$ lb/ft^2. This is representative of the Model 410 configuration.

To reduce the load factors, a maneuver was conducted at abort which returned the velocity vector parallel to the local horizontal at propellant burnout. This type of maneuver is not necessarily optimum, but is presented here to show that the load factor can be reduced to less than 10g for the extreme case.

Velocity impulses of 3000 fps and 6000 fps are reflected in Fig. II-34 for this maneuver, with the latter being representative of the lunar orbit mission capability. Figure II-34 assumes full reaction and aerodynamics control during abort and re-entry. Figure II-35 presents a typical abort trajectory at 15,000 fps from the Case IV ascent trajectory. The load factor levels are satisfactory for an emergency condition.

Some concern has been expressed regarding failure of the roll control system during re-entry. In the event of this type failure, the vehicle will be trimmed to zero lift attitude and make a ballistic type of re-entry. This method minimizes uncontrolled rolls and re-entry at negative lift. However, failure of roll control would mean that the backup system also would have failed. Although this is a double failure, investigations have been made to gain an insight of the ballistic re-entry capability during typical ascent trajectories. Figure II-36 illustrates the load factor encountered if such a ballistic re-entry is made from aborted flight during the suborbital phase. Again Case IV proves most severe. Also the critical ascent speed shifts from 15,000 fps to 19,000 fps for ballistic entries. The peak load factor experienced is 22 g with no maneuvering.

An effort was made to reduce the peak loading by performing maneuvers with the propulsion module at various points along the "free fall" portion of the trajectory prior to entry. The first series of maneuvers is performed immediately after separation from the launch vehicle. An empty weight of the Apollo vehicle was assumed to be 10,000 lb. Various fuel loadings were used that resulted in potential velocity impulses of 1500 fps, 2700 fps and 5300 fps. Thrust is applied at various angles relative to the velocity vector with the mission engine. Figure II-37 shows the load factor for the abort trajectories as a function of firing angle. As can be seen, the optimum thrust angle is close to the forward direction ($\delta = 10^o$). The peak g loading of 22 is reduced to 12.3 g for ΔV = 5300 fps, 18.7 g for ΔV = 2700 fps and 20 g for ΔV = 1500 fps.

Next the maneuvering was initiated when the escape vehicle was at apogee after separation from the booster. The results (Fig. II-38) are similar to

those where the maneuvering was done immediately after separation. The optimum direction of thrust application was again in the forward direction ($\delta = +10^{o}$) and the peak acceleration (22 g) was reduced by approximately the same amount as in the previous maneuver.

Thirdly, maneuvering was delayed until just prior to re-entry. Figure II-39 indicates that the direction of optimum thrust application (δ) has shifted from 40^{o} to 50^{o} and that the peak load factor is somewhat reduced when compared with the previous type maneuvers. The discontinuity for the ΔV = 5300 fps curve stems from the fact that the full 5300 fps cannot be obtained before the propulsion module must be separated from the re-entry vehicle at re-entry. If complete burning were allowed, both modules would be in the atmosphere at burnout.

Although the full gamut of initial conditions for typical Saturn C-2 trajectories have not been investigated nor other schemes such as programmed pitch rates, constant spatial alinement, etc., it nevertheless is felt that the present method gives some insight as to the amount of reduction in peak g possible.

It appears that over 5300 fps is required at (L/D) = 0 to adequately reduce g-levels to tolerable values with the above scheme. Equally important are the dynamic pressures. These pressures must not exceed structural limits. With a $W/C_{D}A$ of 220, for example, the peak load factor must not exceed 7 g to stay below a maximum dynamic pressure of 1500 lb/ft^{2}.

Figure II-40 shows a time history of an (L/D) = 0 abort at the most critical point on the Case IV trajectory. The available maneuvering impulse is 5300 fps and the maximum dynamic pressure experienced is 2600 psf.

The requirement of making an aborted flight in this critical region at an (L/D) of zero is dependent upon the double failure in the roll control system. At worst, a period of only two to three minutes exists where abort would be critical in the event of this double failure. The other ascent trajectories in Ref. 1 are less critical. It is most probable that the final Apollo ascent trajectory will have less critical abort characteristics than those presented.

2. Superorbital Abort

As previously defined, this phase includes coast or parking orbits plus injection of the spacecraft into a translunar trajectory. Here again, as will be the case for the remainder of the mission, the combined mission and command modules are separated from the S-IV stage by the mission engine.

Upon separation from the third stage, the programmed and/or computed thrust vectoring follows to establish the return trajectory.

No critical problems are foreseen concerning abort in the parking orbit phase. Therefore, little effort was expended in this area.

However, consideration has been given to the feasibility and practicability of returning the spacecraft immediately to earth during the entire injection phase. A study has been conducted to resolve questionable areas of performing a maneuver to attain such an immediate re-entry. This type of maneuver has been previously referred to as a "direct return to earth" or "single-pass return." The maneuver represents an emergency turnaround, taking place when the spacecraft is injected into the translunar orbit. The technique is to attain a maximum deflection of the spacecraft's velocity vector toward the earth. The resulting vector will be below the local horizontal plane and will be so aligned that the spacecraft will achieve acceptable re-entry conditions within a few minutes.

In order to assess the feasibility of providing for "immediate return," trades were established whereby propulsion variables and injection conditions can be evaluated. The propulsion variables that affect the performance of the maneuver are thrust levels, specific impulse (I_{sp}) and fuel quantities. The injection conditions consist of various altitudes, flight path angles and speeds. This study used a constant specific impulse of 420 sec and a constant injection speed of 36,100 fps.

The thrust application angle also is fixed at -100^{o} measured from the flight path direction.

One other important factor is the configuration of the re-entry vehicle which defines a re-entry corridor. For this purpose, a lift-to-drag ratio of 0.5. and a ballistic coefficient ($W/C_D A$) of 73 lb/ft^2 was assumed. The resulting re-entry corridor, representative of lifting configurations, is shown in terms of perigee attitude and velocity in Fig. II-41.

Listed below are the thrust levels, fuel quantities and burning times that were investigated.

Thrust (lb)	Fuel (lb)	ΔV (fps)	t_B (burning time)(sec)
30,000	1000	1280	14
	3000	3550	42
	5000	5450	70
	10000	9360	140
50,000	1000	1280	8.4

Thrust (lb)	Fuel (lb)	ΔV (fps)	t_B(burning time)(sec)
	3000	3550	25.2
	5000	5450	42
	10000	9360	84
80,000	1000	1280	5.2
	3000	3550	15.8
	5000	5450	26.3
	10000	9360	52.6

The weight of the spacecraft without fuel is 10,000 lb. The results of the study are presented in a manner that will allow quick evaluation of injection limitations. Figures II-42 to II-44 present a summary of the findings. Each figure shows a minimum injection altitude of 300,000 ft. Injecting into translunar orbit at a lower altitude than this will result in adverse heating and dynamic pressure conditions. For a given thrust level, ΔV (velocity impulse) capability and injection altitude, it can be determined whether or not the spacecraft can make an immediate return to the overshoot boundary. If the initial injection conditions are to the right of a constant ΔV curve, the re-entry vehicle will miss the corridor and will continue into orbit. Thus, an envelope is defined which describes the flexibility of injection conditions. The unbroken curves denote maximum performance since they represent reaching the overshoot boundary. The broken curves indicate reaching the corridor center, thereby reflecting a safety tolerance. The degradation of injection flexibility in providing this tolerance is easily seen. For a given injection angle the allowable altitude is reduced by 100,000 ft.

Figure II-45 shows the variation of the maximum allowable injection angle with thrust level for two values of maneuvering impulse. The injection altitude is 400,000 ft. The curves change slope considerably at a thrust level of approximately 100,000 lb. Beyond this, little gain in the allowable angle is realized. Therefore, from the performance standpoint, this thrust level will be considered optimum for the requirement of an immediate return. Powerplant studies have indicated that thrust levels of this magnitude result in a propulsion system 500 to 700 lb heavier than one having a thrust level of approximately 20,000 lb. Of course, the thrust level can be reduced to decrease this penalty, but in doing so another penalty comes to bear. This penalty arises from the necessity of shaping the trajectory to obtain a low burnout flight path angle. Figure II-46 shows these requirements as a function of thrust levels.

For lower thrust levels (approx. 25,000 lb), the burnout angles must be either negative or close to zero. To obtain these burnout conditions, the booster flight path must be "shaped" and, as can be seen from Fig. II-4, with a loss in velocity potential. This loss will result in a payload penalty of at least 550 lb for the lower thrust levels. For higher thrust levels (80,000 lb) the minimum payload penalty is 160 lb. These penalties are referenced to a (ΔV) capability of approximately 6000 fps. With lower (ΔV) potential, the penalties increase. Also from Fig. II-46, for every 100,000-ft increase in injection altitude, the allowable injection angle decreases by 1°. Furthermore, payload penalties increase rapidly as the thrust level is reduced below 25,000 lb.

If injection flexibility is one goal, indications are that for any reasonable flexibility at all, a velocity impulse of over 6000 fps is required, together with a thrust level of 80,000 lb. This adequately meets Cases I and II as shown in Figs. II-42 to II-44, but is insufficient to cope with Cases III and IV. With a lower thrust level of 30,000 lb, only Case I can be satisfied. For Case III impulses of 8000 fps and 10,000 fps for respective thrust levels of 80,000 lb and 30,000 lb are required.

* * *

In designing for an immediate return capability, it is concluded that a 600- to 800-lb payload penalty will be realized whether this capability is provided by trajectory shaping or by high thrust levels. For thrust levels lower than 20,000 lb, it becomes impractical and unfeasible to incorporate such capability. In addition, if such capability were provided at injection, it would exist for less than a minute, since flight path angle and altitude change very rapidly.

In absence of a direct return capability, it appears that the most applicable mission engine at this time would have a thrust level of approximately 15,000 lb. A study was made utilizing a Saturn boost trajectory (Case III) to ascertain what performance can be expected for a typical mission.

Thrust was applied opposite (retro) to the velocity vector in order to decrease the orbital energy. Return times were noted for given fuel loadings and injection speeds. Figure II-47 presents these findings together with the apogee altitudes attained. For a ΔV of 1800 fps (representative of the circumlunar mission) the return time is 16 hr and the maximum altitude reached is close to 30,000 naut mi if the abort was initiated at injection. For a ΔV of 5300 fps (representative of the lunar orbit mission) the return time is 3.6 hr and the peak altitude is 9000 naut mi. Naturally, the return times and apogee altitudes decrease as the initial abort velocity decreases.

Also noted in the figure is the area where an immediate return can be conducted with this engine. With a velocity impulse potential of 5300 fps, direct returns can be made at speeds up to 30,500 fps.

3. Abort Recovery Capability

Part of the operational concept concerns recovery locations from an abort maneuver during the ascent phase. Figure II-48 presents a summary of recovery locations and requirements that portray the capability of the Apollo spacecraft. Downrange recovery location is shown as a function of elapsed time from launch. The Atlantic Missile Range (AMR) is arbitrarily defined as extending 5000 naut mi downrange from Cape Canaveral. Ten thousand miles downrange the Pacific Missile Range (PMR) begins.

Figure II-48 denotes the recovery distance if an abort were initiated at various times during boost. This curve points out that recovery can be made on the AMR until well into third-stage burning (565 seconds after liftoff). This is over 70% of the total burning time of the C-2 launch vehicle. At this time recovery is made just short of the end of the AMR. Velocities at this point begin to approach satellite speeds, and recovery ranges increase very rapidly. Therefore, there is a short period (approximately 10 sec) when recovery cannot be made on the AMR or PMR. This is evident from the fact that, at 584 seconds after launch, the Saturn vehicle is at satellite speed.

If an abort should occur at 565 sec, the maximum velocity impulse (ΔV) required to reach either the PMR or Edwards AFB is 900 fps. Since the Apollo vehicle will be carrying a minimum of 1800 fps (ΔV) in the propulsion and equipment module, there is sufficient propulsion on board to recover either on the AMR, PMR or Edwards AFB at all times.

This minimum amount of fuel -- carried for circumlunar missions -- therefore affords a choice of landing areas. Figure II-48 notes a point where 1500 fps (ΔV) is required to achieve orbital conditions. Some allowance is made for de-orbit maneuvers later on. At this point -- 545 seconds after launch -- the crew has a choice of recovering on the AMR, PMR or Edwards AFB.

Also noted on the graph is the (ΔV) potential (5300 fps) of a lunar orbit mission where a greater amount of fuel is carried. This allows the choice to occur sooner, about 415 seconds after launch. In summary, the command module can be recovered either on the AMR, PMR or Edwards AFB. In addition, depending on the amount of fuel carried in the propulsion-equipment module, at some time during ascent there will be a choice as to which missile range may be selected as a recovery area.

III. LUNAR TRAJECTORY PHASE

The Apollo study has investigated a general lunar trajectory for circumlunar trajectories, lunar orbit characteristics for the general trans-lunar trajectories, return from lunar orbit trajectories and velocity requirements, and minimum midcourse guidance fuel requirements.

The study of the general lunar trajectory, using an N-body model, becomes very complex because of the number of variables involved and the lack of exact solutions to the equations of motion. The restricted three-body problem itself is complex enough that solutions for useful trajectories have not yet been found. Systematic studies using electronic computers could be made, but again the number of variables involved makes this a long, tedious and expensive job for even the simpler trajectories situated in the moon's orbital plane. Trajectories out of the moon's orbital plane are extremely difficult to obtain without some additional guide.

An effort was made during this study to find a guide which would enable a general picture of possible lunar trajectories to be developed and which would help in obtaining any specific circumlunar trajectory using an electronic computer.

A technique using a series of two-body models similar to the "sphere of influence" technique has been successfully developed. The technique does not use a "sphere of influence," but rather a "volume of influence," which is a somewhat distorted sphere. Correlation with restricted three-body trajectories obtained by integrating the equations of motion using a digital computer (hereinafter called "integrated trajectories") will be shown later in this chapter, as well as a technique for using the results of this correlation method to obtain any exact integrated trajectories shown possible with the "volume of influence" method. The equations used in the volume of influence analysis are presented in Appendix A.

A. GENERAL LUNAR TRAJECTORY ANALYSIS

1. Lunar Trajectory Injection Conditions

Figure III-1 presents a definition of the terms used in the following analysis. The general study was performed using a geocentric X_e axis along the intersection of the moon's orbital plane and the translunar orbital plane. The Z_e axis is normal to the moon's orbital plane; and the Y_e axis, in the right-hand axis system, lies in the moon's orbital plane. For trajectories entirely in the moon's orbital plane, the X_e axis lies along the major axis of the translunar orbit. The moon's orbital plane was used as a reference plane because of the symmetry of the results about this plane. Equations are presented in Appendix

A which interpret the results in terms of true latitude, longitude and inclination of the orbit to the equatorial plane for both the injection point for the translunar orbit and the return vacuum perigee point for the transearth orbit. In the general lunar trajectory study, the inclinations of the translunar, transearth and lunar orbital planes are referenced to the moon's orbital plane.

The initial study was made using an injection point altitude of 760, 000 ft and a flight path angle of 3° above the local horizontal, this matching the burnout conditions of the Saturn C-2 Case III trajectory in Ref. 1. The return vacuum perigee altitude in all cases is 150, 000 ft.

The conditions required to make circumlunar trajectories to various periselenium altitudes for various transearth orbital plane inclinations to the moon's orbital plane are presented in Figs. III-2 through III-14 for various translunar trajectory orbital plane inclinations. These curves define the booster requirements, vehicle and moon position at injection, possible variations in total orbit flight time, and transearth orbital plane inclination to the moon's orbital plane.

Figures III-2 and III-3 present the required injection velocity for various translunar orbital plane inclinations to the moon's orbital plane for any transearth orbital plane inclination from direct returns to retrograde returns for various periselenium altitudes. The data show returns from the north or south for all return inclinations, all for translunar trajectories leaving the earth towards the north. North and south, as used here, represent above and below the moon's orbital plane, respectively. Trajectories which return from the south are those which are moving from below the moon's orbital plane at transearth trajectory vacuum perigee to above the moon's orbital plane.

The first point of interest in these figures is that the return trajectory can approach vacuum perigee from any direction for any nonplanar translunar trajectory. This will allow the return of the spacecraft to any desired landing base from any desirable direction. Equally important, the transearth orbital plane inclination can be from either north or south at approximately the same inclination for a given translunar orbital plane inclination and flight direction with essentially the same injection velocity. This allows the translunar trajectory to leave earth through either the north or south hole in the Van Allen belt, for instance, and also return through either.

Other trends illustrated in Figs. III-2 and III-3 are the obvious increases in initial velocity required when the return trajectory shifts from direct return to retrograde return, and the decrease in required velocity as the periselenium altitude is increased. The required injection velocity also decreases as the translunar orbital plane inclination increases. These trends are shown later in this chapter to be accurate in magnitude and direction in comparison with integrated restricted three-body trajectory results.

The inclination of the translunar trajectory plane to the equatorial plane depends upon the day of the lunar month. Figure III-4 presents the relationship between the inclination of the translunar trajectory plane referenced to the moon's orbital plane and equatorial plane. The nature of the circumlunar trajectory makes Fig. III-4 almost correct for the transearth trajectory as well.

The position of the vehicle at injection is presented in Figs. III-5 through III-9 for various periselenium altitudes and translunar orbital plane inclinations. The position angle, ψ , is measured in the translunar orbital plane from the X_e axis in the moon's orbital plane, positive in the direction of flight. This angle plotted against V_0 yields curves which are characteristically closed loops that shrink in size as the translunar orbital plane inclination is increased. For any given translunar orbital plane inclination, the direction of the transearth orbital plane varies from direct, for the points on the lower left half of the curves, to retrograde for the points on the upper right part of the loop, as shown. The upper part of the closed loops represents conditions required for returning to earth from the south for northbound translunar trajectories, while the lower part represents trajectories returning from the north at vacuum perigee. As the periselenium altitude is increased, the loops expand in size and move toward the earth-moon plane.

The moon position at injection is presented in Figs. III-10 through III-12 for several periselenium altitudes and translunar trajectory plane inclinations. This lead angle is measured from the X_e axis opposite to the direction of the moon's motion. These data exhibit the same trends as the injection point data. They are characteristically closed loops for a constant translunar orbital plane inclination, which shrink in size as the inclination is increased. The points on the lower right portion of the loops represent direct returns, while those on the upper left portion represent retrograde returns. The upper portion of the curves represents trajectories approaching return vacuum perigee from the south, and the lower portion represents trajectories returning from the north. As the periselenium altitude is increased, these curves expand in size and shift towards higher lead angles.

The data presented in Figs. III-2 through III-14 completely define the required velocity at 760,000 ft and flight path angle of three degrees for a vehicle and moon position at the time of injection into translunar orbit. The time of flight from injection into translunar orbit to transearth orbit vacuum perigee for circumlunar missions for the various trajectories is shown in Figs. III-15 and III-18.

Figure III-15 presents the maximum and minimum flight times for direct returns and various translunar orbital plane inclinations as a function of periselenium altitude. It should be noted that the distinction between direct returns and retrograde returns in these data is a transearth orbital plane inclination of 90^o to the moon's orbital plane from either the north or south. However, the high inclinations may be either direct or retrograde relative to the

rotating earth depending upon the orientation of the moon's orbital plane to the earth equatorial plane. The data presented in Fig. III-15 are for returns from the south, but the data for returns from the north are nearly identical. The minimum flight times occur for planar orbits. Orbits which leave on any translunar orbital plane and return in the moon's orbital plane have close to minimum times. The maximum flight times for direct returns occur for transearth orbital plane inclinations of 90°, and the flight times increase as the translunar orbital plane inclination decreases. As can be seen, the variation in flight time to any given periselenium increases as the periselenium altitude increases, and varies from 1.2 hr at a periselenium altitude of 100 naut mi to 5.4 hr at 2000 naut mi. The margin of possible periselenium altitudes at constant flight time varies from 70 naut mi for a six-day trip to 475 naut mi for a seven-day trip. These factors play an important part in obtaining particular trajectories starting at a given launch point on earth and returning to a given landing base on earth for missions during various days of the lunar month. This will be discussed in more detail later in this section with regard to launch time tolerances.

Figures III-16 through III-18 present the total flight time at constant translunar orbital plane inclination to various periselenium altitudes corresponding to any transearth orbital plane inclination. The total time of flight data exhibits the same loop characteristics as the injection point and lead angle data. The size of these loops increases as the periselenium altitude increases, as do the previous data. But unlike the previous data, the size of the loops at constant periselenium altitude increases as the translunar orbital plane inclination increases.

2. Injection Into Lunar Orbit

The characteristics of the above trajectories at or near periselenium are of particular interest if a lunar orbit mission is to be made. The following analyses are based on the assumption that lunar orbit missions will be made only from circumlunar trajectories, which nominally return to earth ballistically to a vacuum perigee of 150,000 ft. This assumption is reasonable for safety in the event of an aborted mission when a lunar orbit is not attempted. It will be shown later in this section that midcourse guidance fuel requirements during the transearth orbit can become excessive quickly if there is much deviation from a nominal return trajectory.

The periselenium velocity for the various circumlunar trajectories is presented in Fig. III-19 as a function of periselenium altitude and translunar orbital plane inclinations. As expected, the periselenium velocity decreases as the periselenium altitude is increased, and increases as the translunar orbital plane inclination increases. As the return trajectory shifts from direct to retrograde, the periselenium velocity increases. The data are presented only for transearth trajectories returning from the south, but the corresponding trajectories from the north have periselenium velocities very nearly equal to those presented.

Figure III-20 presents the required velocity impulse to go into lunar orbit at periselenium altitude, plus the additional velocity increment required to perform an orbit transfer (Hohman type) to lower altitudes and go into circular lunar orbit at these altitudes. The figure presents a band of required velocity impulses for each condition, which is representative of that required for missions performed on various days of the lunar month (different translunar orbital plane inclinations). As the inclination of the translunar orbital plane is increased, the required velocity impulse increases. As expected, the required velocity impulse is minimized by flying directly to the desired lunar orbit altitude and injecting into lunar orbit without an orbit transfer.

The inclination of the lunar orbit to the moon's orbital plane will vary from zero to approximately 15° for the trajectories presented. Although higher inclinations up to polar are possible, the translunar orbits required to establish them either will not return to earth or will not return to suitable vacuum perigee along ballistic paths, and the velocity impulse required to go into lunar orbit increases. For these reasons, such trajectories are not considered feasible for early lunar exploration and should not be attempted until more experience is gained with the safer trajectories.

The orientation of the lunar orbits established with the presented trajectories, relative to the earth-moon geometry, fall broadly into two categories. The trajectories which leave earth towards the north and return to earth from the south result in lunar orbits which intersect the moon's orbital plane along a line roughly parallel with the line joining the earth-moon centers when injection into lunar orbit is performed at periselenium. The portion of the lunar orbit ahead of the moon (its path around the earth) will be above the moon's orbital plane. The opposite is true for translunar trajectories leaving earth towards the south and returning to earth from the north. Translunar trajectories leaving the earth towards the north and returning to earth from the north result in lunar orbits which intersect the moon's orbital plane along a line approximately perpendicular to the line joining the earth-moon centers when injection into lunar orbit is performed at periselenium. The orbit is above the moon's orbital plane between the earth and moon. These characteristics, illustrated in Fig. III-21, show the distinction between the trajectories leaving earth towards the north and returning to earth from either the north or south. Trajectories which return to earth from the south approach the moon from higher above the moon's orbital plane than those which return from the north and leave the moon lower below the moon's orbital plane. The actual trajectories around the moon, except for inclination, are very similar in all respects.

3. Ejection From Lunar Orbit

The required velocity impulse to leave a lunar orbit and return to earth is dependent upon lunar orbit altitude, inclination and orientation of the lunar orbit to the moon's orbital plane, time of return flight, length of time in orbit (number of orbits or days in orbit), and the point at which ejection from lunar orbit

is made. The following analysis of ejection requirements from lunar orbits at 50, 500, and 1000 naut mi considers only trajectories which return to earth with a vacuum perigee altitude of 150, 000 ft. The geometry and symbols used in the ejection from lunar orbit are presented in Fig. III-22. The intersection of the lunar orbit plane and the moon's orbital plane is measured from the line joining the earth-moon centers, and the angular distance between the two is referred to as the "earth lead angle" (ϕ_E). The position of the spacecraft at ejection is measured from the intersection line of the lunar orbital plane and moon's orbital plane in the direction of vehicle motion. It is referred to as the "spacecraft ejection position" (γ). These parameters, along with the inclination of the lunar orbit to the moon's orbital plane (iM) and the lunar orbit altitude, define the conditions at ejection from lunar orbit. The following analyses also assume a flight path angle relative to the moon of zero degree at ejection.

For each ejection condition, there are generally two velocity impulses (added to the circular orbit velocity) which will return the spacecraft to earth with a vacuum perigee of 150, 000 ft. The lower of the two represents a direct return and the higher a retrograde return. Velocity impulses between these two essentially result in earth impact, while velocity impulses lower than the smaller or greater than the larger result in vastly greater perigees. Only the lower velocity impulse (direct return) is presented here.

Of primary concern in this study was the determination of the required velocity impulse to return to a vacuum perigee of 150, 000 ft from any position on a circular lunar orbit (where such a return is possible) and the total return flight time. Figure III-23 presents the required velocity impulse for orbit ejection as a function of return flight time for various lunar orbit altitudes. The data are presented for two inclinations of the lunar orbit plane (iM). The minimum required velocity impulse occurs for lunar orbits in the moon's orbital plane for any given return flight time. The data are also presented for several earth lead angles. For each lunar orbit altitude, there is a specific point which will give a minimum required velocity impulse (Fig. III-24).

The above data show that the required velocity impulse to return in a given flight time decreases as the lunar orbit altitude increases and as the inclination of the lunar orbit decreases. As the return flight time decreases, the required velocity impulse is substantially increased. This is shown graphically in Fig. III-25, where $(\partial \Delta V / \partial t_R)$ is shown as a function of return time (t_R). When the lunar orbit does not lie in the moon's orbital plane, the required velocity impulse to return at a given time decreases as the earth lead angle (ϕ_E) increases from zero to 90°. At this point, the minimum required velocity impulse approaches to within 1 fps of the coplanar minimum velocity impulse. It is interesting to note that, regardless of the inclination of the lunar orbit and the earth lead angle, the position of the ejection point for a minimum velocity impulse lies ahead of the moon $132 \pm 5^{\circ}$ from the line joining the earth-moon centers. The minimum velocity for ejection at this point

approaches the absolute minimum velocity impulse (coplanar orbit) as the earth lead angle approaches 90°.

Figure III-26 presents the time to return as a function of spacecraft position at ejection from a circular lunar orbit. Lines of constant orbit altitude are shown and occur in clusters of constant earth lead angle. The return time for the minimum velocity impulse, also presented in this figure, is between four and one-half and five days. It can be seen that the time to return for a given lunar orbit and earth lead angle is decreased by advancing the ejection point, τ, around the moon (with an accompanying increased velocity impulse as shown in Fig. III-23), and by reducing the lunar orbit inclination angle and lunar orbit altitude for a fixed spacecraft ejection point.

Figure III-27 presents the variation of required velocity impulse with ejection point position for various lunar orbit inclinations and earth lead angles. This figure illustrates the rapid increase in required velocity impulse as the ejection point deviates from optimum.

The relationships among the results presented above and the actual return from a lunar orbit are dependent upon the translunar trajectory and the time in orbit. If a translunar trajectory is used leaving the earth towards the north and which normally would return from the south, the earth lead angle would generally be close to zero degrees. If the spacecraft were held in orbit approximately seven days, the earth lead angle would approach 90° since the orientation of the lunar orbit relative to inertial space is relatively fixed over this time. Thus, the minimum required velocity impulse would be decreased. On the other hand, the use of a translunar trajectory leaving the earth towards the north which normally returns from the north results in an earth lead angle of approximately 90°. For this case, the opposite trend in required velocity impulse would occur. Two typical trajectories showing these variations are presented in Figs. III-28 and III-29.

The results presented above assume that the moon oblateness and earth presence will not affect the lunar orbit over a period of time. A study has been made to determine the effects of the tri-axiality of the moon's mass and the presence of the earth on the lunar orbit. This study, presented in Appendix B, has resulted in Fig. III-30, which presents the precession rate of near-circular lunar orbits as a function of orbit altitude and inclination of the moon's orbital plane. As can be seen, this precession rate is not small enough to be neglected, particularly for the low altitude orbits being considered. But it is not high enough to seriously affect the conclusions drawn in the preceding analyses.

4. Launch Time Tolerance

A launch time tolerance can be obtained in several ways. Most launches require a change in heading during boost to parking orbit or an orbital plane inclination change either while in parking orbit or during the acceleration to

injection. The ascent trajectory can also be modified, along with a lateral direction change, to obtain a launch time tolerance. All these techniques require a significant surplus in booster capability, and the launch time tolerance obtained is measured in one to four minutes. Another technique which can be used to advantage is to modify the translunar trajectory. This technique can give large launch time tolerances, measured in hours, with no significant difference in booster requirements.

The problem of using a variable translunar trajectory to obtain a launch time tolerance reduces itself primarily to the task of determining the right place over the surface of the earth and getting to it at the right time while traveling in the right direction. If the direction is in error at vehicle speeds between circular satellite velocity and parabolic velocity, corrections of any amount require considerable propellant. The following analysis assumes an inflight turn is not required.

Arrival at a given location over the earth for injection from a single launch point (Cape Canaveral used here) is possible, within reason, by modifying the launch azimuth from the launch point. The time of day during which the launch must be made is fixed by the moon position. However, there is a leeway of one to four hours about this nominal time, during which the vehicle possesses the capability of getting to a required injection point, which also varies from the nominal. As will be shown next, the available launch time tolerance depends upon the moon's position with respect to the earth.

The variation in the translunar trajectory with time is primarily a variation of the inclination of the translunar orbital plane to the equatorial plane, as well as a variation in the required injection point. As the launching is delayed, this inclination must be increased, and this in turn implies an increase in launch azimuth (measured from true north). The variation in translunar orbital plane inclination also means a variation in total time of flight for a given periselenium altitude. Thus, if the transearth trajectory must terminate at a given return base along a given inclination to the equatorial plane, the periselenium altitude will also vary over a few miles during the launch time tolerance.

The general lunar trajectory study has been used to determine the launch time tolerance as a function of day of the lunar month for a particular set of trajectories. The restrictions placed on the trajectory were a given launch point, Cape Canaveral, a given return base, Edwards Air Force Base, and an inclination of the transearth orbital plane to the equatorial plane of 35°. Also, the injection point is restricted to lie in the Pacific Missile Range (PMR). Further, the maximum allowable launch azimuth was set at 110° in compliance with range safety requirements. The minimum launch azimuth is restricted by the re-entry vehicle's lateral maneuverability and its ability to reach Edwards AFB from lower inclination parking orbits in the event of an aborted flight prior to injection into the translunar trajectory. With these restrictions, as well as the no-inflight-turn restriction, the available launch time tolerance as a function of day of the lunar month is shown in Fig. III-31. As can be seen,

the available launch time tolerance varies from approximately 0. 17 hr, with the moon at its most northerly declination, to approximately 3. 40 hr with the moon at its most southerly declination. If the restriction of injecting over the PMR is removed, and if the injection point is moved to the Atlantic Missile Range (AMR), thus having a parking orbit of approximately 1. 2 orbits, the curve shown in Fig. III-31 can be shifted 14 days, resulting in a launch time tolerance of 3. 40 hr for the moon at the most northerly declination, and 0. 17 hr with the moon at the most southerly declination. In this fashion, the total launch time tolerance would vary from 1. 95 hr to 3. 40 hr for launchings during the lunar month. In the above calculations, the moon's orbital plane was inclined to the equatorial plane 28. 5°, consistent with the summer of 1968 period.

The choice of operational concept, detailed in Chapter V of this report and outlined above, allows a relatively large launch time tolerance. The restrictions of parking orbit inclinations between 29. 0° and 34. 2°, which allow good ground tracking of the vehicle, lend themselves nicely to the launch time tolerance with "out-of-the-plane" lunar trajectories. The variation of launch time tolerance with translunar orbital plane inclination change is greatest when the initial inclination is equal to the inclination of the moon's orbital plane. Thus, trajectory plane inclination variations in the neighborhood of 28. 5° are more desirable than similar variations about some higher nominal inclination. These trends also fit in nicely with the radiation hazard of the Van Allen belts. The operational concept restricts the translunar orbital plane inclination to the equatorial plane to between 29° and 34. 2°. The upper limit is a range safety limit, but steeper inclinations do not increase the launch time tolerance very much. The minimum inclination of the translunar plane is restricted by lateral maneuverability, but the lower the inclination, the deeper the translunar trajectory passes through the edge of the Van Allen belt. Thus, the lower limit is also restricted by Van Allen belt penetration as well as lateral maneuverability to a given return base from parking orbit.

The total available launch time tolerance, varying with the day of the lunar month during which the spacecraft reaches periselenium, is made up primarily of the tolerance obtained from translunar trajectory modification. Other techniques, mentioned previously, can be used to give additional minutes if there is a surplus in vehicle performance.

It should be pointed out that the available launch time tolerance presented above is concerned only with the tolerance in leaving the launch pad about some nominal, pre-established launch time. Another interesting possibility is to put the spacecraft into a parking orbit in the moon's orbital plane with the capability to leave this parking orbit once about every 90 min. In this manner, the spacecraft plus injection booster could be placed into this parking orbit roughly once each day by firing due east from Cape Canaveral (latitude 28. 525°) during the summer of 1968 period when the moon's orbital plane is inclined approximately 28. 5° to the equatorial plane. The translunar flight would be in the moon's orbital plane. Although this technique seems quite flexible, it has some drawbacks. If the vehicle is to stay in parking orbit for

CONFIDENTIAL

more than a few orbits, the parking orbit altitude must be increased to minimize the effects of the upper atmosphere. This will reduce the effective booster performance. More important, the attaining of the parking orbit with the desired inclination again means a liftoff from the launch pad at some precise time if the parking orbit is to lie in the moon's orbital plane. In this instance, a launch time tolerance about the nominal time can be obtained only by ascent trajectory shaping and in-flight lateral turns at near orbital speeds. Again, the launch time tolerance available using these tools is measured in very few minutes for a surplus velocity impulse (and therefore propellant weight) on the order of 1000 fps.

5. Correlation Studies

The predominant portion of the studies presented in this section thus far were based on the "volume of influence" technique mentioned at the beginning of this section and detailed in Appendix A. These results and conclusions have been substantiated with integrated trajectories using a restricted three-body model. Four widely separated trajectories are shown here to illustrate the correlation, and additional trajectories which correspond to operational concept trajectories for four widely separated days of the lunar month are shown in Chapter V. These eight trajectories substantiate the analysis technique and emphasize the significance of its use to closely approximate any desired integrated trajectory.

The four trajectories are presented here to substantiate the analysis technique and to verify the trends (magnitude and direction) that the "volume of influence" technique predicts. These trajectories have a constant periselenium altitude of 1000 naut mi. Two of the trajectories have a translunar orbital plane inclination of 30^{o} to the moon's orbital plane toward the north and the other two an inclination of 15^{o}. These four trajectories verify the trend of the variation in required injection velocity with transearth orbital plane inclination. They also verify the fact that a given translunar trajectory can be made to return to earth from either the north or south with the same inclination and essentially the same initial velocity. The two trajectories which return to earth with transearth orbital plane inclinations of approximately zero degrees verify the trend of reduced injection velocity requirement as the translunar orbital plane inclination angle is increased. Tables 1 through 4 compare the "volume of influence" (VOICE) results with integrated trajectory results for these four trajectories. Comparisons of injection conditions, conditions at the moon, and return to earth conditions are shown.

The data shown on these tables reflect the improvement in the comparison from the initial iteration through the second or third iteration. The technique used to obtain these iterations is presented in Appendix C. The trajectories have not been modified to complete correlation, but from the data presented it is obvious that this is possible with one or two more iterations.

CONFIDENTIAL

TABLE 1

Comparison of VOICE Trajectory with Integrated Trajectory

	Item	Integrated Trajectory			
		VOICE	1st	2nd	3rd
At Injection into Trans-lunar Orbit	Altitude (ft)	760, 000	760, 000	760, 000	760, 000
	Velocity	35779. 185	35779. 585	35775. 483	35775. 319
	Flight path angle (deg)	3. 0	3. 0	3. 0	3. 0
	Inclination to moon's orbital plane (deg)	30.	30.	30.	30.
	Injection position (ψ) (deg)	12. 368	12. 368	12. 118	12. 102
	Moon lead angle (ϕ) (deg)	43. 9791	43. 9791	44. 7666	44. 8061
At Moon	Periselenium altitude (naut mi)	1000.	788. 1	969.	993.
At Transearth	Altitude (ft)	150, 000	404, 550	144, 450	145, 000
Orbit Vacuum	Total flight time (hr)	154. 51	150. 95	154. 36	154. 55
Perigee	Inclination to moon's orbital plane (deg)	11. 23	11. 51	12. 82	11. 89
	Direction of return	Direct from north			

TABLE 2

Comparison of VOICE Trajectory with Integrated Trajectory

Item		Integrated Trajectory			
		VOICE	1st	2nd	3rd
	Altitude (ft)	760, 000	760, 000	760, 000	760, 000
At Injection	Velocity	35779. 348	35779. 748	35775. 609	35774. 117
into Trans-	Flight path angle (deg)	3. 0	3. 0	3. 0	3. 0
lunar Orbit	Inclination to moon's orbital plane (deg)	30.	30.	30.	30.
	Injection position (ψ) (deg)	12. 259	12. 259	11. 999	11. 940
	Moon lead angle (ϕ) (deg)	44. 0596	44. 0596	44. 8551	45. 0258
At Moon	Periselenium altitude (naut mi)	1000.	789. 56	964.	999. 7
At Transearth	Altitude (ft)	150, 000	413, 000	145, 220	151, 200
Orbit Vacuum	Total flight time (hr)	154. 31	151. 36	154. 02	154. 30
Perigee	Inclination to moon's orbital plane (deg)	7. 92	8. 35	6. 62	6. 96
	Direction of return	Direct from south			

TABLE 3

Comparison of VOICE Trajectory with Integrated Trajectory

Item		VOICE	Integrated Trajectory 1st	2nd	3rd
	Altitude (ft)	760, 000	760, 000	760, 000	
At Injection	Velocity	35782. 081	35782. 481	35778. 070	
into Trans-	Flight path angle (deg)	3. 0	3. 0	3. 0	
lunar Orbit	Inclination to moon's orbital plane (deg)	15.	15.	15.	
	Injection position (ψ) (deg)	12. 3816	12. 3816	12. 0980	
	Moon lead angle (ϕ) (deg)	43. 6860	43. 6860	44. 5160	
At Moon	Periselenium altitude (naut mi)	1000.	788. 06	986. 3	
At Transearth	Altitude (ft)	150, 000	404, 550	134, 300	
Orbit Vacuum	Total flight time (hr)	154. 20	151. 56	154. 186	
Perigee	Inclination to moon's orbital plane (deg)	7. 83	11. 51	8. 03	
	Direction of return	Direct from south			

TABLE 4

Comparison of VOICE Trajectory with Integrated Trajectory

Item		Integrated Trajectory			
		VOICE	1st	2nd	3rd
	Altitude (ft)	760, 000	760, 000	760, 000	
At Injection	Velocity	35809. 116	35809. 666	35807. 322	
into Trans-	Flight path angle (deg)	3. 0	3. 0	3. 0	
lunar Orbit	Inclination to moon's orbital plane (deg)	15.	15.	15.	
	Injection position (ψ) (deg)	14. 572	14. 572	14. 499	
	Moon lead angle (ϕ) (deg)	39. 5159	39. 5159	39. 8203	
At Moon	Periselenium altitude (naut mi)	1000.	795. 15	984. 7	
At Transearth	Altitude (ft)	150, 000	2, 158, 000	121, 000	
Orbit Vacuum	Total flight time (hr)	157. 22	154. 51	157. 87	
Perigee	Inclination to moon's orbital plane (deg)	88. 53	84. 38	87. 79	
	Direction of return	Direct from north			

B. TRANSLUNAR MIDCOURSE GUIDANCE FUEL REQUIREMENTS

The minimum midcourse guidance fuel requirements during the translunar trajectory were determined for two trajectories. One is typical of the operational concept trajectories. The other is a trajectory in the moon's orbital plane. The studies were made using a digital computer program employing a restricted three-body model. All trajectories are integrated trajectories.

The perturbing effects for which the midcourse guidance fuel requirements are determined consist of velocity errors at injection due to guidance system accuracy. The errors used are felt to be larger than those expected by a factor of at least two. The one-sigma errors used are:

$$\sigma_x = 5.3 \quad fps$$

$$\sigma_y = 12.3 \quad fps.$$

$$\sigma_z = 14.1 \quad fps.$$

(1) Where the X-direction is in the direction of flight and parallel to the local horizontal,

(2) The Y-axis is perpendicular to the plane of flight in a right-handed sense, and

(3) The Z-axis is parallel to the local vertical.

These errors were combined in such a manner as to give a three-dimensional 99% probability (3.368σ) in arbitrary directions relative to the nominal velocity vector. Since the one-sigma values are not the same, the total velocity vector error is not a constant, but depends upon its orientation and varies from 30 fps to 45 fps.

The study was performed by first obtaining the position coordinates of the nominal trajectory as a function of time. The same data was obtained for a trajectory perturbed at injection by the above amounts. A correction point on the perturbed trajectory was chosen and the correction trajectory from that point to a point on the nominal trajectory was determined. The correction trajectory was such that it returned to the proper position on the nominal trajectory at the correct time. At this point, a second velocity correction was made to align the correction trajectory along the nominal trajectory. This is illustrated on the sketch below, where ΔV_p is the initial (position) velocity impulse and ΔV_v (velocity) is the final velocity impulse.

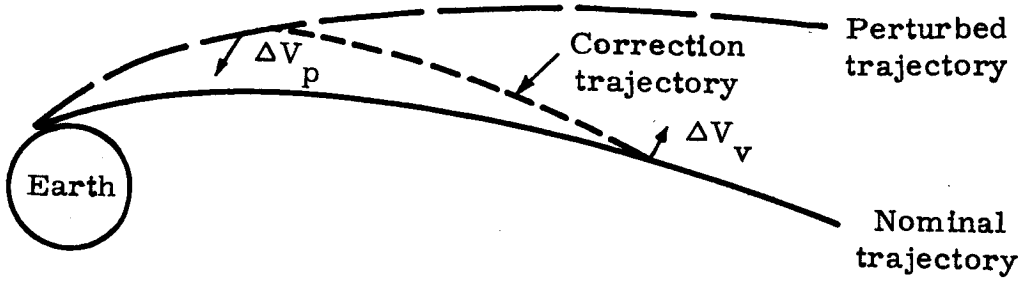

The point on the nominal trajectory where the correction trajectory reaches it was varied from fast corrections (within five hours) to long correction times (80 hr). The above procedure was repeated for several initial correction points on the perturbed trajectory.

The correction trajectory was obtained by determining the sensitivities of the nominal trajectory at various times during the translunar orbit and assuming that they were reasonably linear for small velocity corrections. Typical sensitivities are presented in Tables 5 through 7 for initial correction times of three hours, 12 hours, and 35 hours after injection. The X-axis for these sensitivities lies in the moon's orbital plane along the intersection of the translunar orbital plane at injection and the moon's orbital plane. The Y-axis is perpendicular to X-axis and also in the moon's orbital plane. The Z-axis is perpendicular to the moon's orbital plane in a right-hand sense. The validity of the linearity assumption was demonstrated by inserting the calculated correction velocity, ΔV_p , and applying it to the perturbed trajectory at the initial correction time. The results are shown in Fig. III-44 where the distance between the nominal trajectory and correction trajectory is shown as a function of time.

As might be expected, the sooner the first correction is made, the less it costs to make the correction. This can be seen in Figs. III-32 through III-34, where initial corrections were made three hours and five hours after injection into the translunar orbit. These figures present the initial velocity correction required (ΔV_p) to correct the position to the nominal trajectory, the second velocity correction (ΔV_v) to align the correction trajectory along the nominal trajectory (both direction and velocity), and the total velocity correction required which is the sum of ΔV_p and ΔV_v magnitudes. These data are shown plotted against the time (position) on the nominal trajectory at which the correction is completed. Similar data are presented in Figs. III-35 through III-43 for corrections initiated three hours after injection and completed at times between 10 hours and 85 hours. These data are for several combinations of initial velocity errors at injection, but all represent 99% probability (3.368σ) conditions.

TABLE 5

Midcourse Correction Sensitivities ($t_{initiation}$ = 3 hr)

Sensitivity Coefficient	t match	10	50	66.98	79.48	82	83	84	85
$\partial X/\partial \dot{x}$	(hr)	7.8	86.0	133.8	168.4	167.8	163.4	158.0	165.2
$\partial Y/\partial \dot{X}$		-0.56	-16.8	-27.0	-42.0	-47.2	-46.6	-38.2	-16.4
$\partial Z/\partial \dot{x}$		-0.10	-2.58	-3.84	-4.0	-3.32	-3.2	-4.36	-9.56
$\partial X/\partial \dot{Y}$		-0.60	-20	-33.6	-45.0	-5.2	-42.8	-36.0	-23.8
$\partial Y/\partial \dot{y}$		6.84	37.6	48.8	63.0	71.2	76.6	82.8	84.0
$\partial z/\partial \dot{y}$		0.06	1.02	1.42	0.96	-0.08	-1.06	-2.82	-4.86
$\partial X/\partial \dot{Z}$		-0.10	-3.2	-5.2	-6.8	-6.6	-6.8	-7.2	-9.6
$\partial Y/\partial \dot{Z}$		0.06	1.0	1.4	1.8	1.4	-0.8	-0.6	-3.6
$\partial z/\partial \dot{z}$		6.3	31.02	37.86	39.8	38.18	36.5	33.38	27.8
$\partial \dot{X}/\partial \dot{x}$		1.24	2.58	3.02	1.34	-2.82	-5.58	-2.66	20.38
$\partial \dot{Y}/\partial \dot{x}$		-0.18	-0.52	-0.74	-2.15	-1.18	3.18	15.2	25.4
$\partial \dot{z}/\partial \dot{x}$		-0.03	-0.076	-0.064	0.16	0.26	-0.22	-2.62	-8.04
$\partial \dot{X}/\partial \dot{y}$		-0.16	-0.70	-0.90	-0.66	1.18	4.06	10.06	12.16
$\partial \dot{Y}/\partial \dot{y}$		0.94	0.66	0.72	2.304	4.70	6.16	5.2	3.94
$\partial \dot{z}/\partial \dot{y}$		0.014	0.028	0.014	-0.212	-0.74	-1.34	-2.12	-1.54
$\partial \dot{X}/\partial \dot{z}$		-0.04	-0.10	-0.14	-0.06	+0.04	-0.60	-1.02	-4.18
$\partial \dot{Y}/\partial \dot{z}$		+0.02	+0.02	+0.02	-0.03	-0.38	-0.98	-2.32	-3.08
$\partial \dot{z}/\partial \dot{z}$		+0.848	0.456	0.322	-0.268	-1.24	-2.26	-4.18	-6.92

TABLE 6

Midcourse Correction Sensitivities ($t_{initiation}$ = 12 hr)

Sensitivity Coefficient	t_{match}	10	50	66.98	79.48	82	83	84	85
$\partial X/\partial x$	(hr)	-	46.8	74.8	94.6	94.4	92.4	90.2	96.6
$\partial Y/\partial \dot{x}$		-	-3.8	-6.2	-12.0	-13.4	-12.2	-6.0	+8.0
$\partial Z/\partial \dot{x}$		-	-0.38	-0.78	-0.8	-0.68	-0.84	-1.96	-5.86
$\partial X/\partial \dot{y}$		-	-2.8	-6.2	-10.4	-10.4	-8.6	-2.6	12.2
$\partial Y/\partial \dot{y}$		-	34.4	45.8	62.4	71.0	77.2	86.0	93.0
$\partial Z/\partial \dot{y}$		-	0	0.52	-0.48	-1.48	-2.54	-4.66	-8.14
$\partial X/\partial \dot{z}$		-	-0.40	-0.80	-1.0	-1.0	-1.4	-2.4	-5.2
$\partial Y/\partial \dot{z}$		-	0	0	-0.4	-1.2	-2.0	-3.8	-6.4
$\partial Z/z$		-	33.62	45.38	50.44	44.92	46.98	43.14	35.92
$\partial \dot{X}/\partial \dot{x}$		-	1.52	1.74	0.8	-1.36	-2.62	-0.12	15.08
$\partial \dot{Y}/\partial \dot{x}$		-	-0.16	-0.28	-0.814	-0.12	2.92	10.2	15.68
$\partial \dot{Z}/\partial \dot{x}$		-	-0.02	-0.02	0.046	-0.02	-0.44	-2.14	-5.76
$\partial \dot{X}/\partial \dot{y}$		-	-0.16	-0.26	-0.36	+0.78	3.24	10.06	18.4
$\partial \dot{Y}/\partial \dot{y}$		-	0.80	0.82	2.275	5.08	7.54	9.34	2.96
$\partial \dot{Z}/\partial \dot{y}$		-	0.004	-0.006	-0.202	-0.74	-1.48	-2.86	-3.78
$\partial \dot{X}/\partial \dot{z}$		-	-0.02	-0.06	0	-0.08	-0.40	-1.66	-4.52
$\partial \dot{Y}/\partial \dot{z}$		-	0	0	-0.162	-0.64	-1.26	-2.36	-2.62
$\partial \dot{Z}/\partial \dot{z}$		-	0.756	0.602	-0.120	-1.34	-2.68	-5.28	-9.28

TABLE 7

Midcourse Correction Sensitivities ($t_{initiation}$ = 35 hr)

Sensitivity Coefficient	t_{match}	50	66.98	79.48	82	83	84	85
$\partial X/\partial \dot{X}$	(hr)	15.2	33.8	47.0	47.6	46.8	46.2	50.8
$\partial Y/\partial \dot{X}$		-0.20	-0.60	-2.4	-2.6	-1.6	+4.2	+10.0
$\partial Z/\partial \dot{X}$		-0.02	+0.60	0	0	-0.16	-0.88	-3.24
$\partial X/\partial \dot{Y}$		0	-0.6	-2.2	-2.0	-0.8	+4.0	+16.00
$\partial Y/\partial \dot{Y}$		14.8	31.4	48.6	54.0	59.2	66.8	73.4
$\partial Z/\partial \dot{Y}$		0	-0.02	-0.44	-1.22	-2.02	-3.74	-6.7
$\partial X/\partial \dot{Z}$		0	0	0	0	-0.40	-1.0	-3.60
$\partial Y/\partial \dot{Z}$		0	-0.2	-0.4	-1.0	-1.8	-3.2	-5.2
$\partial Z/\partial \dot{Z}$		14.82	30.86	40.0	39.9	38.76	36.06	17.16
$\partial \dot{X}/\partial \dot{X}$		1.04	1.12	0.65	-0.36	-0.92	0.72	9.42
$\partial \dot{Y}/\partial \dot{X}$		-0.02	-0.06	-0.254	+0.36	+1.9	+5.86	+8.50
$\partial \dot{Z}/\partial \dot{X}$		0	-0.002	-0.014	-0.060	-0.34	-1.32	-3.42
$\partial \dot{X}/\partial \dot{Y}$		0	-0.06	-0.180	0.58	2.44	7.92	14.52
$\partial \dot{Y}/\partial \dot{Y}$		0.98	0.98	2.04	4.26	6.34	8.14	3.46
$\partial \dot{Z}/\partial \dot{Y}$		0	0	-0.148	-0.58	-1.18	-2.36	-3.32
$\partial \dot{X}/\partial \dot{Z}$		0	0	0	-0.08	-0.36	-1.4	-3.66
$\partial \dot{Y}/\partial \dot{Z}$		0	0	-0.118	-0.52	-1.02	-1.88	-2.04
$\partial \dot{Z}/\partial \dot{Z}$		0.974	0.882	0.32	-0.66	-1.74	-3.90	-7.30

The data presented all show a similar trend. The initial correction is the bigger one and increases as the initial correction time is delayed. The magnitude of the initial correction velocity decreases as the final correction point moves closer to the moon. The second velocity correction (ΔV_v) decreases as the final correction point moves toward the moon and then characteristically increases rapidly as the moon begins accelerating the vehicle. The total velocity correction required shows a definite region of desirable final correction point that lies between 50 and 70 hours for the data shown.

The ideal correction technique is one in which the first correction is made as soon as possible and is designed to return to the nominal trajectory at approximately 180, 000 naut mi from earth and 45, 000 naut mi from the moon. This is the combination for which the minimum midcourse guidance fuel requirements exist. The data presented use three hours after injection into the translunar orbit (approximately 30, 000 naut mi from earth) as the initial correction point. This is felt to be the minimum time for enough onboard tracking data to be accumulated to allow reasonable curve fits of position and velocity (using Keplerian equations) to determine the initial correction. A more detailed explanation of determining present position can be found in Ref. 4.

Further studies have been made in which only a partial correction was made at three hours after injection, followed by second and third corrections at 10 hours and 25 hours, all attempting to return the vehicle to the nominal trajectory at 50 hours after injection. The trend of increasing correction velocity with delayed initial correction time is also apparent when only a partial correction is made initially with several additional corrections applied later. The total velocity requirements using this technique increased by a factor of four to six. This points to the necessity of not only making the initial correction as soon as possible, but making it as good as possible. If second or third corrections are required between the initial correction and final correction, they characteristically become large quite rapidly.

The concept of making an initial correction only (nominally) to adjust the periselenium altitude, instead of returning to the nominal translunar trajectory, has many implications, but most of these are quite adverse. This will be discussed later in this section after the transearth midcourse guidance fuel requirements are presented.

The fuel requirements presented herein are for velocity impulses which are assumed perfectly made. The main purpose of defining the minimum fuel requirements is to provide a yardstick by which to measure various guidance systems as they are programmed into the problem. The trends exhibited are accurate and can be used to aid in determining guidance system requirements.

A guidance technique proposed for the lunar trajectory makes use of Keplerian two-body equations to supply the midcourse guidance corrections (Ref. 4). This technique has been partially examined with regard to the increase in fuel requirements.

The use of two-body equations in themselves is not sufficient to obtain a satisfactory initial correction. This is illustrated on Fig. III-44, where a first and second correction were made at three hours and eight hours, respectively. The additional corrections required, even after the second correction, are very large, and increasing in magnitude rapidly with time. The Keplerian trajectories were determined by fitting a Kepler orbit through both the initial point and the desired point at 50 hr after injection into the translunar orbit with the time being fixed to arrive at the aim point at 50 hr. The inadequacy of this simple approach is obvious.

A technique for biasing the aim point has been developed in Ref. 4. This technique is quite simple in itself, but its use gives dramatic results. A single correction at three hours after injection into translunar orbit returns the vehicle to within 35 naut mi of the aim point at 50 hr, and a relatively small second and third corrections could eliminate this error. The difference in the total Keplerian correction at three hours and the perfect three-body correction is only approximately 0.2 fps in magnitude, with errors in the various velocity components varying from 0.7 to 2.1 fps. This accuracy is not too much different from the ability of the guidance system to measure the velocity impulse supplied by rocket motors.

The simplicity of the overall guidance system using this technique and the flexibility which comes from the simplicity are coupled with satisfactory trajectory results. Continued study of the technique and the resulting midcourse guidance fuel requirements is certainly in order.

C. TRANSEARTH MIDCOURSE GUIDANCE FUEL REQUIREMENTS

The transearth midcourse guidance fuel requirements are divided into two parts. The first is concerned with circumlunar flights and the second is concerned with leaving lunar orbit.

The major perturbing effects used to determine the velocity impulse (or fuel) required for transearth guidance corrections for circumlunar flights come from two sources. The first perturbing effect is the assumption of incomplete translunar trajectory guidance corrections. It is assumed that the final correction velocity (ΔV_v) is not made, and the vehicle is allowed to continue its orbit around the moon on the translunar correction orbit with no additional corrections. The transearth midcourse correction is made at 105 hr after injection (57,400 naut mi beyond the moon) and also at 115 hr after injection (77,300 naut mi beyond the moon). The corrections are designed to result in returning to the nominal trajectory at various times from 120 hr after injection for the correction at 105 hr, and 135 hr after injection for the correction at 115 hr, to perigee. The correction velocity requirements are shown in Figs. III-45 through III-47 for three different translunar perturbed trajectories.

The second major perturbing effect considered is variations in the mass of the earth and moon. It is assumed that the mass of the earth is known within 0.0022%. The nominal ratio of earth mass to moon mass used in these studies is 81.45. Measurements made by several astronomers over a long period of time are usually claimed to be accurate within $\pm$0.05 or less, but the several measurements vary between approximately 81.15 and 81.75. The values of the earth mass to moon mass ratio used in these studies are 81.15, 81.30, 81.45 (nominal), 81.60 and 81.75. This range of mass uncertainty is considered to be far in excess of expected uncertainties at the time the first manned circumlunar mission is made.

The required correction velocities for three typical cases are shown in Figs. III-45 through III-47. These correction velocities include the lack of final translunar correction, and the variation of the mass of the moon in the more adverse direction. As above, the corrections are initiated at either 105 hr or 115 hr after injection, and the correction velocity is presented for return to the nominal trajectory at the correct time and place for several positions along the return trajectory. The correction velocity shown includes both the initial position velocity correction (at 105 hr or 115 hr) and the final velocity correction at the return to the nominal trajectory point.

These illustrations show the expected trends of reduced correction velocity required for corrections made as early as possible and reduction of total correction velocity as the final correction point approaches perigee. The initial correction times used in this study insured that the vehicle position at correction is sufficiently beyond the effect of the moon's gravity field to allow reasonable tracking of position and velocity without major moon effects. The variations of required correction with initial correction time again point to the necessity of obtaining good position and velocity tracking as soon as possible after entering a region where reasonably accurate return midcourse guidance corrections can be computed.

The magnitude of the required corrections, although felt to be quite conservative, indicates the need of controlling the translunar trajectory as closely as possible. The lack of a two-foot per second correction during the translunar trajectory at 50 hr after injection becomes a required 60 fps correction (at 105 hr) on the transearth trajectory. The sensitivity of transearth vacuum perigee to variations in periselenium altitude varies over a wide range, but a factor of ten is not unreasonable. Not only does the return vacuum perigee vary, but the inclination of the return orbit and the time of return orbit also vary, making the task of returning to a prescribed point on earth even more difficult. Therefore, the need for close, accurate control on the translunar trajectory is a necessity if the transearth midcourse guidance correction velocities are not to increase to very large magnitudes. Suggested translunar techniques of making one correction (at three hours, for example) which corrects only the periselenium are not satisfactory for the same reasons. Unless this correction is made to reach the correct periselenium altitude at the right time and place relative to the earth-moon geometry, the distortion in the transearth trajectory is enough to

require very large transearth midcourse guidance corrections, particularly if the return trajectory is to terminate at a given point on earth.

It should also be noted that major midcourse guidance shaping corrections to the general lunar trajectory are purposely avoided near the moon (within 56, 000 naut mi). The only corrections made within the moon's influence on circumlunar missions are the final corrections to insure the proper periselenium altitude. To attempt to make primary trajectory corrections in a region where the dynamics of the trajectory are significantly affected by both the earth and moon is an unnecessary complication. To make corrections near the moon to modify the transearth trajectory, other than those necessary to remain on a preselected trajectory, can result in very large transearth midcourse guidance corrections; the drawbacks associated with such corrections do not warrant their use.

The transearth midcourse guidance fuel requirements after leaving a lunar orbit have also been studied. The major perturbing effect is the guidance system uncertainty in burnout velocity. Although the position at burnout is also important, the intrinsic nature of a guidance concept which continuously tries to place the actual spacecraft within a phantom spacecraft on the nominal trajectory tends to reduce the position errors to very small amounts (See Ref. 4). The one-sigma velocity uncertainties used in this study are one foot per second in all three directions. The studies were made using the three-dimensional 99% probability (3. 368σ) velocity errors in arbitrary directions.

In all cases, the velocity error at injection is propagated to the point corresponding to the point at 105 hr after injection used in the circumlunar flight studies. Figures III-48 through III-50 present the initial (position) velocity corrections(ΔV_p), and the final (velocity) corrections (ΔV_v), as well as the total velocity correction required. As in the translunar case, the initial correction, made at the 105-hour point, corrects the position of the vehicle so that it crosses the nominal transearth trajectory at a predetermined position and time, which is varied from the 120-hr point to perigee. The final velocity correction (ΔV_v) realigns the spacecraft along the nominal trajectory with the correct velocity.

The required correction velocities presented in these figures are quite low, but are strong functions of the uncertainties concerning the physical constants of the earth-moon system. The required transearth midcourse guidance fuel requirements for a closely defined lunar orbit should be significantly lower then those on early, less-well defined circumlunar flights.

D. TRANSLUNAR ABORT

1. General Considerations

Abort in the translunar phase is more commonly termed "turnaround maneuver." Abort is conducted by utilizing the propulsion and equipment module and

the mission engine. For a starting point in this phase, a preliminary tradeoff study of turnaround performance was conducted. The study consisted of trades in propulsion requirements and time-to-return to earth from any point in a translunar trajectory. Requirements for turnaround maneuvers which result in return trajectories out of the initial flight plane are also included.

The purpose of this tradeoff is to gain a more complete understanding of the turnaround problem. Since orders of magnitude of the various parameters of interest will suffice for this purpose, the following simplifying assumptions are made:

(1) Spherical earth.

(2) No perturbations due to moon or sun.

(3) Corrections to initial velocity vector applied instantaneously.

(4) The translunar, transearth and turnaround trajectories have a perigee whose distance (Rp) from the center of the earth is equal to the earth's radius.

(5) Radiation belts are ignored.

The first concern is to determine the velocity impulse (ΔV) requirements, together with the time-to-return to earth when performing turnaround maneuvers. Before this can be done, the initial velocity (V_i) and flight path angle (γ_i) must be known for any point along any translunar trajectory. For simplification of calculations, expressions are derived which are normalized with respect to the earth's surface. Resulting normalized velocity is then expressed as

$$V = \left[\frac{2}{R} - (1-e)\right]^{0.5}$$

Where (R) is the distance from earth in earth radii and (e) is the eccentricity of the orbit.

The flight path angle (γ), which is measured from the local horizontal to the velocity vector, may be found by use of the following:

$$\cos\gamma = \left[\frac{(1+e)}{R\{2-R(1-e)\}}\right]^{0.5}$$

Next, the bounds of allowable eccentricities for the turnaround trajectories are required. For one constant and continuous bound, a return eccentricity of one is arbitrarily selected. Actually this may be interpreted as a design

limit and will be referred to as such. Having defined the maximum eccentricity allowed, it naturally follows to determine the allowable minimum (e min). For a given distance from earth (R) and a required perigee condition, the minimum return eccentricity obtainable is realized when the semi-major axis (a) is as small as possible. This would necessitate that R= apogee and thus:

$$a = \frac{R+1}{2}$$

The resulting equation for the minimum allowable eccentricity is:

$$e_{MIN} = \frac{(R-1)}{(R+1)}$$

and if the eccentricity of the return trajectory is lower than (e min), the vehicle will miss the earth and will not be "captured".

Figure III-51 shows an envelope of allowable return eccentricities as a function of distance from the earth. Of course there isn't any real upper limit above e = 1 provided that a proper negative γ_F is achieved. In other words the following is true:

γ_F = initial flight path angle of return trajectory

$\pm\gamma_F$: $\{e_{MN} < e_R < 1.0\}$: eccentricity of turnaround trajectory $= e_R$

$-\gamma_F$: $\{e_R \geq 1.0\}$: (restricted only by design limit)

Knowing the orbital elements of the translunar trajectory plus the required turnaround eccentricity, both the initial conditions prior to turnaround (V_L , γ_i) and immediately after the maneuver (V_F , γ_F) are easily found.

The time to return to earth along any of the allowable orbits was computed with standard time equations and the results are shown in Fig. III-52. This plot is true regardless of the eccentricity of the translunar trajectory and shows the trade in time for the allowed return eccentricities for any given distance from earth (R).

One of the main objectives of the study was to ascertain the consequences of changing the heading of the return trajectories from the initial flight plane. The definition of "change in heading (ϵ)" and the general problem is sketched below.

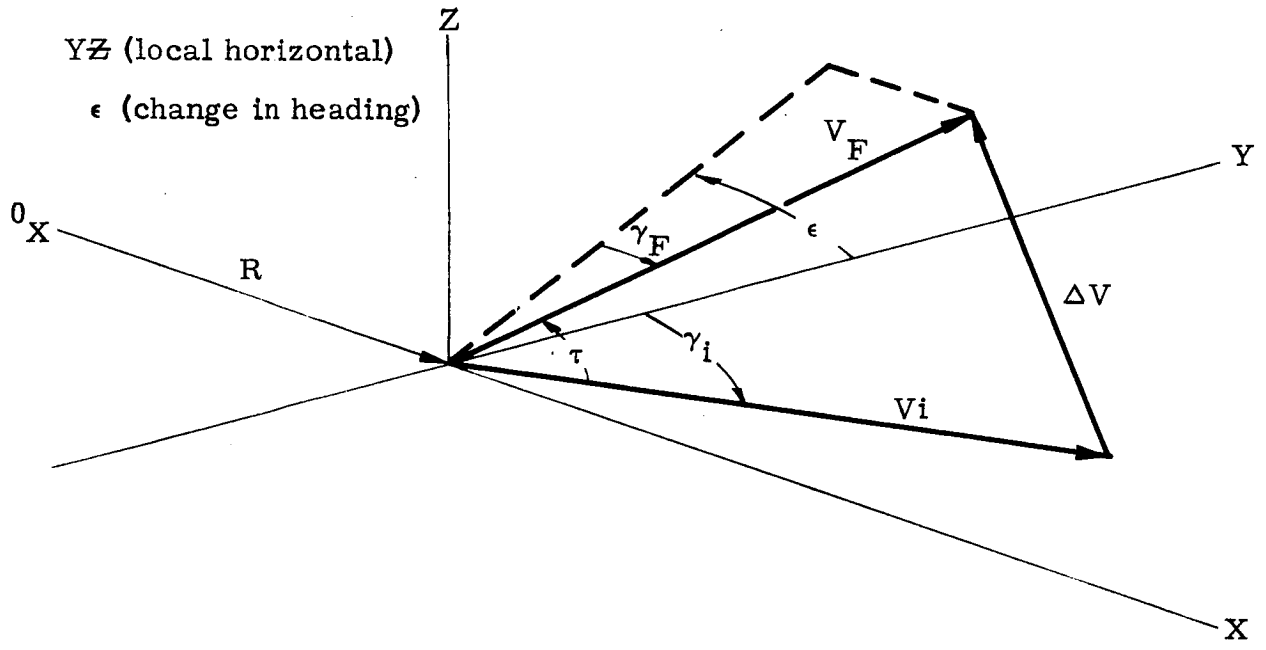

The change in heading is identically the angle between the original flight plane and the turnaround trajectory plane. A heading change may also be described as being the difference in directions reflected upon the earth between the initial translunar velocity vector (V_i) and the return velocity vector (V_F).

Taking the vector dot product of the initial and final velocities ($\bar{V}_F \cdot \bar{V}_i$), the included angle $\uparrow$ may be found.

$$\uparrow = \cos^{-1}\left[\sin\gamma_i \sin\gamma_F + \cos\gamma_i \cos\gamma_F \cos\epsilon\right]$$

$\uparrow$ increases when ϵ increases for a given γ_i; and γ_F.

From the cosine law, it is seen that as $\uparrow$ increases,

$$\Delta V^2 = V_i^2 + V_F^2 - 2 V_i V_F \cos\uparrow$$

the required velocity impulse also increases for a given V_i and V_F. Therefore, for given initial conditions of V_i and V_F and a specific time-to-return, any change in heading will result in an increase in the required maneuvering impulse.

Barring other requirements, Figs. III-53 and III-54 bear out the inefficiency of conducting such turnaround flights with a change in heading. However, when attempting to have a specific perigee target, it may become more efficient timewise to maneuver out of the initial flight plane.

These illustrations also provide trades in propulsion requirements as a function of distance from earth and time-to-return. The figures are based on a translunar trajectory with an eccentricity of one. Correction factors for translunar eccentricities less than one also are provided in Figs. III-55 to III-58. These correction factors point out the trade in fuel requirements as a function of the translunar orbit eccentricity (e_0). They indicate that maximum performance for a given velocity impulse is realized when the eccentricity of the translunar trajectory is as low as possible.

It also becomes evident that in view of the expected propulsion potential of Apollo ($\Delta V \approx$ 2000 to 6000 fps) significant changes in heading can only be accomplished when nearing or departing in the vicinity of the moon.

On the return leg, after circumnavigating the moon, emergencies might arise which would require major maneuvers. The tradeoffs in time and fuel requirements for transearth trajectories may be found by reversing the sign of the flight path angle in Figs. III-53 and III-54 letting the eccentricity scale apply to both e_0 and e_R.

Below are two examples emphasizing the turnaround from a translunar trajectory.

Example 1

GIVEN: $e_0 = .985$
R = 20 EARTH RADII
ΔV = 4000 FPS (CAPABILITY OF VEHICLE)
$\mathcal{E} = 0$

Find the return eccentricity and time to return. From Fig. III-53 for e_0-1; e_R = 0.927 and γ_F = (+). From Figs. III-55 to III-58: ΔV required = 0.95 (4000) = 3800. ΔV equivalent = 4000 + 4000 = 3800 = 4200 fps. Again from Fig. III-53, e_0' = 0.985, e_R = 0.925 and γ - (+). From Fig. III-52, the time to return is 51 hr.

Example 2

GIVEN: $e_0 = 1.0$
R = 20 EARTH RADII
TIME-TO-RETURN = 20 HOURS
$\mathcal{E} = 0$

Find the propulsion requirements and the return eccentricity. From Fig. III-52, the return eccentricity (e_R) = 0.91 and γ_E = (-). Figure III-53, ΔV required = 9700 fps.

2. In-Plane Abort

Even during emergency situations, advanced selected landing sites would be desirable. An investigation was made into the potential of performing in-plane turnaround maneuvers that would return to a given perigee longitude. The results of the investigation have proven very promising and are presented in the following discussion.

For the investigation, classical two-body equations of motion have been used and instantaneous maneuvers have been assumed.

The nominal trajectory prior to the maneuver is an ellipse with a perigee at 150, 000 ft, and a perigee velocity of 36, 270 fps giving an eccentricity of 0.9668. This ellipse has an apogee altitude about the same as the moon's average orbital radius.

Figure III-59 presents the necessary information to estimate return perigee longitudes for various ΔV and maneuver radii. The right hand side of Fig. III-59 shows the "return time" (time from maneuver to return perigee) (h_p = 150, 000 ft) as a function of the radius of the maneuver and velocity impulse applied. The left hand side of the figure converts the return time into the location of perigee relative to the injection perigee.

It has been assumed in this conversion that the return perigee latitude is equal to the injection perigee latitude. The degree of approximation involved in this assumption is indicated in Fig. III-60. The line labeled $\Delta\Phi$ shows the angular rotation of the major axis of the ellipse caused by ΔV's of various magnitudes. These values of $\Delta\Phi$ would be the maximum error in the return perigee longitudes using Fig. III-59 if the inclination of the trajectory plane to the earth's equator were zero. It can be seen that even at large values of velocity impulse, the errors due to the assumption would be small.

The second curve on Fig. III-60 shows change in return perigee latitude due to the change in argument of perigee for a typical inclination of 36.5° and injection perigee at latitude 16.5°S. The assumption of Fig. III-59 that the return perigee latitude is equal to the injection perigee latitude can be seen to be nearly correct.

In order to illustrate the use of Fig. III-59, the following example is presented:

Given:

Injection perigee at latitude 35°N, longitude 135°W of Greenwich.

Find:

The ΔV and time to return to Edwards AFB, latitude 35°N, longitude 120°W of Greenwich for an in-plane turnaround maneuver at 10 earth radii.

Solution:

The longitude of return perigee is 345°W of injection perigee longitude. From Fig. III-59:

n	Return Time (hr)	Velocity Required (ft/sec)
$0 < n < 1$	18.4	5500
$1 < n < 2$	42.4	2600
$2 < n < 3$	66.4	1500

Note that the assumption of equal perigee latitude for injection and return results in the removal of trajectory inclination from the problem. However, the particular inclination and injection perigee latitude are indirectly involved in the problem when making the choice of return perigee longitude. For example, assume it is desired to land in Australia after a turnaround from a southeasterly launch out of Canaveral. The southeasterly inclination will result in an approach to Australia from the northwest. Therefore, return perigee longitudes somewhat west of Australia are desirable.

Figures III-61 through III-64 have been obtained from Fig. III-59 for three typical situations. Figure III-61 shows the ΔV's and return times for turnarounds at various R/R_E with the requirement of landing in Australia. The injection perigee longitude is taken as 8.8°W representative of a southeasterly launch from Canaveral with no coast. The longitudes used for Australian landings reflect the assumption of an approach from the northwest.

Figure III-62 presents the same information for landing in the United States. The injection perigee is assumed to be directly over Edwards. This would be representative of a launch from Canaveral on a 35° inclination trajectory with a coasting period prior to injection. The downrange maneuverability in this case enters into the selection of return perigee longitude because the aerodynamic maneuver "foot print" is nearly tangent to the landing site latitude. Therefore, four possible return perigee longitudes have been shown on Fig. III-62. Perigee at 190°W longitude is representative of a return to Edwards AFB with about

4500 stat mi of re-entry glide range. The other extreme would be a return perigee longitude at the east coast of the United States. This would be representative of a minimum range re-entry that could still remain within the boundaries of the United States. The much wider selection of return times compared to the Australian landings is apparent. This is due primarily to the fact that re-entry longitudinal maneuverability can be used to extend the choice of return perigee longitudes. Figure III-63 is similar to III-62 except that injection perigee occurs at 165° W.

* * *

Figure III-59 can be used to estimate velocity impulse and return times for planar maneuvers with any specified difference in the longitude of injection and return perigee. The advantages in terms of turnaround flexibility for the 35° inclination trajectory with return to the United States have been illustrated.

3. Out-of-Plane Abort

Although the previous discussion dealt with in-plane aborts during the translunar phase, it did mention the possibility of performing returns out of the nominal flight plane. In fact, propulsion requirements were given in Fig. III-53 to return 90° out of the nominal flight plane to no specific place on earth.

The present discussion will demonstrate the feasibility of performing a turnaround maneuver with a change in heading. The benefits derived from such maneuvers are in the form of reduced return flight times to acquire a specific landing site.

A study was made with a typical translunar trajectory. From this nominal trajectory, maneuvers were conducted in and out of the flight plane at various distances from earth. The return landing site is Edwards Air Force Base and the orbital characteristics of the translunar trajectory are:

Nominal Translunar Trajectory

Injection	Conditions
Velocity	35, 785 fps
Altitude	761, 000 ft
Flight path angle	3°
Longitude	1. 65°W
Latitude	26. 35°N
Orbit inclination	35°
Eccentricity	0. 9728

The results are presented in Fig. III-64. All maneuvers were performed instantaneously.

Figure III-64 gives the time to return from an abort as a function of the distance from earth for various conditions.

For reference purposes, the first condition presented does not make use of any maneuvering at all. This condition is the nominal trajectory and for various distances from earth shows the time remaining to complete a circumlunar mission.

The Apollo vehicle will have a capability of possessing a 6000 fps characteristic impulse for the lunar orbit mission and an 1800 fps for the circumlunar mission.

When one thinks of an emergency in space, naturally the question arises: "How quick can a return be made"? The answer, of course, depends on whether one particular landing site is desired, or a choice of a number of sites is available, or a return to anywhere on earth is suitable.

If a return to anywhere on earth is suitable, it has already been proven in the previous section that the most efficient use of maneuvering fuel is realized when all maneuvers are conducted within the nominal flight plane. Figure III-64 shows two smooth curves representing the absolute minimum return time to earth for velocity impulses of 1800 fps and 6000 fps. As can be seen, there are major reductions in the total flight time remaining.

If a return is desired to a particular landing site, say Edwards Air Force Base, then the problem of "timing" the arrival is present.

The "stepped" curves shown represent the minimum time to return to Edwards AFB in case of an emergency and make evident the "timing" problem for two cases of impulse potential. As noted, four of the "stepped" curves represent return flights of 10° and 20° out of the nominal flight plane. The return times for these flights to Edwards Air Force Base are less than the in-plane flights up to certain points. The intersections of the out-of-plane curves with the absolute minimum time curves denote where these points occur and require that the planar change must be reduced as altitude is gained to achieve minimum return times in these areas.

The portion of the"return-to-Edwards" curves before this intersection requires more and more velocity impulse as they approach the intersection. At the intersection the available amount of characteristic impulse is required, and thus, the necessity for reducing the planar change is seen.

In summary, there are definite benefits to be gained in performing turn-around maneuvers out of the plane when a specific landing site is desired. Reductions in time-to-return of five hours over the in-plane returns can be realized. If there is a multi-choice of landing sites, this would further reduce the times to return.

The restriction of inadequate tracking facilities or any other restrictions are not reflected here. The purpose, at this time, is to prove feasibility and performance gains in conducting aborted flights out of the nominal flight plane.

E. TRANSEARTH ABORT

The term "abort" during this phase is somewhat ambiguous. Actually, the spacecraft is on its return leg and any maneuvering would affect perigee conditions only. Therefore studies were conducted to ascertain the effect of such maneuvers on perigee velocity, time to perigee and argument of perigee. All maneuvers hold the altitude of perigee constant at 150, 000 ft.

1. Time to Perigee Control

Figure III-65 presents the change in arrival time at (earth) perigee as a function of the characteristic velocity required and the altitude above the earth's surface at which the maneuver is performed. The same information is presented in Figs. III-66 and III-67 in other convenient forms. The change in longitude of perigee is defined as the change in time to perigee multiplied by the angular rotation rate of the earth. These curves indicate that if 3000 fps is available for maneuvering and it is all applied at a point half way between the earth and the moon, then the vehicle can arrive at earth perigee one quarter of an earth's circumference ahead or one half an earth's circumference behind the original perigee longitude.

2. Effect on Argument of Perigee

Figure III-68 shows the change in the argument of perigee associated with the various maneuvers. The change in argument of perigee is defined as the angular rotation of the major axis of the return elliptic trajectory during the maneuver. Note that the angular changes in argument are very small compared with the changes in longitude of perigee. Also, the argument of perigee changes by about 3.2^{0} for each 1000 fps of maneuver and is almost independent of the altitude of the maneuver.

3. Effect on Re-entry Velocity

Figure III-69 shows the change in velocity at perigee as a function of the characteristic velocity and radius of the maneuver. This curve indicates the degree to which the initial re-entry velocity is affected by midcourse maneuvers. For the 3000-fps maneuver at the half-way point used earlier, the change in perigee velocity would be about minus 300 fps or plus 500 fps.

* * *

Significant changes in time to perigee by midcourse maneuvers will require characteristic velocities on the order of 500 to 3000 fps. Argument of perigee and velocity at perigee are not greatly affected by such maneuvers.

The above analyses were performed with a nominal orbit having an eccentricity of 0. 9668 and perigee velocity of 36, 270 fps.

IV. RE-ENTRY PHASE

This section describes the re-entry trajectory analysis, in which the significant features of the re-entry phase were determined, and the influence of these features on the re-entry vehicle design parameters was evaluated. Parametric studies of corridor width, maneuver requirements and maneuver capabilities are presented, as well as the corridor characteristics of several configurations. Also described is a maneuverability study in which the effects of control technique were determined. The maneuvering capabilities of representative configurations employing these techniques are shown.

It is shown that a lifting capability greatly increases the g-limited corridor width available; also that life modulation provides a still further extension of this corridor.

The required longitudinal range is determined to vary between 3000 and 10,000 naut mi depending on the moon's declination. The lateral range requirement is shown to be less critical than the longitudinal range and is dependent on return trajectory errors in time and inclination.

The parametric study of maneuver capability shows that the corridor width determines the L/D required to get a specific maximum range. It is also shown that if an apogee altitude limit exists, this altitude will determine the maximum range capability for constant L/D trajectories. For a constant L/D entry, a 10,000 naut mi range requirement from a 30 naut mi corridor boundary requires an L/D $\simeq$ 0.45. This study also shows that corridor width exerts a strong influence on maneuver capability of vehicles with relatively low values of $(L/D)_{max}$ ($L/D < 0.4$).

Three of the re-entry vehicles studied (L-2C, Mercury and M-1) are incapable of limiting maximum g to six on the 30-naut mi corridor boundary. Modulation of the L-2C configuration is shown to decrease the available g-limited corridor width.

The range control technique has a strong influence on the maneuver capability of a given configuration. The maximum capabilities of the Model 410 vehicle are determined to be approximately 17,000-naut mi longitudinal range and $\pm$ 1000-naut mi lateral range for entry at 36,000 fps on the 40-naut mi corridor boundary

Definition of Terms

The re-entry phase is defined as that part of the return trajectory after the vehicle first crosses 400,000-ft altitude inbound. Subsequent skips back above this altitude are considered to be part of the re-entry phase.

All corridor widths mentioned in this document refer to the vacuum perigee width as used by Chapman. This width is the difference, measured in nautical miles, between the perigee altitudes of the overshoot and undershoot return trajectories. For a fixed perigee velocity, the difference in perigee altitudes can be related to a difference in flight path angle at the re-entry altitude. The re-entry altitude has been arbitrarily defined as 400,000 feet. The following terms are defined for later discussion.

Negative C_L max overshoot. There are a variety of definitions in use for the overshoot boundary. For example, there is the "single pass overshoot," defined as the maximum perigee altitude at which the vehicle can enter at maximum negative lift coefficient and reach the earth within a range of one earth's circumference from the entry point. There is also in use the definition of overshoot based on the abrupt change in range to impact described in the sketch below:

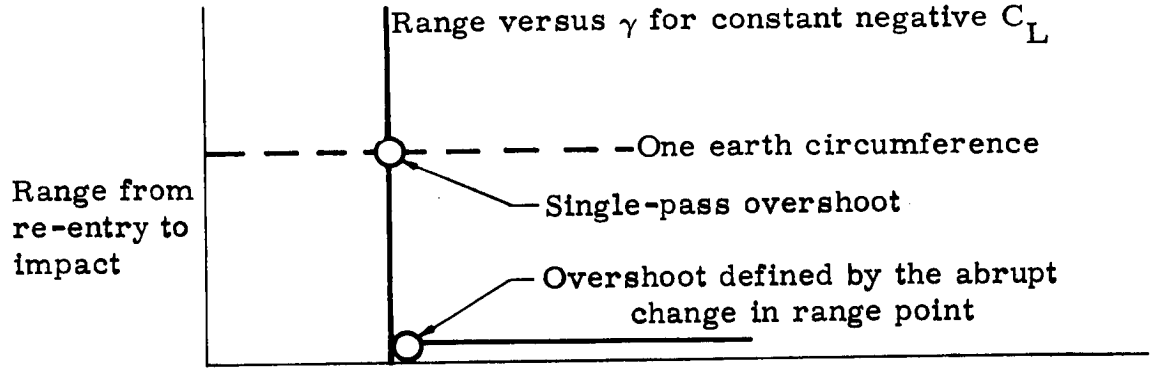

The difference in overshoot entry angle between these two definitions is about 0.05°, which is equivalent to about one-half mile in corridor width.

The negative C_L max overshoot definition employed here falls somewhere between these two definitions. The negative C_L max overshoot boundary is defined as the maximum perigee altitude at which the vehicle can enter at negative C_L max and remain within the atmosphere (400,000ft).

The primary point is that the overshoot definition has a negligible effect on the corridor widths presented.

Positive C_L max overshoot. The positive C_L max overshoot boundary is defined arbitrarily as the maximum perigee altitude for which the vehicle

can enter at positive C_L max to the point where $\gamma = 0^o$ at which time negative $C_L$max is applied and the vehicle is able to remain within the atmosphere.

The purpose of introducing this overshoot definition is to illustrate the reduction in corridor width which would occur if it were necessary to enter the atmosphere without precise flight path angle information. For example, in emergency situations in which knowledge of the exact re-entry conditions is not available, the vehicle would have to enter at positive lift until it is determined (from a load factor time history, for example) that an overshoot condition exists. Once this is determined, a roll to negative lift would be performed. The positive C_L max overshoot boundary is then representative of a practical boundary for this emergency condition.

This overshoot boundary is approximately five to seven naut mi below the negative C_L max boundary.

Guidance corridor. The guidance corridor is the 3 σ corridor width attainable for a final midcourse correction at 30,000 naut mi from the earth. This corridor width is estimated to be 10 naut mi or $\pm$5 naut mi about the desired perigee altitude. The reason for making no midcourse corrections closer than 30,000 naut mi is the rapid increase in propulsive velocity increments required to produce a given change in perigee altitude as the altitude decreases. The improvement in altitude measurement accuracy at the point where the radar altimeter becomes effective results in improved knowledge of the re-entry conditions. It is estimated that the entry flight path angle will be known to within $\pm 0.05^o$ by the time re-entry is initiated. This means that the location of the vehicle within the 10-naut mi guidance corridor will be known to within about 0.5 naut mi. This accuracy is sufficient for re-entry trajectory predictions required for re-entry guidance.

Design corridor. It is not considered practical to design the re-entry vehicle for only the 10-naut mi guidance corridor. However, it is not yet clear how much additional corridor width should be provided. Until such information becomes available, it will be assumed that the re-entry vehicle will be designed for a 30-naut mi corridor width. In addition, it has been assumed that this 30-naut mi corridor is measured with respect to the positive C_L max overshoot.

The combination of these two assumptions will result in a conservative re-entry vehicle design.

g-limited undershoot. The minimum perigee altitude at which the vehicle can re-enter and not exceed a specified maximum load factor (g) is referred to as the g-limited undershoot boundary of the corridor. To be able to

determine this boundary for a given vehicle, two quantities must first be specified: (1) the maximum allowable load factor and (2) the technique by which the vehicle's attitude is to be controlled.

* * *

The analysis of re-entry is initiated with a parametric study of the factors that influence corridor width, followed by parametric studies to determine maneuver requirements and capabilities. Specific configurations are then considered, and corridor characteristics and maneuver capabilities are determined for these configurations.

A. CORRIDOR WIDTH PARAMETRIC STUDIES

A number of studies (Ref. 9 through 13) have been made of the motion of vehicles entering planetary atmospheres and many of the interrelationships between vehicle parameters and resulting trajectory characteristics have been established. The work of Chapman (Ref. 9 and 10) has been particularly valuable for studying re-entry at supercircular velocities.

From Ref. 9, it is possible to determine g-limited re-entry corridors as a function of the re-entry vehicle's lift-to-drag ratio, L/D, and ballistic parameter, W/C_DA. This information, in terms of the overshoot and undershoot boundaries defined in Ref. 9, is shown in Figs. IV-1 and IV-2.

Vacuum perigee altitude for the single-pass overshoot and for 10- and 6-g max undershoot, respectively, are presented with W/C_DA and L/D as parameters. The assumptions are constant C_L and C_D and an entry velocity of 35,000 fps at an altitude of 400,000 ft.

The significant characeristics to be noted from these curves are:

(1) Corridor width is independent of W/C_DA if W/C_DA is the same for overshoot and undershoot.

(2) Overshoot perigee altitude is primarily a function of the W/C_LA attainable.

(3) Undershoot perigee altitude for a constant value of W/C_DA is decreased significantly by relatively low values of L/D. As L/D increases beyond 1.0, the benefits become small. When particular lift-drag polars were superimposed on the undershoot curves of Figs. IV-1 and IV-2 it was found that minimum perigee altitude was obtained in the region of L/D max for each case.

(4) For ballistic re-entry, (i.e., L/D = 0,) the corridor width is only 6.9 naut mi for 10-g max, and is non-existent for 6-g max undershoot.

(Note the undershoot boundary for L/D = 0 is not shown on Fig. IV-2 for reasons of clarity, since this boundary lies above the L/D = overshoot boundary shown.)

Further parametric studies of g-limited corridors are complicated by the fact that maximum corridor widths are realized when operating the re-entry vehicle at different points of the C_L, C_D polar for the overshoot and undershoot re-entries. In order to limit the number of parameters to manageable proportions, particular lift-drag curves have been selected.

The C_L, C_D relationships selected for use are those presented in Ref. 9. For most configurations maximum g-limited corridor widths are obtained when re-entry is initiated near $C_{L_{max}}$, applied negatively in the case of overshoot and near $(L/D)_{max}$ on the undershoot. It has been found, however, that little error is introduced if $C_{L_{max}}$ applied negatively on the overshoot boundaries and $(L/D)_{max}$ on the undershoot boundaries are assumed to give maximum corridor widths. These are the only additional restrictions placed on Figs. IV-1 and IV-2, while the results of such a study are limited by the particular selection of C_L, C_D relationship, important trends are nevertheless established.

The effect of entry velocity on corridor width, obtained from Ref. 9, is shown in Fig. IV-3. The 10-g limited corridor width variation with entry velocity is presented for several values of L/D. It is apparent that relatively large velocity reductions, corresponding to large propellant ratios, are required to obtain significant increases in corridor width for a fixed L/D.

The results presented thus far have concerned re-entry at constant lift and drag coefficients. Grant, in Ref. 11, has indicated that substantial increases in g-limited corridor width can be obtained by employing variations of C_L during re-entry. Such re-entries are commonly referred to as modulated re-entries.

The term "modulated re-entry" is somewhat ambiguous since it is necessary to modulate lift during almost all lifting re-entries at some time prior to landing in order to stay within the design limitations of the vehicle or to avoid exiting from the atmosphere to extreme altitudes. "Modulated re-entries" therefore refer to re-entries in which lift and/or drag are modulated prior to the first maximums of load factor or heating rate. Constant C_L and C_D re-entries are those in which C_L and C_D are constant only until the initial maximums of load factor or heating rate are reached. Beyond these maximums, C_L and C_D are unspecified except that sufficient variation is employed to avoid exceeding the initial maximums.

Modulation from $C_{L_{max}}$ to $C_L = 0$ is shown analytically by Grant to provide the largest increases in g-limited corridor width. Again specific C_L, C_D polars are necessary in order to develop results involving a limited

number of parameters. The polars for the M-1, M-2, and winged vehicle shown in Fig. IV-4, have been selected for this purpose. These curves are representative of re-entry vehicles having maximum L/D's of about 0.5, 1.25 and 1.75. Using these polars, the ratio of modulated to unmodulated g_{max}, as a function of $(L/D)_{max}$, for any entry angle or velocity is shown in Fig. IV-5 for modulated re-entry from $C_{L_{max}}$ to $C_L = 0$ and $C_{L_{max}}$ to $(L/D)_{max}$, respectively. These data may then be combined with Chapman's constant C_L, C_D results to give the 10-g and 6-g modulated re-entry corridors. Figures IV-6 and IV-7 present such results for the case of modulation from $C_{L_{max}}$ to $C_L = 0$. Comparison of Figs. IV-6 and IV-7 with Figs. IV-1 and IV-2 indicates the large improvements in corridor widths obtained through modulation. For example, the 10-g single-pass re-entry corridor for a vehicle with L/D of 1.0 and W/C_DA of 100 is increased from 52 naut mi to 122 naut mi by modulation. The 6-g modulated corridor, more desirable from the standpoint of crew comfort and capability for long load factor durations, is increased from 32 naut mi to 72 naut mi.

The limiting value of load factor affects the corridor width at an entry velocity of 36,000 fps in the manner shown in Fig. IV-8. Unmodulated and modulated re-entry corridor width variation with maximum allowable load factor is presented for several values of L/D. The time history of load factor is such that a 6-g_{max} represents approximately the upper limit at which the crew may be expected to perform useful control functions during re-entry. As is apparent in Fig. IV-8, the maximum allowable load factor represents an important parameter in determining available corridor widths. This figure also indicates the increase in corridor width obtained by modulated re-entry.

The maximum load factor has been the only determining factor of the undershoot boundary of the re-entry corridor in the results presented. In some instances, aerodynamic heating may represent a more severe limitation than load factor in determining the vehicle's undershoot boundary. In such cases, the heating rate, q, or total heat, Q, limited corridors would replace the g-limited corridor as the criterion for midcourse accuracy required.

B. MANEUVER REQUIREMENTS PARAMETRIC STUDY

A major factor in determing the L/D requirements of the re-entry vehicle is the maximum range (maneuverability) required from the re-entry point to touchdown for the return from a circumlunar mission. This section deals with a study which determined the range requirements of the re-entry vehicle. Both longitudinal and lateral maneuverability requirements were determined from calculations involving simple spherical trigonometric relationships.

Although the approach was conservative, it should be noted that the results are quite dependent on the assumptions used to limit the problem to a reasonable size.

1. Longitudinal Maneuverability

The longitudinal range required is defined as the distance from the point of re-entry to the latitude of the landing site measured along the earth's surface in the plane of the re-entry trajectory. This in-plane range is a function of the return trajectory inclination and is primarily dependent on the location of the re-entry point with respect to the landing site latitude.

In order to locate the re-entry point, the location of the conic perigee of the return ellipse must first be considered. The conic perigee varies from northern to southern latitudes depending on the moon's declination. The perigee occurs in the Southern Hemisphere when the moon is at northern declination and in the Northern Hemisphere when the moon is southerly declined. Consider the earth-moon line at the start of the transearth trajectory as shown in the following sketch for the conditions of the moon at its maximum northern and southern declinations.

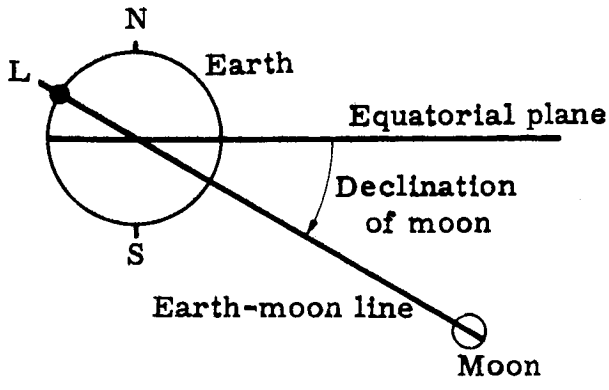

Moon at Southern Declination

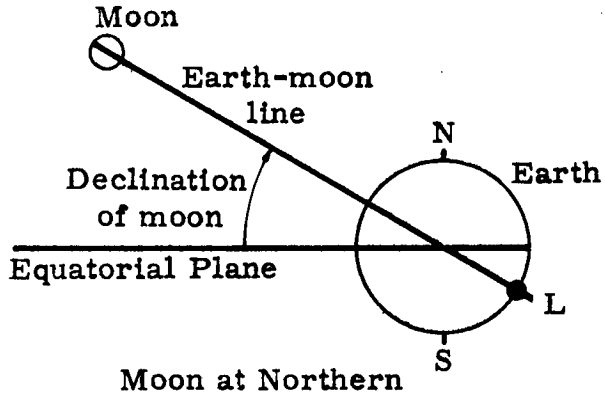

Moon at Northern Declination

This earth-moon line can be considered the line of nodes of the trajectory plane and the earth-moon plane. A projection of this line through the earth intersects the earth's surface at the points denoted by L in the above sketch,

i.e., in the northern and southern hemispheres when the moon is at its southern and northern declinations, respectively.

From Ref. 14 the angular arc between the conic perigee and the node line is of the order of 7.5° for typical direct re-entry circumlunar trajectories. For re-entry vehicles having some lift capability (with L/D of the order of 0.5), the 10-g_{max} corridor at 400,000-ft altitude is defined by re-entry angles ranging from -8 to -5°. For the purposes of this study, an average value of γ_E equal to -6.5° was selected. Therefore the angle between the re-entry point and the conic perigee is about twice this value, or 13°.

Combining the angular values obtained for the location of the conic perigee relative to the node, and the location of the re-entry point relative to the conic perigee, we obtain the location of the re-entry point relative to the node as being 20.5°.

Figures IV-11 and IV-12 show the geometric relationships and equations used in calculating the longitudinal range requirements for the conditions of the re-entry point in the Northern and Southern Hemispheres. The results obtained by these calculations are shown in Fig. IV-9, given as the longitudinal range required as a function of the return trajectory inclination angle with the target latitude, i.e., with landing site latitude as the parameter. The range requirements when the moon is at its maximum northern and southern declinations are shown.

Considering the present operational concept of the return trajectory inclined 35° and Edwards AFB as the landing site (35° N latitude), Fig. IV-9 shows the longitudinal re-entry range required is 10,000 naut mi when the moon is at its most northern declination (28.5°N). This required range is reduced to 3300 naut mi when the moon is at its most southern declination. In order to have complete flexibility of launch time for the lunar missions, it will be necessary to be able to complete the mission when the moon is at any point in its orbit. Therefore, the 10,000 naut mi requirement has been selected as the minimum longitudinal range in defining the L/D requirement for the re-entry vehicle.

2. Lateral Maneuverability

The lateral range required is defined as the great circle arc length measured from the target perpendicular to the plane of the re-entry trajectory. For purposes of this study, the lateral range requirements have been determined as a function of the errors in return trajectory inclination and the longitude at the equatorial crossing of the re-entry trajectory. In this manner the lateral range is independent of the moon's declination. The nominal return trajectory used in this study is at an inclination of 35°, which is tangent to the 35th parallel at Edwards AFB.

The geometric relationships and equations used to calculate the lateral range required are shown in Fig. IV-13. The results obtained from these calculations are shown in Fig. IV-10. This figure presents the lateral range required for combinations of errors in trajectory inclination of -18 to +20° and errors in longitude at the equator of ±45°. These results show that rather large errors in these trajectory parameters must be experienced before a lateral range of 1000 naut mi is required.

For landing at Edwards AFB, Fig. IV-10 shows that for a maximum lateral maneuver capability of ± 1000 naut mi, the tolerance in inclination error is ±17°. The tolerance in longitude at the equator crossing of the return trajectory is ±60° for a 1000 naut mi range requirement. This is equivalent to ±5 hr in arrival time at the equatorial crossing. A combined error of -11° in inclination and ±3 hr (±45° in longitude) could be accepted for a required lateral range of 1000 naut mi. These tolerances are significantly greater than the expected errors in inclination and arrival time. For this reason, lateral maneuverability required from the return trajectory is considered not as critical a requirement as longitudinal maneuverability in defining the L/D requirements for the re-entry vehicle.

The analysis of launch time tolerance (Chapter III, Section A) showed the maneuver requirement for returning to Edwards AFB from the parking orbit prior to injection. For the minimum parking orbit inclination considered (27.5°) this requirement is about 400 naut mi lateral range. A more realistic minimum inclination of about 29° reduced this requirement to 300 naut mi. Therefore it appears that this lateral maneuver requirement for abort during the parking orbit phase (at satellite velocity) is more severe than that to be expected from the return trajectory requirements if reasonable launch time tolerances are expected.

Having determined the maneuverability required, the next analysis will consider the factors that influence maneuvering capabilities during re-entry.

C. MANEUVER CAPABILITY PARAMETRIC STUDY

This section describes the parametric studies of downrange and lateral maneuvering capability. Consideration is restricted to atmospheric maneuverability defined as that obtainable after the vehicle has initially crossed an arbitrary reference altitude of 400,000 ft. It should be noted, however, that the vehicle is permitted to exceed the reference altitude after it has once descended through it in order to extend downrange maneuverability, but in no case are trajectories which penetrate the inner radiation belt considered acceptable (400 naut mi). It is possible that atmospheric maneuverability may be augmented by appropriate midcourse powered maneuvers. This additional capability is dependent on propulsion capability and not the re-entry vehicle configuration and will not be discussed here.

Parametric studies have been conducted to determine the effects of the various factors that influence the maneuvering capability of re-entry vehicles. Both longitudinal and lateral maneuverability studies were conducted.

The longitudinal maneuverability investigations were made using an analog computer for a re-entry velocity of 36,000 fps. All digital computed trajectories were limited to particular vehicles. Supplementing the analog study are the results of a parametric study provided by the NASA Space Task Group for an entry velocity of 35,000 fps.

The lateral maneuvering capabilities were analytically determined using a technique developed during the course of this study. This analytical technique was based on the assumption that the vehicle roll attitude was maintained constant from initial entry to impact. It will be shown in Section E of this chapter that this procedure gives the maximum lateral range.

These longitudinal and lateral maneuver capabilities were combined to form maneuvering envelopes, obtained for several (L/D)'s at various corridor depths. These envelopes define the total re-entry maneuver capability available from the initial point of re-entry at these corridor depths.

1. Longitudinal Maneuverability

Maneuvering capability is primarily a function of the re-entry vehicle's maximum L/D. For re-entry at parabolic velocities, however, a second variable must be considered, i.e., the location of the vacuum perigee altitude of re-entry within the vehicle's particular perigee corridor.

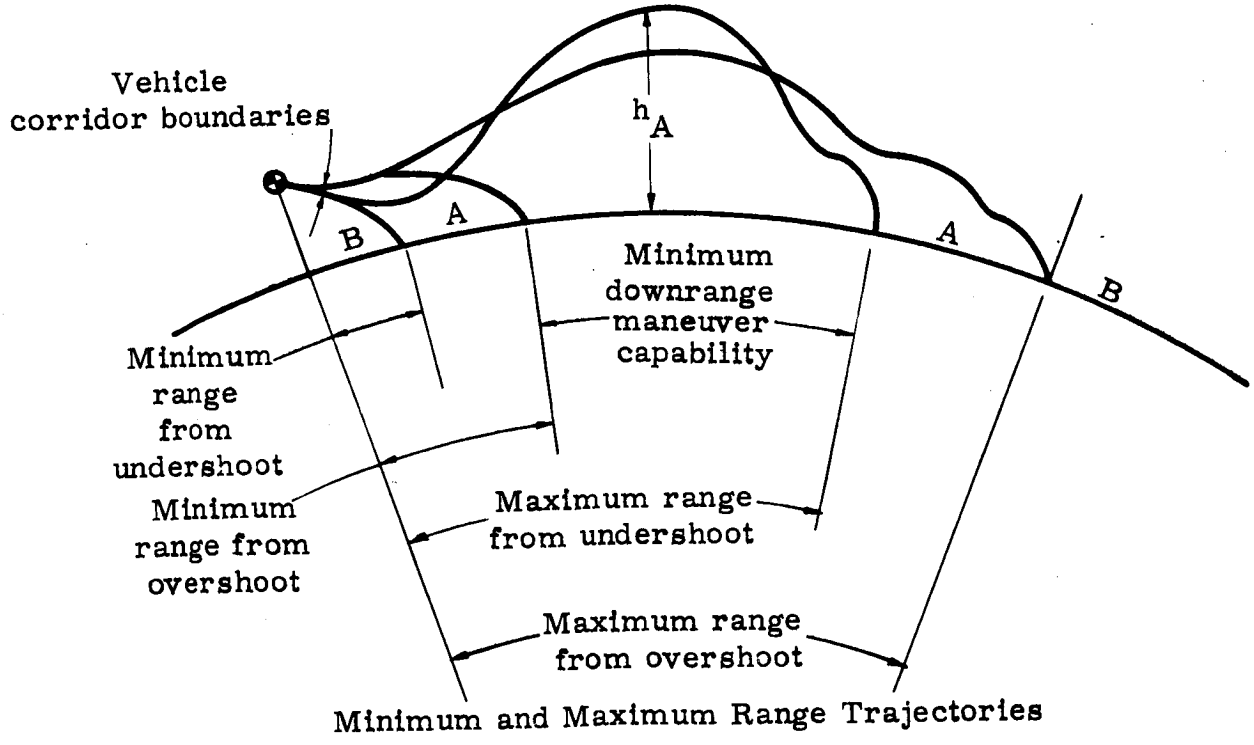

Minimum and Maximum Range Trajectories

Consider, first, the problem of determining downrange maneuverability. The sketch shows minimum and maximum range trajectories of a typical vehicle entering along the undershoot and overshoot boundaries of its corridor. The range segments called "Minimum Down Range Maneuver Capability" are the ranges attainable from any location within the corridor. The segments marked "A" can be reached only from restricted portions of the corridor. The segments marked "B" cannot be reached from any point in the corridor. The actual values of maximum and minimum range from overshoot and minimum range from undershoot are strongly dependent upon the control technique used to obtain them. For example, the overshoot re-entries are performed initially at negative $C_{L_{max}}$. This value must be modified after single-pass entry is assured or the vehicle will experience excessive load factors. The manner in which lift is modified by the control system then determines the maneuverability that is obtained.

The maximum range from the undershoot trajectory can be performed at constant L/D maximum for low L/D vehicles and, therefore, with no concern given to any particular control technique. For ranges greater than about 12, 000 naut mi the apogee altitudes (marked h_A in the sketch) during undershoot maximum range trajectories will increase to the point where penetration of the inner radiation belt becomes a limitation. Beyond such a point, the particular control technique used to restrict apogee altitude becomes the determining factor of maximum undershoot range and, therefore, minimum downrange maneuver capability.

The following results must be interpretated in the light of the various assumptions and ground rules which have just been stated.

The results of previous studies (Ref. 17) indicate that the minimum range from the overshoot boundary does not vary greatly with (L/D). The minimum range is almost totally a function of maximum allowable load factor. For any given maximum load factor and (L/D) the minimum range does not vary more than 500 naut mi throughout the entire corridor. It was felt, therefore, that this variable could be eliminated, and that the parametric study would be concerned only with determining maximum range.

The longitudinal range is not only dependent on (L/D) and the vehicle's location in its corridor, but also on the trajectory control techniques. In order to simplify the study and to eliminate the control technique as a variable, the trajectories used were computed for constant angles of attack only. A detailed discussion of the effects of the various range control techniques is contained in Section E of this chapter. However, it should be noted that most of the constant L/D trajectories skip out of the atmosphere.

In light of the above considerations, the parametric study to determine longitudinal maneuverability was reduced to determining maximum range as a function of re-entry angle for various constant values of (L/D).

This study was conducted on an analog computer. The Z-function technique introduced by Chapman in Ref 15 was used for this study. The detailed description of the mechanization of this program on the computer is given in Ref 4. This program consistently achieved results in range that were within 1% of those computed on the digital program (IBM 7090). These results are considered to be well within the accuracy requirements for a parametric study.

The results of this study are shown in Fig.IV-14, where longitudinal range for several re-entry angles is plotted as a function of L/D. In addition to the range information, conditions for an apogee altitude of 400 naut mi during the skip are shown. This apogee limit represents an upper bound on the longitudinal range available.

To supplement the information presented in Fig.IV-14, the results of a parametric range study conducted by the NASA Space Task Group are included in Fig IV-15. A comparison of these two figures shows that a significant increase in range is realized when the re-entry velocity is increased from 35,000 fps to 36,000 fps. Another expected result that may be determined is that the same vehicle (same L/D) skips to the altitude limit at a steeper entry angle from the higher velocity than from the lower velocity.

The information in Figs. IV-14 and IV-15 also indicates that the maximum allowable apogee attitude will determine the maximum range obtainable, for any flight path and L/D combination. The L/D determines the maximum corridor depth (re-entry flight path angle) at which this range can be attained. For example, in order to have a longitudinal range capability of 10,000 naut mi throughout a 30-naut mi corridor, dorresponding to an undershoot flight path angle of 7.4^{o} for $W/C_{D}A \approx 70$, the re-entry vehicle should have an (L/D) of 0.45.

2. Lateral Maneuverability

Lateral range is defined as the perpendicular distance measured along the surface of a spherical earth from the landing point to the vertical plane containing the original re-entry trajectory. This lateral range is not only a function of the same factors that influence longitudinal range (L/D, corridor depth, initial velocity, vertical lift control technique), but also of bank angle and longitudinal range itself.

It was readily apparent that, to limit the study to reasonable proportions, some of these variables would have to be eliminated. Other studies (Section E of this report) show that maximum lateral range could be expected if the bank angle were maintained constant throughout re-entry. For this reason, no other control technique was considered in the parametric study.

The initial velocity was limited to 36,000 fps, since it was found that velocity differences of as much as 1000 fps from this value would not affect

the results of the parametric study. This conclusion was based on the results of a brief study (presented in Section E of this chapter) conducted to determine the effects of increasing the re-entry velocity from 35,000 fps to 36,000 fps.

It is also shown in Section E that for a particular vehicle and control technique, the corridor depth does not greatly affect the maximum lateral range. This data indicates that there is only a 100 naut mi difference in maximum lateral range, out of 600 naut mi total, for the same control technique, between the overshoot boundary and the 40-naut mi corridor undershoot boundary. Therefore, it was assumed that initial entry angle would not affect the maximum lateral range. However, the influence of the vehicle's position in the corridor is by no means eliminated by this assumption because the downrange impact distance is greatly affected by entry flight path angle.

After making the above simplifying assumptions, the remaining list of variables to be considered in a parametric study of lateral range capability are (L/D), bank angle and longitudinal range. During the course of this study, an empirical method of predicting the maximum lateral range capability of a re-entry vehicle was derived, considering only these variables. This method may be used to calculate maximum lateral range as a function of down range impact distances for constant banked entry trajectories for various L/D ratios.

This method can also be used to calculate an entire maneuvering envelope if certain range information is available. If this range information is not available, then only the maximum lateral range potential can be obtained. First the method will be derived, and then its application to each of these two situations will be illustrated.

The change in heading angle, $\Delta\psi_1$, measured from the plane of the original re-entry trajectory, is given by Eq (1) from Ref.16:

$$\Delta\psi_1 = (L/D)\sin\Phi_B \ln(\overline{V_i}), \text{ rad.} \qquad (1)$$

where Φ_B = bank angle

$\overline{V_i}$ = initial velocity/satellite velocity

This is the heading change accomplished from initial entry only to that point on the trajectory where the velocity is equal to satellite velocity. If at this point the bank angle were changed to zero, the lateral range measured around a spherical earth normal to the original plane of re-entry would be given by Eq (2).

$$y_1 = \Delta\psi_1 R_e \sin\psi_c \qquad (2)$$

where R_e = radius of the earth, naut mi

ψ_c = range central angle to impact

y_1 = lateral range, naut mi

Now to this lateral range, y_1, is added the lateral range capability of the vehicle when entering at satellite velocity, y_2. The lateral range for satellite re-entries at bank angles of 45^o is obtained from Fig. 3 of Ref.16. This data is repeated here as Fig. IV-16. Equation (3) has been derived to approximate this lateral range for a west to east entry and to account for bank angles other than 45^o.

$$y_2 = 620\,(L/D)^{1.78} \sin(2\,\Phi_b), \text{ naut mi} \qquad (3)$$

Equation (3) is not applicable for bank angles greater than about 80^o. For bank angles exceeding 80^o, Ref.16 should be used to find y_2.

The total lateral range is given by adding Eq (3) to Eq (2).

$$y \text{ total} = (L/D) \ln(\bar{V}_i)\, R_e(\sin\psi_R)(\sin\psi_c) + 620\,(L/D)^{1.78} \sin(2\,\Phi_b) \qquad (4)$$

Figure IV-17 shows the results of a correlation of Eq (4) with values obtained from the Martin N-stage, 2-D trajectory program using the IBM 7090 computer. Range central angles and vehicle bank angles were obtained from the IBM calculated trajectories and were used in Eq (4) to calculate lateral range. The results of this correlation indicate that accuracies within 10% can be expected from this equation.

Equation (4) can be used directly to estimate the influence of the vehicle characteristics (lift-to-drag ratio) on the maximum lateral range potential even though the down-range impact distance is not available for various bank angles. This estimate is made by assuming that $\phi_c = 90^o$ for $\phi_B = 45^o$. The accuracy of this assumption will vary greatly with entry conditions and $(L/D)_{max}$ of the vehicle. The estimate will be low for vehicles with large values of (L/D) since $\phi_c = 90^o$ could be achieved with bank angles greater than 45^o. Obviously the downrange capability for a given $(L/D)_{max}$ and bank angle would be strongly dependent on entry angle.

Making the above assumptions, the maximum lateral range estimate would be given by Eq (6)

$$y_{max} = (L/D)\ .707\ R_e \ln(\overline{V}_i) + 620\ (L/D)^{1.78},\ \text{naut mi} \quad (6)$$

For $\overline{V}_i = 36,000$ fps and $R_e = 3440$ naut mi, Eq (6)

reduces to $$y_{max} = 810\ (L/D) + 620\ (L/D)^{1.78},\ \text{naut mi} \quad (7)$$

This equation is plotted in Fig. IV-18 along with the results of several machine computed trajectories from Ref. 19 and 20. As reported in Ref.18, these machine computed trajectories include a wide variety of control techniques and corridor depths. The equation shows reasonably good agreement with the calculated trajectories, where constant banked and constant L/D control techniques were used. These techniques are labeled "skip trajectories" on the figure.

In order to use Eq (4) to calculate maneuvering envelopes, it is necessary to have consistent values of ϕ_C and ϕ_B. The results of the parametric study of longitudinal range may be used to obtain these values. If the L/D values shown in Figs. IV-14 or IV-15 are considered to be the vertical component of L/D, then each of these L/D's can be related to a bank angle, ϕ_B by:

$$\cos \phi_B = \frac{(L/D)\ \text{Fig. IV-14 or IV-15}}{(L/D)\ \text{vehicle}} \quad (5)$$

So that if a vehicle L/D is selected, Fig. IV-14 can be interpreted as giving range vs bank angle for various entry angles.

Returning to Eq (4), it is seen that all the information necessary for calculating maneuvering envelopes is available if Eq (5) is applied to the results of the parametric study of longitudinal maneuverability. This procedure has been followed. The results are presented in Figs. IV-19 through IV-22. These figures show the variation with L/D of the total maneuvering envelopes for specific re-entry angles of -5.6°, -6.2°, -6.85° and -7.6°. It should be kept in mind that these maneuvering envelopes are for re-entries in which the bank angles, C_L and C_D, are maintained at constant values throughout the trajectory. The maneuvering envelopes clearly show the effectiveness of L/D in increasing the landing site capability of a re-entry vehicle. The variation of maximum lateral range with longitudinal range is also apparent.

Comparing Figs. IV-19 through IV-22 gives an indication of the effect of corridor depth on the maneuvering envelopes. The high L/D vehicles

were not greatly affected by increasing corridor depth over the range of re-entry angles investigated. The lower the $(L/D)_{max}$ of the vehicle, the greater is the change in maximum lateral range with changing entry angle. The landing site capability of a vehicle with an $(L/D)_{max} = 0.35$ varies considerably with corridor depth. For example, a vehicle with an $L/D = 0.8$ has a maximum lateral range of 1150 naut mi when re-entering at either 7.6^{o} or 6.85^{o}. For an $L/D = 0.35$, however, the maximum lateral range decreases from 310 naut mi to 200 naut mi when the entry angle is increased from 6.85^{o} to 7.6^{o}.

The requirement of returning to Edwards AFB from the parking orbit prior to injection can also be used to evaluate lateral maneuverability requirements. In Chapter III, this lateral range was shown to be on the order of 300 naut mi and would correspond to entry at satellite velocity. Figure IV-16 can be used to determine the L/D required using this criteron assuming no propulsion was available for this maneuver. From this figure, it can be seen that the minimum L/D to meet this requirement is 0.63.

D. RE-ENTRY VEHICLE STUDIES

The re-entry vehicle characteristics analyzed in this Chapter are stagnation point heating rates and load factor. Two modes of heating were considered, convective and radiative. These heating rates, as well as load factor, were obtained for several configurations re-entering along various corridor boundaries.

The load factors experienced by a vehicle re-entering the atmosphere at different locations in the corridor can be used as a measure of the vehicle's suitability as a re-entry configuration. Therefore, this information as a function of corridor depth was obtained for several re-entry vehicles. The configurations are shown in Fig. IV-23. The aerodynamic characteristics are summarized in Fig. IV-24. The effects of corridor depth on maximum aerodynamic heating rates and maximum load factor are summarized for each vehicle in Figs. IV-27 through IV-36. These figures have been called corridor maps and are applicable only to the initial portion of the trajectory, that is, from initial entry at 400,000 ft to approximately the point where flight path angle equals zero. The entry velocity in each case was 36,000 fps. The aerodynamic heating rates shown in these maps are convective, q_c, and radiative, q_r, experienced at a reference stagnation point. The equations used to calculate these heating rates are:

$$q_c = 0.61 \sqrt{\frac{\sigma}{R_n}} \left(\frac{V}{1000}\right)^{3.15} \quad \text{Btu/ft}^2\text{-sec}$$

$$q_r = R_n \left(\frac{E}{2}\right) \left(\frac{\Delta}{R_n}\right) \quad \text{Btu/ft}^2\text{-sec}$$

where: E = energy radiated from boundary layer (Ref 21)

Δ = shock wave standoff distance, ft

R_n = stagnation point nose radius, ft

σ = atmosphere density ratio

V = velocity, fps

For vehicles with hemispherical noses, the actual nose radius is used. Hence, the references q_c and q_r are the actual stagnation points q_c and q_r. When the vehicle does not have a hemispherical nose, as in the case of the Mercury and L-2-C configuration, then some fictitious nose radius is used. For Mercury and L-2-C, the radius of the circular plot for area is used. In this case the heating rates plotted do not represent actual heating rates existing on the vehicle. At $\alpha = 90^o$ the actual stagnation point heating rates are approximately 60% of the reference stagnation point values. These variations in reference nose radius, and the large differences in heating rate distribution around the vehicles, precluded the use of the stagnation point heating rates for comparing the different configurations. The principal value of the stagnation point heating rate was its use as an indicator to show the effects of corridor depth and re-entry technique on each vehicle. Stagnation point heating rates, therefore, were not used to compare the different configurations.

A comprehensive analysis of the aerodynamic heating investigation is presented in Ref. 22. Reference 22 describes the methods used and the estimated heating rate distributions over the entire re-entry vehicle. The total integrated heat loads for the entire trajectories using specific control techniques are also presented.

The aerodynamic load factor, η, was defined as:

$$\eta = \frac{\sqrt{L^2 + D^2}}{W}$$

where L = vehicle lift, lb

D = vehicle drag, lb

W = vehicle weight, lb

The magnitude, duration and orientation of the load factor determine the stresses imposed on the crew during re-entry. The maximum value of η is shown for each vehicle as a function of corridor depth for the different re-entry techniques on the corridor maps.

The total time that η exceeds 5g is also shown on these maps. This value of 5g was arbitrarily selected as being a representative number for load factor duration comparison, based on information regarding human tolerance to long time accelerations.

The load factor orientation angle is not shown. This angle varied througout many of the trajectories while the load factor was being held constant. For this reason, it was impossible to plot the orientation angle on the corridor maps. A complete analysis of load factor orientation and its effect is contained in Ref.3.

The absolute values of abscissas of the corridor maps are re-entry flight path angle at 400,000-ft altitude. A relative scale is also used to show corridor depth, measured from the positive $C_{L_{max}}$ overshoot boundary as defined in the introduction. This corridor depth serves as a basis of comparison of the several configurations and also of the relative merits of the different entry techniques for a given configuration.

The re-entry techniques previously referred to were different angle of attack programs. These programs may be divided into two types; constant angle of attack, and varied or modulated angle of attack. The constant angle of attack data was obtained for angles of maximum lift coefficient, $C_{L_{max}}$, and maximum lift-to-drag ratio, L/D. These attitudes provided minimum heating rates and minimum load factor, respectively, for constant angle of attack re-entries.

Lift modulation technique was described earlier in this chapter. Basically, this principle required a reduction in resultant force coefficient, C_R ($C_R = \sqrt{C_L^2 + C_D^2}$), as the dynamic pressure increased so that the load factor was maintained at a constant value. The amount of g reduction that can be realized is determined by the amount of change in C_R that can be accomplished. Increasing L/D increases the amount of change in C_R available. It has been shown in Ref.11 that modulation from $C_{L_{max}}$ provides the greatest reduction in load factor. Several modulation techniques were used. All of these techniques were initiated from the $C_{L_{max}}$ attitude. However, the degree of modulation was varied to obtain different results.

To achieve the minimum load factor, the lift was modulated from $C_{L_{max}}$ to $C_L = 0$. The maximum value of dynamic pressure was reached just as C_L was reduced to zero. This technique uses the full modulation capability of the vehicle and results in the minimum load factor obtainable for each entry angle. For the same entry angle, this gives higher values of stagnation heating rates than any of the other modulation techniques. The curves in Figs. IV-27 to IV-36 labeled "$C_{L_{max}}$ Mod to $C_L = 0$" show the results of this type of modulation.

The second type of modulation employed was very similar to the first. The difference was that the angle of attack reached at the maximum dynamic pressure was that for maximum (L/D). Using this technique required that the load factor held constant during modulation be somewhat higher than that when full modulation was used. The maximum heating rates were correspondingly lower than those for full modulation. This type of modulation is labeled "$C_{L_{max}}$ Mod to L/D_{max}".

The third type of modulation was somewhat less explicit than the first two. In this technique the vehicle was not modulated to any specific angle of attack, but to whatever value greater than zero was required to maintain a particular load factor. This type of modulation, shown only for the Model 410 and M-2 vehicles, is labeled "$C_{L_{max}}$ Mod to $C_L > 0$" on the corridor maps.

These three types of modulation are illustrated in Fig. IV-25.

The corridor map of the Model 410 is shown as Fig. IV-27. It is clear from this figure that modulation greatly increases the allowable corridor depth for a given maximum load factor. It can also be seen that for a given corridor depth modulation reduces the maximum heating rates below those for entries at (L/D) max as well as the maximum load factor. For this configuration, then, modulation capability could be used to very good advantage to reduce the severity of the re-entry for both the vehicle and the crew.

The M-1 corridor map (Fig. IV-28) shows only a small improvement in corridor depth could be gained through lift modulation. This was attributed to the relatively small reduction in resultant force coefficient, C_R, that could be achieved. This change in C_R was about 0.31 for the M-1 and 0.99 for the Model 410. The trend of the results, however, was the same as for the Model 410.

Figure IV-29 shows the corridor summary for the W-1 vehicle. The results, although not as complete as those for the Model 410 show that the two vehicles had very similar corridor characteristics. The W-1 maximum load factor was slightly higher than that for the Model 410 for unmodulated entries, but the maximum heating rates were slightly lower. This was a result of the difference in W/C_DA between the two vehicles. Modulation of the W-1 showed the same degree of reduction in load factor and heating rates compared to $(L/D)_{max}$ re-entry as it did for the Model 410.

The comparatively mild characteristics of the M-2 vehicle can be seen in Fig. IV-30. At the 30-naut mi corridor boundary, the maximum load factor could be held to a value less than 3g by modulation to $C_L = 0$. If modulation were continued only to $(L/D)_{max}$ the maximum load factor would be 4g and the heating rates would be much lower than those for a constant $(L/D)_{max}$ re-entry. The 6g maximum corridor is approximately 90 naut mi. It is doubtful, however, that the full corridor potential of this vehicle could be utilized. The

extreme increases in maximum heating rates beyond a 40 naut mi corridor would impose a severe heat shield design requirement for this vehicle.

The corridor map for the L-2-C vehicle is shown in Fig. IV-31. The constant $C_{L_{max}}$ 6G corridor is 18 naut mi and is 33 naut mi for a 10g limit. Only entries at constant $C_{L_{max}}$ are shown, since this represents the minimum g condition for the vehicle. This vehicle was limited in usable angle of attack to values between 55° and 90°, as shown in the sketch below, by heating of the afterbody structure. The 55° angle of attack limit represents both the maximum lift and the maximum lift-to-drag ratio attitude. In order to verify that the

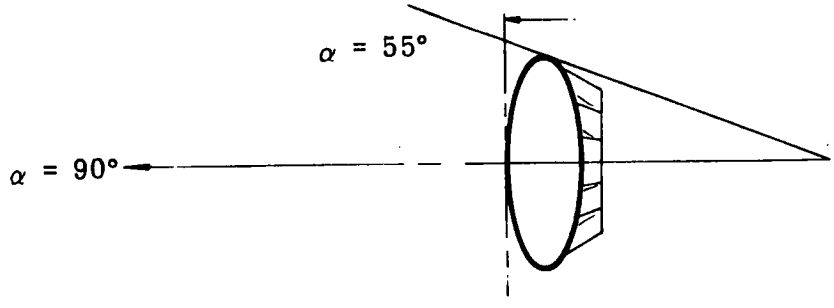

constant $C_{L_{max}}$ entry resulted in the deepest corridor for a given maximum load factor, entry trajectories using other techniques were computed.

Modulation has been shown to greatly increase the g-limited corridors of the other configuration. It was felt therefore that it should also provide an increase in corridor width for this vehicle. There is an important difference between the L-2-C and the other configurations, however. For the L-2-C the maximum resultant force coefficient does not occur at $C_{L_{max}}$. In fact, over the usable angle of attack range, C_R is a minimum at $C_{L_{max}}$ as shown in the following sketch. Since the whole point of modulation is to reduce C_R, it was obvious that modulation with the L-2-C could not begin at $C_{L_{max}}$. Full modulation would be defined as starting at some higher angle of attack and terminating at $C_{L_{max}}$. The problem then became one of finding the g-limited corridor width variation with variation in initial angle of attack. The g-limited corridors for modulation to $C_{L_{max}}$ from initial angles of attack of 80°, 70° and 60° were computed. The results, in Fig. IV-32, show that the constant $C_{L_{max}}$ attitude provides the deepest corridor, and that the corridor is decreased as initial angle of attack is increased.

This study was expanded to find the optimum initial angle of attack from which to begin modulation if the minimum angle of attack were reduced to 35°.

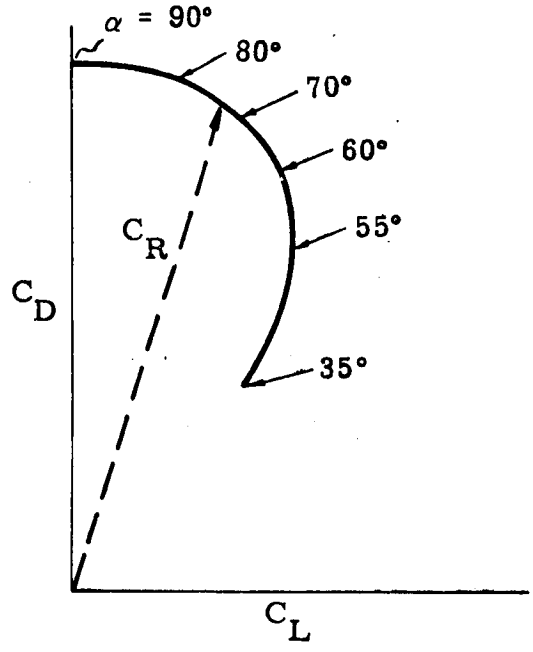

The study was conducted in the same manner as that for modulation to 55° angle of attack. The initial angle of attack was varied between 80° and 50°; full modulation was employed to 35° angle of attack. The results, presented in Fig. IV-33, show that modulation from $C_{L_{max}}$ provides the deepest corridor.

Only the minimum amount of data required to define the corridor limits of the L-1 configuration was determined. This data is shown in Figs. IV-34 and IV-35. This vehicle had characteristics very similar to the Model 410 and the W-1. The vehicle was not considered in further study because of balance problems.

The corridor map for the Mercury configuration is given in Fig. IV-36. This vehicle had characteristics similar to those of the L-2-C. The maximum allowable angle of attach of 21° provided a $(L/D)_{max} = 0.35$. This angle of attack was used to determine the vehicle corridor characteristics. Maximum allowable load factor limitations would impose very narrow corridor restrictions on this configuration. The 6 g limited corridor width would be about 12 naut mi, and a 30-naut mi corridor would result in a load factor that exceeded 11.5 g.

The data presented in the corridor maps afford many comparisons among the different vehicles and control techniques. Since the heating and load factor problems increase with increasing corridor, the most significant comparison would be made at the required corridor undershoot boundary. The present investigation has shown that a 30-naut mi corridor, measured from the

positive $C_{L_{max}}$ overshoot, would be required. A summary of the characteristics of the seven configurations employing different re-entry techniques is presented in Table 8 for re-entry on the 30-naut mi corridor boundary. When using this table, it should be remembered that the heating rates can be used only to compare the effects of different techniques for a particular vehicle. The load factor information can be used to compare the vehicles.

Some of the significant results shown in Table 8 are:

(1) All of the configurations exhibited the same general trends in increasing load factor and heating rates with increasing corridor depth.

(2) The maximum heating rates increased as the amount of modulation increased.

(3) Entries initially at $C_{L_{max}}$ (even when partially modulated) have lower maximum heating rates than entries at $(L/D)_{max}$.

(4) The maximum heating rate varied inversely with the maximum load factor.

(5) The M-1, L-2-C, and Mercury vehicles could not meet a 6g maximum load factor requirement at this corridor depth.

Table 9 was constructed to show the various corridor depths available for the different configurations and techniques, assuming a maximum allowable load factor of 6g. This table indicates the large 6g corridor potential available to the vehicles with the higher maximum lift-drag ratios.

The final study in this Section will determine the maneuvering capabilities of some of the configurations whose corridor characteristics have been analyzed.

TABLE 8

Summary of Vehicle Characteristics

(30-naut mi corridor)

TABLE 8

Vehicle	Re-entry Technique	η max (g)	Time that $\eta > 5$ g (sec)	q_c (Btu/ft^2-sec)	q_r (Btu/ft^2-sec)
Model 410	Constant $C_{L_{max}}$	8.9	32	480	100
	Constant $(L/D)_{max}$	6.5	20	625	290
	$C_{L_{max}}$ modulated to $(L/D)_{max}$	5.0	40	510	150
	$C_{L_{max}}$ modulated to $C_L = 0$	3.0	0	620	325
	6 g modulated	6.0	34	500	100
M-1	Constant $C_{L_{max}}$	9.0	30	400	120
	7 g modulated	7.0	40	404	120
W-1	Constant $C_{L_{max}}$	9.5	30	420	60
	Constant $(L/D)_{max}$	6.8	23	550	160
	$C_{L_{max}}$ modulated to $C_L = 0$	3.1 (est)	0	575 (est)	175 (est)
	$C_{L_{max}}$ modulated to $(L/D)_{max}$	5.6	40	460	80
	6 g modulated	6.0	37	440	75
M-2	Constant $C_{L_{max}}$	7.7	25	460	20
	Constant L/D	5.2	14	660	60
	$C_{L_{max}}$ modulated to $(L/D)_{max}$	4.1	0	520	40
	$C_{L_{max}}$ modulated to $C_L = 0$	2.0	0	800	220
	6 g modulated	6	33	490	25
L-2C	Constant $C_{L_{max}}$	9.2	26	260	170
L-1	Constant $C_{L_{max}}$	9.0	29	720	35
	$C_{L_{max}}$ modulated to $C_L = 0$	4.4	29	790	40
Mercury	Constant C_L	11.6	40	235	140

TABLE 9

Summary of Corridor Depths for 6 g max.

Vehicle	Re-entry Technique	Corridor Depth (naut mi)	Time that n_L >5g (sec)
Model 410	Constant $C_{L_{max}}$	18	15
	Constant (L/D)	27.5	16
	$C_{L_{max}}$ modulated to (L/D)max	37	41
	$C_{L_{max}}$ modulated to $C_L = 0$	56	89
M-1	Constant $C_{L_{max}}$	17	15
	$C_{L_{max}}$ modulated to $C_L = 0$	26	43
W-1	Constant $C_{L_{max}}$	17	23
	Constant (L/D) max	26	20
	$C_{L_{max}}$ modulated to (L/D) max	33	40
	C_{L}max modulated to $C_L = 0$	56 (est)	90 (est)
M-2	Constant $C_{L_{max}}$	22	20
	Constant L/D	35	17
	$C_{L_{max}}$ modulated to (L/D) max	49	40
	$C_{L_{max}}$ modulated to $C_L = 0$	93	63
L-2C	Constant $C_{L_{max}}$	18	12
L-1	Constant $C_{L_{max}}$	17	20
	$C_{L_{max}}$ modulated to $C_L = 0$	43	34
Mercury	L/D = 0.35	12	21

E. MANEUVERABILITY STUDIES

Maneuvering studies were conducted to determine the effects of different control techniques on maneuver performance and to determine the maneuver capabilities of three representative configurations employing these techniques. Several control techniques were investigated; they included both skip and non-skip trajectories. Maneuver capabilities were obtained for the Model 410 vehicle controlled by both skip and non-exit techniques, for the M-1 vehicle using a skip technique, and the M-2 using a non-skip technique.

Re-entry maneuverability requirements based on The Martin Company's Operational concept of the Apollo mission were evaluated in Section B of this chapter. These requirements were found to be functions of changes in the moon's declination for the longitudinal maneuverability and of errors in return trajectory arrival time and inclination for the lateral maneuverability. The expected errors in the return trajectory were shown to require a lateral range capability somewhat less than $\pm$ 100 naut mi. This is an inherent characteristic of the return trajectory, and was one of the factors that influenced the selection of this trajectory. The inclination of the return trajectory is approximately equal in magnitude to the latitude of Edwards AFB. As the vehicle approaches the landing site along the return trajectory, its flight path becomes tangent to this latitude so that large errors in return time must be experienced before any appreciable lateral maneuvering is required. The longitudinal re-entry range requirement was shown to vary from 3, 300 naut mi to 10, 000 naut mi depending on the moon's declination. When these figures were examined, it became apparent that any vehicle capable of satisfying the longitudinal requirements could more than meet the lateral requirements. However, it was considered necessary to determine the total lateral capability of the vehicle so that attainable alternate landing sites could be selected. A landing site capability would also show the largest errors in the return trajectory for which the vehicle was capable of correcting.

There are many factors that influence the maneuvering capability of a given vehicle of fixed L/D max. The more significant factors and a brief discussion of each is given below.

(1) A reduction in the maximum allowable load factor increases the minimum longitudinal range a vehicle can achieve. Load factor limits also decrease the allowable bank angle during re-entry. The decrease in allowable bank angle varies with corridor depth, but the influence on minimum range is independent of the re-entry corridor.

(2) The maximum allowable apogee altitude limits the maximum range of constant L/D skip trajectories. However, if lift and drag are varied to control exit conditions, the restriction on range is a function of the $(L/D)_{max}$ of the vehicle. The higher L/D's are less restricted than low L/D's.

(3) The minimum allowable dynamic pressure, dictated by a requirement for aerodynamic control, limits the maximum range of some classes of non-exit trajectories.

(4) Increasing corridor depth decreases the maximum range.

(5) The range control technique has a strong influence on the maximum longitudinal and lateral range capability and also on the minimum longitudinal range.

1. Influence of Range Control Techniques on Maneuver Performance

The influence of control technique on maneuver performance of the Model 410 was obtained for entry along the 40-naut mi corridor boundary. Several techniques were investigated. These techniques were divided into two general classes: (1) skip trajectories that exit the atmosphere after the initial entry phase, and (2) non-exit trajectories that may or may not skip. A skip trajectory is defined as one in which the flight path becomes positive at any time after initial entry.

No attempt was made in this study to control the vehicle to a specific range, and all effort was directed toward achieving maximum range while staying within the trajectory restraints. These restraints varied with the control technique. The control techniques were all "open loop," and as such were extremely sensitive to changes in the various control parameters.

The control techniques were selected early in the study. They are based on the re-entry criterion that initial entry would always be made at $C_{L\ max}$ and would be held constant until pullout at $\gamma = 0^{o}$ unless it is necessary to modulate to hold the load factor within specified limits. This criterion imposes some restriction on the maneuver capability since no maneuvering is allowed during the initial portion of the re-entry. The actual range control technique proposed in Ref. 4 is a slight modification of the above procedure. The difference is that range control is allowed during the initial portion of the entry as long as load factor remains within the specified limit.

The results of analog studies of this range control technique are reported in Ref. 4. Basically, Chapman's Z-function is used to solve for an L/D required to obtain a desired range. This solution is obtained every ten seconds, and a new value of L/D is computed. The technique is thus a form of "closed loop" control, with a constant value of L/D held until updated by a later solution. Using the Z-function solution, a prediction of maximum load factor is also obtained. If this value is greater than the allowable load factor, a solution is obtained for the minimum L/D that will keep the vehicle within the g-limits. This is the L/D value used until the next calculation.

The results of this analog study have led to the conclusion that this prediction of L/D, using Chapman's Z-function technique, is a practical means

of re-entry range control. Although the studies are by no means complete, the indications are that this method can be made to work satisfactorily.

2. Skip Trajectories

Range control of trajectories that skip out of the atmosphere was achieved by controlling the exit conditions. This could be compared to controlling the burnout conditions of an ICBM to achieve a given range. The velocity and flight path angle at exit determine the range during the skip to the second entry. The vehicle L/D and entry conditions (velocity and flight path angle) determine the range from this point to touchdown. The exit conditions also control the apogee altitude. The maximum allowable altitude was 400 naut mi.

Two techniques were used to vary the effective aerodynamic characteristics to control the exit conditions: roll control and angle of attack variation.

A "two-roll procedure" was adopted, involving two, properly timed, 180^{o} rolls to control the exit conditions to provide longitudinal range control as well as apogee altitude control. By using roll angles other than 180^{o}, this procedure could also be used to give lateral range control. If the roll angle were less than 90^{o}, then only one roll would be required; this technique is called simply "roll control."

The effect of rolling the vehicle is to change the trajectory by changing the vertical component of L/D. If no lateral range is required, the roll angle can be changed from plus to minus the desired value to cancel out any tendency to maneuver out of the re-entry plane. It should be pointed out that using either of the roll procedures does not change the effective (W/C_DA) of the vehicle.

The second technique--angle of attack variation--requires one or two step changes as in the roll procedures. For corridor depths less than 30 naut mi and vehicle (L/D)'s > 0.35, negative lift is required. Under these conditions a 180^{o} roll, combined with the angle of attack change, was used. In cases where the angle of attack change was large, a correspondingly large change in (W/C_DA) was experienced. When these changes in angle of attack were made at velocities much greater than satellite, the change in (W/C_DA) had more influence on range than the change in (L/D).

3. Non-exit Trajectories

The non-exit range control techniques had the one principal advantage of being able to use aerodynamic control from the initial re-entry to initiation of the recovery procedure. The main disadvantage of this procedure is that a severe maximum range penalty is imposed on vehicles with relatively low (L/D)'s.

Two fundamentally different non-exit control techniques were considered. The first is actually a skip that does not go above the atmosphere. These skips

were controlled so that an equilibrium glide trajectory was intercepted just past apogee, if possible. If the velocity and altitude conditions were such that an equilibrium glide could not be achieved, a glide with oscillatory characteristics was experienced. The maximum range with this control technique is dependent only on $(L/D)_{max}$ and corridor depth. The control procedure is the same as for the exit skip trajectory--either roll or angle of attack variation.

The maximum altitude allowed for these trajectories was approximately 300,000 feet. The upper limit on altitude was in reality a lower limit on dynamic pressure, imposed by aerodynamic control considerations. This altitude limit has a very strong influence on maximum range. If the maximum altitude were reduced to 250,000 feet, the maximum attainable range with the Model 410 dropped from 10,000 naut mi to approximately 5500 naut mi for re-entries along the 30-naut mi corridor.

The second non-exit trajectory was called "constant altitude glide." As the name implies, the pullout altitude is held constant as the vehicle decelerates to a desired glide velocity. The constant altitude portion is followed by a constant (L/D) glide. Since the pullout altitudes were generally around 200,000 feet ($\pm$ 30,000 ft), the vehicle decelerated fairly rapidly. The rapid deceleration results in large reductions in maximum range from those attainable with the other technique.

4. The Maneuver Performance of Three Configurations

The maneuver performance of the Model 410 was obtained for several trajectory control techniques. Both skip and non-exit range control methods were employed.

The re-entry conditions at the positive lift overshoot boundary and at the 40-naut mi undershoot boundary were used in order to determine the effects of re-entry angle on the maneuvering capability.

On the undershoot boundary, four techniques for obtaining lateral range were evaluated. Three of these techniques were employed in such a manner as to keep the vehicle in the atmosphere.

On the overshoot boundary, only one technique was investigated.

For both the undershoot and overshoot trajectories, the following restrictions were placed on the maneuvering techniques:

(1) Initial entry was at $C_{L\,max}$ attitude (regardless of bank angle), and angle of attack was modulated as necessary to hold maximum load factor equal to 10g.

(2) The pitch attitude was shifted to that for $(L/D)_{max}$ as soon as possible, considering load factor and apogee altitude limits.

The re-entry conditions at the 40-naut mi undershoot boundary were:

V_E = 36,000 fps

γ_E = -8^o

h_E = 400,000 ft

The four non-exit range control techniques employed at this re-entry angle are described below.

Technique 1. This is a constant bank angle turn resulting in trajectories that skip. The bank angle was restricted to values between 50^o and 80^o to keep the apogee altitude within the atmosphere and the maximum load factor less than 10g. The time at which C_L is changed to $(L/D)_{max}$ is very important, and in order to get maximum capability, it is necessary to shift to $(L/D)_{max}$ as soon as possible. This time was determined by trial and error procedure.

Technique 2. Here the initial re-entry is made in an unbanked attitude. At the bottom of the pullout (γ = 0), C_L is shifted to $(L/D)_{max}$, and at the same time various roll angles are assumed from 45^o to 80^o. Since the 80^o

roll resulted in an apogee altitude of 345,000 ft, this trajectory was selected for continued study. The roll angle at this point (h = 345,000 ft) was changed to values between 0^{o} and 80^{o} and then held constant to impact.

Technique 3. Initial re-entry is the same as technique 2; however, at γ = 0^{o}, a constant altitude turn is initiated at $(L/D)_{max}$. Bank angle is varied as a function of velocity to maintain a constant altitude. From various positions along this turn, trajectories were calculated for continuations at the appropriate constant bank angle. Trajectories were also computed for continuations from these points with zero bank angle.

Technique 4. This is the same as technique 1, except that the apogee altitude limit is raised to 400 naut mi, and the bank angle restrictions are somewhat eased.

The results obtained from these four range control techniques on the 40-naut mi undershoot boundary are shown in Fig. IV-37. This figure shows the variation of maximum lateral range with longitudinal range measured from the re-entry point. The enclosed region represents the total landing site capability of the vehicle at this re-entry condition.

It is readily apparent that technique 4 gives the greatest landing site flexibility. This is due to both a greater maximum lateral range and a greater variation in longitudinal range. The maximum lateral range was approximately $\pm$ 1,000 naut mi. Lateral ranges of $\pm$500 naut mi could be achieved as far downrange as 10,000 naut mi.

Of the non-exit methods, technique 1 provides much greater maneuver performance than the other two. The maximum lateral range was approximately $\pm$ 900 naut mi, and the maximum longitudinal range was 5,400 naut mi.

The re-entry conditions at the overshoot boundary were

$$\gamma_E = -5.3^{o} \text{ for } V_E = 36,000 \text{ fps at } 400,000 \text{ ft.}$$

The only technique investigated for this condition was the constant altitude turn. The method was the same as technique 3 used for the 40-naut mi undershoot corridor with one exception. It was necessary to delay the shift to $(L/D)_{max}$ since C_L at $(L/D)_{max}$ was not large enough to maintain constant altitude immediately upon reaching the pullout altitude even at an inverted attitude.

The maneuvering envelope utilizing this technique on the overshoot boundary is shown in Fig. IV-38. It is of interest to note that the maximum lateral range is only $\pm$100 naut mi greater than that at the 40-naut mi undershoot

boundary, using the same technique. However the longitudinal range control is greater by a factor of four (ΔR = 5,600 naut mi versus 1,400 naut mi).

The results of a study of the M-1 maneuver capability are presented in Fig. IV-39. Results for entries at both 35,000 fps and 36,000 fps are included. Figure IV-39(c) shows the lateral displacement capability of the M-1 for re-entry at constant roll angles held from 400,000 ft to landing. Figure IV-39(b) shows the roll angles which could be held without exceeding a load factor of 10 g during re-entry at 35,000 fps as a function of the initial re-entry angle at 400,000 ft. Maximum lateral range was 550 naut mi, occurring at a roll angle of about 45^{o}.

Maneuvering from the 40-naut mi undershoot boundary ($\gamma_E = -7.75^{o}$) was not begun until the peak load factor was passed. No lift modulation was employed. Figure IV-39(d) shows the lateral displacement obtained for various roll angles initiated at pullout ($\gamma = 0^{o}$). Maximum load factor of 10g is experienced prior to pullout and is not exceeded during the constant roll condition after $\gamma = 0^{o}$. Maximum lateral range from the 40-naut mi undershoot boundary is about 450 naut mi.

Maneuverability for entry on the 30-naut mi corridor ($\gamma_E = -7.4^{o}$) is shown in Fig. IV-39(e). A roll angle of 45^{o} was permissible prior to peak load factor (10g) for entry at this corridor depth. The maximum lateral range was only about 50 naut mi greater than that obtained on the 40-naut mi corridor boundary, although the maximum longitudinal range was increased considerably. The effect of the 1000-fps re-entry velocity increase is clearly shown in this figure.

A very limited study was made of the lateral range capability of the M-2. Only two trajectories were calculated, and both of these were constant altitude turns. The difference between the two trajectories was the vehicle's angle of attack during the initial entry. The entry conditions were a velocity of 35,000 fps and a flight path angle of -7.9^{o}. This corresponds roughly to a 40-naut mi corridor position.

A $C_{L\,max}$ attitude was assumed during the initial entry of the first trajectory. At the bottom of the pullout, the angle of attack was changed to give $(L/D)_{max}$, and the bank angle was varied to maintain the altitude constant. After the bank angle was reduced to zero, a constant (L/D) glide was followed to touchdown. The longitudinal range to impact for this trajectory was about 2250 naut mi and the lateral range was 1250 naut mi.

The second trajectory was computed at an $(L/D)_{max}$ attitude during the initial entry. The procedure for the constant altitude turn and glide to touchdown were the same as the first trajectory. The results of this trajectory show a longitudinal range of 1600 naut mi and a lateral range of 1150 naut mi.

It may seem unusual that the entry at $(L/D)_{max}$ did not have the greater range. The explanation lies in the second phase of the trajectory where the constant altitude turns were accomplished. The deceleration during constant altitude flight exerts the main control on the maximum range. Since the $C_{L_{max}}$ entry pulled out at a higher altitude than the $(L/D)_{max}$ entry the reduced density resulted in lower deceleration (the C_D for both trajectories was the same during this phase) for the higher altitude trajectory. Consequently, the trajectory flown at the higher altitude had the greater range.

A summary of longitudinal range capability for constant L/D re-entries at 36,000 fps is presented in Fig. IV-40 for the Mercury configuration, the M-1, and the Model 410. Range as a function of corridor depth is shown for three constant values of L/D. The effects of g-modulation on the M-1 and the Model 410 re-entry range are also shown. This g-modulation should not be classified as a range control technique; its purpose is to limit the maximum load factor. The constant L/D = 0.5 curve applies to both the M-1 and the Model 410 at $C_{L_{max}}$. The differences in $\frac{W}{C_D A}$ between these two vehicles at the $C_{L\ max}$ attitude was considered negligible (62.5 for the M-1 and 73 for the Model 410).

Lines of constant load factor are shown in Fig. IV-40, that are applicable to the constant L/D entries. A 400-naut mi apogee altitude limit line is also included in the figure. For ranges less than the values on this line, the apogee altitude is less than 400 naut mi.

The configuration parameters are summarized in the following table.

Vehicle	L/D	$\frac{W}{C_D A}$ psf
Mercury	0.35	36
M-1	0.5	62.5
Model 410	0.5	73
	0.73	156

Figure IV-40 shows that the Mercury configuration (L/D = 0.35) has a maximum range of approximately 2500-naut mi on the 30-naut mi undershoot boundary. In order to have a 10,000 naut mi range capability, the corridor width must be reduced to about 18 naut mi. At this narrower corridor boundary, the maximum load factor exceeds 8g.

The M-1 range capability is given by the curves labeled "L/D = 0.5" and "7-G Mod". The constant L/D = 0.5 curve shows that on the 30-naut mi corridor boundary this vehicle can achieve a range of approximately 15,000

naut mi. However, the maximum load factor is 9g. When the lift is modulated to hold 7g, the range is reduced considerably so that the maximum range on the 30-naut mi corridor boundary is only about 7500 naut mi. Very close to full modulation is necessary to hold 7g at the 30-naut mi corridor boundary. Because the $C_{L_{max}}$ attitude is also the attitude for L/D_{max} for the M-1, modulation reduces the L/D. This reduction in L/D is the cause of the reduction in range when modulation is employed.

As noted previously, the curve for L/D = 0.5 is also applicable to the Model 410 entering at a constant $C_{L_{max}}$ attitude. Modulation of this vehicle, however, produces significantly different results from that of the M-1. Modulation from $C_{L_{max}}$ initially increases the L/D of the Model 410 so that the range is increased compared to constant $C_{L_{max}}$ entries at the same corridor depth. The 6-g Mod curve shows that the maximum range on the 30-naut mi corridor is in excess of 20,000 naut mi, and that 10,000 naut mi can be achieved for entries on a 50-naut mi corridor boundary while limiting the maximum load factor to 6 g.

The maximum range of the Model 410 entering at a constant L/D_{max} is shown by the curve labeled "L/D = 0.73." It can be seen from this curve that the maximum range at the 30-naut mi undershoot boundary is 24,000 naut mi, and that 10,000 naut mi could probably be achieved for corridor depths greater than 60 naut mi.

All studies to date have been made on the basis of a non-rotating earth. The effects of the earth's rotation can be separated into two areas. The first area would be those effects that influence the corridor studies, and the second would be those that influence the maneuverability studies.

The 35,000-fps velocity used to determine the effect of entry velocity was obtained by subtracting a velocity component due to earth's rotation (approximately 1200 fps) from the nominal return perigee velocity (36,200 fps).

The normal re-entry will be in a generally West to East direction and the effect of the moving atmosphere would be to decrease the magnitude of the aerodynamic forces encountered. Similarly, the maximum heating rates would also be reduced. Some examples of the reductions that might be expected are shown in the table below, where the maximum heating rates and load factors encountered by the M-1 vehicle entering at a constant $C_{L_{max}}$ attitude are shown.

γ_E	V_E	g_{max}	$q_{c_{max}}$	$q_{r_{max}}$
-7.3	35,000 fps	8.3	364	95
-7.3	36,000	8.45	390	117

The effect of the earth's rotation on range was found to be insignificant for a constant inertial velocity. The range relative to a target on the earth's surface will be reduced by an amount proportional to the return trajectories inclination and time elapsed during entry.

However, the lower decelerations experienced during re-entry with the rotating atmosphere would tend to increase the inertial range. The effect of these two phenomena is to give practically no change in range. The lateral range covered will either be increased or decreased, depending on whether maneuvers are made to the right or left of the entry trajectory. The effect would be to warp the maneuver envelope without changing the overall lateral dimensions.

During this study, considerable effort was required to obtain re-entry trajectories with certain desired characteristics. An example of this is the maneuverability study described previously. Arbitrary control programs were selected to give maximum range. These selections were further complicated by the necessity to keep the trajectories within certain constraints regarding load factor and maximum apogee altitude. It became apparent that a trajectory optimization program to solve these problems was not only desirable but was actually mandatory if further effort were to be continued in this area. The initial steps have been taken to obtain this capability. A re-entry trajectory optimization program is currently being programmed for the IBM 7090 computer (see Appendix D).

This program will determine an angle of attack time history that will maximize or minimize the heat input to the vehicle while satisfying the following constraints:

(1) Acceleration levels remain within specified duration limits.

(2) Trajectory terminates at a specified range.

(3) Trajectory remains below a specified altitude limit.

(4) Dynamic pressure remains above a specified minimum value.

The direct variational method of optimization was selected because of its accuracy and the short computation time required. It is felt that with this trajectory optimization capability, the re-entry analysis will be greatly facilitated.

From such a program, the exact control program required to produce a desired trajectory would be obtained. Not only could the maximum and minimum heat inputs be determined for any location on the vehicle and any re-entry range, but information regarding maximum range could also be obtained. The control program to maximize range for any given vehicle could be determined. The resulting trajectories would remain within the specified constraints.

* * *

A comprehensive analysis of the re-entry phase of the return trajectory has been made. This analysis has included parametric studies as well as studies of particular vehicles. The important results determined by these studies are listed below:

(1) The re-entry corridor width is independent of $W/C_D A$ if $W/C_D A$ is the same for both overshoot and undershoot.

(2) The positive lift and negative lift overshoot boundaries are dependent only on $W/C_L A$.

(3) Lift provides large increases in the g-limited corridor widths. Modulating the lift provides even greater increases in this corridor.

(4) Longitudinal range requirements are dependent on the return trajectory. For the selected operational concept of return to Edwards AFB along a 35^o inclination trajectory, the range requirement is shown to vary between 3300 and 10,000 naut mi depending on the moon's declination.

(5) Lateral range requirements imposed by the return trajectory are dependent on errors in trajectory inclination and arrival time. This requirement is shown to be on the order of $\pm$ 100 naut mi.

(6) To obtain the 10,000-naut mi longitudinal range from re-entry requires a $L/D \approx .45$.

(7) The lateral range required to return to Edwards AFB from the parking orbit prior to injection is 300 naut mi and requires a vehicle with a $(L/D_{max} \simeq .63$.

(8) Lift-to-drag ratio is the principal parameter that influences the size of the maneuvering envelope.

(9) Increasing corridor width has strong effect on the maneuver envelopes of vehicles with (L/D)'s < 0.4.

(10) The corridor maps of all configurations studied show the same trend of increasing maximum load factor and maximum heating rate with increasing corridor depth.

(11) Entries at $C_{L_{max}}$ result in the lowest maximum heating rates.

(12) Entries at $(L/D)_{max}$ result in the lowest maximum load factors.

(13) Lift modulation can be used to decrease the maximum load factors encountered. It also provides lower heating rates than entries at $(L/D)_{max}$.

(14) Three of the configurations studied (M-1, L-2C, and Mercury) cannot hold the maximum allowable load factor to 6g on the 30-naut mi corridor boundary.

(15) Modulation of the L-2C does not increase the g-limited corridor width for a given allowable load factor.

(16) Skip trajectories give larger maneuver envelopes than any of the other range control techniques studied.

(17) For non-exit trajectories, lowering the maximum altitude reduces the maximum range.

(18) The maneuver envelope of the Model 410 vehicle entering on the 40-naut mi corridor boundary at 36,000 fps has dimensions of $\pm$ 1,000-naut mi lateral range and about 17,000-naut mi longitudinal range. The maneuver envelope of the M-1 for these same conditions is $\pm$500-naut mi lateral range and 13,000-naut mi longitudinal range.

(19) Increasing entry velocity from 35,000 fps to 36,000 fps does not affect maximum lateral range. However, large increases in longitudinal range are noted.

V. OPERATIONAL CONCEPT

A relatively simple and practical operational concept has been developed. Incorporating desirable trajectory characteristics, the concept takes account of the use of existing facilities where possible for the launching, return base, and tracking during flight, particularly during the critical injection into translunar orbit and re-entry phases.

A single launch facility, Cape Canaveral, will always be used. The vehicle will be launched down the Atlantic Missile Range (AMR) and injected into a parking orbit at 650, 000 ft. The vehicle will continue in this parking orbit until it is over the Pacific Missile Range (PMR), where injection into the translunar orbit will take place. The injection point will be determined by the moon position, relative to earth, at which periselenium is desired. For circumlunar trajectories, the vehicle will travel to the moon and return on a nominally ballistic path inclined to the equatorial plane by 35^{o}. The periselenium altitude (i. e., time of flight) will be such that the vehicle will return and re-enter up the PMR and always land at Edwards Air Force Base.

For lunar orbit missions, the vehicle will travel an identical trajectory, where possible, and be injected into lunar orbit at or near periselenium at approximately 250 naut mi. If a lunar orbit cannot be initiated, the vehicle will return to earth along a ballistic trajectory and land at Edwards Air Force Base. If a lunar orbit is established, an orbital transfer will be made to the desired lunar orbit altitude. Ejection from lunar orbit will be such that a free return will be made to Edwards Air Force Base along a trajectory inclined 35^{o} to the equatorial plane.

There are many advantages to such an operational concept. The trajectories from launch to injection and from re-entry to landing will be identical for all days of the lunar month except for the ground ranges covered. The ground track of these trajectories will travel the AMR and PMR ranges where excellent tracking facilities are already in existence or planned. The major portions of the launch, parking orbit, and re-entry and return to base will be over water, removing the danger of dropping parts of the booster on land masses.

If an abort is necessary during the launch into parking orbit, the spacecraft will return to earth on the AMR. If the mission must be aborted during the parking orbit (due to unsuccessful equipment checkout, for instance), the spacecraft can return to Edwards Air Force Base unless immediate re-entry is required. If an immediate re-entry is called for, it will be along the PMR. Thus, the possibilities of hitting undesirable land masses with either portions of the booster or with the spacecraft in the event of an abort are minimized.

The lunar trajectory characteristics dictated by the operational concept have been a significant factor in the choice of the operational concept.

Factors such as radiation hazards, launch time tolerances and relative ease of returning to a given return base must all be included.

The operational concept trajectories are all designed to leave the earth through the northern hole in the Van Allen belts. Translunar trajectories with inclinations to the equatorial plane of 29° have been established as the minimum inclination allowed. Trajectories which reach the moon when it is at its maximum southern declination will pass through the hole, while trajectories which reach the moon when it is at its maximum northern declination will pass through the fringes of the Van Allen belts.

The major portion of the launch time tolerance will be obtained by modifying the translunar trajectory orbital plane inclination. This will be done by changing the launch azimuth from 99.5° to 110° as the vehicle is delayed on the pad. This results in parking orbit and translunar trajectory plane inclinations varying from 29° to 34.2°. The launch time tolerance obtained in this fashion varies from approximately 10 minutes when the moon is at the most northerly declination to 3.4 hr when the moon is at its most southerly declination. This technique puts no additional burden upon the booster since special ascent trajectory shaping and orbit inclination changes in flight are not necessary.

Both the radiation and launch time tolerance become closer to marginal as the moon approaches its most northerly declination. Both problem areas might be removed by moving the injection point to the Southern Atlantic Ocean region for times of the lunar month when the moon is at its northern declinations. The translunar trajectory would then pass through the southern hole in the Van Allen belts. The launch time tolerance for injection points in this region ranges from 10 minutes with the moon at its maximum southern declination to 3.4 hr with the moon at its most northern declination.

There are several reasons why this apparently simple fix was not incorporated into the operational concept for early manned lunar journeys. To launch in this region means either a very short parking orbit or a parking orbit which travels about the earth approximately 1.25 times. In the first case, the parking orbit would not be long enough to perform a reasonable systems checkout (Ref. 3). If the parking orbit were extended to 1.25 orbits, the earth rotation during the orbit would remove the AMR ground tracking facilities from the injection point into lunar orbit.

Another reason for restricting the injection points to the Pacific Ocean region is the available altitude range at periselenium. With the injection point in the Pacific Ocean region, the required periselenium altitudes for circumlunar flights are restricted to approximately 250 naut mi or 2100 naut mi. This is a result of the variation of total flight time with periselenium altitude as shown in Fig. V-1. The time must be controlled so that the landing base will be rotated to a position under the transearth trajectory after re-entry. A typical required periselenium altitude as a function of the day of the lunar month is presented in Fig. V-2 for injection points in the Pacific Ocean region.

Injection in the Atlantic Ocean region would require periselenium altitudes of approximately 700 naut mi if the vehicle were to return to Edwards Air Force Base.

The use of translunar trajectories which pass through the southern hole in the Van Allen belts has both advantages and disadvantages. The suggested operational concept restricts the injection points to the Pacific Ocean region, but recognizes that later flights might very well use the south-bound translunar trajectories to advantage.

The transearth trajectory will nominally return to earth up the PMR with an inclination of 35° to the equatorial plane. A landing will be made at Edwards Air Force Base after coasting from re-entry approximately 3500 to 10, 000 naut mi (Fig. V-3), depending upon the day of the lunar month and the accuracy of the total trip time. The 35° inclination was chosen to increase the flexibility of the transearth orbit time. A variation of 50 minutes is available without exceeding a lateral maneuverability requirement of approximately 20 naut mi at Edwards Air Force Base.

Typical trajectories for four days of the lunar month have been determined, using the "volume of influence" results. and are shown as ground traces in Figs. V-4 to V-7. The initial conditions used to obtain these trajectories and the comparison to the "volume of influence" results are shown in Tables 7 through 10. Again, the usefulness of the technique is demonstrated. The final trajectories shown have not been carried through to complete correlation as yet. But the results are close enough to give satisfactory trajectories, and final trajectories could be obtained with one or two more iterations.

This operational concept makes full use of existing or planned launch, return base and tracking facilities. The same launch trajectory is used regardless of the day of the lunar month, and the return trajectory to Edwards Air Force Base is unchanged. An adequate launch time tolerance is available throughout the lunar month and does not impose any penalty on the booster requirements. The hot regions of the radiation belts will be avoided during both the translunar and transearth trajectories. Finally, the return trajectory is flexible enough so that a landing at Edwards AFB is possible even with relatively large return time errors. The concept is simple and flexible, and gives the early astronaut even higher chances of success.

CONFIDENTIAL

CONFIDENTIAL

TABLE 10

Comparison of VOICE Trajectory with Integrated Trajectory

(moon position: approximate maximum southerly declination)

	Item	VOICE	Integrated Trajectory 1st	2nd	3rd
At Injection into Translunar Orbit	Altitude (ft)	760,000	760,000	760,000	
	Velocity	35807.151	35808.348	35803.055	
	Flight path angle (deg)	3.0	3.0	3.0	
	*Inclination to moon's orbital plane (deg)	15.	15.	15.	
	Injection position (ψ) (deg)	13.735	13.735	13.474	
	Moon lead angle (ϕ) (deg)	234.0137	234.0137	234.6418	
	Longitude (deg)	166.12W	166.12W	166.40W	
	Latitude (deg)	32.02N	32.02N	31.95N	
At Moon	Periselenium altitude (naut mi)	243.0	151.0	240.0	
At Transearth Orbit Vacuum Perigee	Altitude (ft)	150,000	468,000	150,000	
	Total flight time (hr)	141.65	139.58	141.40	
	Inclination to moon's orbital plane (deg)	14.21	19.51	16.86	
	Inclination to equatorial plane (deg)	35.02	35.00	36.97	
	Longitude (deg)	163.00W	164.80W	158.0W	
	Latitude (deg)	24.11N	24.27N	23.0N	
	Direction of return	Direct from south			

*All translunar orbits inclined 35^{o} to Equatorial plane

TABLE 11

Comparison of VOICE Trajectory with Integrated Trajectory

(moon position: approximate descending node)

	Item	VOICE	Integrated Trajectory 1st	2nd	3rd
At Injection into Translunar Orbit	Altitude (ft)	760,000	760,000	760,000	
	Velocity	35807.600	35808.800	35804.715	
	Flight path angle (deg)	3.0	3.0	3.0	
	*Inclination to moon's orbital plane (deg)	7.5	7.5	7.5	
	Injection position (ψ) (deg)	13.723	13.723	13.467	
	Moon lead angle (ϕ) (deg)	-16.7800	-16.7800	-16.2431	
	Longitude (deg)	124.62E	124.62E	124.42E	
	Latitude (deg)	7.60S	7.60S	7.75S	
At Moon	Periselenium altitude (naut mi)	235.0	160.0	219.0	
At Transearth Orbit Vacuum Perigee	Altitude (ft)	150,000	-450,000	175,000	
	Total flight time (hr)	141.53	139.32	141.00	
	Inclination to moon's orbital plane (deg)	9.41	12.30	14.80	
	Inclination to equatorial plane (deg)	36.53	38.98	41.24	
	Longitude (deg)	135.08E	167.23E	141.20E	
	Latitude (deg)	20.16S	21.00S	20.73S	
	Direction of return	Direct from south			

*All translunar orbits inclined 35° to Equatorial plane

CONFIDENTIAL
MA 12009

TABLE 12

Comparison of VOICE Trajectory with Integrated Trajectory

(moon position: approximate maximum northerly declination)

	Item	VOICE	Integrated Trajectory 1st	2nd	3rd
At Injection into Translunar Orbit	Altitude (ft)	760,000	760,000		
	Velocity	35807.706	35808.398		
	Flight path angle (deg)	3.0	3.0		
	*Inclination to moon's orbital plane (deg)	30.	30.		
	Injection position (ψ) (deg)	13.752	13.752		
	Moon lead angle (ϕ) (deg)	54.1178	54.1178		
	Longitude (deg)	102.71E	102.71E		
	Latitude (deg)	21.65S	21.65S		
At Moon	Periselenium altitude (naut mi)	260.0	192.0		
At Transearth Orbit Vacuum Perigee	Altitude (ft)	150,000	192,000		
	Total flight time (hr)	141.80	140.19		
	Inclination to moon's orbital plane (deg)	31.99	35.58		
	Inclination to equatorial plane (deg)	35.23	36.99		
	Longitude (deg)	105.59E	130.0E		
	Latitude (deg)	29.98S	28.50S		
	Direction of return	Direct from south			

*All translunar orbits inclined 35° to Equatorial plane

TABLE 13

Comparison of VOICE Trajectory with Integrated Trajectory

(moon position: approximate ascending node)

	Item	VOICE	Integrated Trajectory 1st	2nd	3rd
At Injection into Translunar Orbit	Altitude (ft)	760,000	760,000	760,000	
	Velocity	35808.863	35808.863	35807.485	
	Flight path angle (deg)	3.0	3.0	3.0	
	*Inclination to moon's orbital plane (deg)	63.3	63.3	63.3	
	Injection position (ψ) (deg)	13.824	13.824	13.724	
	Moon lead angle (ϕ) (deg)	124.29339	124.32339	124.584	
	Longitude (deg)	141.78E	141.78E	141.71E	
	Latitude (deg)	5.27N	5.27N	5.21N	
At Moon	Periselenium altitude (naut mi)	273.0	78	272.0	
At Transearth Orbit Vacuum Perigee	Altitude (ft)	150,000	400,000	151,000	
	Total flight time (hr)	141.56	137.33	141.30	
	Inclination to moon's orbital plane (deg)	63.43	46.62	67.0	
	Inclination to equatorial plane (deg)	35.3	---	38.5	
	Longitude (deg)	153.24E	---	154.0E	
	Latitude (deg)	6.05S	---	7.2S	
	Direction of return	Direct from south			

*All translunar orbits inclined 35° to Equatorial plane

VI. REFERENCES

1. "Saturn C-1 and C-2 Booster Systems, "NASA Project Apollo Working Paper No. 1002, 9 November 1960.

2. "Mechanical Systems," Apollo Final Report, Martin ER 12005-1, June 1961, CONFIDENTIAL.

3. "Life Sciences," Apollo Final Report, Martin ER 12008-2, June 1961, CONFIDENTIAL.

4. "Guidance and Control System," Apollo Final Report, Martin ER 12007-2, June 1961, CONFIDENTIAL.

5. "Investigation of the Explosive Characteristics of RP-1 and Liquid Oxygen," Martin-Denver Report, 10 September 1959.

6. "Nuclear Safety Test Report for the Task II Thermoelectric Generator," Martin MND P-2357.

7. "Aerodynamics," Apollo Final Report, Martin ER 12017, June 1961, CONFIDENTIAL.

8. "Onboard Propulsion," Apollo Final Report, Martin ER 12009, June 1961, CONFIDENTIAL.

9. Chapman, D. R., "An Analysis of the Corridor and Guidance Requirements for Supercircular Re-entry into Planetary Atmospheres," NASA TR-55, August 1959.

10. Chapman, D. R., "An Approximate Analytical Method for Studying Entry into Planetary Atmospheres," NASA TR-11, 1959.

11. Grant, F. C., "Modulated Entry," NASA TN D-452, August 1960.

12. Phillips, R. L., Cohen, D. B., "Use of Drag Modulation to Reduce Declaration Loads During Atmosphere Entry," ARS Journal, p. 414, June 1959.

13. Wong, T. J., Goodwin, G., and Slye, R., "Motion and Heating During Atmosphere Re-entry of Space Vehicles," NASA Joint Conference on Lifting Manned Hypervelocity and Re-entry Vehicles, April 11-14, 1960.

14. Michael, W. H., Jr., Crenshaw, J. W., "Trajectory Considerations for Circumlunar Missions," IAS Paper 61-35, IAS 29th Annual Meeting, New York, January 23-25, 1961.

15. Chapman, D. R., "An Approximate Analytical Method for Studying Entry into Planetary Atmospheres,"NASA RE R-11, 1959.

16. Slye, R. E., "An Analytical Method of Studying the Lateral Motion of Atmosphere Entry Vehicles," NASA TN D-325.

17. "Manned Lunar Vehicle System," Martin ER 11245M.

18. "Interim Summary Report on Re-entry Trajectory Analysis," Apollo Midterm Review, Martin TM-30.

19. Unpublished Martin data.

20. Unpublished NASA data.

21. Kivel, B., "Radiation from Hot Air and its Effects on Stagnation-Point Heating," Journal of Aerospace Sciences, February 1961.

22. "Aerodynamic Heating." Apollo Final Report, Martin ER 12006, June 1961, CONFIDENTIAL.

VII. ILLUSTRATIONS

Figure	Title	Page
II-1.	Reference Ascent Trajectory	VII-11
II-2.	Time in Parking Orbit and Range to Injection	VII-12
II-3.	Payload Loss Versus Launch Azimuth	VII-13
II-4.	Burnout Velocity Loss Versus Burnout Flight Path Angle	VII-14
II-5.	Little Joe I Characteristics	VII-15
II-6.	Saturn C-1 Capabilities	VII-16
II-7.	Angle of Attack Versus Time During Abort	VII-17
II-8.	Abort Performance off the Pad	VII-18
II-9.	Effect of Drogue Chute Deployment During Abort	VII-19
II-10.	Abort Trajectory Time History	VII-20
II-11.	Abort Trajectory Time History	VII-21
II-12.	Effect of 40-fps Headwind on Abort Trajectory	VII-22
II-13.	Effect of 40-fps Tailwind on Abort Trajectory	VII-23
II-14.	L-2C Configuration Abort Trajectory	VII-24
II-15.	Model 410 Escape Trajectory at Maximum q	VII-25
II-16.	Load Factor and q During Maximum q Abort	VII-26
II-17.	Escape at Maximum q from Saturn C-1 Booster	VII-27
II-18.	Abort Trajectories at Low q	VII-28
II-19.	Load Factor Versus Time for Low q Abort Maneuver	VII-29
II-20.	Effect of Tailoff on Load Factor	VII-30
II-21.	Booster Lift Characteristics	VII-31
II-22.	Booster Drag Characteristics	VII-32

ILLUSTRATIONS (continued)

Figure	Title	Page
II-23.	Hazard Volume Versus Time After Abort	VII-33
II-24.	Abort at Maximum Dynamic Pressure	VII-34
II-25.	Explosive Potential: RP-1 and Liquid Oxygen	VII-35
II-26.	Effect of Ballast on Model 410 Static Stability	VII-36
II-27.	Stabilizing Effect of Drogue Chute	VII-37
II-28.	Tumbling Rate After Abort: Autopilot Failure	VII-38
II-29.	Angle of Attack After Abort: Autopilot Failure	VII-39
II-30.	Tumbling Versus Thrust Eccentricity: Pad Abort	VII-40
II-31.	Abort Trajectories at Maximum q: Autopilot Failure	VII-41
II-32.	Autopilot Response During Abort Initiation	VII-42
II-33.	Payload Penalty for Launch Escape System	VII-43
II-34.	Load Factor Versus Velocity Summary	VII-44
II-35.	Abort Trajectory (V = 15,000 fps)	VII-45
II-36.	Abort Trajectory at (L/D) = 0	VII-46
II-37.	Effect of Thrust Vector Orientation	VII-47
II-38.	Abort Maneuvering at Escape Trajectory Apogee	VII-48
II-39.	Abort Maneuvering at Escape Trajectory Re-entry	VII-49
II-40.	Abort Trajectory at (L/D) = 0 with V = 5300 fps	VII-50
II-41.	Perigee Altitude at Injection	VII-51
II-42.	Immediate Re-entry Capability: T = 30,000 lb	VII-52
II-43.	Immediate Re-entry Capability: T = 50,000 lb	VII-53
II-44.	Immediate Re-entry Capability: T = 80,000 lb	VII-54

ILLUSTRATIONS (continued)

Figure	Title	Page
II-45.	Summary: Thrust Versus Flight Path Angle for Immediate Re-entry	VII-55
II-46.	Allowable Injection Burnout Flight Path Angle	VII-56
II-47.	Abort at Injection Trajectory	VII-57
II-48.	Recovery Position After Abort	VII-58
III-1.	Lunar Trajectory Geometry and Definitions	VII-59
III-2.	Injection Velocity Requirements (Direct Returns)	VII-60
III-3.	Injection Velocity Requirements (Retrograde Returns)	VII-61
III-4.	Inclination of Trajectory to Moon's Orbital Plane and Equatorial Plane	VII-62
III-5.	Vehicle Position at Injection (periselenium = 500 naut mi)	VII-63
III-6.	Vehicle Position at Injection (periselenium = 100 naut mi)	VII-64
III-7.	Vehicle Position at Injection (periselenium = 1000 naut mi)	VII-65
III-8.	Vehicle Position at Injection (periselenium = 1500 naut mi)	VII-66
III-9.	Vehicle Position at Injection (periselenium = 2000 naut mi)	VII-67
III-10.	Moon Position at Injection (periselenium = 100 naut mi)	VII-68
III-11.	Moon Position at Injection (periselenium = 500 naut mi)	VII-69
III-12.	Moon Position at Injection (periselenium = 1000 naut mi)	VII-70
III-13.	Moon Position at Injection (periselenium = 1500 naut mi)	VII-71
III-14.	Moon Position at Injection (periselenium = 2000 naut mi)	VII-72
III-15.	Time Versus Periselenium Altitude	VII-73
III-16.	Time for Various Injection Conditions to Constant Periselenium Altitude ($L_{VTL} = 5^{o}$)	VII-74

ILLUSTRATIONS (continued)

Figure	Title	Page
III-17.	Time for Various Injection Conditions to Constant Periselenium Altitude ($L_{VTL} = 30^{o}$)	VII-75
III-18.	Time for Various Injection Conditions to Constant Periselenium Altitude ($L_{VTL} = 15^{o}$)	VII-76
III-19.	Periselenium Velocity	VII-77
III-20.	Velocity Increment Required to go into Lunar Orbit	VII-78
III-21.	Lunar Orbit Characteristics	VII-79
III-22.	Lunar Orbit Ejection Geometry	VII-80
III-23.	Velocity Impulse Versus Return Flight Time	VII-81
III-24.	Minimum Required Velocity Impulse for Lunar Orbit Ejection	VII-82
III-25.	Increased Required Velocity Gradient Versus Return Time	VII-83
III-26.	Return Time Versus Ejection Position	VII-84
III-27.	Required Velocity Impulse Versus Ejection Position	VII-85
III-28.	Required Velocity Impulse Versus Time in Orbit ($\phi_0 \sim 0$)	VII-86
III-29.	Required Velocity Impulse Versus Time in Orbit ($\phi_0 \sim 90$)	VII-87
III-30.	Precession Rate of Lunar Orbit due to Moon Oblateness and Presence of the Earth	VII-88
III-31.	Launch Time Tolerance Versus Day of Lunar Month	VII-89
III-32.	Midcourse Guidance Velocity Requirements ($\Delta\dot{Y}_{N_0} = 0$ fps; $\Delta\dot{Z}_{N_0} = 30.61$)	VII-90
III-33.	Midcourse Guidance Velocity Requirements ($\Delta\dot{Y}_{N_0} = 18.882$ fps; $\Delta\dot{Z}_{N_0} = 21.645$)	VII-91
III-34.	Midcourse Guidance Velocity Requirements ($\Delta\dot{Y}_{N_0} = 26.702$ fps; $\Delta\dot{Z}_{N_0} = 0$)	VII-92

ILLUSTRATIONS (continued)

Figure	Title	Page
III-35.	Midcourse Guidance Velocity Requirements (99% probability of injection errors < $\Delta\dot{X}_{N_0}$ = 13.65 fps; $\Delta\dot{Y}_{N_0}$ = 0; $\Delta\dot{Z}_{N_0}$ = 30.61)	VII-93
III-36.	Midcourse Guidance Velocity Requirements (99% probability of injection errors < $\Delta\dot{X}_{N_0}$ = 13.65 fps; $\Delta\dot{Y}_{N_0}$ = ±18.88; $\Delta\dot{Z}_{N_0}$ = 21.65)	VII-94
III-37.	Midcourse Guidance Velocity Requirements (99% probability of injection errors < $\Delta\dot{X}_{N_0}$ = 13.65 fps; $\Delta\dot{Y}_{N_0}$ = 26.70; $\Delta\dot{Z}_{N_0}$ = 0)	VII-95
III-38.	Midcourse Guidance Velocity Requirements (99% probability of injection errors < $\Delta\dot{X}_{N_0}$ = 0 fps; $\Delta\dot{Y}_{N_0}$ = ±31.73; $\Delta\dot{Z}_{N_0}$ = 30.61)	VII-96
III-39.	Midcourse Guidance Velocity Requirements (99% probability of injection errors < $\Delta\dot{X}_{N_0}$ = 8.1 fps; $\Delta\dot{Y}_{N_0}$ = ±31.73; $\Delta\dot{Z}_{N_0}$ = 21.6)	VII-97
III-40.	Midcourse Guidance Velocity Requirements (99% probability of injection errors < $\Delta\dot{X}_{N_0}$ = 11.51 fps; $\Delta\dot{Y}_{N_0}$ = ±31.67; $\Delta\dot{Z}_{N_0}$ = 0)	VII-98
III-41.	Midcourse Guidance Velocity Requirements (99% probability of injection errors < $\Delta\dot{X}_{N_0}$ = 11.51 fps; $\Delta\dot{Y}_{N_0}$ = 0; $\Delta\dot{Z}_{N_0}$ = 36.31)	VII-99
III-42.	Midcourse Guidance Velocity Requirements (99% probability of injection errors < $\Delta\dot{X}_{N_0}$ = 8.1 fps; $\Delta\dot{Y}_{N_0}$ = ±18.88; $\Delta\dot{Z}_{N_0}$ = 36.31)	VII-100
III-43.	Midcourse Guidance Velocity Requirements (99% probability of injection errors < $\Delta\dot{X}_{N_0}$ = 0 fps; $\Delta\dot{Y}_{N_0}$ = ±26.70; $\Delta\dot{Z}_{N_0}$ = 36.31)	VII-101
III-44.	Error Distance Versus Time Along Correction Trajectory	VII-102
III-45.	Transearth and Midcourse Velocity Requirement ($\Delta\dot{X}_{N_0}$ = 13.65 fps; $\Delta\dot{Y}_{N_0}$ = 0; $\Delta\dot{Z}_{N_0}$ = 30.61)	VII-103
III-46.	Transearth and Midcourse Velocity Requirement ($\Delta\dot{X}_{N_0}$ = 13.65 fps; $\Delta\dot{Y}_{N_0}$ = 18.88; $\Delta\dot{Z}_{N_0}$ = 21.645)	VII-104

ILLUSTRATIONS (continued)

Figure	Title	Page
III-47.	Transearth and Midcourse Velocity Requirement ($\Delta\dot{x}_{N_0} = 13.65$ fps; $\Delta\dot{y}_{N_0} = 26.70$; $\Delta\dot{z}_{N_0} = 0$)	VII-105
III-48.	Transearth and Midcourse Guidance Required Velocity Impulse due to Errors in Velocity at Ejection from Lunar Orbit ($\Delta\dot{x}_{N_0} = 2.575$ fps; $\Delta\dot{y}_{N_0} = 0$; $\Delta\dot{z}_{N_0} = 2.1709$)	VII-106
III-49.	Transearth Midcourse Guidance Required Velocity Impulse due to Errors in Velocity at Ejection from Lunar Orbit ($\Delta\dot{x}_{N_0} = 2.575$ fps; $\Delta\dot{y}_{N_0} = 1.5357$; $\Delta\dot{z}_{N_0} = 1.5357$)	VII-107
III-50.	Transearth Midcourse Guidance Required Velocity Impulse due to Errors in Velocity at Ejection from Lunar Orbit ($\Delta\dot{x}_{N_0} = 2.575$ fps; $\Delta\dot{y}_{N_0} = 2.1709$; $\Delta\dot{z}_{N_0} = 0$)	VII-108
III-51.	Envelope of Allowable Return Orbit Eccentricity for Translunar Orbit Abort	VII-109
III-52.	Time to Return after Translunar Orbit Abort	VII-110
III-53.	Required Velocity Impulse for Abort ($\epsilon = 0$)	VII-111
III-54.	Required Velocity Impulse for Abort ($\epsilon = 90$)	VII-112
III-55.	Correction Factors for Translunar Orbit Eccentricities Less than 1.0 (eccentricity of turnaround trajectory = 1.0)	VII-113
III-56.	Correction Factors for Translunar Orbit Eccentricities Less than 1.0 (eccentricity of turnaround trajectory = e_{min})	VII-114
III-57.	Correction Factors for Translunar Orbit Eccentricities Less than 1.0 (eccentricity of turnaround trajectory = $1/2(1 + e_{min})$)	VII-115
III-58.	Correction Factors for Translunar Orbit Eccentricities Less than 1.0 (eccentricity of turnaround trajectory = $1/2(1 + e_{min})$)	VII-116
III-59.	Return Perigee Longitude After Abort from Translunar Orbit	VII-117
III-60.	Change in Argument of Perigee and Latitude of Return Perigee After Abort from Translunar Orbit	VII-118

ILLUSTRATIONS (continued)

Figure	Title	Page
III-61.	Required Velocity Impulse at Abort to Return to Australia	VII-119
III-62.	Required Velocity Impulse at Abort to Return to United States	VII-120
III-63.	Required Velocity Impulse at Abort to Return to Edwards AFB	VII-121
III-64.	Minimum Return Time for Turnaround Maneuvers	VII-122
III-65.	Change in Arrival Time at Perigee as a Function of Characteristic Velocity of Maneuver and Altitude of Maneuver	VII-123
III-66.	Altitude of Maneuver as a Function of Velocity of Maneuver and Change in Longitude of Perigee	VII-124
III-67.	Change in Longitude of Perigee as a Function of Characteristic Velocity of Maneuver and Altitude of Maneuver	VII-125
III-68.	Change in Argument of Perigee as a Function of Characteristic Velocity of Maneuver and Altitude of Maneuver	VII-126
III-69.	Change in Perigee Velocity as a Function of Characteristic Velocity of Maneuver and Altitude of Maneuver	VII-127
IV-1.	G-Limited Re-entry Corridors (overshoot boundary)	VII-128
IV-2.	G-Limited Re-entry Corridor (undershoot boundary)	VII-129
IV-3.	Effect of Entry Velocity on Corridor Width	VII-130
IV-4.	Drag Polar for M-1 and M-2 Configurations	VII-131
IV-5.	Effects of Lift Modulation on Load Factor	VII-132
IV-6.	Ten-G Modulated Re-entry Corridor	VII-133
IV-7.	Six-G Modulated Re-entry Corridor	VII-134
IV-8.	Limiting Load Factor Effect on Corridor Width	VII-135
IV-9.	Longitudinal Range Requirements Versus Inclination Angle	VII-136

ILLUSTRATIONS (continued)

Figure	Title	Page
IV-10.	Tolerance on Inclination Versus Lateral Maneuverability	VII-137
IV-11.	Geometric Relationships for Longitudinal Range Requirements (Northern Hemisphere)	VII-138
IV-12.	Geometric Relationships for Longitudinal Range Requirements (Southern Hemisphere)	VII-139
IV-13.	Geometric Relationship for Lateral Range Requirements	VII-140
IV-14.	Longitudinal Range Versus (L/D)	VII-141
IV-15.	Re-entry Range Versus Flight Path Angle	VII-142
IV-16.	Lateral Range for Satellite Re-entry	VII-143
IV-17.	Lateral Range Correlation of Empirical Results with Machine Calculations	VII-144
IV-18.	Maximum Lateral Range Versus (L/D)	VII-145
IV-19.	Maneuvering Envelope Versus (L/D) for Re-entry Angle = -5.6 Degrees	VII-146
IV-20.	Maneuvering Envelope Versus (L/D) for Re-entry Angle = -6.2 Degrees	VII-147
IV-21.	Maneuvering Envelope Versus (L/D) for Re-entry Angle = -6.85 Degrees	VII-148
IV-22.	Maneuvering Envelope Versus (L/D) for Re-entry Angle = -7.6 Degrees	VII-149
IV-23.	Re-entry Body Configurations	VII-150
IV-24.	Aerodynamic Characteristics of Re-entry Configurations	VII-151
IV-25.	Modulation Techniques	VII-152
IV-26.	Effect of Corridor Width on Maximum Heating Rate and Load Factor (Model 410, V_E = 36,000 fps; W/A = 81.5; R_N = 2.5 ft)	VII-153

ILLUSTRATIONS (continued)

Figure	Title	Page
IV-27.	G-Duration Versus Corridor Depth for Skip Trajectory (Model 410, V_E = 36,000 fps; W/A = 81.5; R_N = 2.5 ft)	VII-154
IV-28.	M-1 Re-entry Vehicle Corridor Summary (V_E = 36,000 fps; W/A = 50; R_N = 3.4 ft)	VII-155
IV-29.	W-1 Re-entry Vehicle Corridor Summary (V_E = 36,000 fps; W/A = 50; R_N = 3.4 ft)	VII-156
IV-30.	M-2 Re-entry Vehicle Corridor Summary (V_E = 35,000 fps; W/A = 48; R_N = 1.5 ft)	VII-157
IV-31.	L-2C Re-entry Vehicle Corridor Summary (V_E = 36,000 fps; W/A = 46; R_N = 6.41 ft)	VII-158
IV-32.	L-2C Re-entry Vehicle, Effect of Lift Modulation on Corridor Depth	VII-159
IV-33.	L-2C Re-entry Vehicle, Variation of 10-G Limit Corridor with Initial Angle of Attack	VII-160
IV-34.	L-1 Maximum Heating Rate and Load Factor Versus Corridor Depth	VII-161
IV-35.	L-1 G Duration Versus Corridor Depth	VII-162
IV-36.	Mercury Re-entry Vehicle Maximum Heating Rate and Load Factor Versus Corridor Depth	VII-163
IV-37.	Undershoot Boundary Maneuvering Envelope	VII-164
IV-38.	Overshoot Boundary Maneuvering Envelope	VII-164
IV-39.	M-1 Maneuver Capability	VII-165
IV-40.	Re-entry Performance	VII-166
V-1.	Total Flight Time Versus Periselenium Altitude	VII-167
V-2.	Required Periselenium Altitude Versus Day of Lunar Month	VII-168
V-3.	Range to Edwards AFB from Re-entry	VII-169

ILLUSTRATIONS (continued)

Figure	Title	Page
V-4.	Ground Trace for Typical Operational Trajectory	VII-170
V-5.	Ground Trace for Typical Operational Trajectory	VII-171
V-6.	Ground Trace for Typical Operational Trajectory	VII-172
V-7.	Ground Trace for Typical Operational Trajectory	VII-173

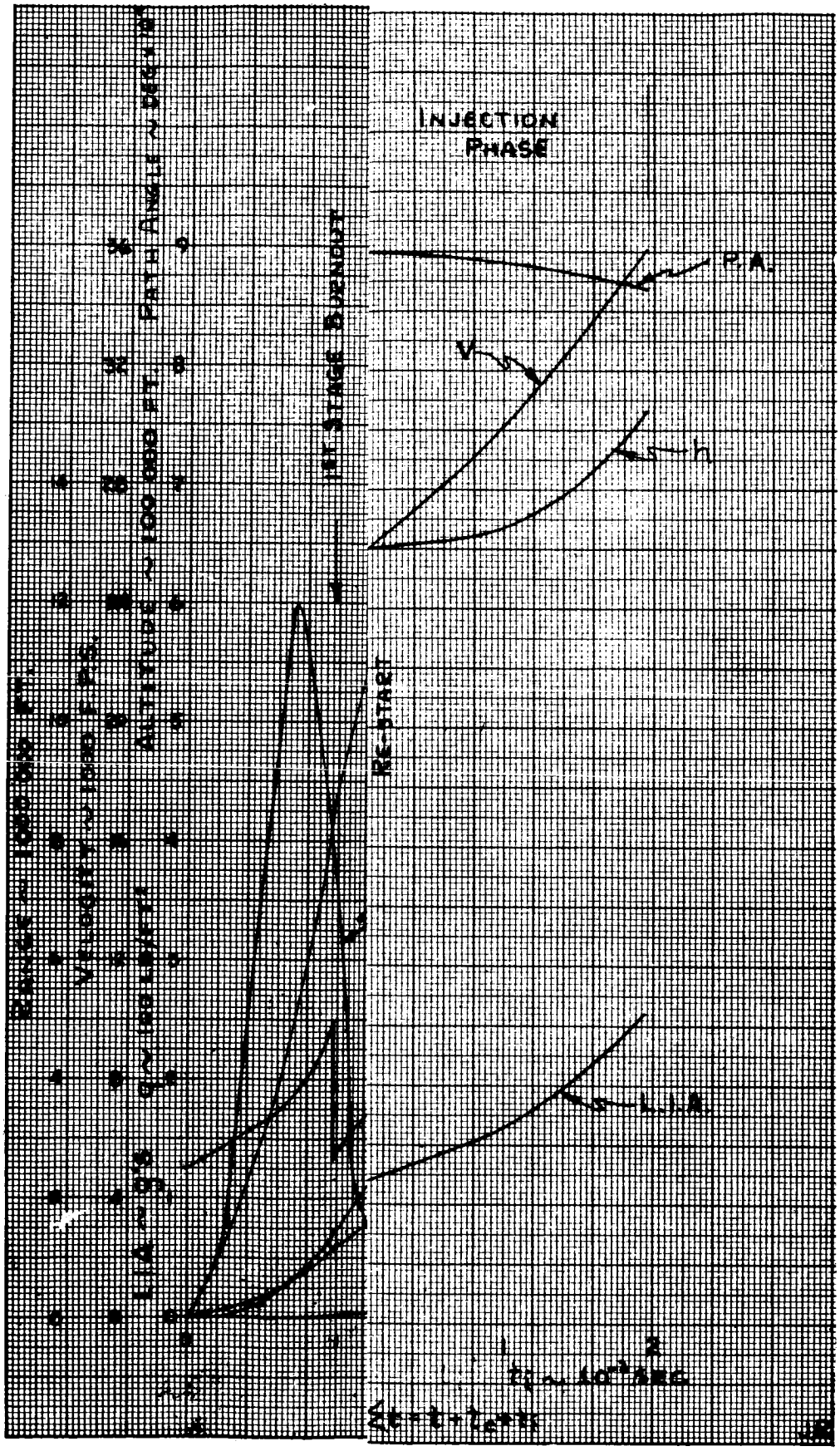

Reference Ascent Trajectory

CONFIDENTIAL

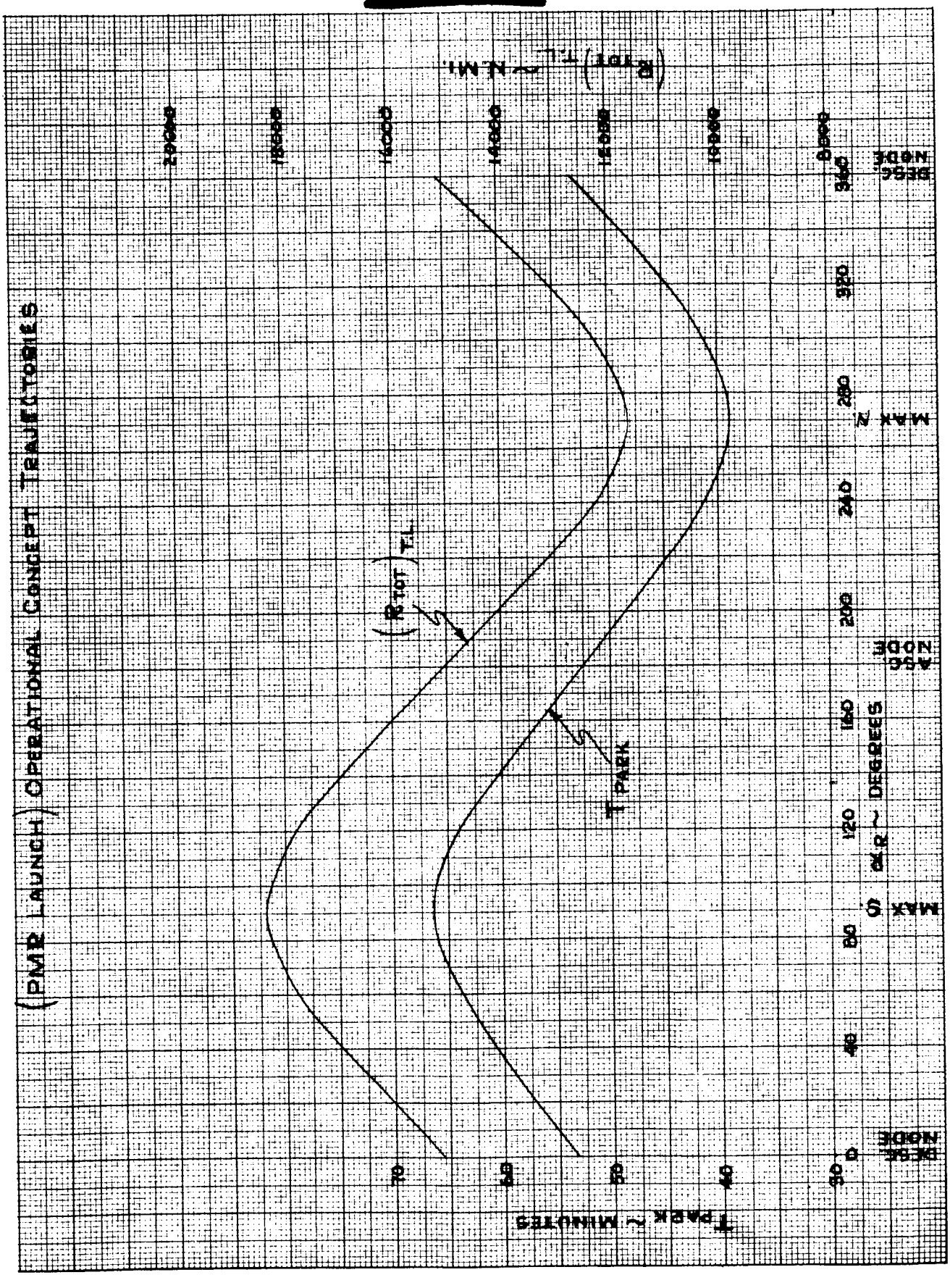

Fig. II-2. Time in Parking Orbit and Range to Injection

CONFIDENTIAL

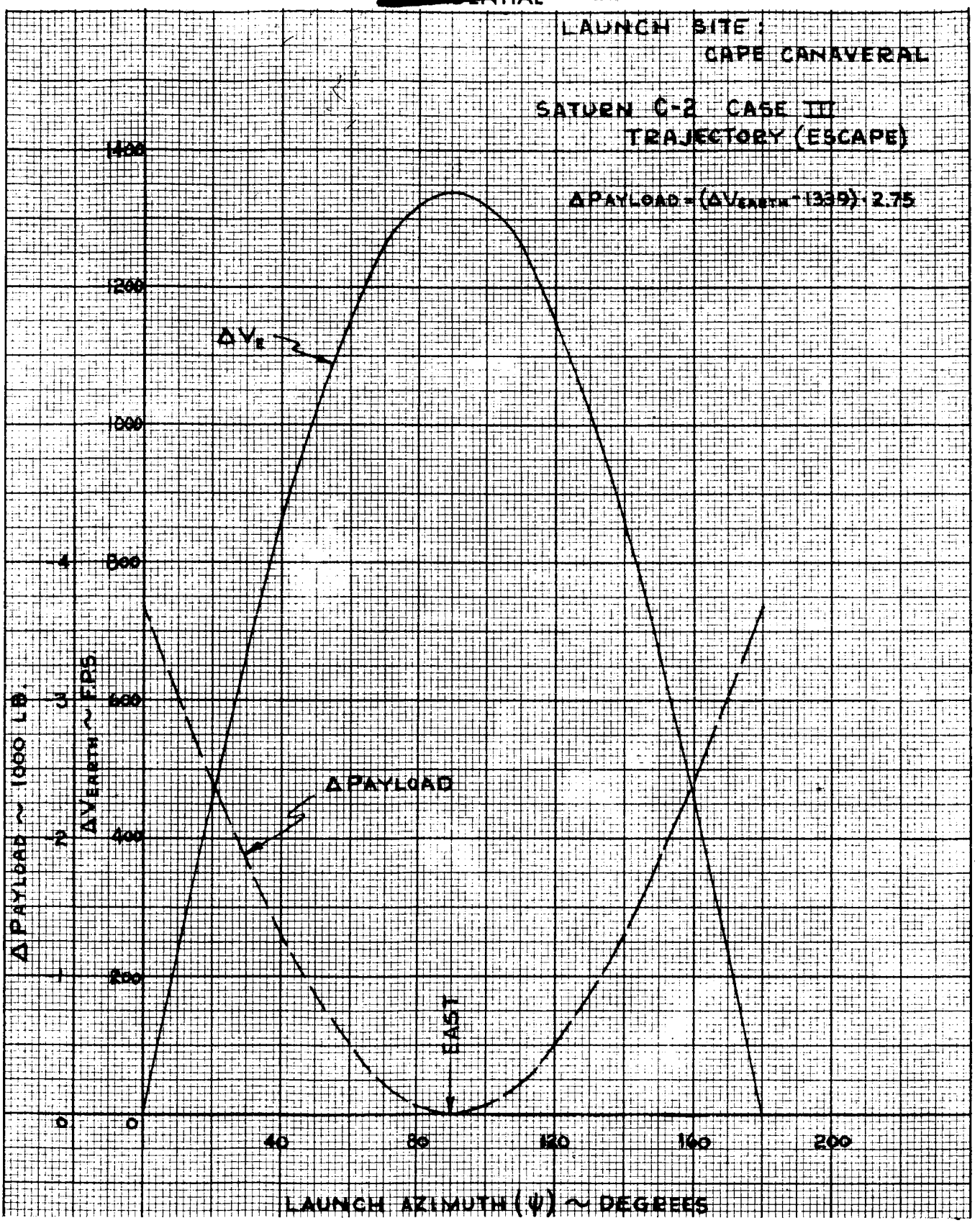

Fig. II-3. Payload Loss Versus Launch Azimuth

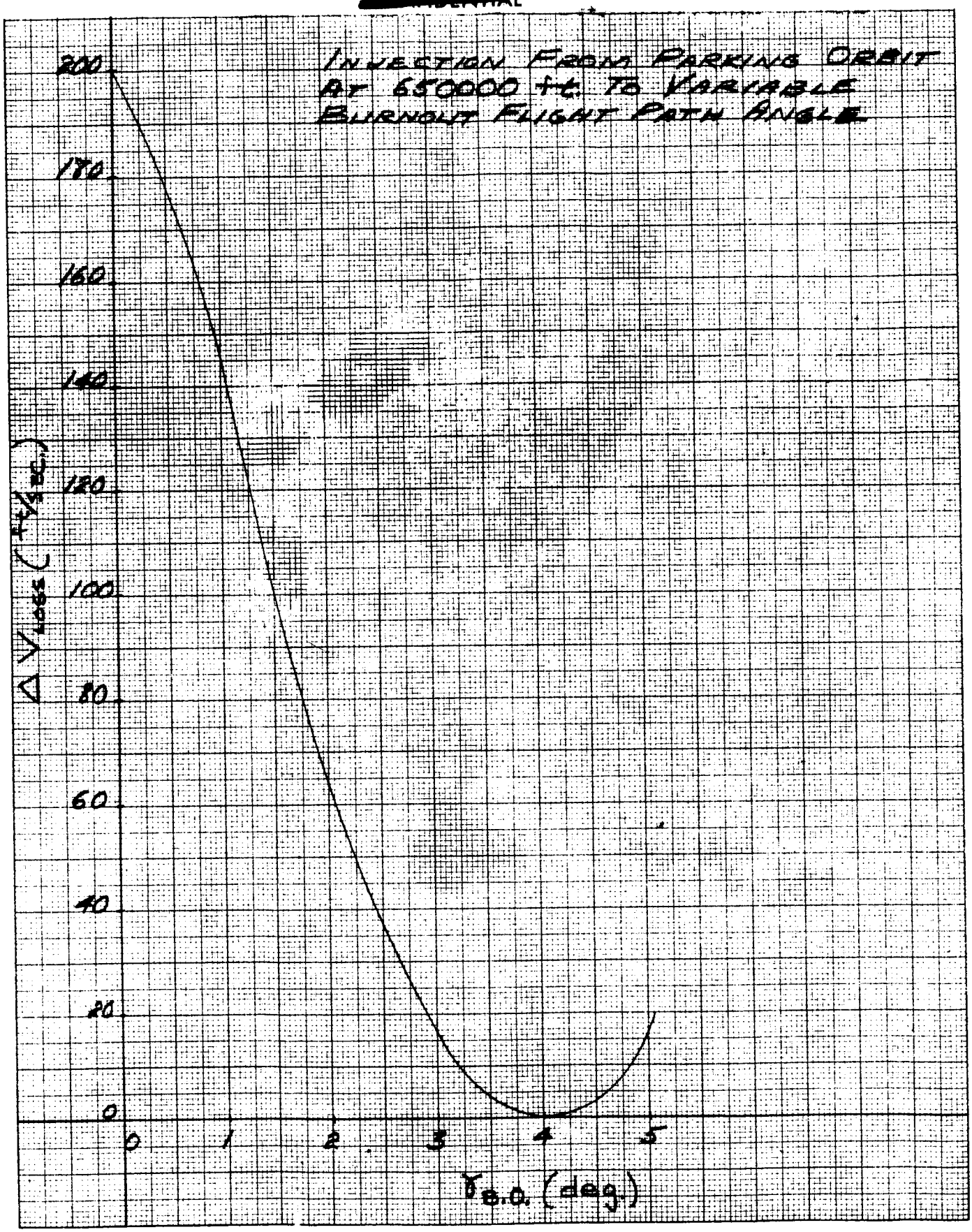

Fig. II-4. Burnout Velocity Loss Versus Burnout Flight Path Angle

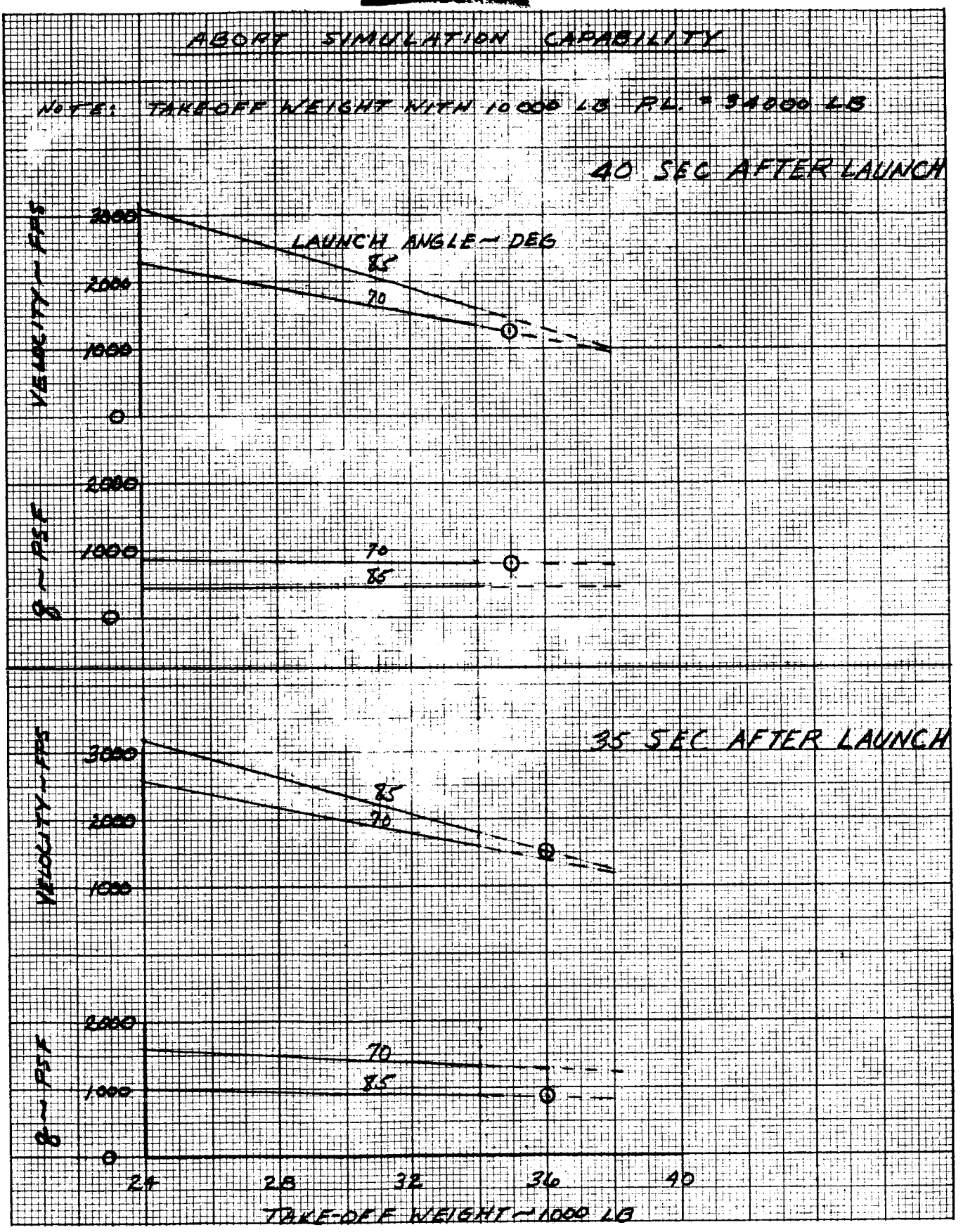

Fig. II-5. Little Joe I Characteristics

PARABOLIC REENTRY TEST

SATURN C-1 + 75000 LB APOLLO COMMAND MODULE

POSITION AND VELOCITY AT S-IV BURNOUT

	S-I	S-IV	APOLLO
FUEL	746000	100,000	0
BURNOUT	109,571	11,700	75000
ISP	257 (SL)	420 (VAC)	
THRUST	1,500,000 LBS	90,000 (VAC)	

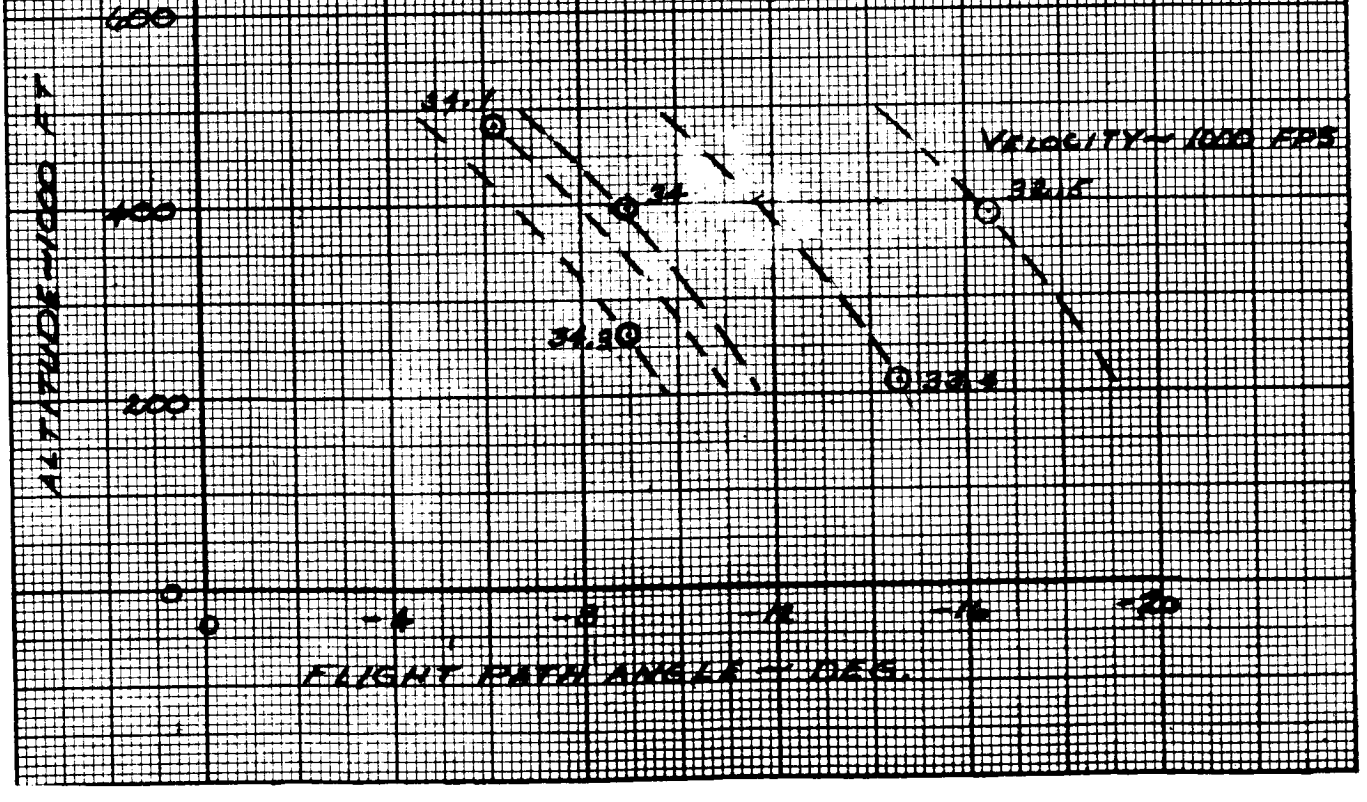

Fig. II-6. Saturn C-1 Capabilities

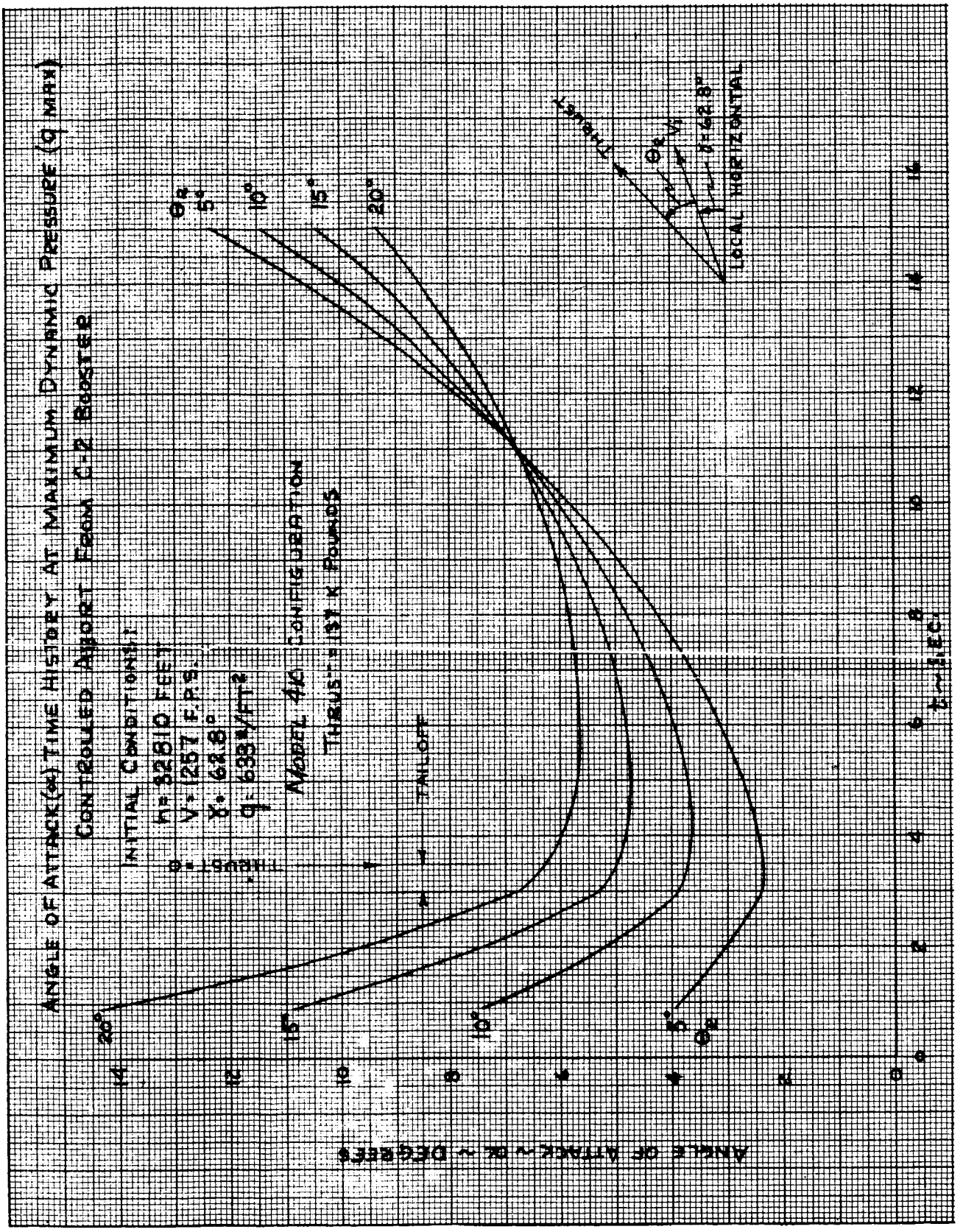

Fig. II-7. Angle of Attack Versus Time During Abort

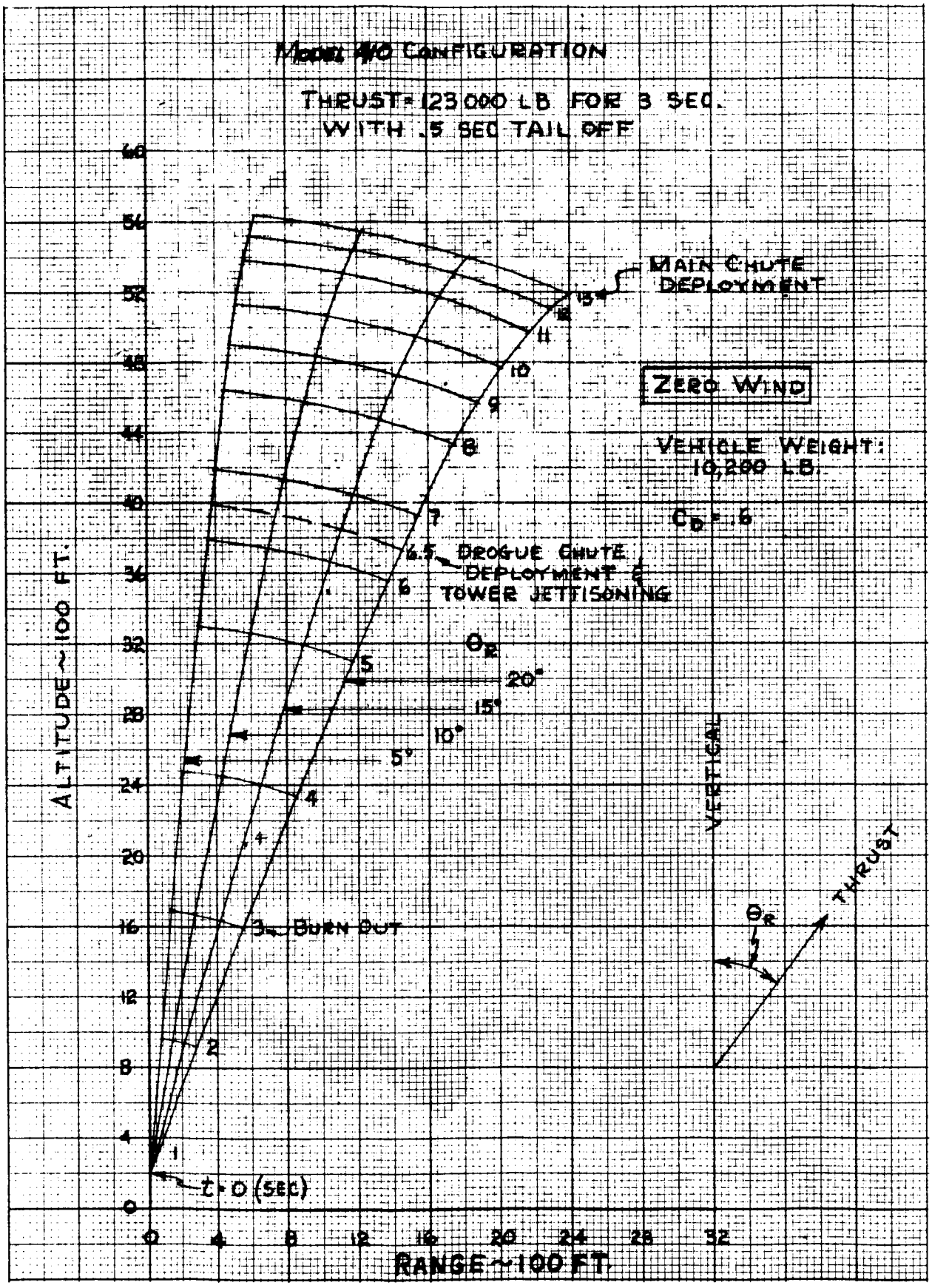

Fig. II-8. Abort Performance off the Pad

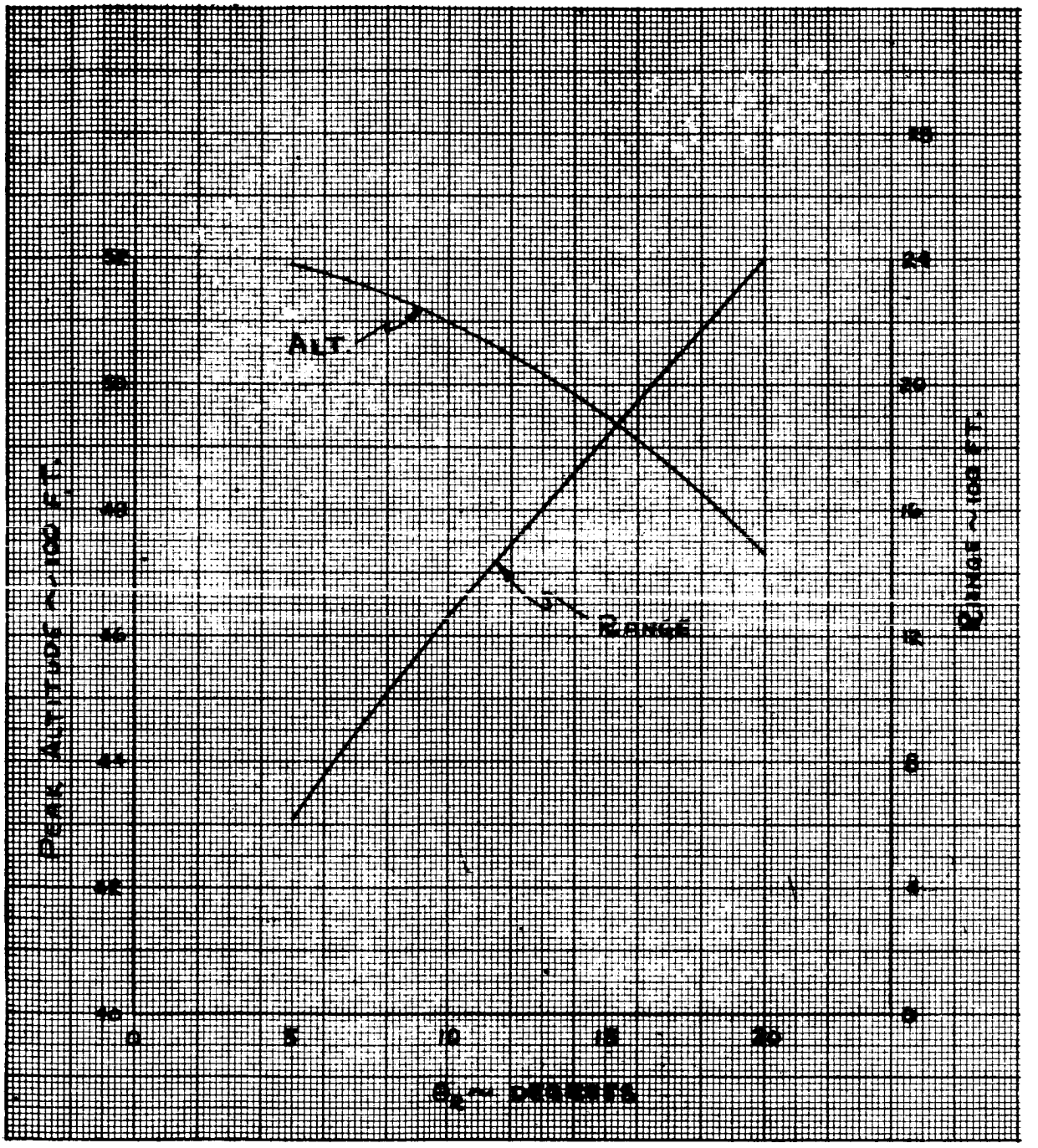

Fig. II-9. Effect of Drogue Chute Deployment During Abort

CONFIDENTIAL

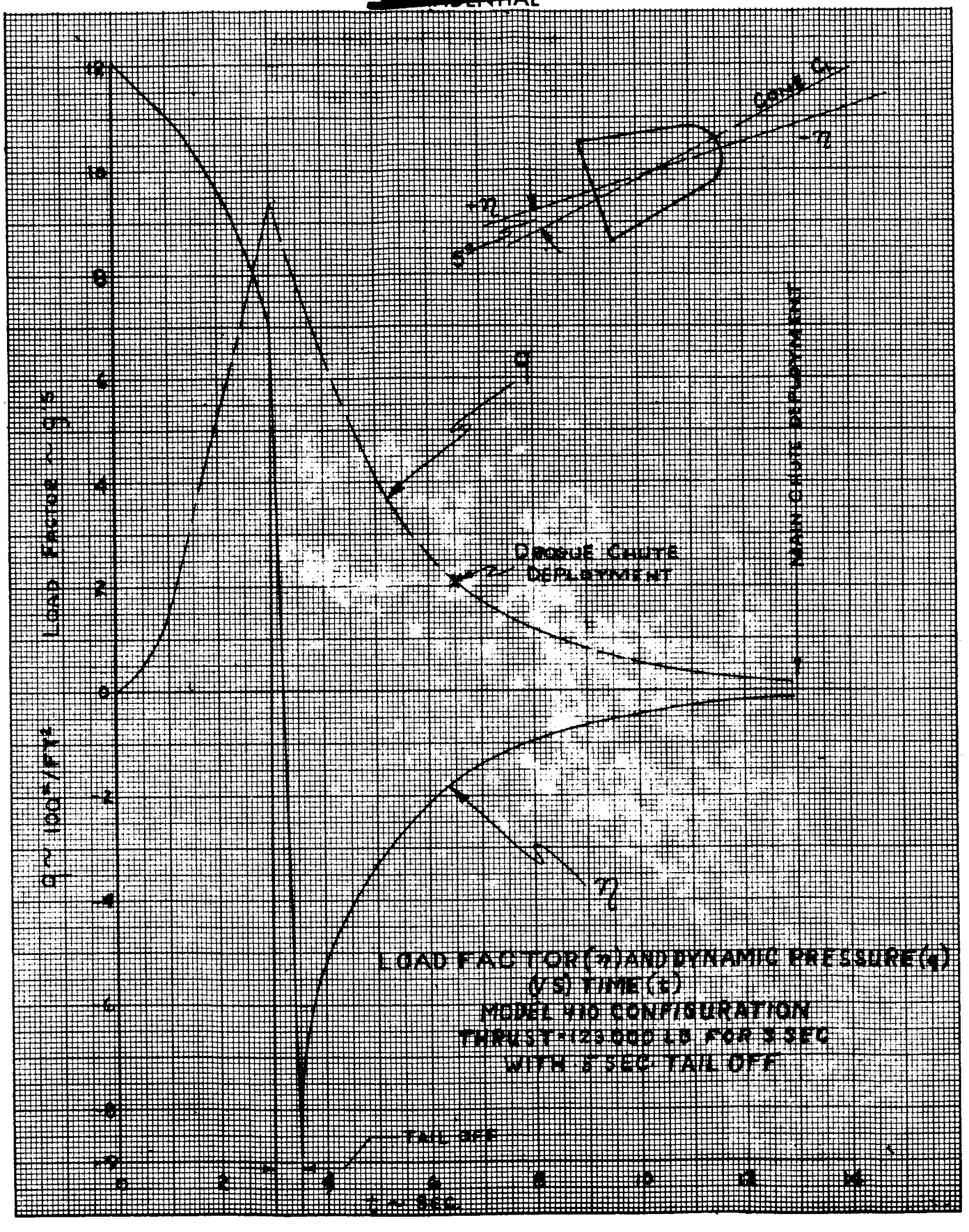

Fig. II-10. Abort Trajectory Time History

CONFIDENTIAL

D-3 (6-60)

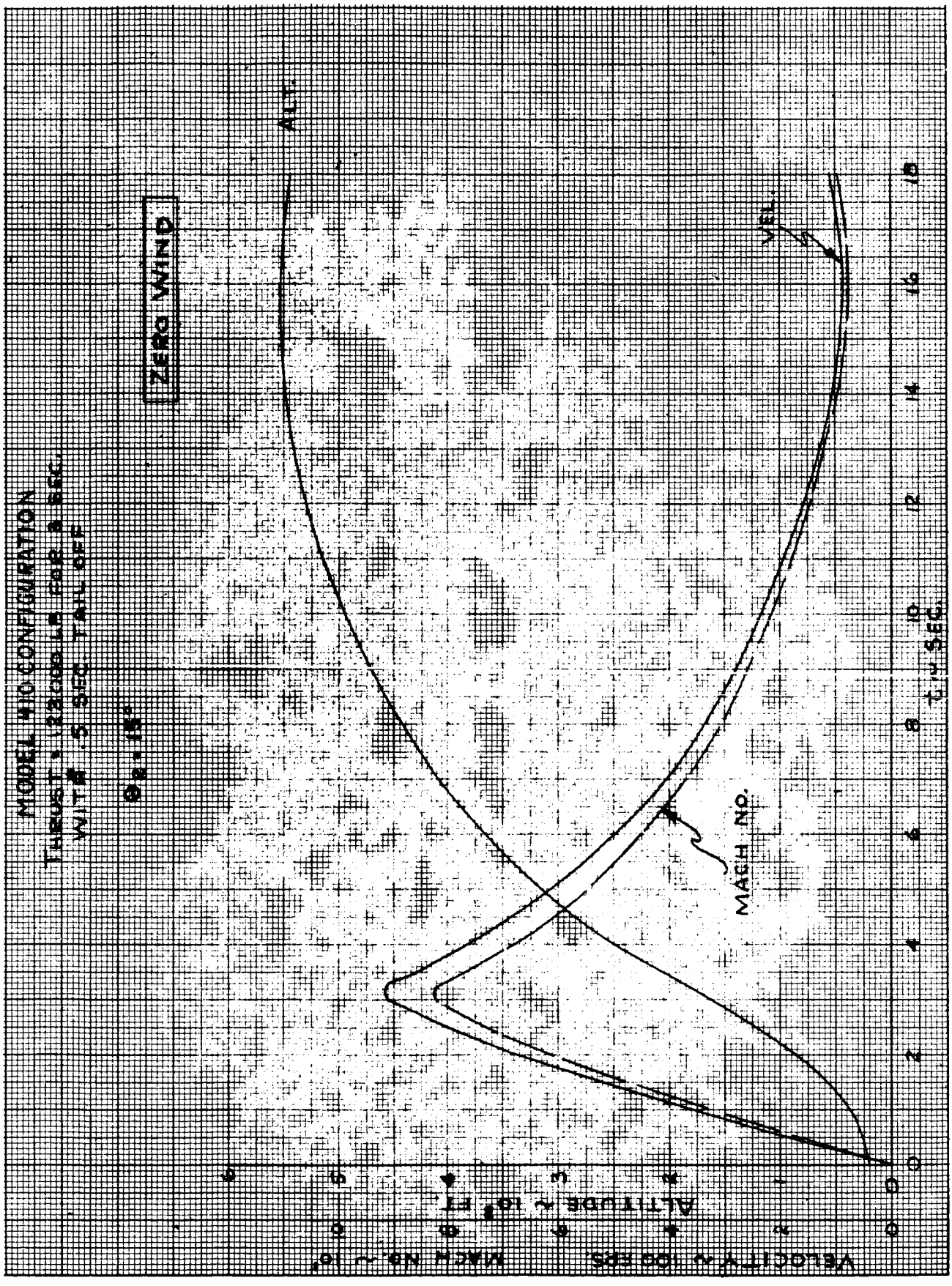

Fig. II-11. Abort Trajectory Time History

CONFIDENTIAL

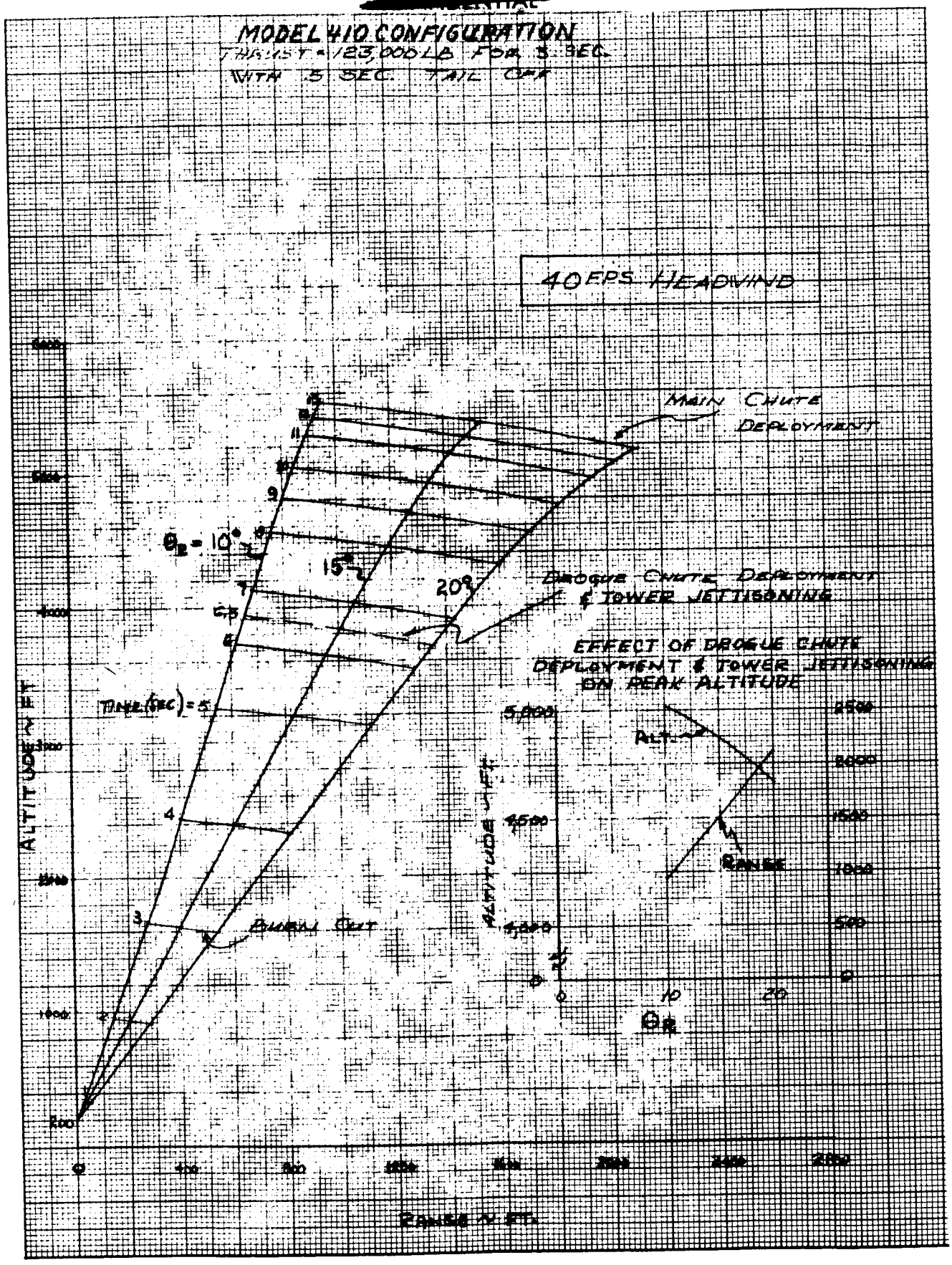

Fig. II-12. Effect of 40-fps Headwind on Abort Trajectory

CONFIDENTIAL

CONFIDENTIAL

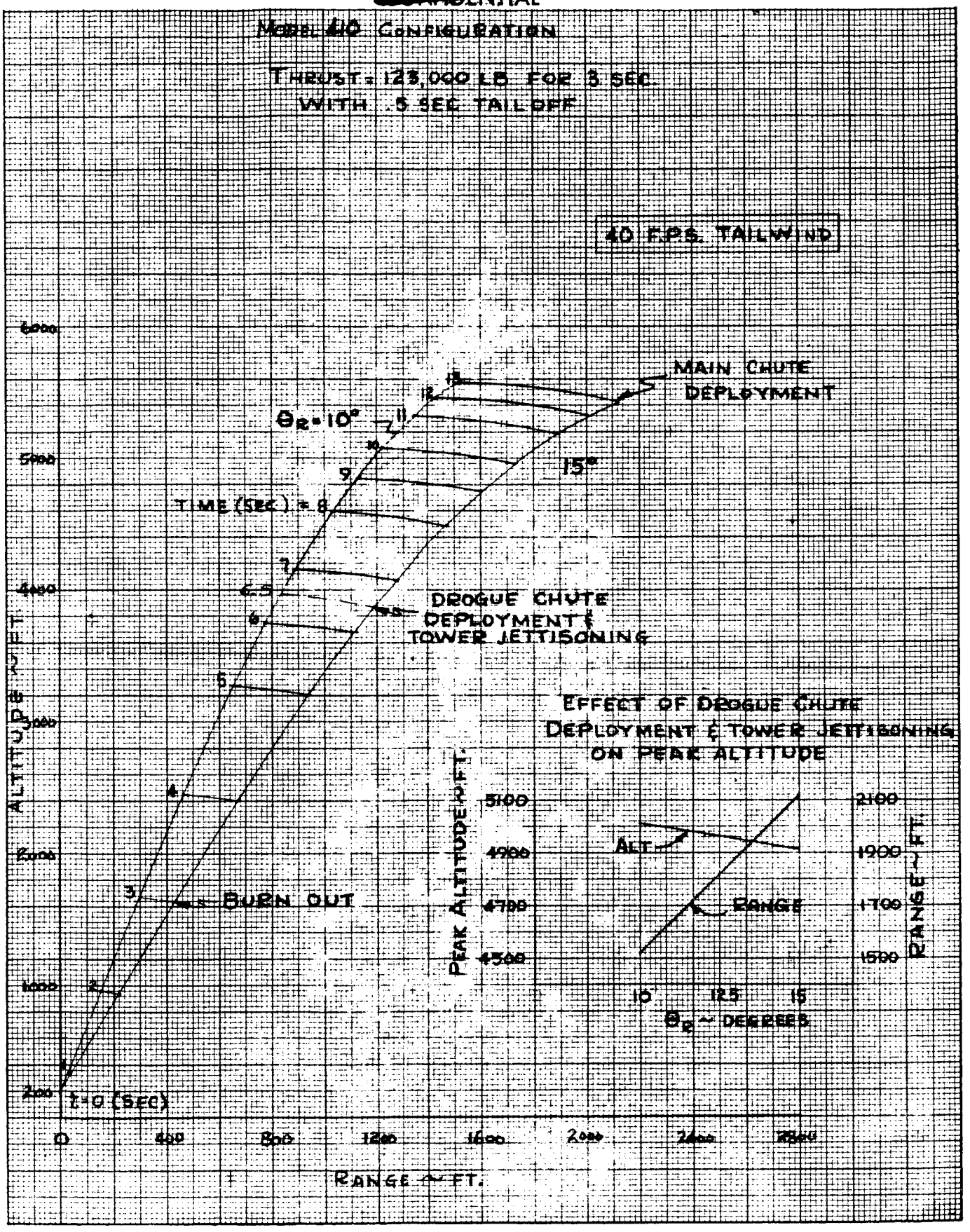

Fig. II-13. Effect of 40-fps Tailwind on Abort Trajectory

CONFIDENTIAL

D-3 (6.60)

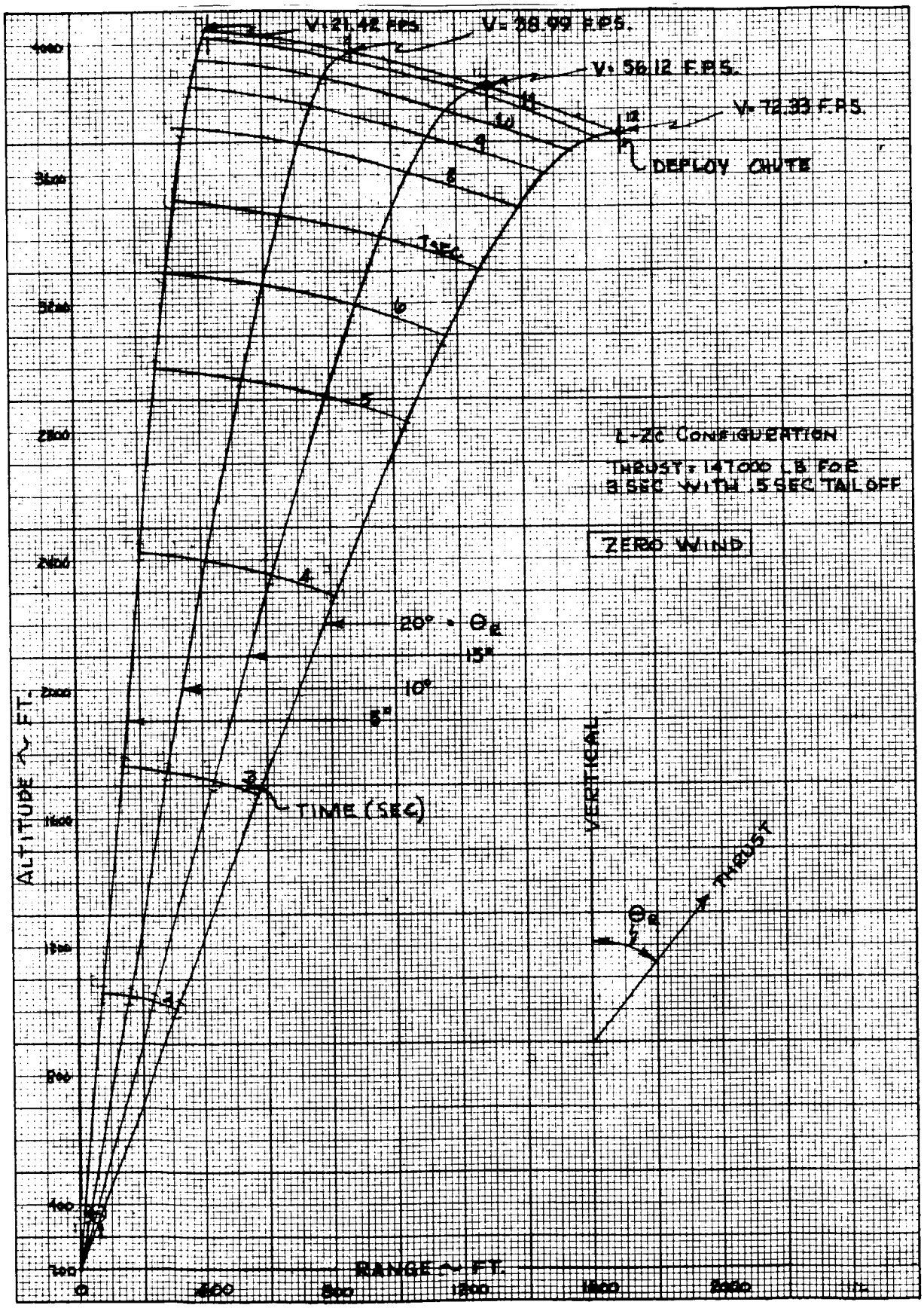

Fig. II-14. L-2C Configuration Abort Trajectory

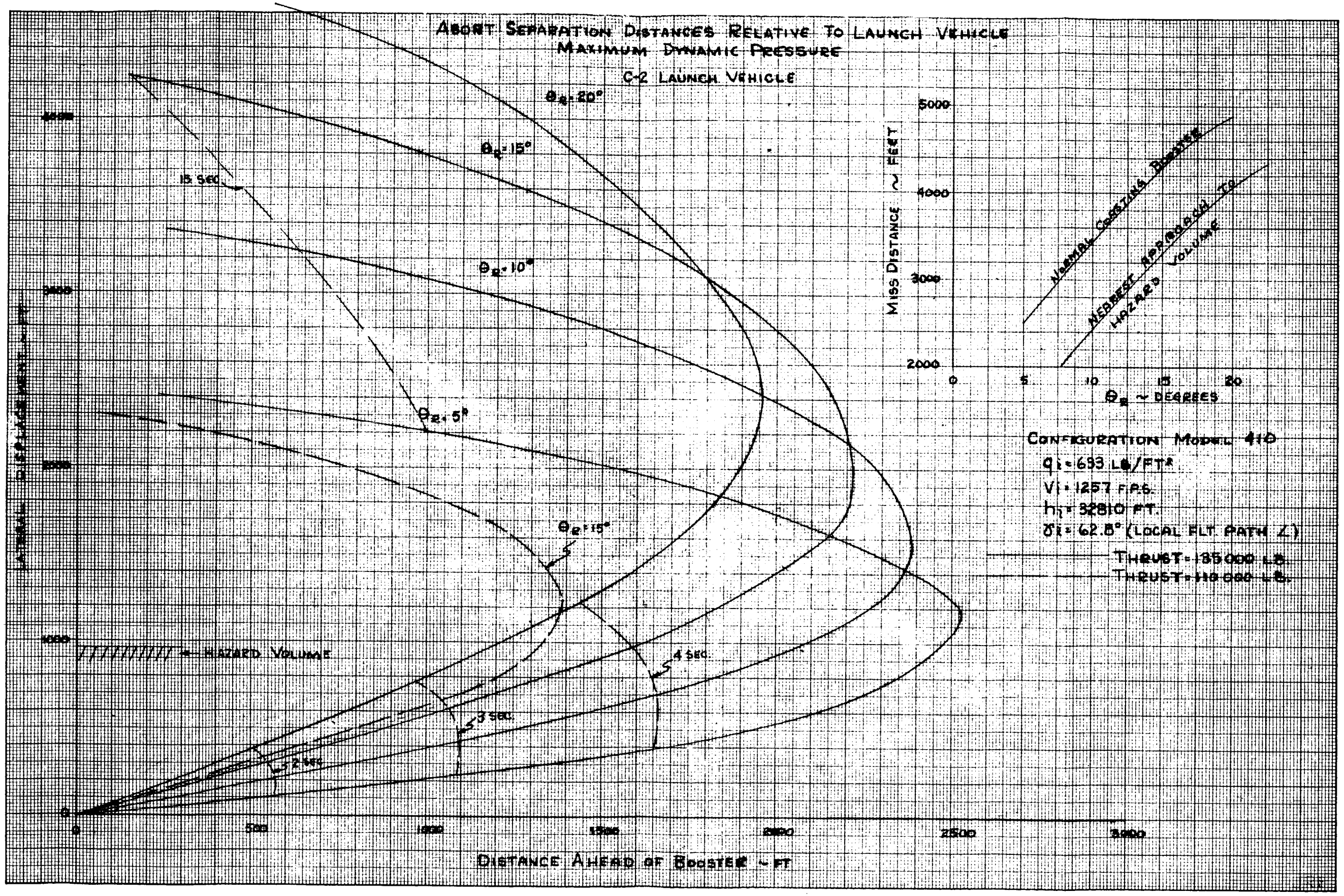

Fig. II-15. Model 410 Escape Trajectory at Maximum q

CONFIDENTIAL

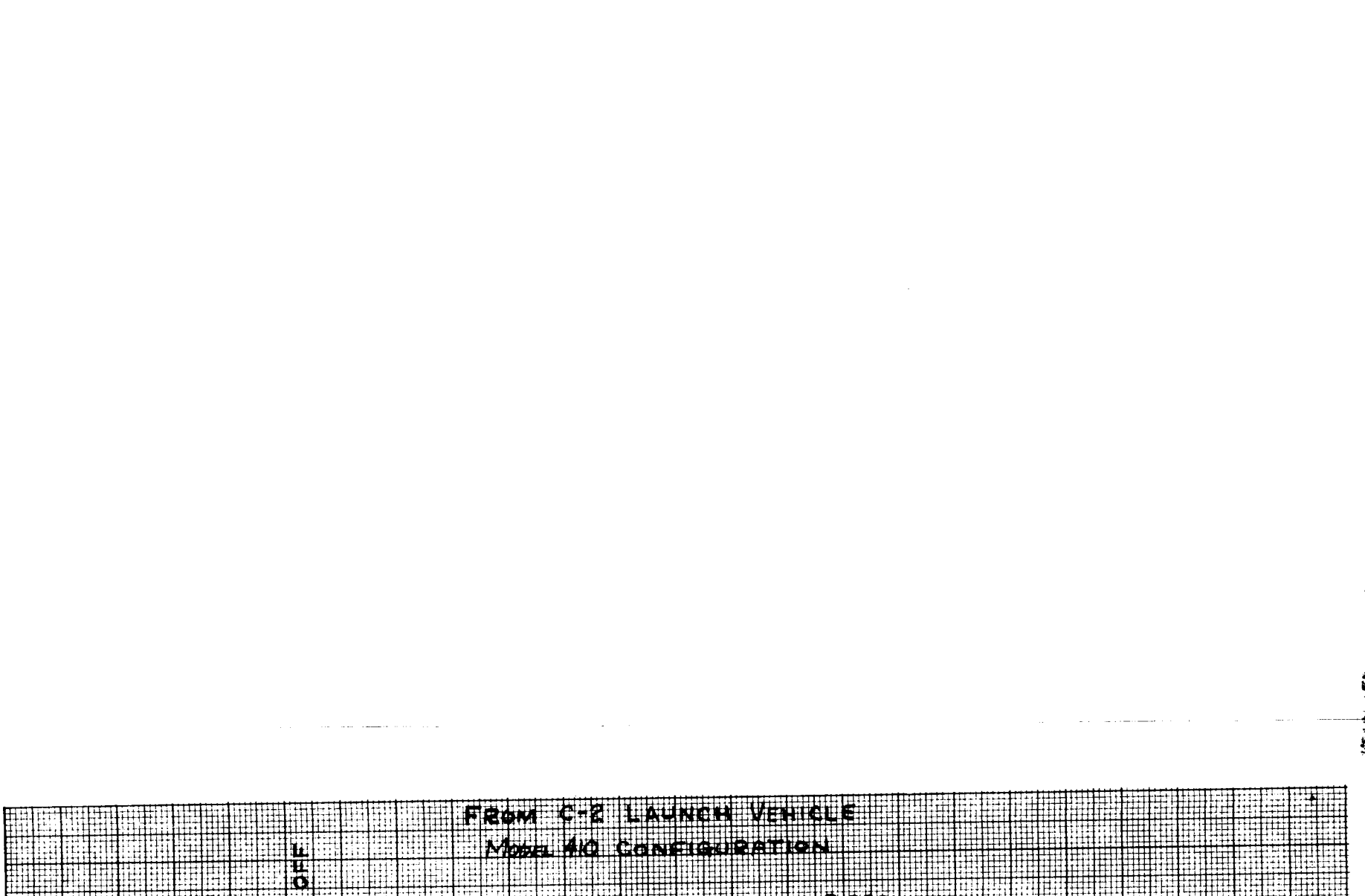

Fig. II-16. Load Factor and q During Maximum q Abort

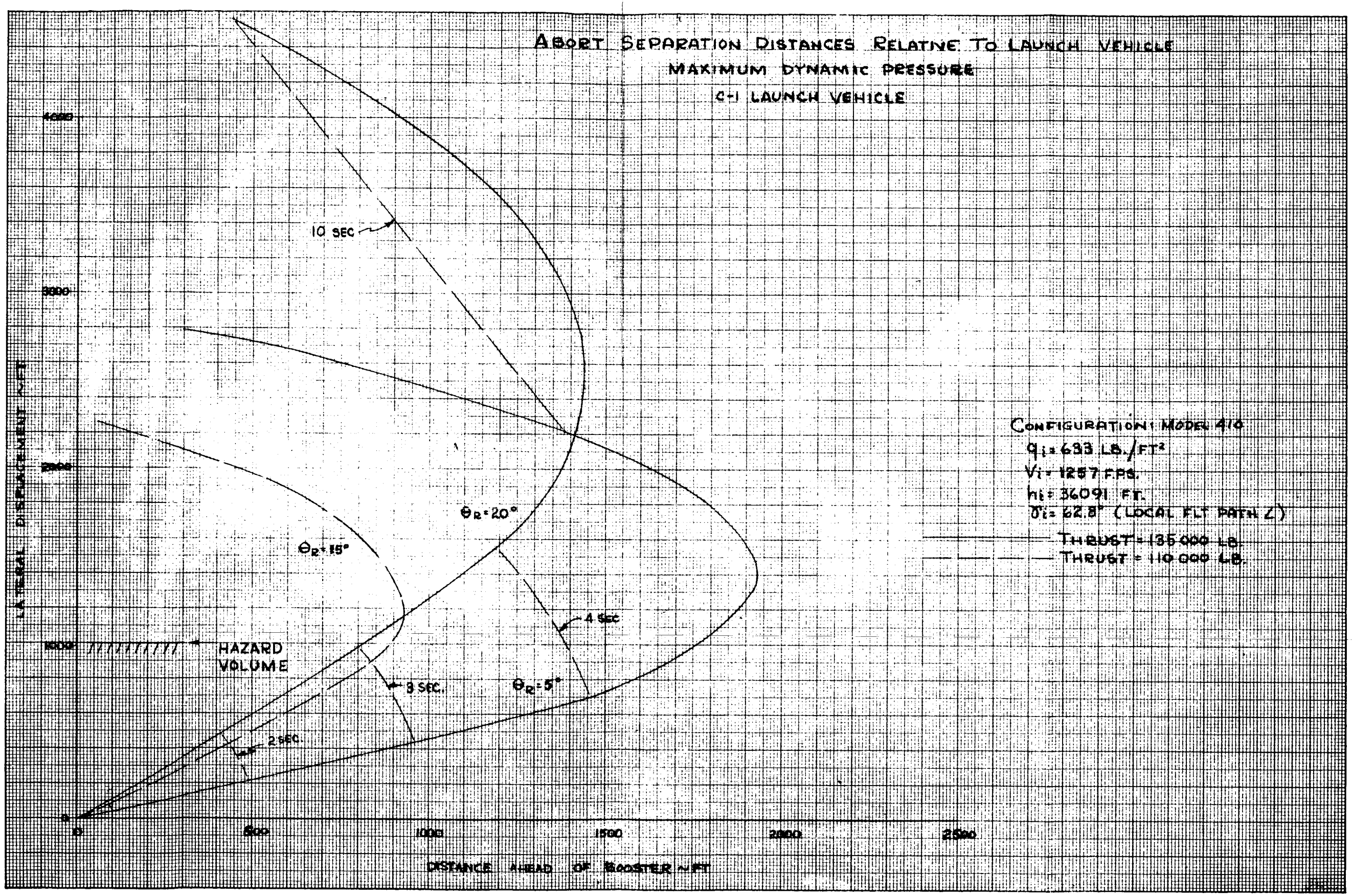

Fig. II-17. Escape at Maximum q from Saturn C-1 Booster

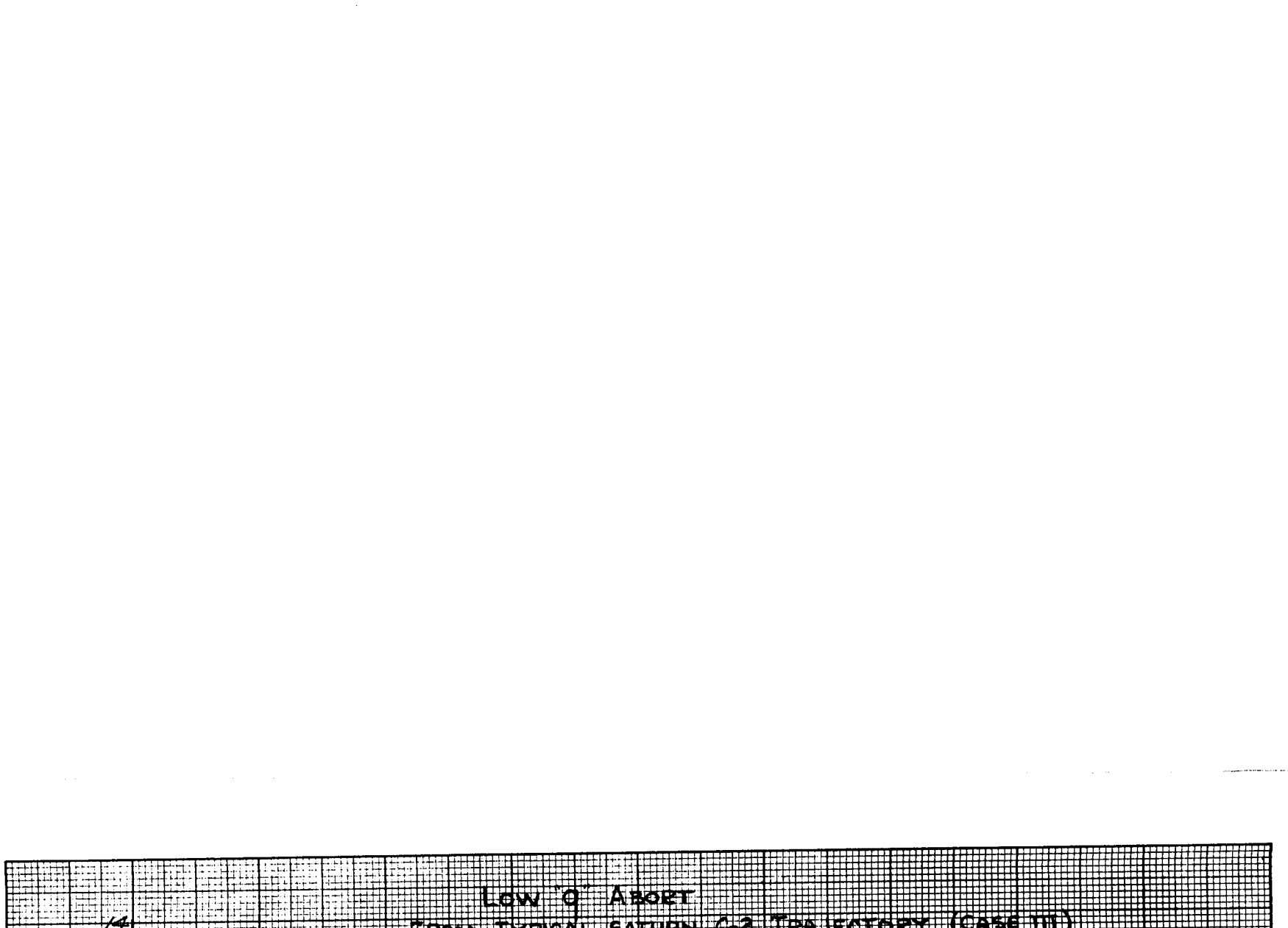

Fig. II-18. Abort Trajectories at Low q

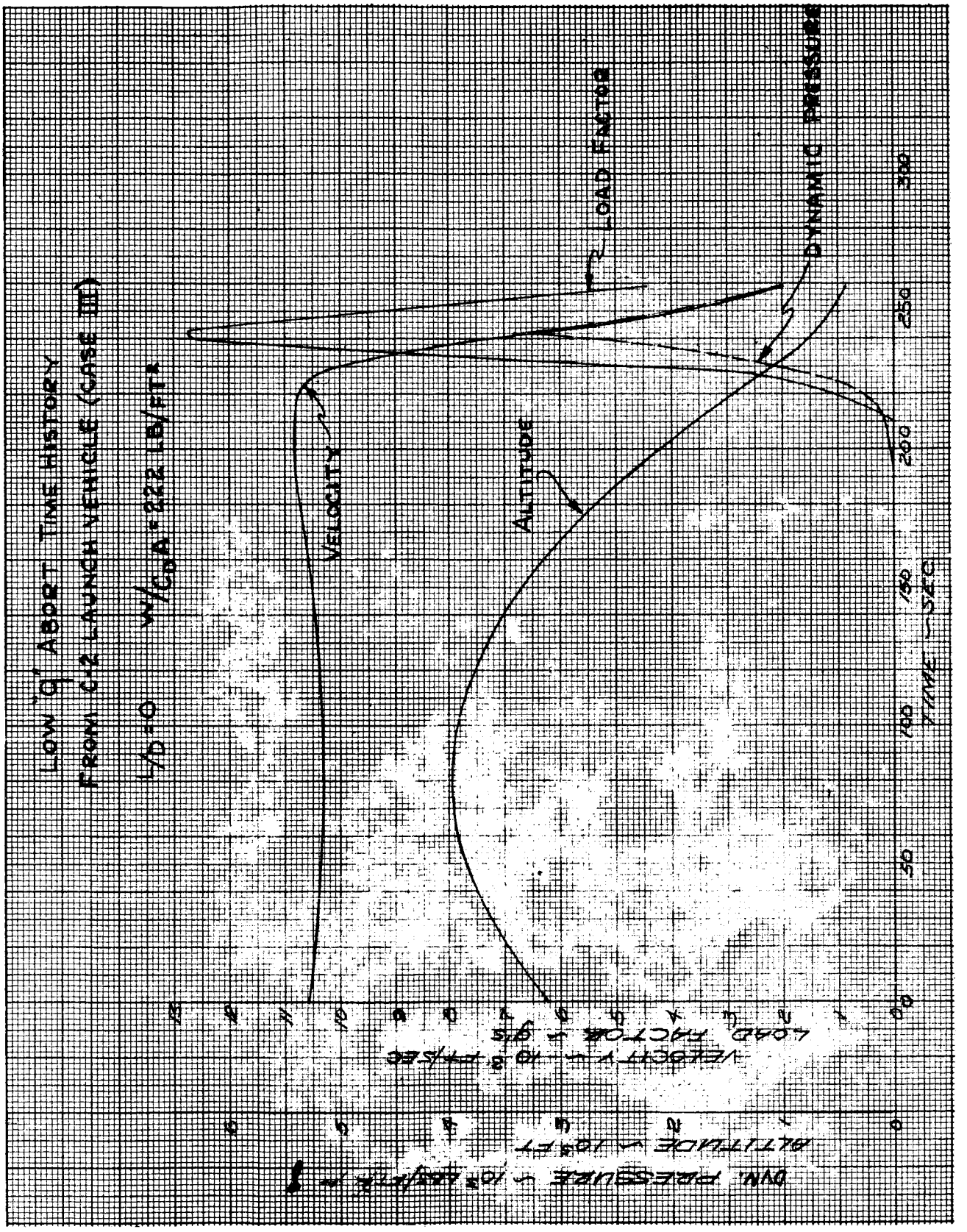

Fig. II-19. Load Factor Versus Time for Low q Abort Maneuver

CONFIDENTIAL

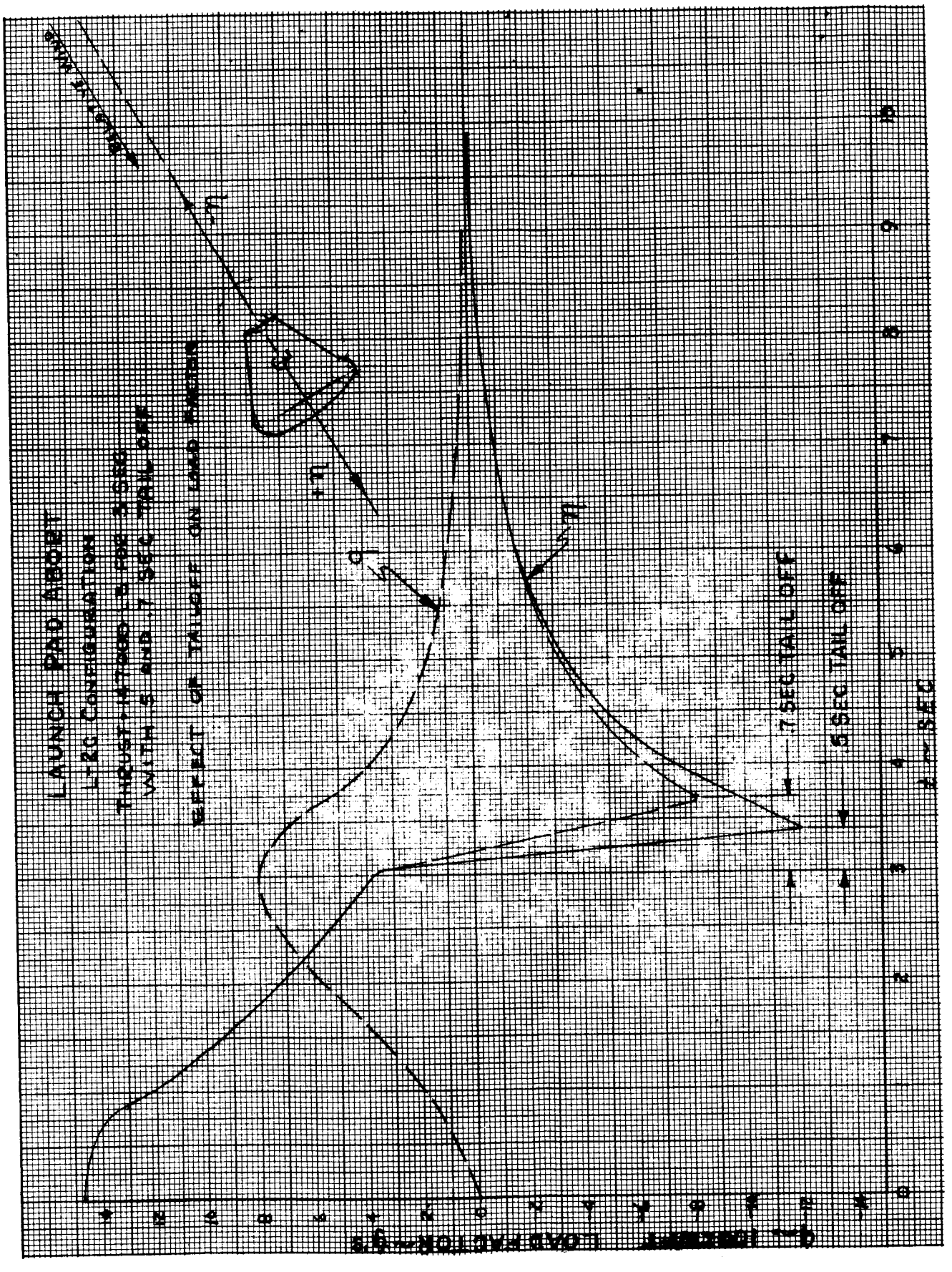

Fig. II-20. Effect of Tailoff on Load Factor

CONFIDENTIAL

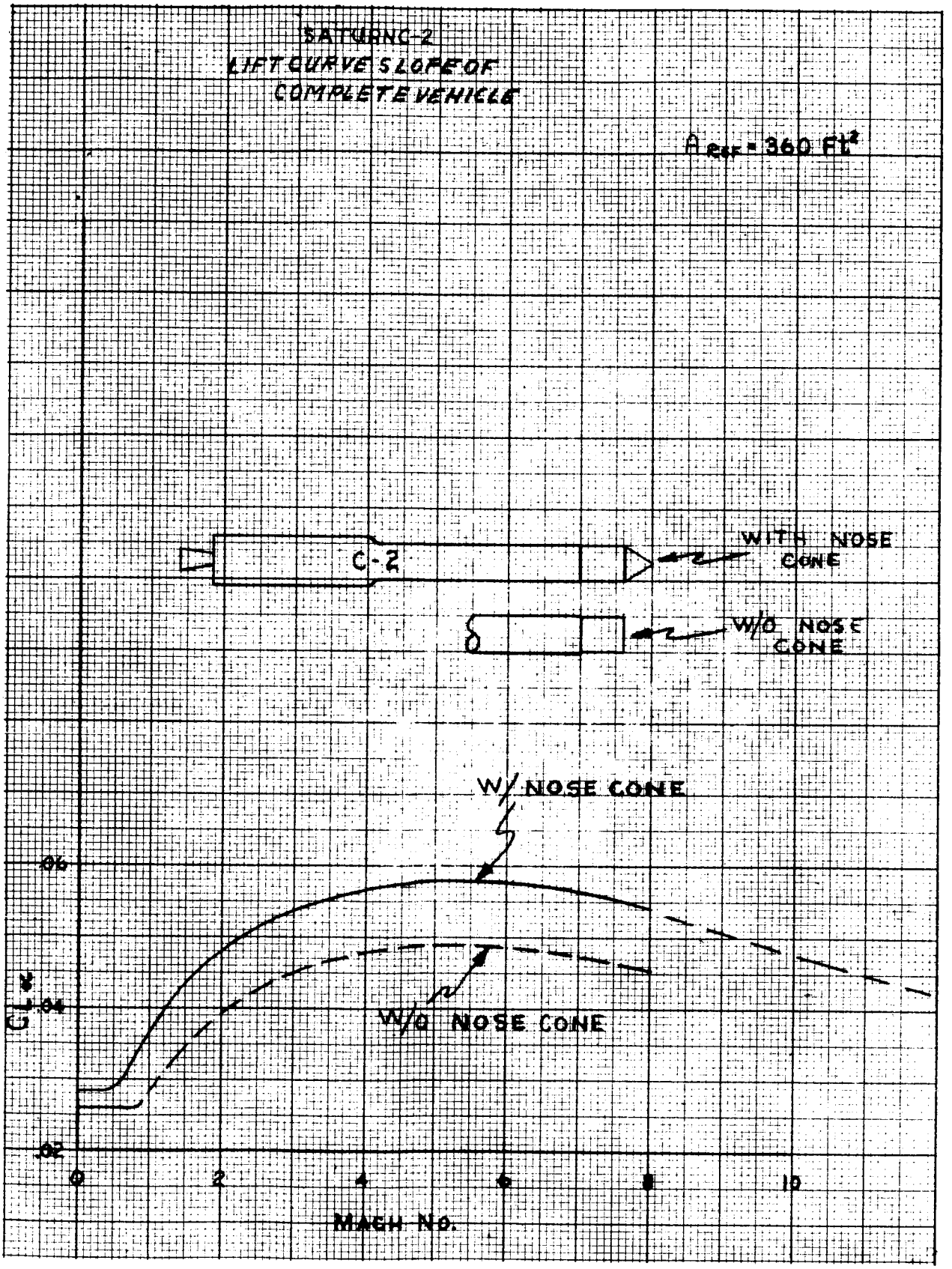

Fig. II-21. Booster Lift Characteristics

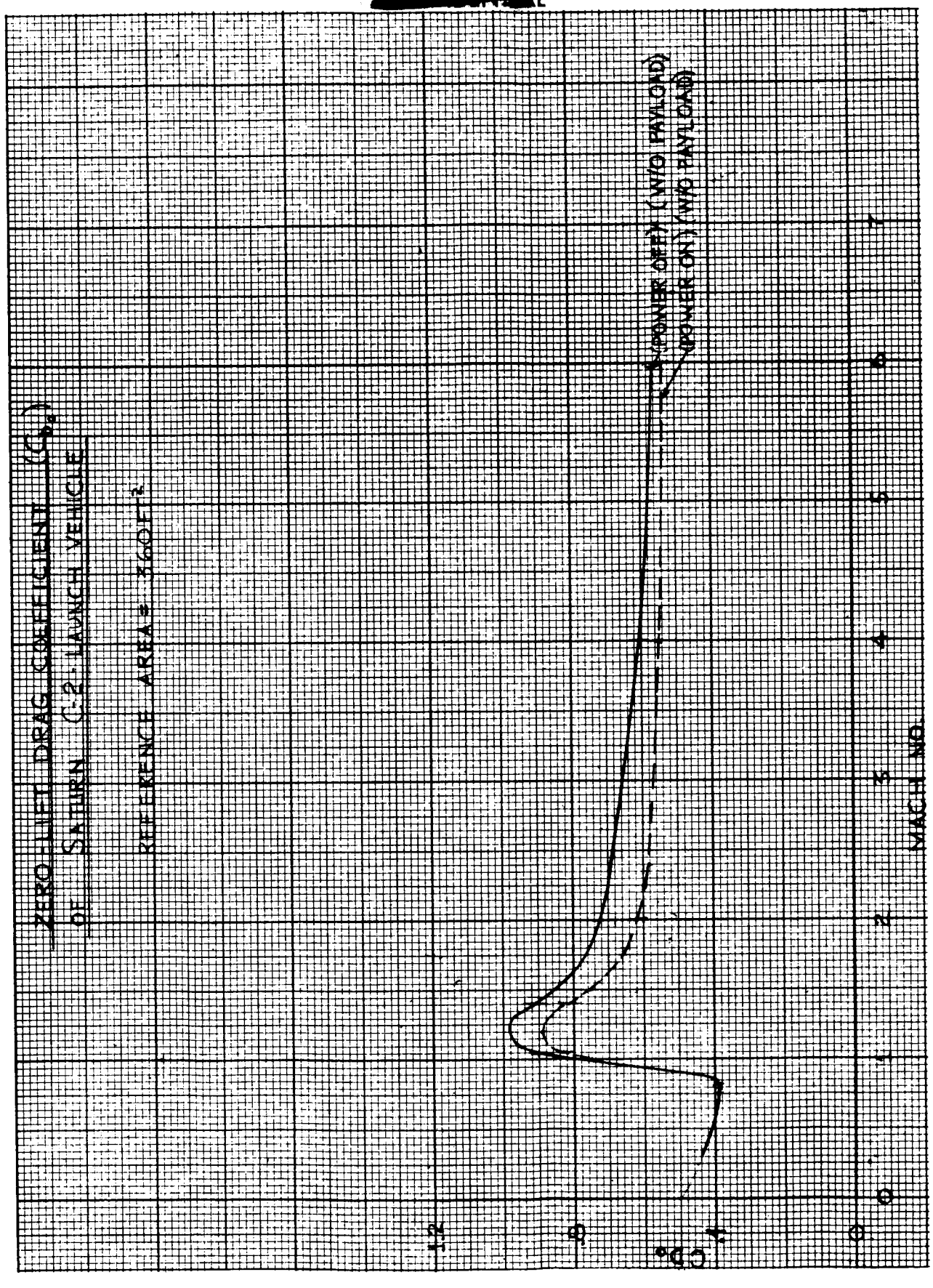

Fig. II-22. Booster Drag Characteristics

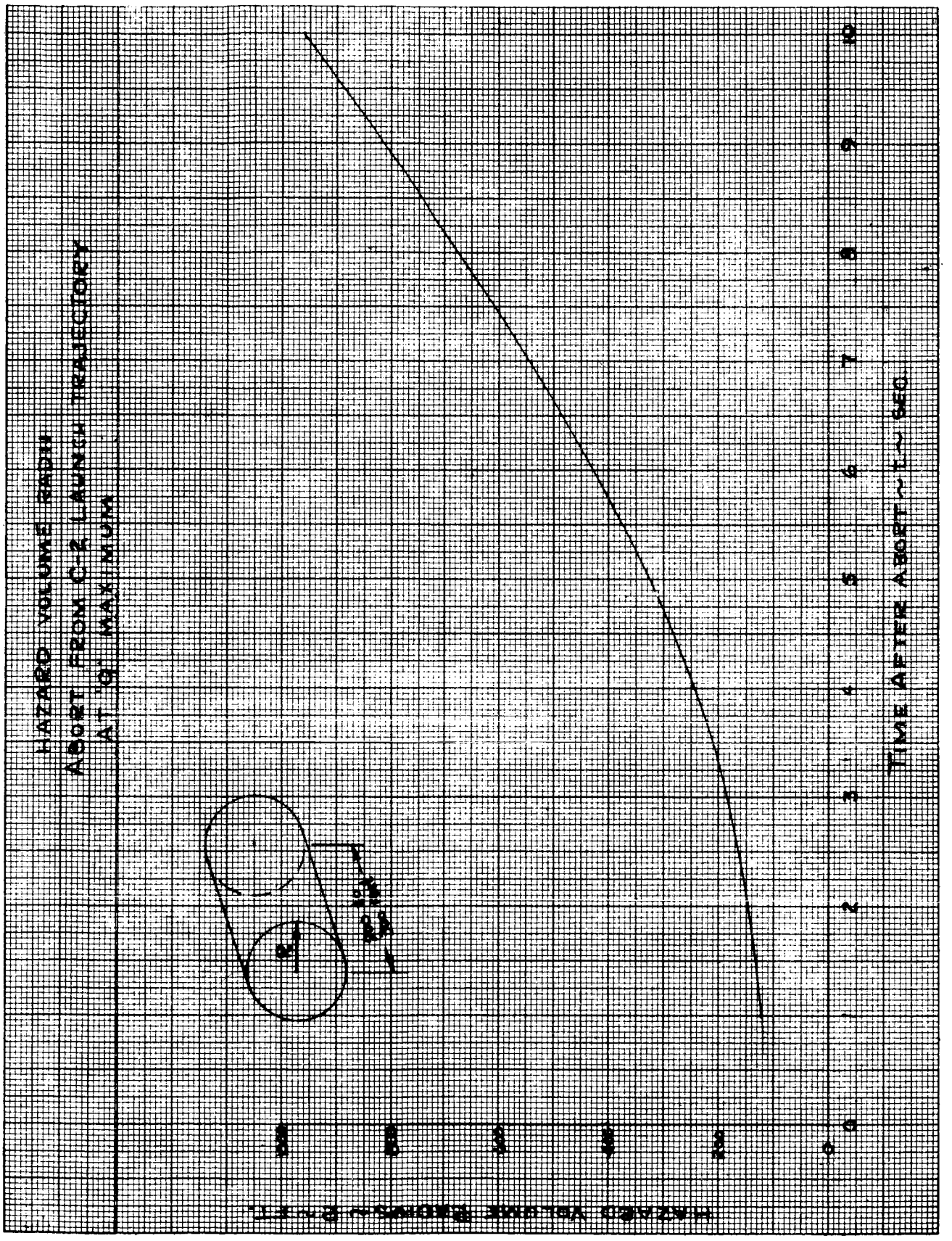

Fig. II-23. Hazard Volume Versus Time After Abort

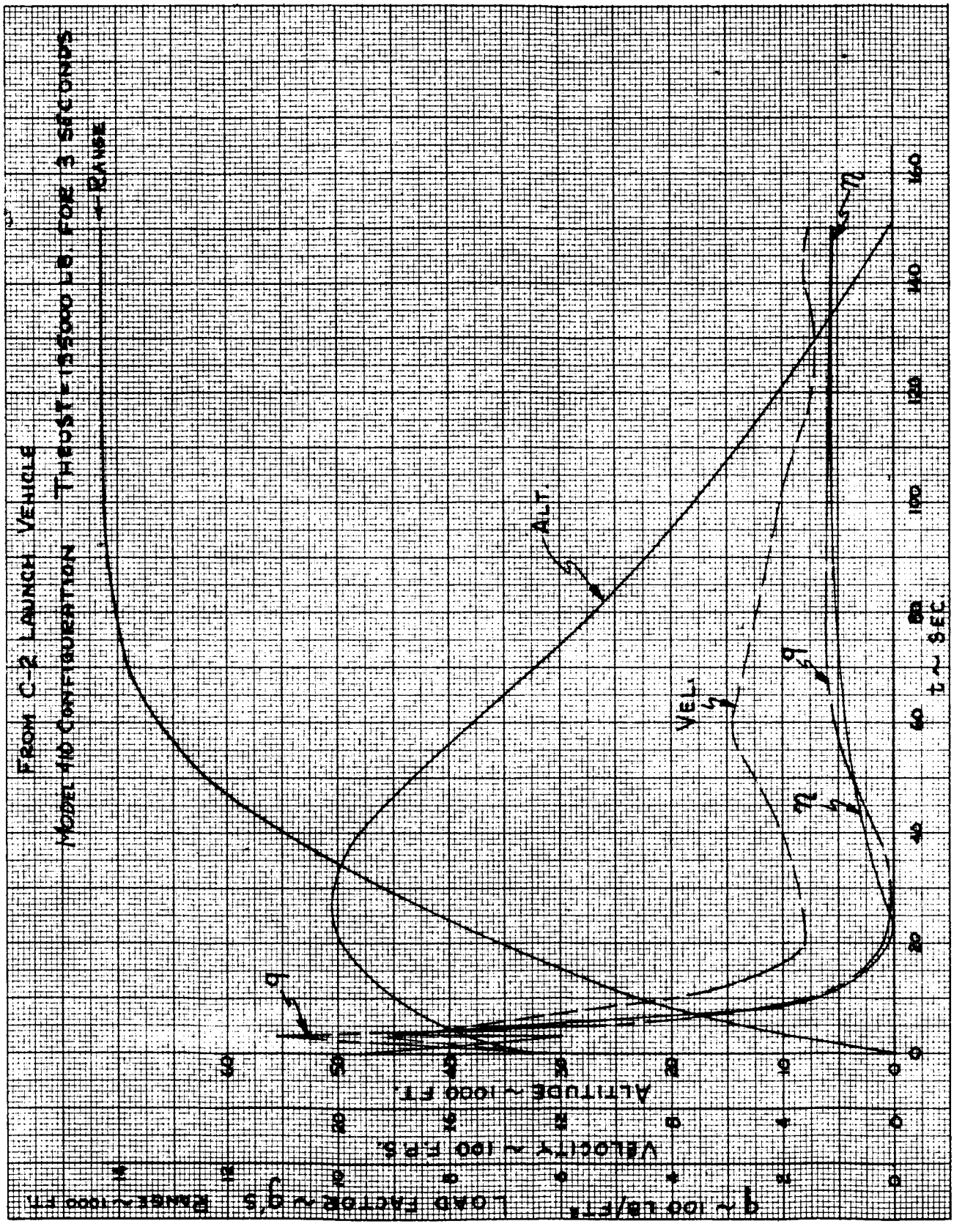

Fig. II-24. Abort at Maximum Dynamic Pressure

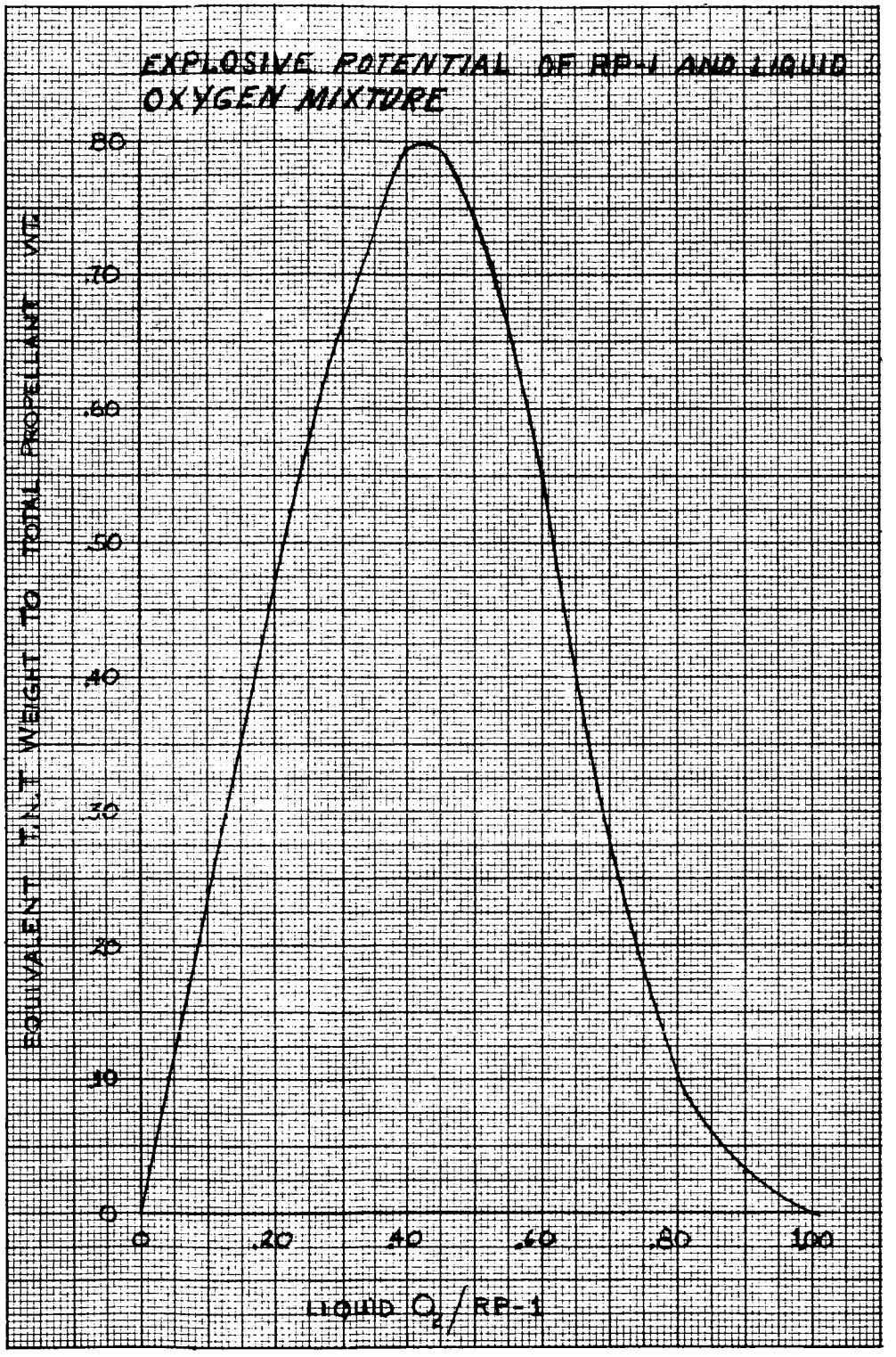

Fig. II-25. Explosive Potential: RP-1 and Liquid Oxygen

CONFIDENTIAL

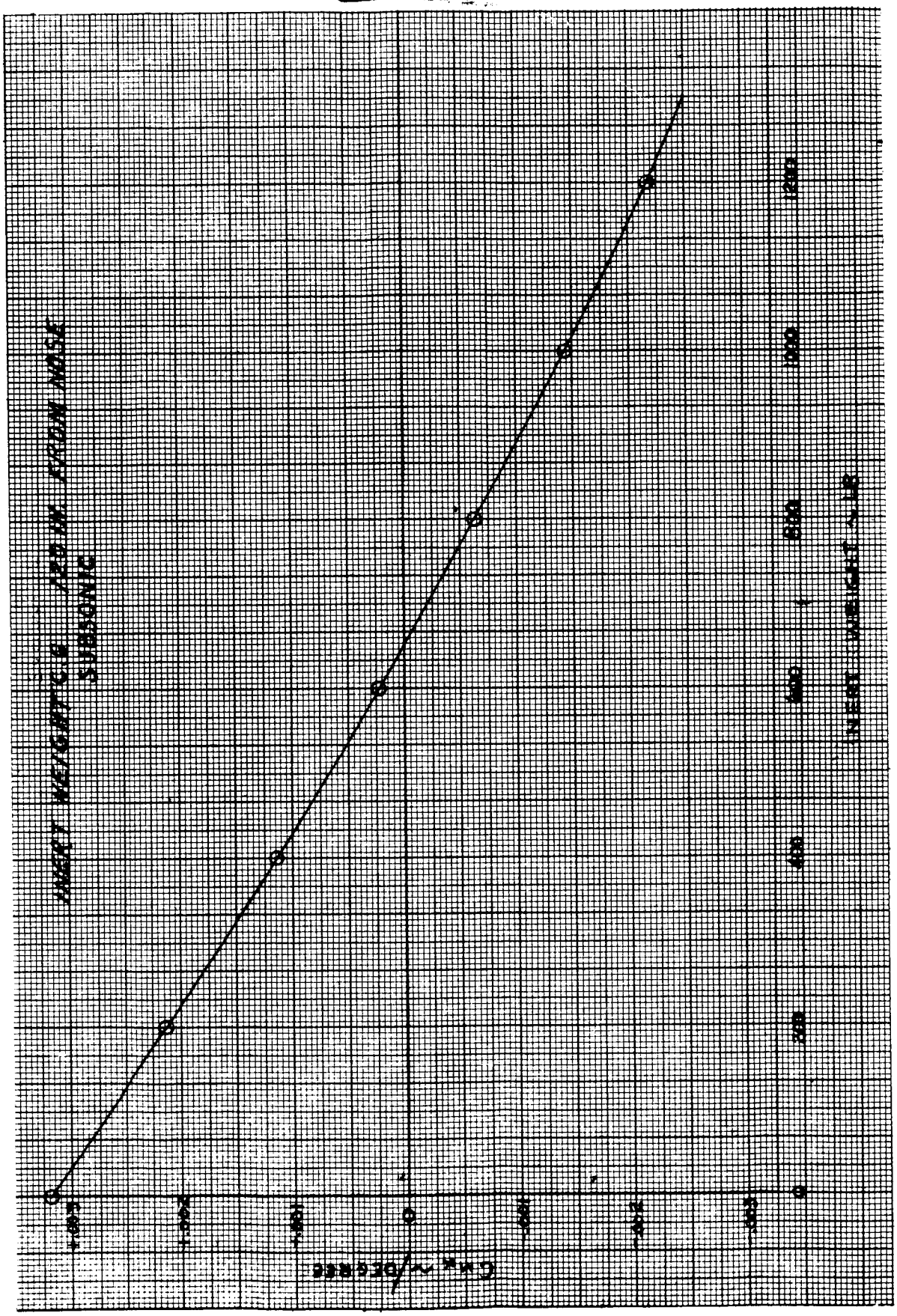

Fig. II-26. Effect of Ballast on Model 410 Static Stability

CONFIDENTIAL

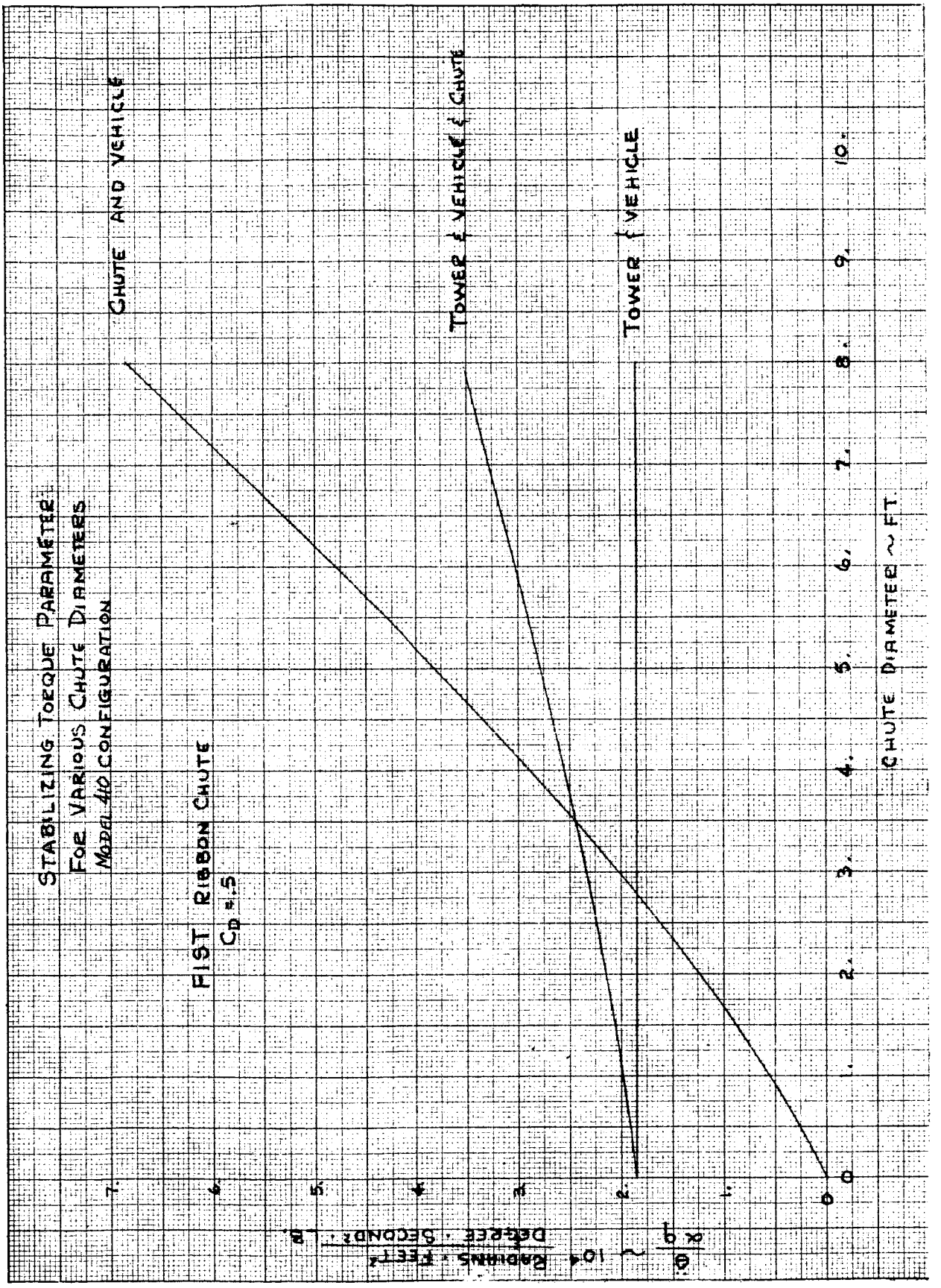

Fig. II-27. Stabilizing Effect of Drogue Chute

CONFIDENTIAL

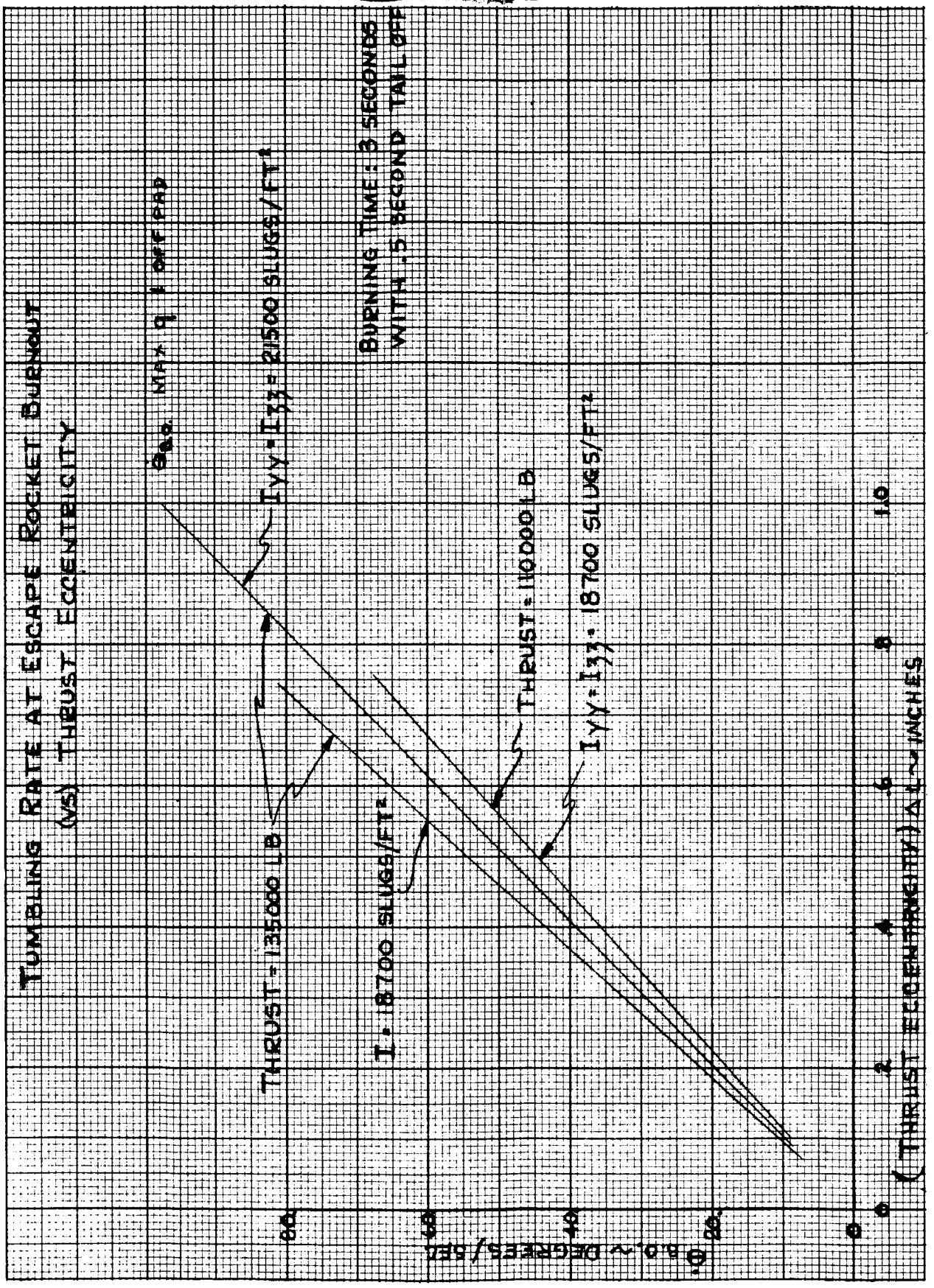

Fig. II-28. Tumbling Rate After Abort: Autopilot Failure

CONFIDENTIAL

D-3 (6-60)

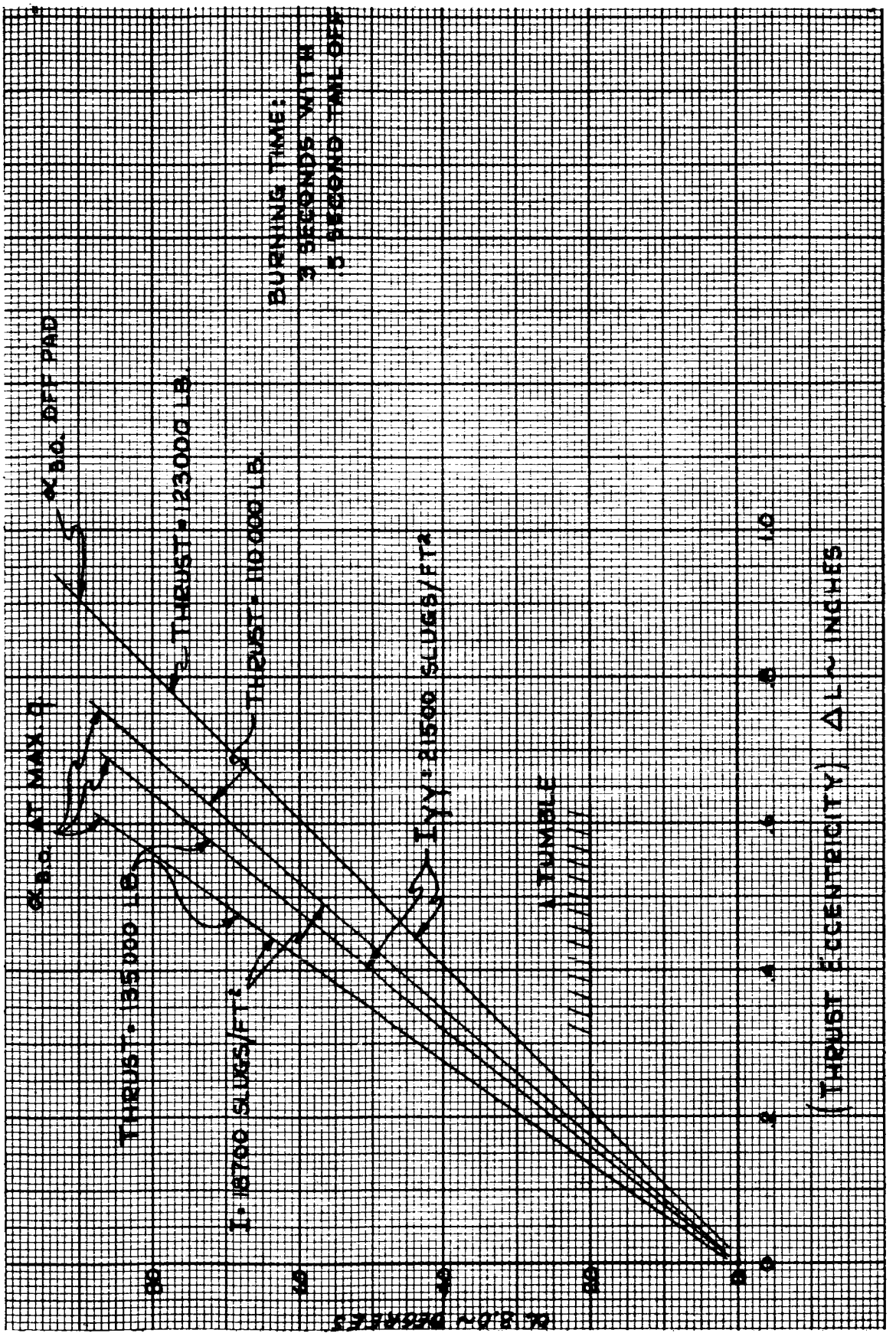

Fig. II-29. Angle of Attack After Abort: Autopilot Failure

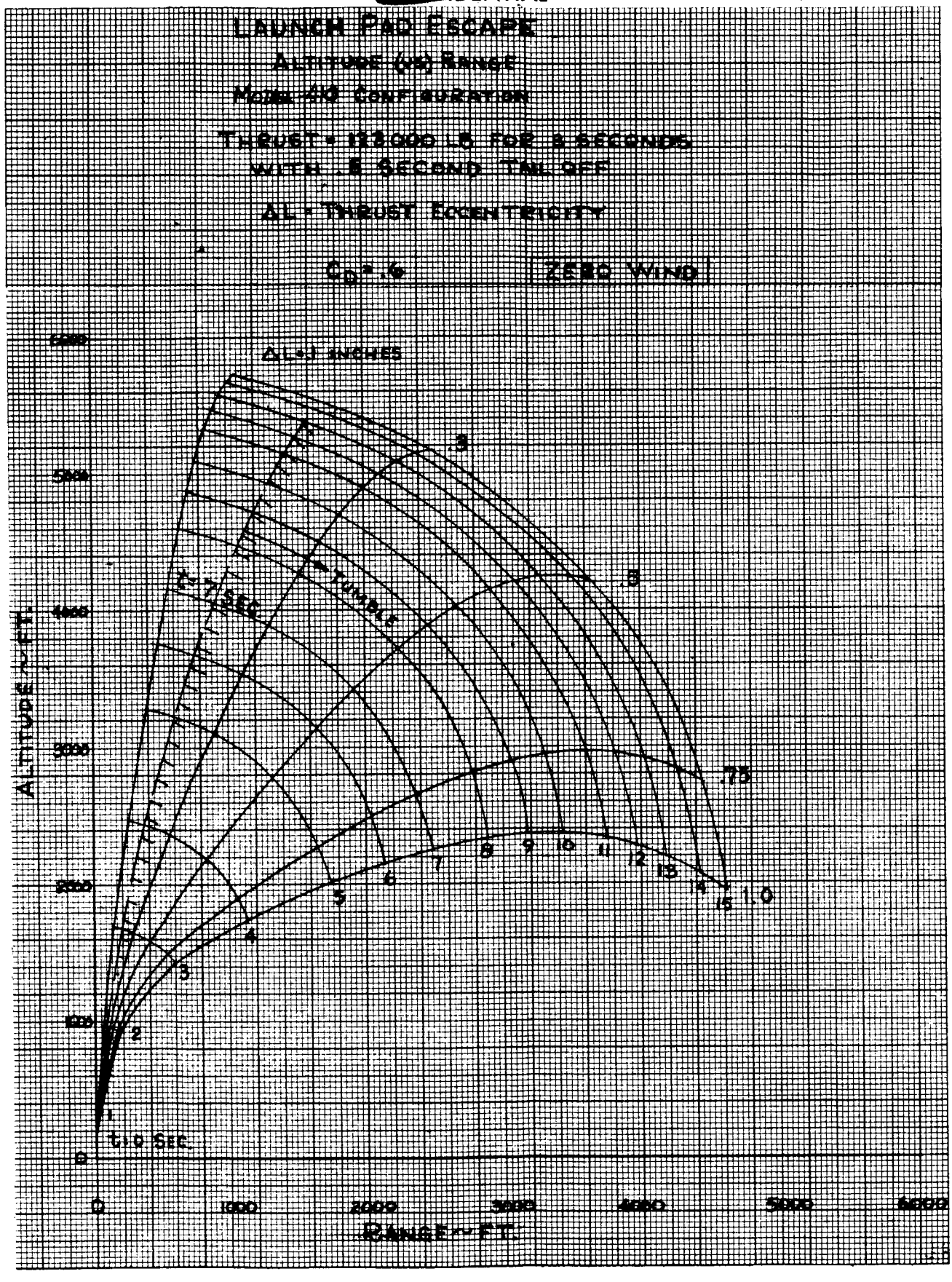

Fig. II-30. Tumbling Versus Thrust Eccentricity: Pad Abort

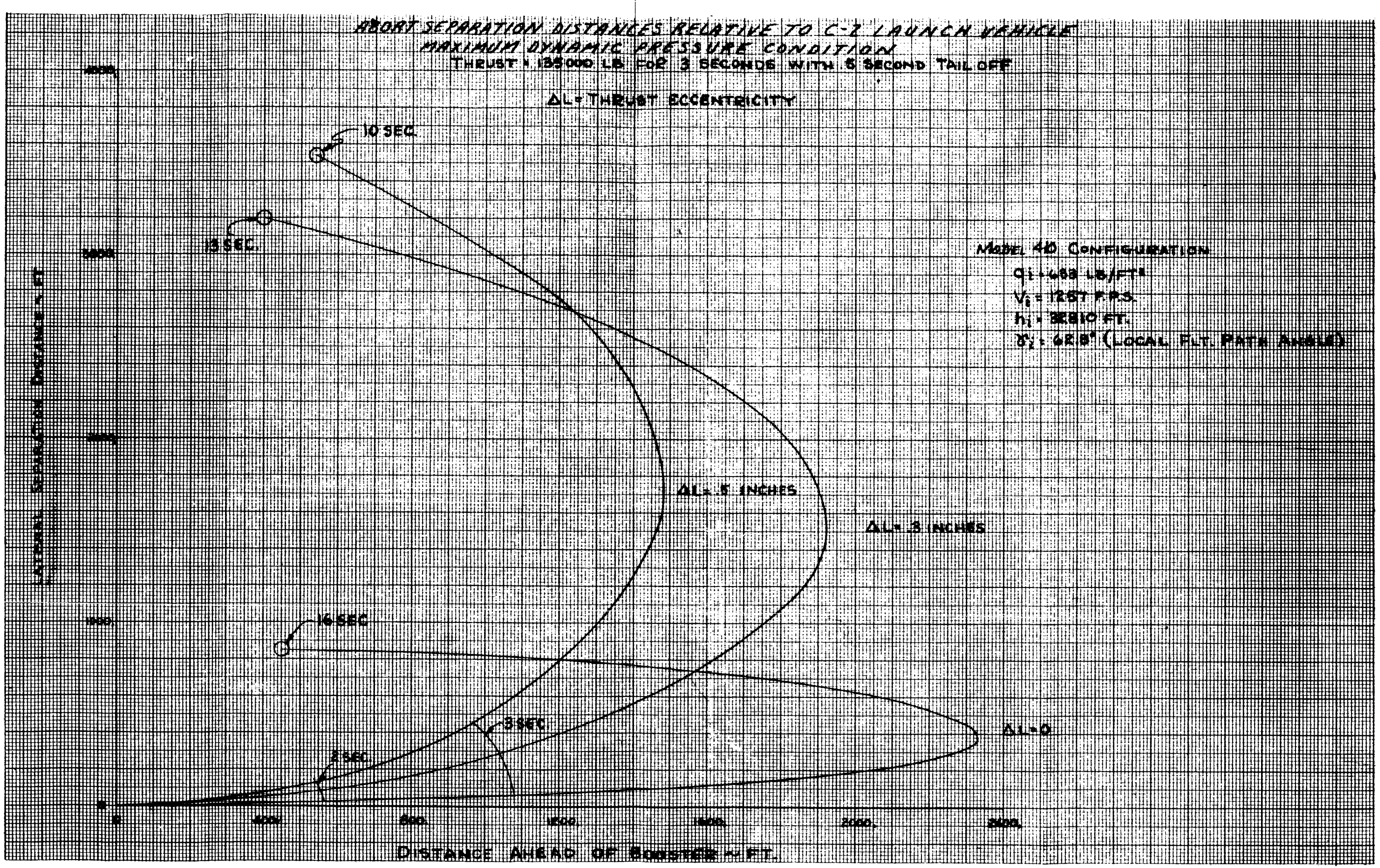

Fig. II-31. Abort Trajectories at Maximum q: Autopilot Failure

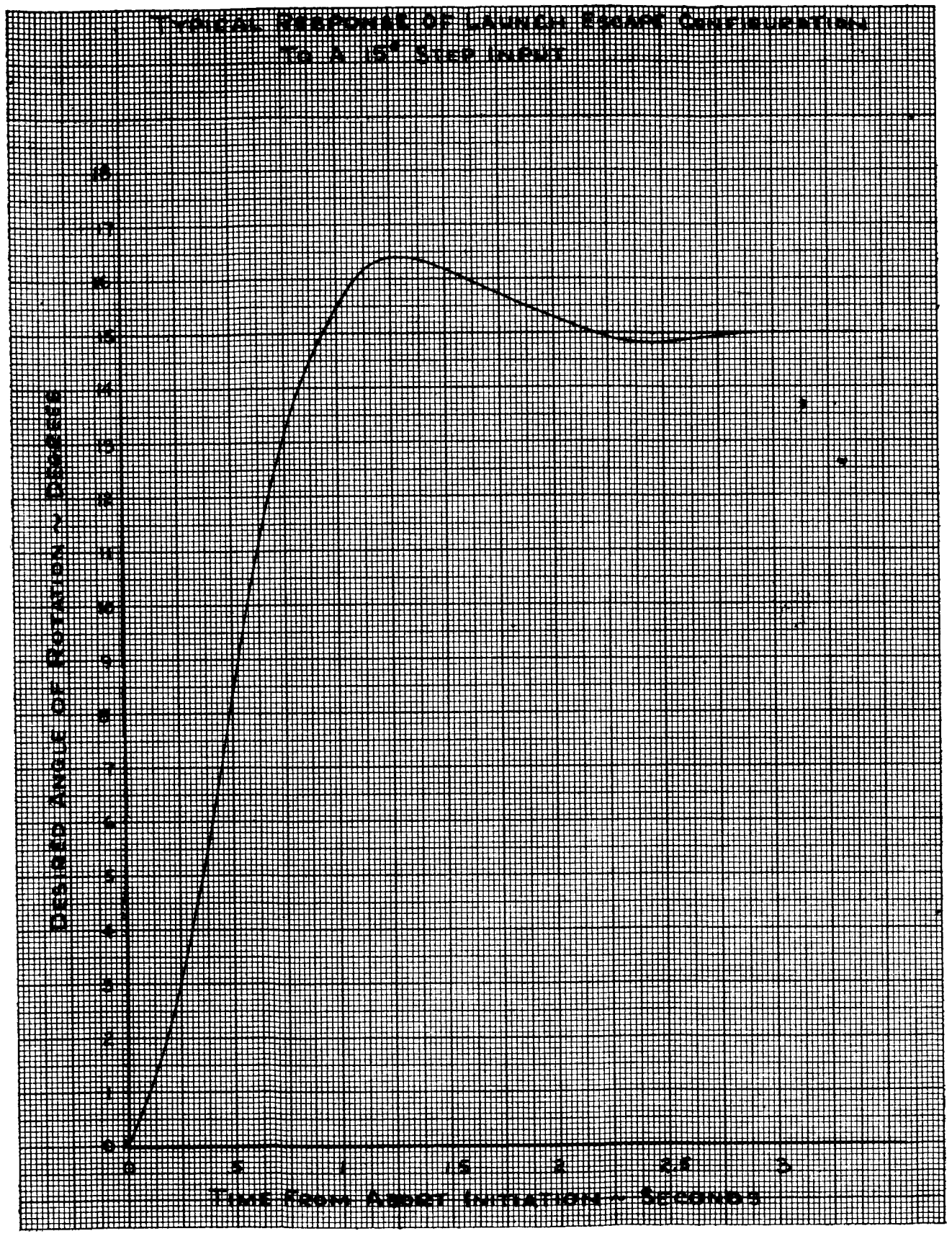

Fig. II-32. Autopilot Response During Abort Initiation

D-(6-60)

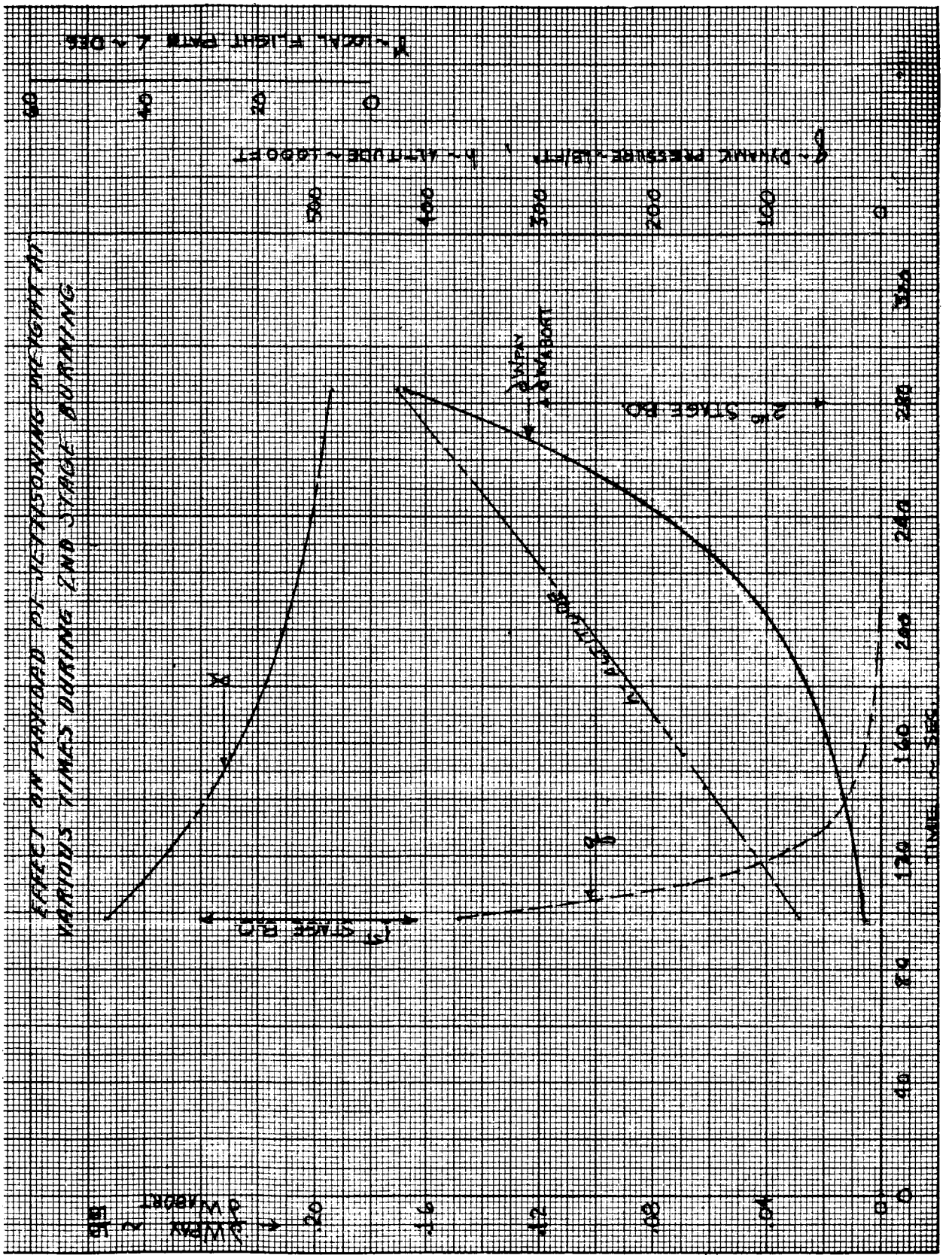

Fig. II-33. Payload Penalty for Launch Escape System

D-3 (6-60)

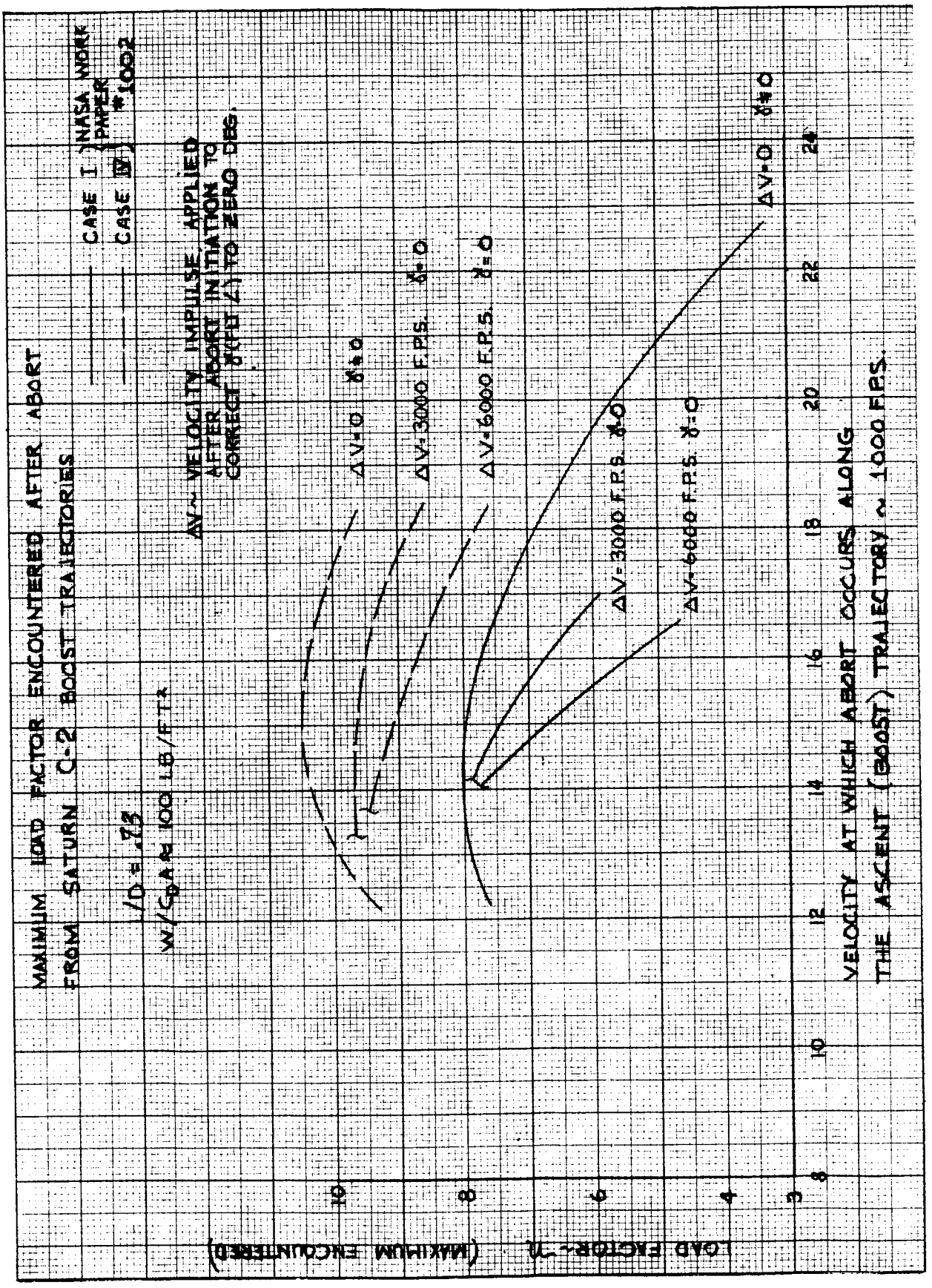

Fig. II-34. Load Factor Versus Velocity Summary

D-3 (6-60)

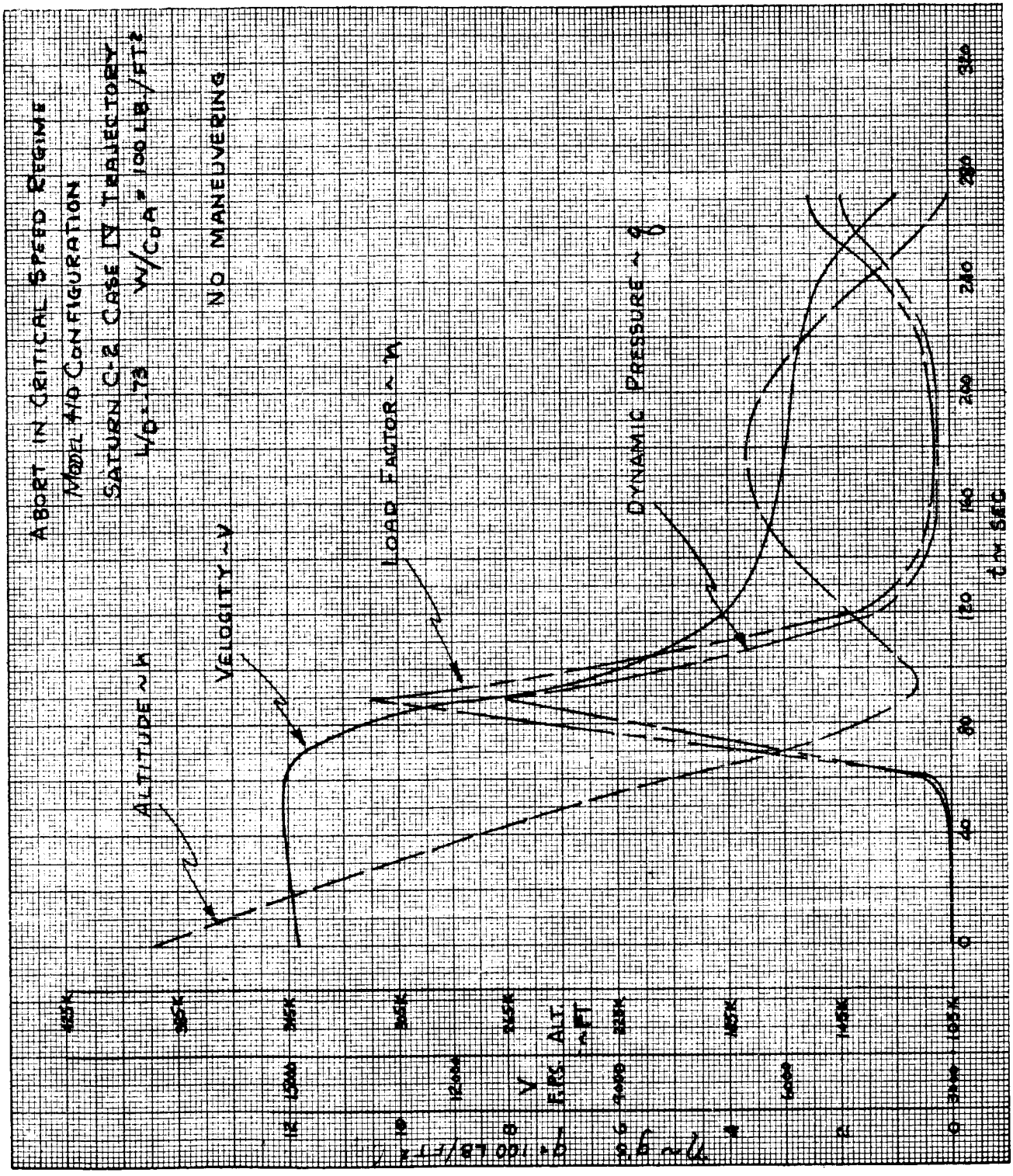

Fig. II-35. Abort Trajectory (V = 15,000 fps)

~~CONFIDENTIAL~~

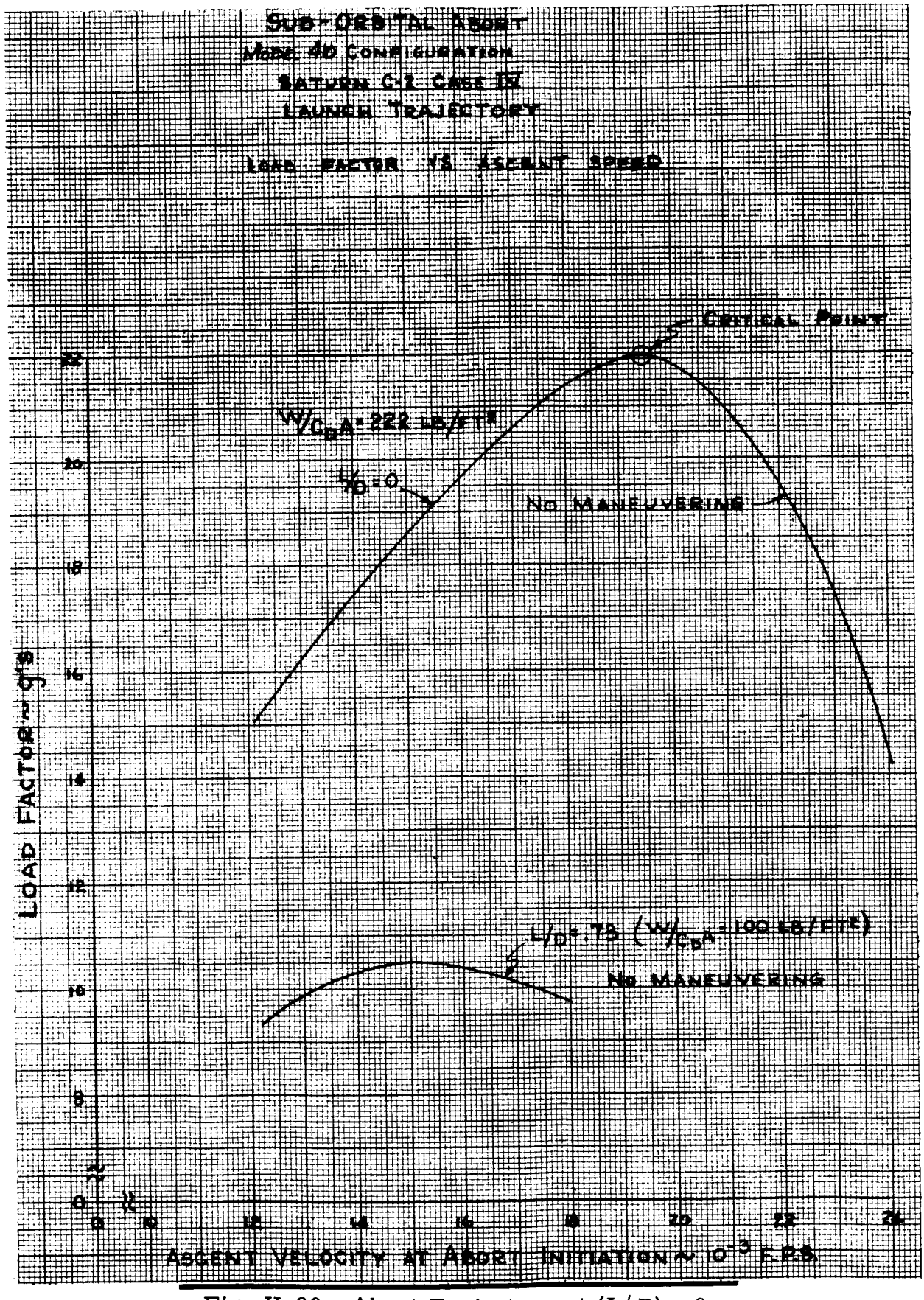

Fig. II-36. Abort Trajectory at (L/ D) = 0

~~CONFIDENTIAL~~

D-3 (6-60)

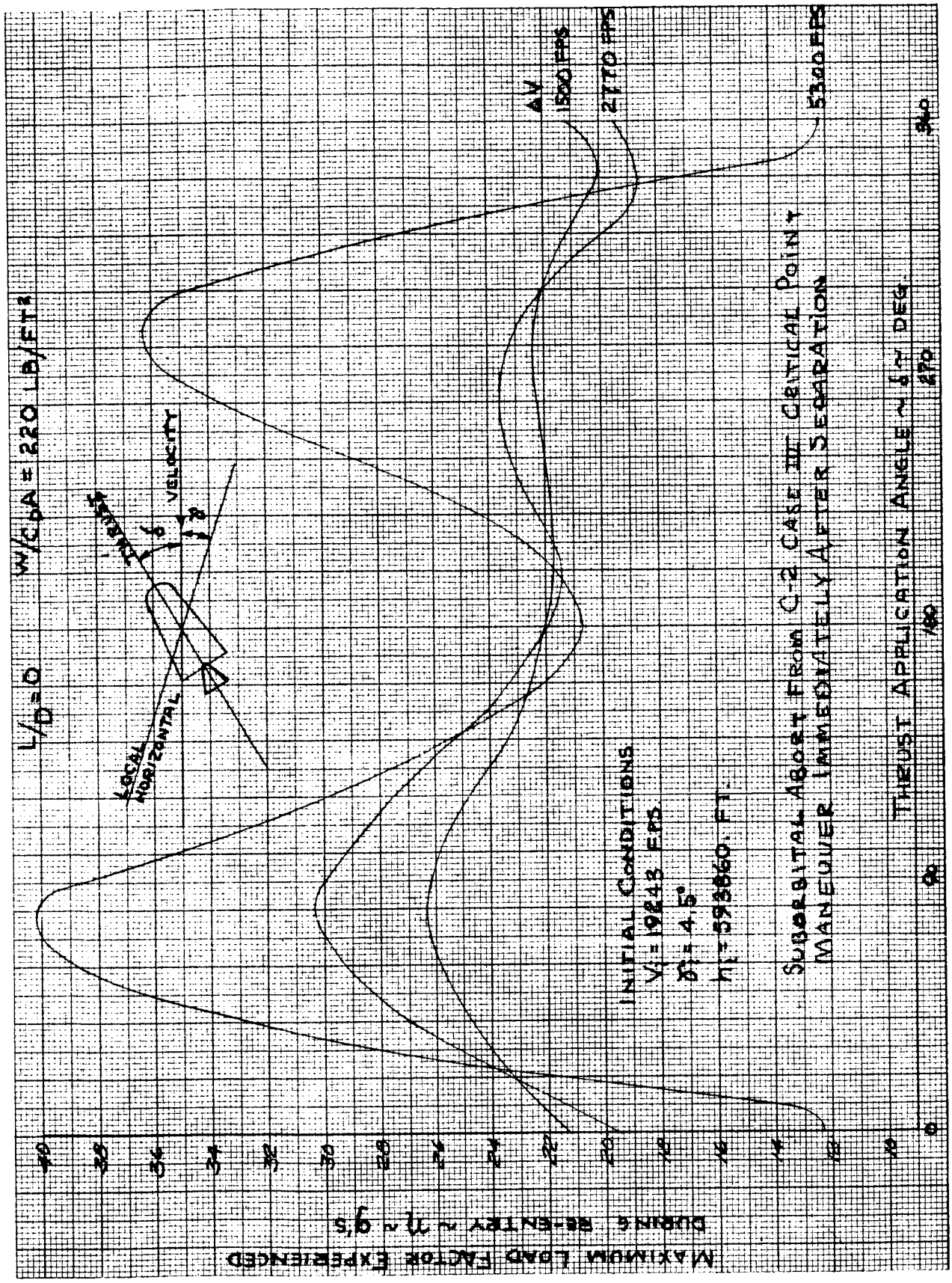

Fig. II-37. Effect of Thrust Vector Orientation

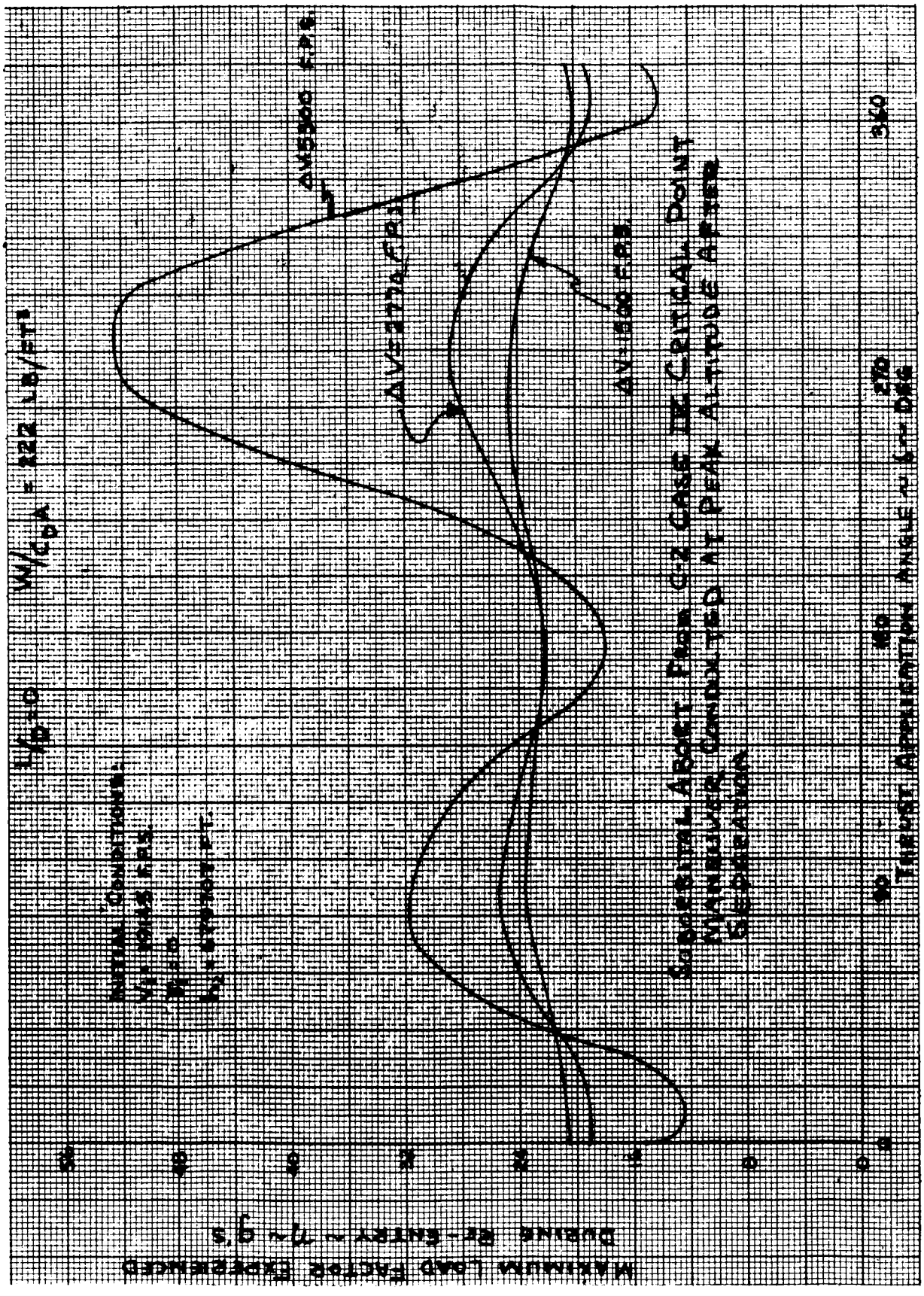

Fig. II-38. Abort Maneuvering at Escape Trajectory Apogee

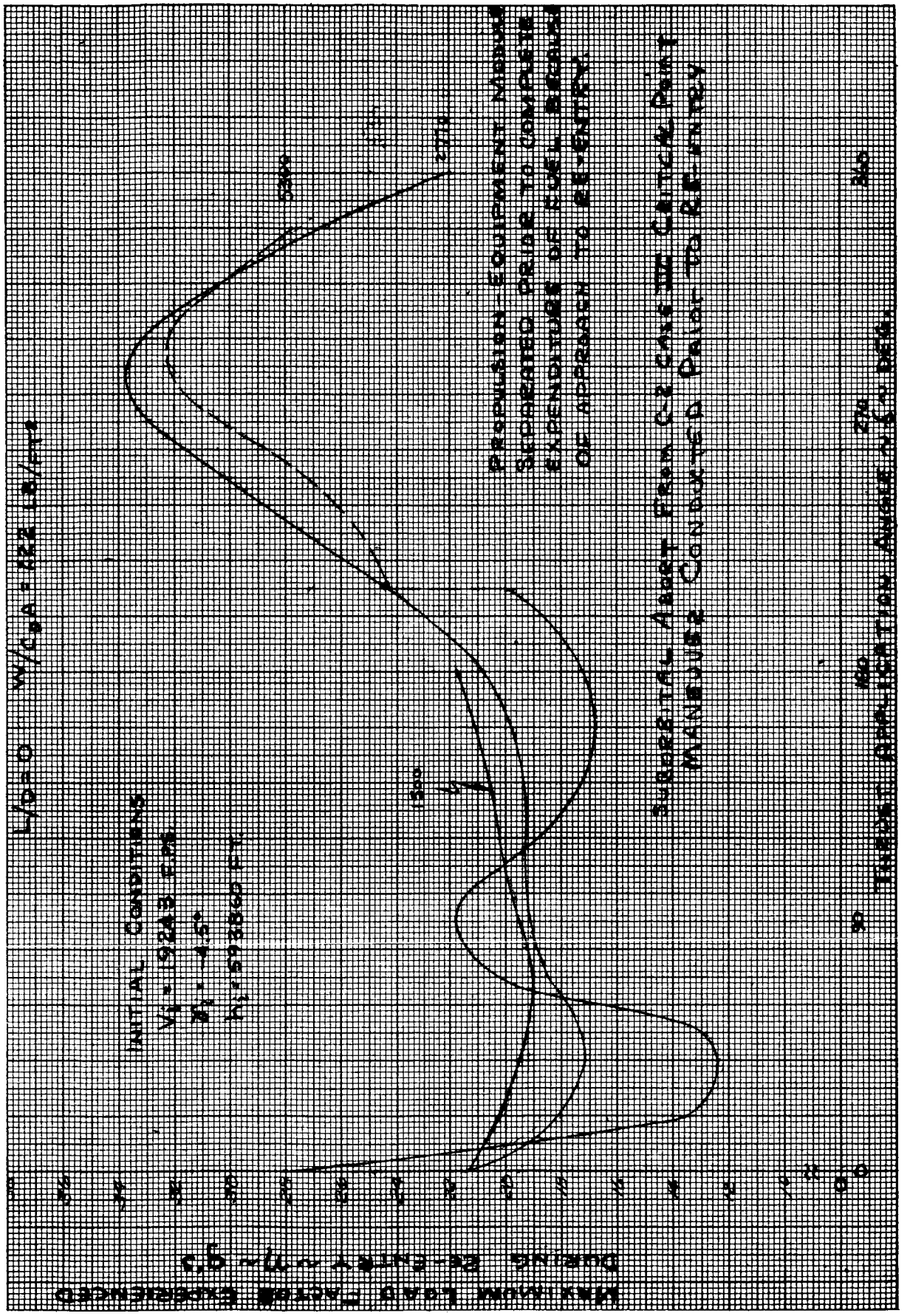

Fig. II-39. Abort Maneuvering at Escape Trajectory Re-Entry

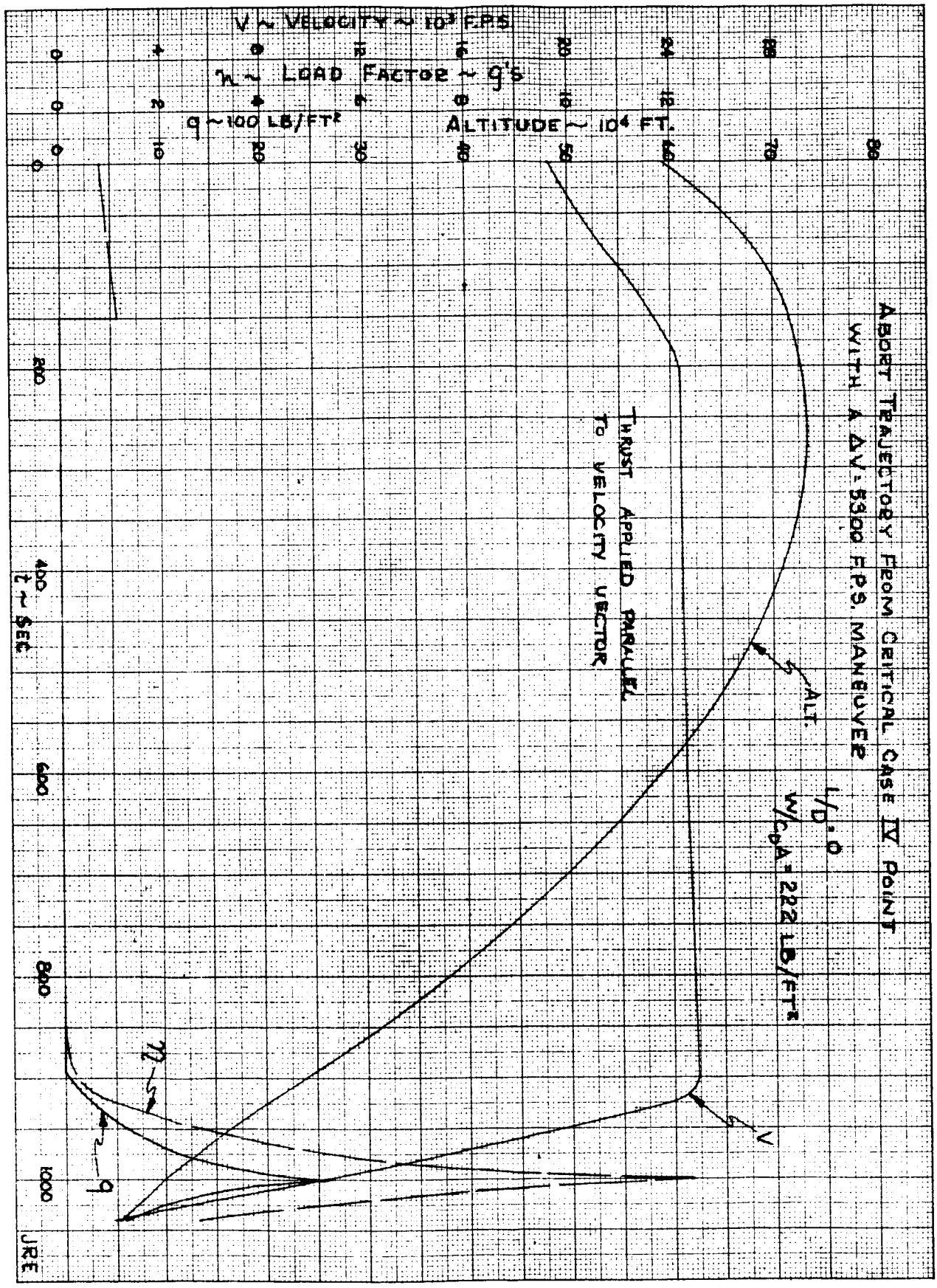

Fig. II-40. Abort Trajectory at (L/ D) = 0 with V = 5300 fps

D-3 (6-60)

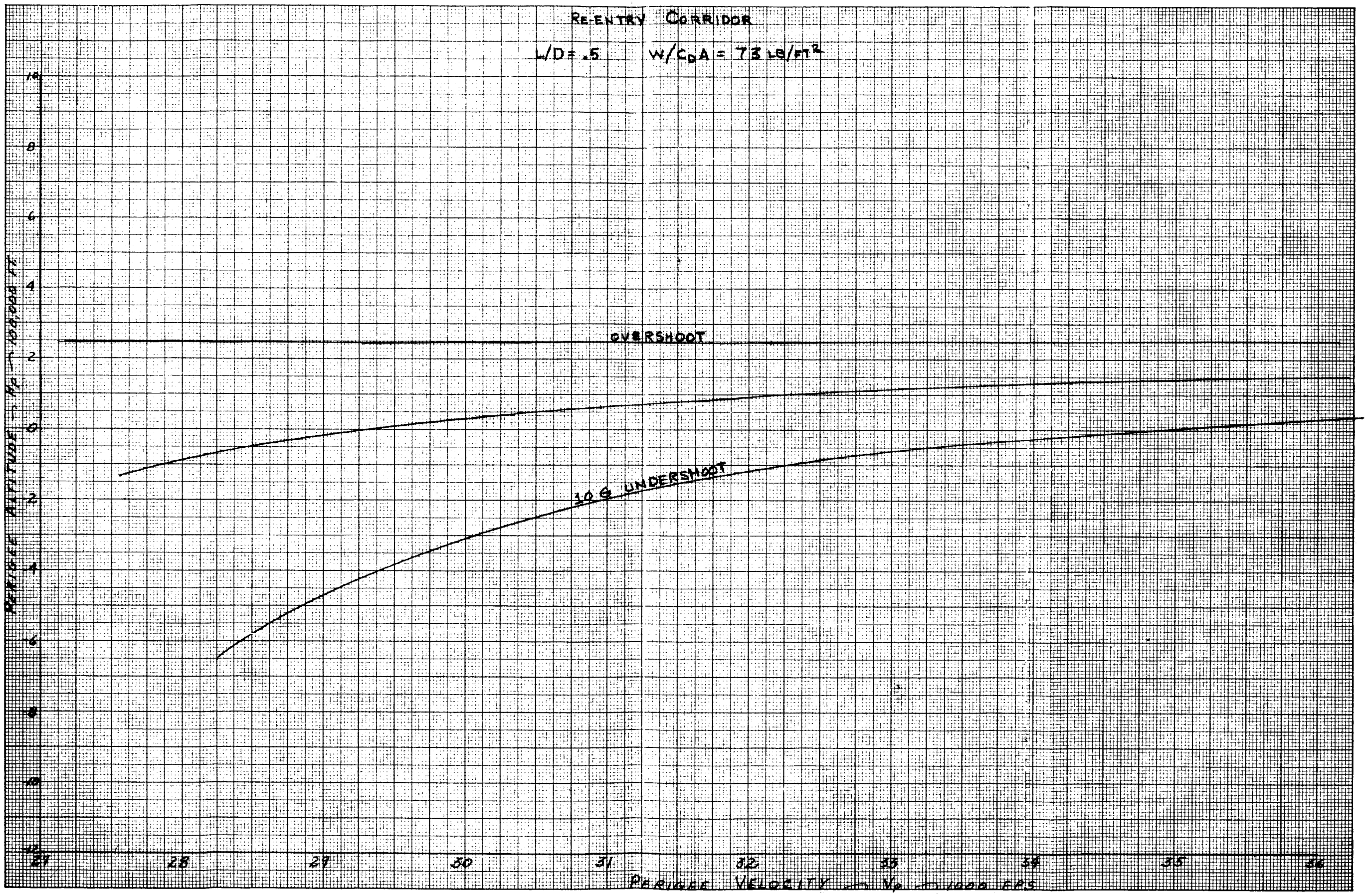

Fig. II-41. Perigee Altitude at Injection

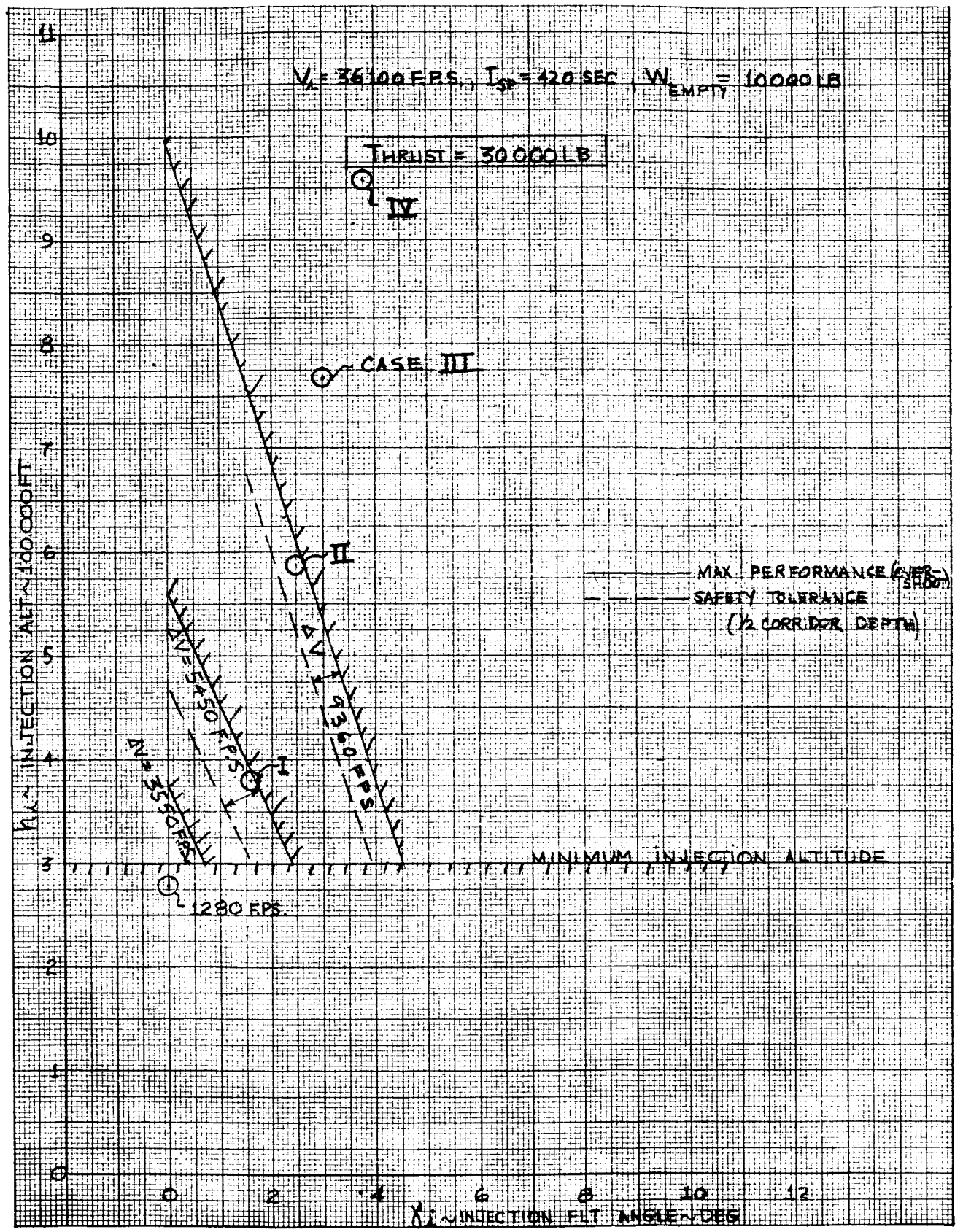

Fig. II-42. Immediate Re-entry Capability: T = 30,000 lb

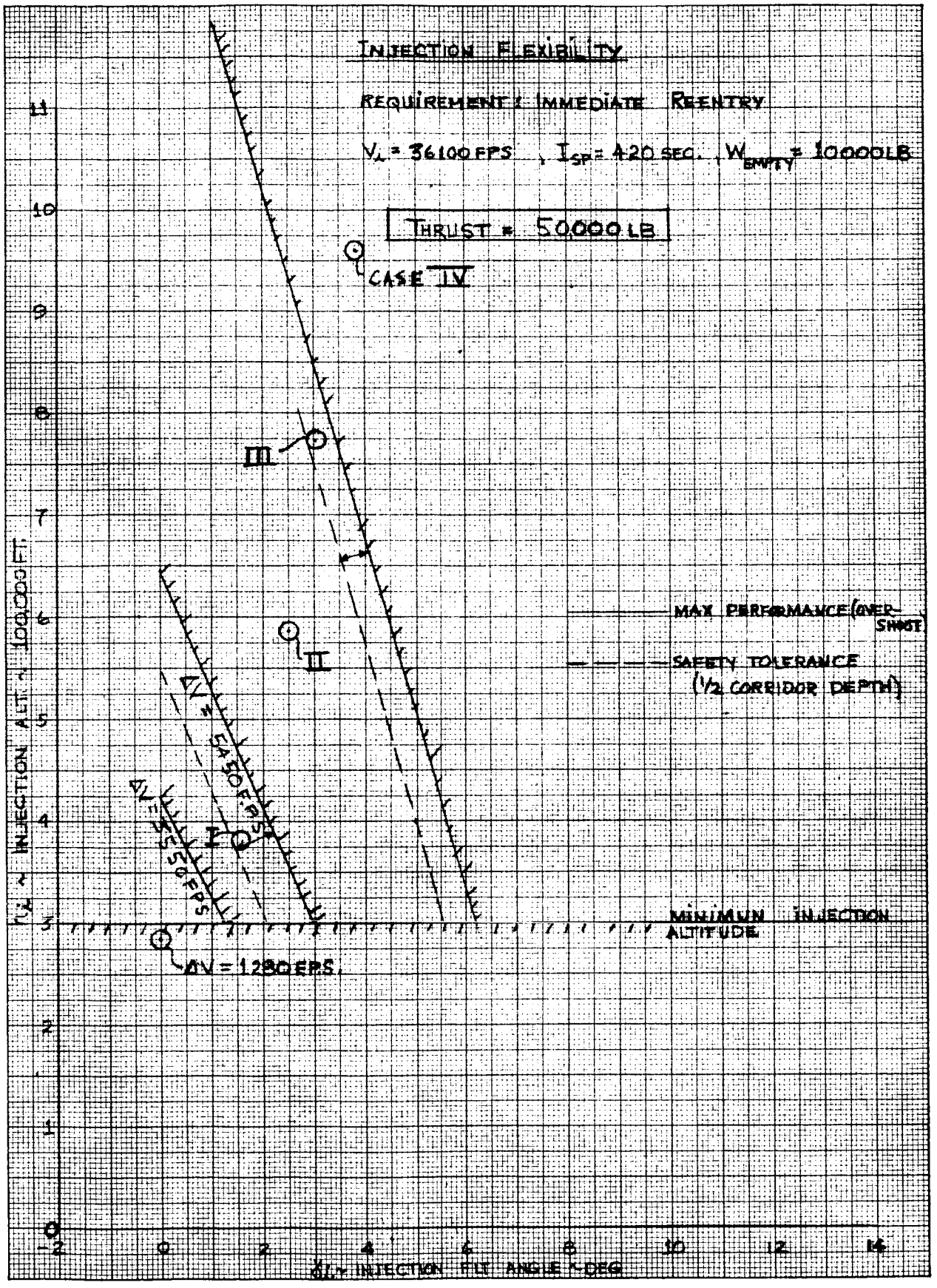

Fig. II-43. Immediate Re-entry Capability: T = 50,000 lb

CONFIDENTIAL

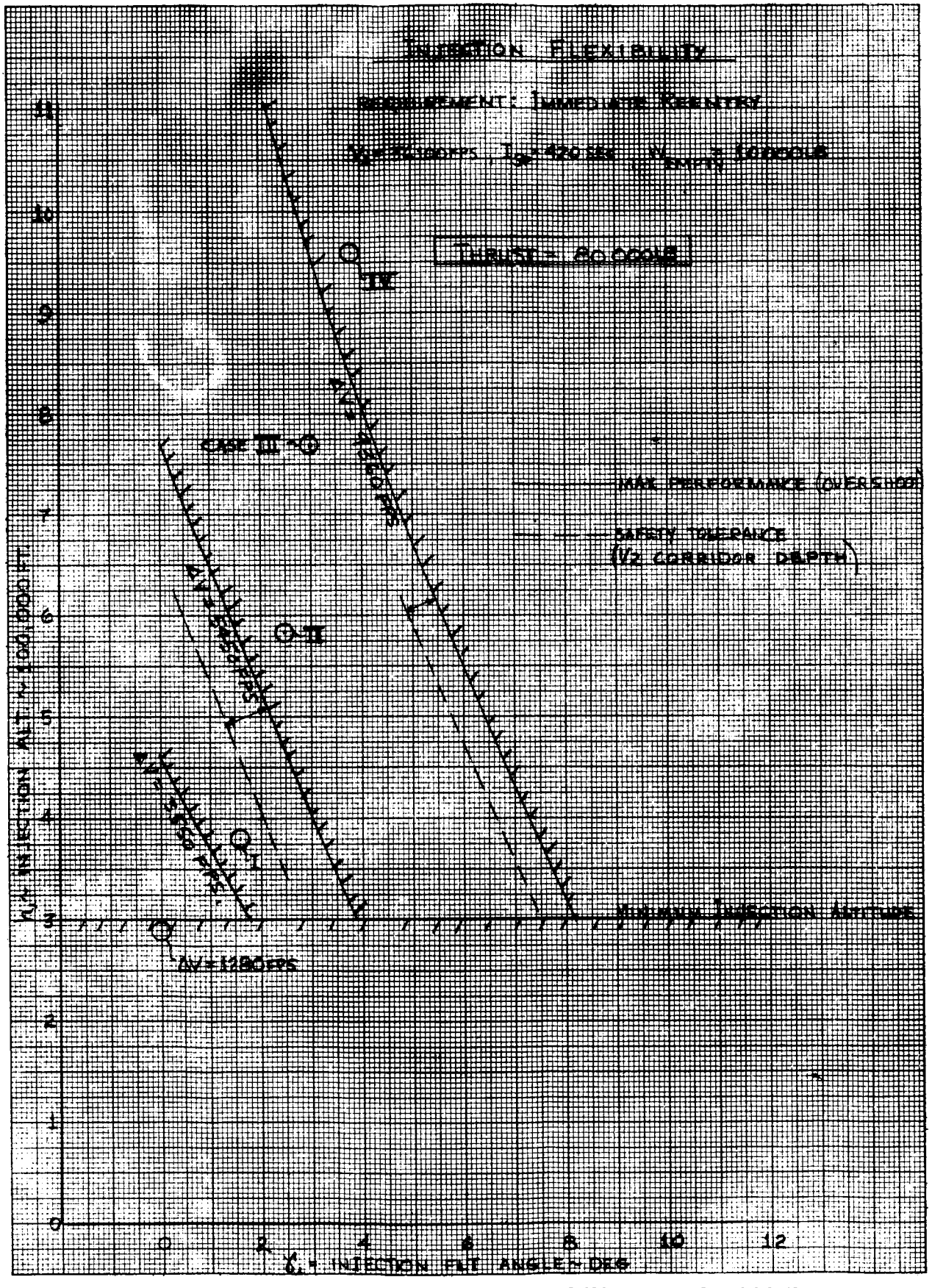

Fig. II-44. Immediate Re-entry Capability: T = 80,000 lb

CONFIDENTIAL

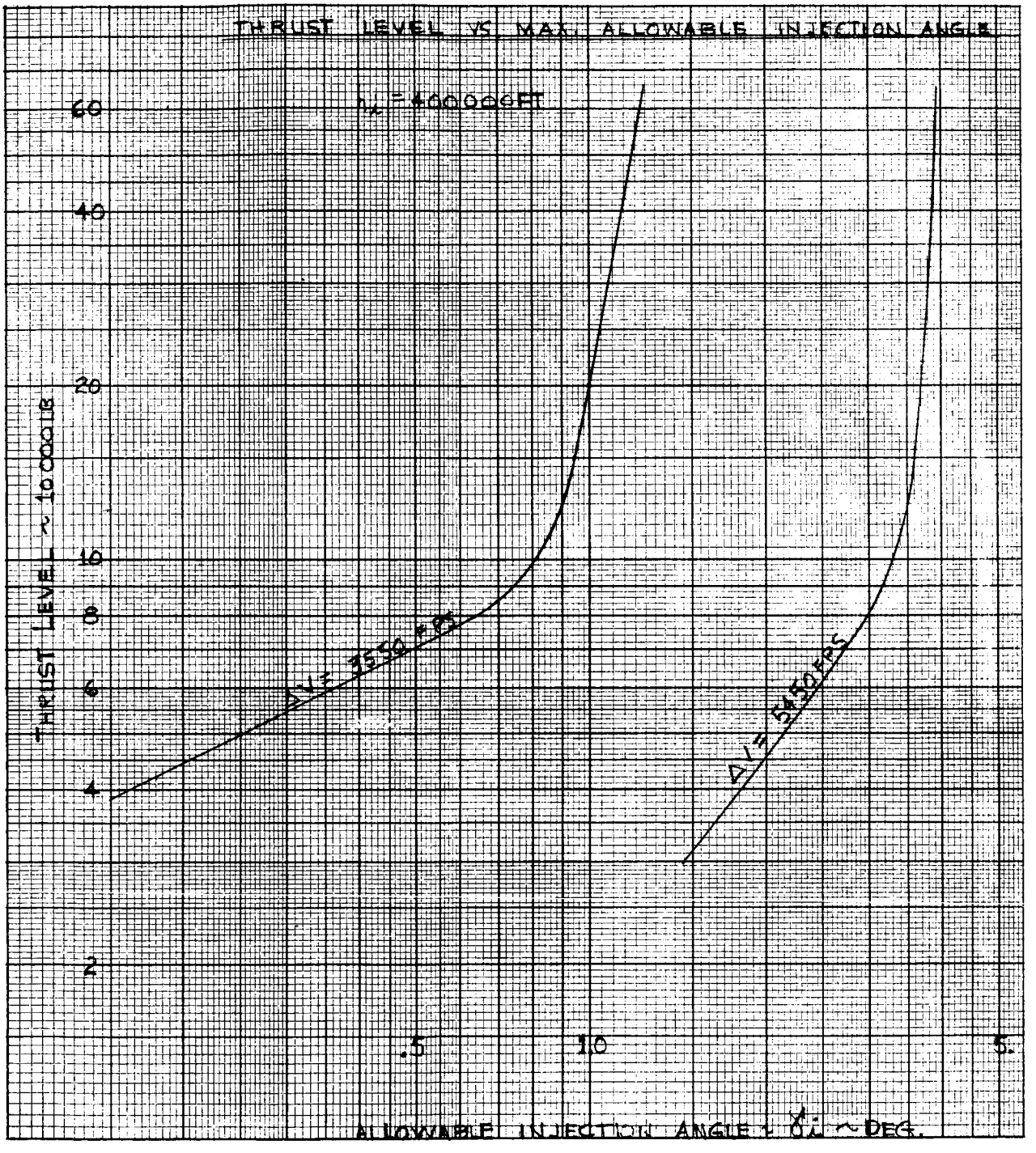

Fig. II-45. Summary: Thrust Versus Flight Path Angle for Immediate Re-entry

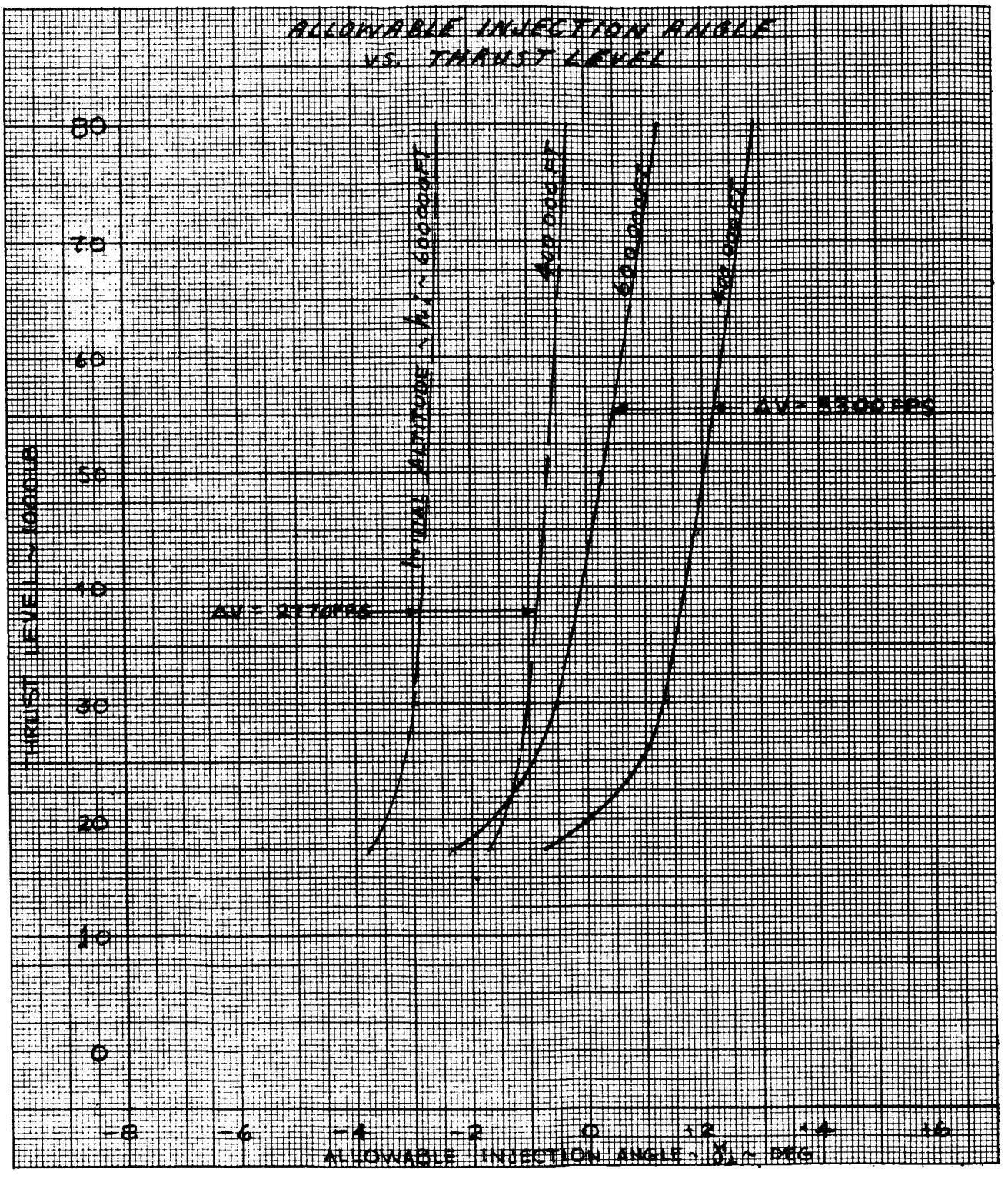

Fig. II-46. Allowable Injection Burnout Flight Path Angle

CONFIDENTIAL

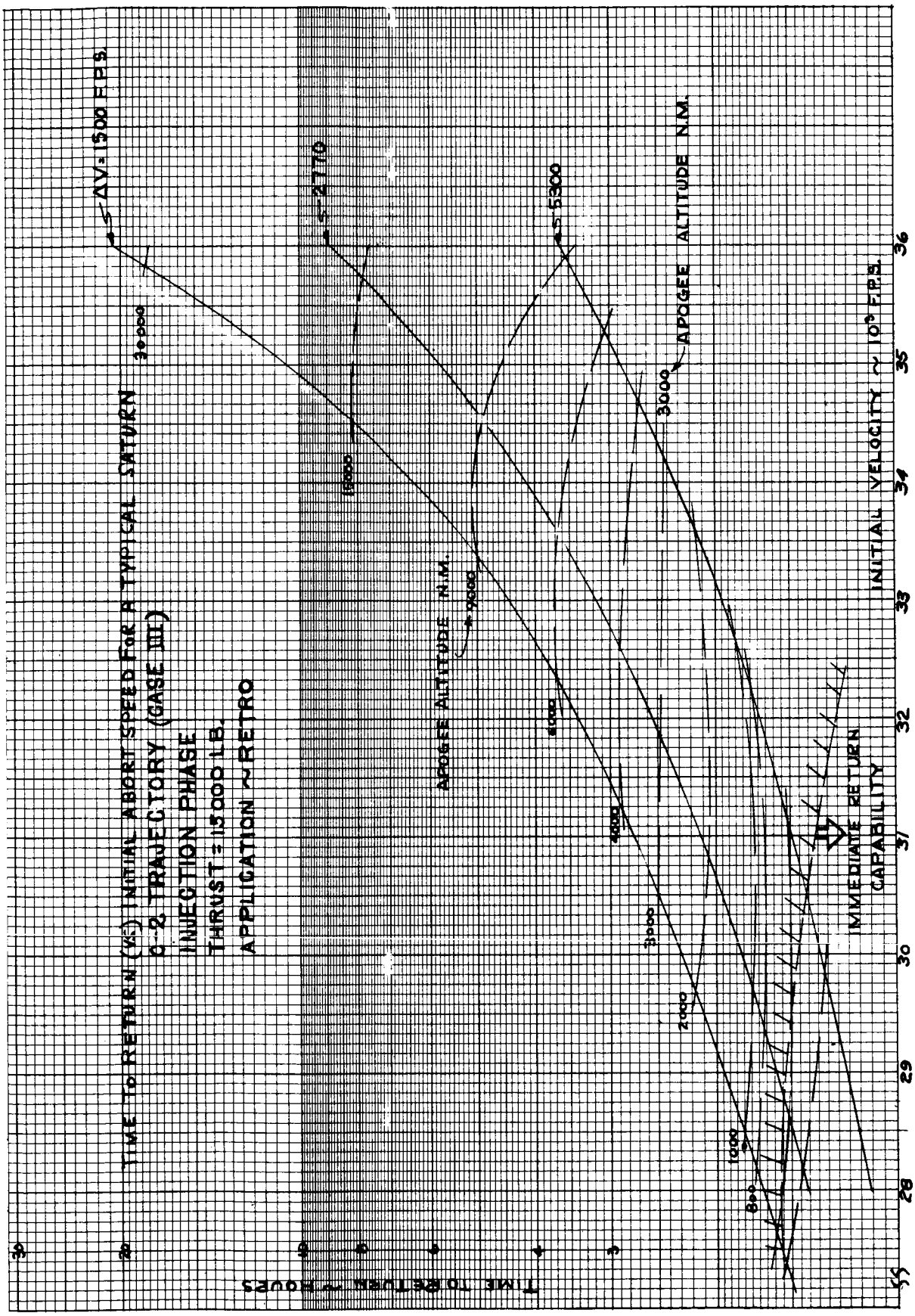

Fig. II-47. Abort at Injection Trajectory

CONFIDENTIAL

D-3 (6-60)

CONFIDENTIAL

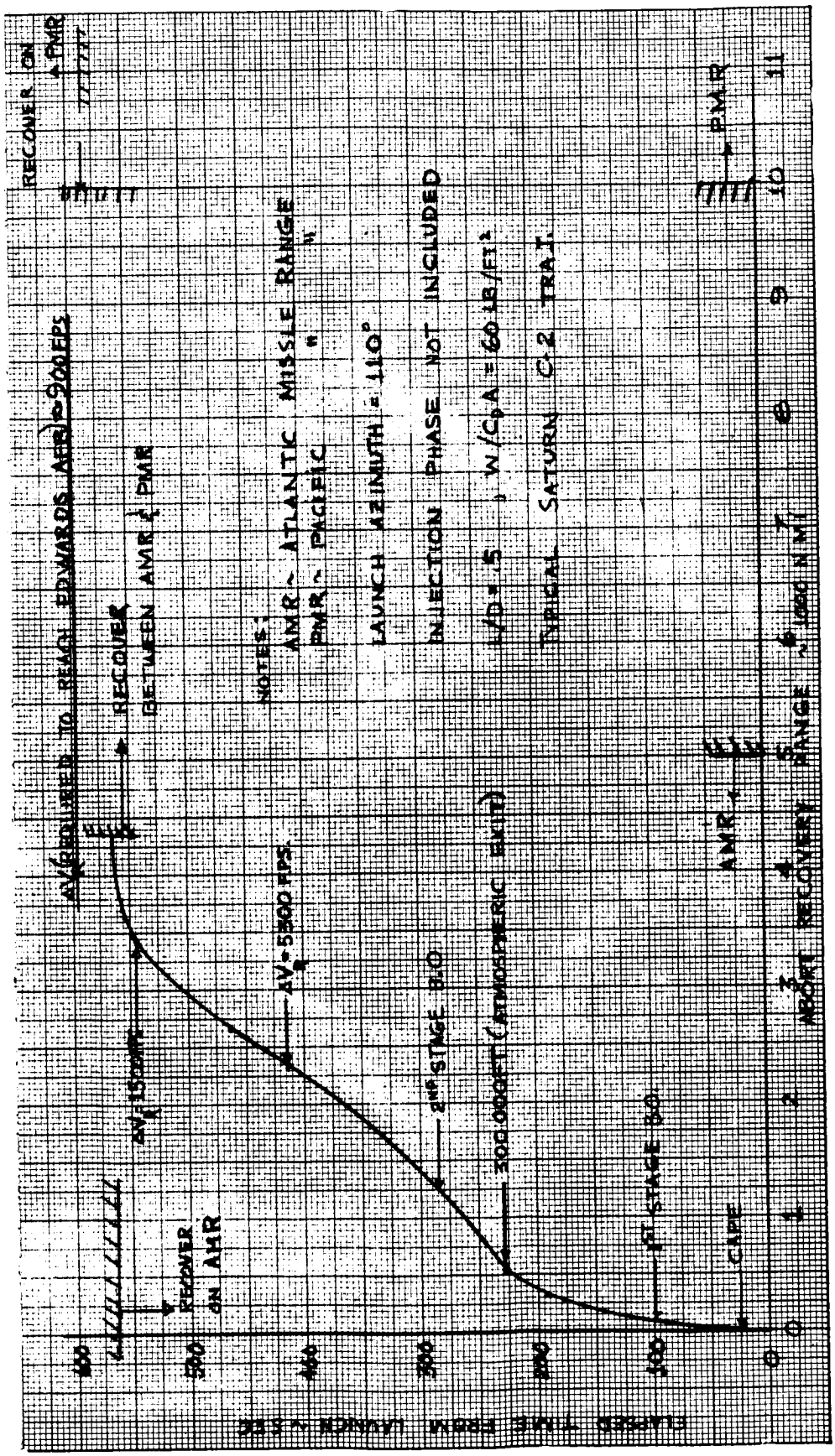

Fig. II-48. Recovery Position After Abort

CONFIDENTIAL

CONFIDENTIAL

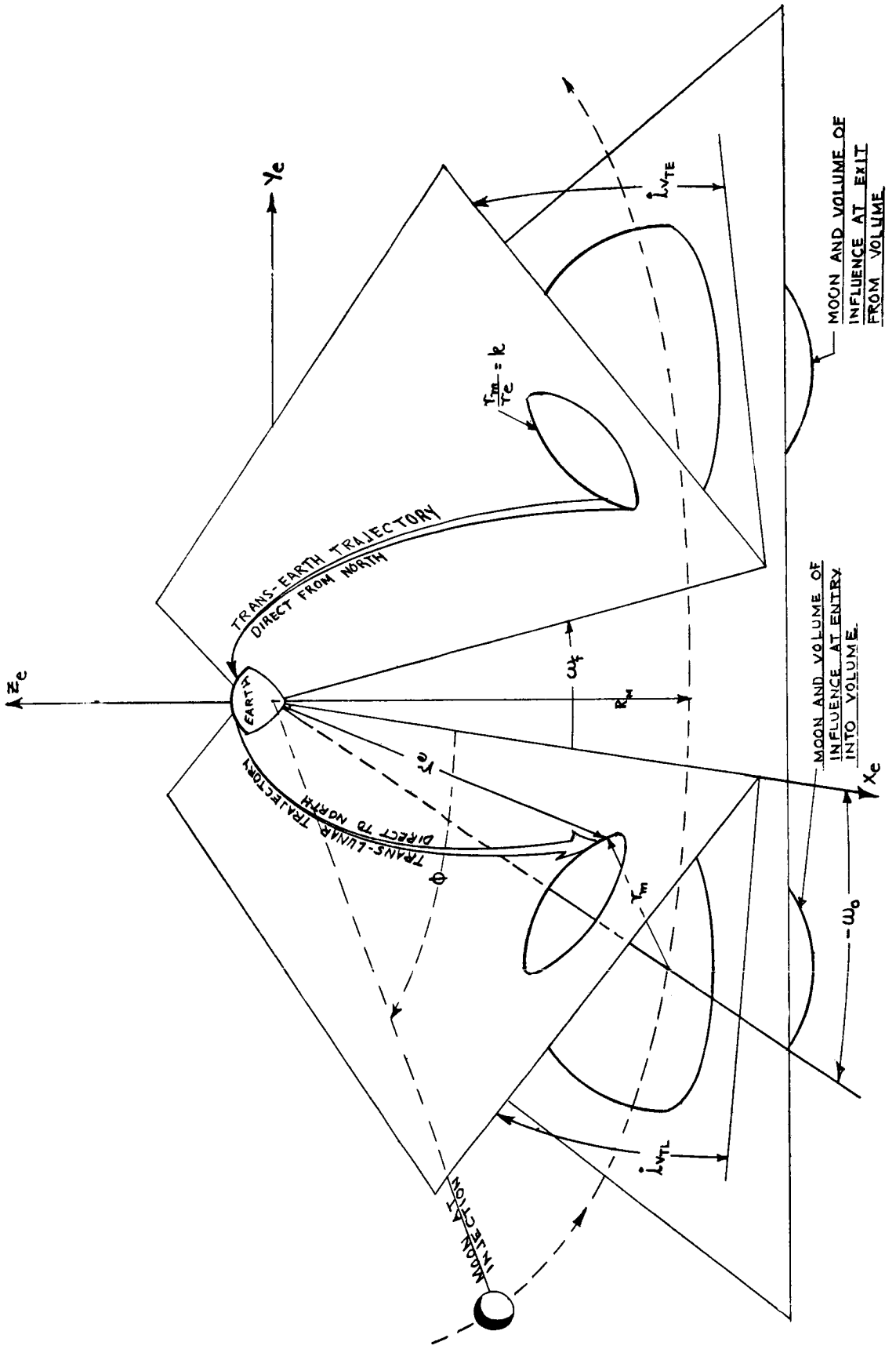

Fig. III-1. Lunar Trajectory Geometry and Definitions

CONFIDENTIAL

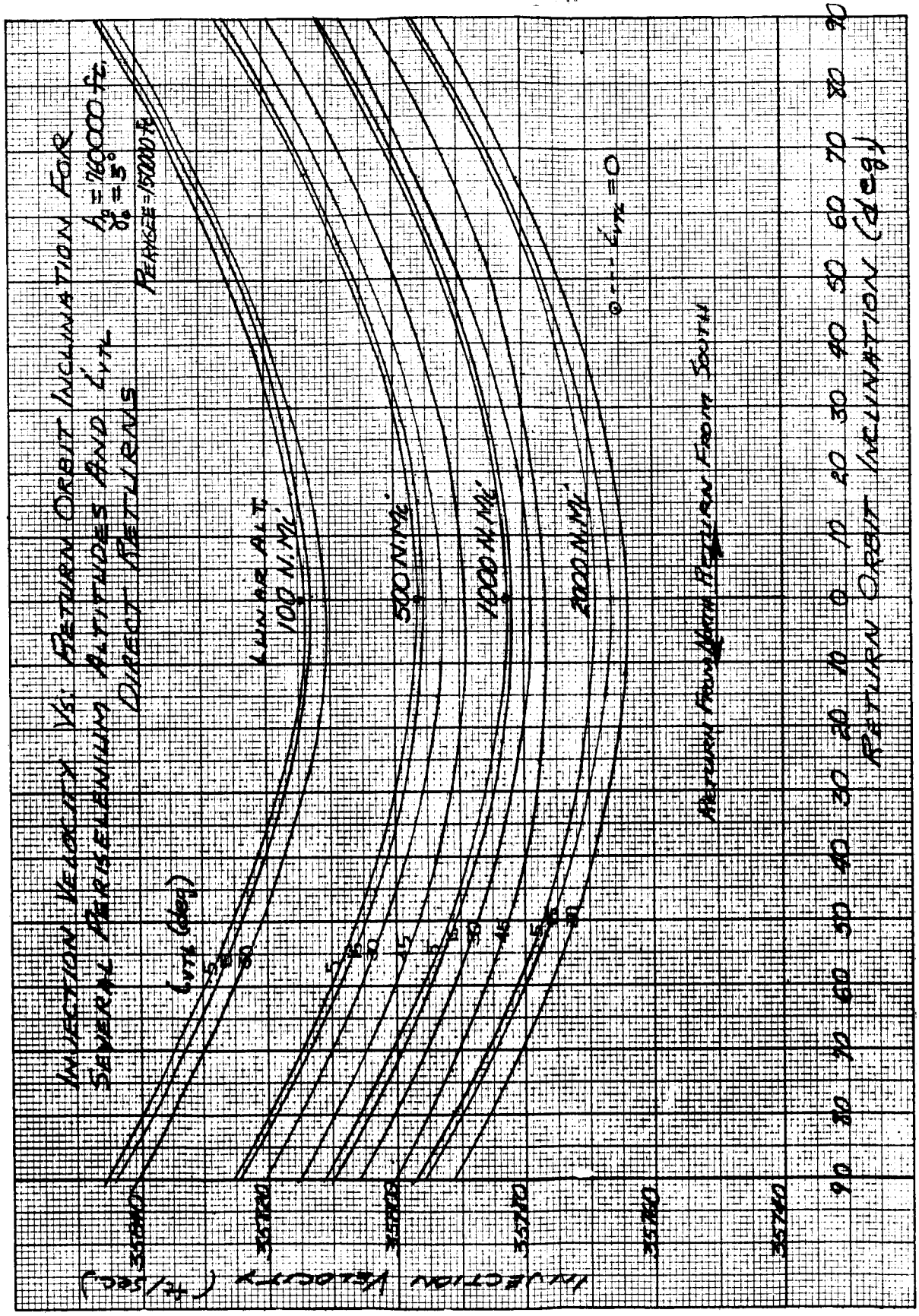

Fig. III-2. Injection Velocity Requirements (Direct Returns)

CONFIDENTIAL

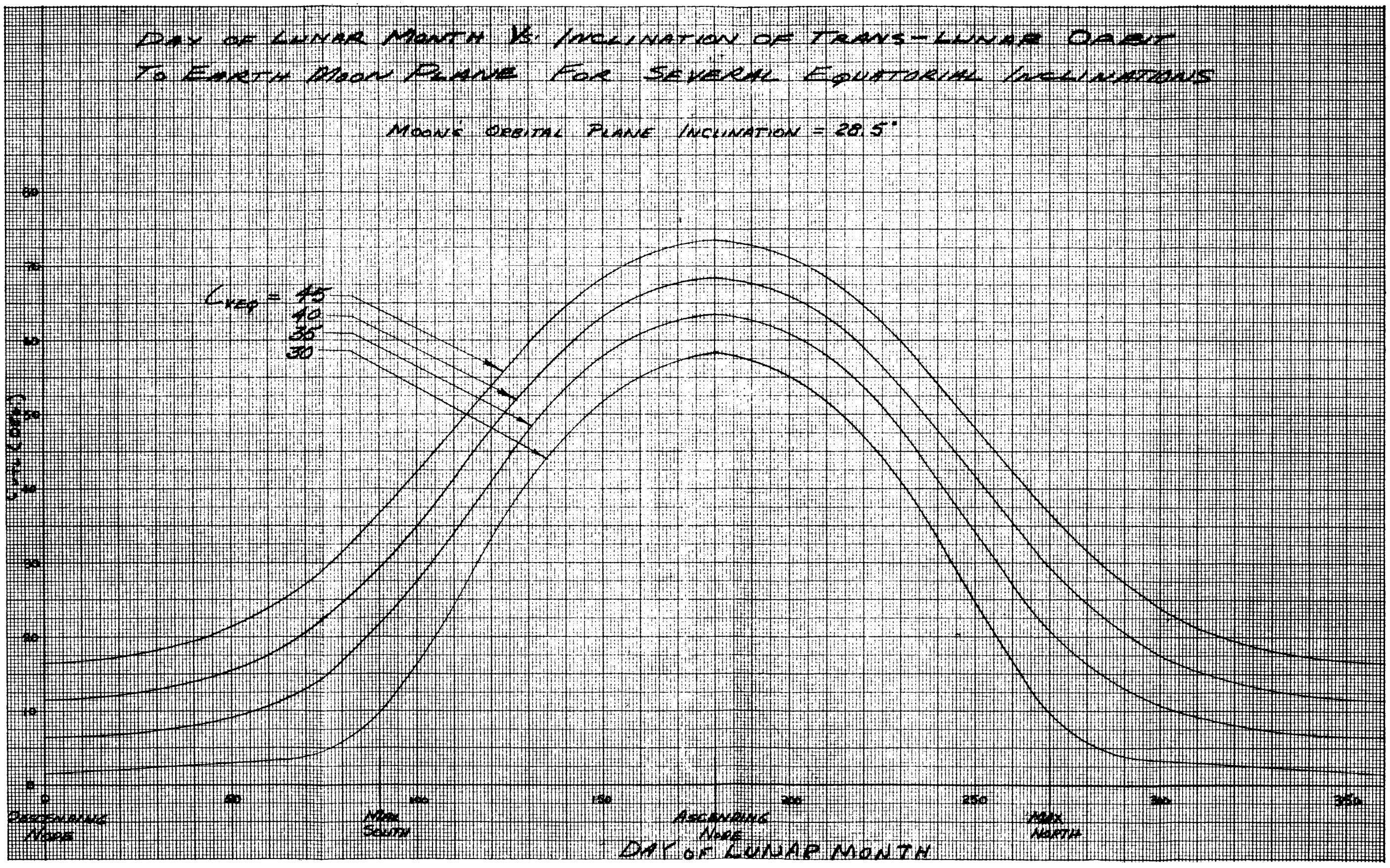

Fig. III-4. Inclination of Trajectory to Moon's Orbital Plane and Equatorial Plane

CONFIDENTIAL

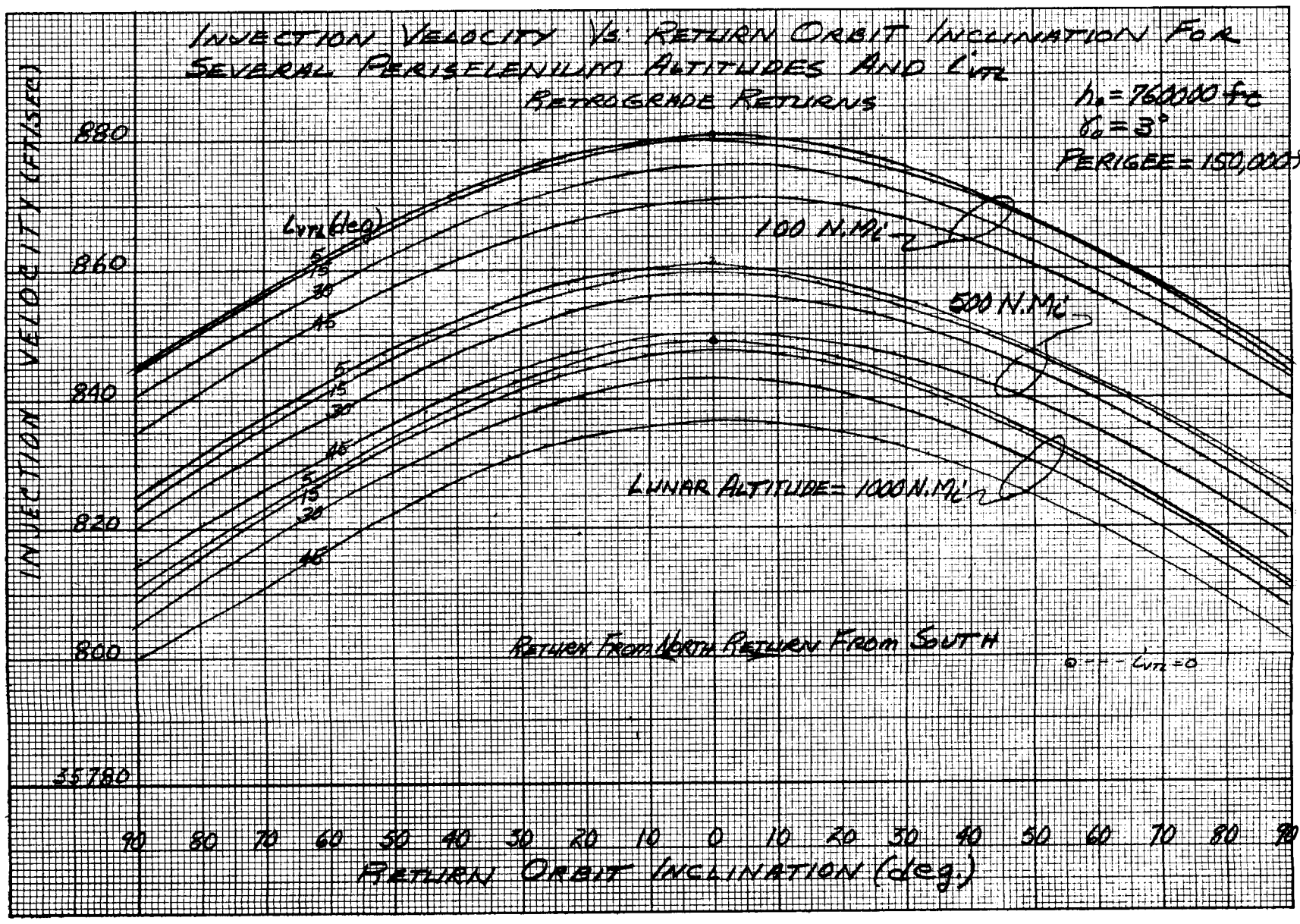

Fig. III-3. Injection Velocity Requirements (Retrograde Returns)

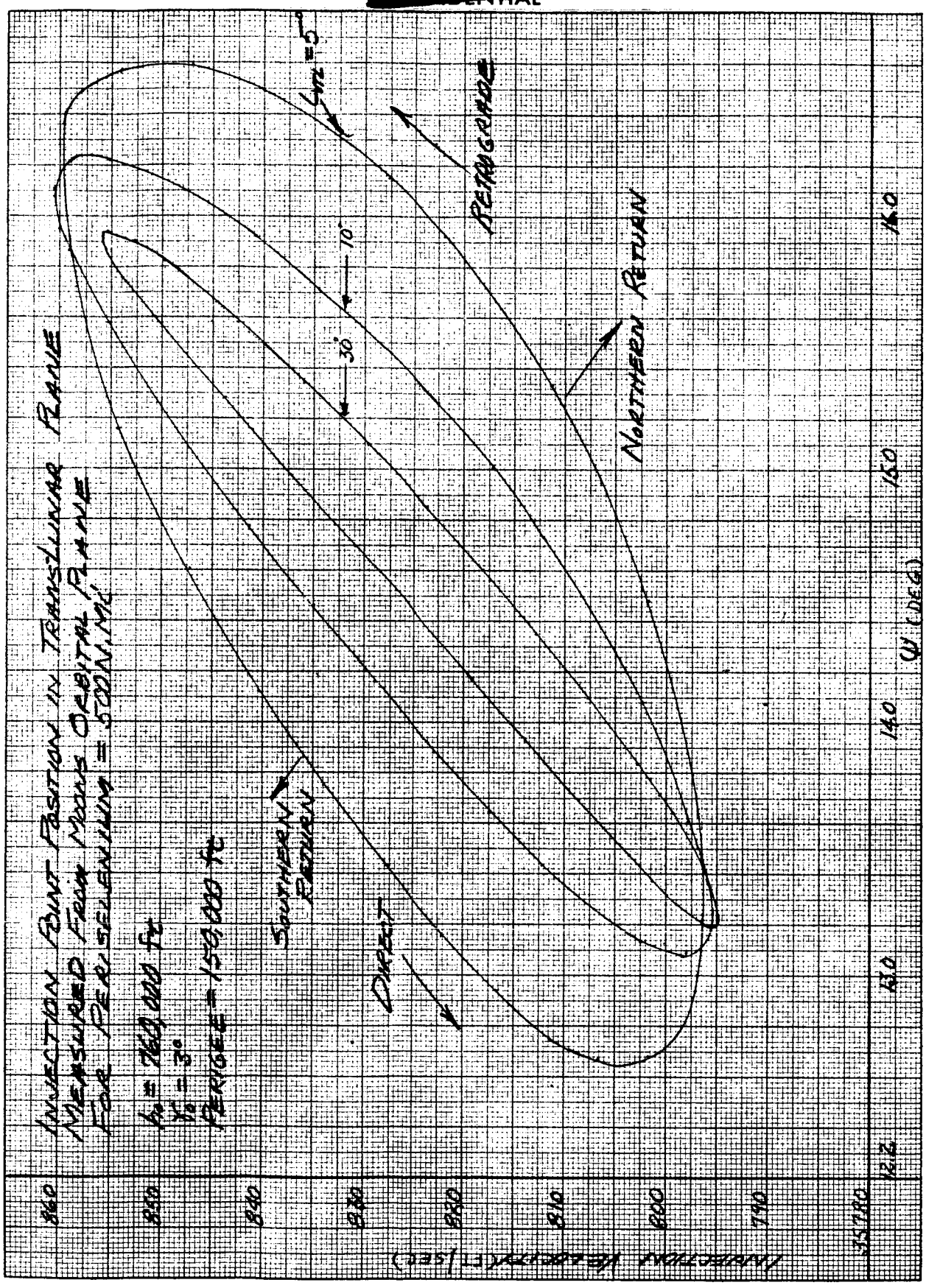

Fig. III-5. Vehicle Position at Injection (periselenium = 500 naut mi)

CONFIDENTIAL

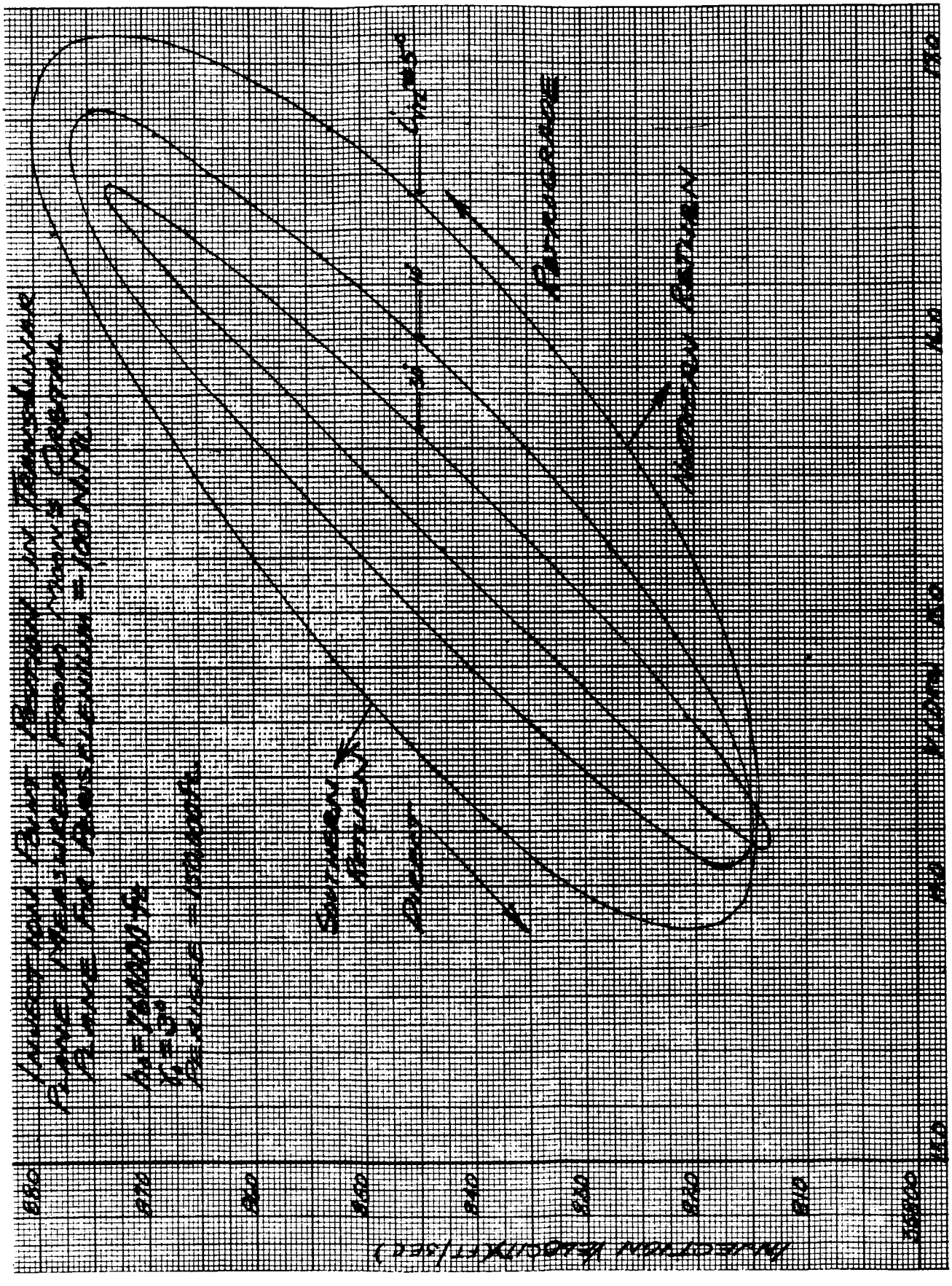

Fig. III-6. Vehicle Position at Injection (periselenium = 100 naut mi)

CONFIDENTIAL

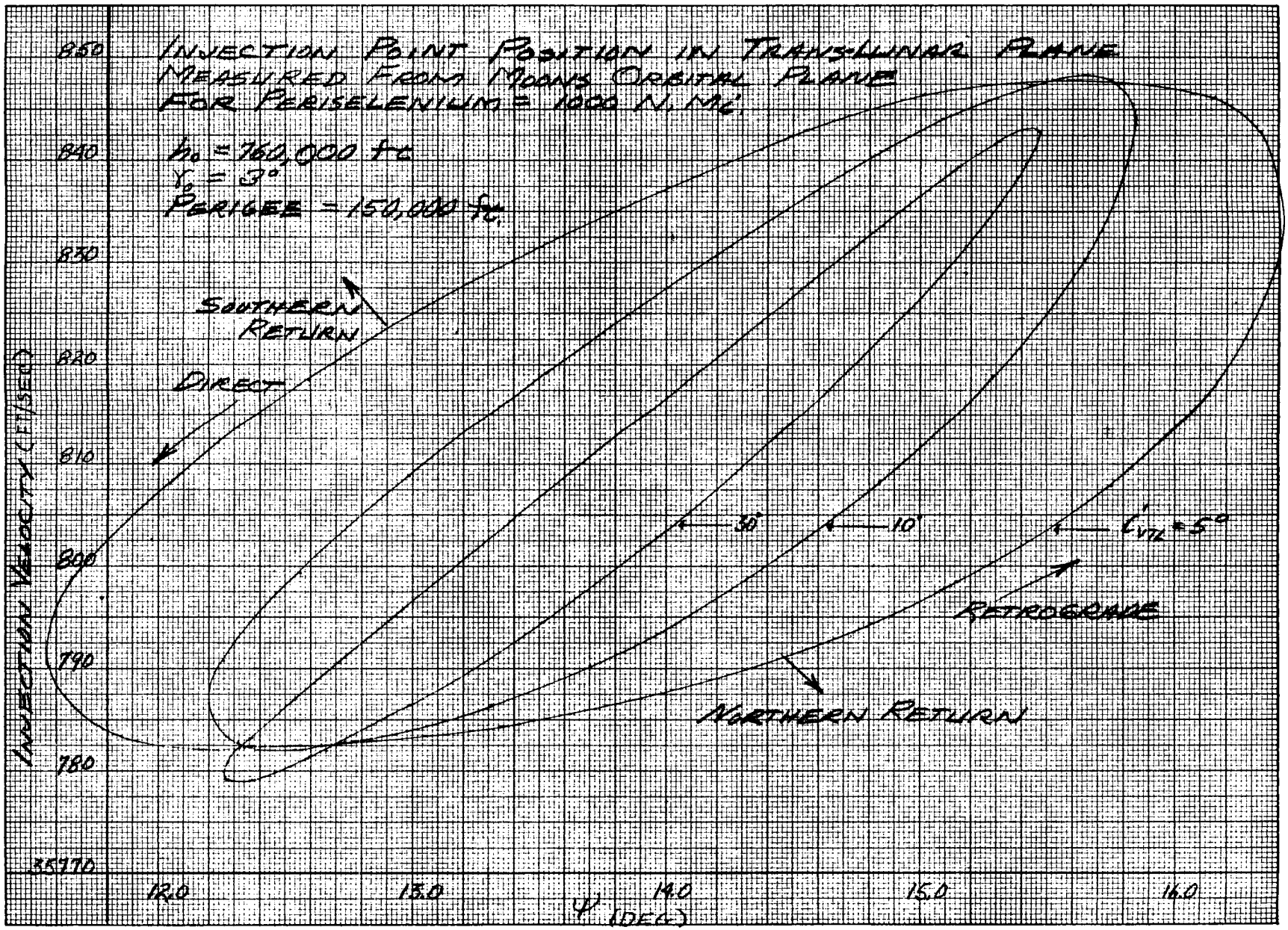

Fig. III-7. Vehicle Position at Injection (periselenium - 1000 naut mi)

CONFIDENTIAL

CONFIDENTIAL

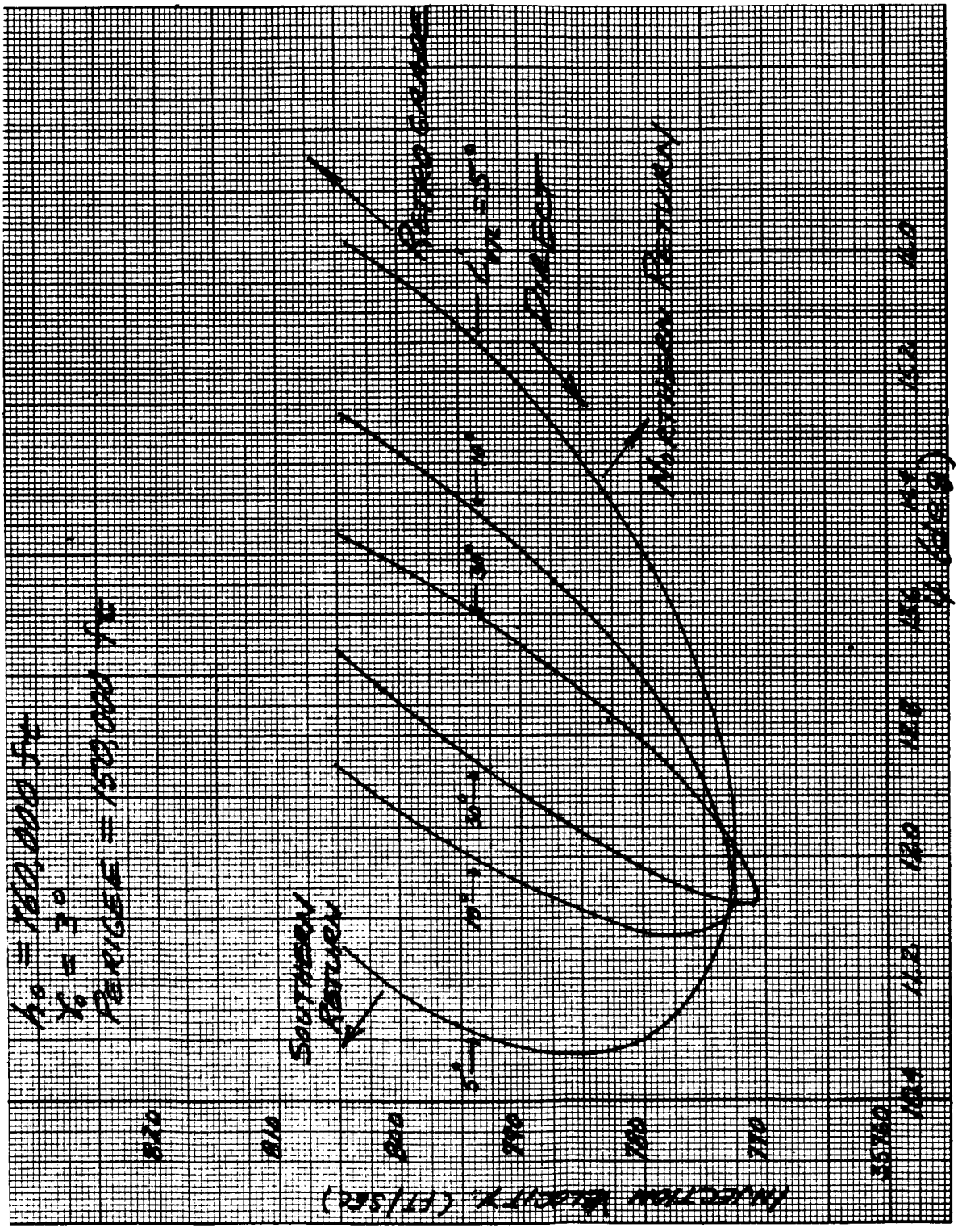

Fig. III-8. Vehicle Position at Injection (perselenium = 1500 naut mi)

CONFIDENTIAL

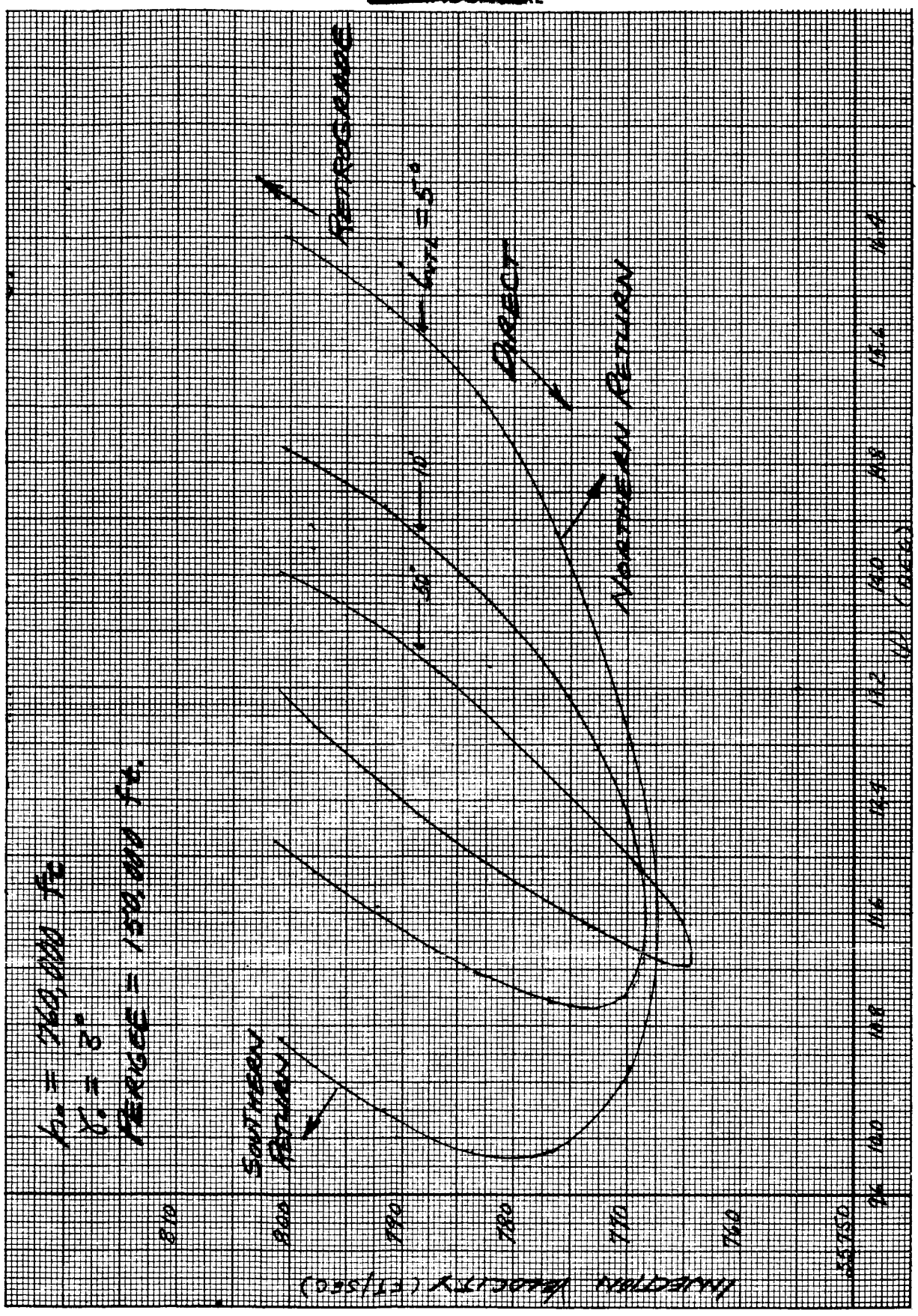

Fig. III-9. Vehicle Position at Injection (periselenium = 2000 naut mi)

D-3 (6-60)

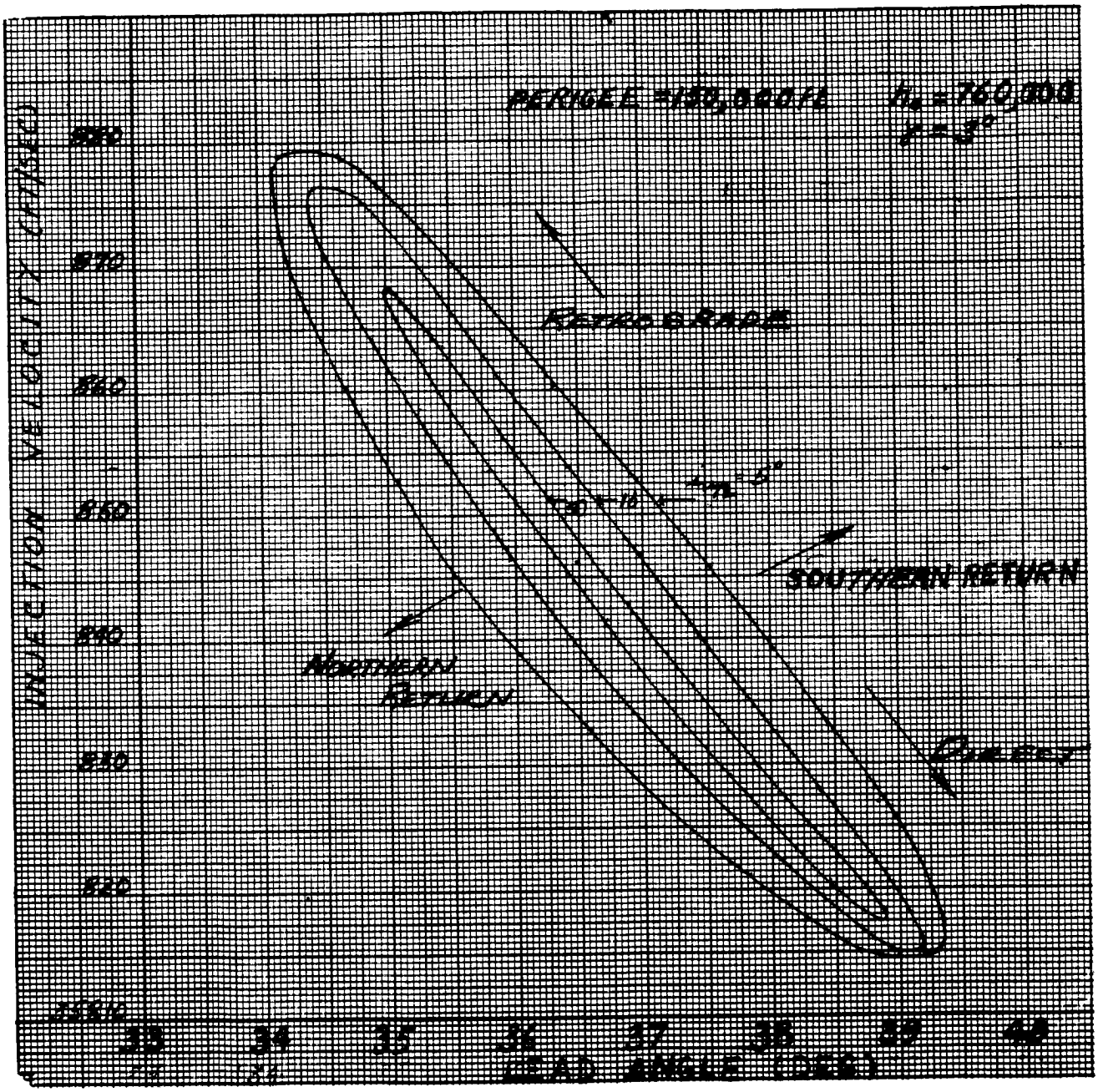

Fig. III-10. Moon Position at Injection (periselenium = 100 naut mi)

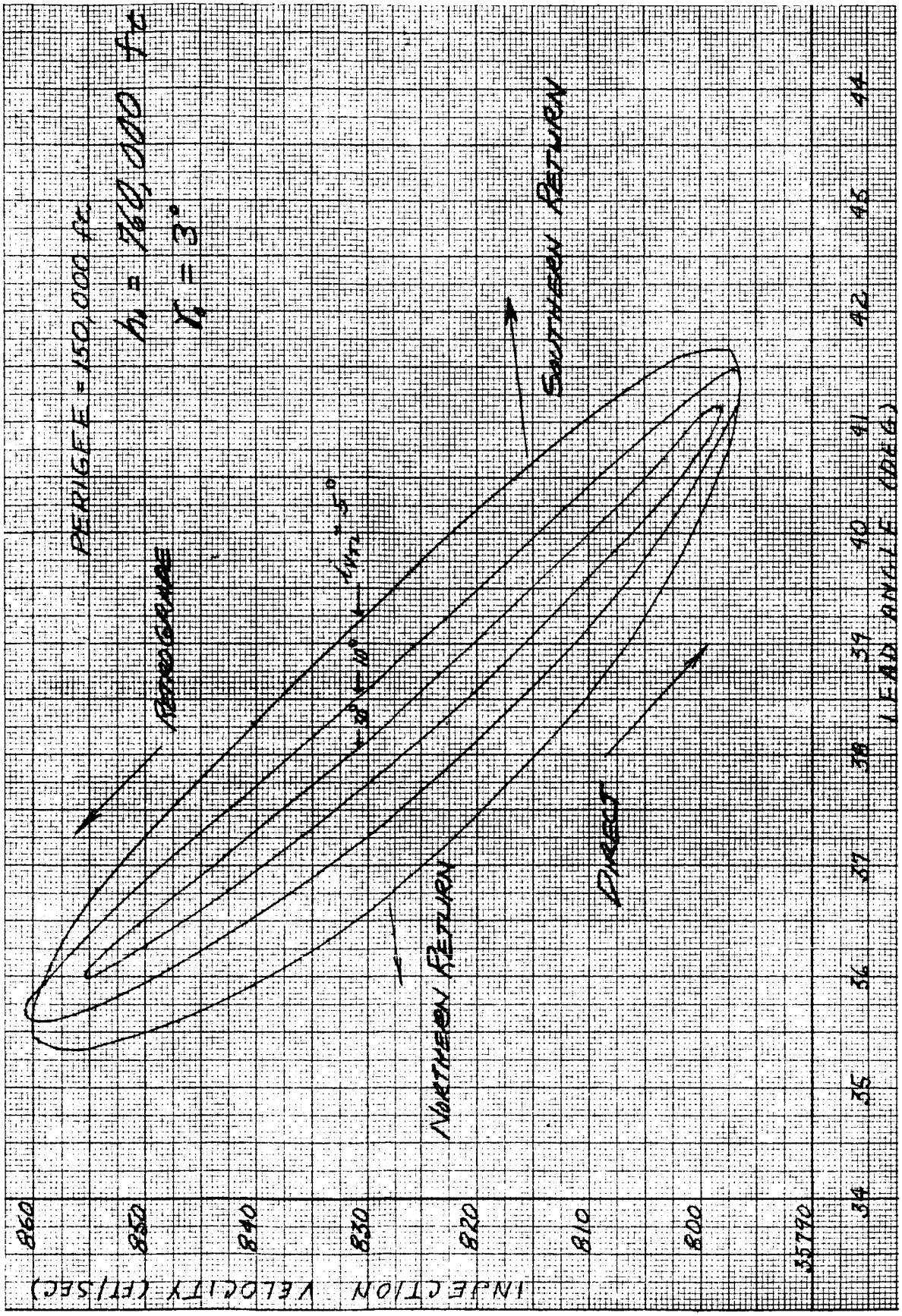

Fig. III-11. Moon Position at Injection (periselenium = 500 naut mi)

D-3 (6-60)

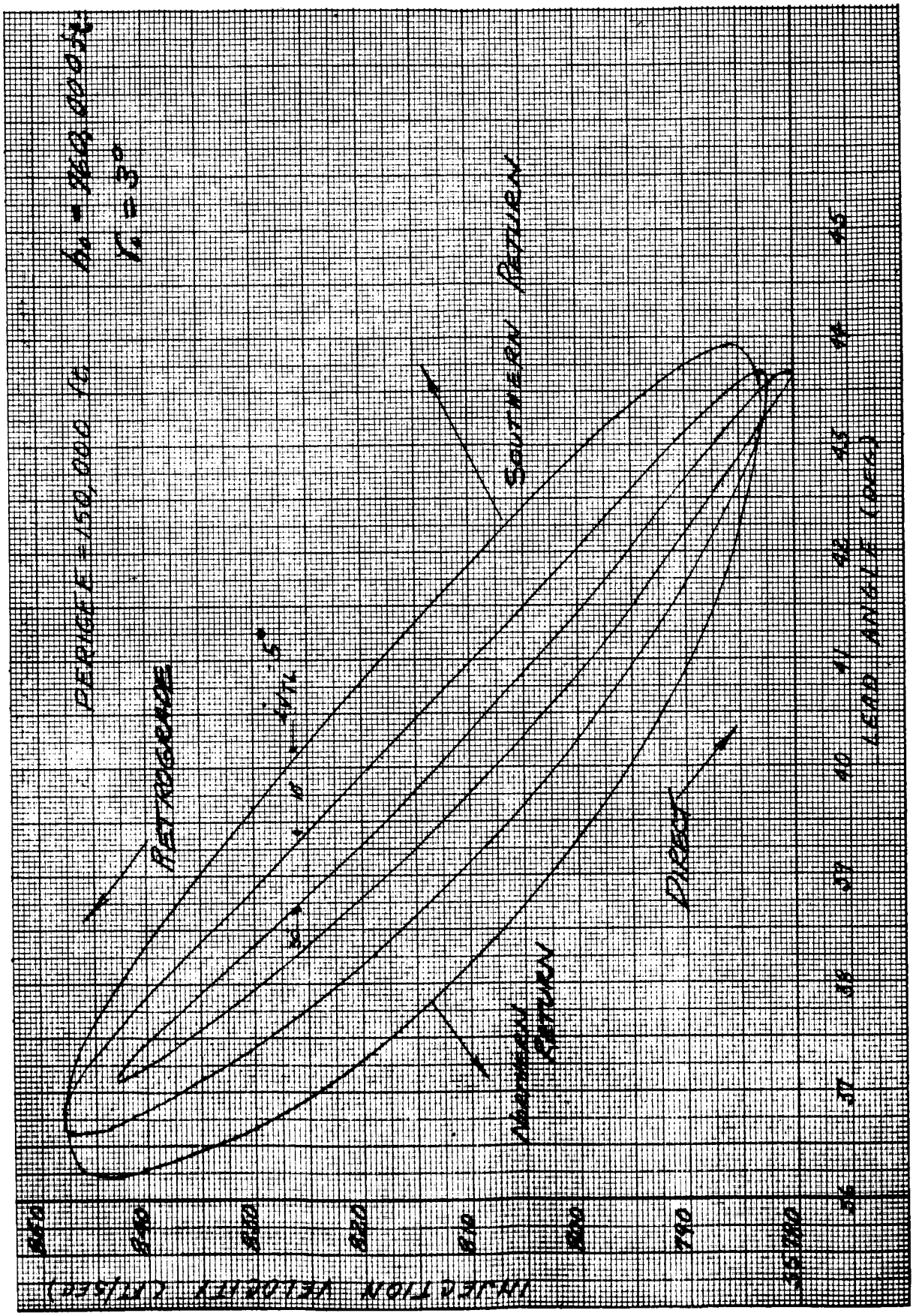

Fig. III-12. Moon Position at Injection (periselenium = 1000 naut mi)

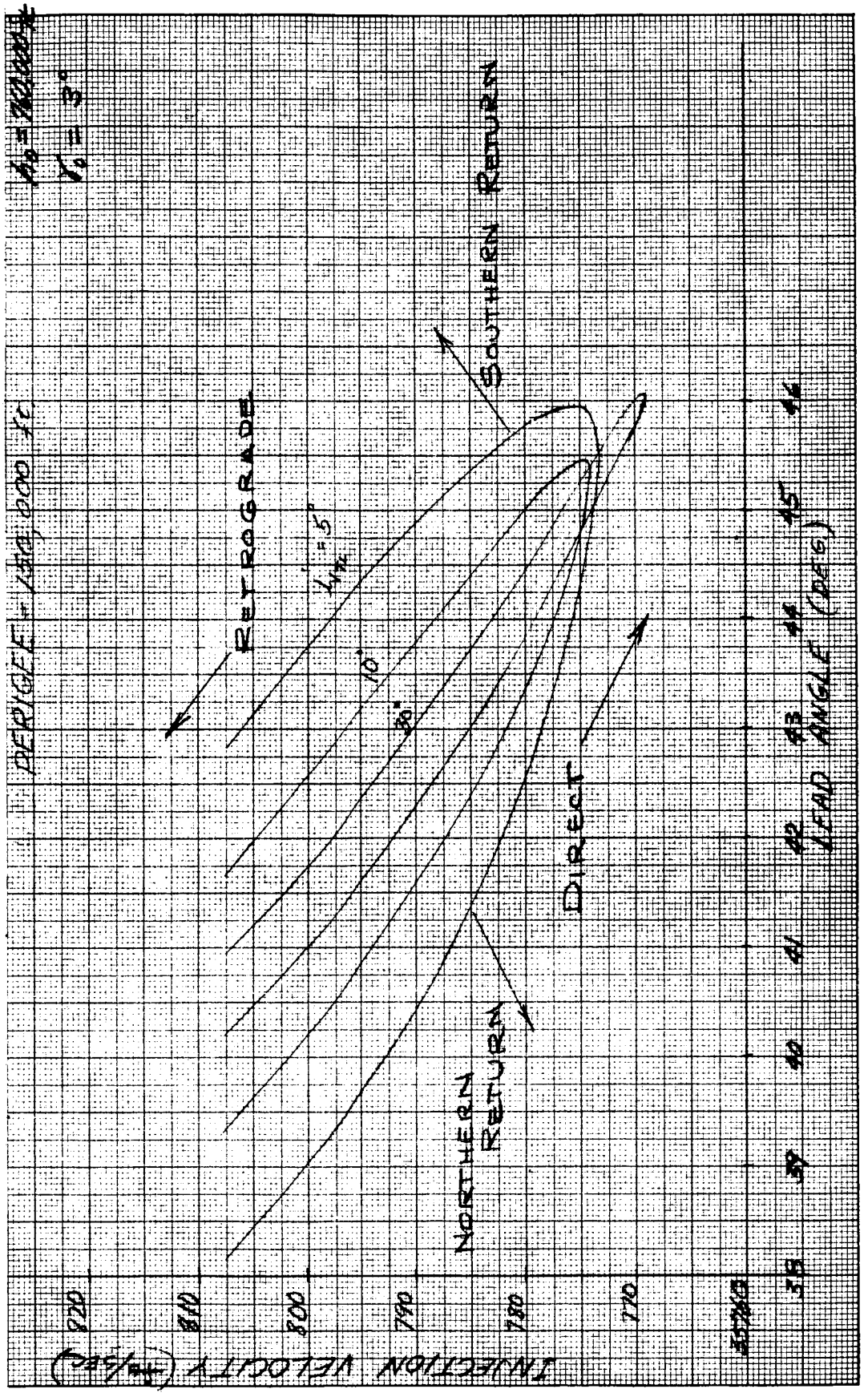

Fig. III-13. Moon Position at Injection (periselenium = 1500 naut mi)

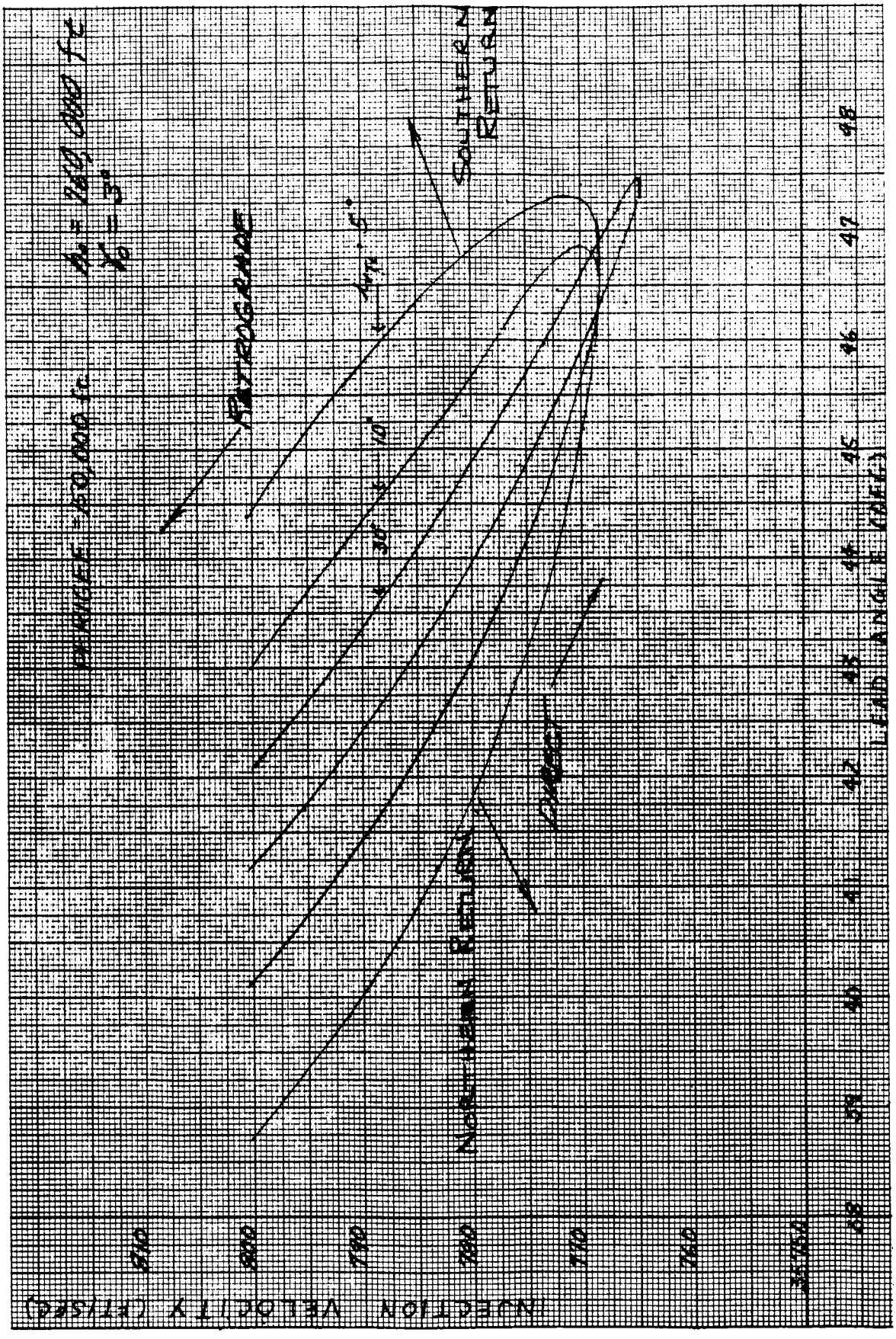

Fig. III-14. Moon Position at Injection (periselenium = 2000 naut mi)

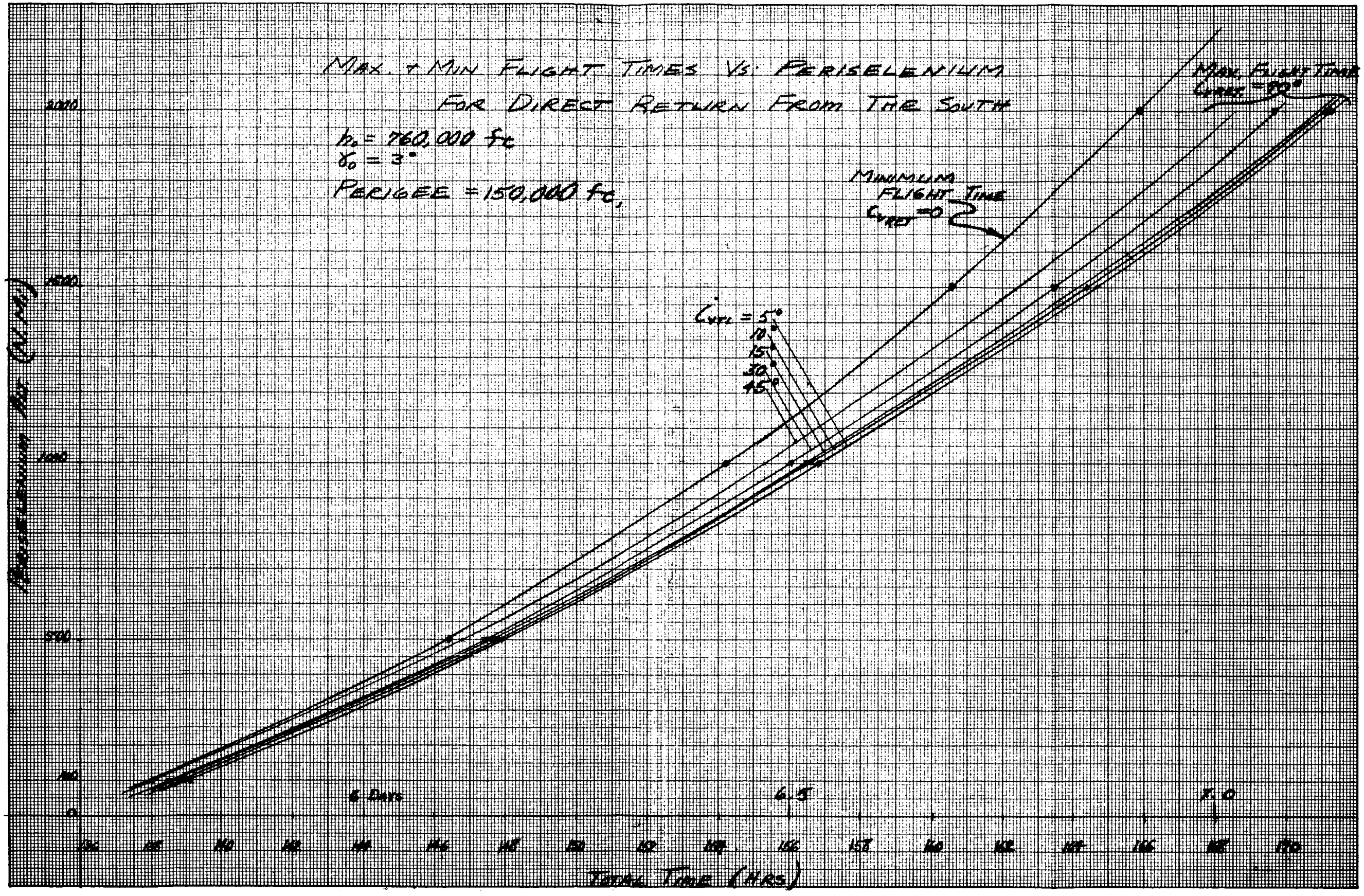

Fig. III-15. Time Versus Periselenium Altitude

CONFIDENTIAL

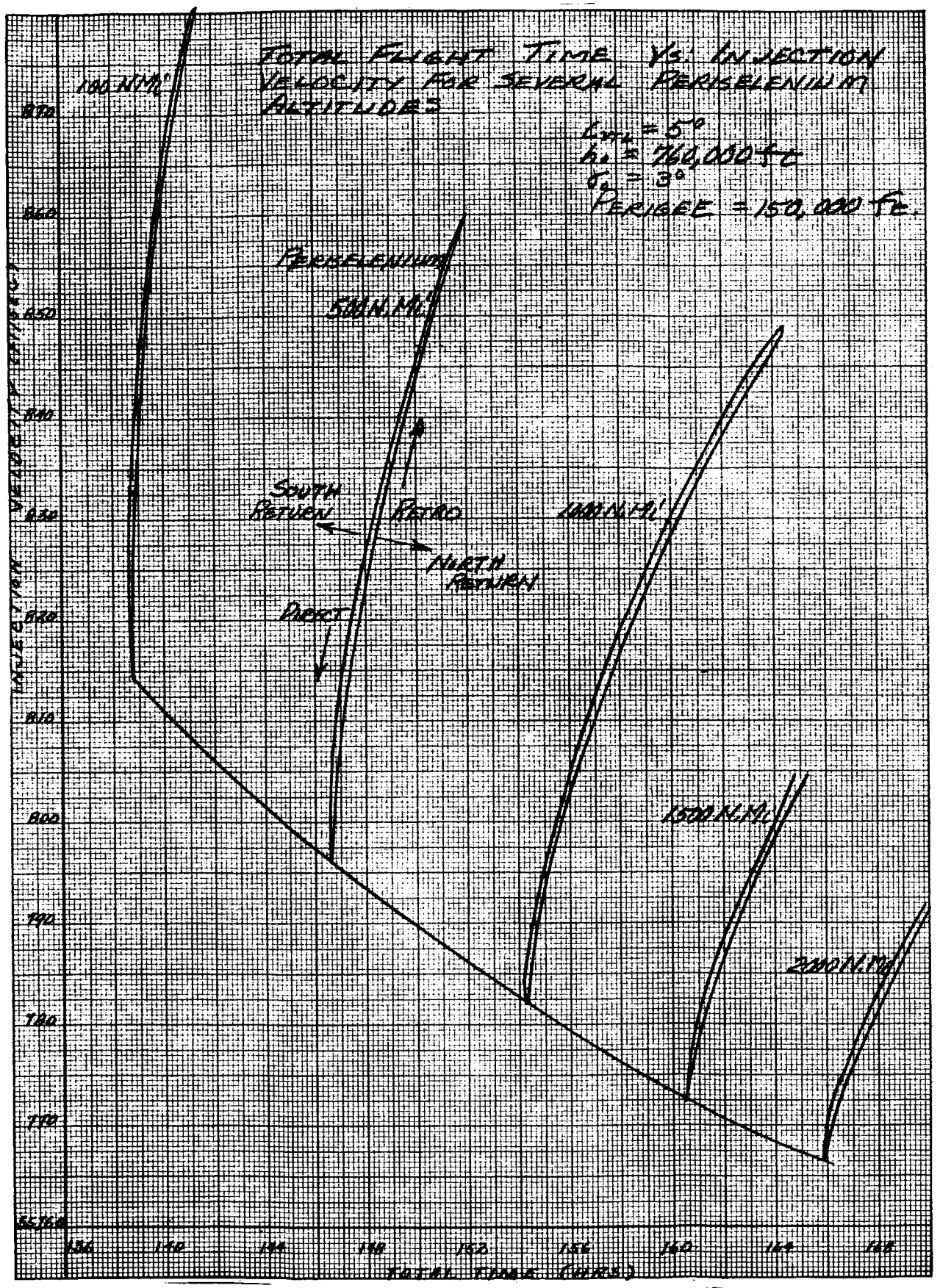

Fig. III-16. Time for Various Injection Conditions to Constant Periselenium Altitude (L_{VTL} = 5°)

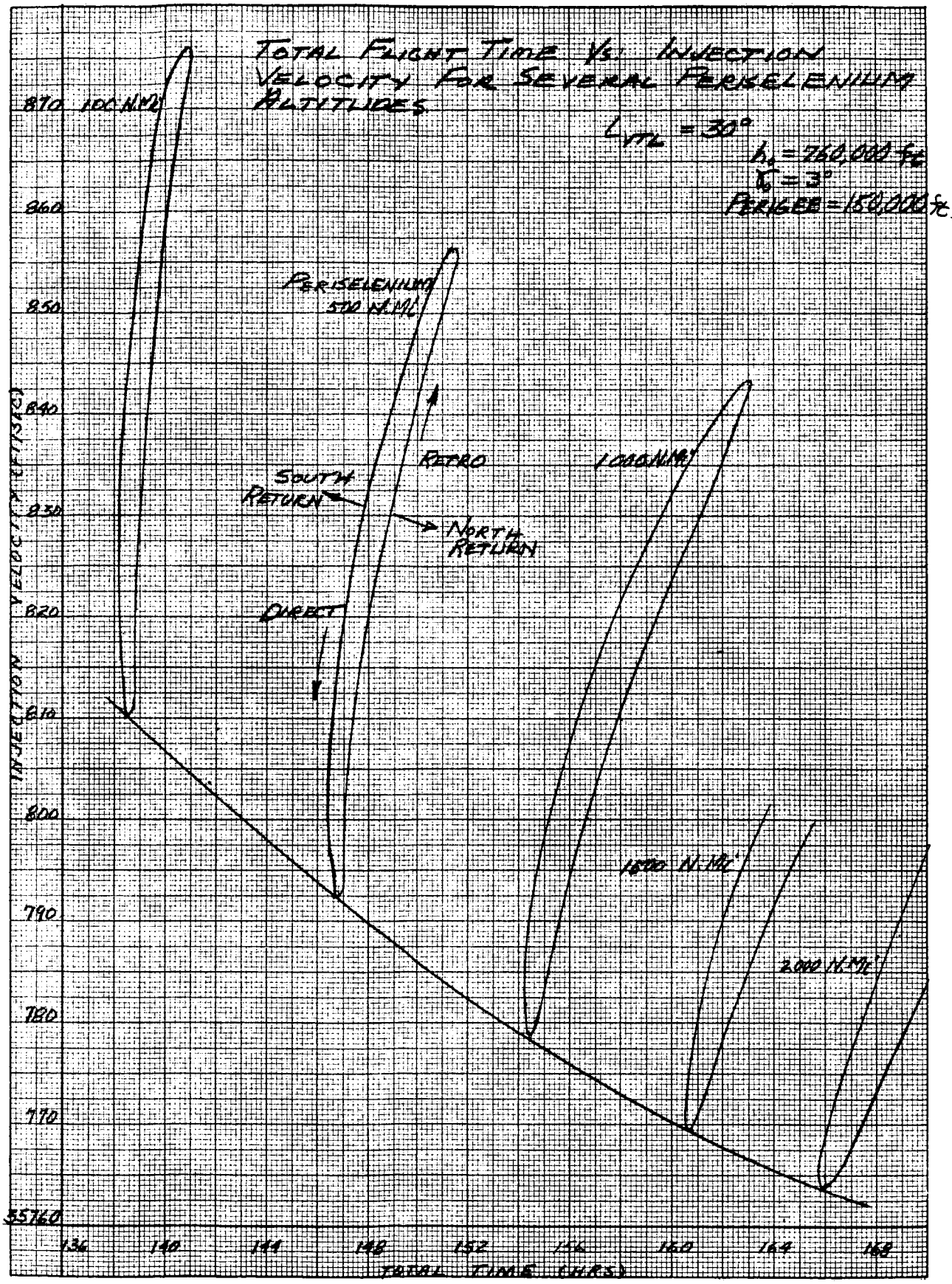

Fig. III-17. Time for Various Injection Conditions to Constant Periselenium Altitude ($L_{VTL} = 30°$)

D-3 (6-60)

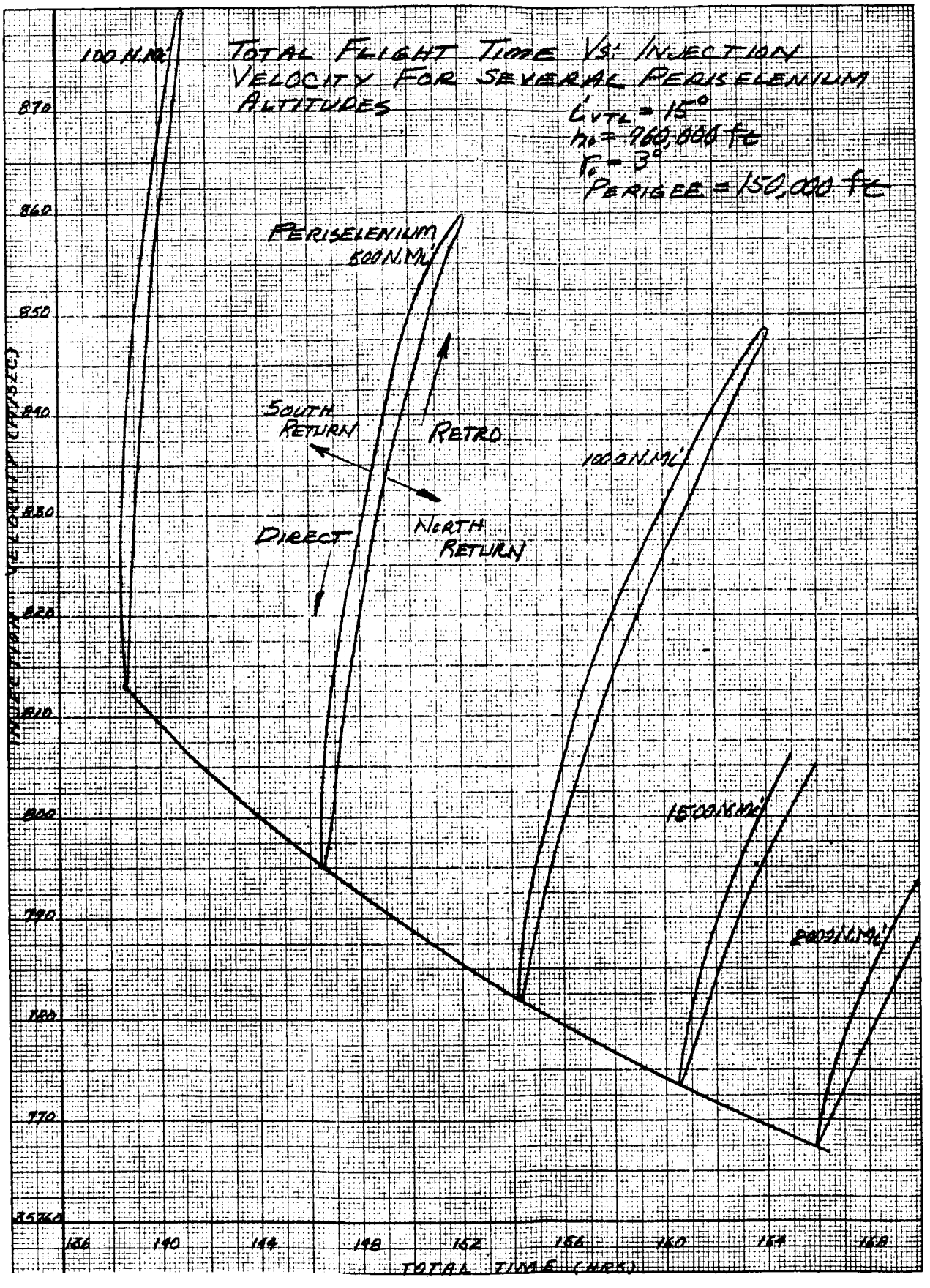

Fig. III-18. Time for Various Injection Conditions to Constant Periselenium Altitude (L_{VTL} = 15°)

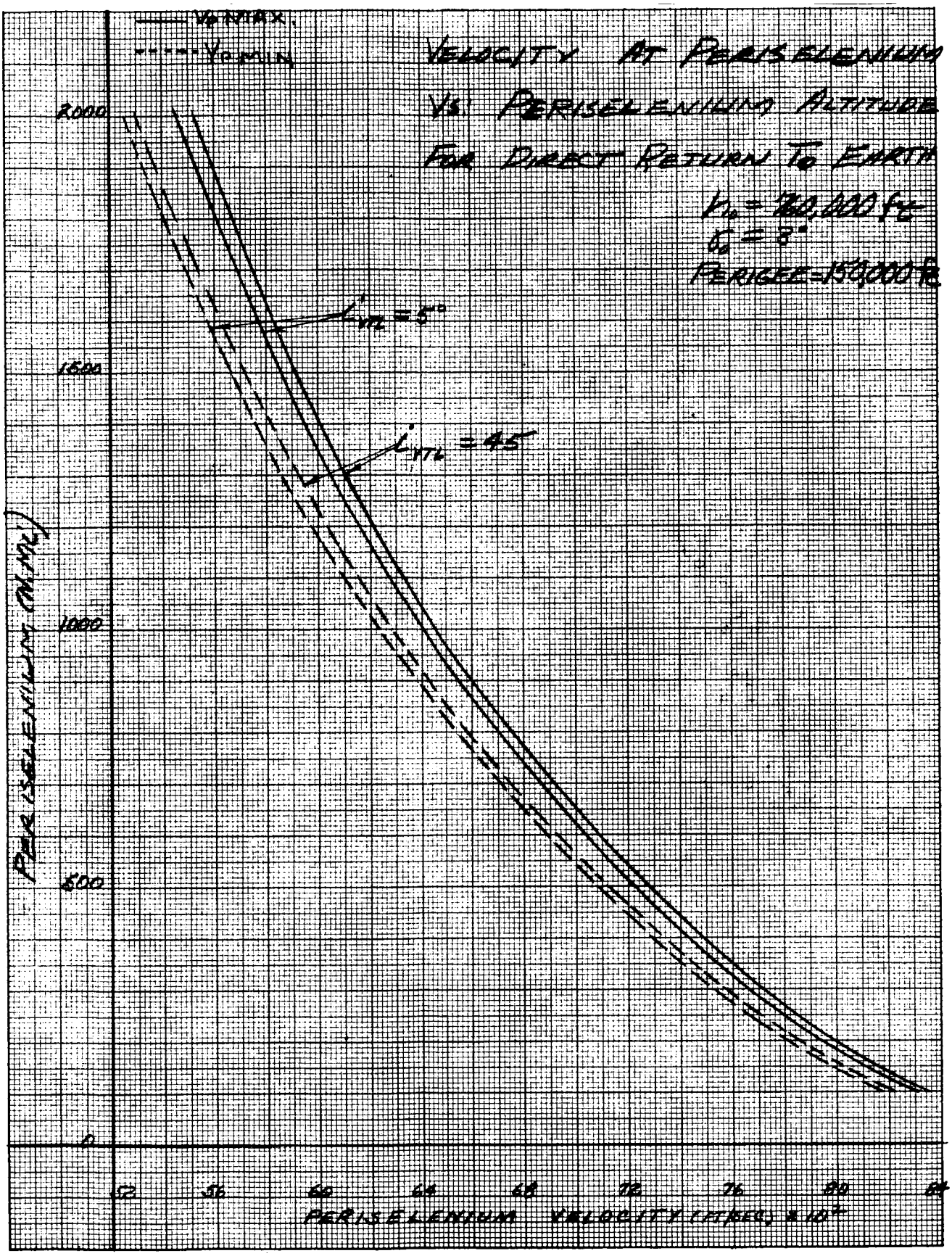

Fig. III-19. Periselenium Velocity

D-3 (6-60)

~~CONFIDENTIAL~~

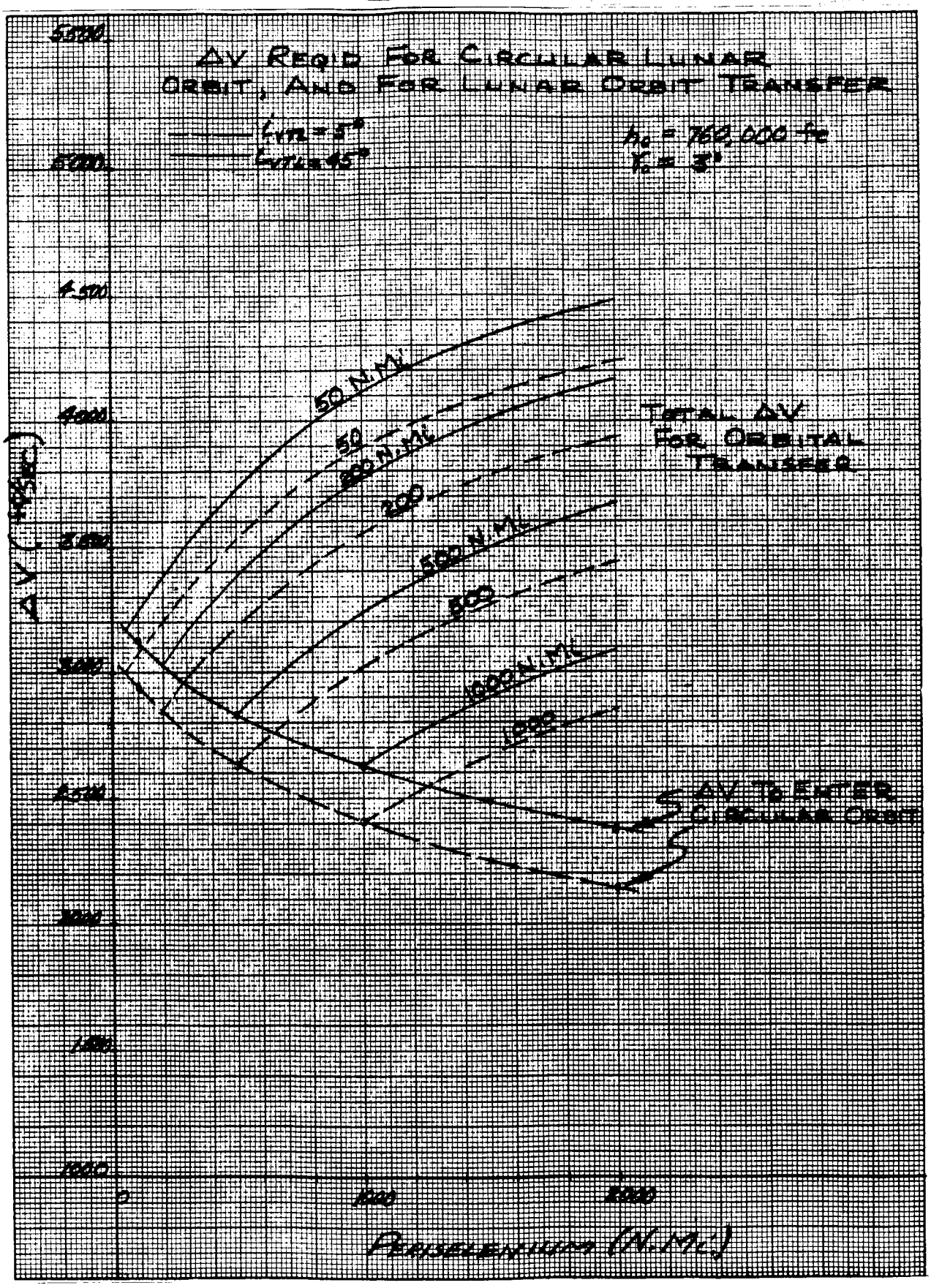

Fig. III-20. Velocity Increment Required to go into Lunar Orbit

D-3 (6.60)

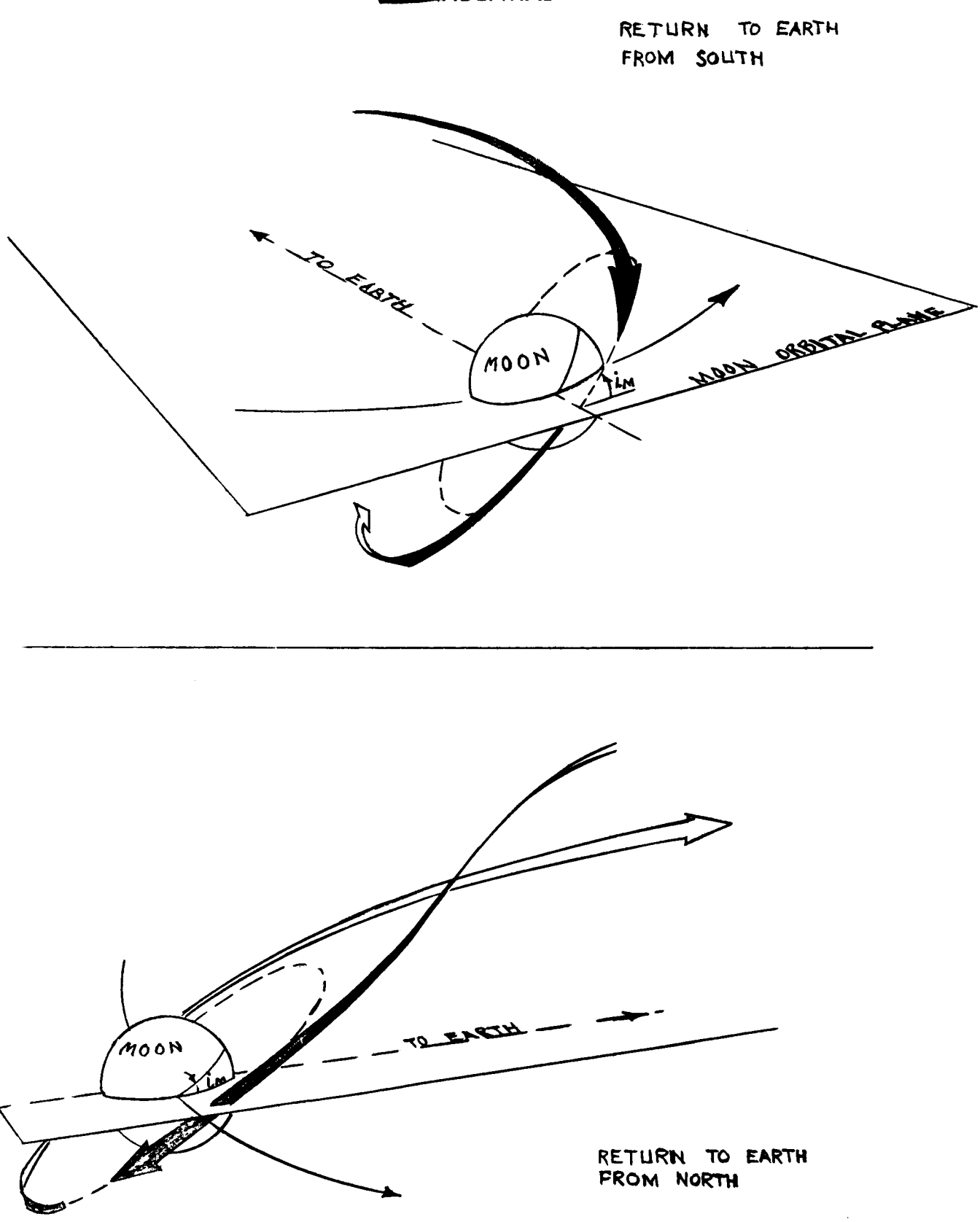

Fig. III-21. Lunar Orbit Characteristics

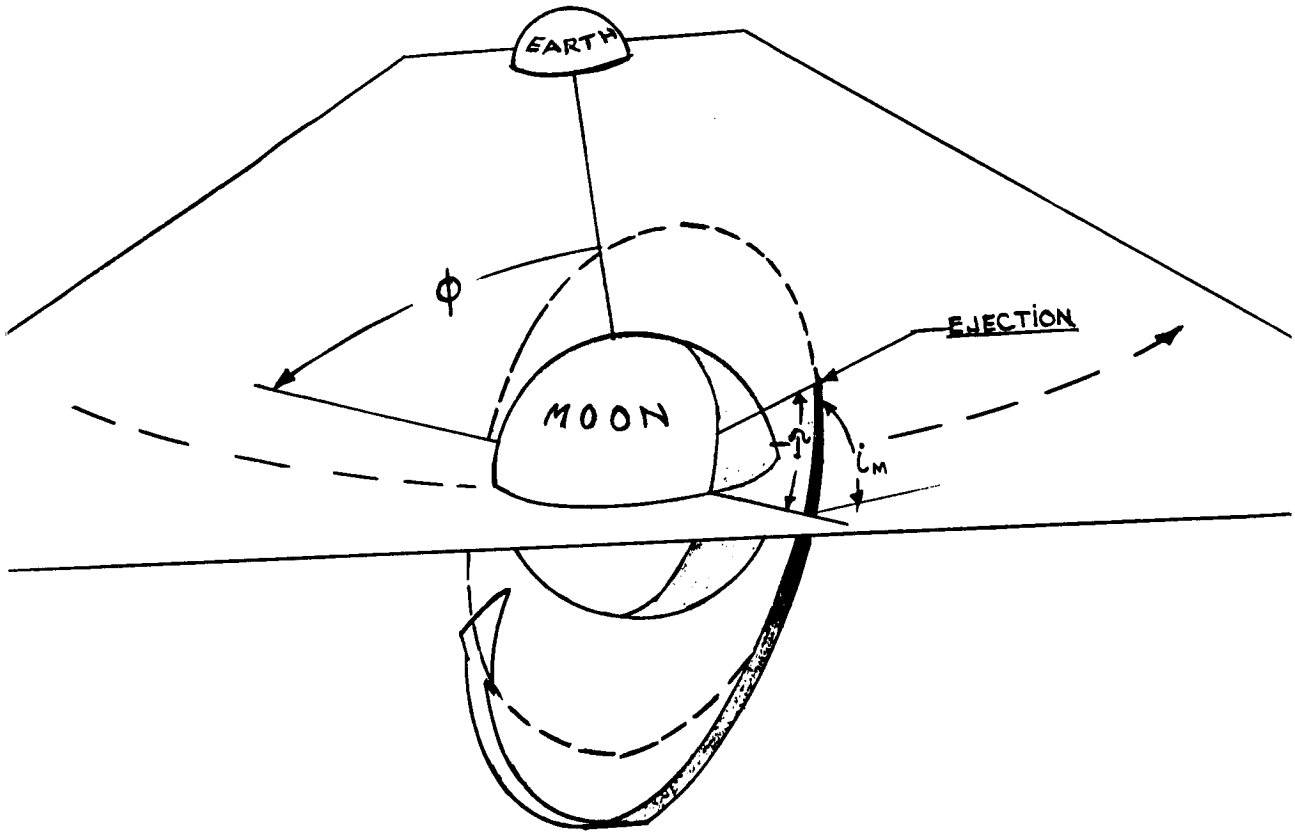

Fig. III-22. Lunar Orbit Ejection Geometry

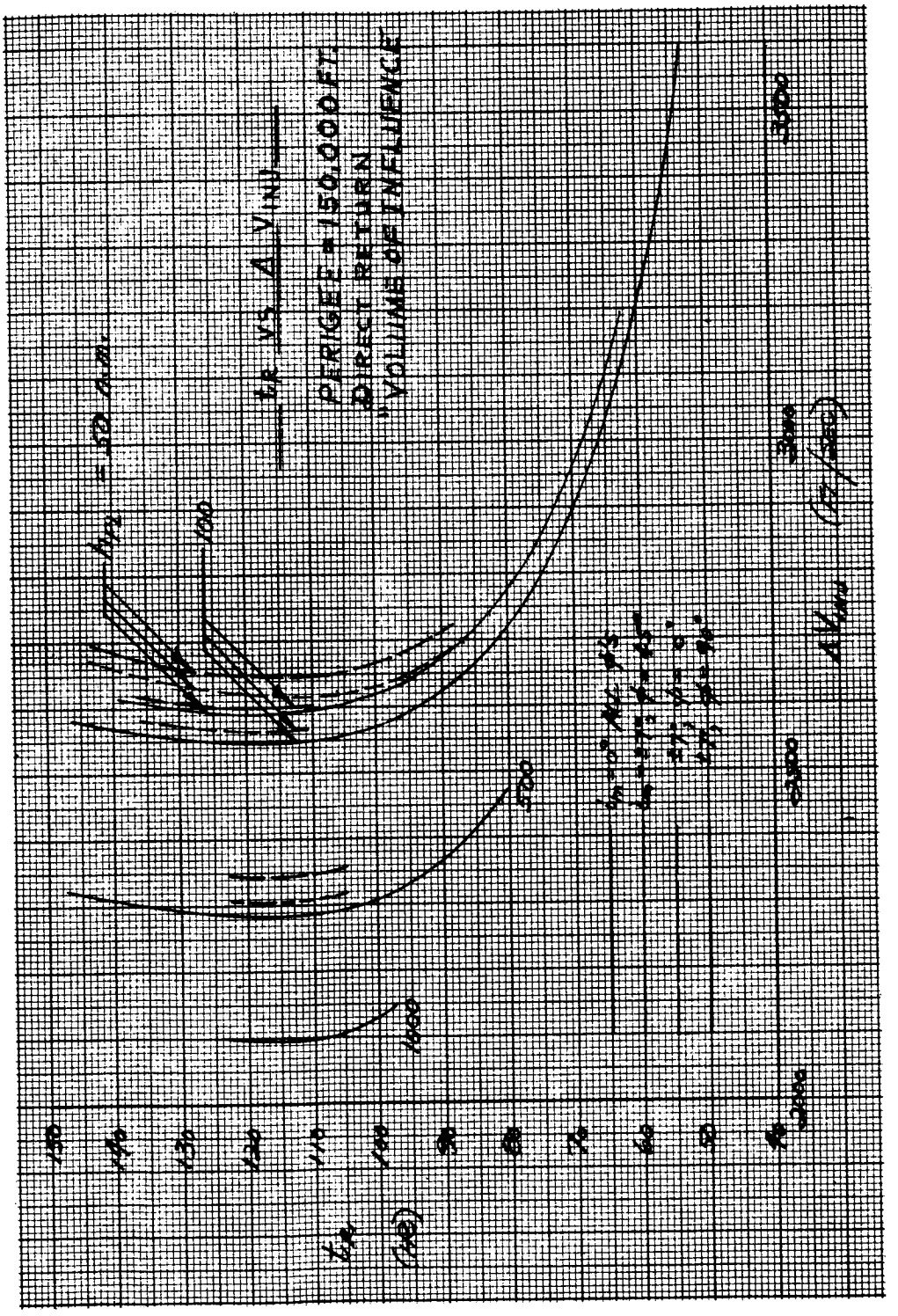

Fig. III-23. Velocity Impulse Versus Return Flight Time

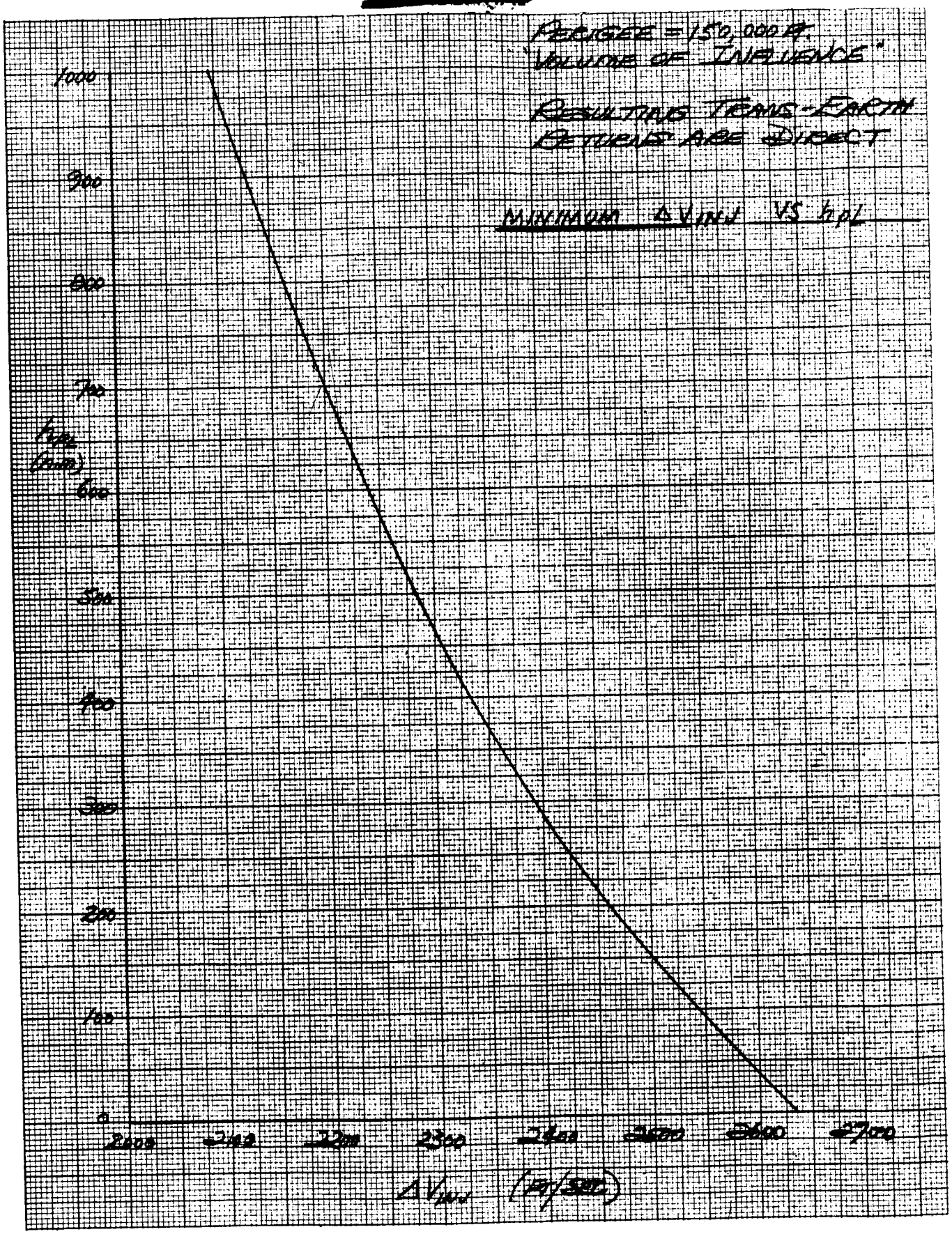

Fig. III-24. Minimum Required Velocity Impulse for Lunar Orbit Ejection

CONFIDENTIAL

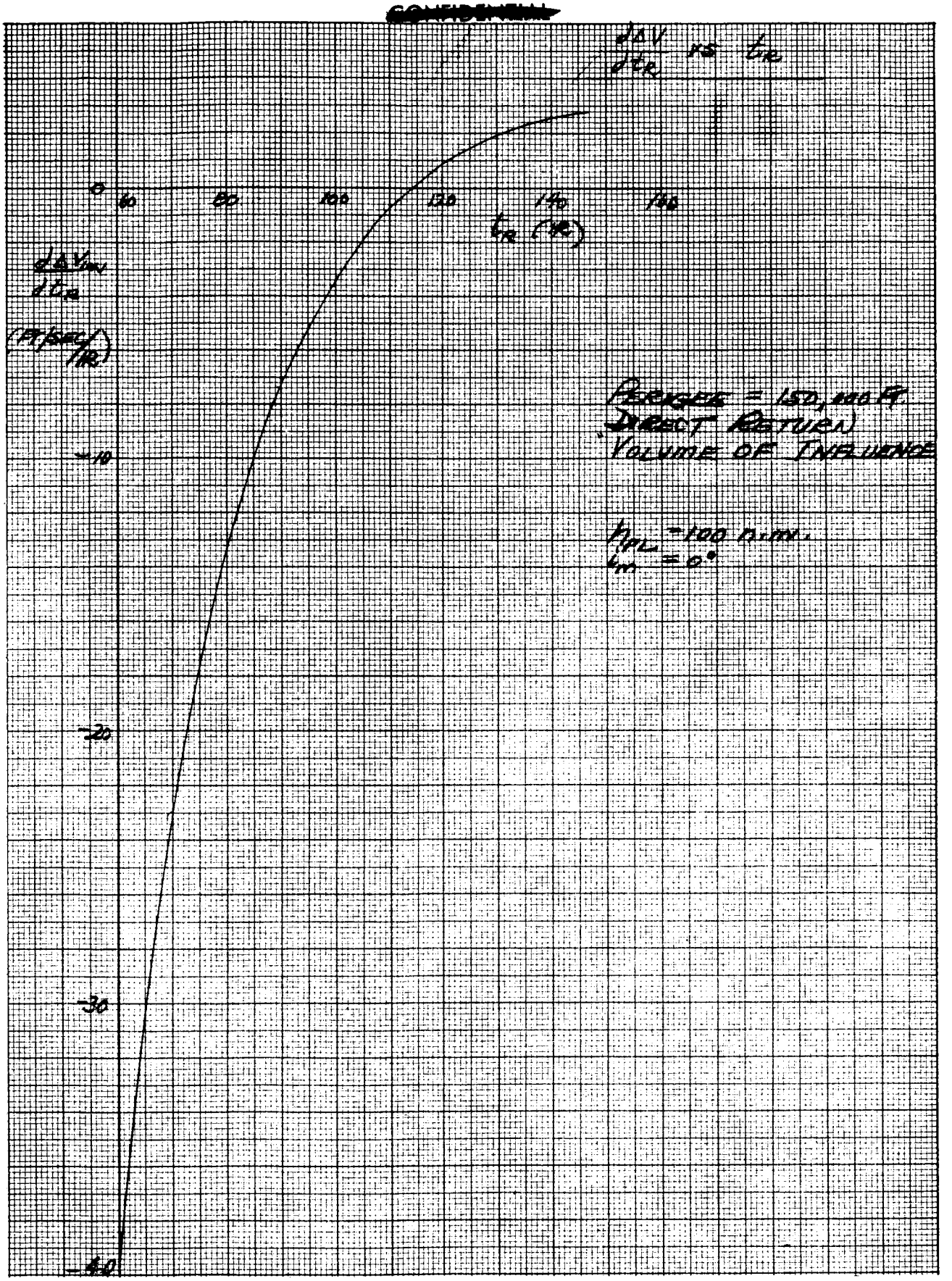

Fig. III-25. Increased Required Velocity Gradient Versus Return Time

CONFIDENTIAL

D-3 (6-60)

CONFIDENTIAL

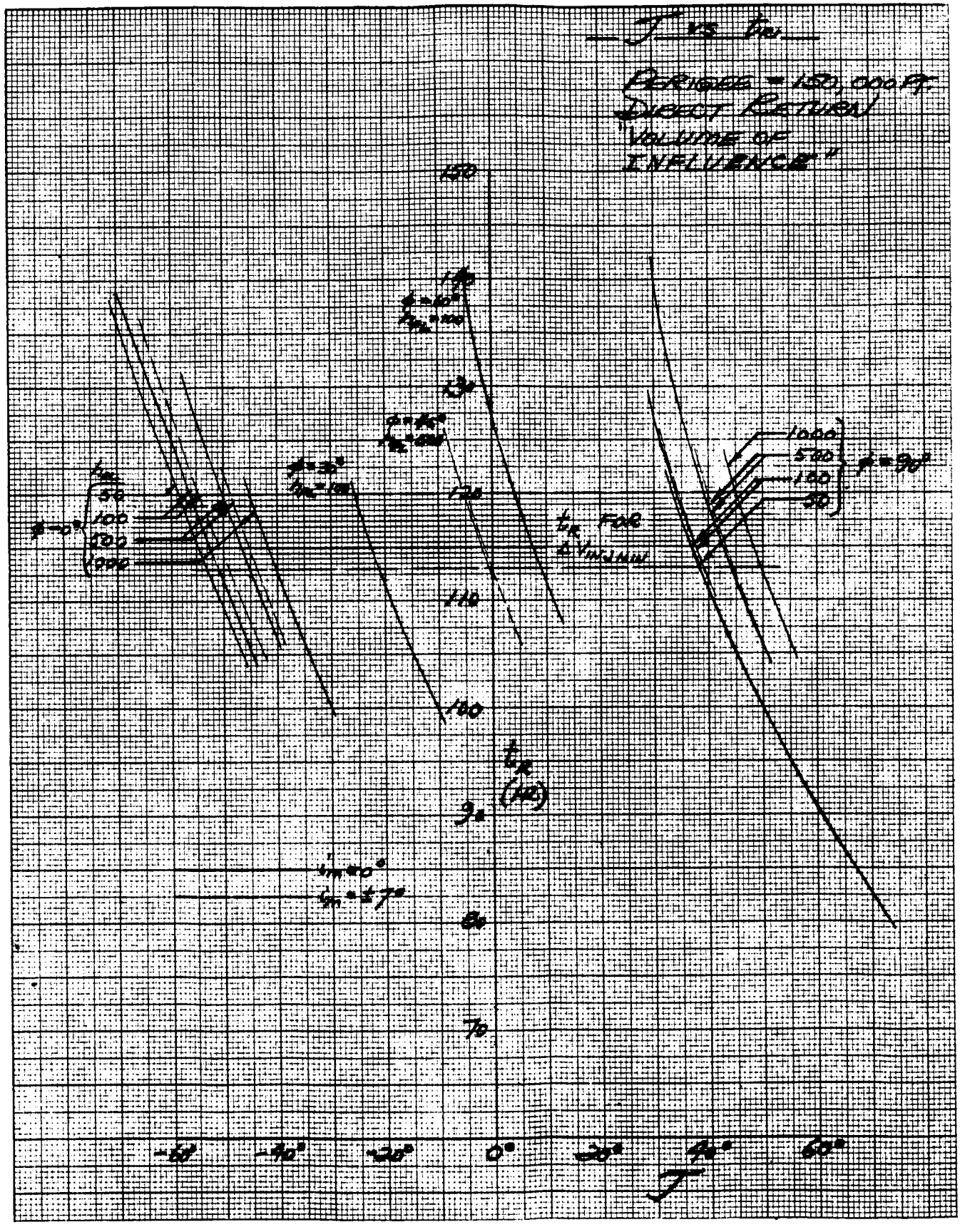

Fig. III-26. Return Time Versus Ejection Position

CONFIDENTIAL

D-3 (6-60)

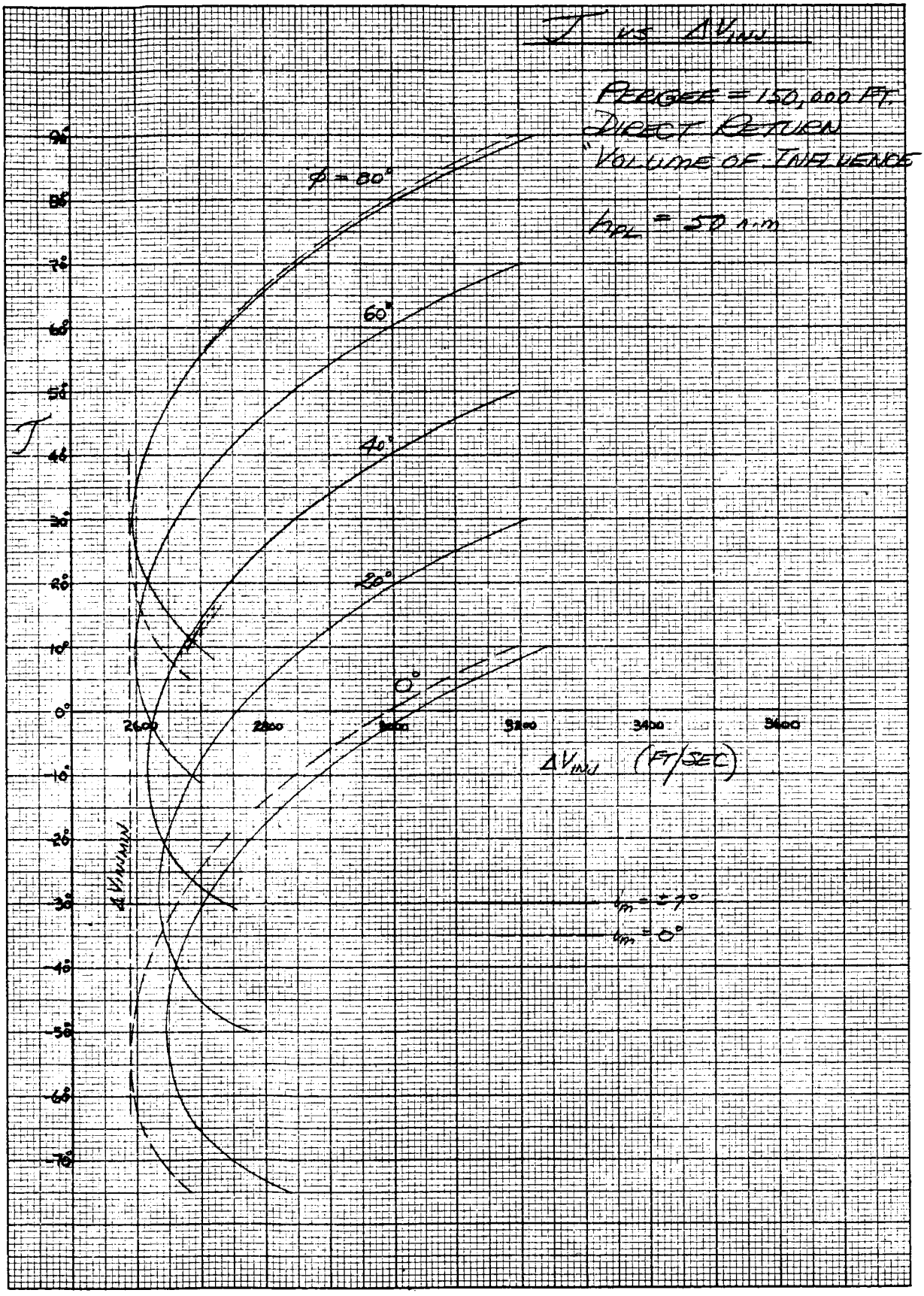

Fig. III-27. Required Velocity Impulse Versus Ejection Position

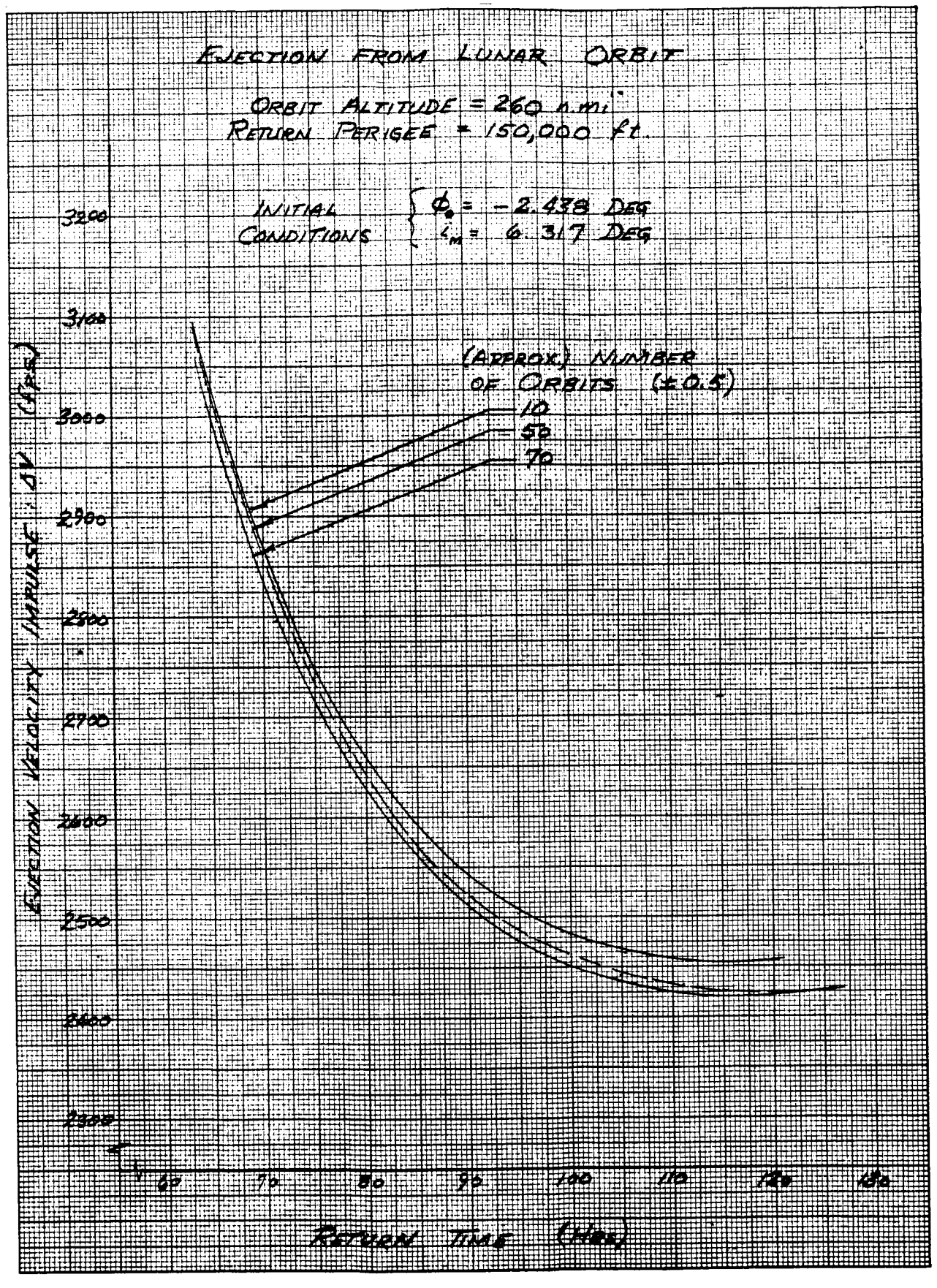

Fig. III-28. Required Velocity Impulse Versus Time in Orbit ($\phi_0 \sim 0$)

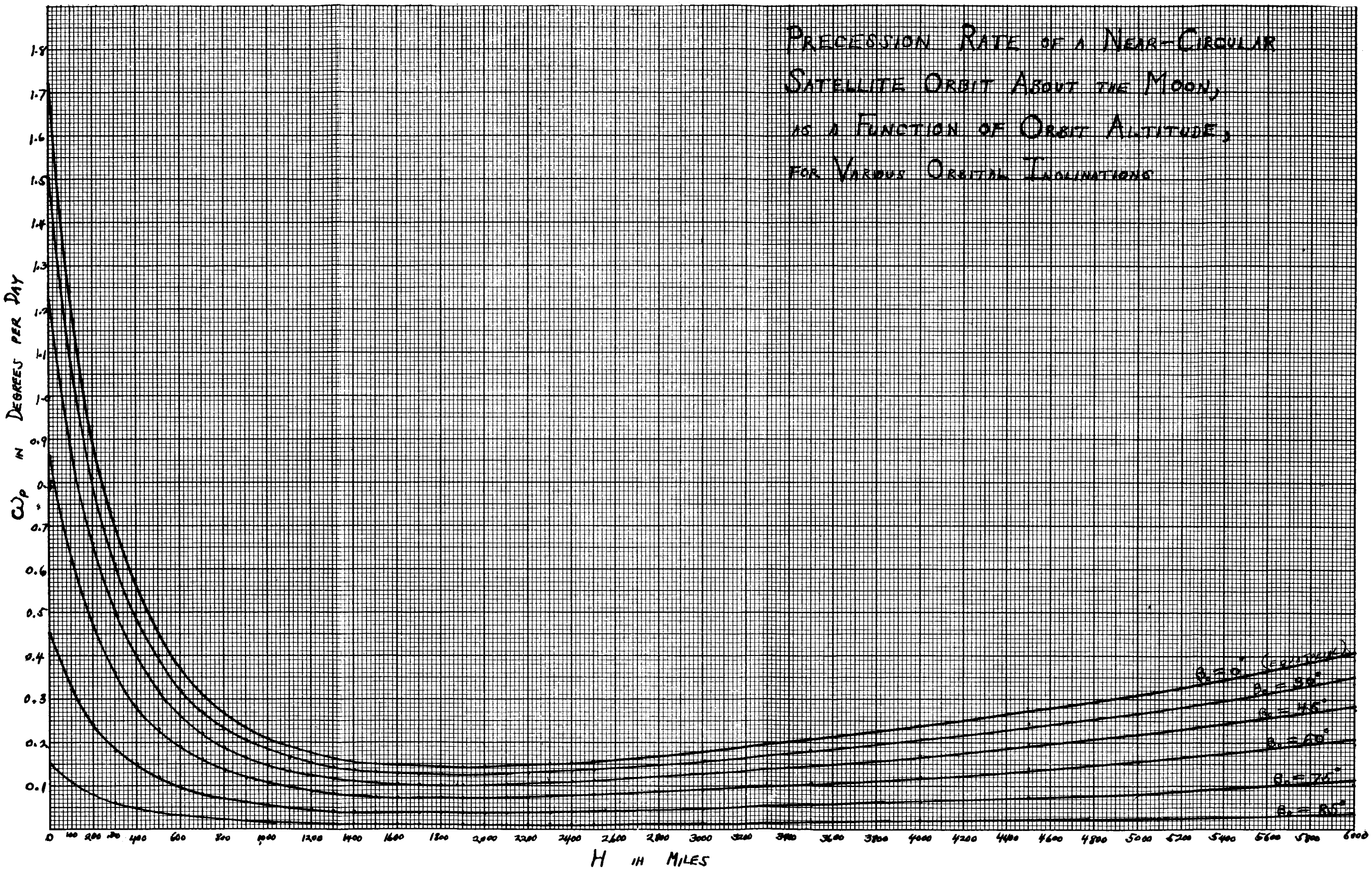

Fig. III-30. Precession Rate of Lunar Orbit due to Moon Oblateness and Presence of the Earth

~~CONFIDENTIAL~~

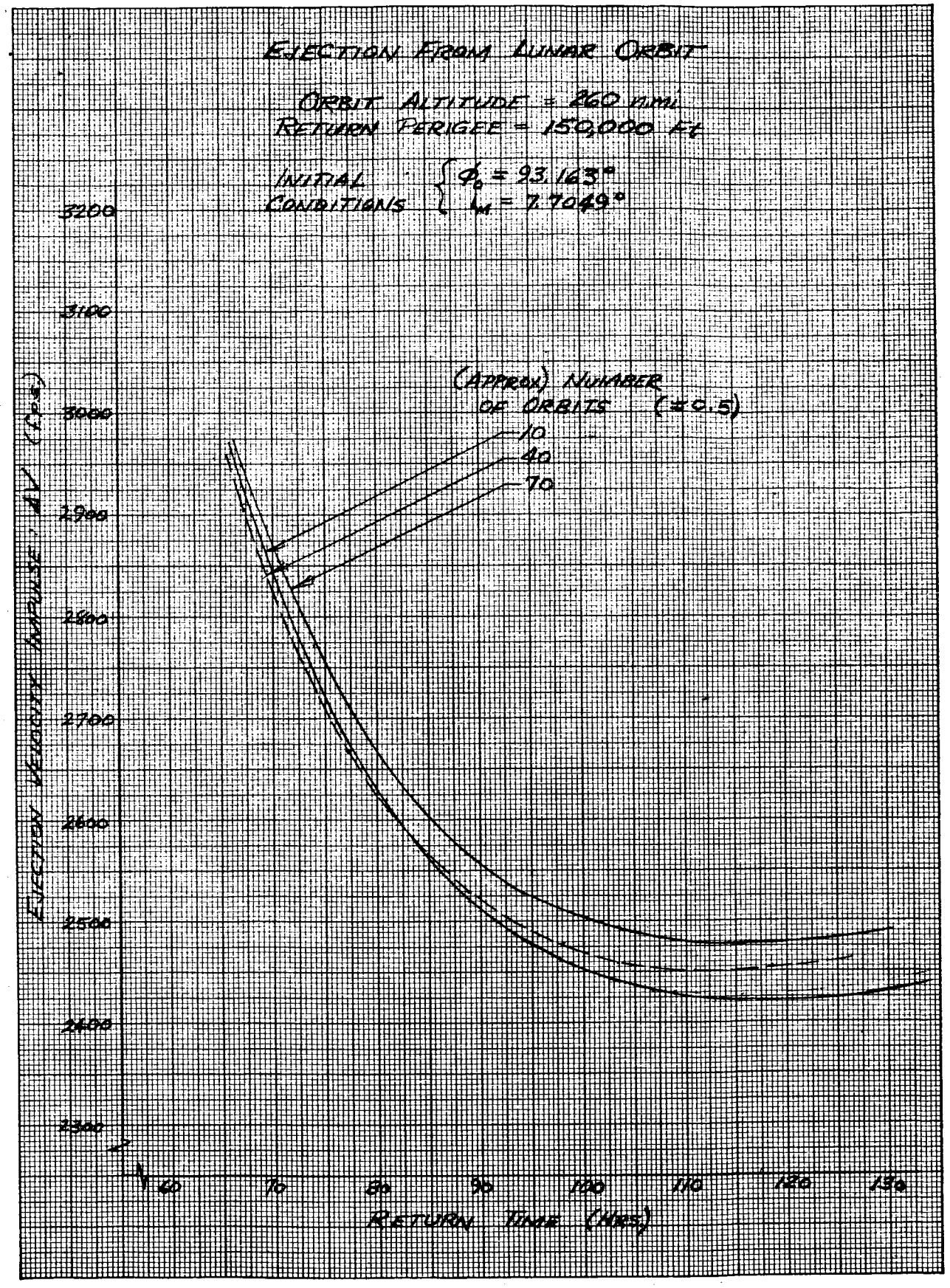

Fig. III-29. Required Velocity Impulse Versus Time in Orbit ($\phi_0 \sim 90$)

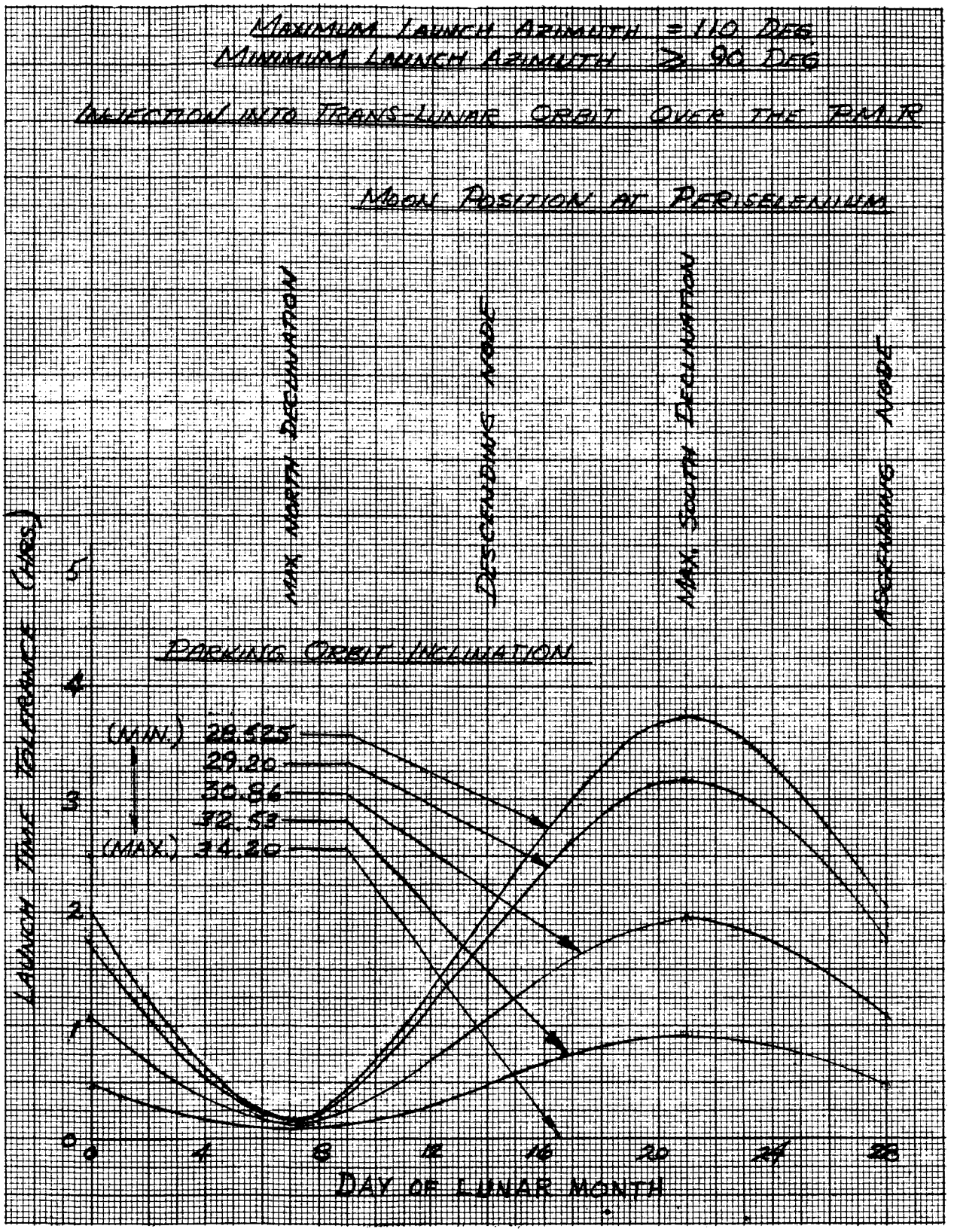

Fig. III-31. Launch Time Tolerance Versus Day of Lunar Month

CONFIDENTIAL

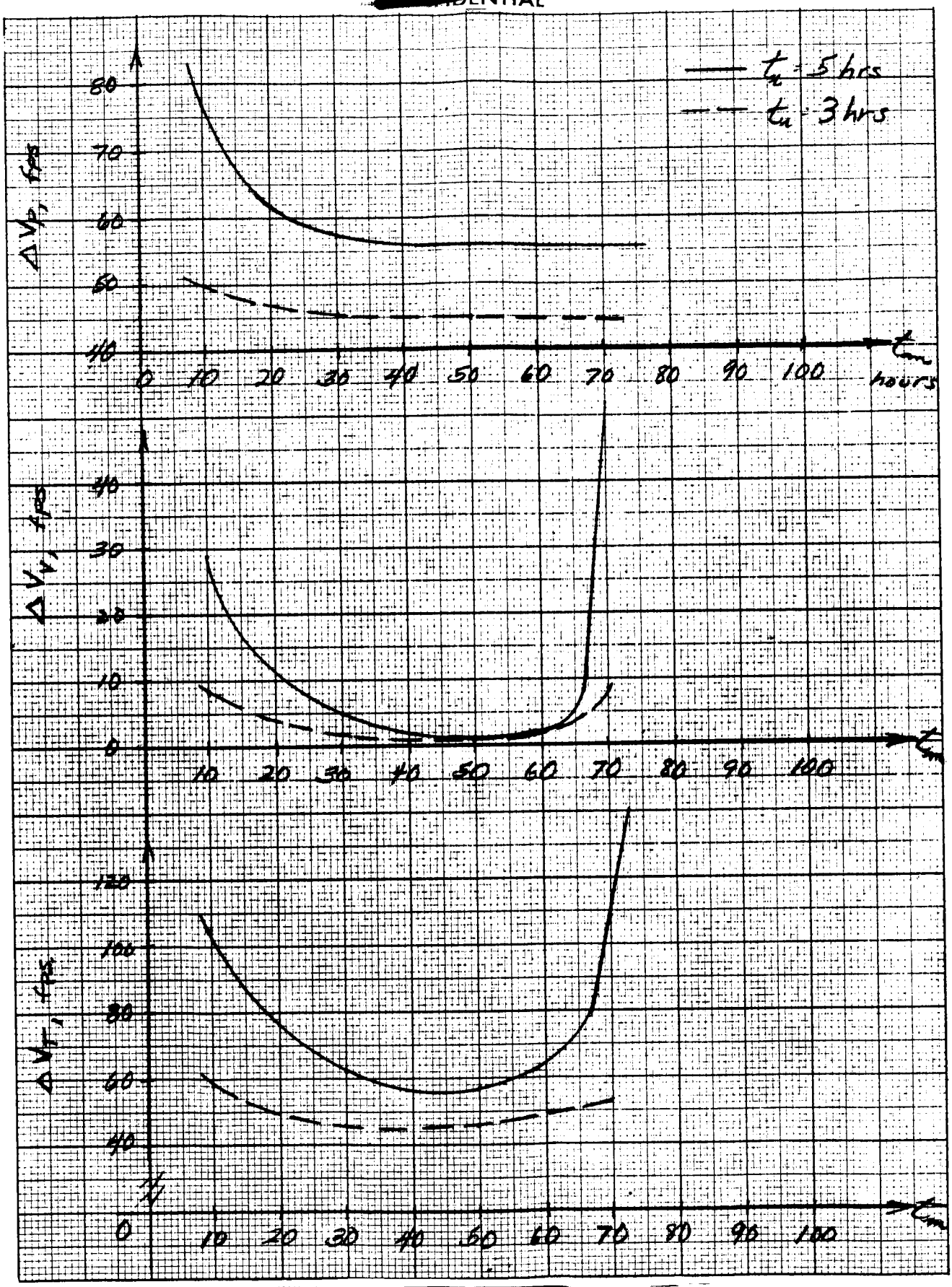

Fig. III-32. Midcourse Guidance Velocity Requirements ($\Delta\dot{y}_{n_0}$ = 0 fps; $\Delta\dot{z}_{n_0}$ = 30.61)

CONFIDENTIAL

D-3 (6.60)

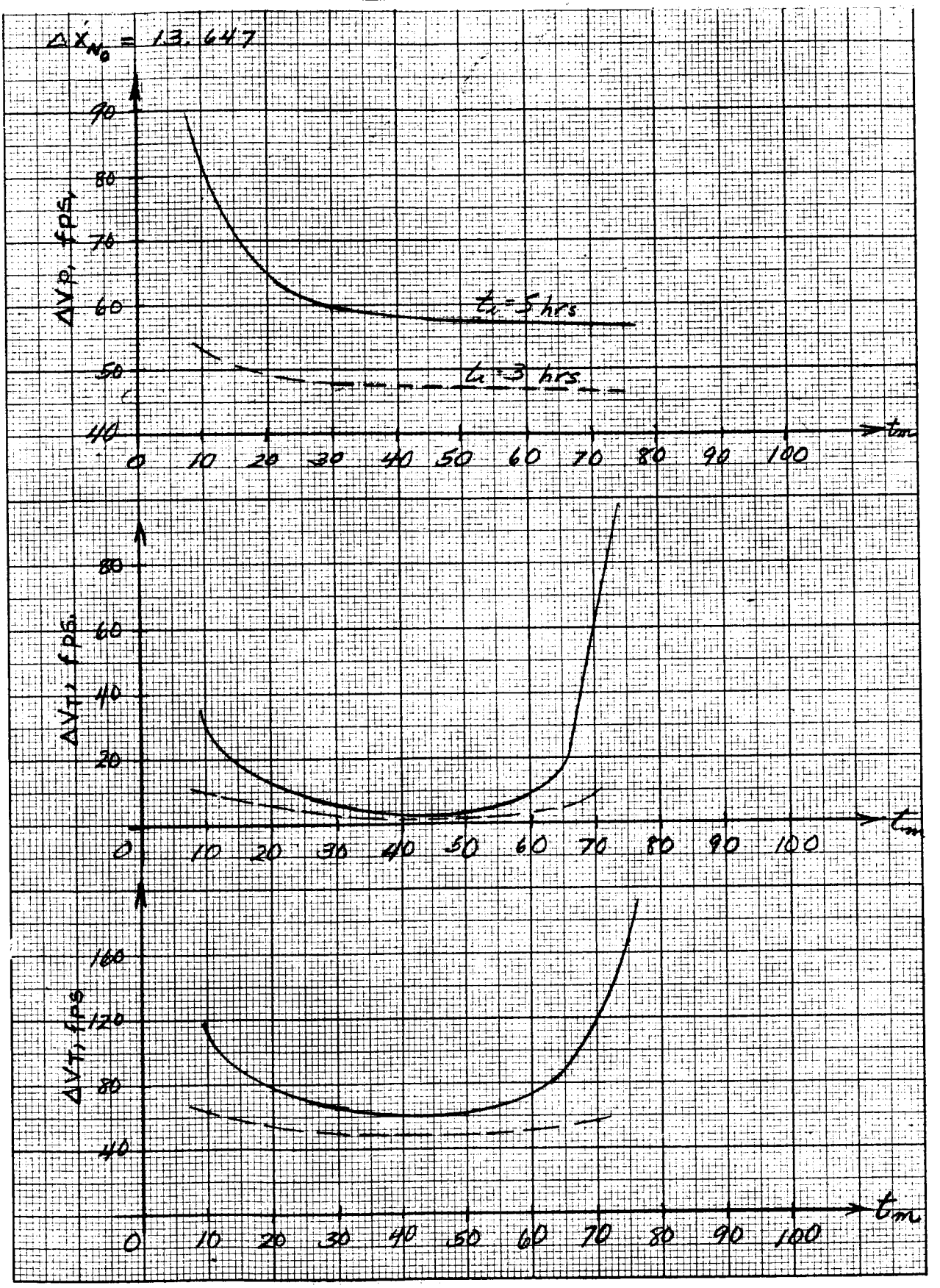

Fig. III-33. Midcourse Guidance Velocity Requirements
($\Delta \dot{y}_{n_0}$ = 18.882 fps; $\Delta \dot{z}_{n_0}$ = 21.645)

CONFIDENTIAL

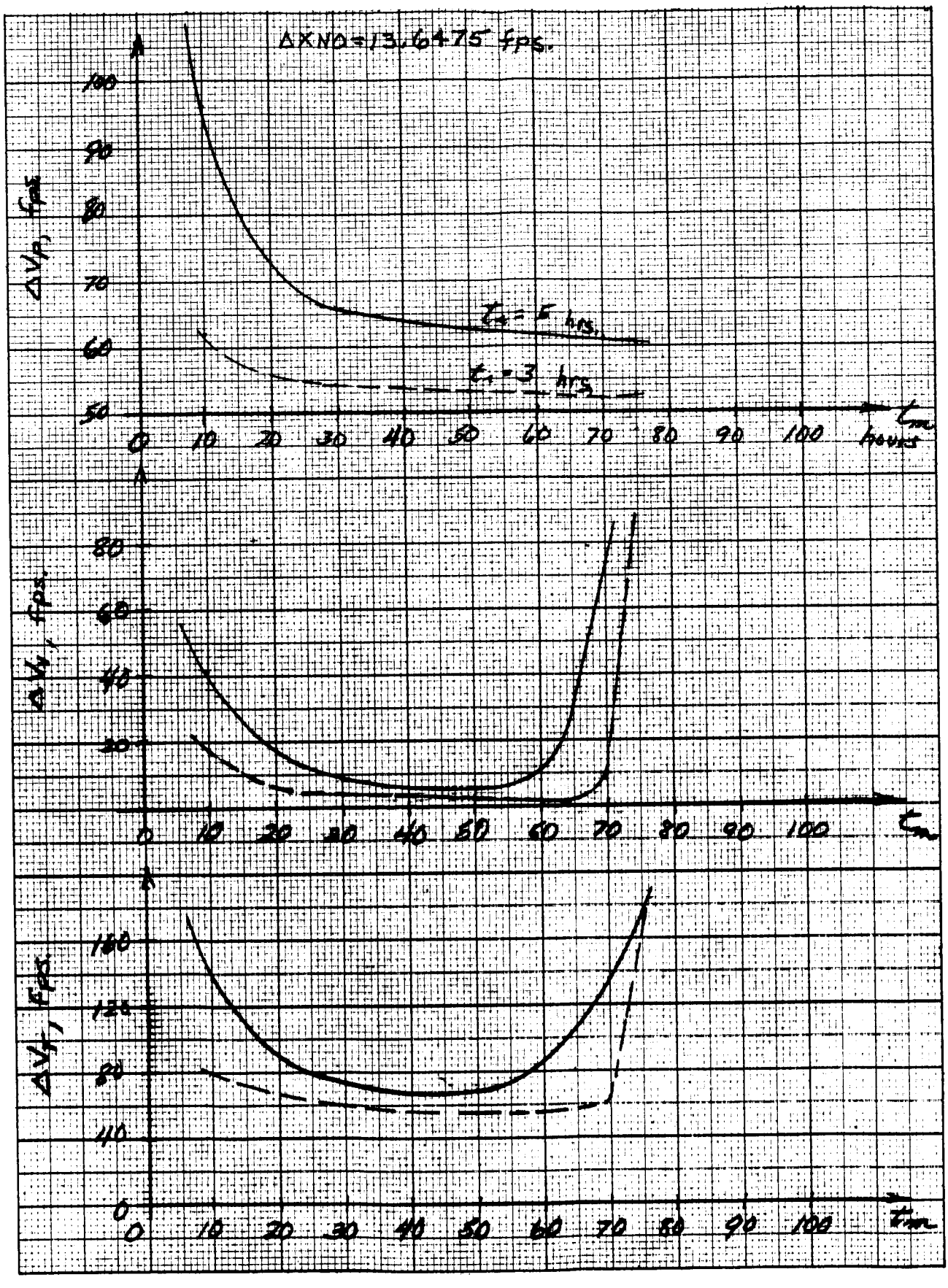

Fig. III-34. Midcourse Guidance Velocity Requirements
($\Delta\dot{y}_{n_0}$ = 26.702 fps; $\Delta\dot{z}_{n_0}$ = 0)

CONFIDENTIAL

D-3 (6-60)

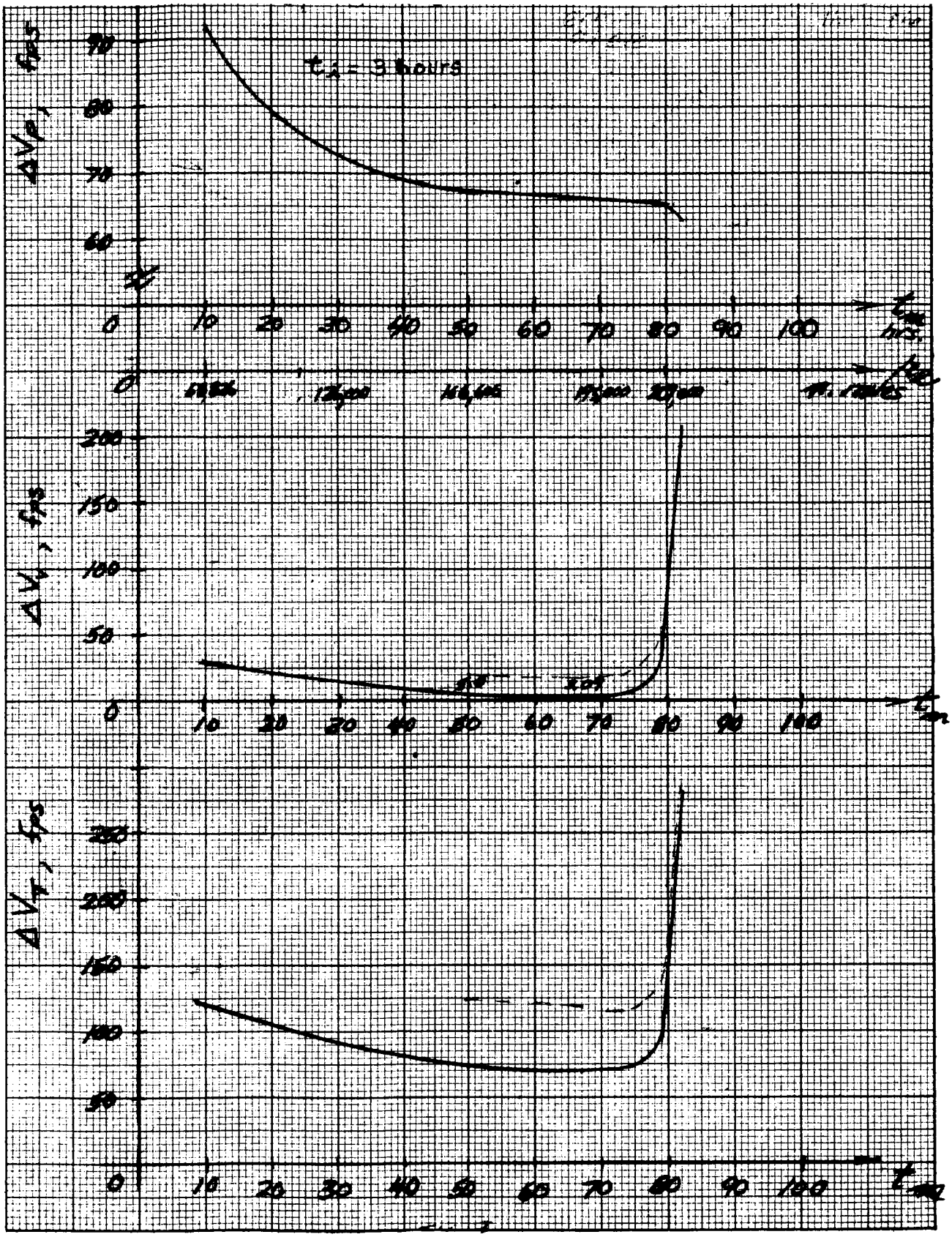

Fig. III-35. Midcourse Guidance Velocity Requirements (99% probability of injection errors $< \Delta \dot{x}_{n_0} = 13.65$ fps; $\Delta \dot{y}_{n_0} = 0$; $\Delta \dot{z}_{n_0} = 30.61$)

D-3 (6-60)

CONFIDENTIAL

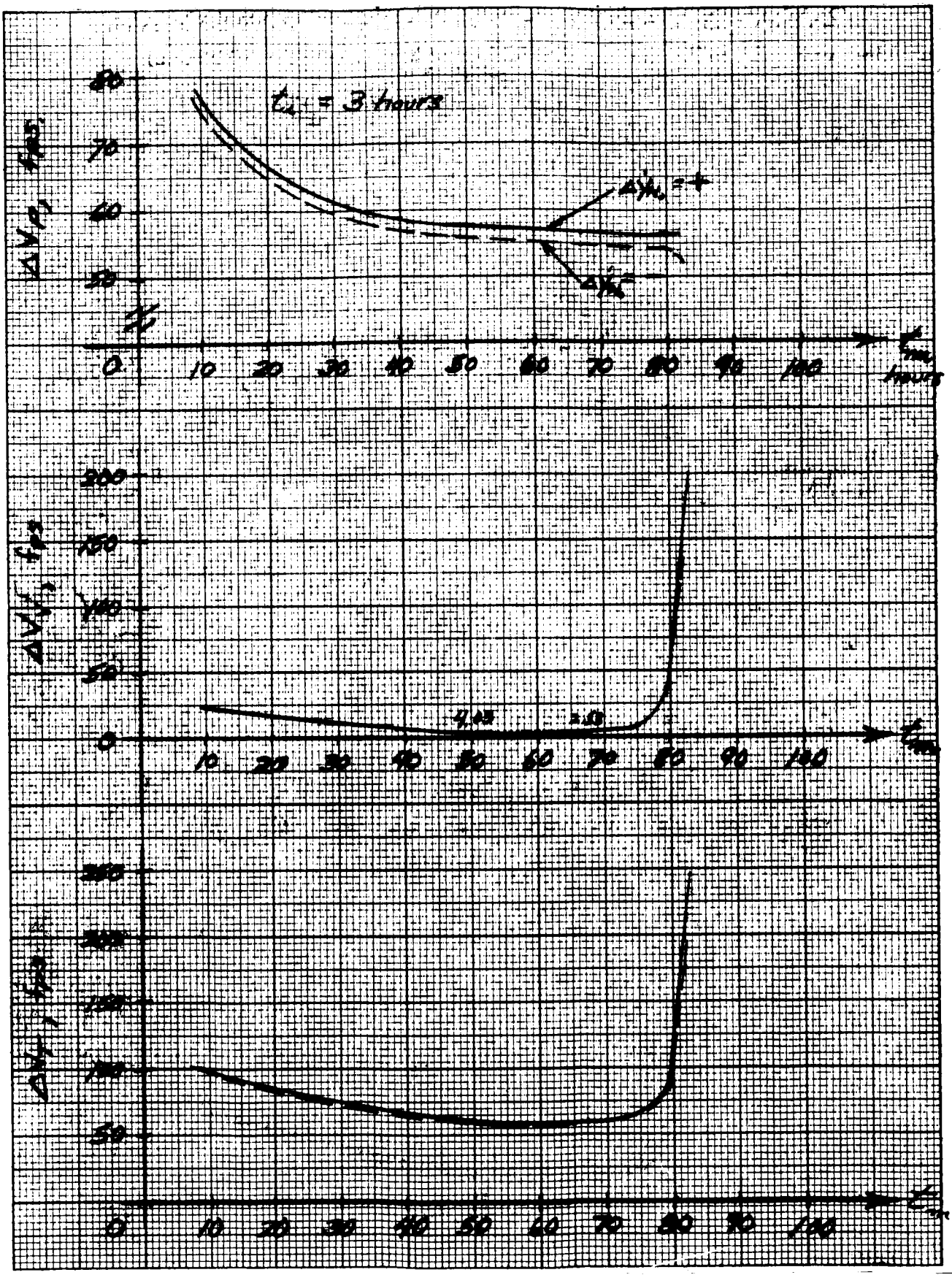

Fig. III-36. Midcourse Guidance Velocity Requirements (99% probability of injection errors $< \Delta \dot{x}_{n_0} = 13.65$ fps; $\Delta \dot{y}_{n_0} = \pm 18.88$; $\Delta \dot{z}_{n_0} = 21.65$)

CONFIDENTIAL

D-3 (6-60)

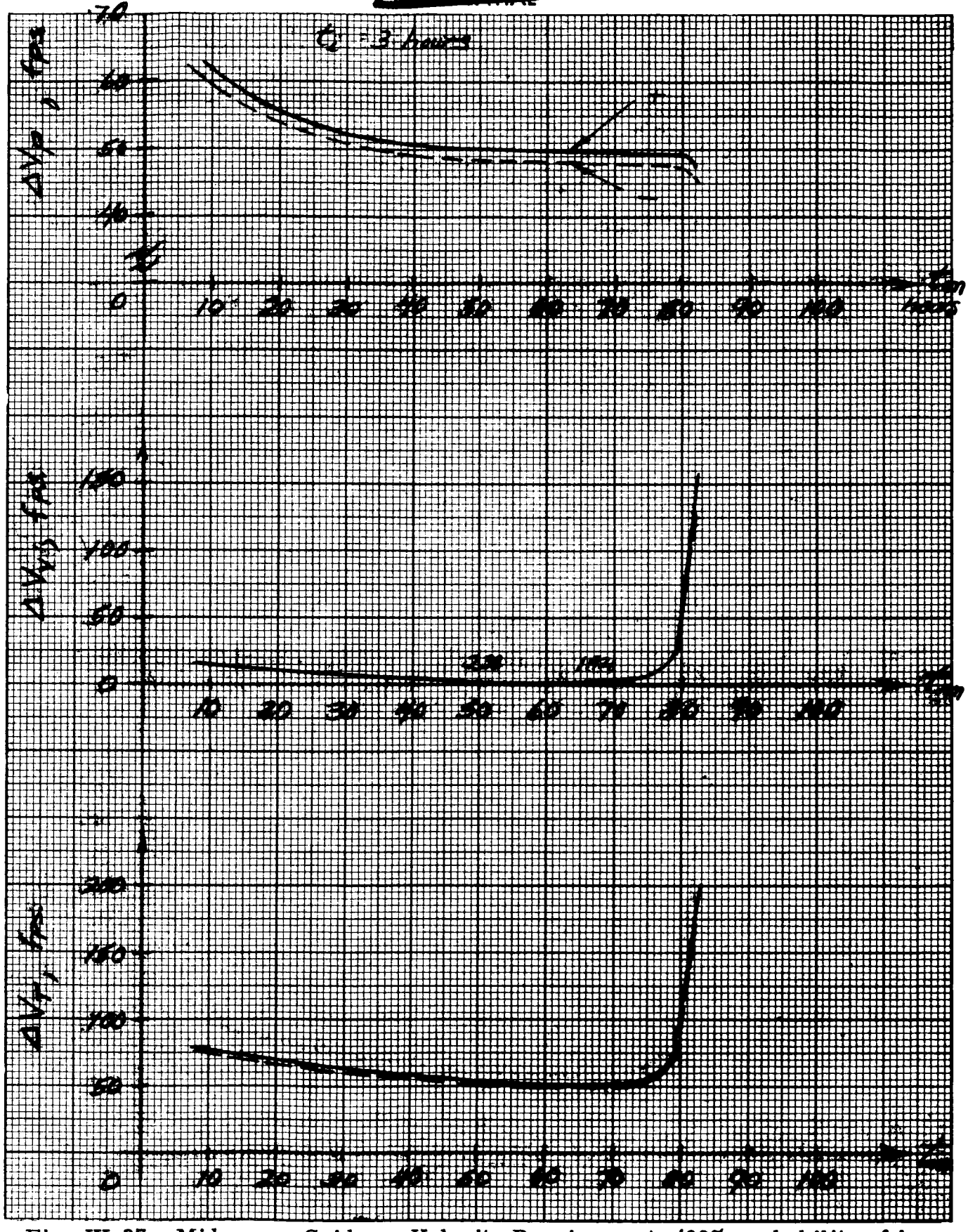

Fig. III-37. Midcourse Guidance Velocity Requirements (99% probability of injection errors $< \Delta \dot{x}_{n_0} = 13.65$ fps; $\Delta \dot{y}_{n_0} = 26.70$; $\Delta \dot{z}_{n_0} = 0$)

D-3 (6-60)

CONFIDENTIAL

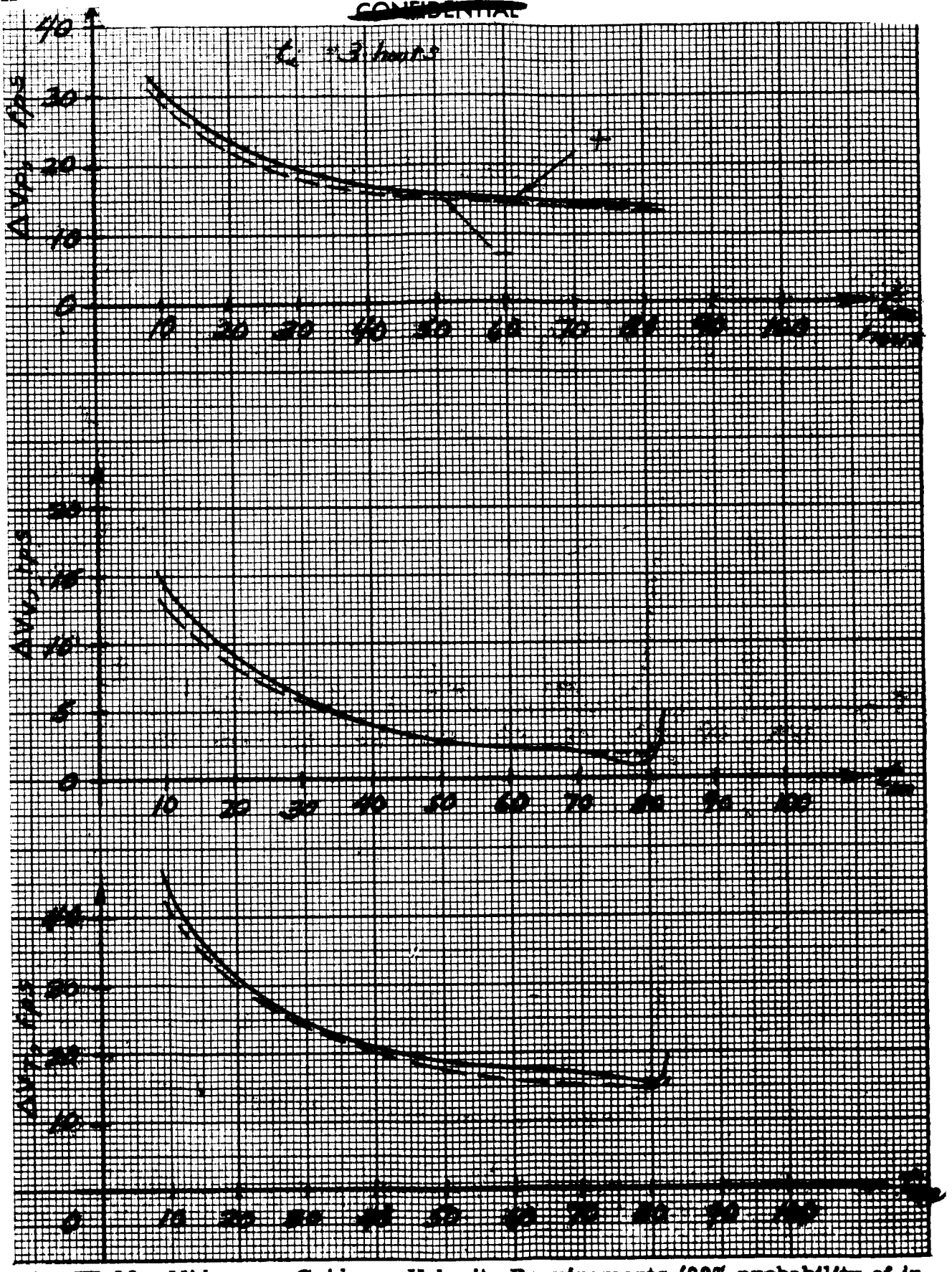

Fig. III-38. Midcourse Guidance Velocity Requirements (99% probability of injection errors < $\Delta \dot{x}_{n_0}$ =0 fps; $\Delta \dot{y}_{n_0}$ = ±31.73; $\Delta \dot{z}_{n_0}$ = 30.61)

CONFIDENTIAL

D-3 (6-60)

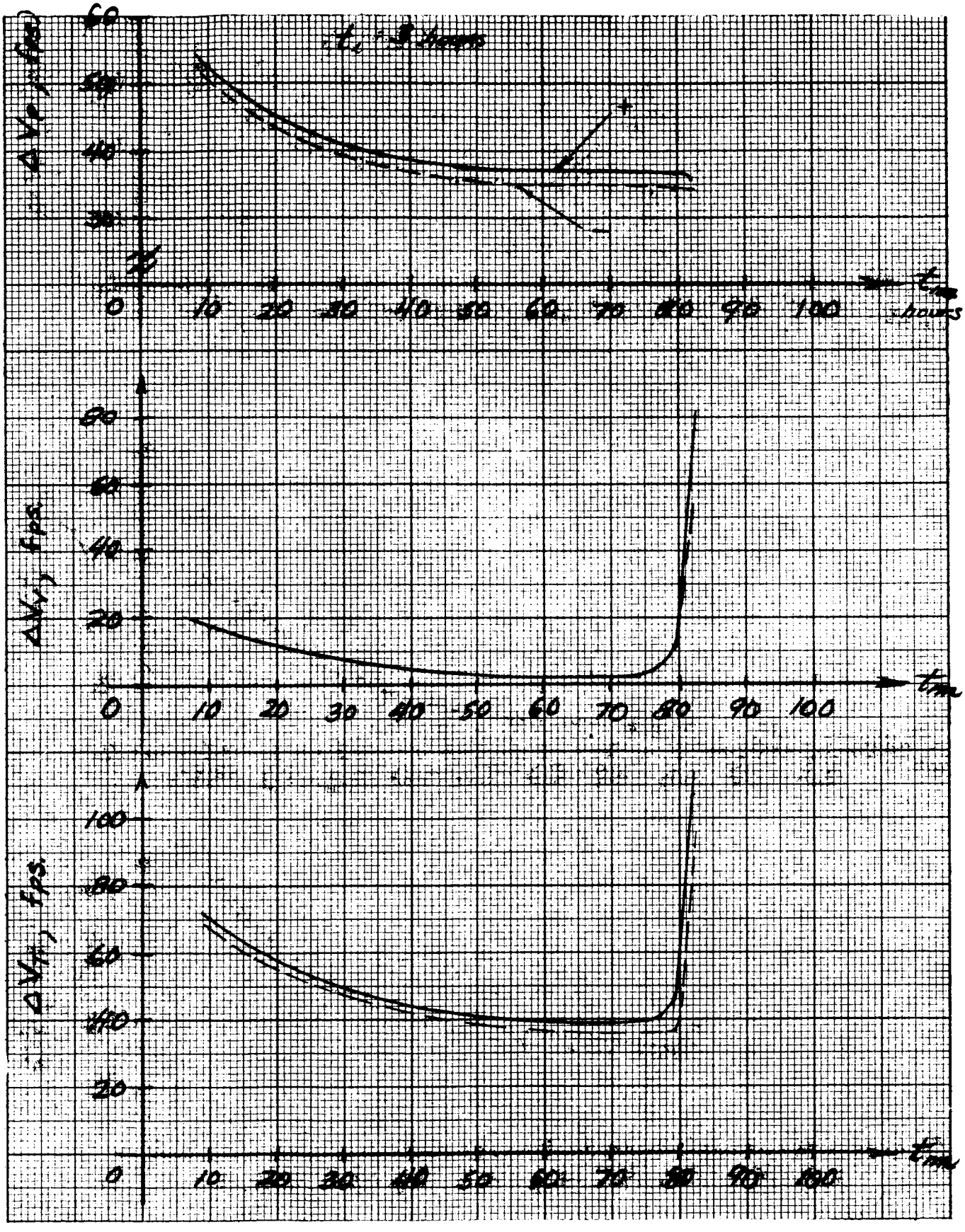

Fig. III-39. Midcourse Guidance Velocity Requirements (99% probability of injection errors $< \Delta\dot{x}_{n_0} = 8.1$ fps; $\Delta\dot{y}_{n_0} = \pm 31.73$; $\Delta\dot{z}_{n_0} = 21.6$)

CONFIDENTIAL

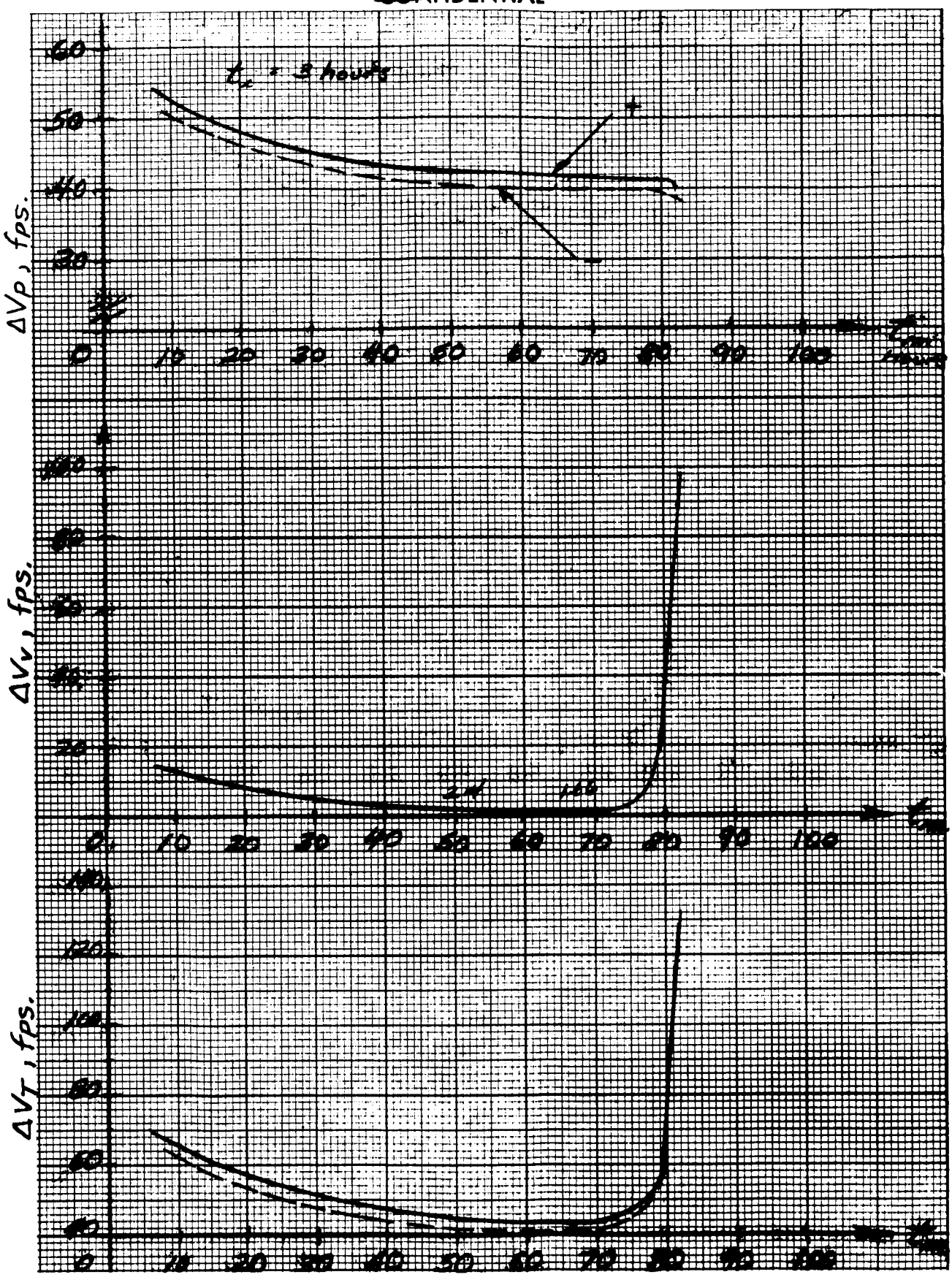

Fig. III-40. Midcourse Guidance Velocity Requirements (99% probability of injection errors $< \Delta \dot{x}_{n_0} = 11.51$ fps; $\Delta \dot{y}_{n_0} = \pm 31.67$; $\Delta \dot{z}_{n_0} = 0$)

CONFIDENTIAL

D-3 (6-60)

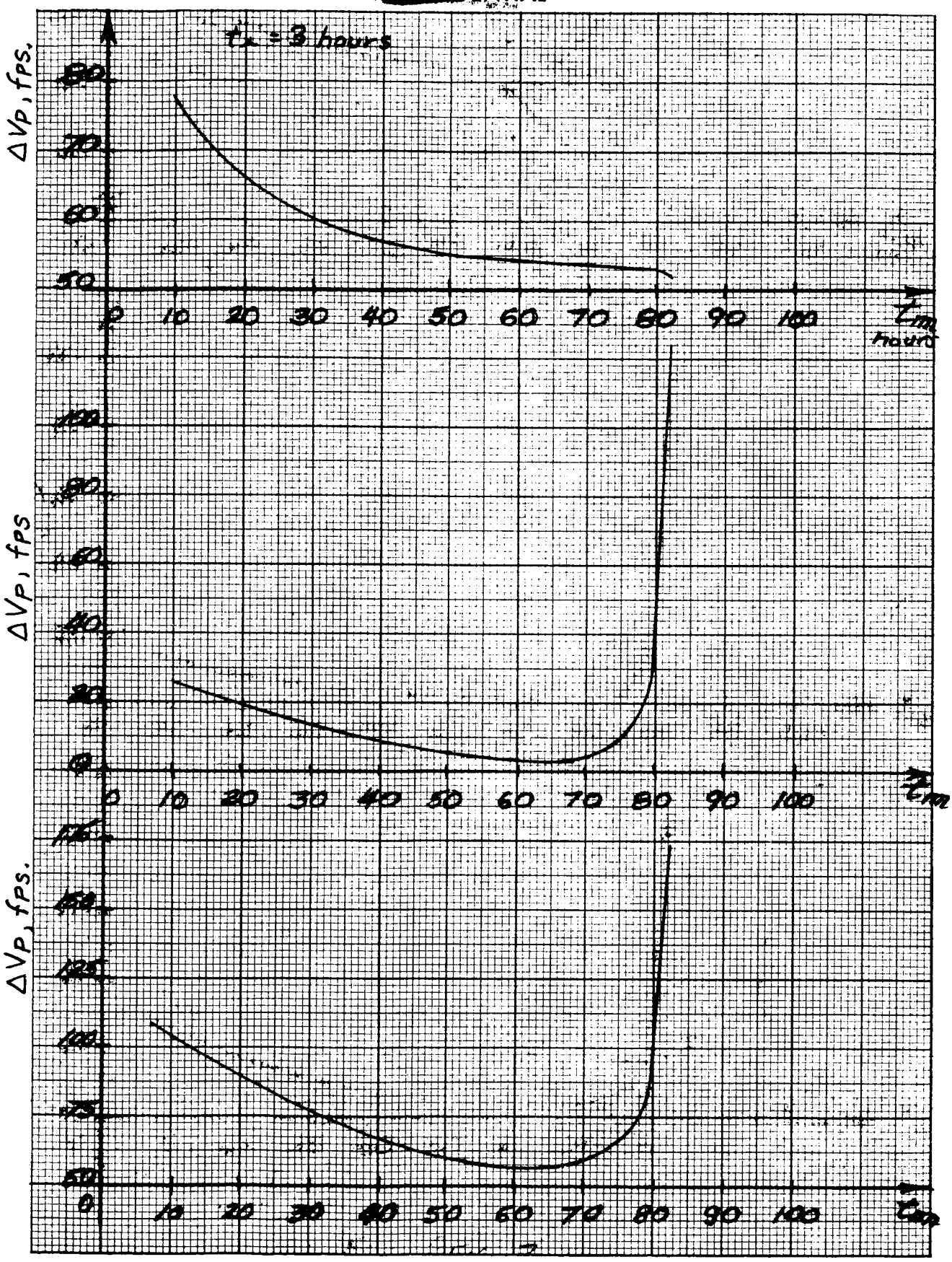

Fig. III-41. Midcourse Guidance Velocity Requirements (99% probability of injection errors $< \Delta\dot{x}_{n_0} = 11.51$ fps; $\Delta\dot{y}_{n_0} = 0$; $\Delta\dot{z}_{n_0} = 36.31$)

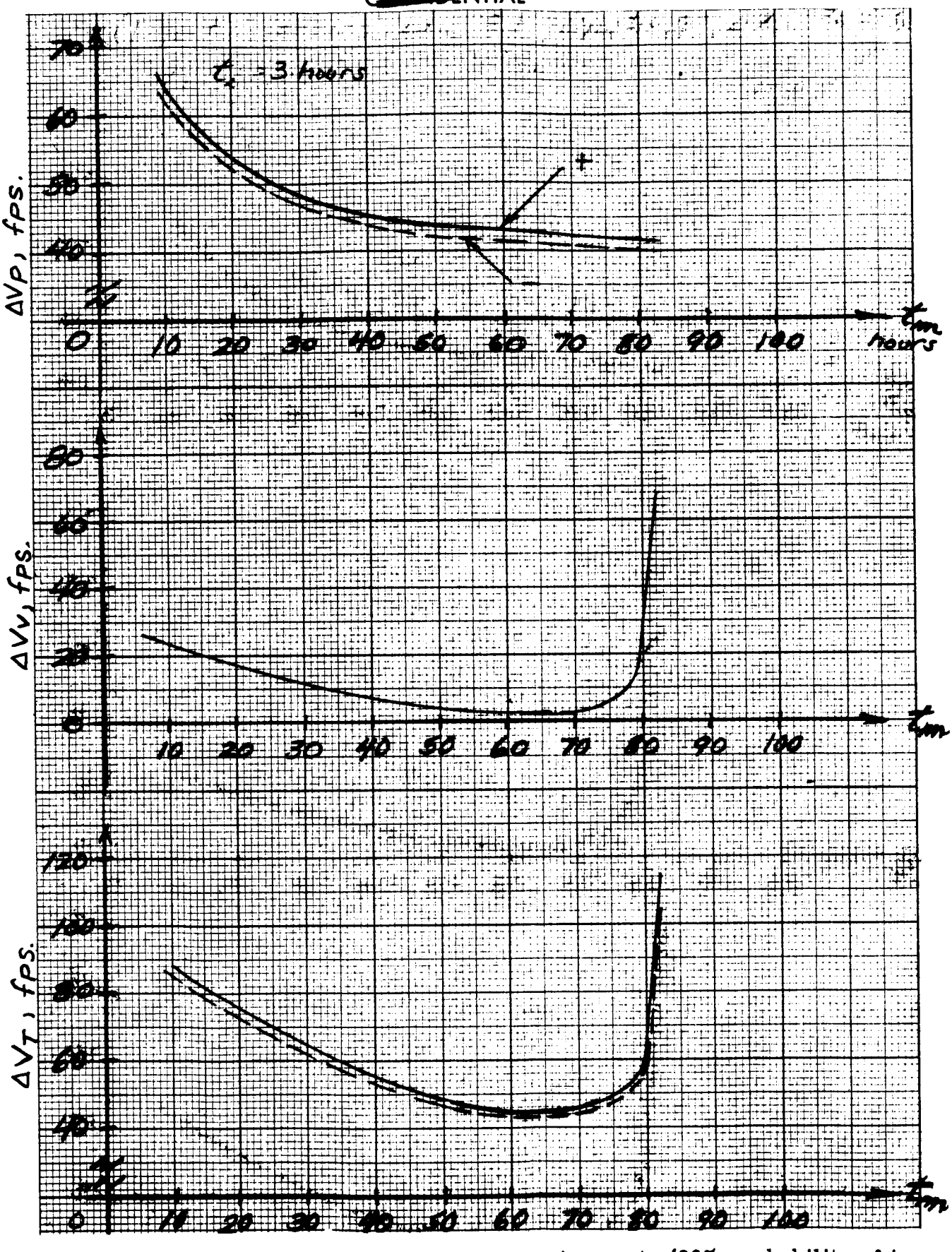

Fig. III-42. Midcourse Guidance Velocity Requirements (99% probability of injection errors < $\Delta \dot{x}_{n_0}$ = 8.1 fps; $\Delta \dot{y}_{n_0}$ = ±18.88; $\Delta \dot{z}_{n_0}$ = 36.31)

CONFIDENTIAL

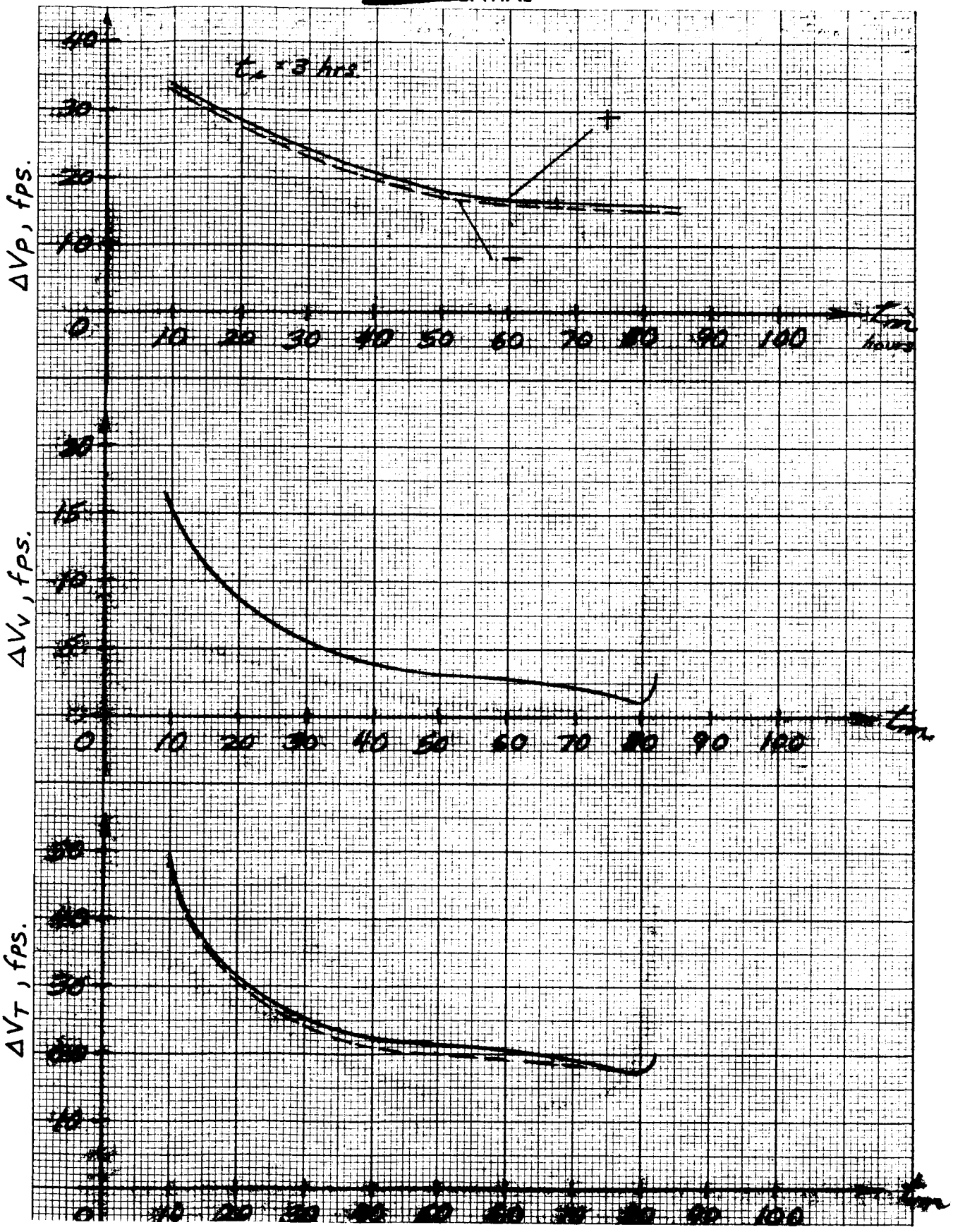

Fig. III-43. Midcourse Guidance Velocity Requirements (99% probability of injection errors < $\Delta \dot{x}_{n_0}$ = 0 fps; $\Delta \dot{y}_{n_0}$ = ±26.70; $\Delta \dot{z}_{n_0}$ = 36.31)

CONFIDENTIAL

D-3 (6.60)

CONFIDENTIAL

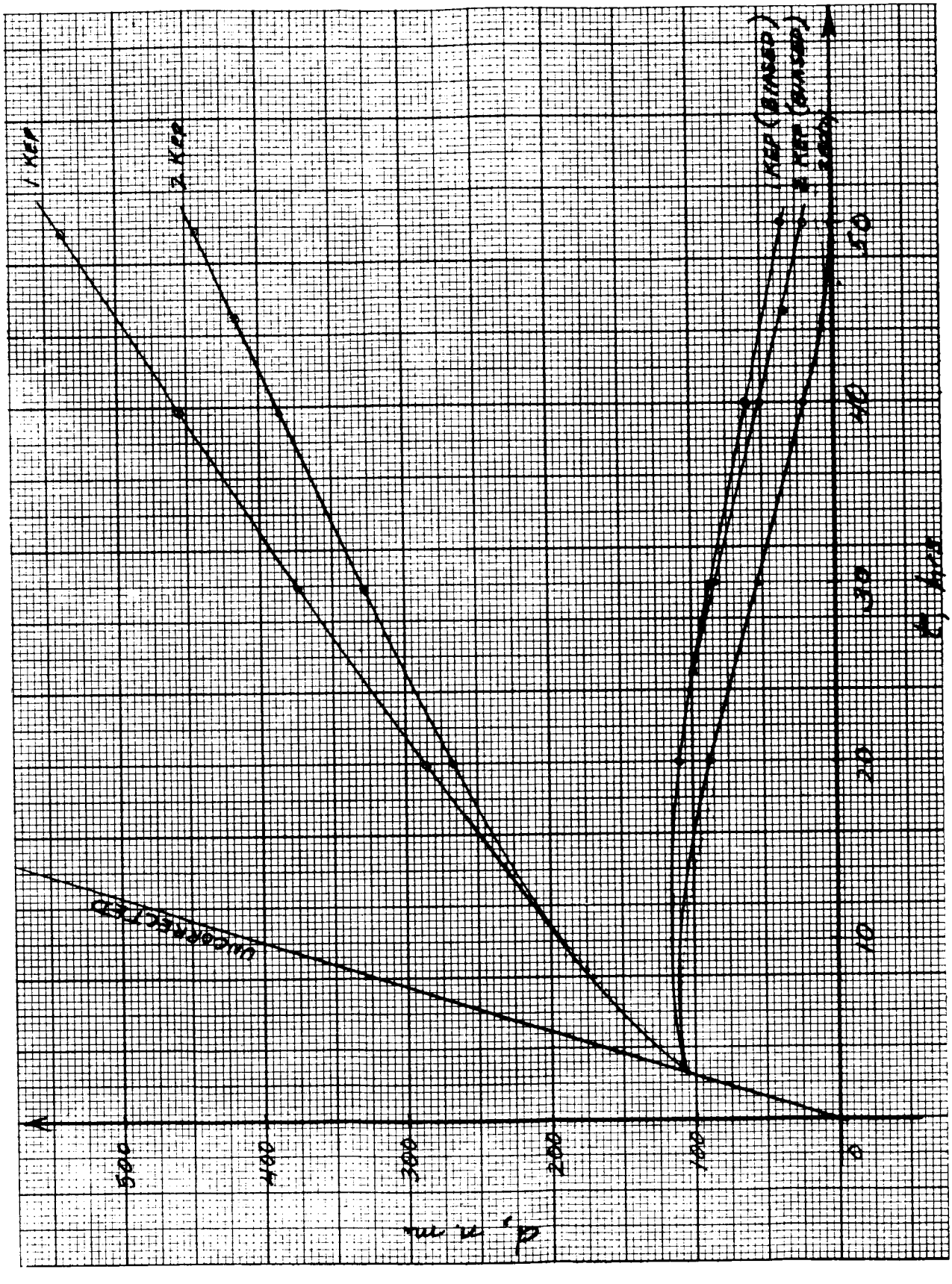

Fig. III-44. Error Distance Versus Time Along Correction Trajectory

CONFIDENTIAL

D-3 (6-60)

CONFIDENTIAL

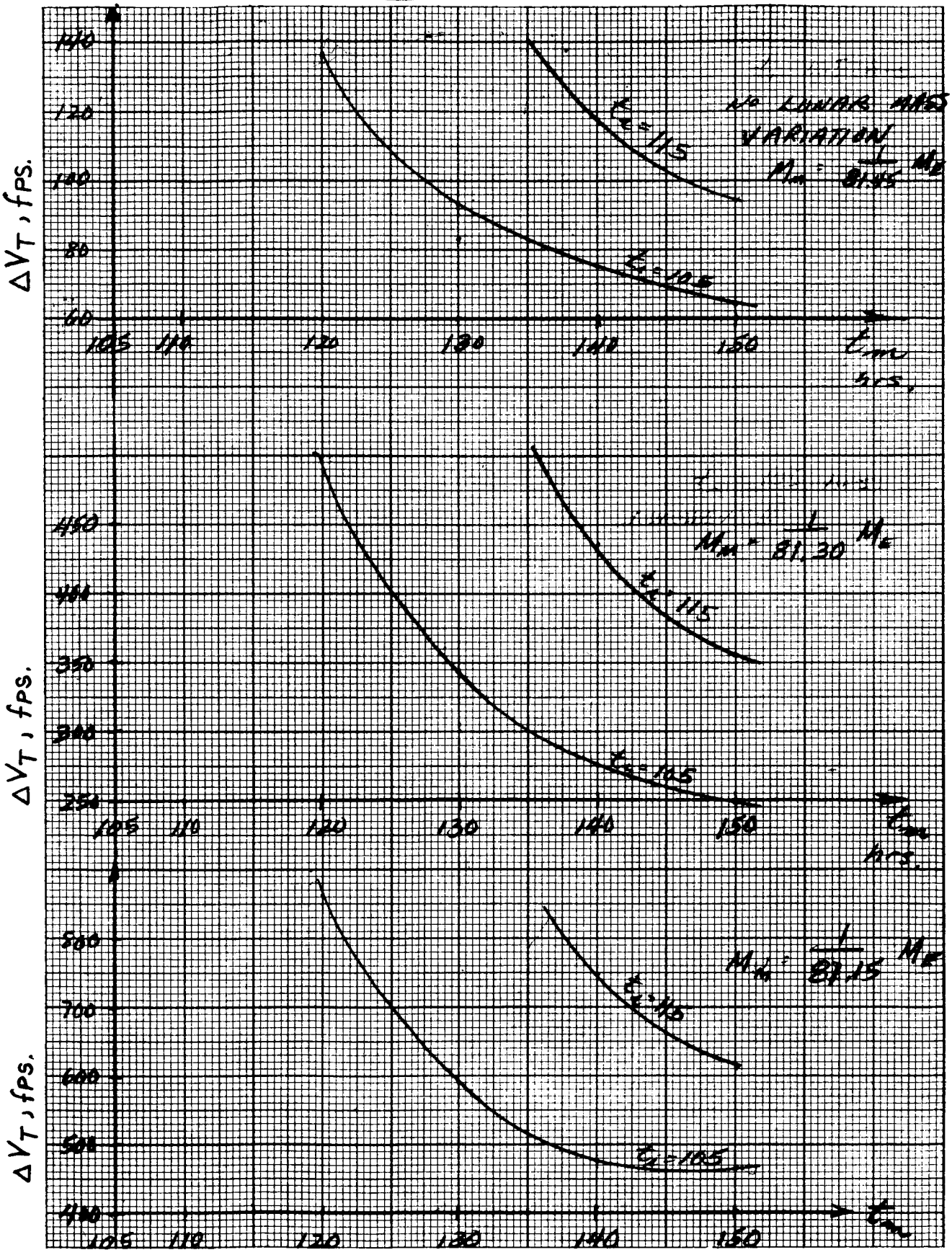

Fig. III-45. Transearth and Midcourse Velocity Requirement ($\Delta \dot{x}_{n_0}$ = 13.65 fps; $\Delta \dot{y}_{n_0}$ = 0; $\Delta \dot{z}_{n_0}$ = 30.61)

CONFIDENTIAL

D-3 (6-60)

CONFIDENTIAL

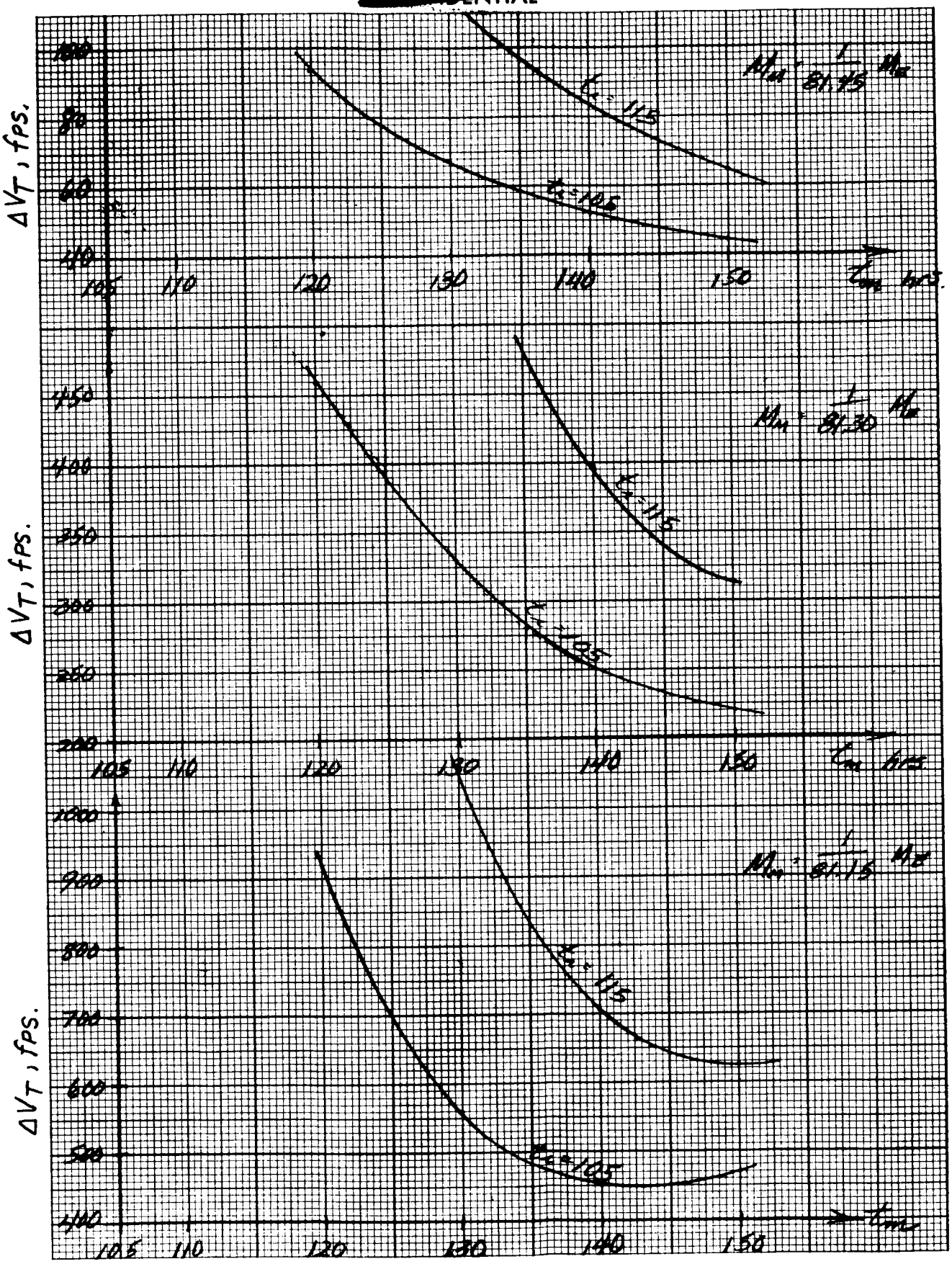

Fig. III-46. Transearth and Midcourse Velocity Requirement ($\Delta \dot{x}_{n_0}$ = 13.65 fps; $\Delta \dot{y}_{n_0}$ = 18.88; $\Delta \dot{z}_{n_0}$ = 21.645)

CONFIDENTIAL

D-3 (6-60)

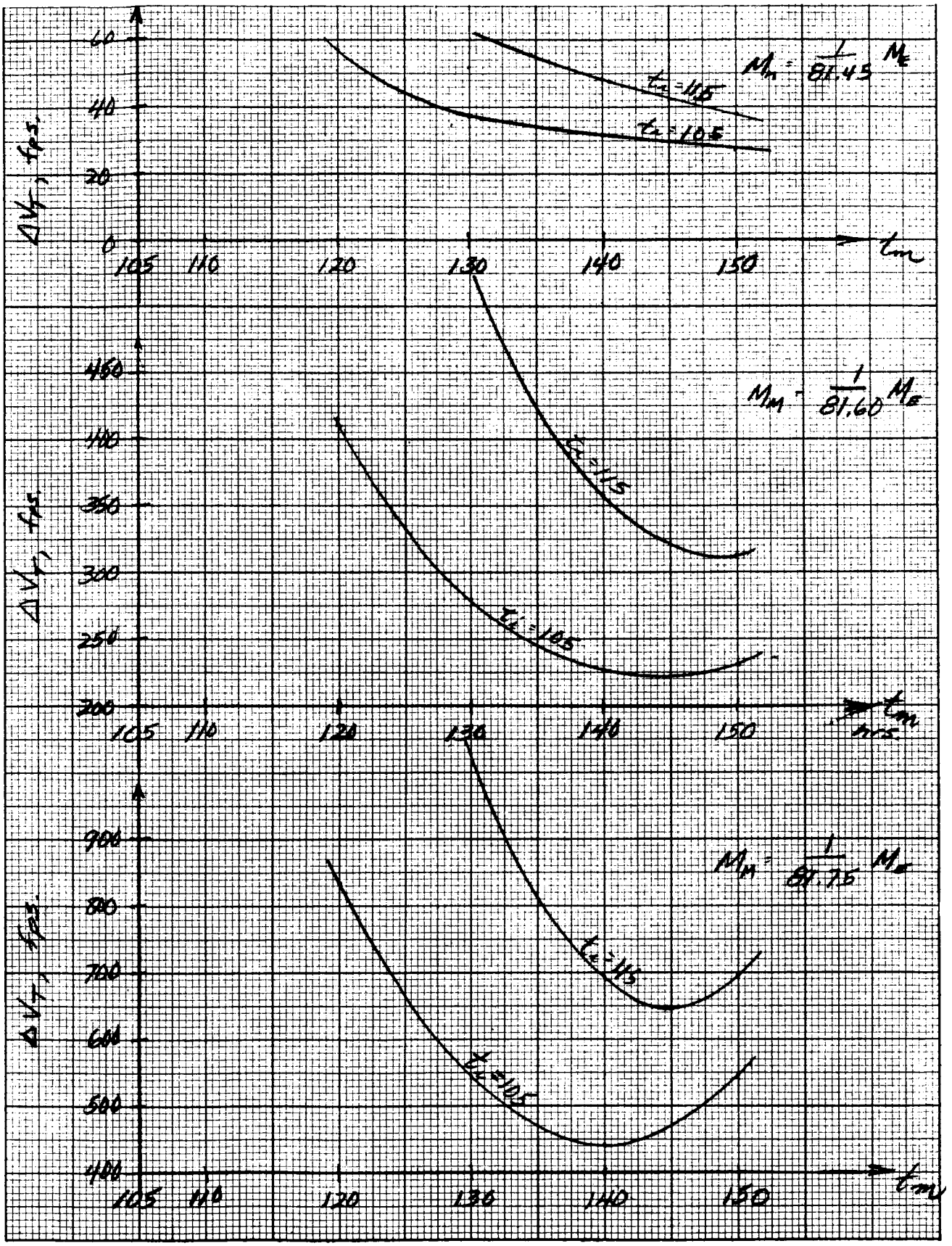

Fig. III-47. Transearth and Midcourse Velocity Requirement ($\Delta \dot{x}_{n_0}$ = 13.65 fps; $\Delta \dot{y}_{n_0}$ = 26.70; $\Delta \dot{z}_{n_0}$ = 0)

CONFIDENTIAL

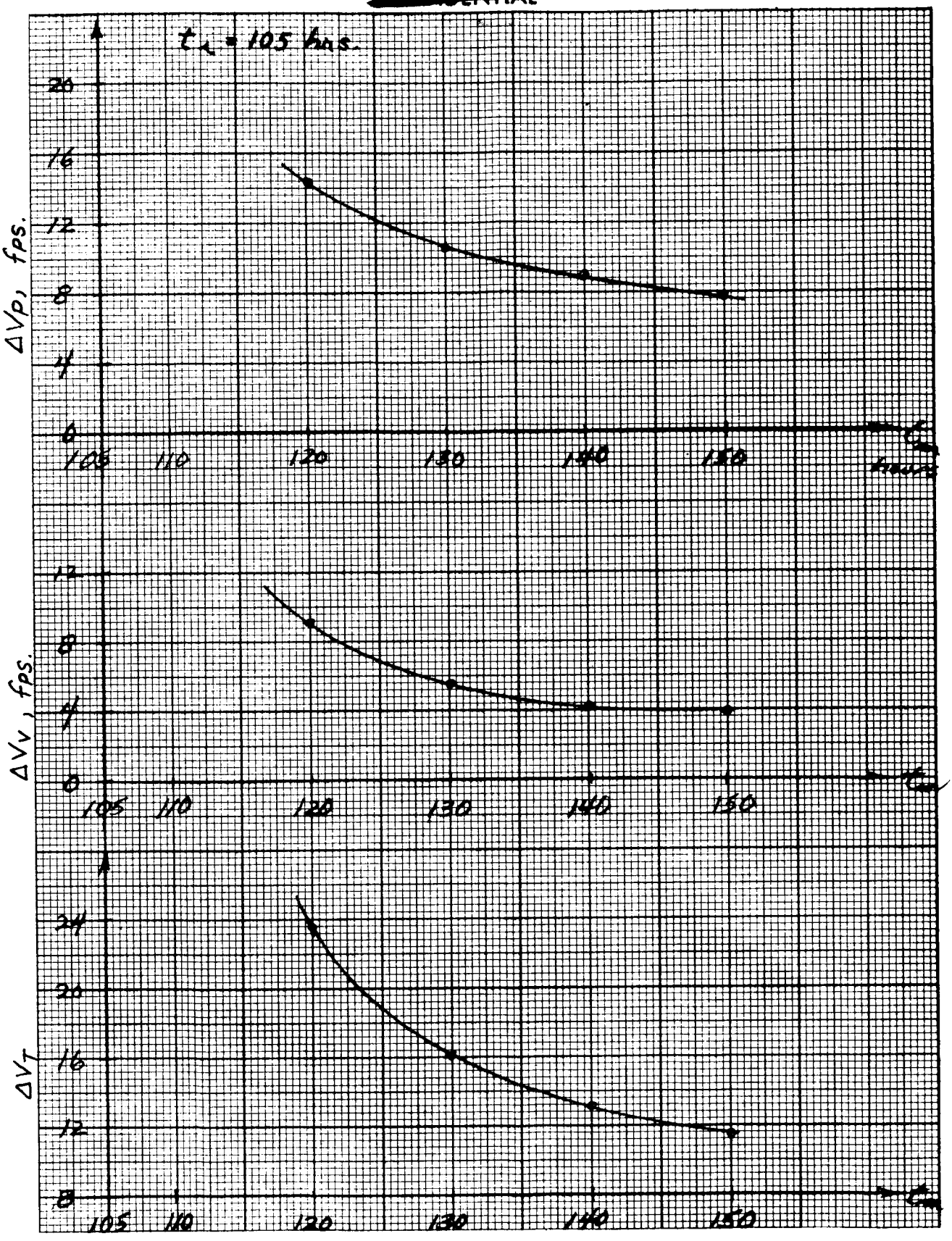

Fig. III-48. Transearth and Midcourse Guidance Required Velocity Impulse due to Errors in Velocity at Ejection from Lunar Orbit ($\Delta \dot{x}_{n_0}$ = 2.575 fps; $\Delta \dot{y}_{n_0}$ = 0; $\Delta \dot{z}_{n_0}$ = 2.1709)

CONFIDENTIAL

D-3 (6-60)

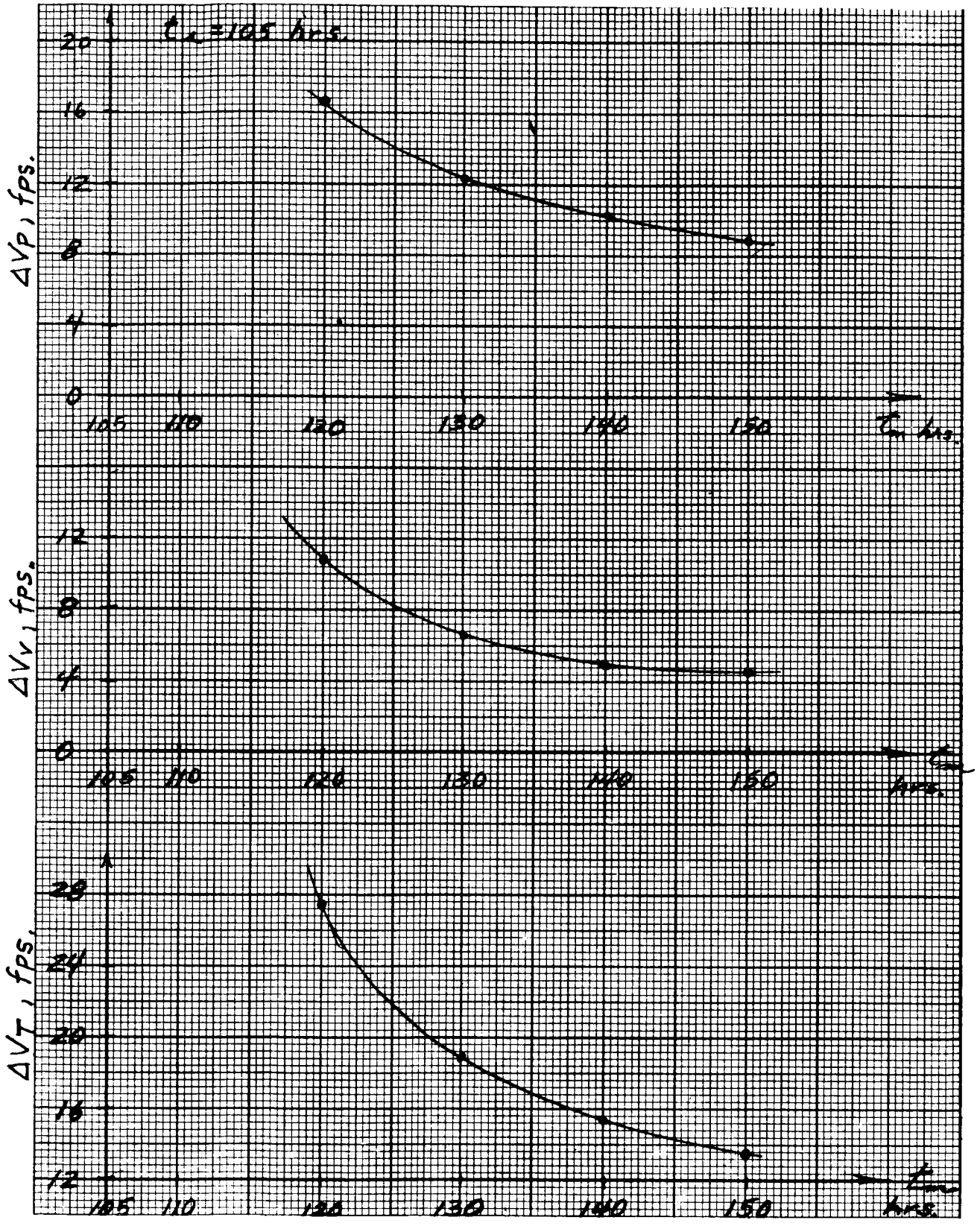

Fig. III-49. Transearth Midcourse Guidance Required Velocity Impulse due to Errors in Velocity at Ejection from Lunar Orbit ($\Delta\dot{x}_{n_0}$ = 2.575 fps; $\Delta\dot{y}_{n_0}$ = 1.5351; $\Delta\dot{z}_{n_0}$ = 1.5351)

D-3 (6-60)

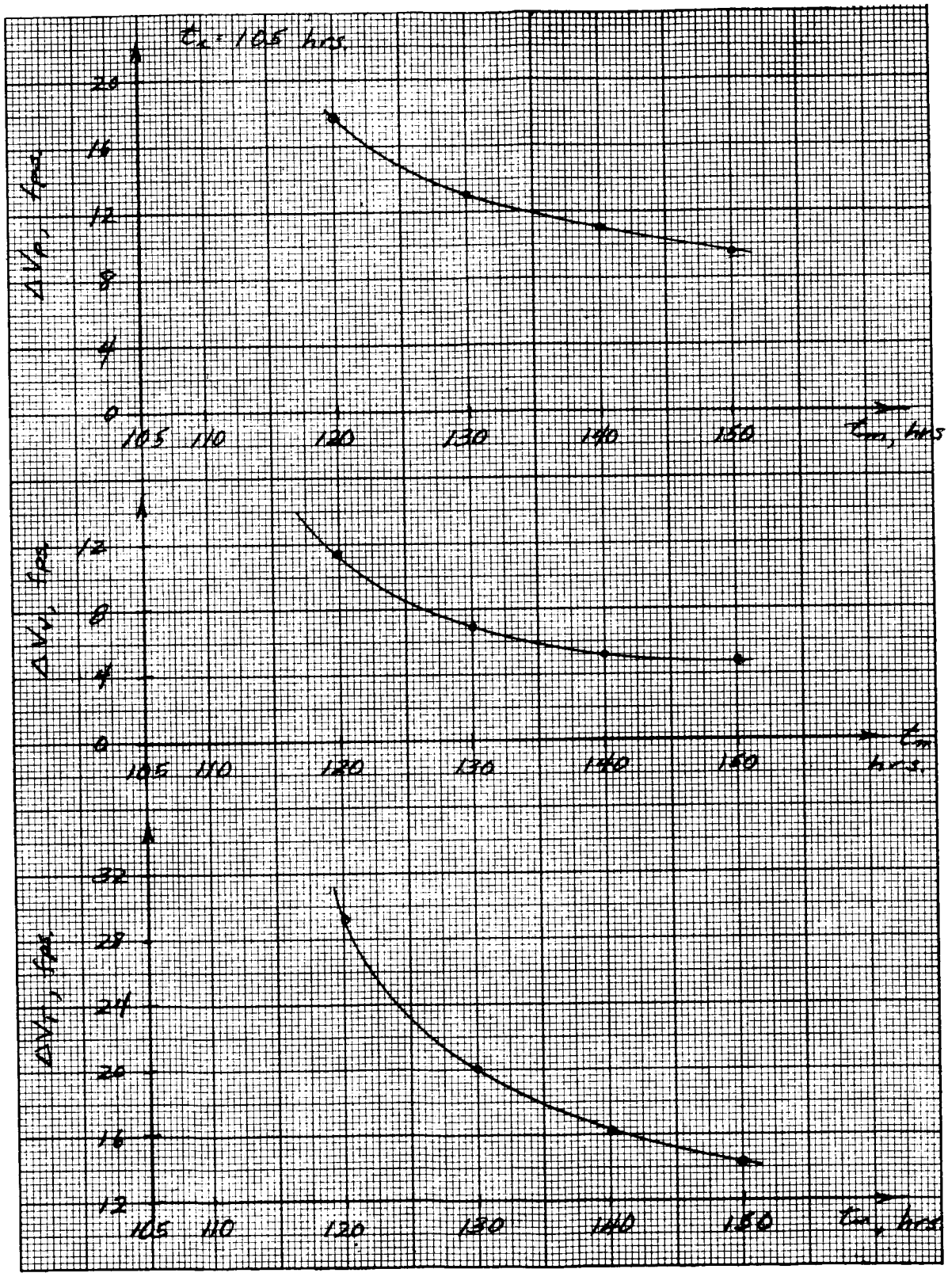

Fig. III-50. Transearth Midcourse Guidance Required Velocity Impulse due to Errors in Velocity at Ejection from Lunar Orbit ($\Delta\dot{x}_{n_0}$ = 2.575 fps; $\Delta\dot{y}_{n_0}$ = 2.1709; $\Delta\dot{z}_{n_0}$ = 0)

D-3 (6.60)

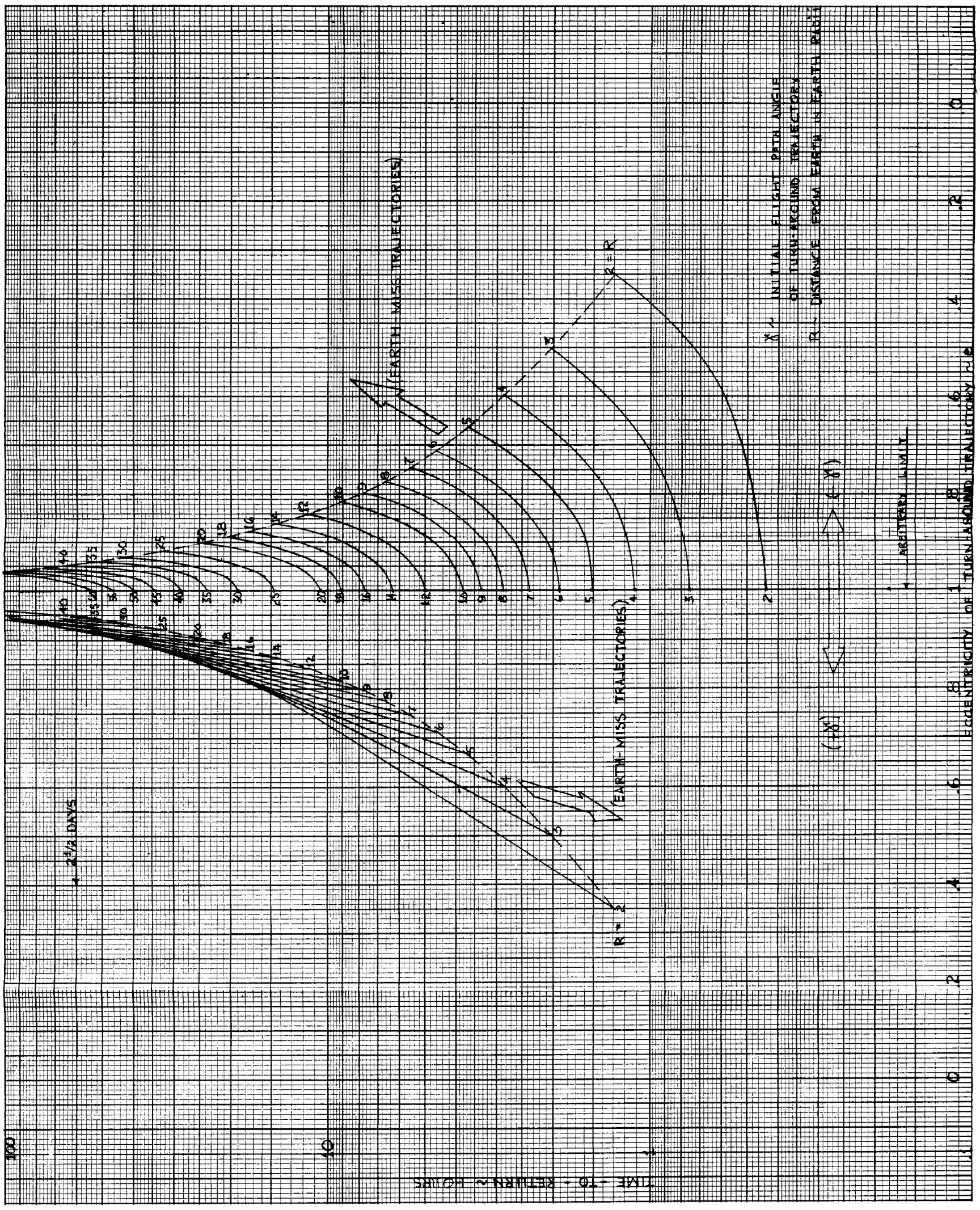

Fig. III-52. Time to Return After Translunar Orbit Abort

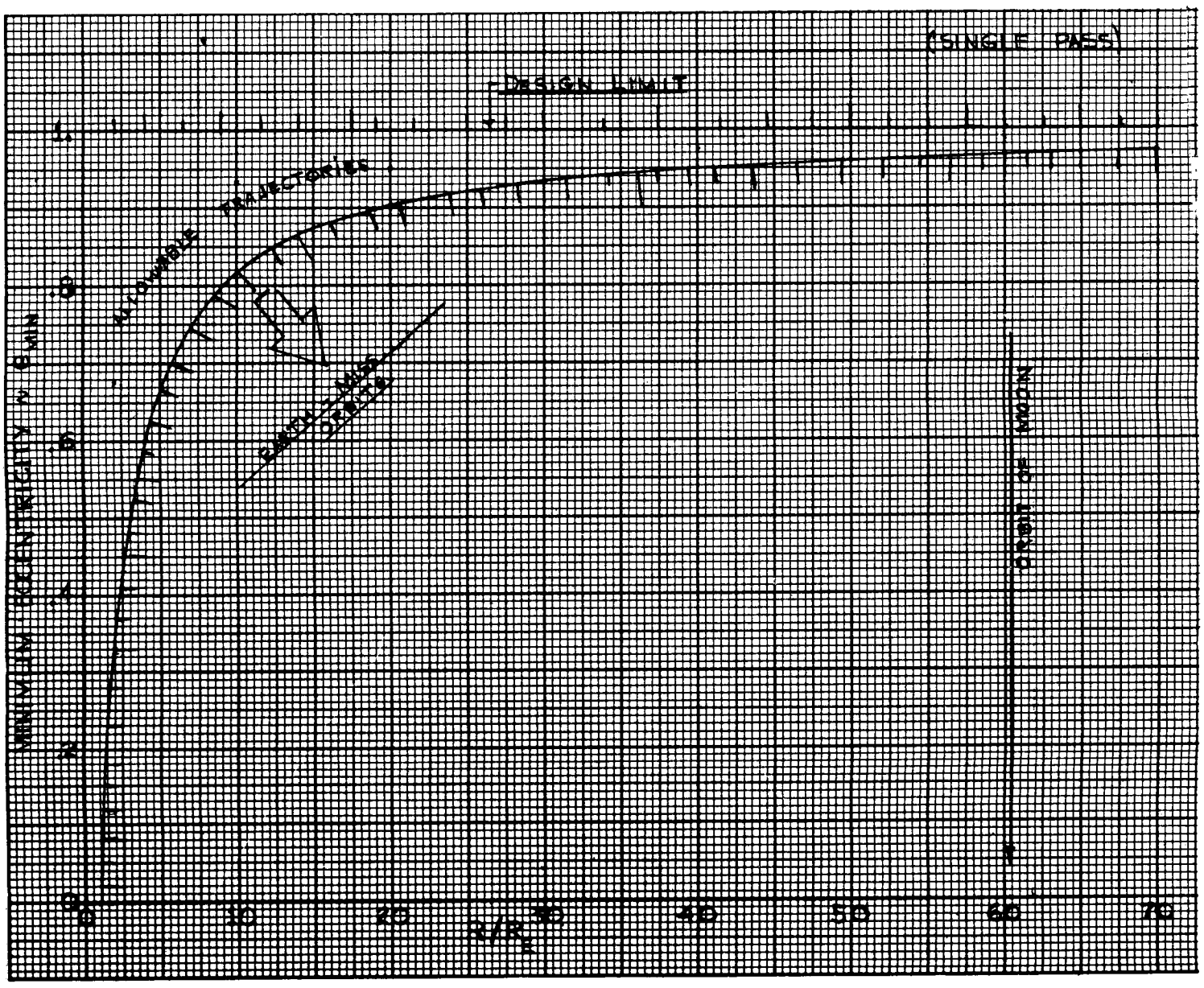

Fig. III-51. Envelope of Allowable Return Orbit Eccentricity for Translunar Orbit Abort

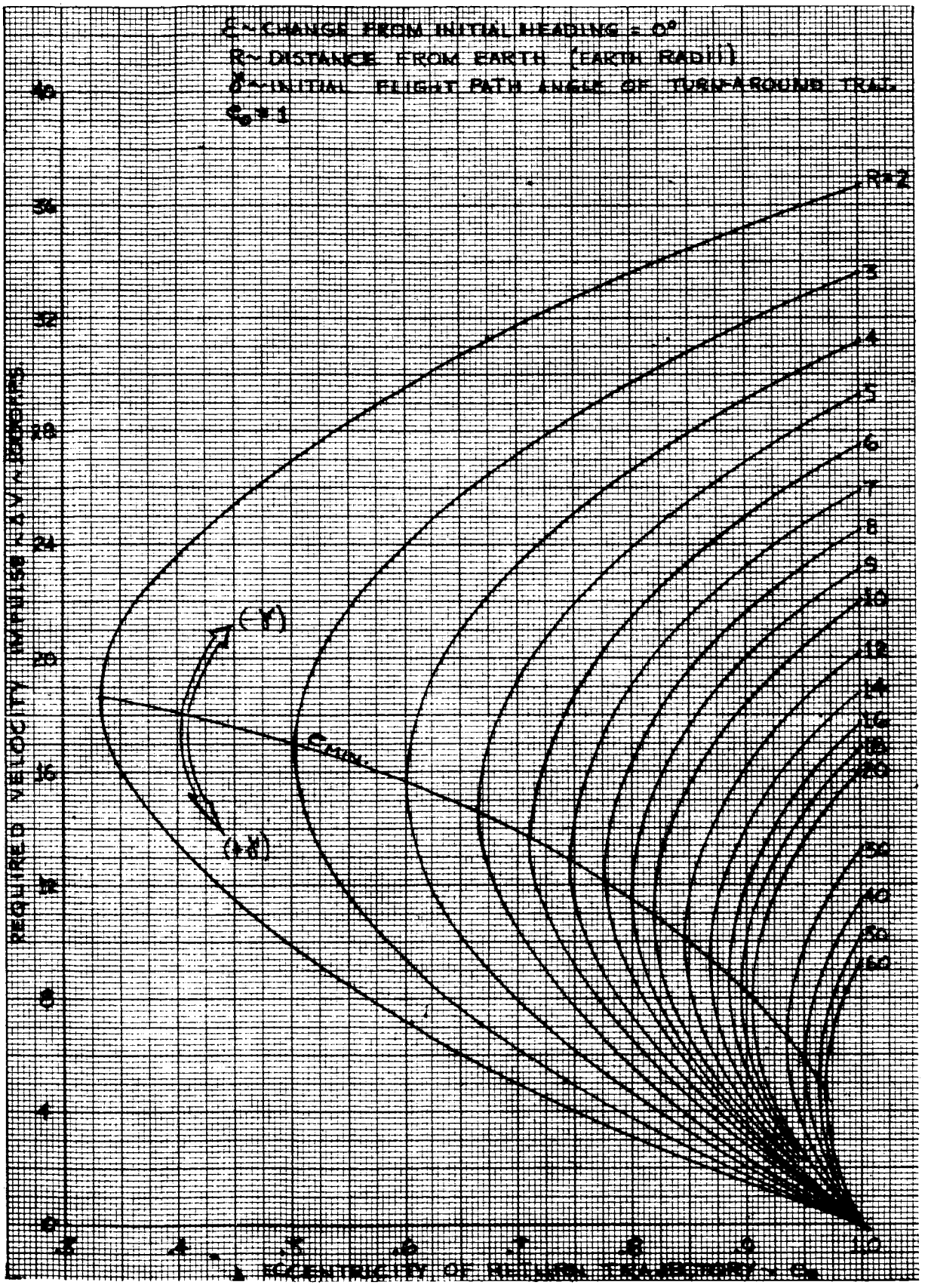

Fig. III-53. Required Velocity Impulse for Abort ($\epsilon = 0$)

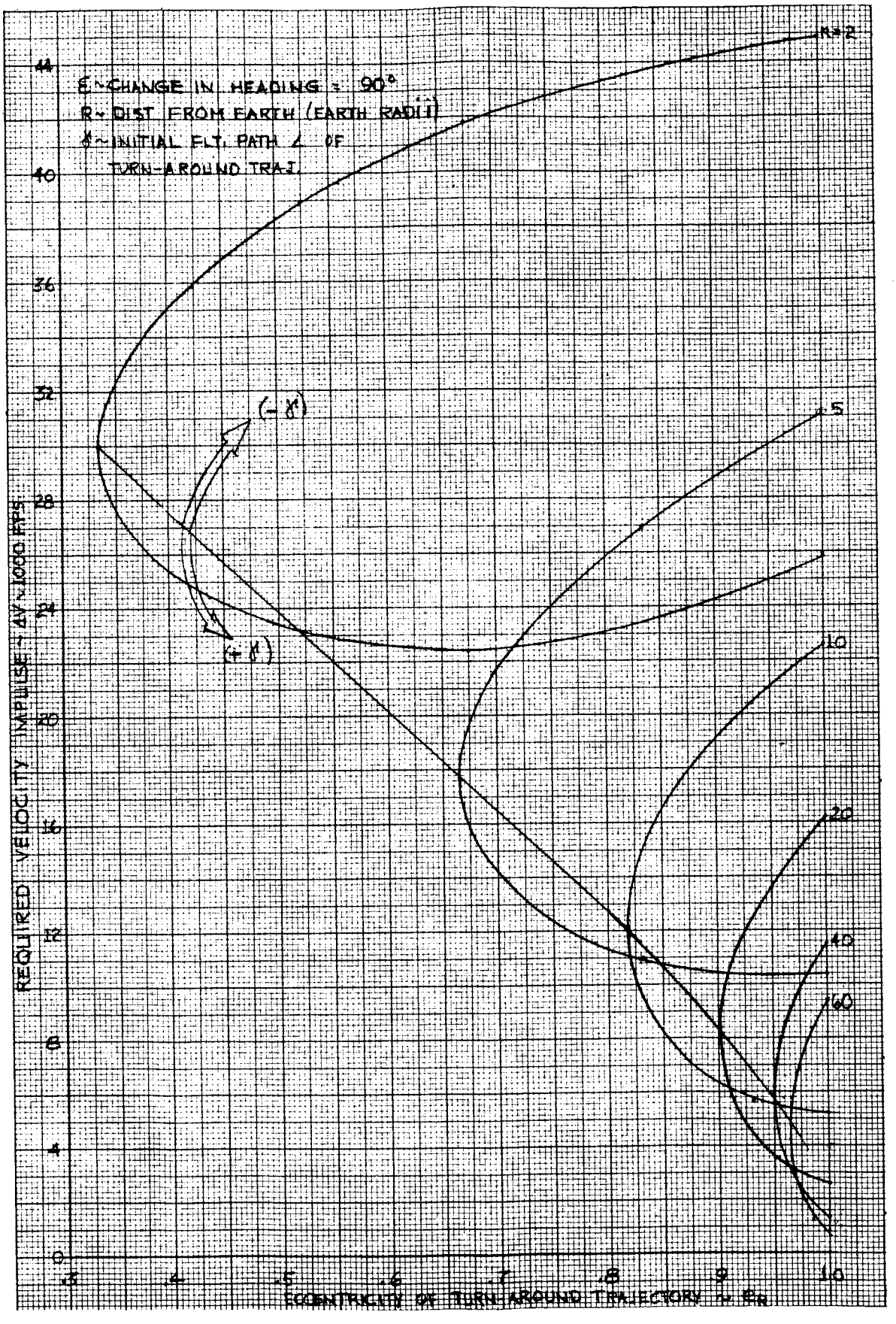

Fig. III-54. Required Velocity Impulse for Abort (ε = 90)

D-3 (6-60)

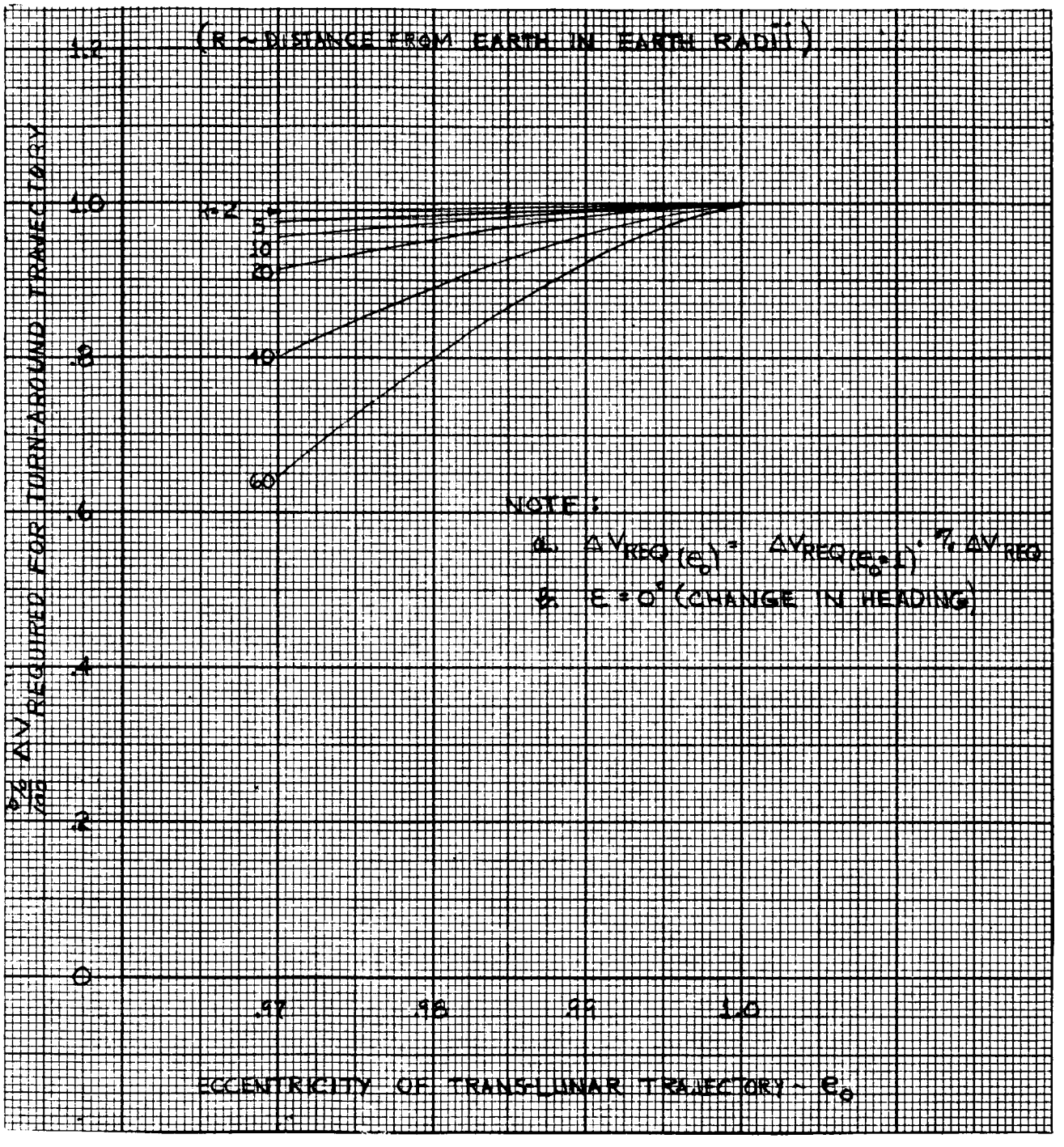

Fig. III-55. Correction Factors for Translunar Orbit Eccentricities Less than 1.0 (eccentricity of turnaround trajectory = 1.0)

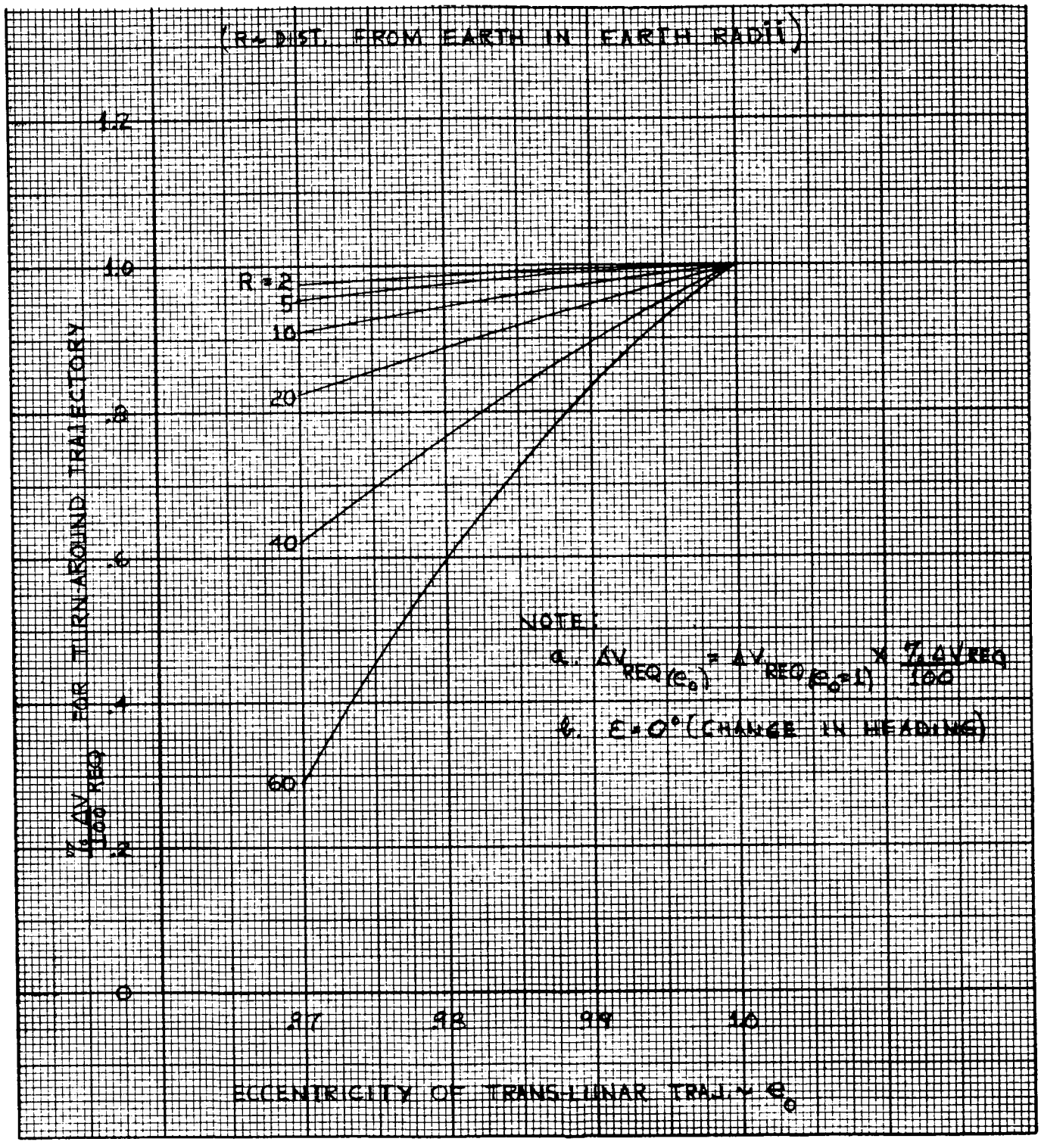

Fig. III-56. Correction Factors for Translunar Orbit Eccentricities Less than 1.0 (eccentricity of turnaround trajectory = e_{min})

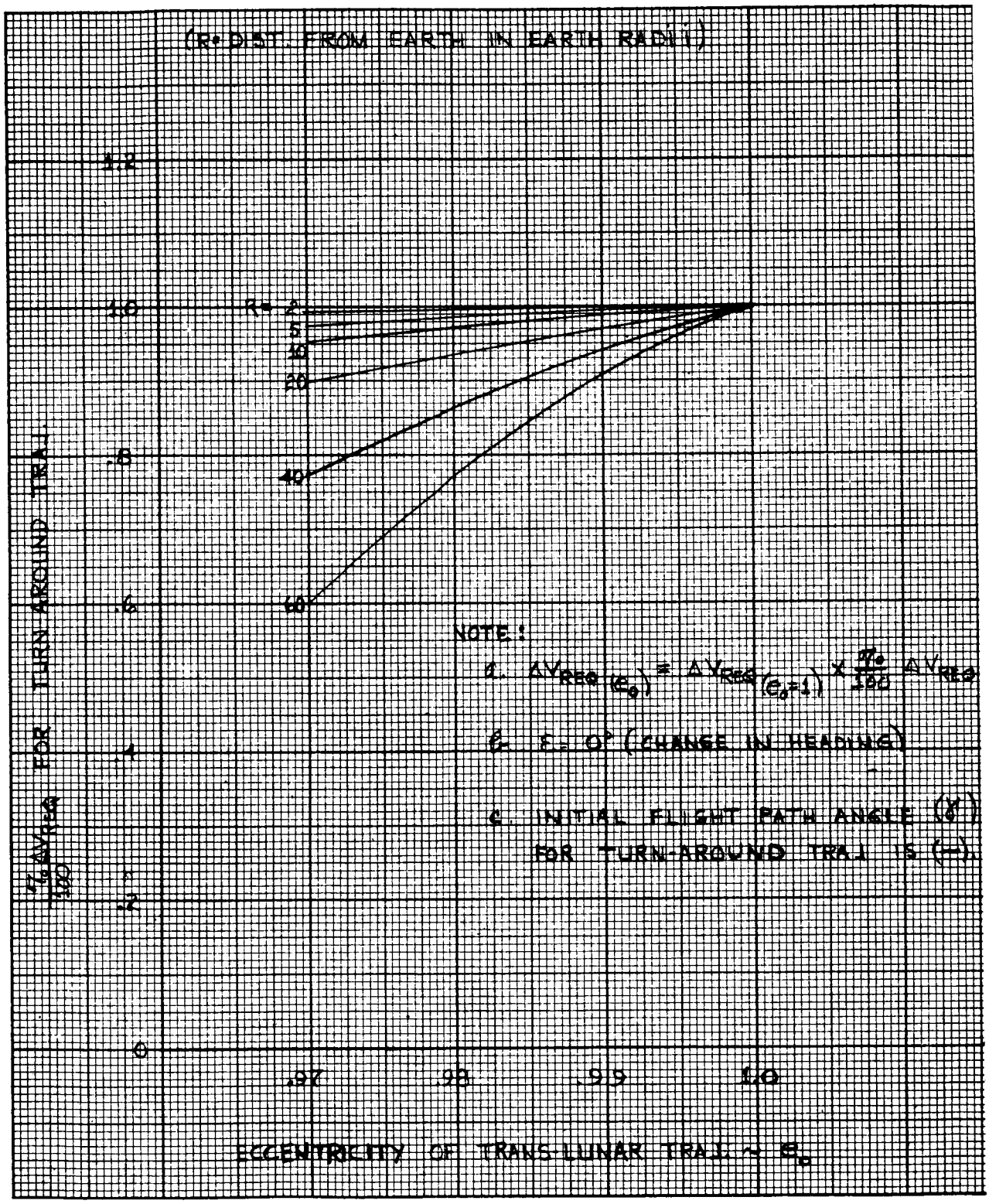

Fig. III-57. Correction Factors for Translunar Orbit Eccentricities Less than 1.0 (eccentricity of turnaround trajectory = 1/2 ($1 + e_{min}$)

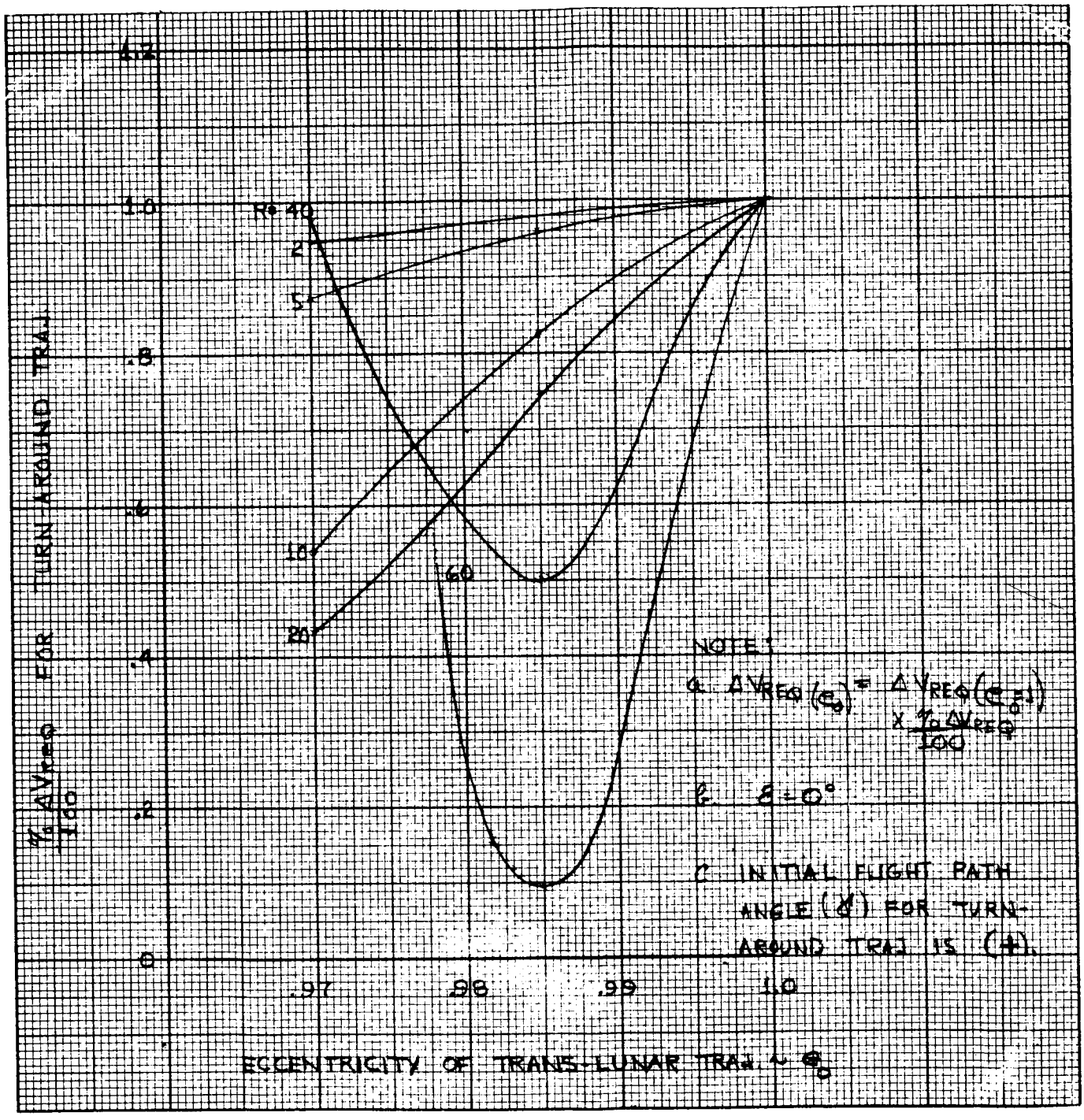

Fig. III-58. Correction Factors for Translunar Orbit Eccentricities Less than 1.0 (eccentricity of turnaround trajectory = $1/2\ (1 + e_{min})$

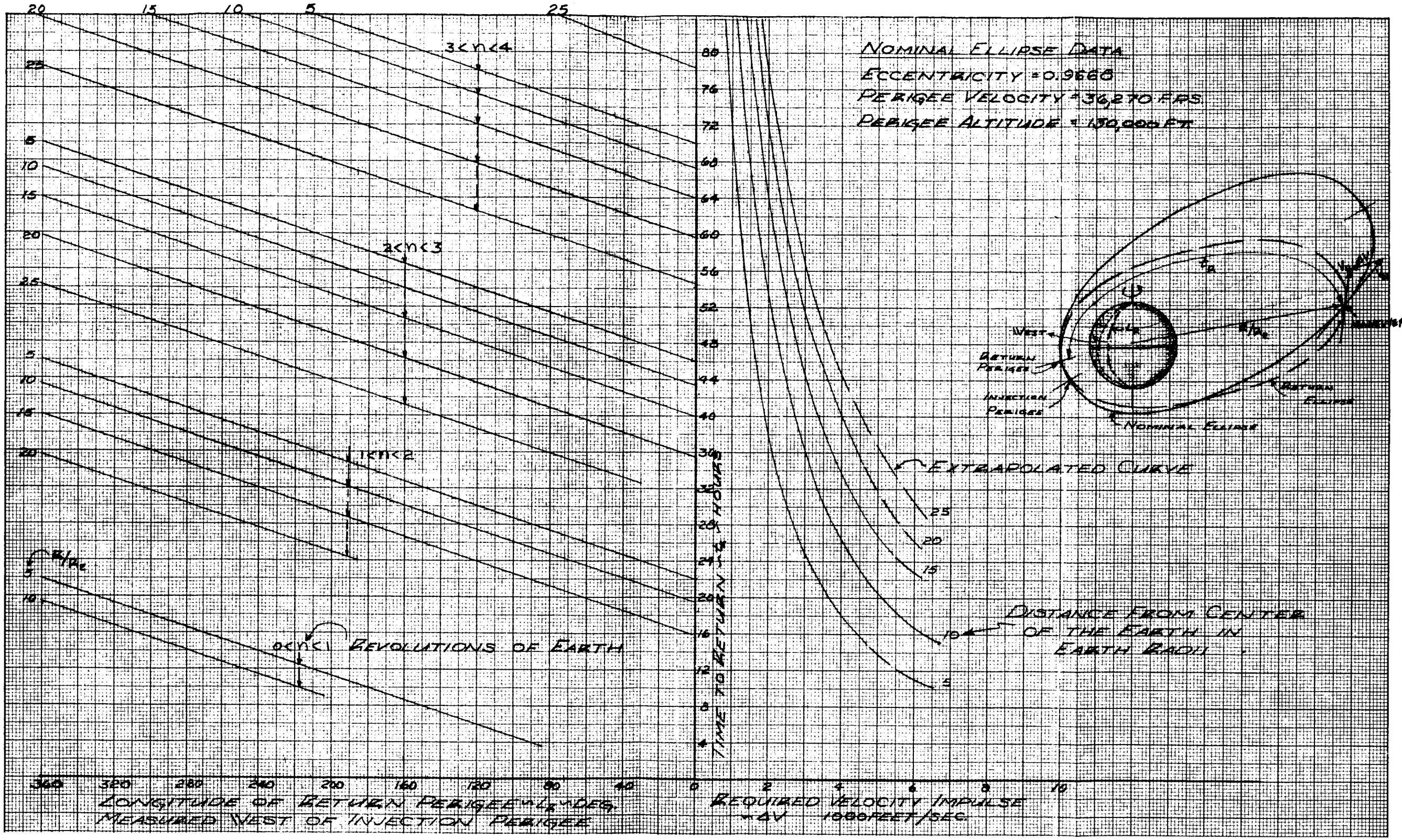

Fig. III-59. Return Perigee Longitude After Abort from Translunar Orbit

CONFIDENTIAL

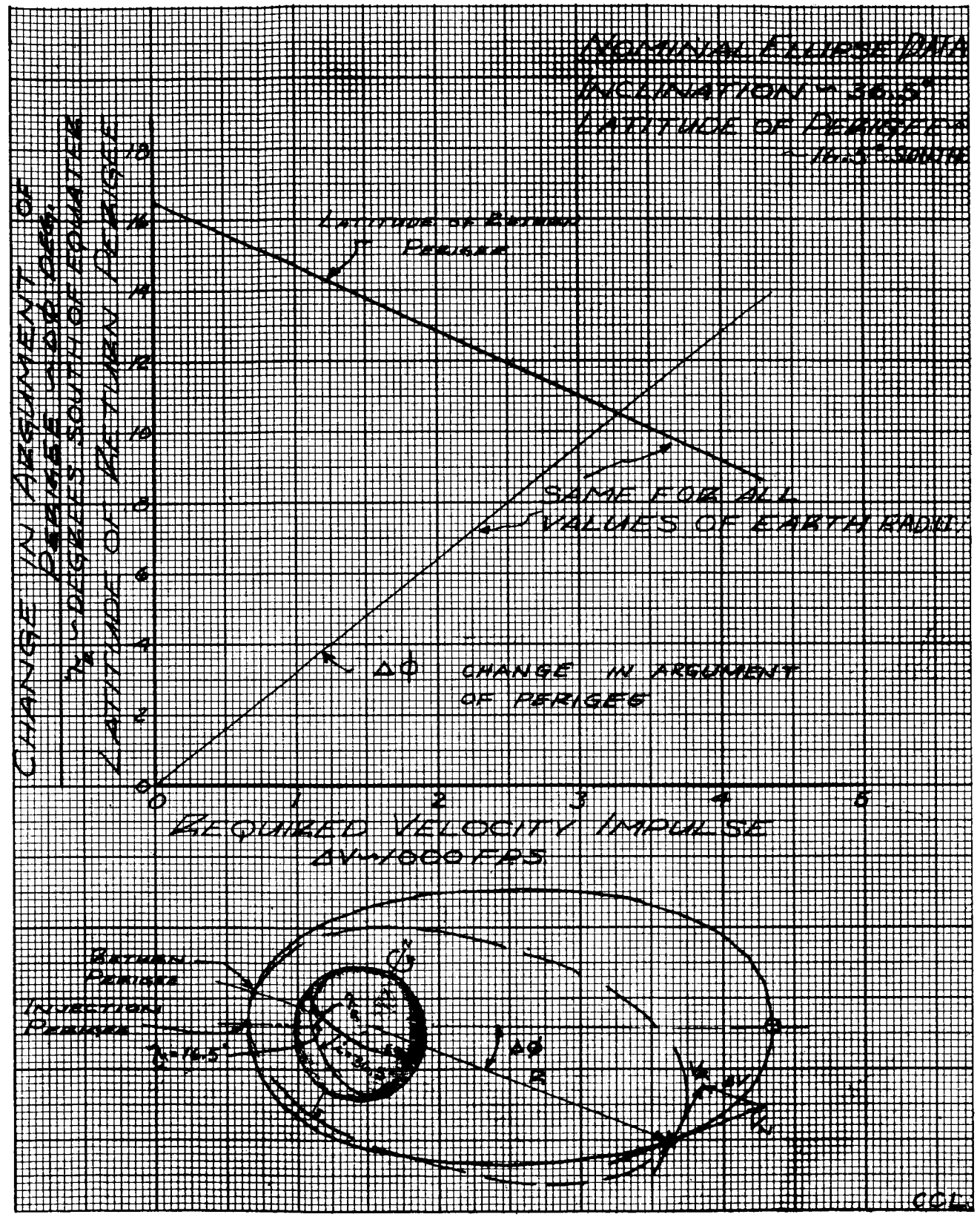

Fig. III-60. Change in Argument of Perigee and Latitude of Return Perigee After Abort from Translunar Orbit

D-3 (6-60)

CONFIDENTIAL

CONFIDENTIAL

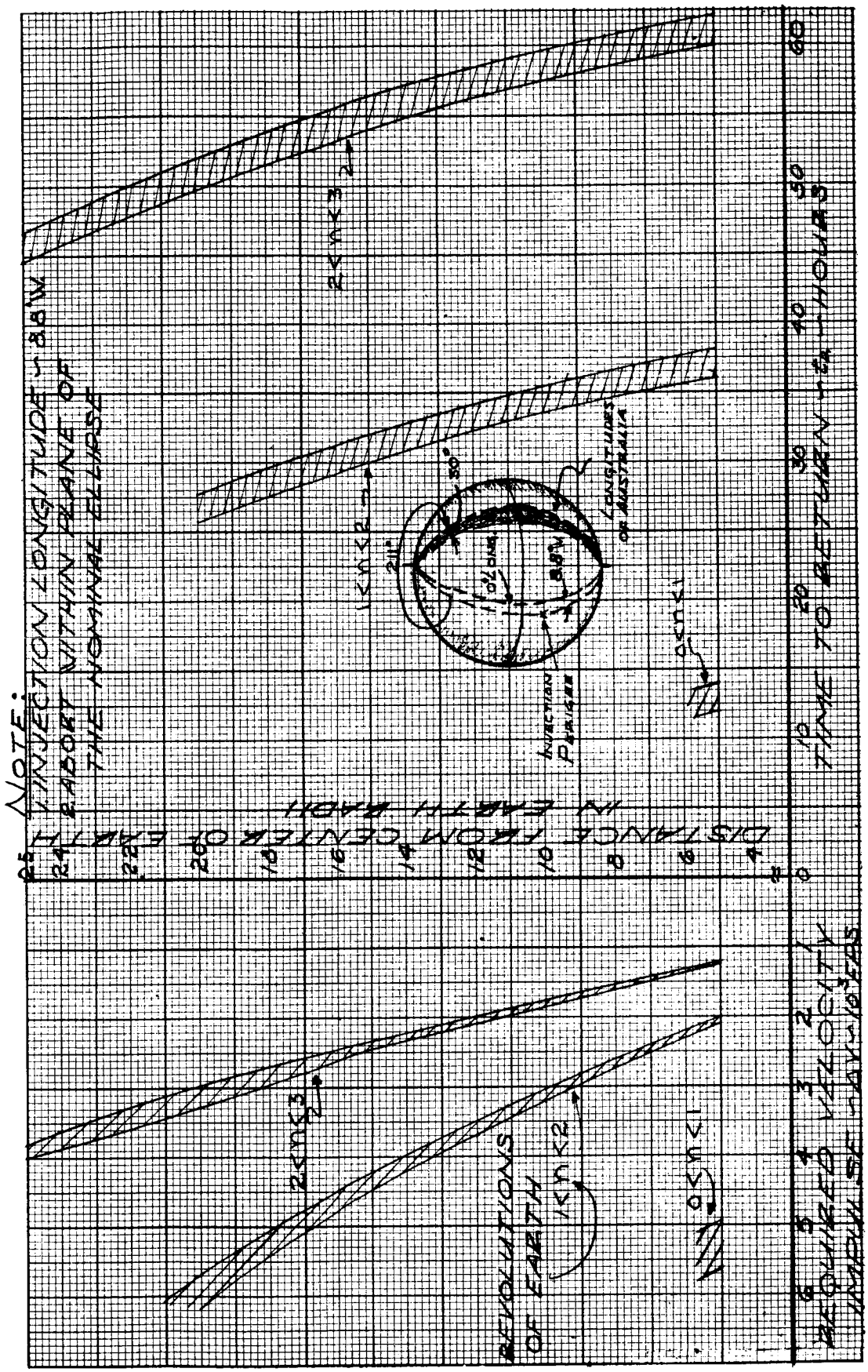

Fig. III-61. Required Velocity Impulse at Abort to Return to Australia

CONFIDENTIAL

D-3 (6-60)

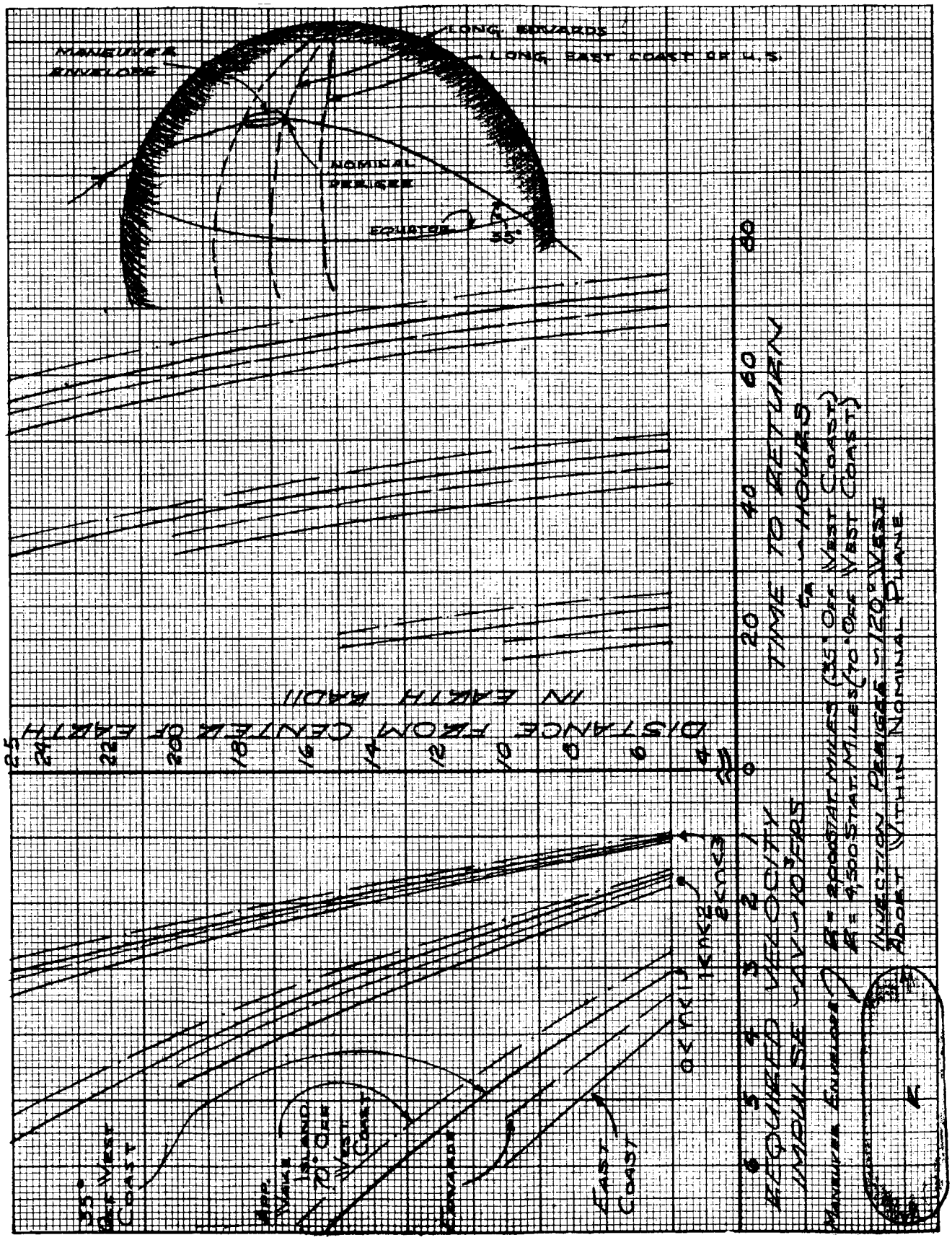

Fig. III-62. Required Velocity Impulse at Abort to Return to the United States

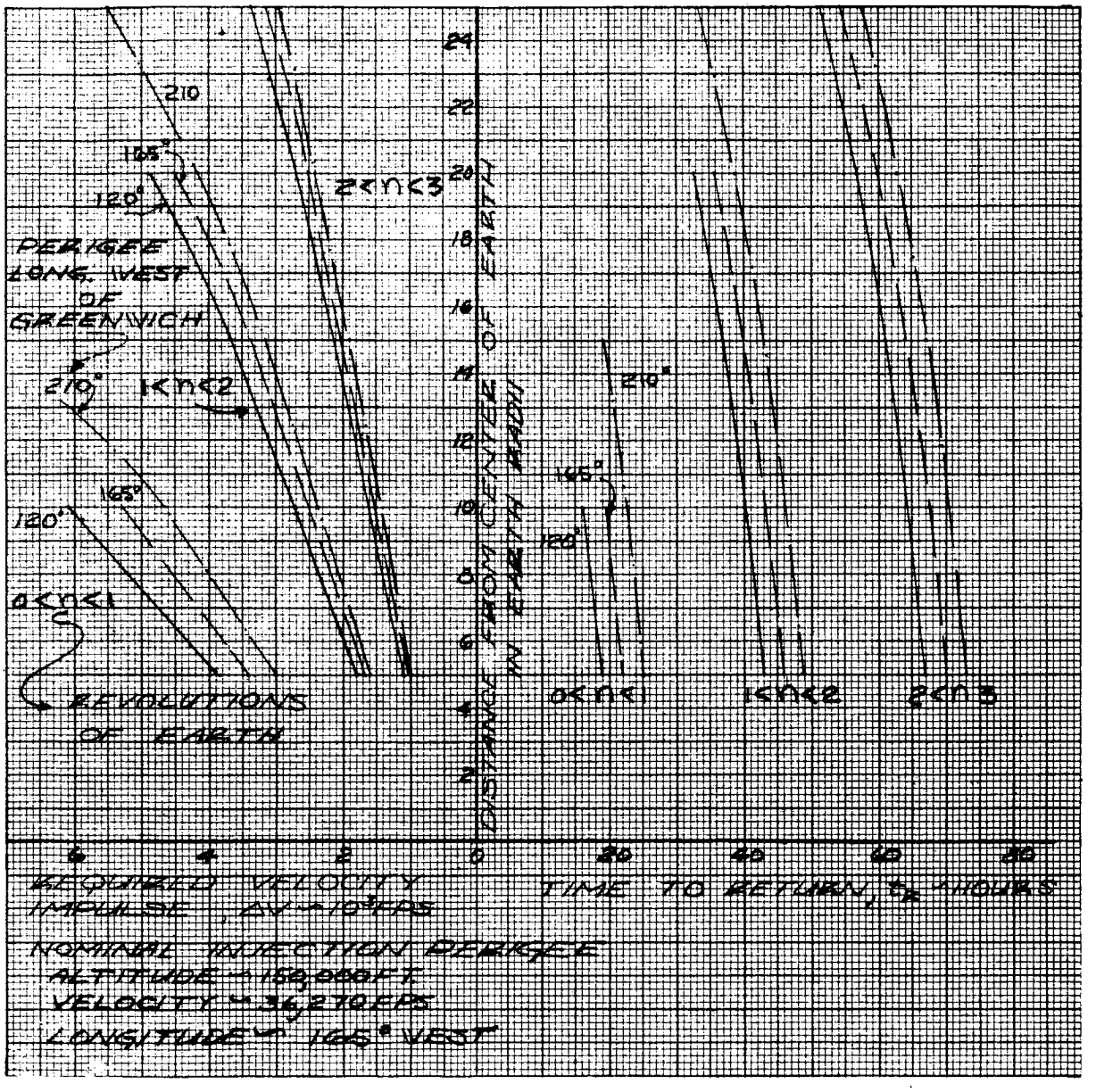

Fig. III-63. Required Velocity Impulse at Abort to Return to Edwards AFB

CONFIDENTIAL

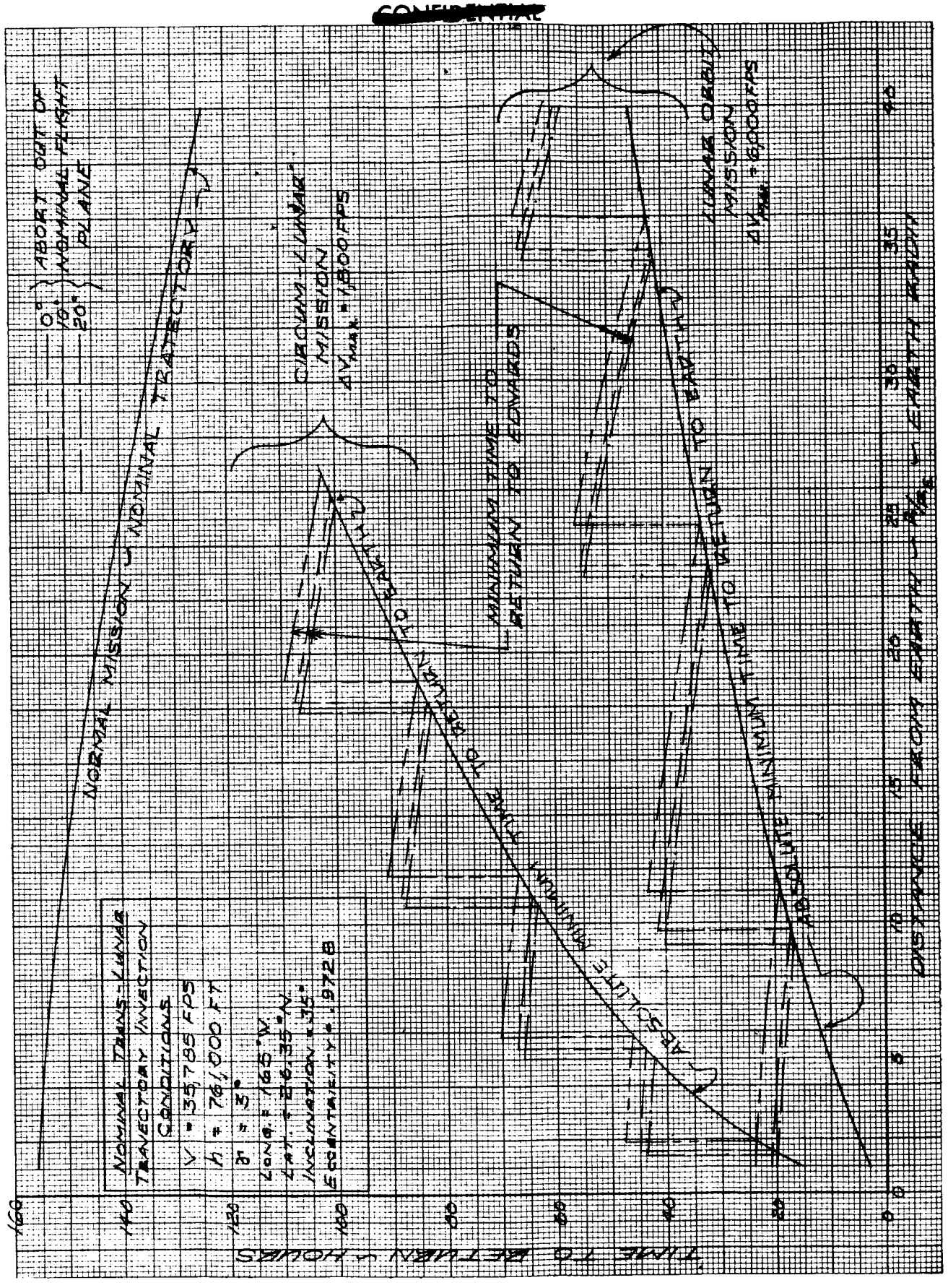

Fig. III-64. Minimum Return Time for Turnaround Maneuvers

CONFIDENTIAL

D-3 (6-60)

CONFIDENTIAL

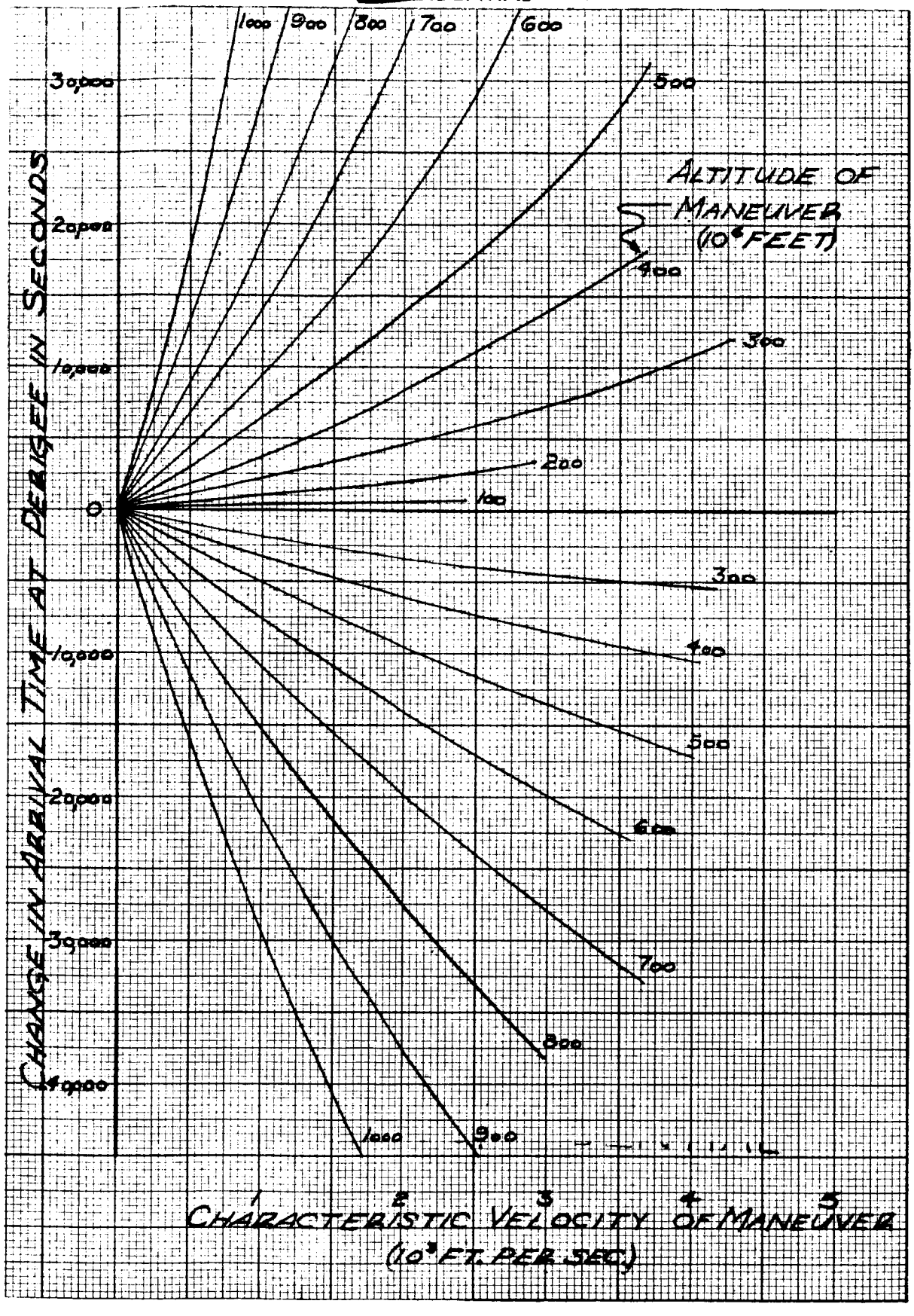

Fig. III-65. Change in Arrival Time at Perigee as a Function of Characteristic Velocity of Maneuver and Altitude of Maneuver

CONFIDENTIAL

D-3 (6-60)

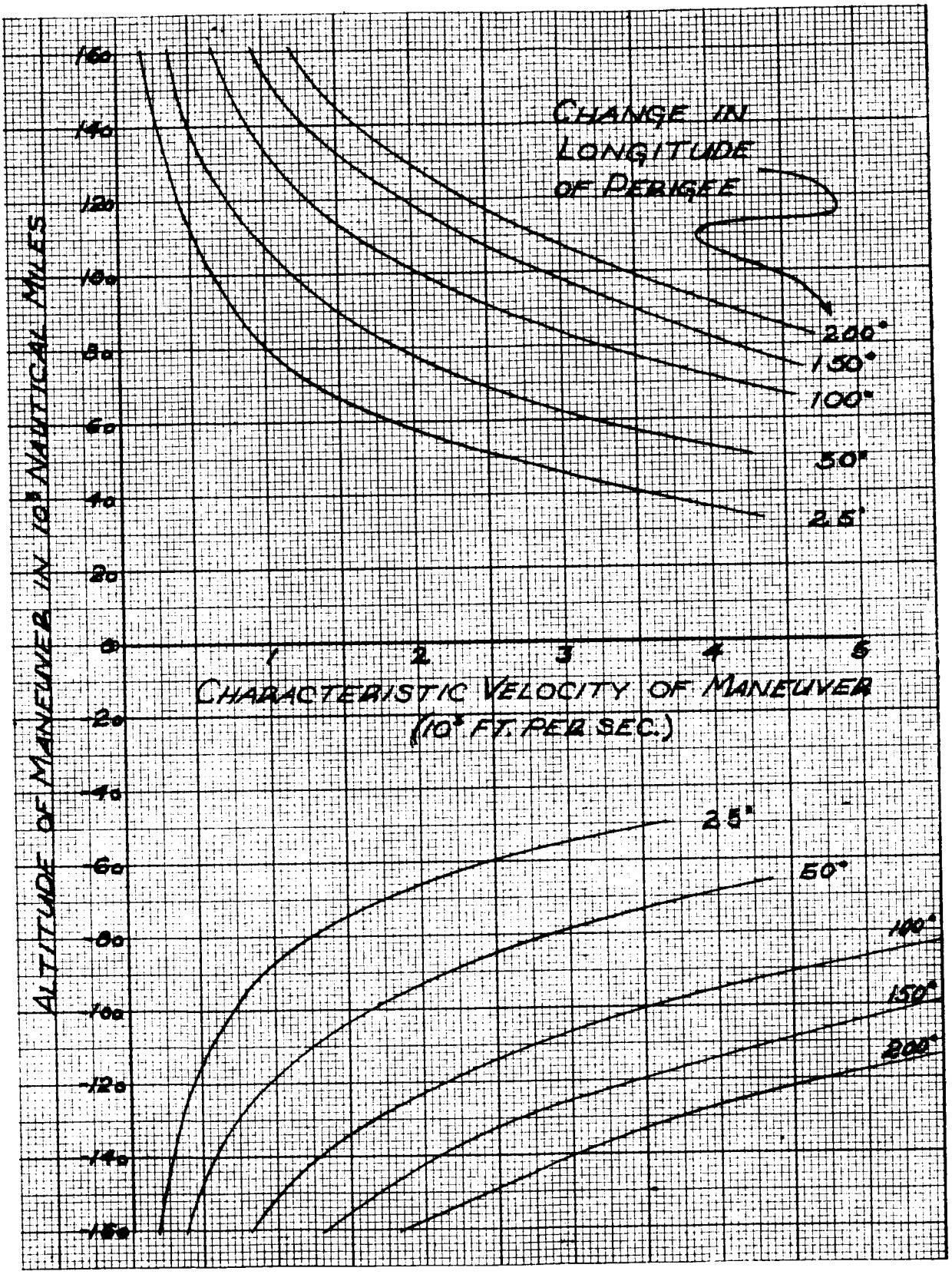

Fig. III-66. Altitude of Maneuver as a Function of Velocity of Maneuver and Change in Longitude of Perigee

D-3 (6-60)

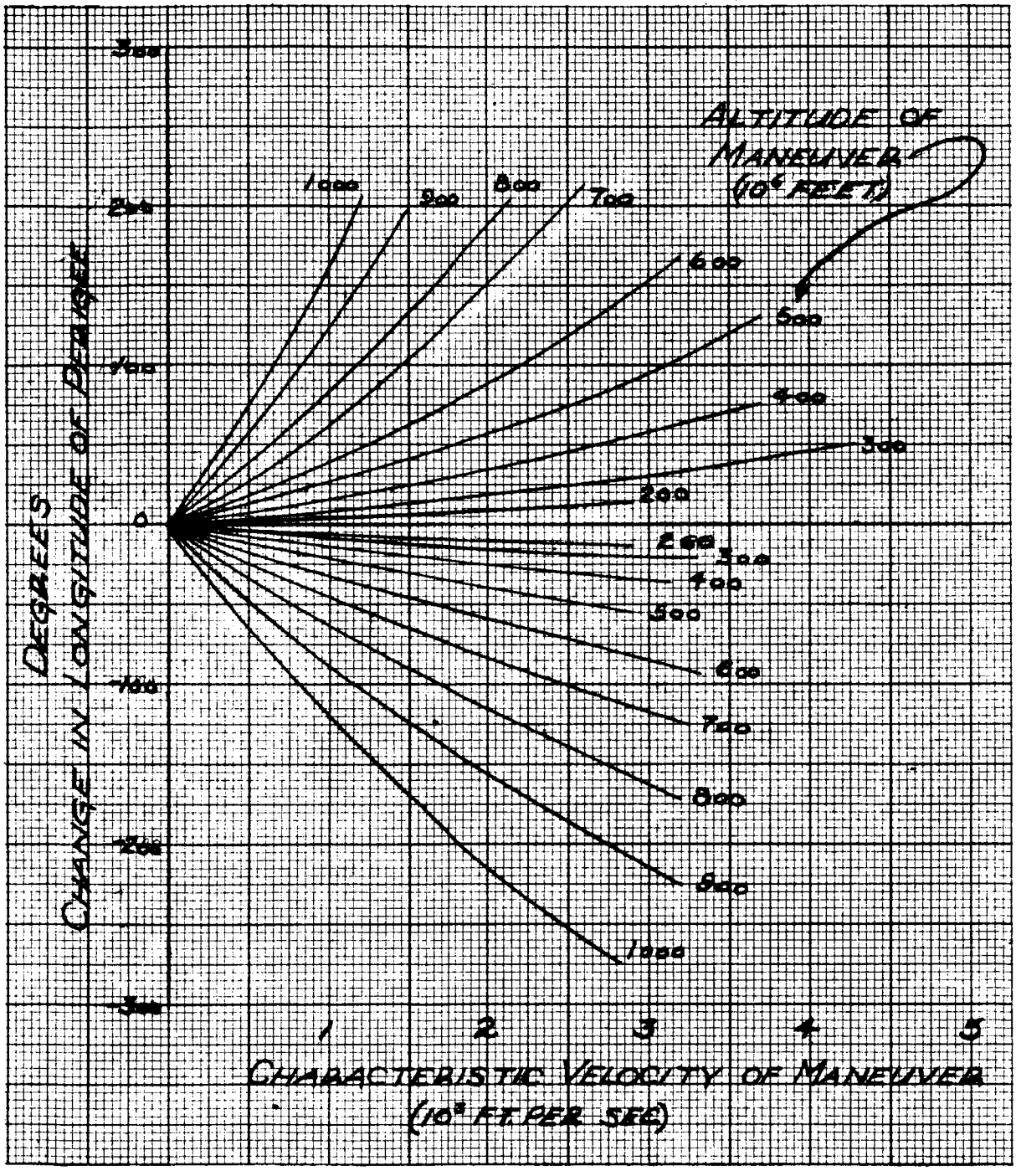

Fig. III-67. Change in Longitude of Perigee as a Function of Characteristic Velocity of Maneuver and Altitude of Maneuver

D-3 (6-60)

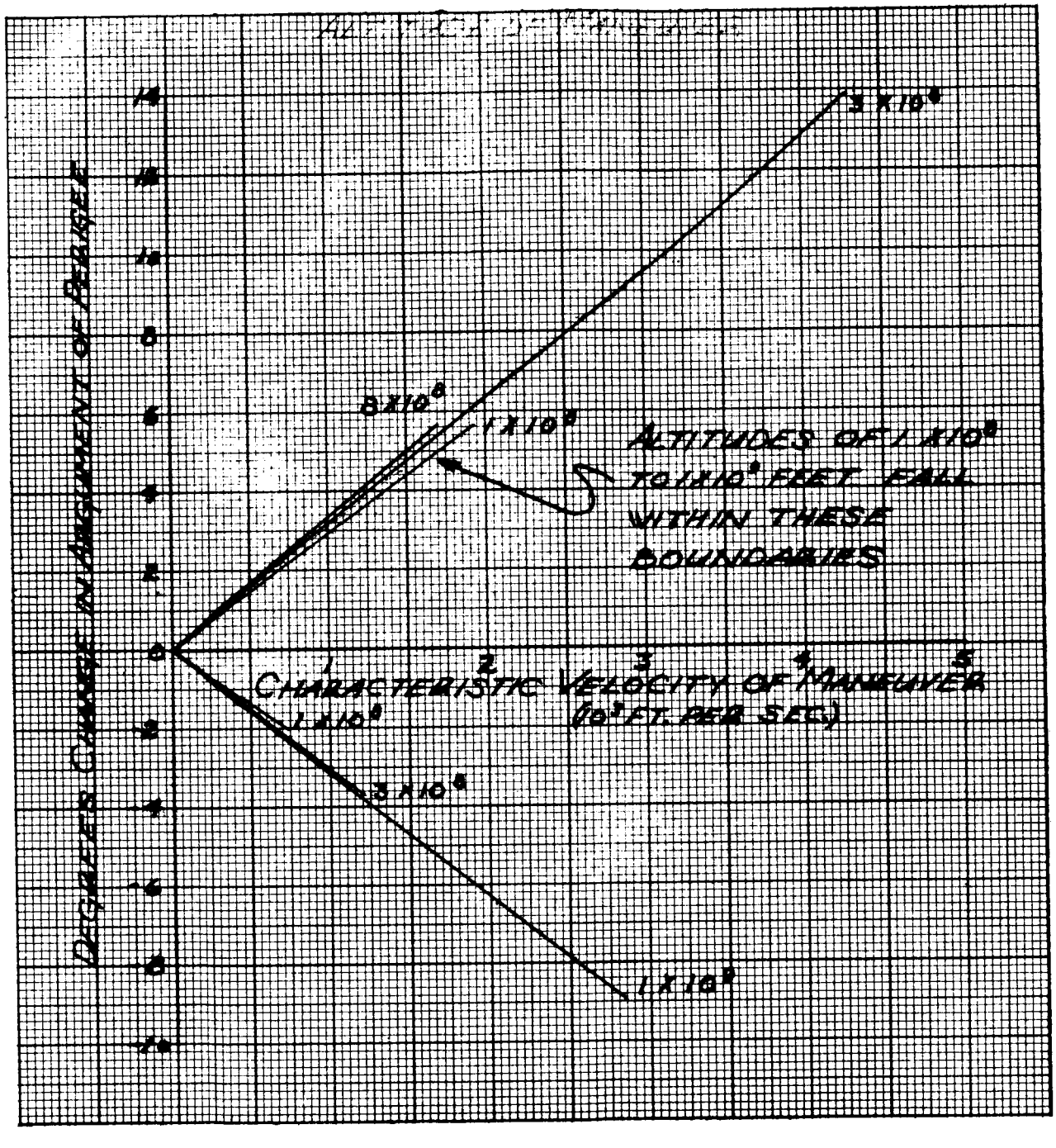

Fig. III-68. Change in Argument of Perigee as a Function of Characteristic Velocity of Maneuver and Altitude of Maneuver

D-3 (6-60)

CONFIDENTIAL

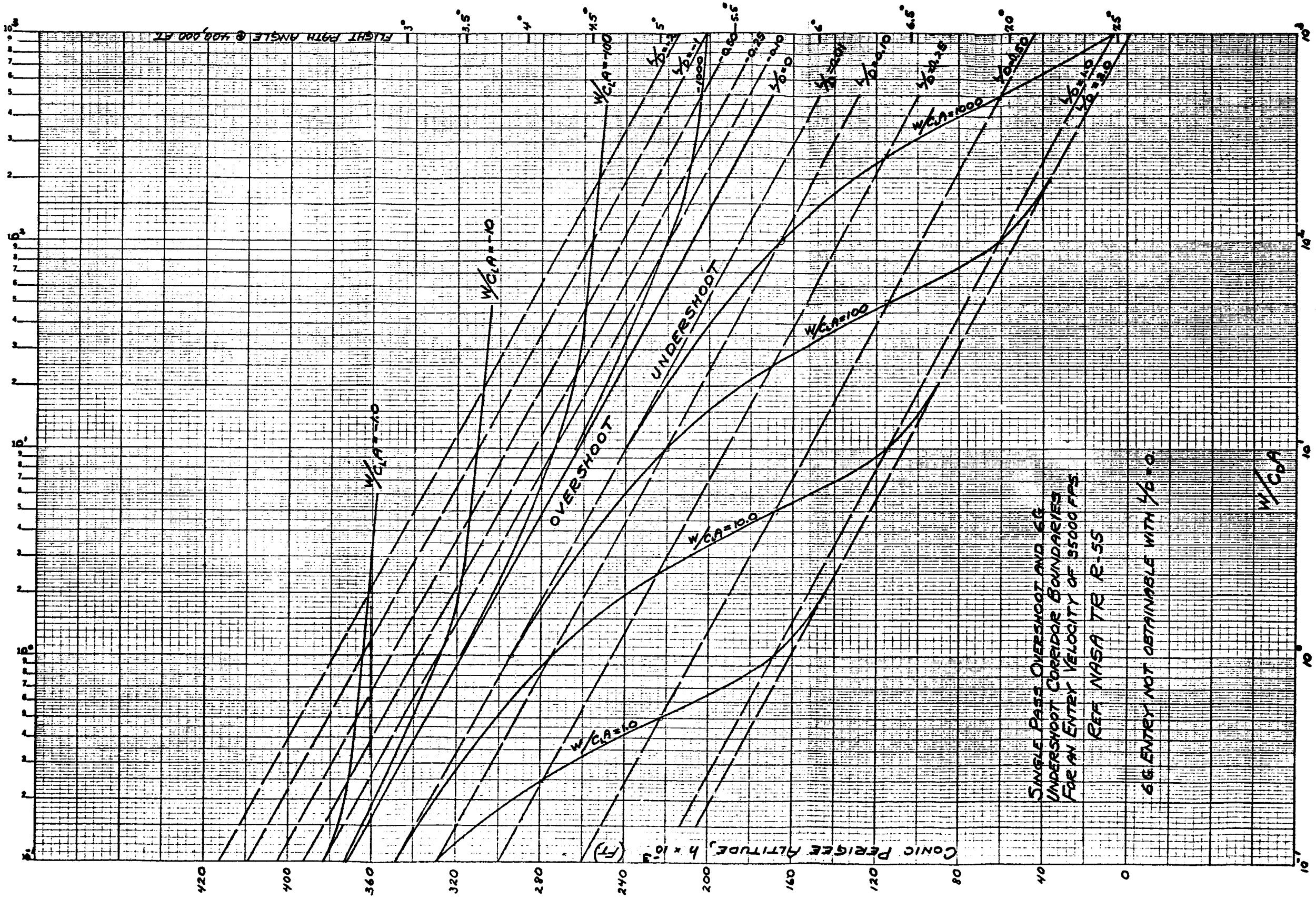

Fig. IV-1. G-Limited Re-entry Corridors (overshoot boundary)

CONFIDENTIAL

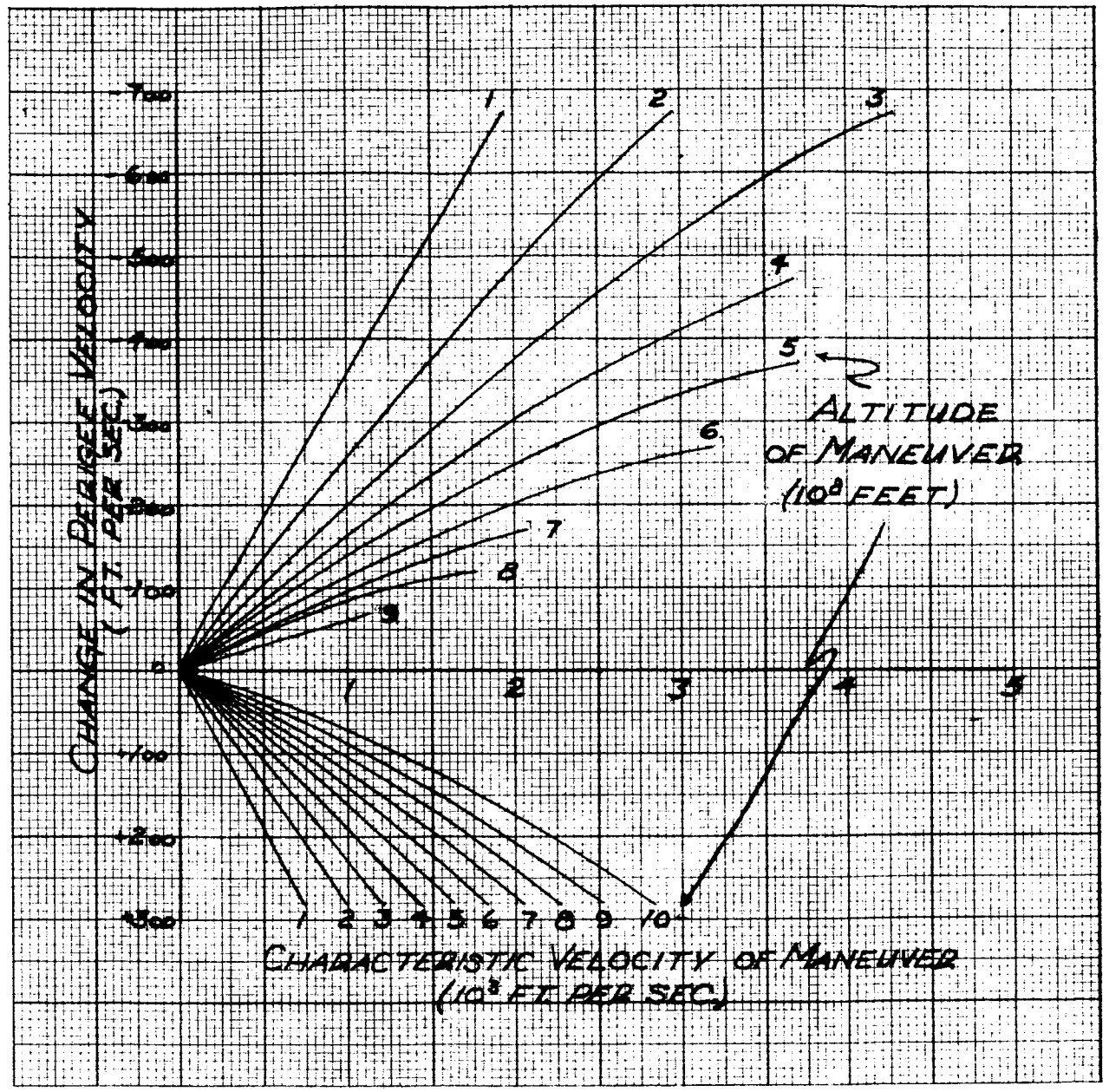

Fig. III-69. Change in Perigee Velocity as a Function of Characteristic Velocity of Maneuver and Altitude of Maneuver

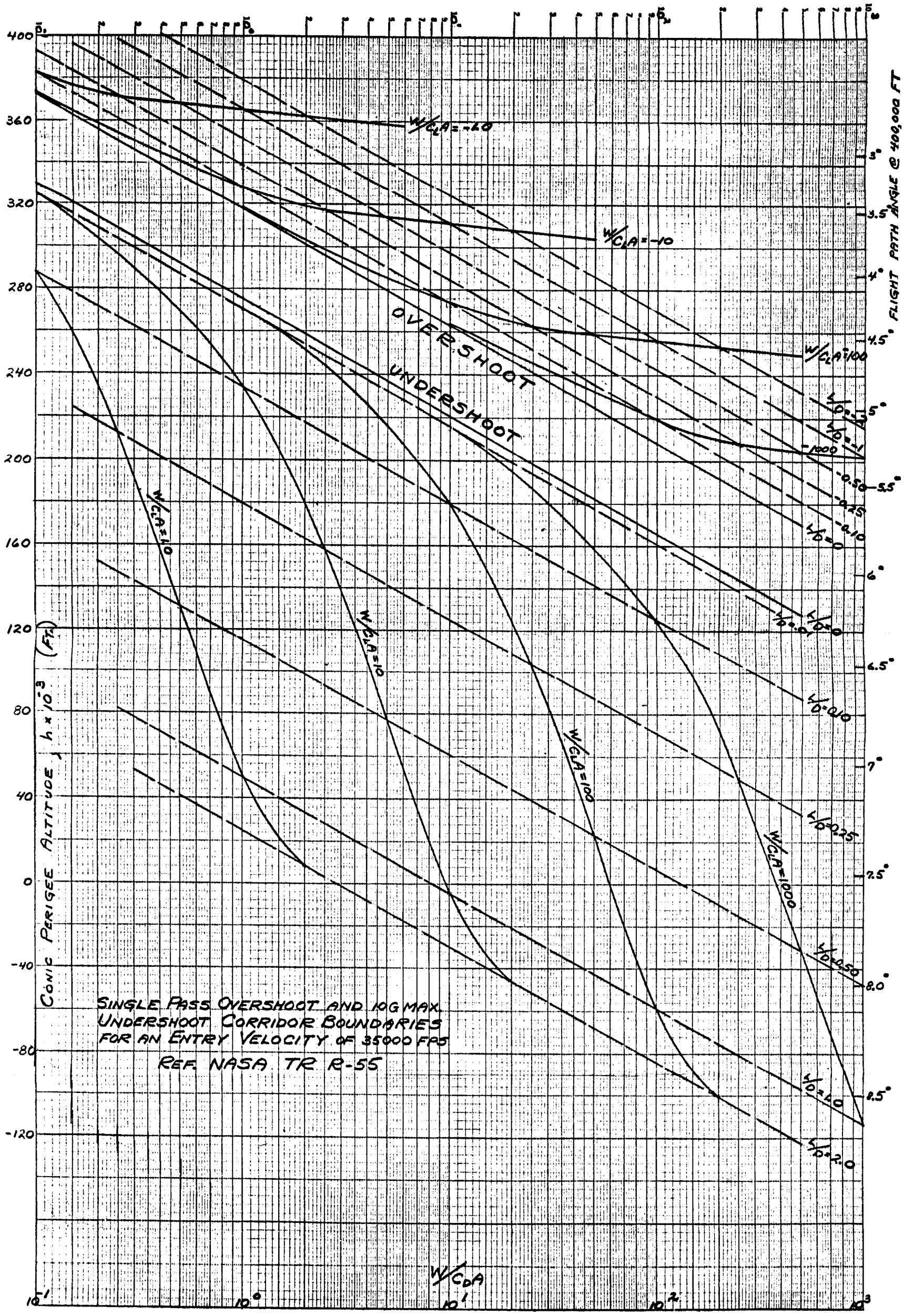

Fig. IV-2. G-Limited Re-entry Corridors (undershoot boundary)

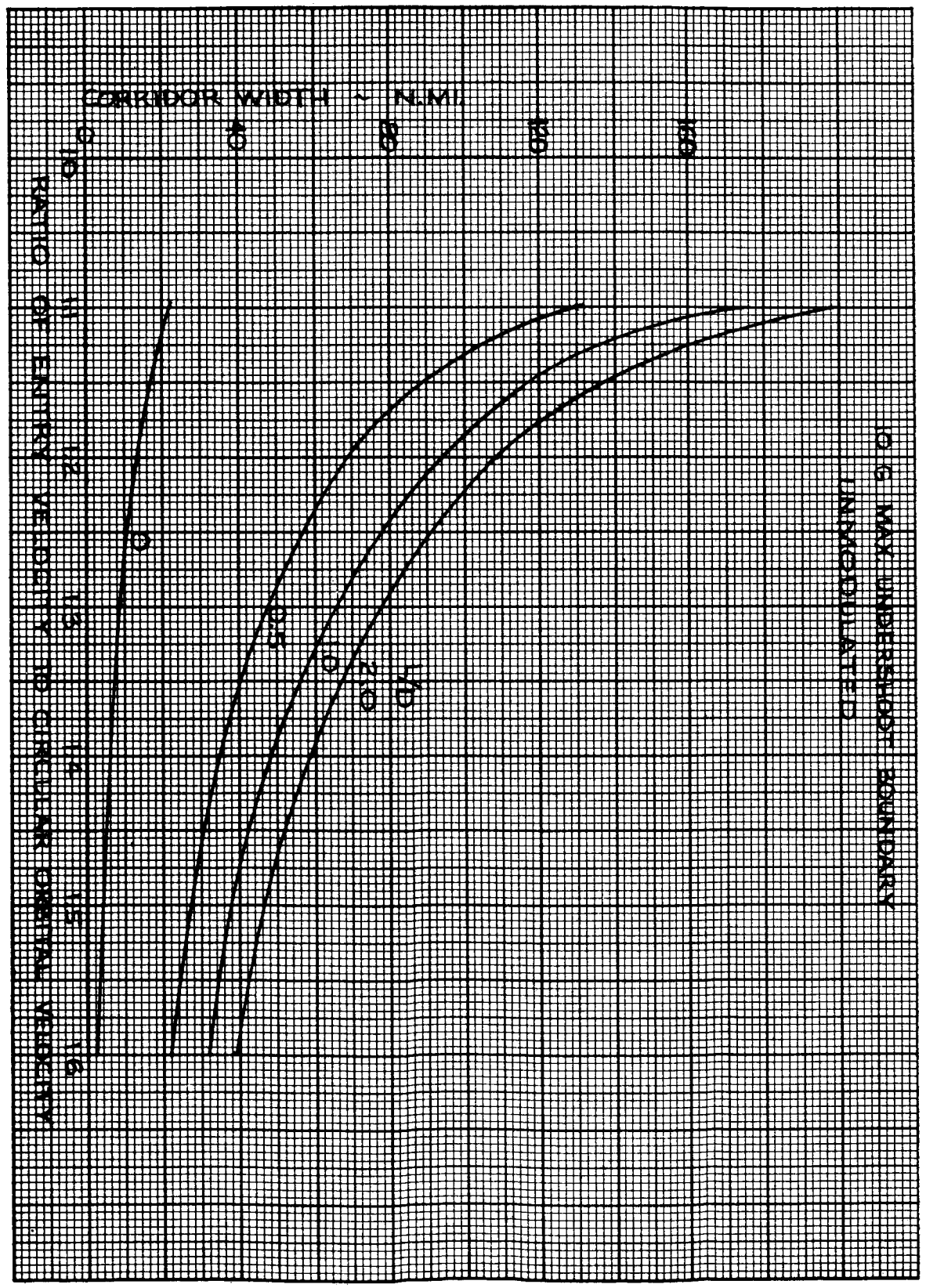

Fig. IV-3. Effect of Entry Velocity on Corridor Width

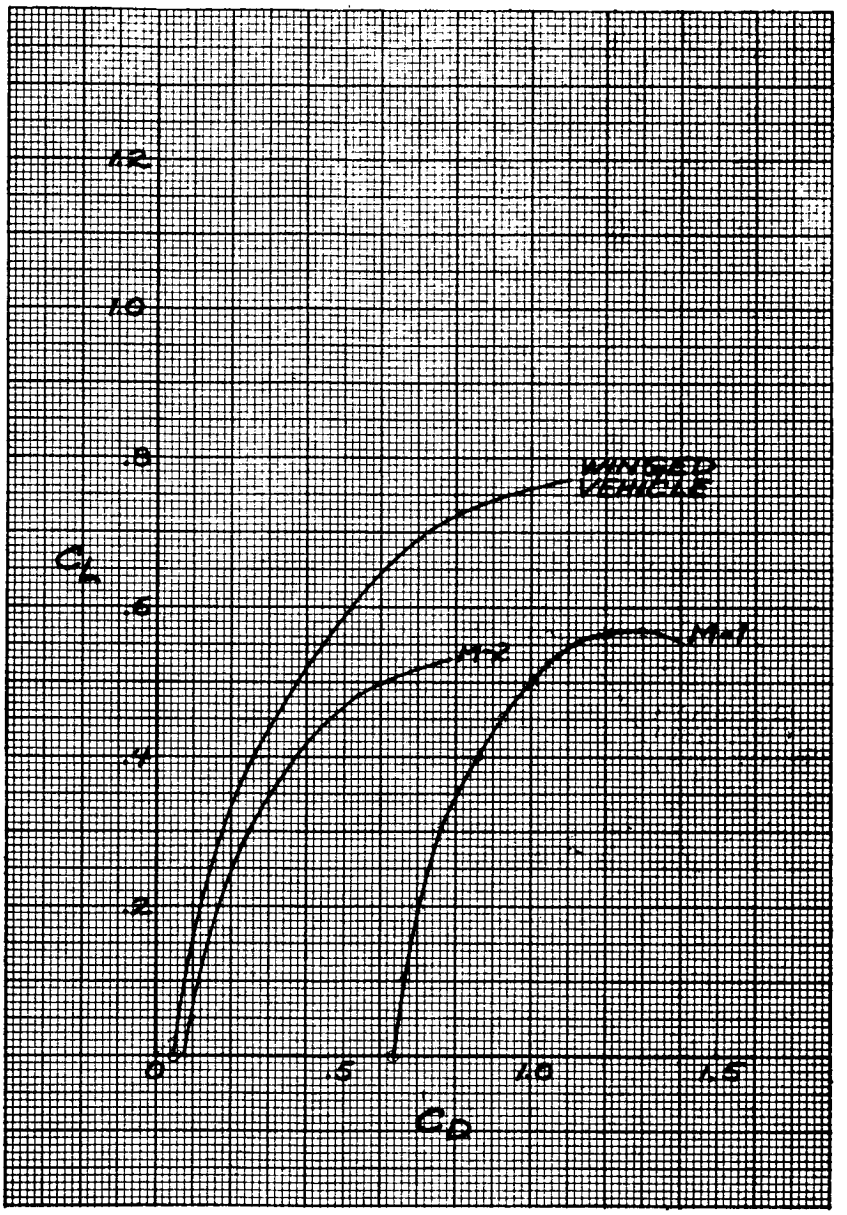

Fig. IV-4. Drag Polar for M-1 and M-2 Configurations

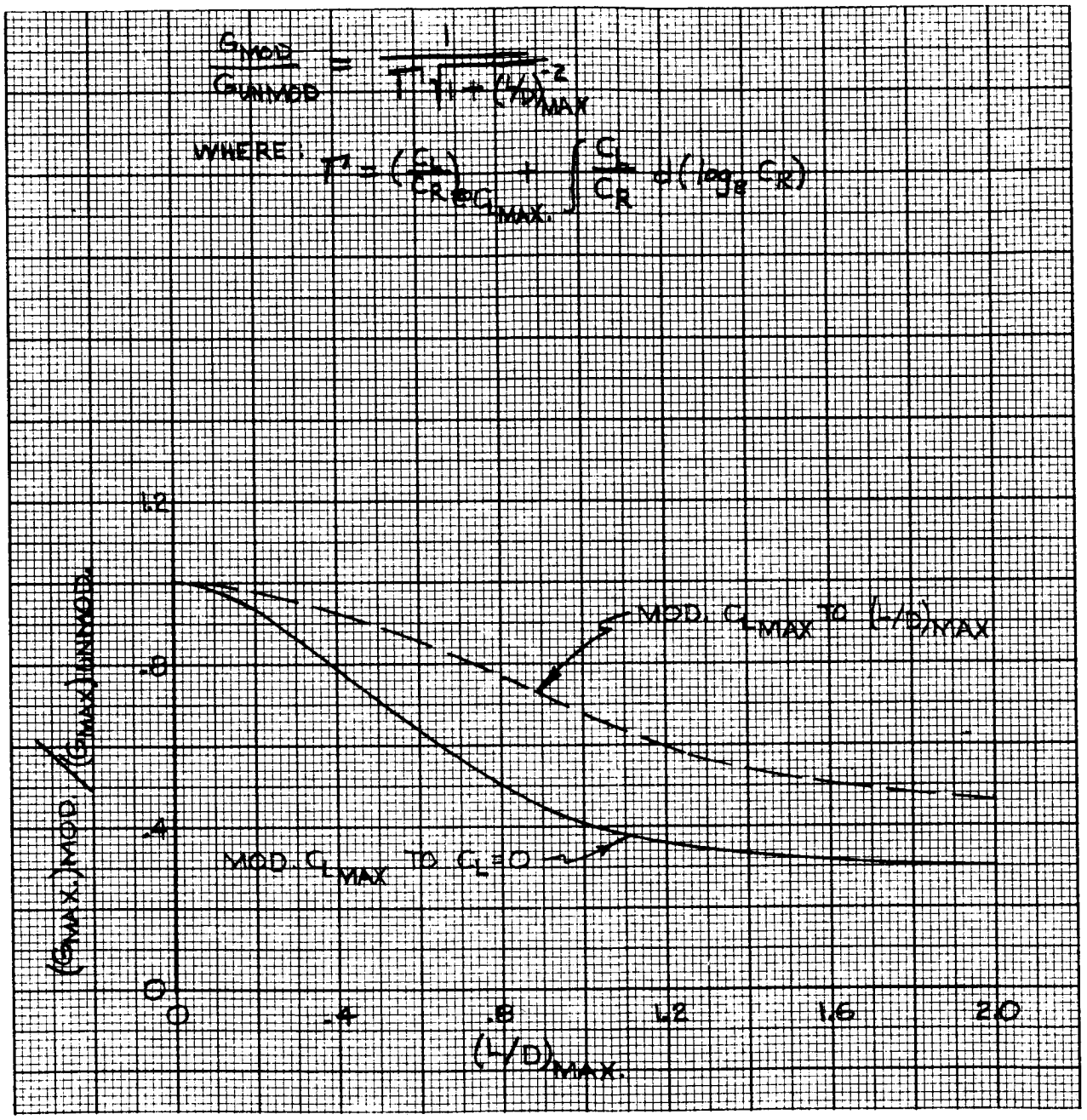

Fig. IV-5. Effects of Lift Modulation on Load Factor

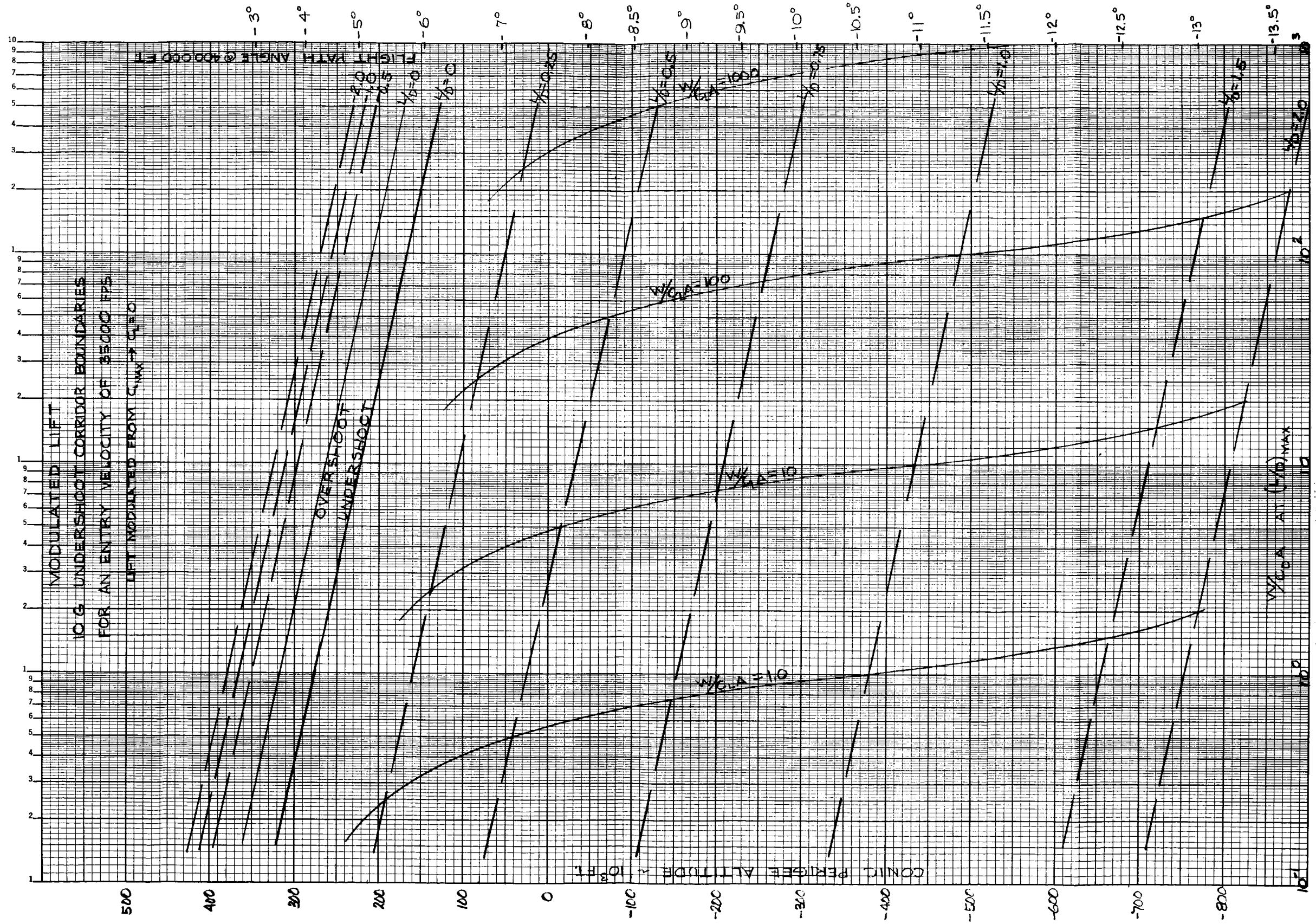

Fig. IV-6. Ten-G Modulated Re-entry Corridor

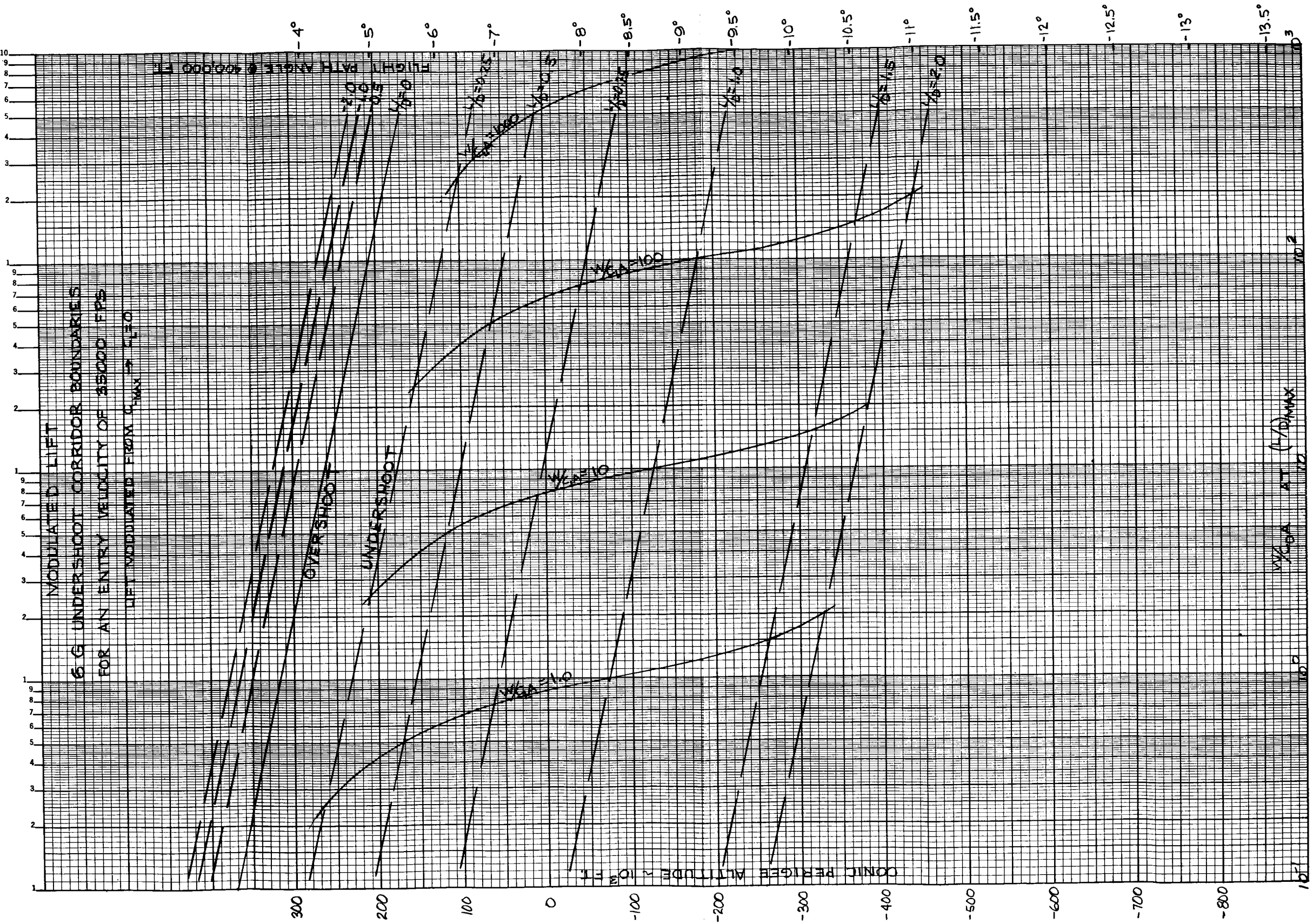

Fig. IV-7. Six-G Modulated Re-entry Corridor

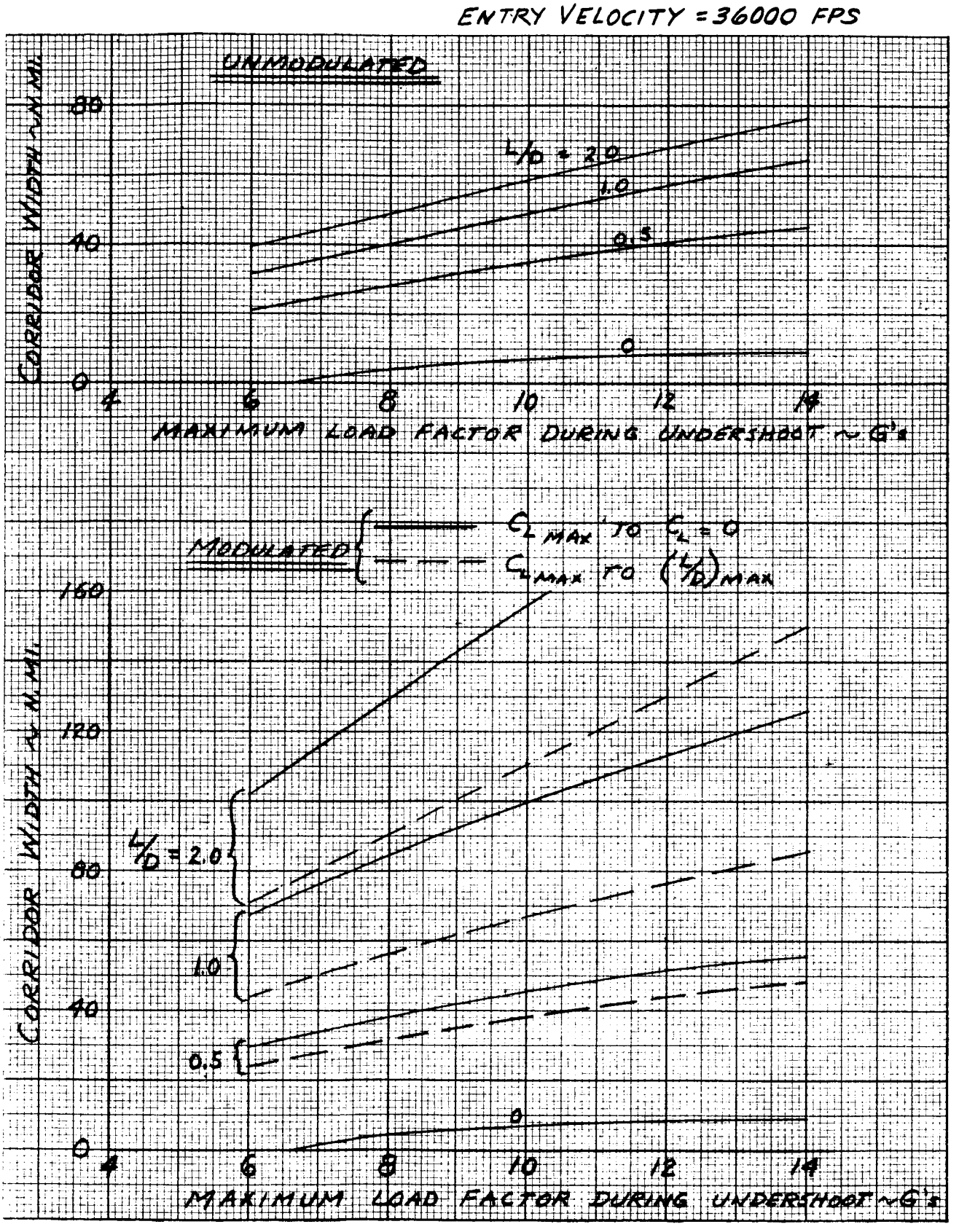

Fig. IV-8. Limiting Load Factor Effect on Corridor Width

D-3 (6-60)

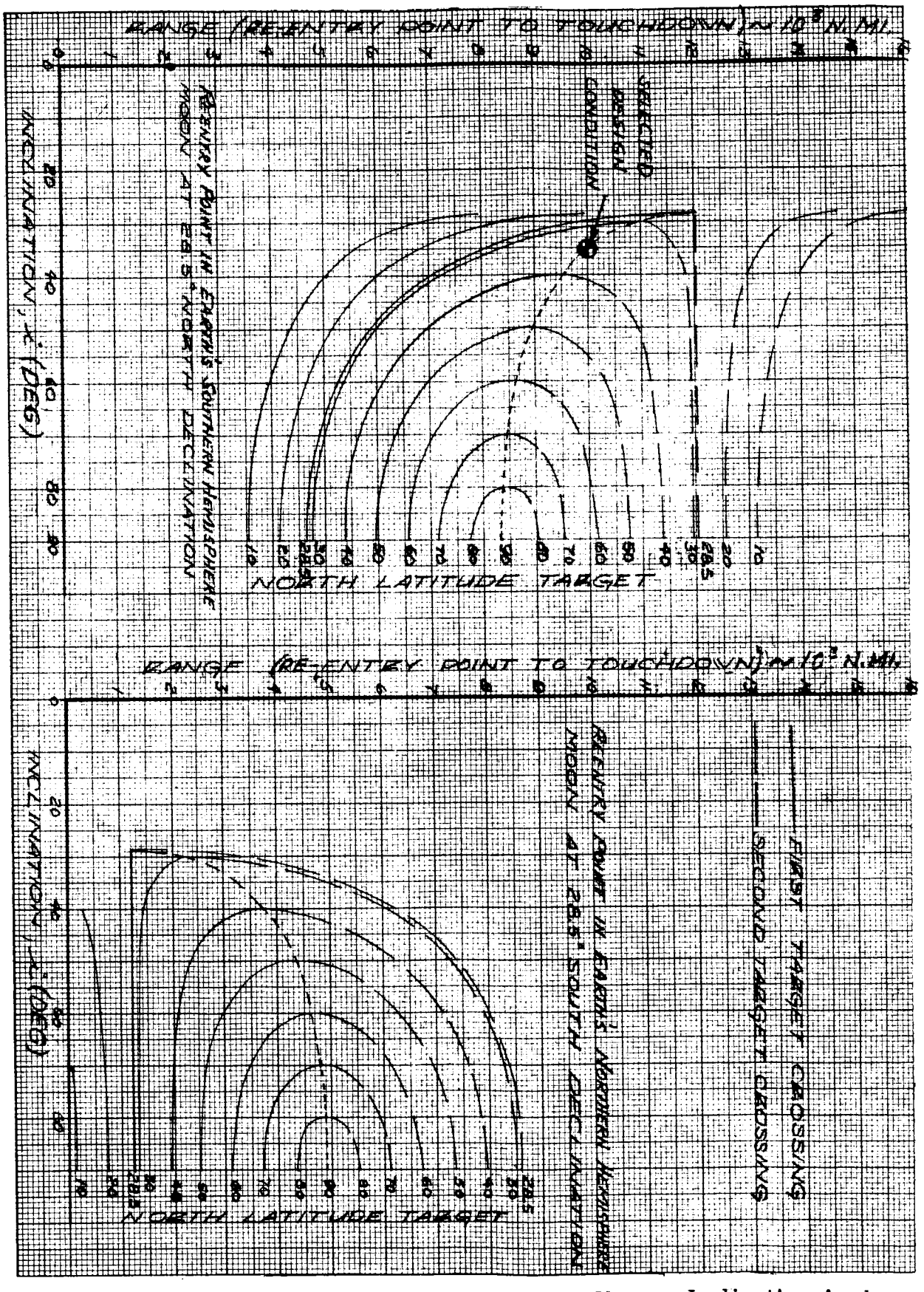

Fig. IV-9. Longitudinal Range Requirements Versus Inclination Angle

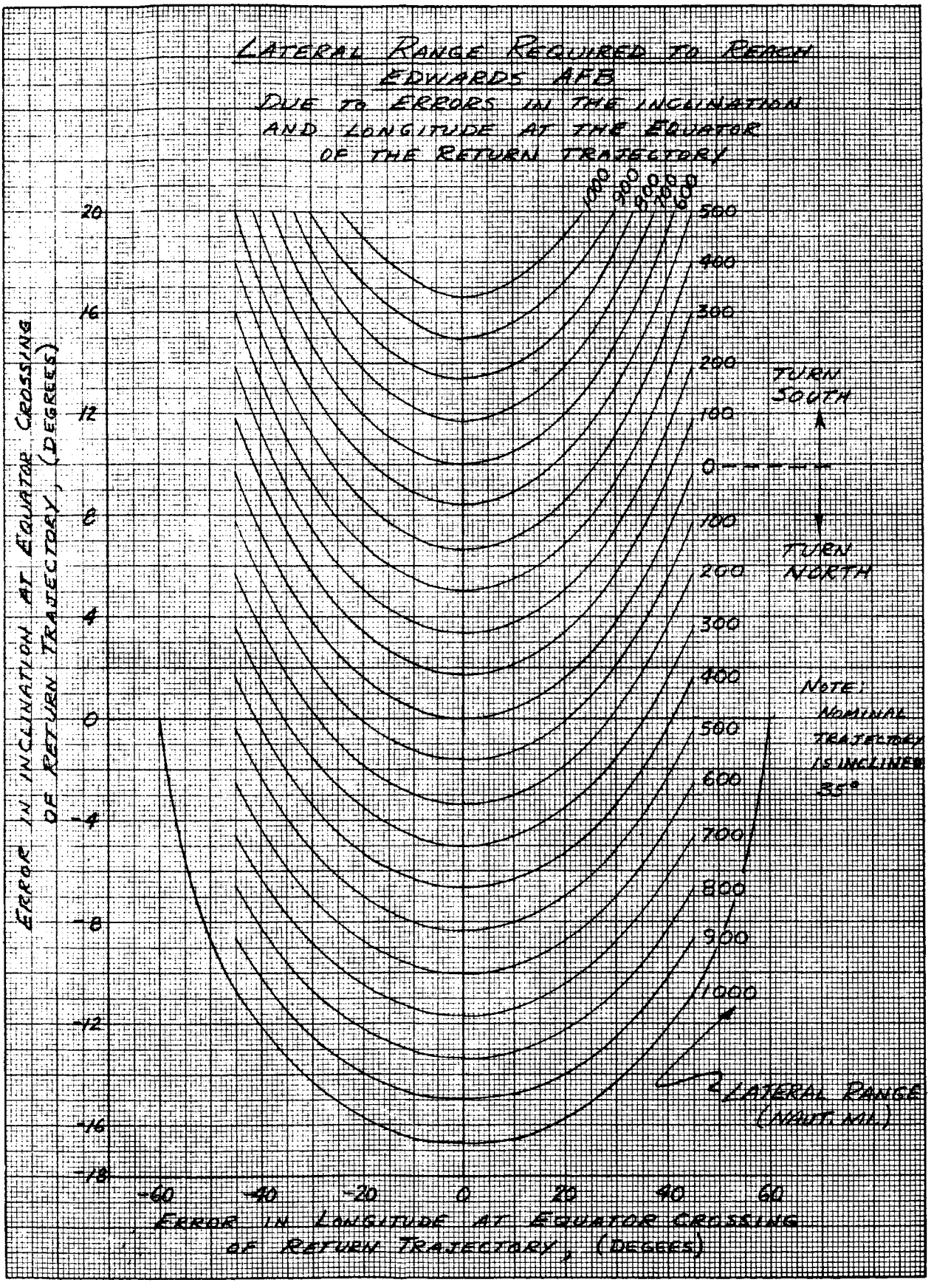

Fig. IV-10. Tolerance on Inclination Versus Lateral Maneuverability

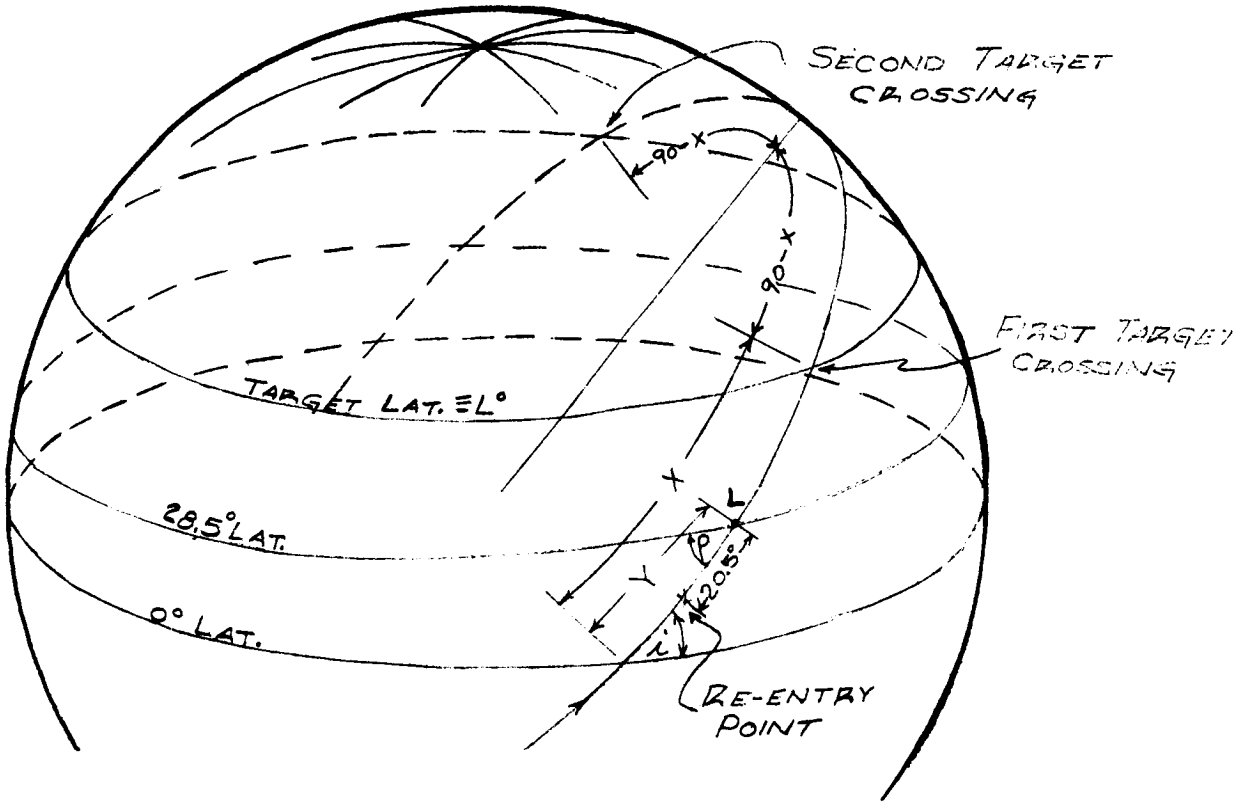

$$Y^\circ = \cos^{-1}\left[\cot i \tan P\right]$$

$$X^\circ = \sin^{-1}\left[\frac{\sin L^\circ}{\sin i}\right]$$

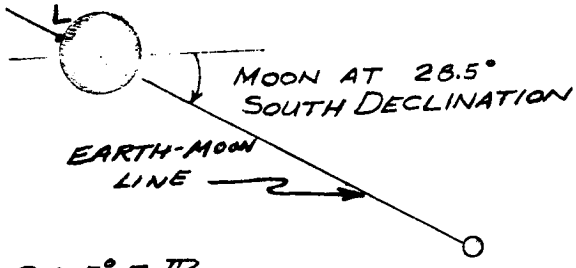

$$\text{RANGE FIRST CROSSING} = X^\circ - Y^\circ + 20.5^\circ \equiv \text{IR}$$

$$\text{RANGE SECOND CROSSING} = X^\circ - Y^\circ + 20.5^\circ + 2(90^\circ - X^\circ)$$

WHERE

$P \equiv$ INCLINATION OF RETURN TRAJECTORY PLANE TO EARTH-MOON PLANE, DEG.

$i \equiv$ INCLINATION OF RETURN TRAJECTORY PLANE TO EQUATORIAL PLANE, DEG.

Fig. IV-11. Geometric Relationships for Longitudinal Range Requirements (Northern Hemisphere)

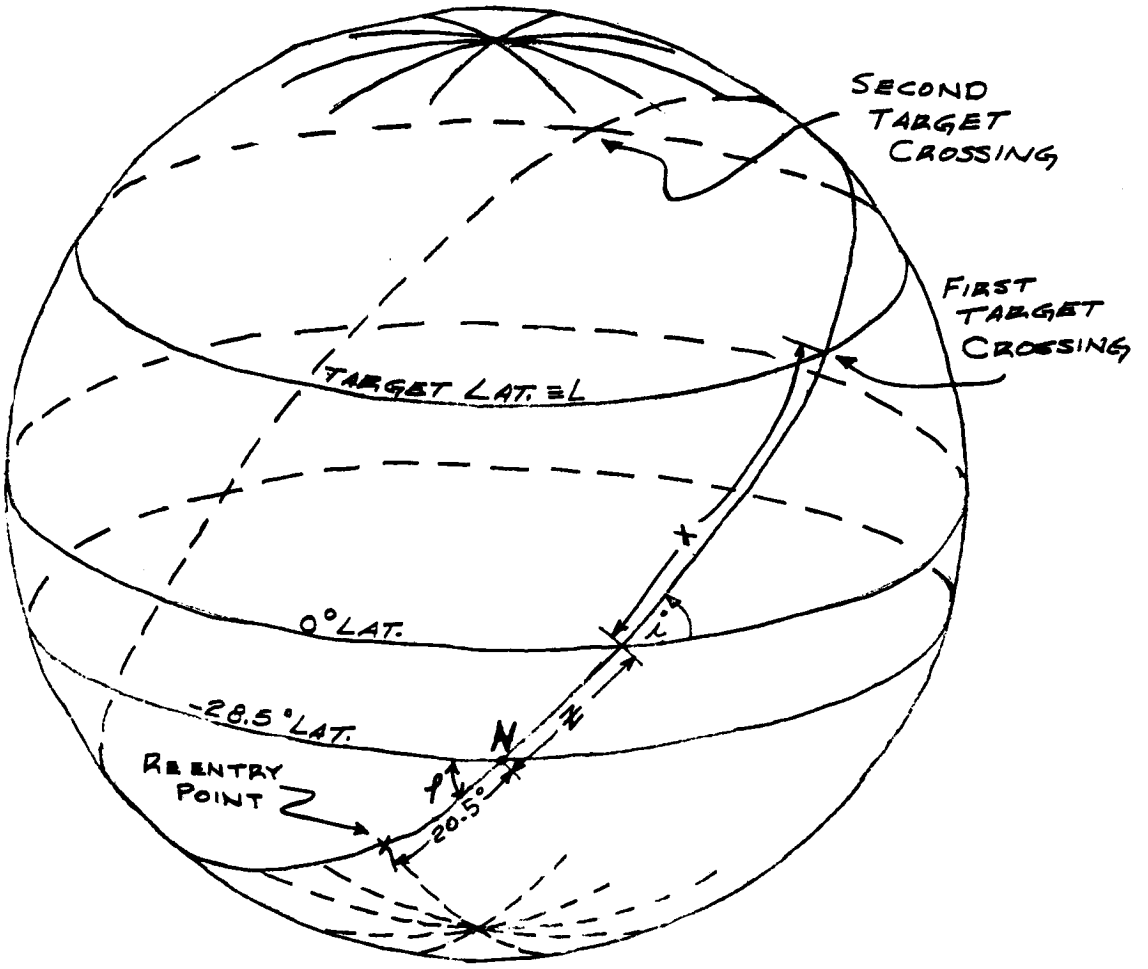

$$Z^\circ = \text{SIN}^{-1}\left[\frac{\text{SIN}\,28.5}{\text{SIN}\,i}\right]$$

$$X^\circ = \text{SIN}^{-1}\left[\frac{\text{SIN}\,L}{\text{SIN}\,i}\right]$$

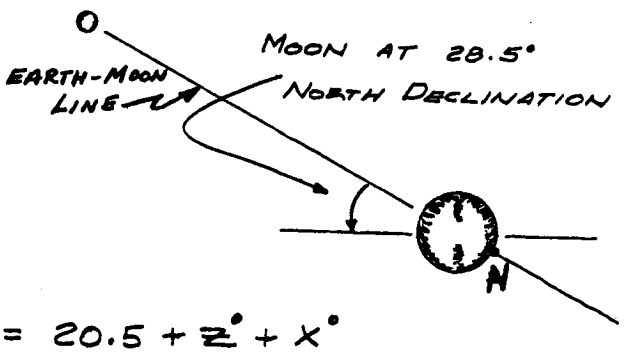

RANGE FIRST CROSSING = $20.5 + Z^\circ + X^\circ$

RANGE SECOND CROSSING = $20.5^\circ + Z^\circ + 180^\circ - X^\circ$

Fig. IV-12. Geometric Relationships for Longitudinal Range Requirements (Southern Hemisphere)

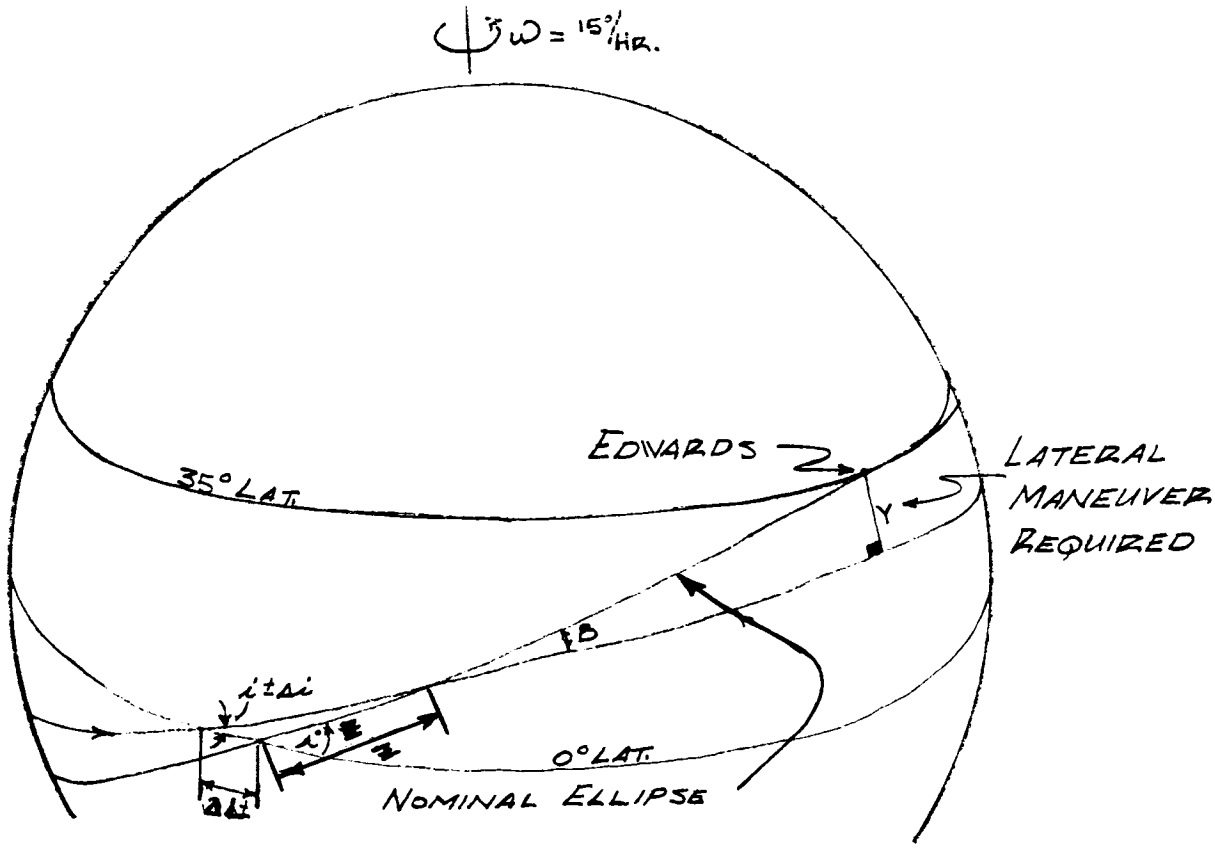

$$\cos B = \cos \Delta i - \sin(i+\Delta i)\sin i\,(1-\cos \omega \Delta t)$$

$$\sin Z = \frac{\sin(i+\Delta i)\sin \omega \Delta t}{\sin B}$$

$$Y^\circ = \sin^{-1}\left[\sin B \cos Z\right]$$

WHERE i ≡ INCLINATION OF NOMINAL TRAJECTORY

Δi = ERROR IN INCLINATION
ΔL = ERROR IN LONGITUDE
} AT EQUATOR CROSSING

Fig. IV-13. Geometric Relationship for Lateral Range Requirements

D-3 (6-60)

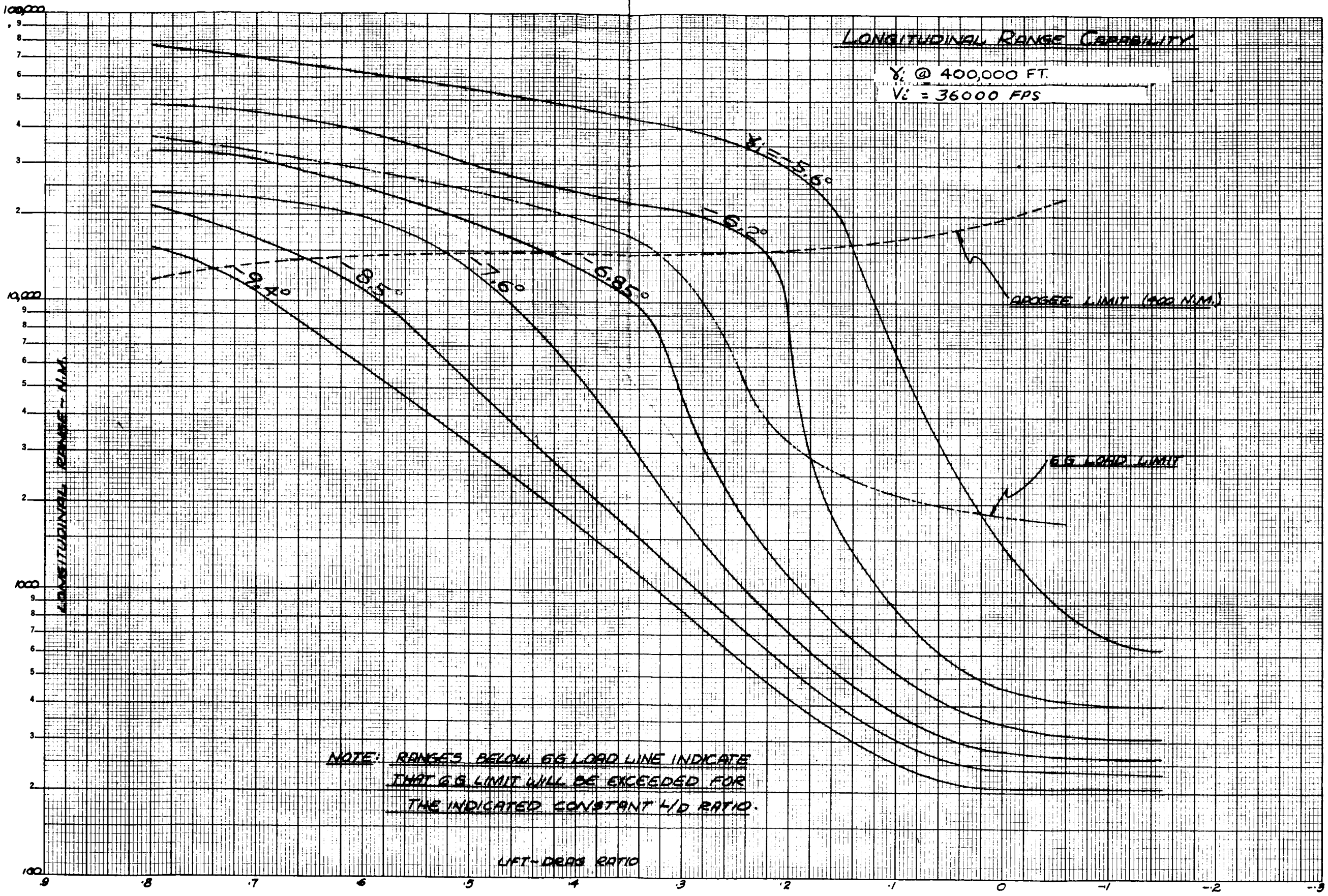

Fig. IV-14. Longitudinal Range Versus (L/D)

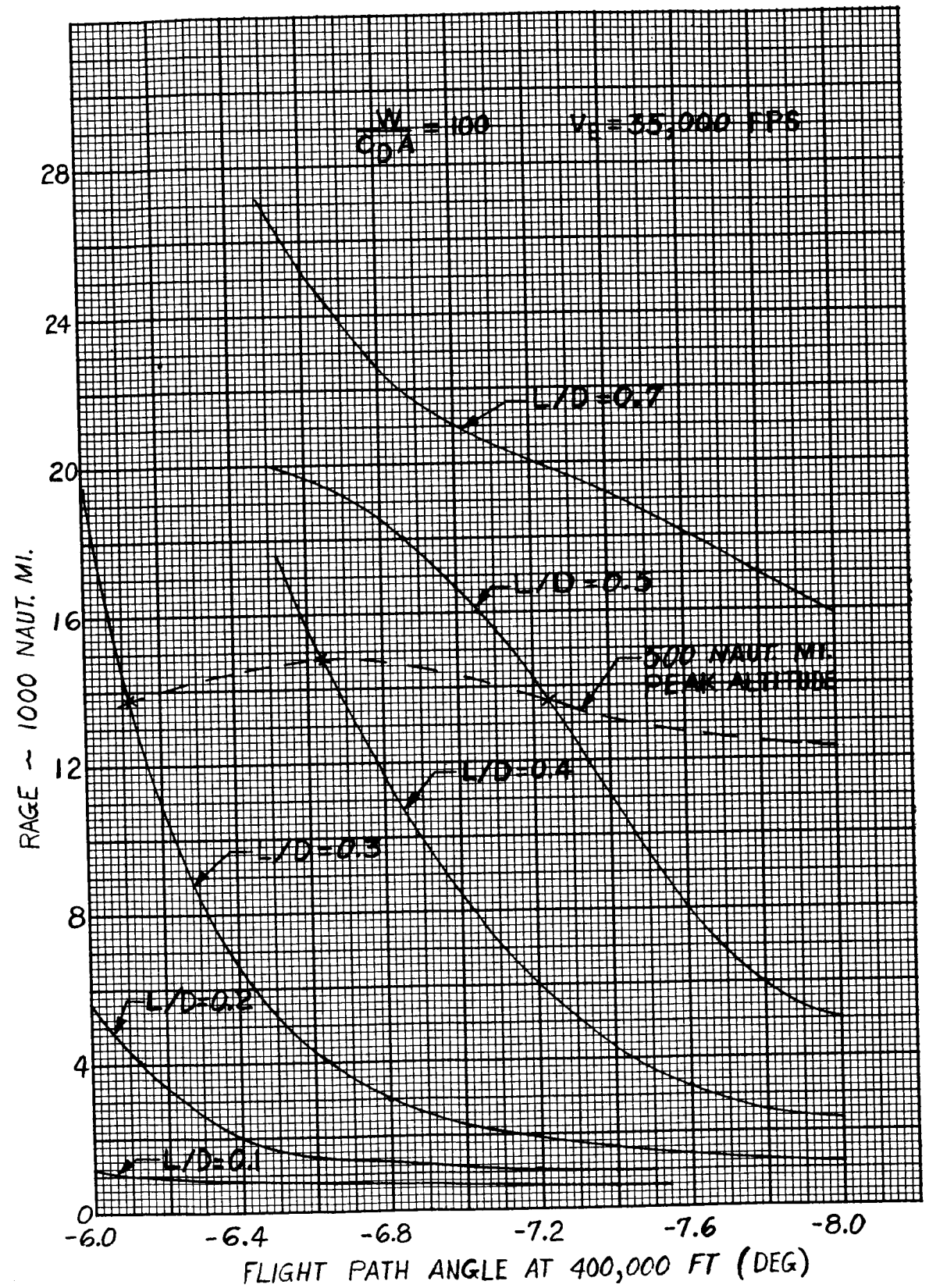

Fig. IV-15. Re-entry Range Versus Flight Path Angle

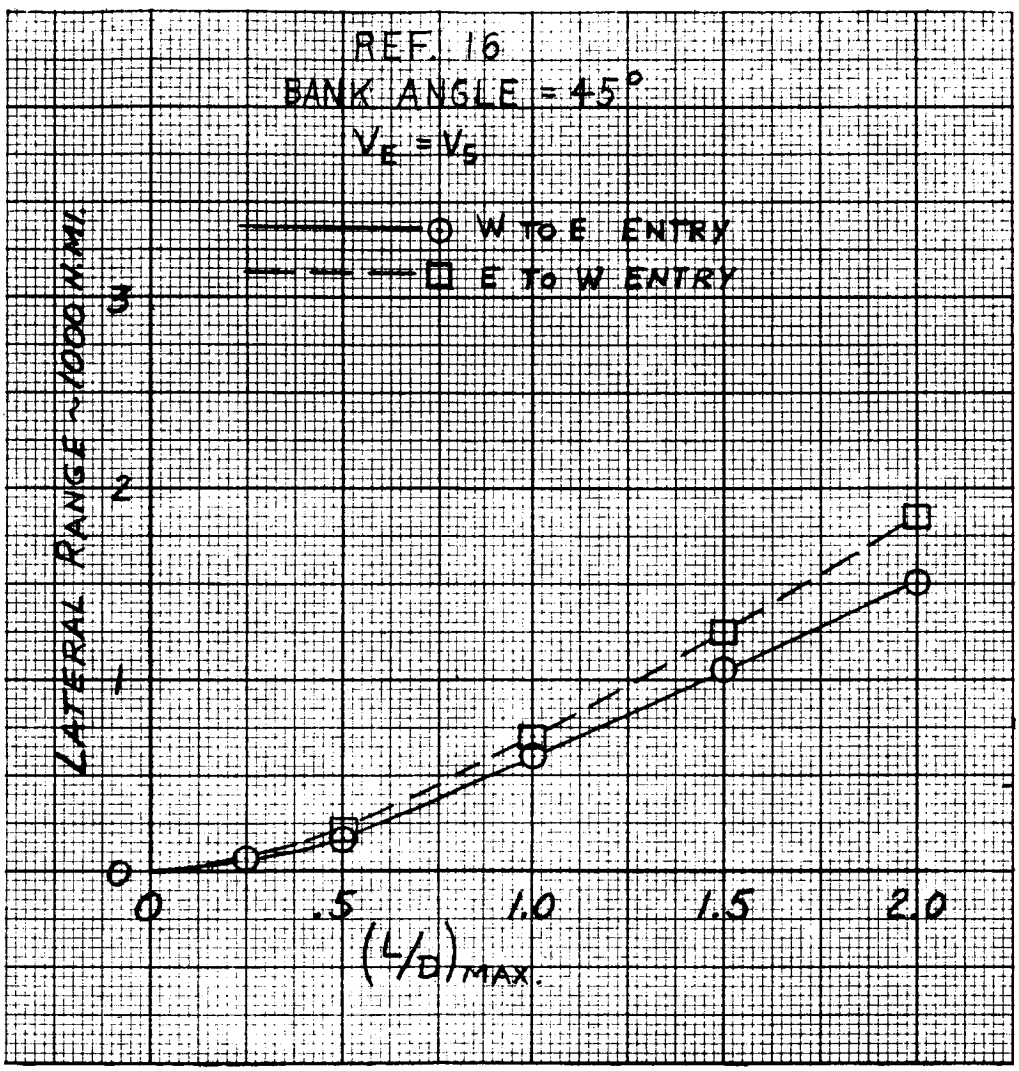

Fig. IV-16. Lateral Range for Satellite Re-entry

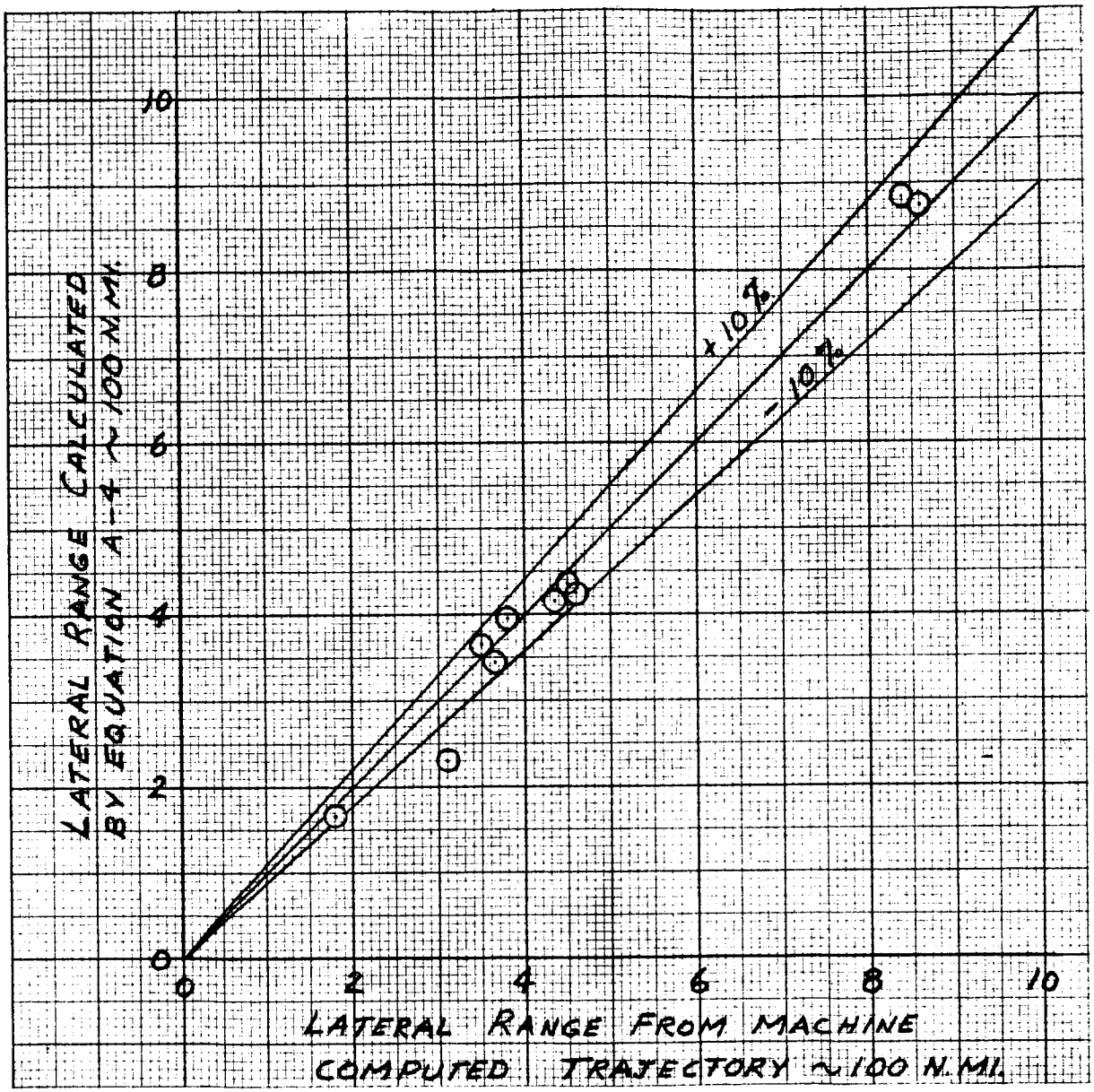

Fig. IV-17. Lateral Range Correlation of Empirical Results with Machine Calculations

D-3 (6-60)

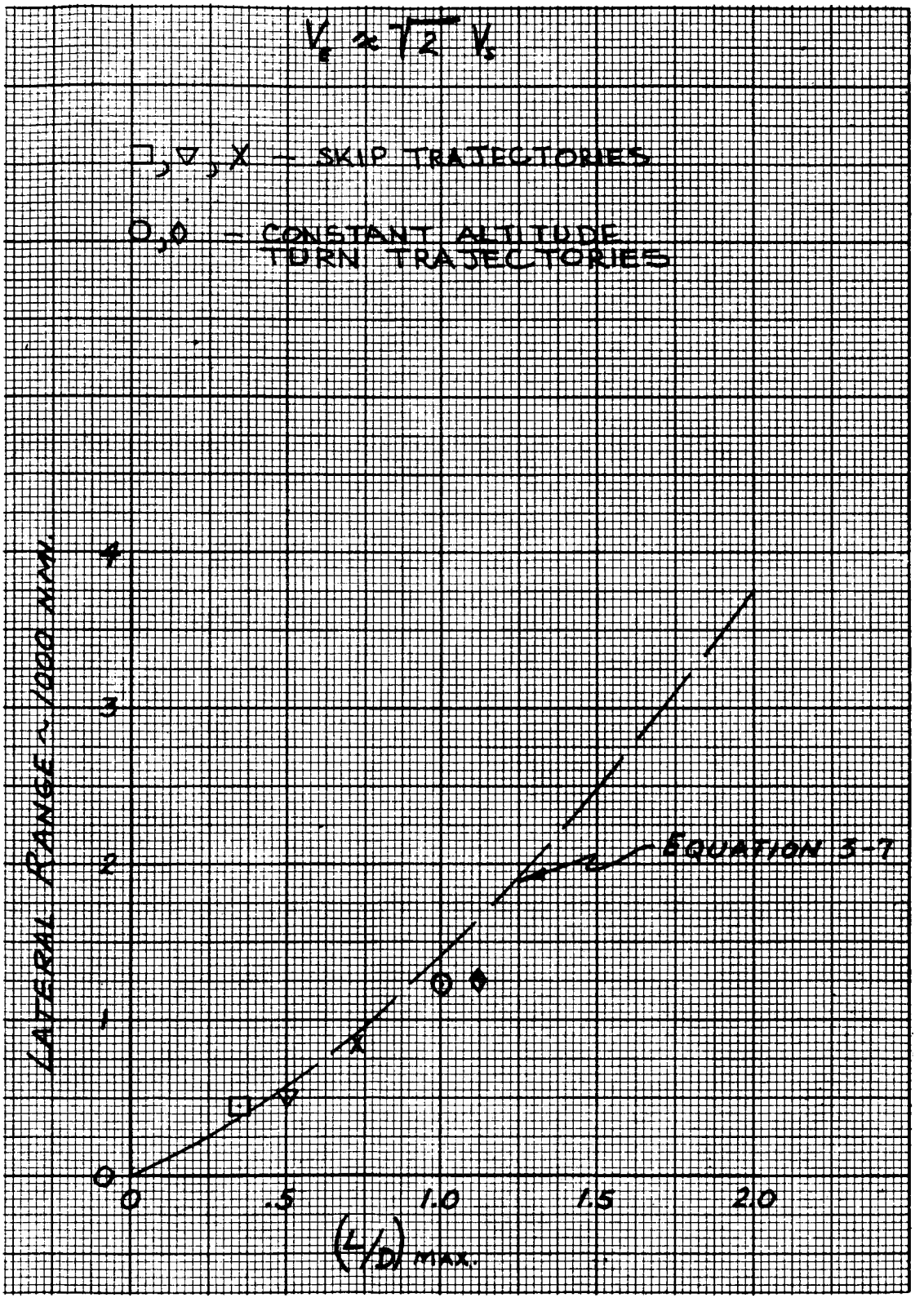

Fig. IV-18. Maximum Lateral Range Versus (L/D)

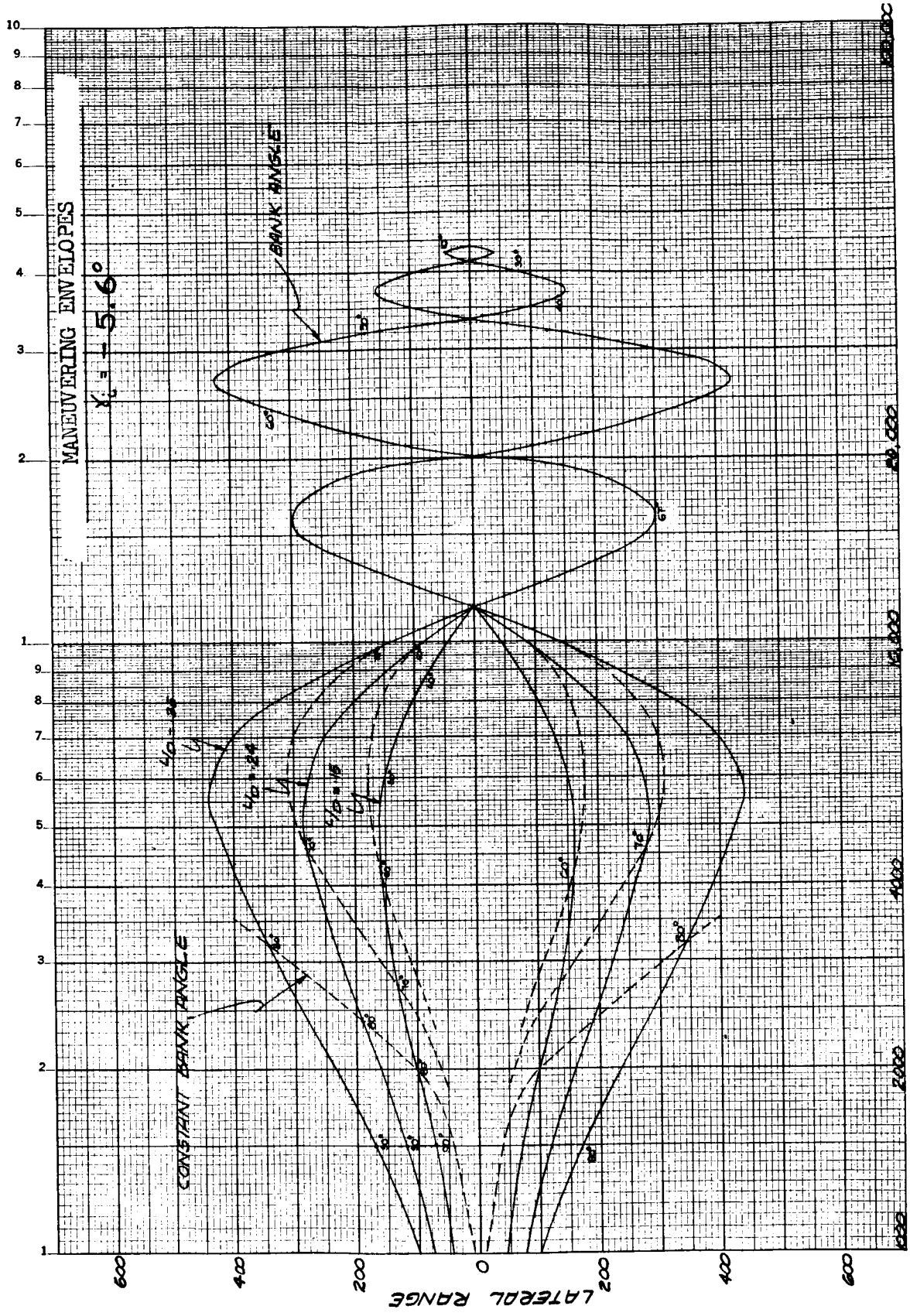

Fig. IV-19. Maneuvering Envelope Versus (L/D) for Re-entry Angle = -5.6 Degrees

D-3 (6-60)

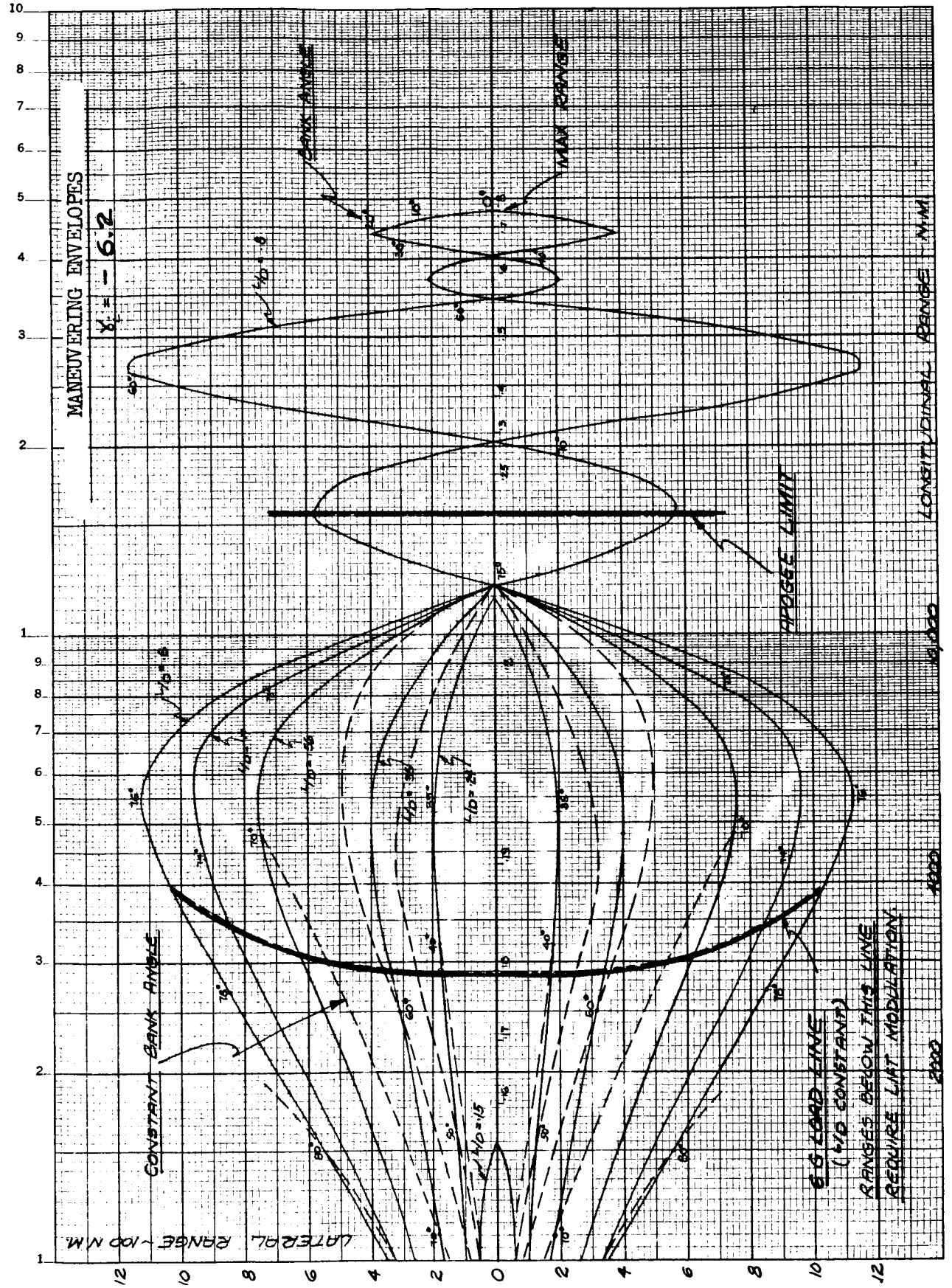

Fig. IV-20. Maneuvering Envelope Versus (L/D) for Re-entry Angle = -6.2 Degrees

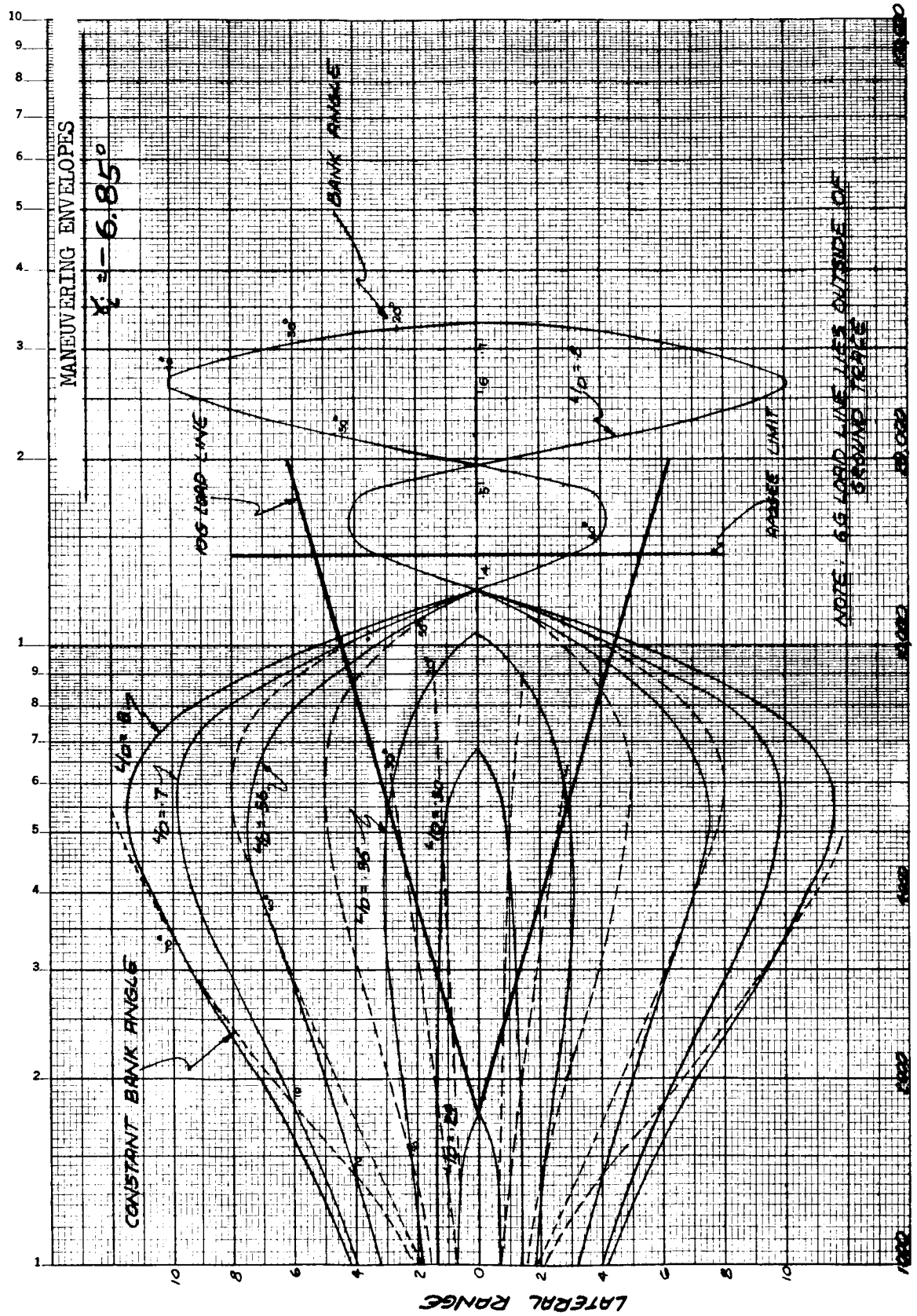

Fig. IV-21. Maneuvering Envelope Versus (L/D) for Re-entry Angle = -6.85 Degrees

~~CONFIDENTIAL~~

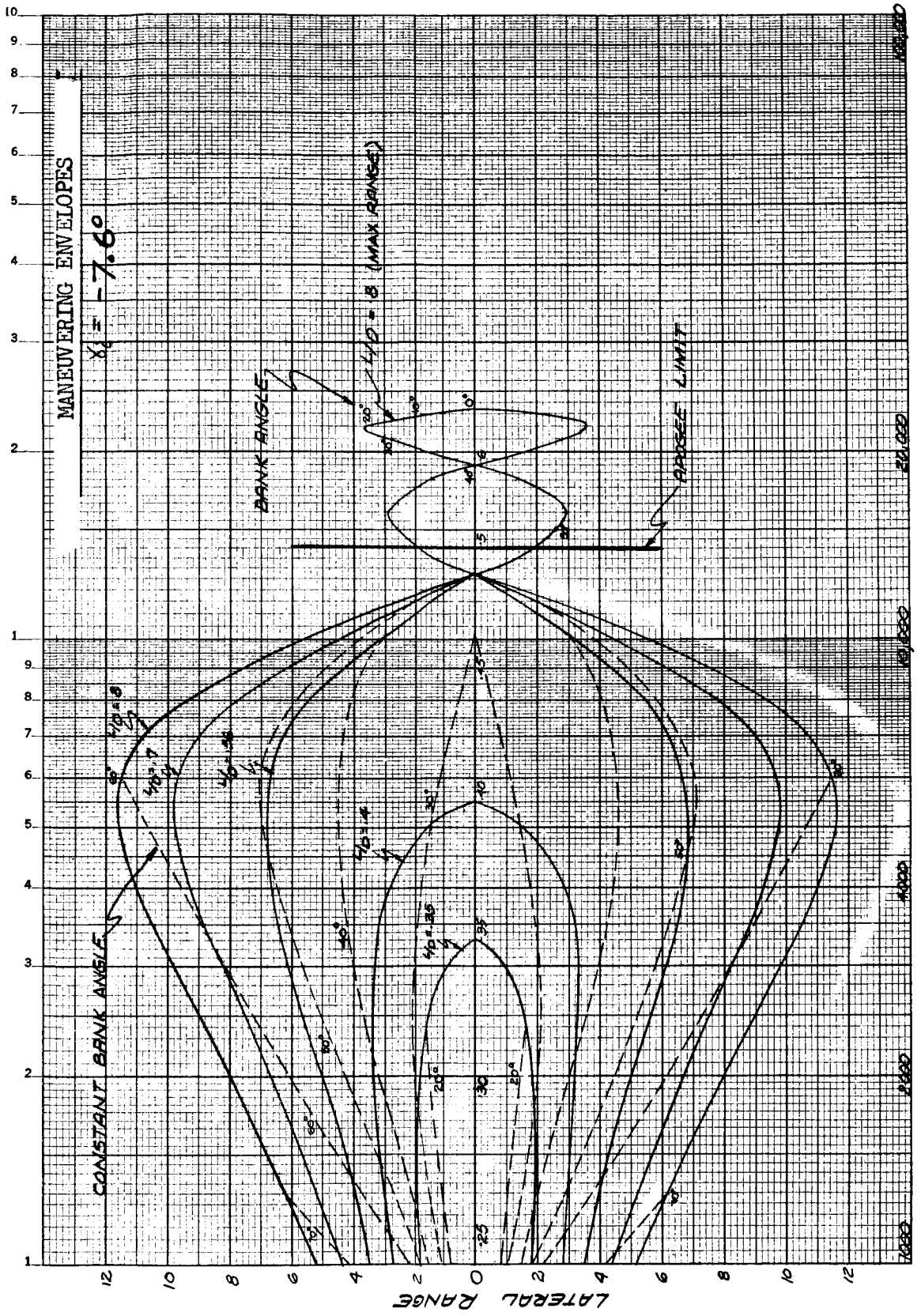

Fig. IV-22. Maneuvering Envelope Versus (L/D) for Re-entry Angle = -7.6 Degrees

D-3 (6-60)

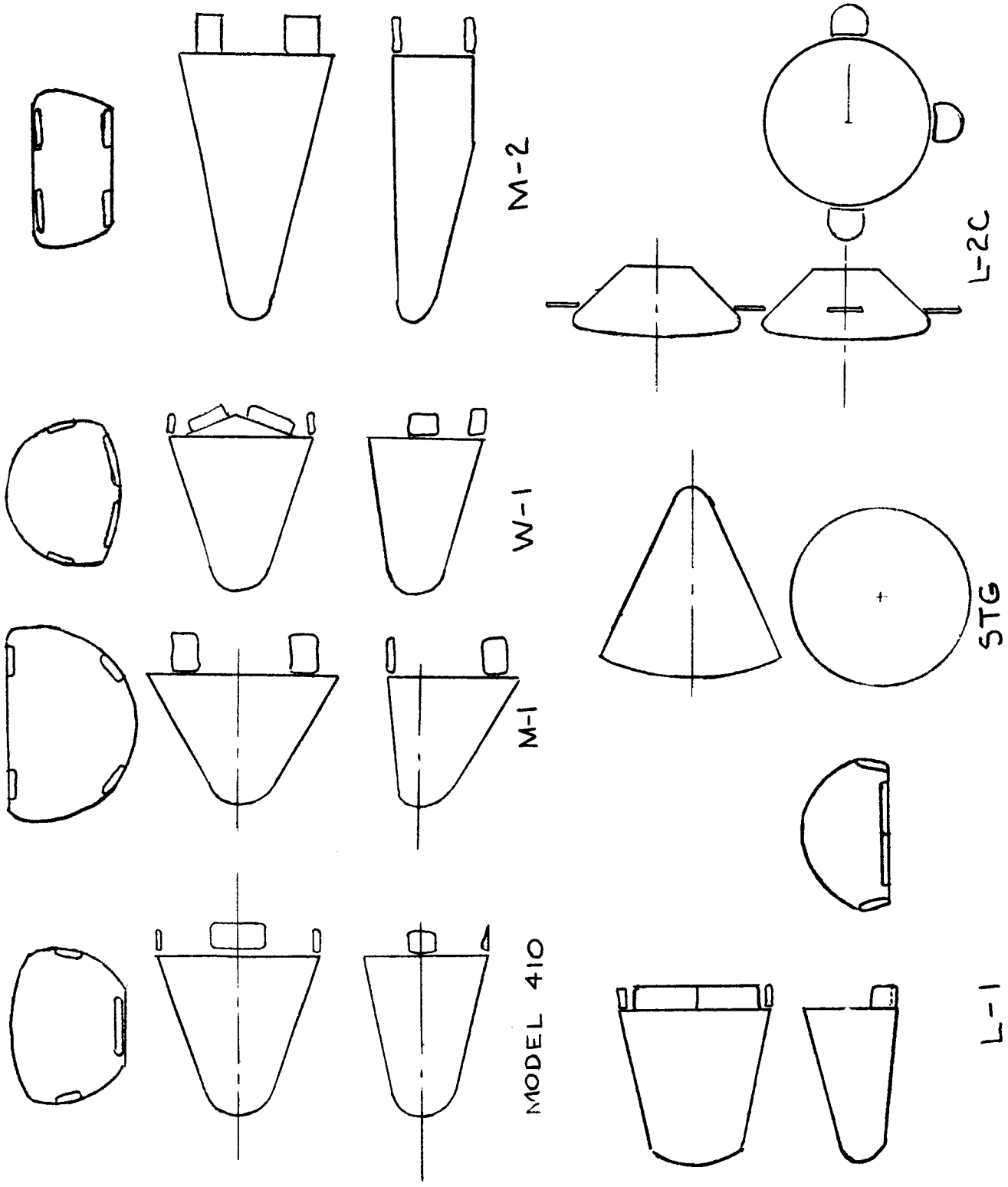

Fig. IV-23. Re-entry Body Configurations

D-3 (6.60)

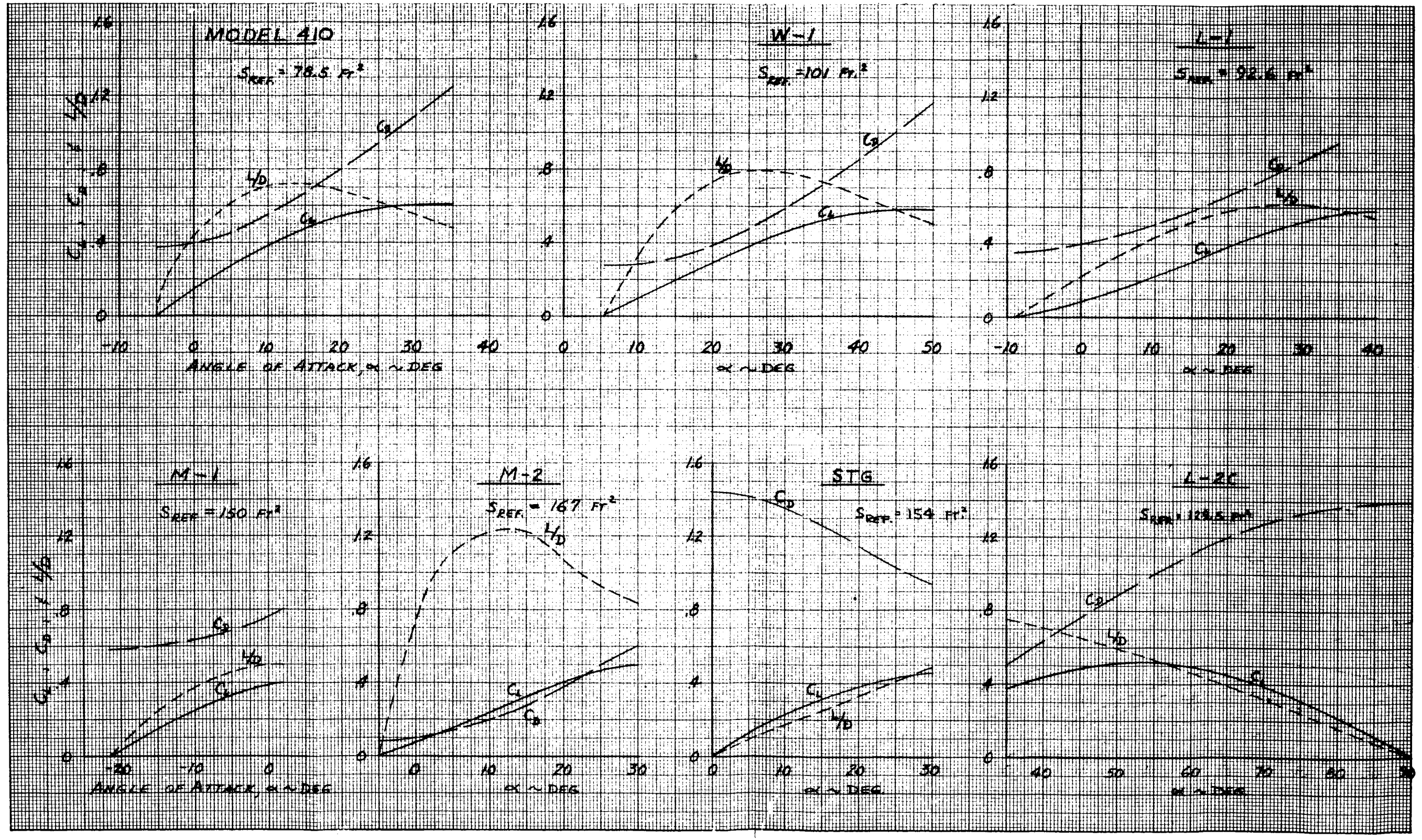

Fig. IV-24. Aerodynamic Characteristics of Re-entry Configurations

CONFIDENTIAL

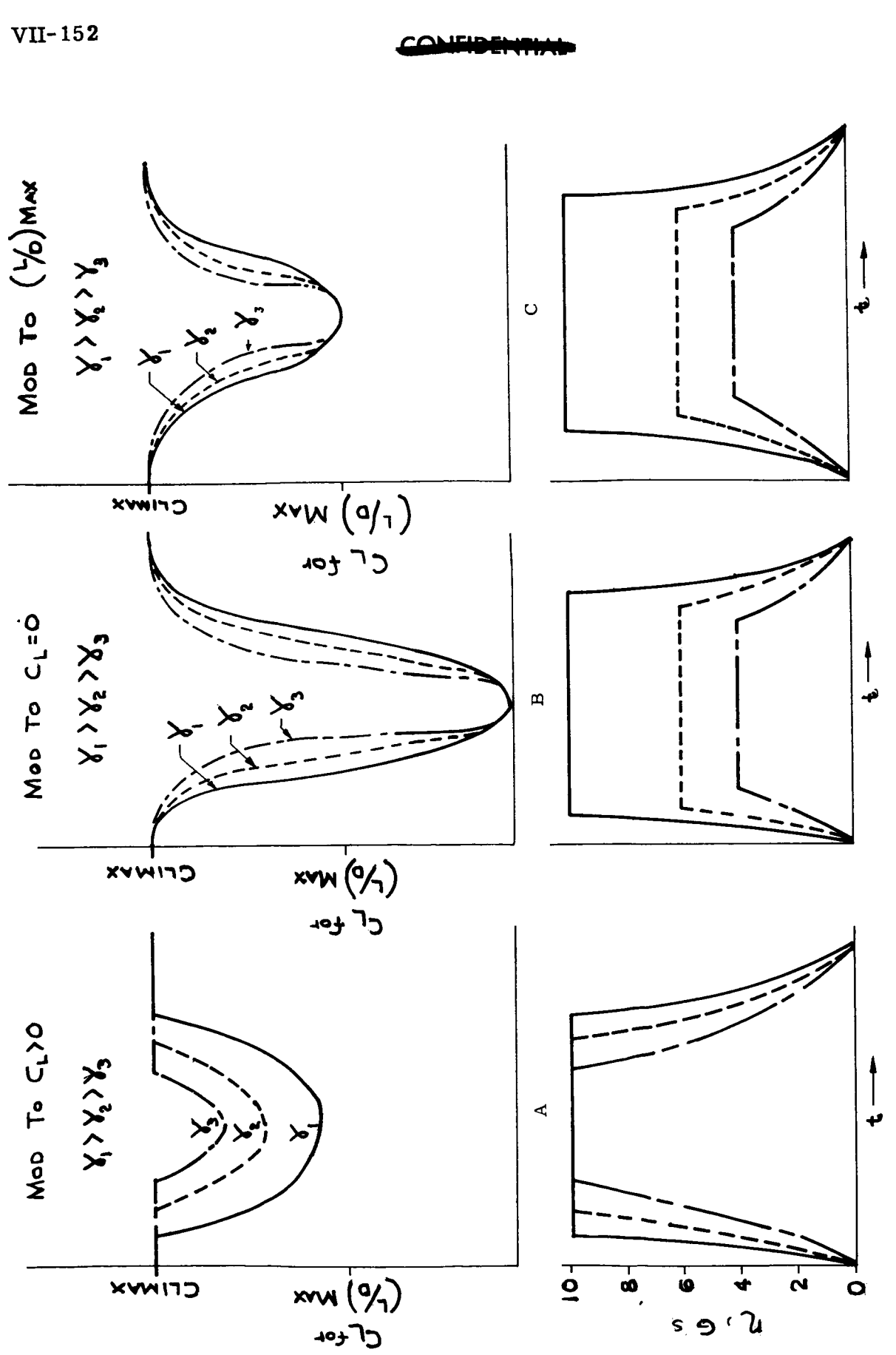

Fig. IV-25. Modulation Techniques

CONFIDENTIAL

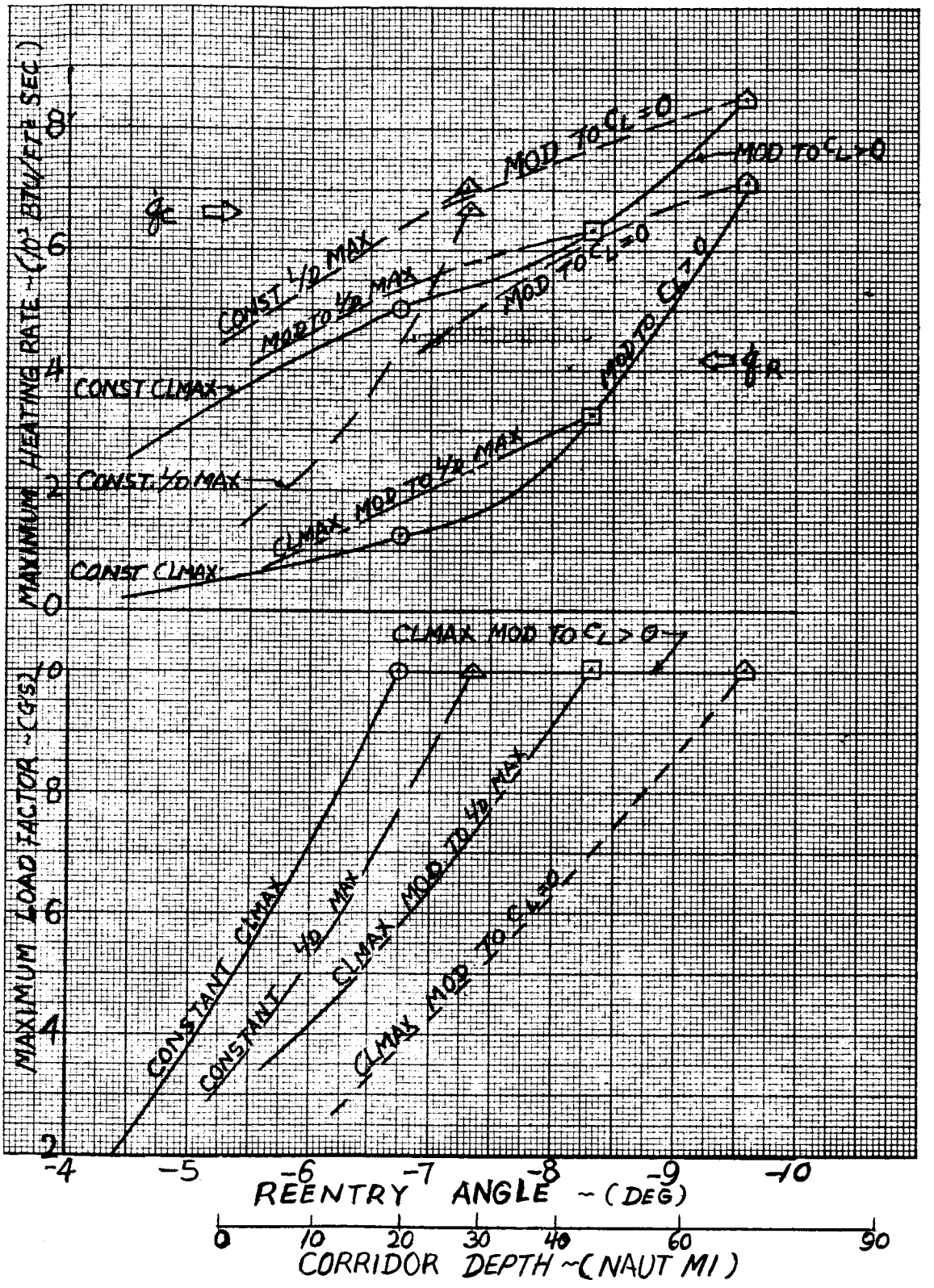

Fig. IV-26. Effect of Maximum Heating Rate and Load Factor on Corridor Width (Model 410, V_E = 36,000 fps; W/A = 81.5; R_N = 2.5 ft)

D-3 (6-60)

CONFIDENTIAL

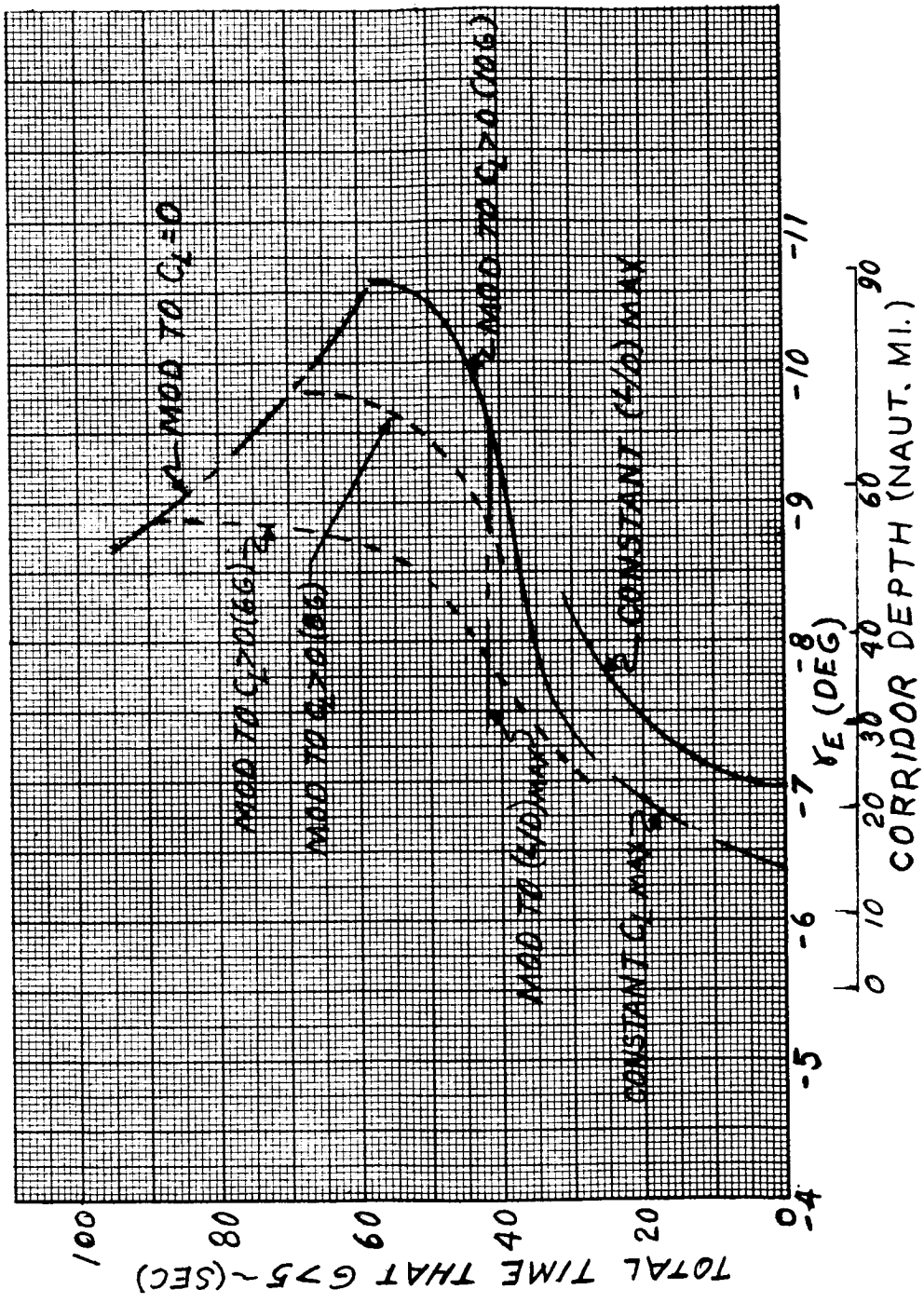

Fig. IV-27. G-Duration Versus Corridor Depth for Skip Trajectory (Model 410, V_E = 36,000 fps; W/A = 81.5; R_N = 2.5 ft)

CONFIDENTIAL

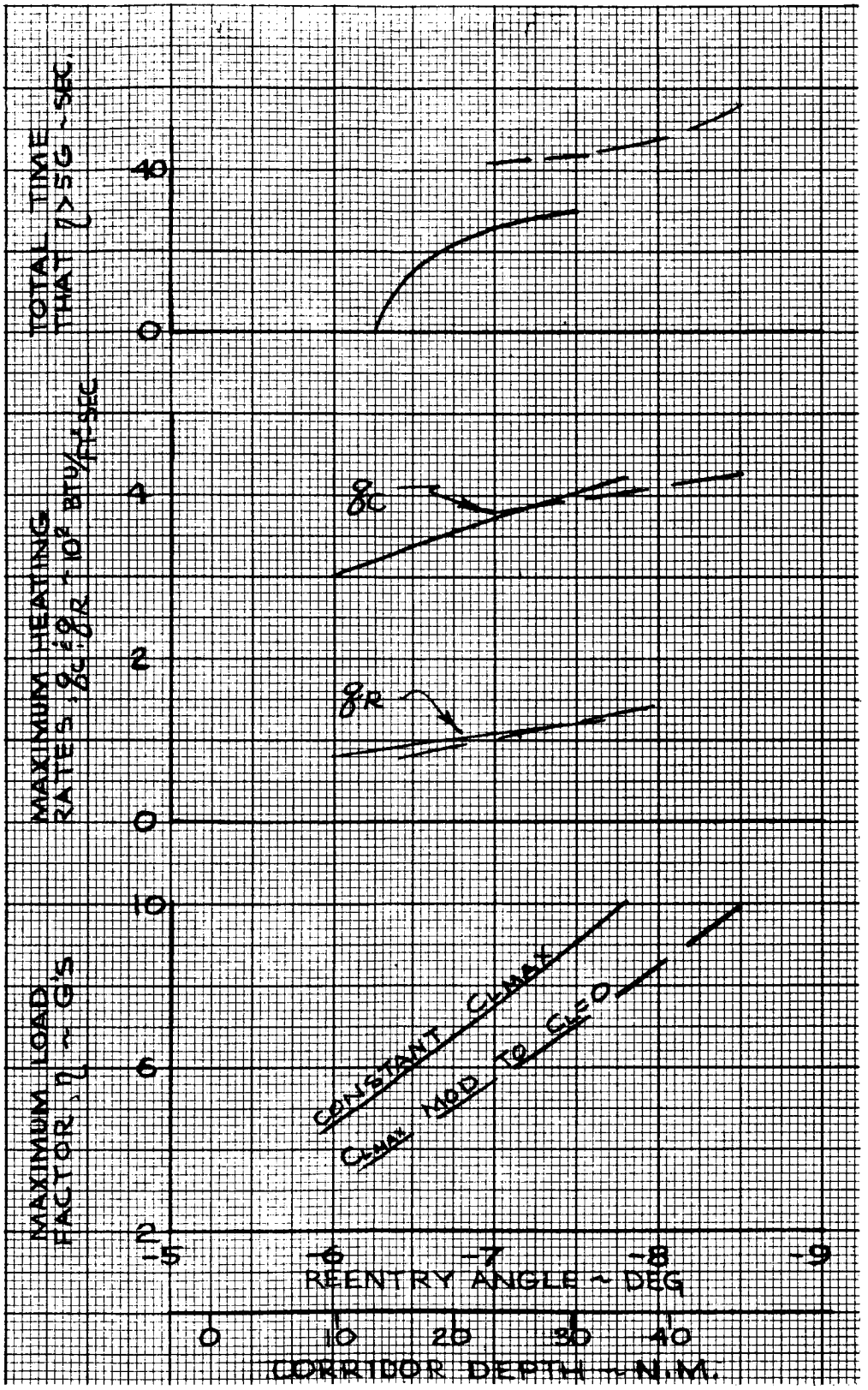

Fig. IV-28. M-1 Re-entry Vehicle Corridor Summary (V_E = 36,000 fps; W/A = 50; R_N = 3.4 ft)

D-3 (6-60)

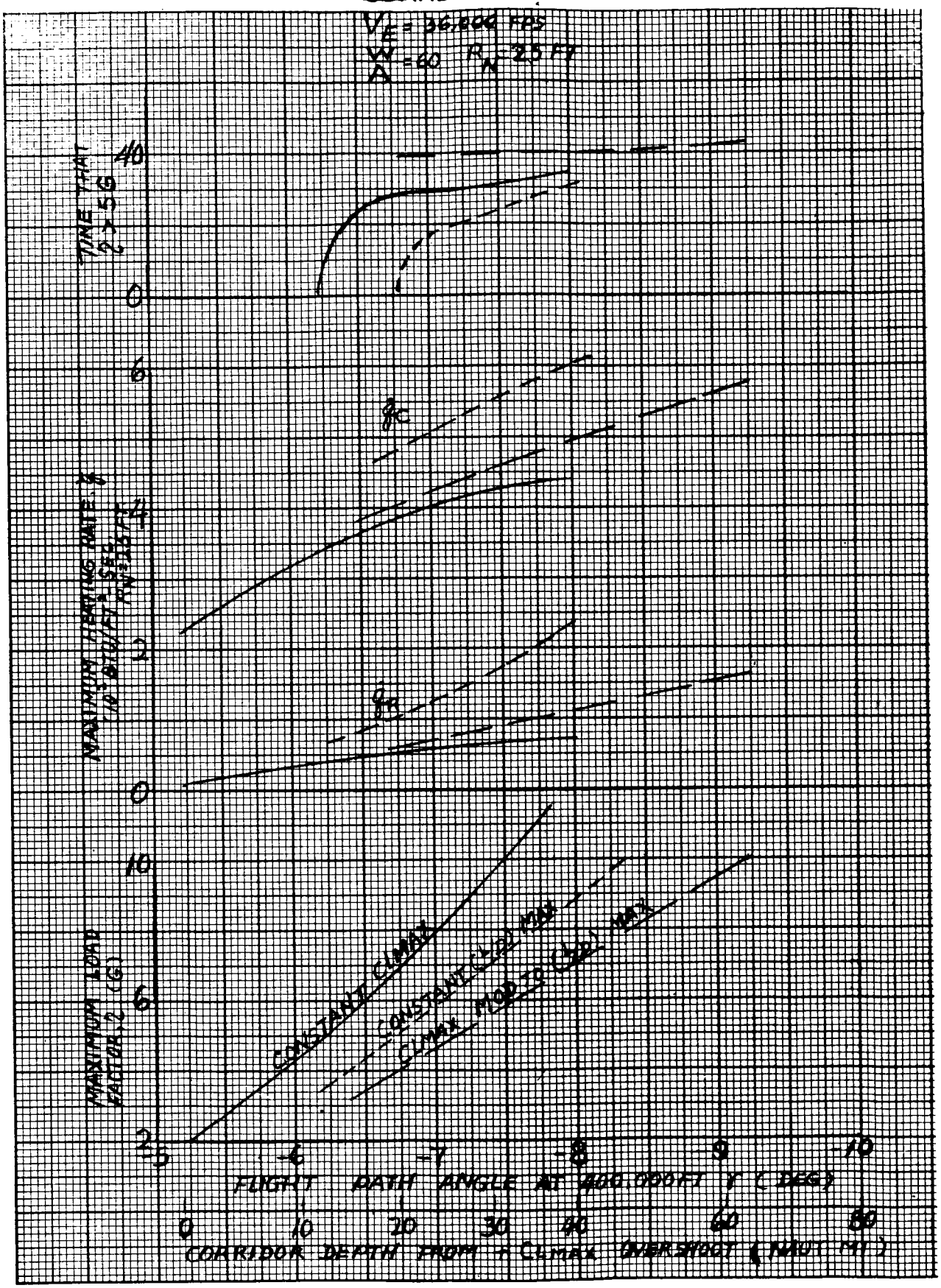

Fig. IV-29. W-1 Vehicle Re-Entry Corridor Summary

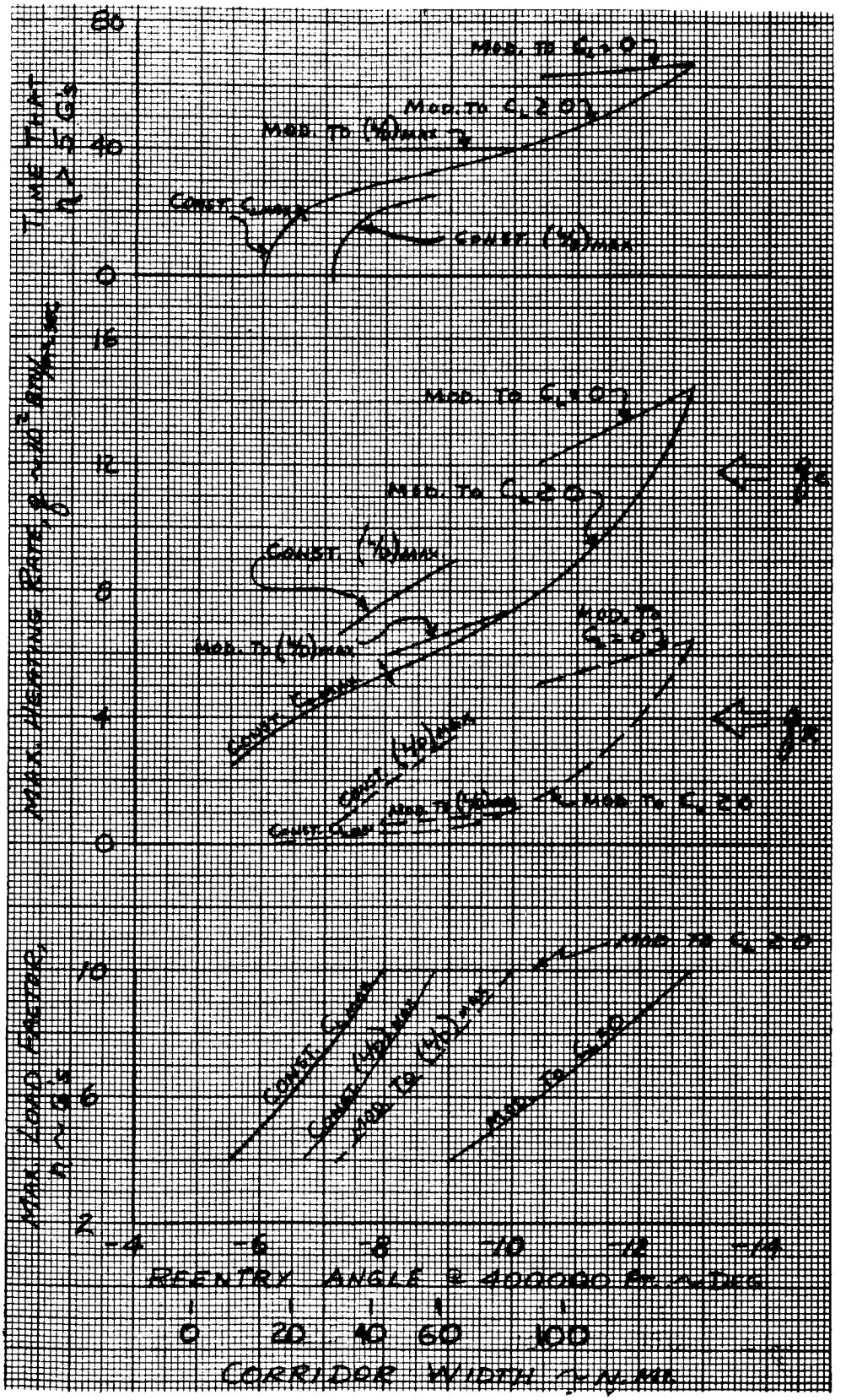

Fig. IV-30. M-2 Re-entry Vehicle Corridor Summary (V_E = 35,000 fps; W/A = 48; R_N = 1.5 ft)

D-3 (6-60)

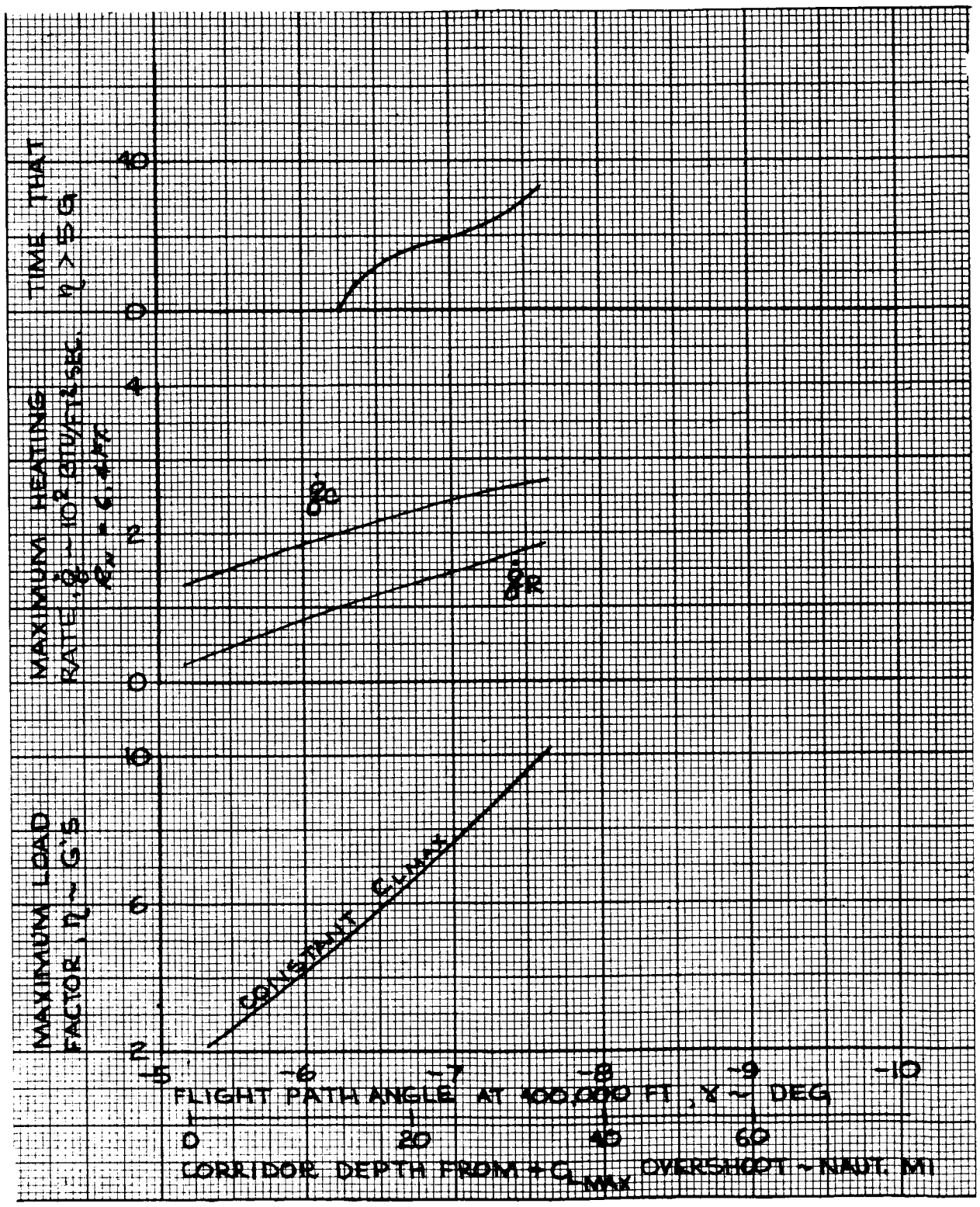

Fig. IV-31. L-2C Re-entry Vehicle Corridor Summary (V_E = 36,000 fps; W/A = 46; R_N = 6.41 ft)

D-3 (6-60)

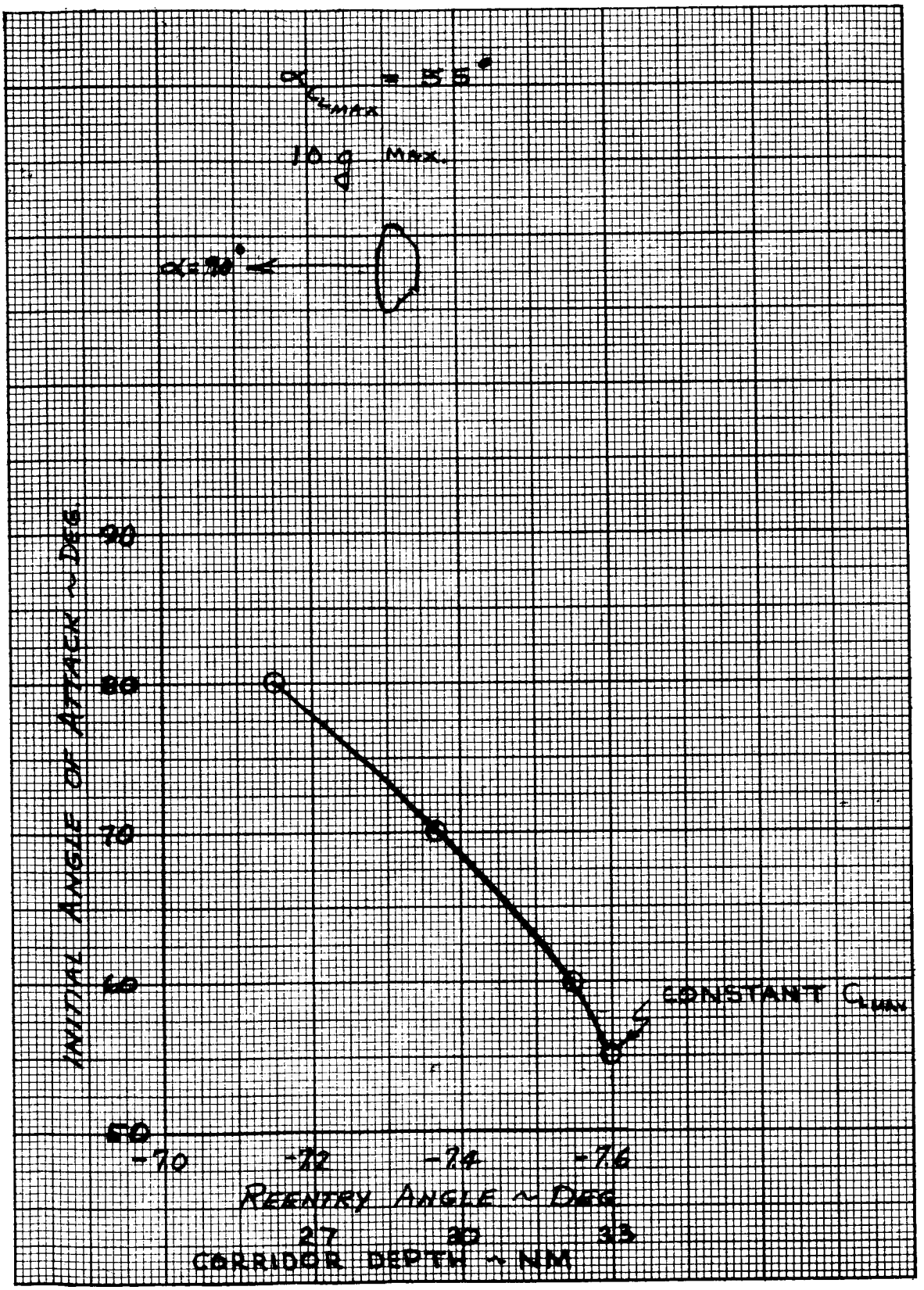

Fig. IV-32. L-2C Re-entry Vehicle, Effect of Lift Modulation on Corridor Depth

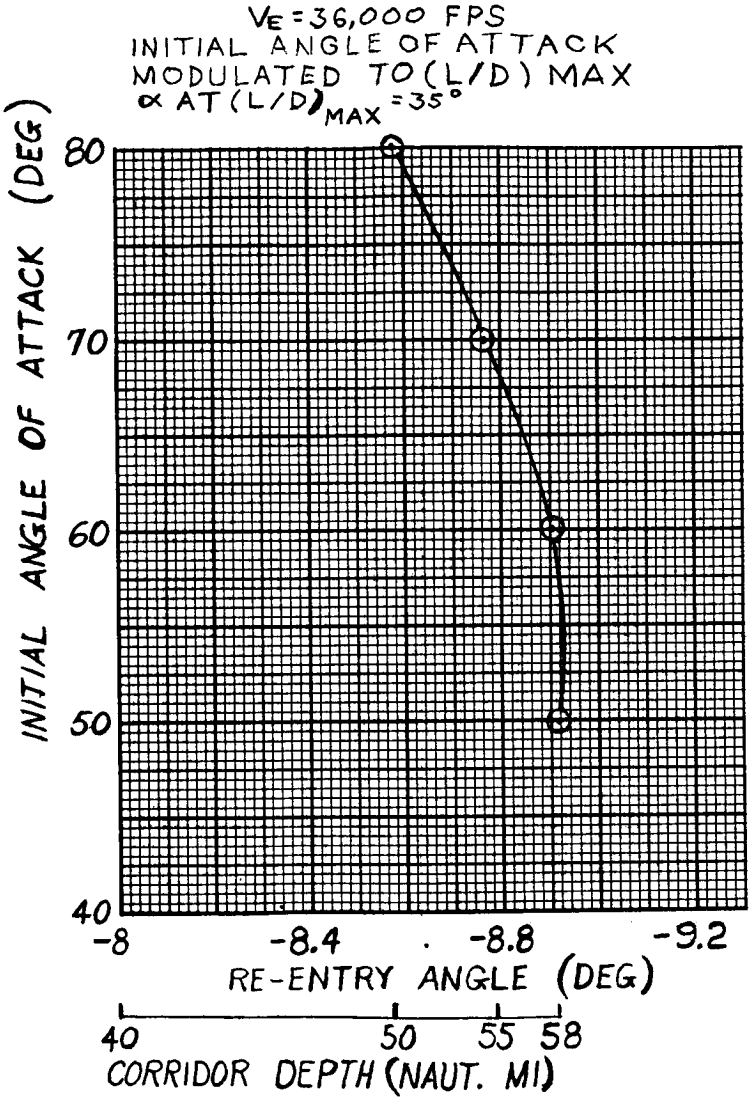

Fig. IV-33. L-2C Re-entry Vehicle, Variation of 10-G Limit Corridor with Initial Angle of Attack

D-3 (6-60)

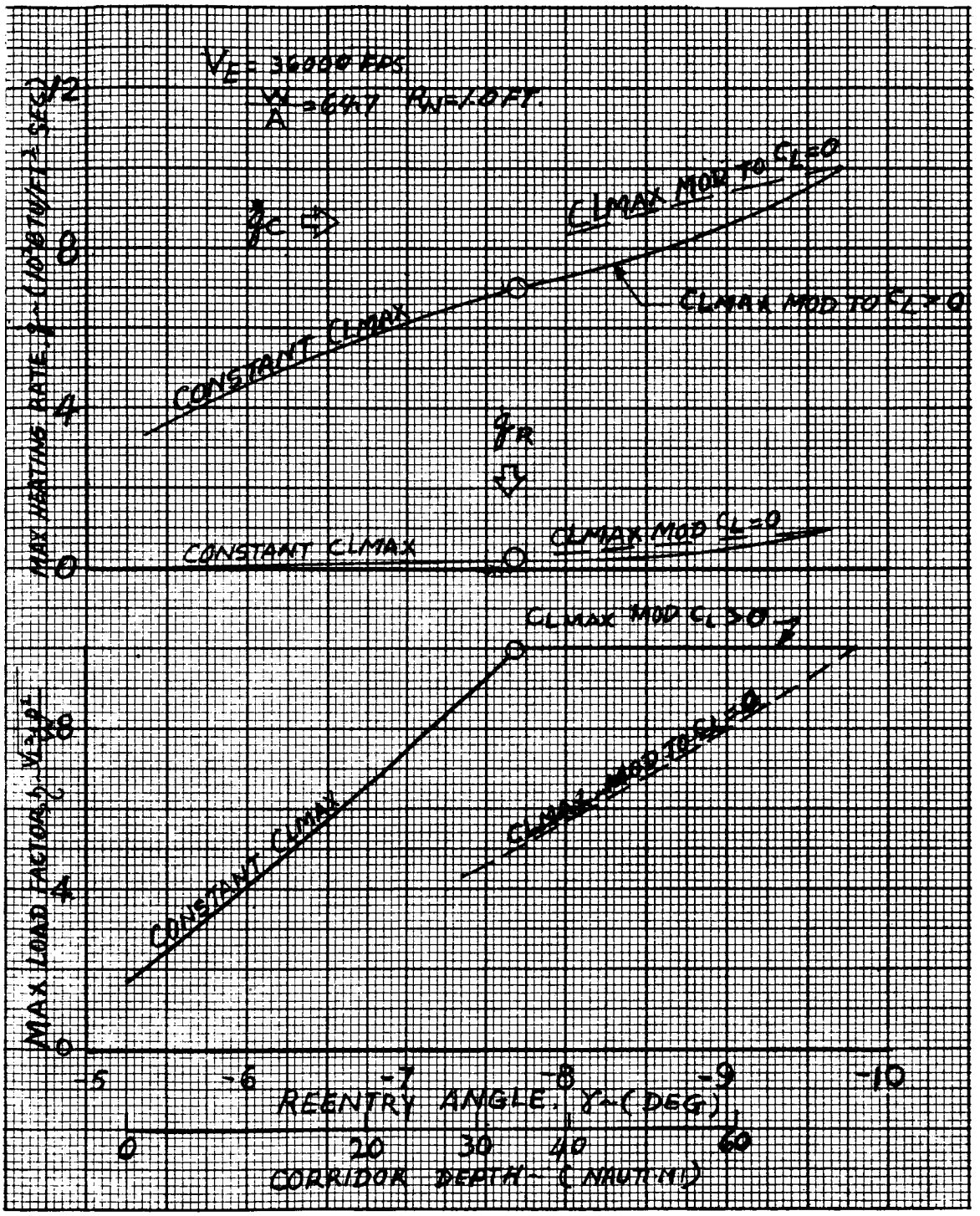

Fig. IV-34. L-1 Maximum Heating Rate and Load Factor Versus Corridor Depth

D-3 (6-60)

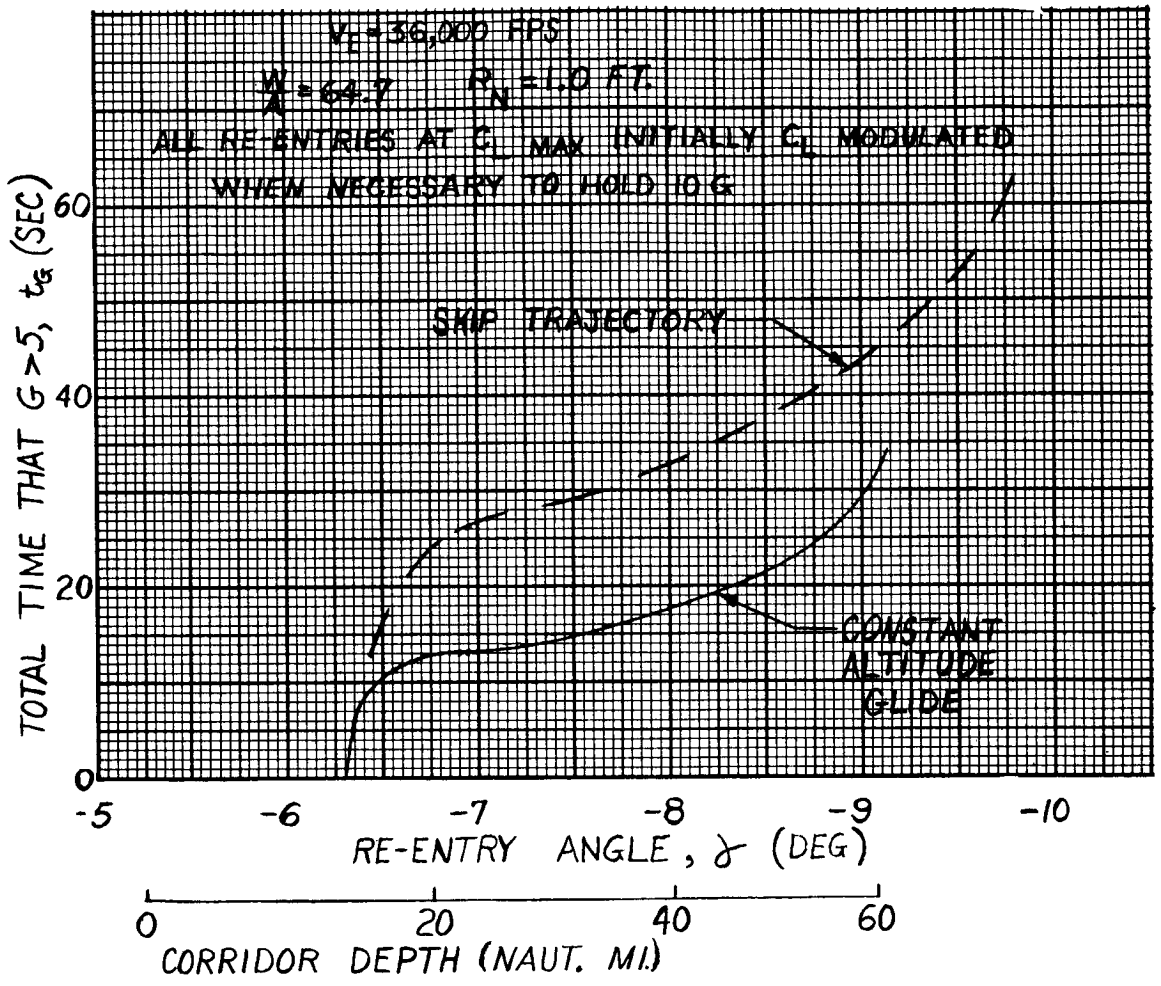

Fig. IV-35. L-1 G Duration Versus Corridor Depth

D-3 (6.60)

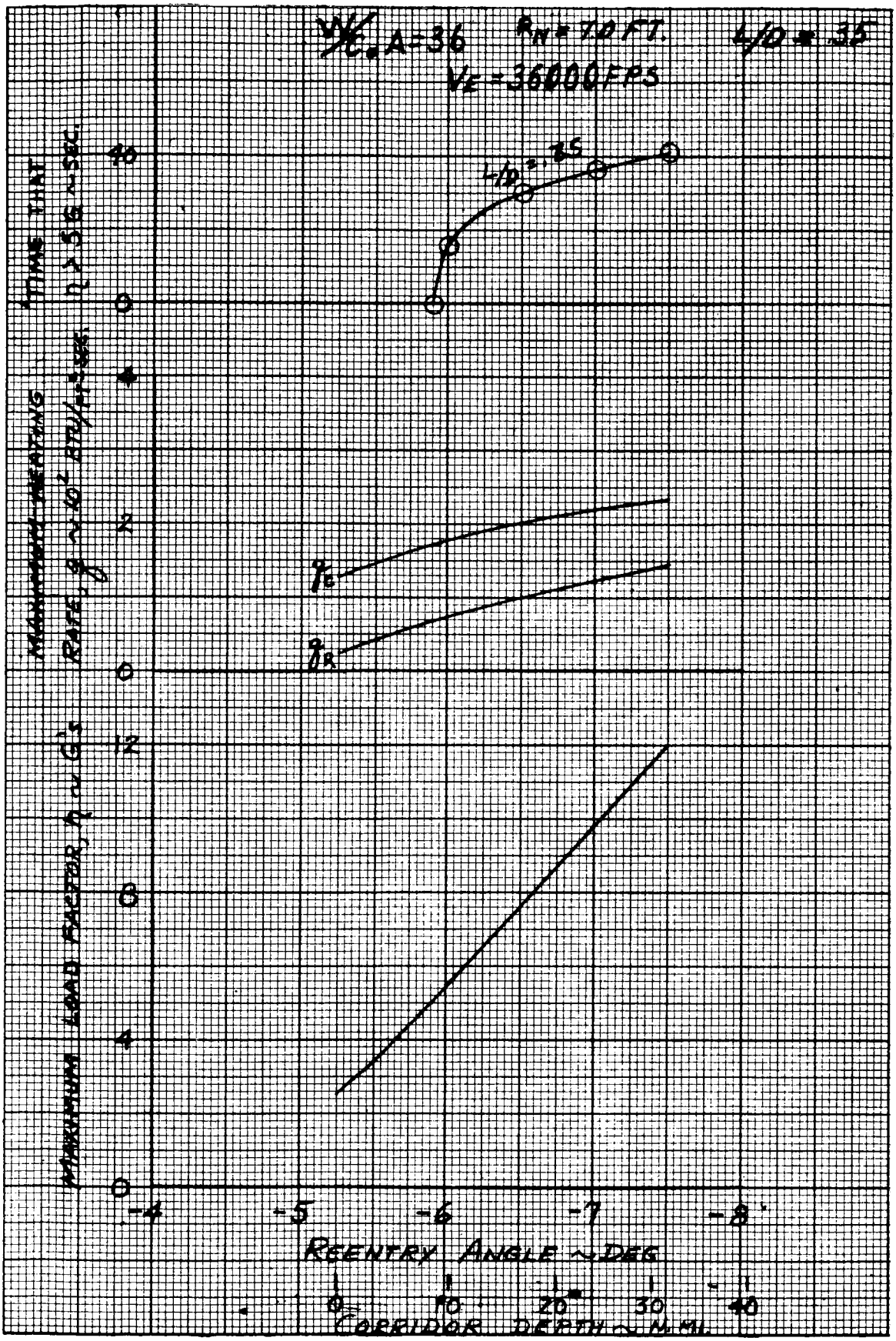

Fig. IV-36. Mercury Re-entry Vehicle Maximum Heating Rate and Load Factor Versus Corridor Depth

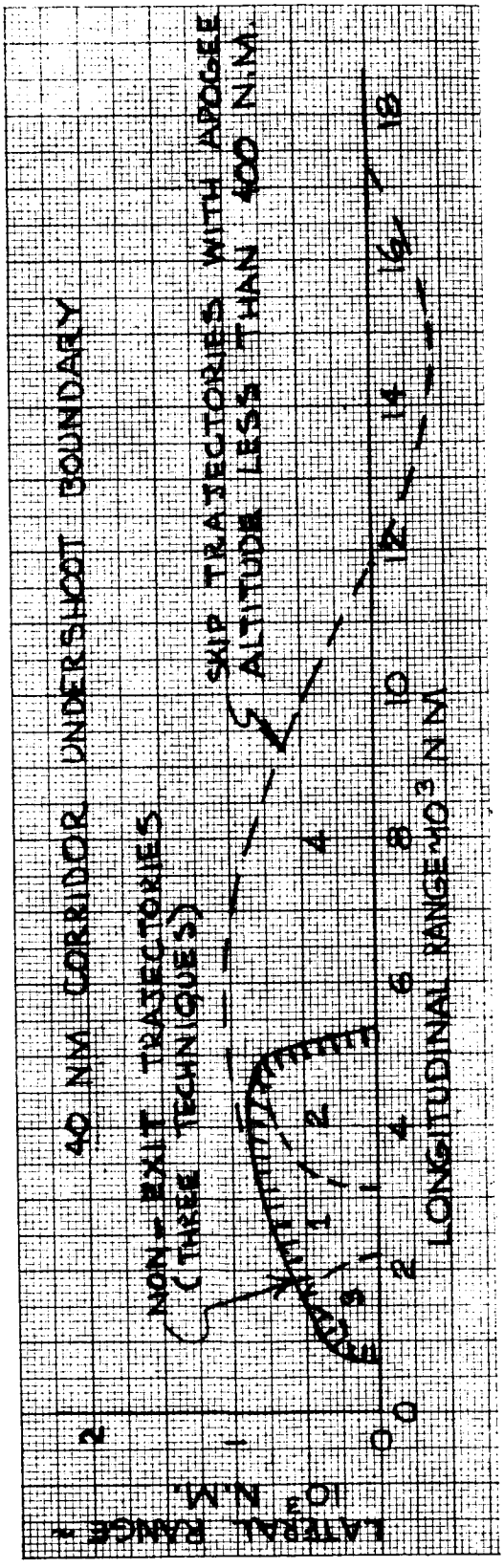

Fig. IV-37. Undershoot Boundary Maneuvering Envelope

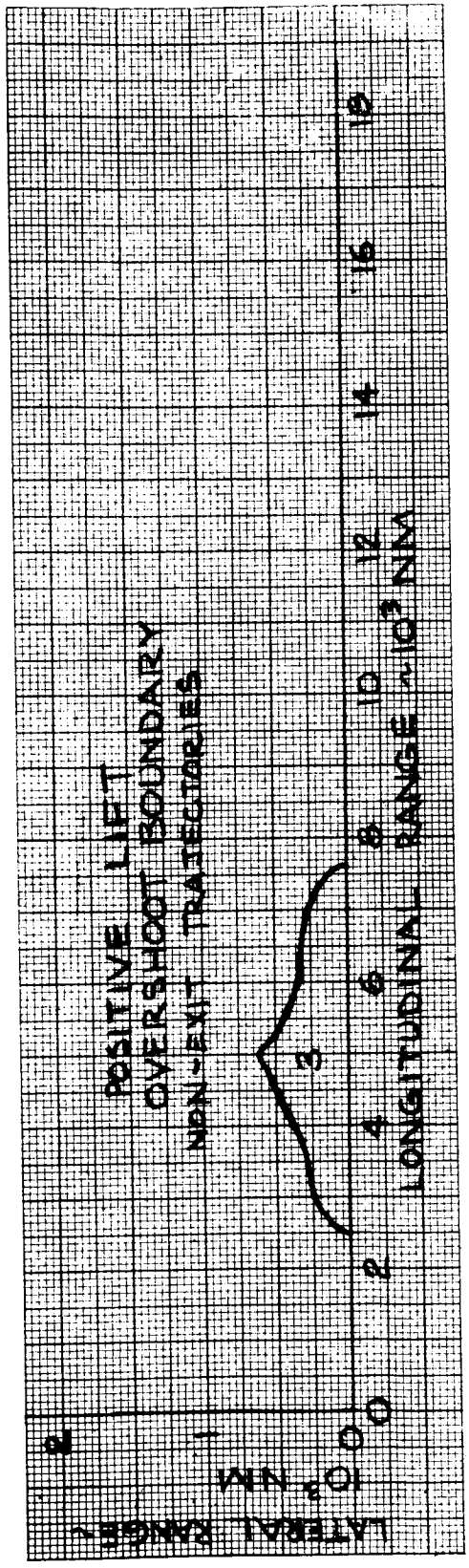

Fig. IV-38. Overshoot Boundary Maneuvering Envelope

CONFIDENTIAL

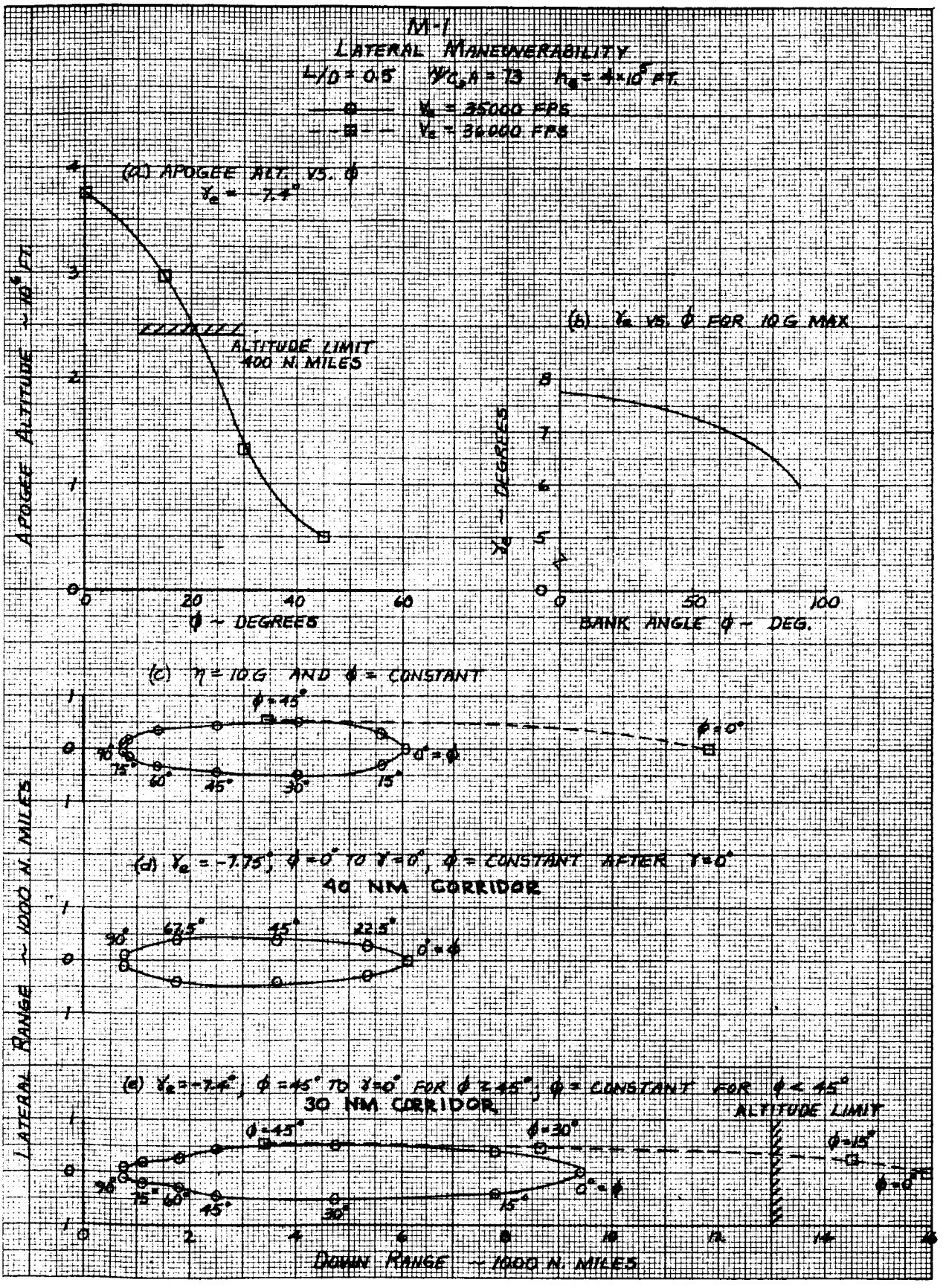

Fig. IV-39. M-1 Maneuver Capability

CONFIDENTIAL

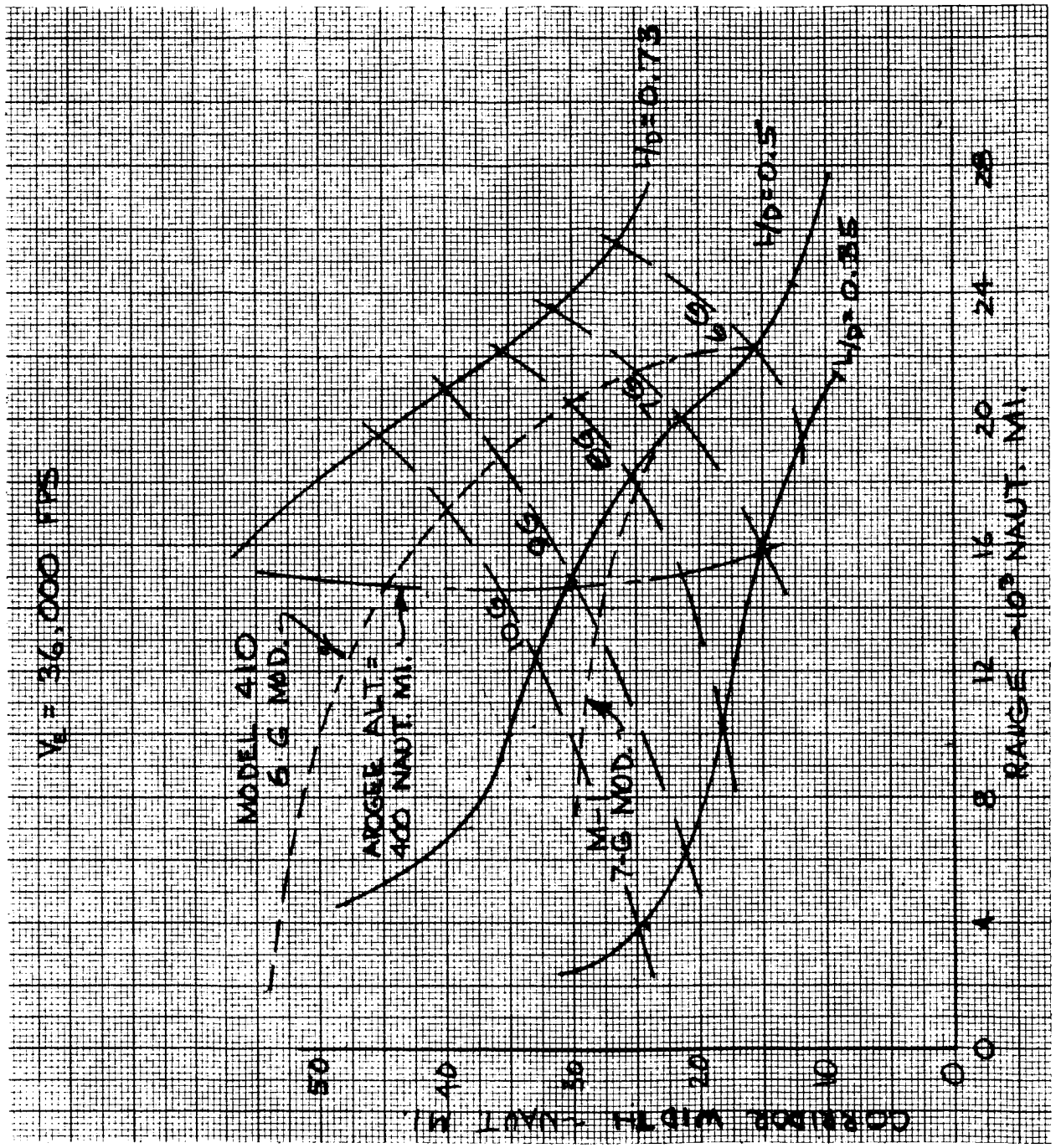

Fig. IV-40. Re-entry Performance

~~CONFIDENTIAL~~

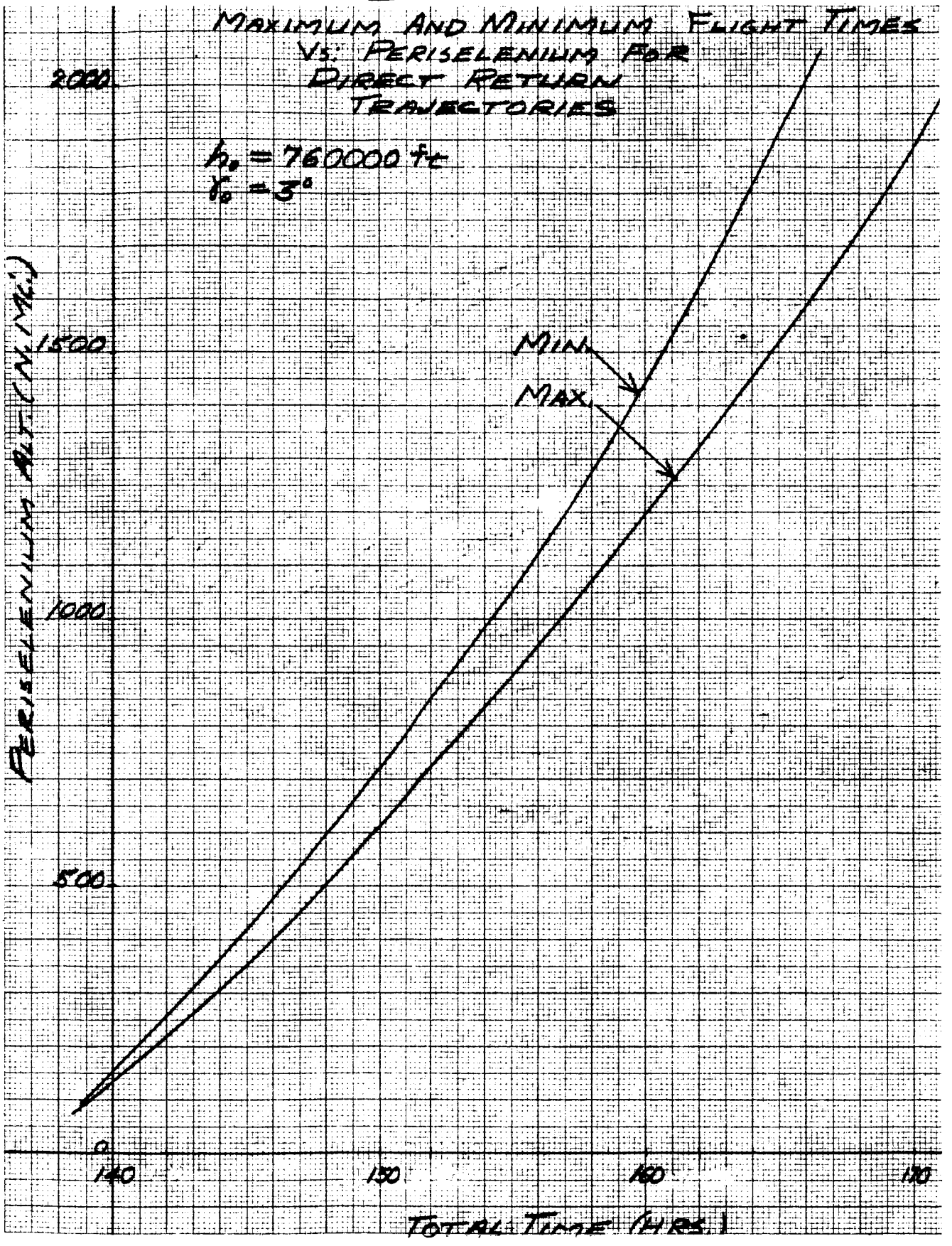

Fig. V-1. Total Flight Time Versus Periselenium Altitude

D-3 (6-60)

CONFIDENTIAL

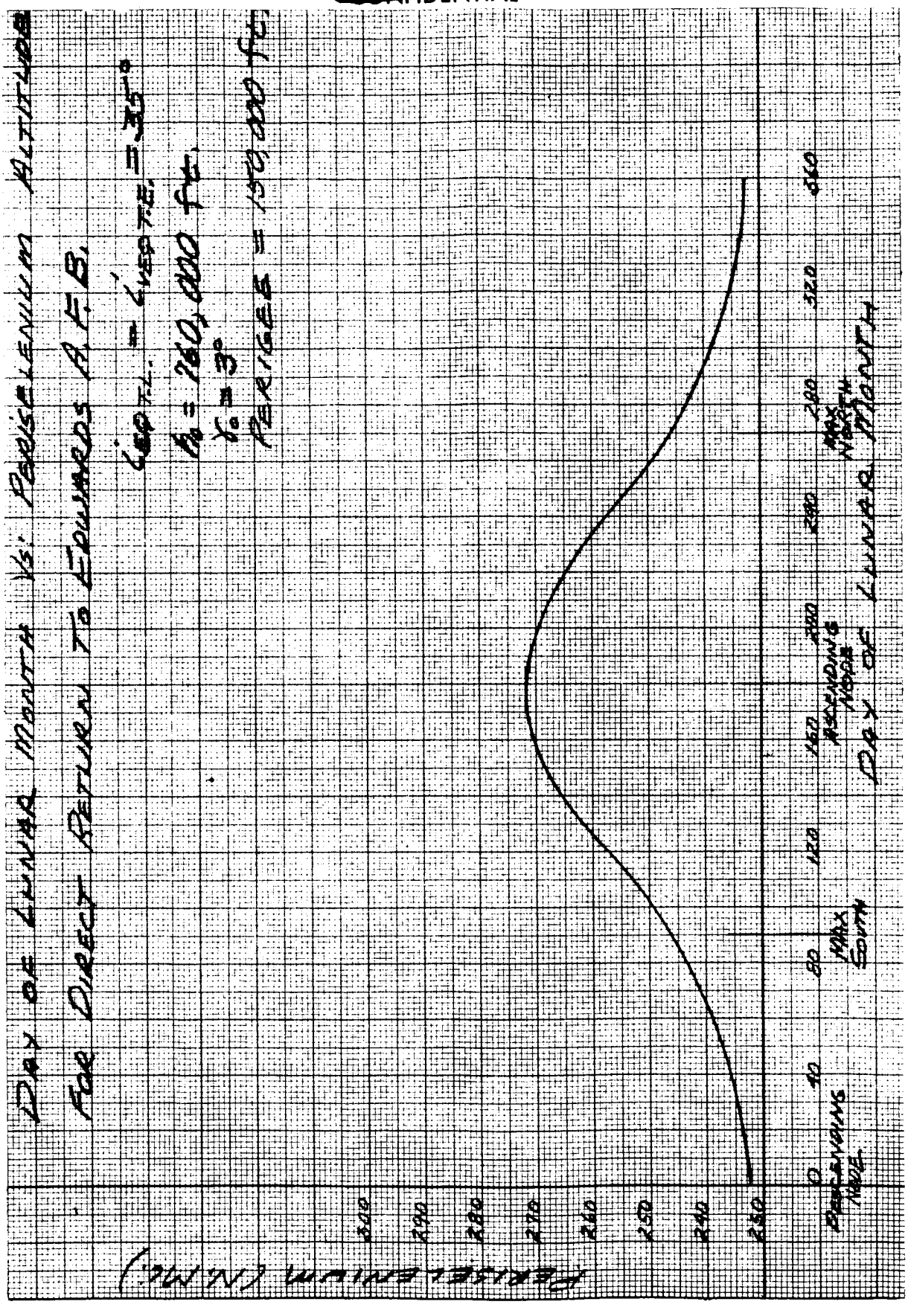

Fig. V-2. Required Periselenium Altitude Versus Day of Lunar Month

CONFIDENTIAL

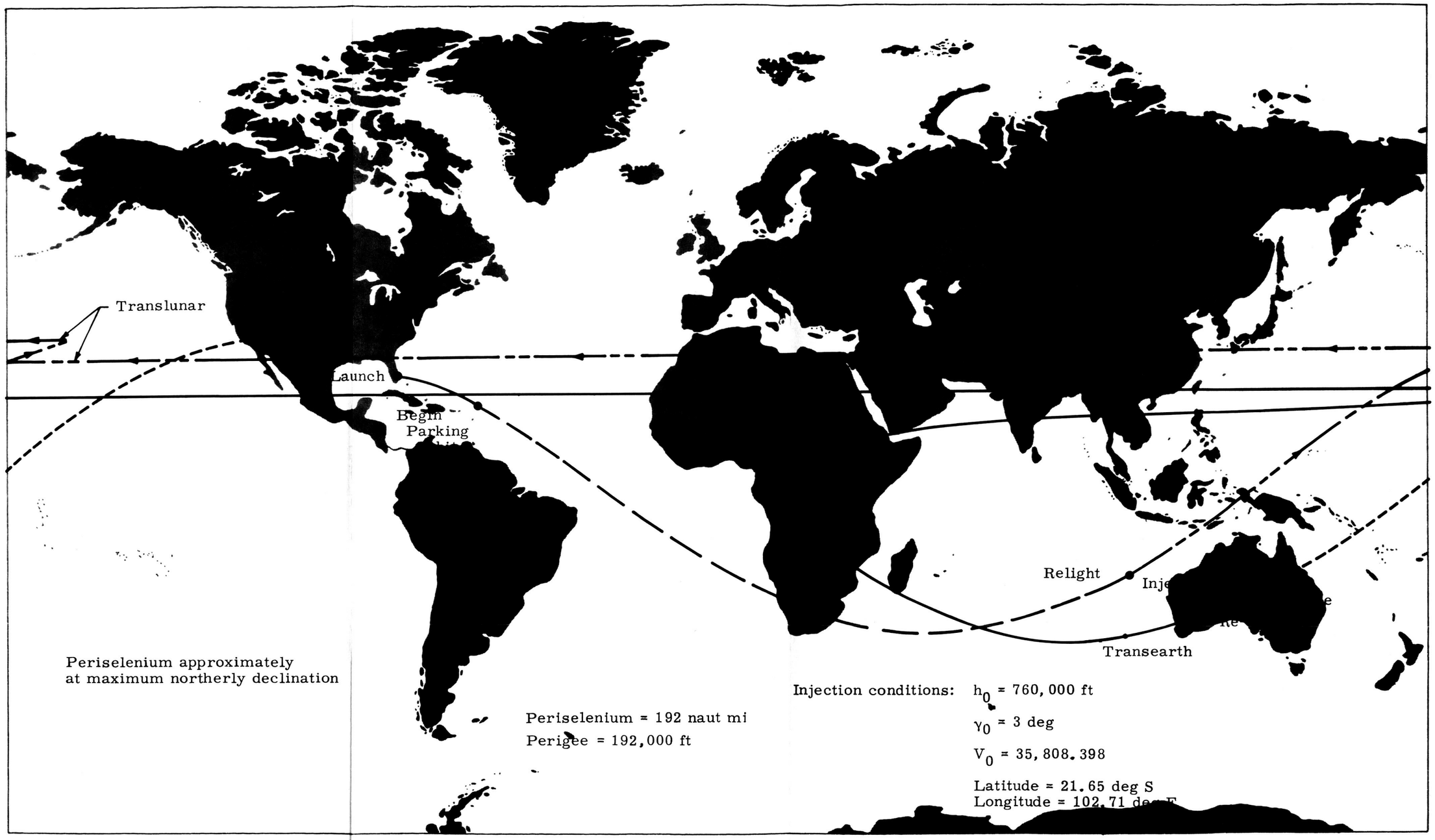

Fig. V-4. Ground Trace for Typical Operational Trajectory

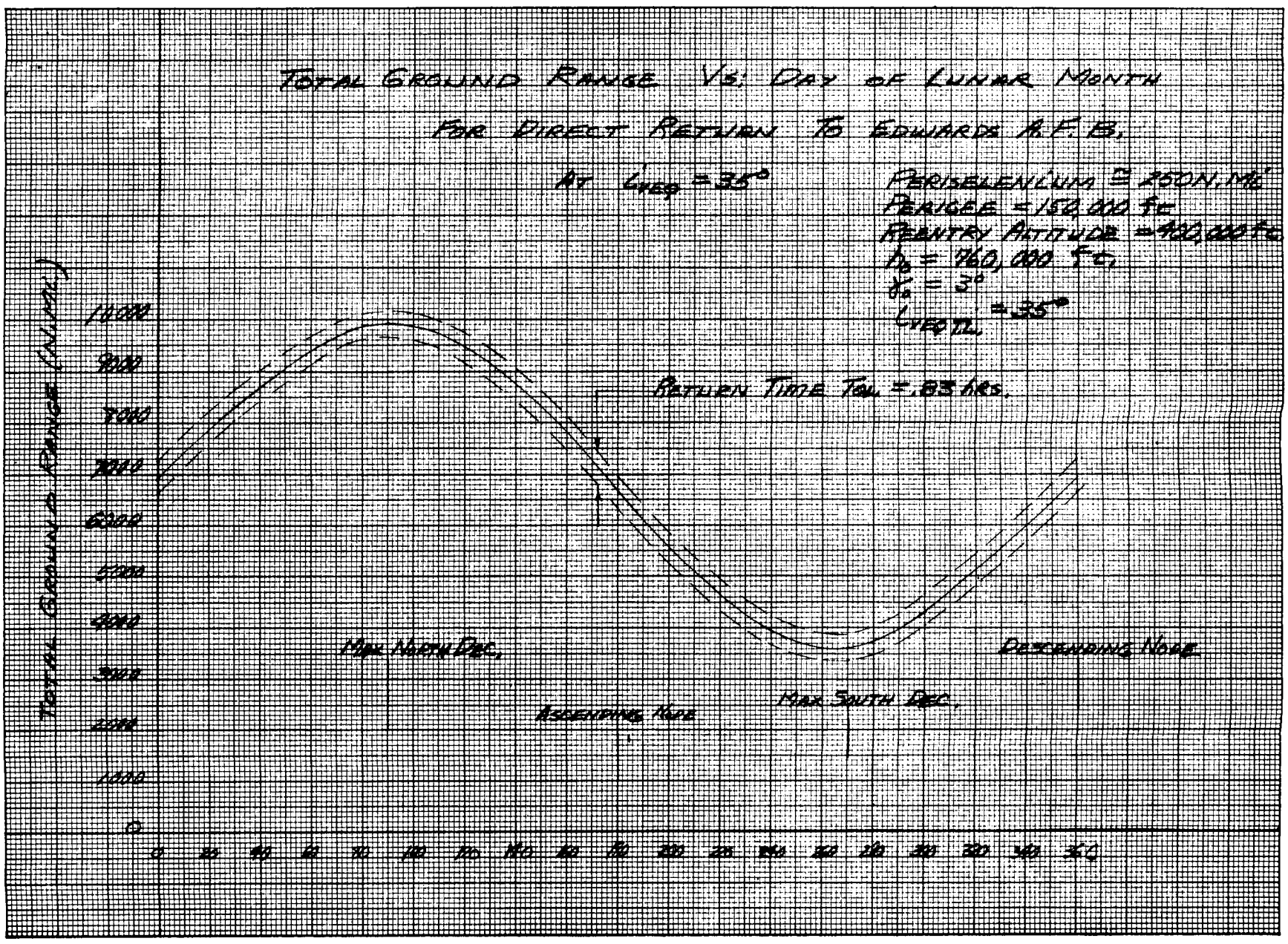

Fig. V-3. Range to Edwards AFB from Re-entry

CONFIDENTIAL
ER 12003

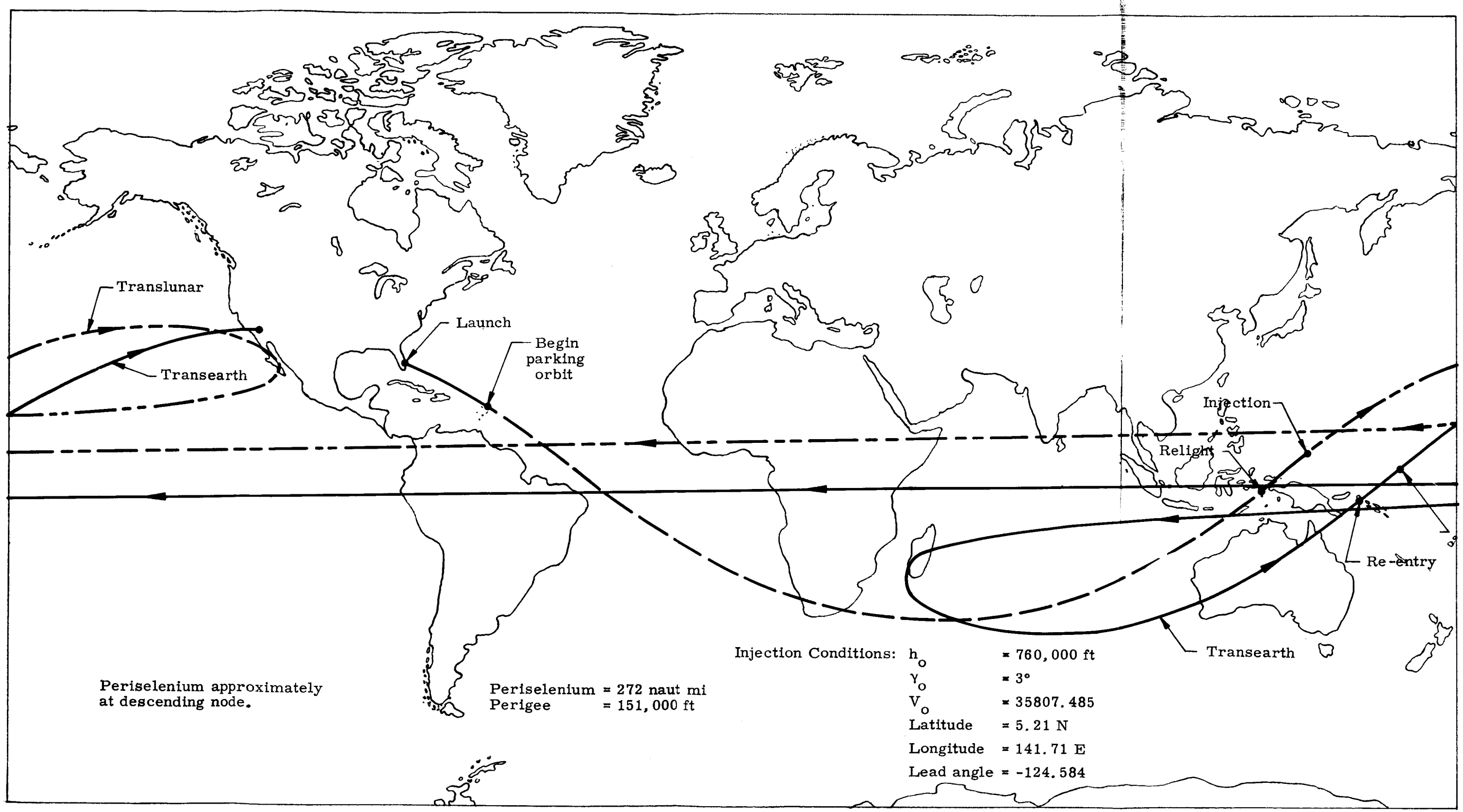

Fig. V-5. Ground Trace for Typical Operational Trajectory

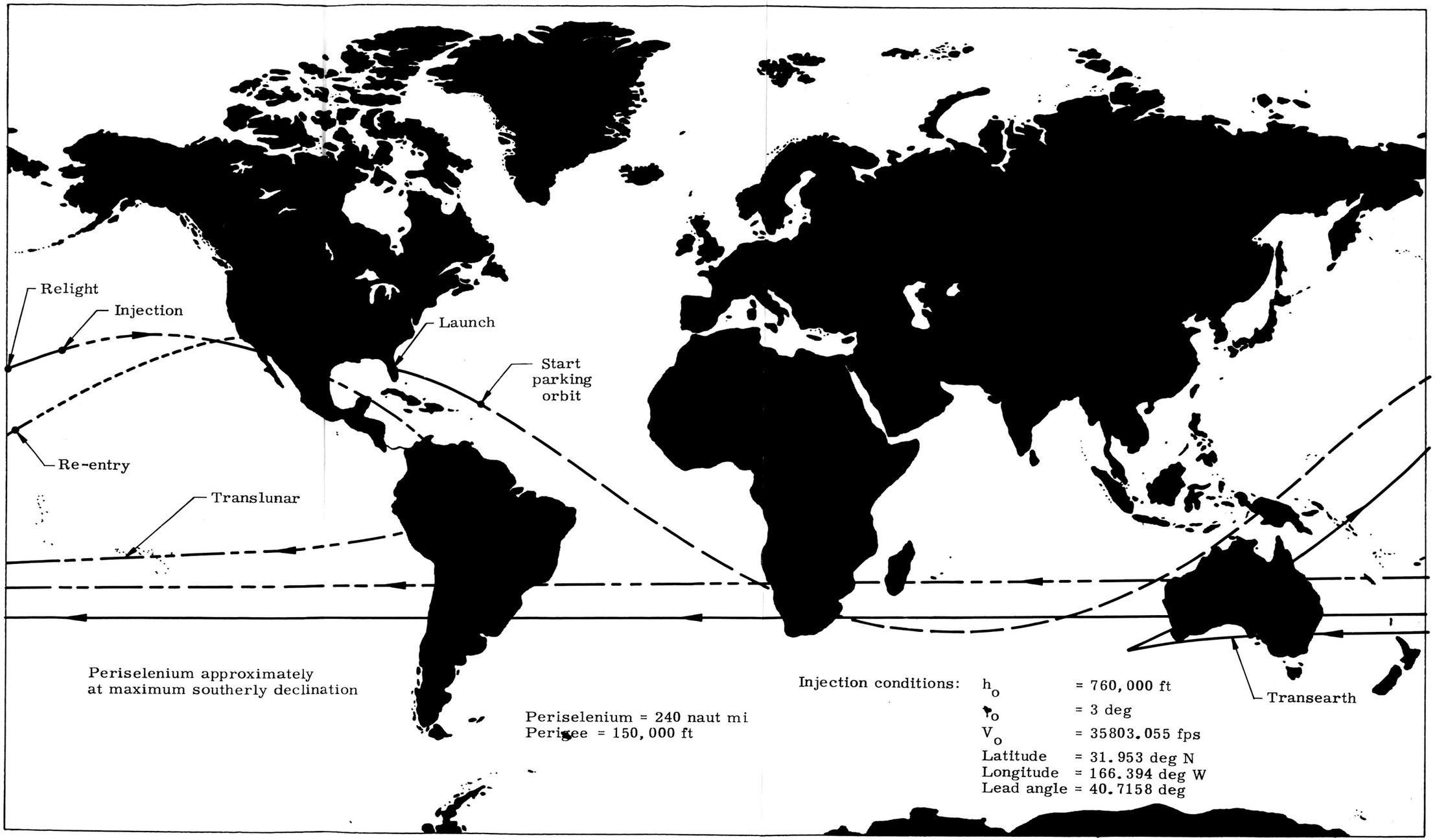

Fig. V-6. Ground Trace for Typical Operational Trajectory

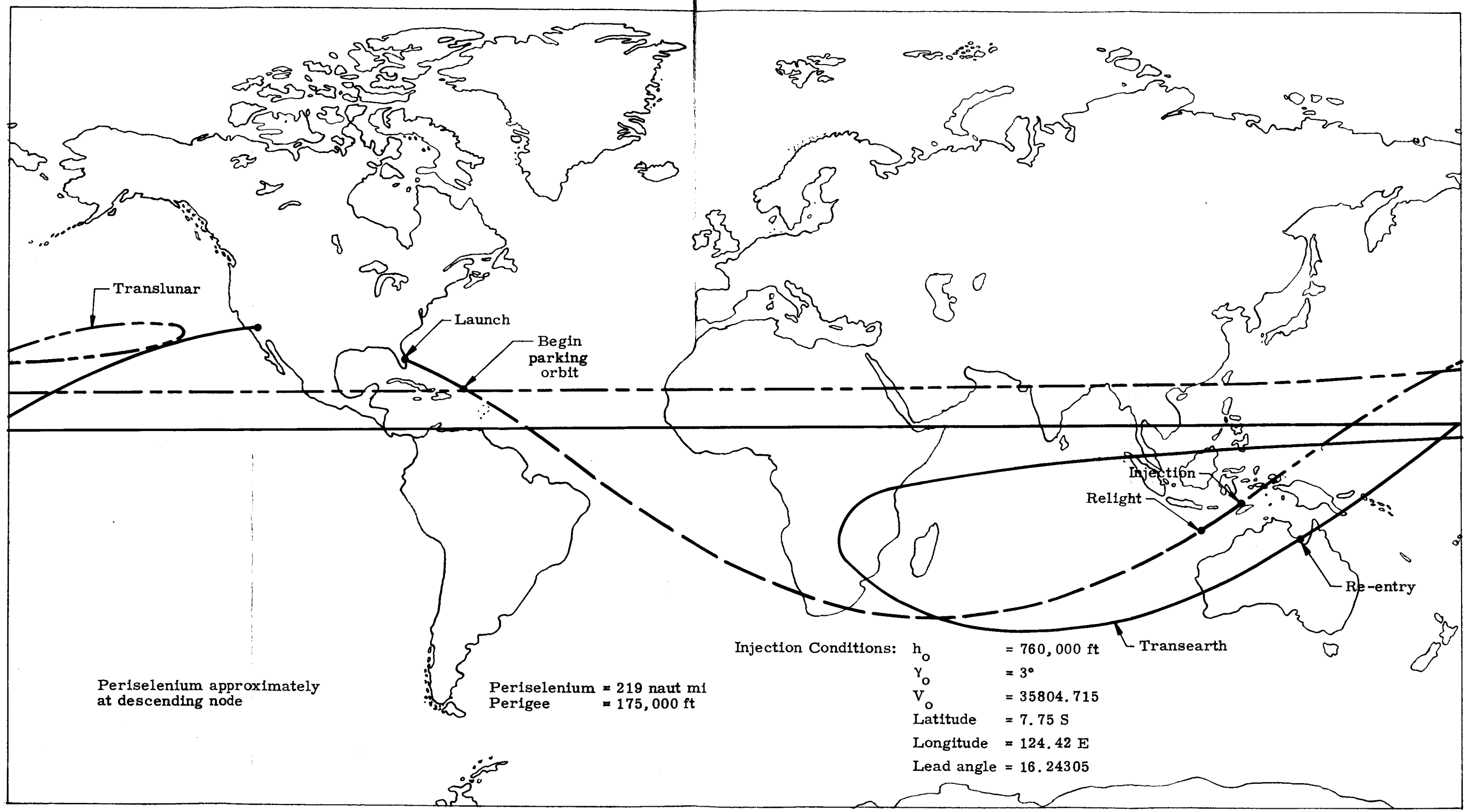

Fig. V-7. Ground Trace for Typical Operational Trajectory

APPENDIX A

EQUATIONS FOR VOLUME OF INFLUENCE TO APPROXIMATE LUNAR TRAJECTORY

The equations used in the volume of influence study are presented along with the equations required to interpret the results of the general lunar trajectory in actual latitude and longitudes of the injection point on a parking orbit originating at Cape Canaveral. The latitude and longitudes of the trans-earth trajectory perigee point on a rotating earth are also determined, as well as the continuation of this trajectory to the return base latitude.

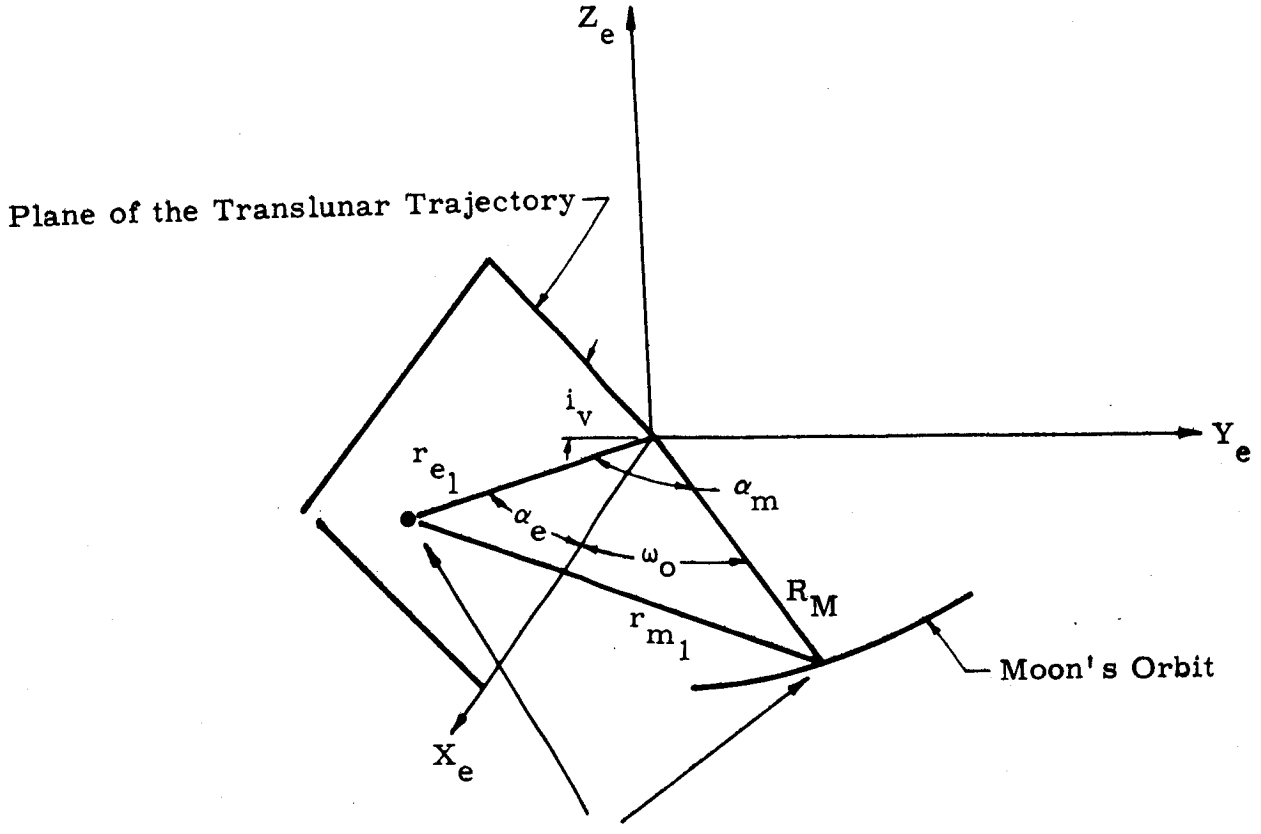

Volume of influence defined by:

$$\frac{r_m}{r_e} = k \tag{A-1}$$

$$\frac{R_M}{r_{e_1}} = \cos \alpha_M \pm \sqrt{\cos^2 \alpha_M - (1 - k^2)} \tag{A-2}$$

Where the (+) sign is used for penetrations on the earth-side of the volume of influence

$$r_{m_1} = k r_{e_1} \tag{A-3}$$

$$\cos \alpha_M = \cos \alpha_e \cos \omega_o - \sin \alpha_e \sin \omega_o \cos \iota_{V_{TL}} \tag{A-3a}$$

$$\begin{aligned} \tilde{r}_{e_1 x_e} &= r_{e_1} \cos \alpha_e \\ r_{e_1 y_e} &= - \tilde{r}_{e_1} \sin \alpha_e \cos \iota_{V_{TL}} \\ \tilde{r}_{e_1 z_e} &= \tilde{r}_{e_1} \sin \alpha_e \sin \iota_{V_{TL}} \end{aligned} \tag{A-4}$$

$$\begin{aligned} \tilde{r}_{m_1 x_e} &= - R_M \cos \omega_o + \tilde{r}_{e_1 x_e} \\ \tilde{r}_{m_1 y_e} &= - R_M \sin \omega_o + \tilde{r}_{e_1 y_e} \\ \tilde{r}_{m_1 z_e} &= \tilde{r}_{e_1 z_e} \end{aligned} \tag{A-5}$$

Using: $V_{se}^2 = \frac{\mu_e}{r_{e_1}}$ $\quad \mu_e = GM = g_o R_o^2$

$$1 - e_e^2 = \left(\frac{V_e}{V_{se}}\right)^2 \left[2 - \left(\frac{V_{e_1}}{V_{se}}\right)^2\right] \cos^2 \gamma_{e_1}$$

$$a = \frac{r_{e_1}}{2 - \left(\frac{V_{e_1}}{V_{se}}\right)^2} \tag{A-6}$$

for some initial V_o, r_o, γ_o, the conditions at the volume of influence. V_{e_1} r_{e_1} and γ_{e_1}, can be evaluated.

Defining: $\beta = 90^\circ - \gamma_{e_1} - \alpha_e$

$$\begin{aligned} V_{e_1 x_e} &= V_{e_1} \cos\beta \\ V_{e_1 y_e} &= V_{e_1} \sin\beta \cos i_{V_{TL}} \\ V_{e_1 z_e} &= -V_{e_1} \sin\beta \sin i_{V_{TL}} \end{aligned} \tag{A-7}$$

$$\begin{aligned} V_{m_1 x_e} &= R_M \dot{w} \sin w_o + V_{e_1 x_e} \\ V_{m_1 y_e} &= -R_M \dot{w} \cos w_o + V_{e_1 y_e} \\ V_{m_1 z_e} &= V_{e_1 z_e} \end{aligned} \tag{A-8}$$

Having r_{m_1} Eq. (5) and V_{m_1} Eq. (8), γ_{m_1} can be determined:

$$\vec{V}_{m_1} \cdot \vec{r}_{m_1} = V_{m_1} r_{m_1} \sin\gamma_{m_1} = V_{m_1 x_e} r_{m_1 x_e} + V_{m_1 y_e} r_{m_1 y_e} + V_{m_1 z_e} r_{m_1 z_e} \tag{A-9}$$

Using

$$r_{m_1} = \frac{P_m}{1 + e_m \cos\theta_{m_1}} \tag{A-10a}$$

$$P_m = r_{m_1}\left(\frac{V_{m_1}}{V_{sm_1}}\right)^2 \cos^2\gamma_{m_1} \qquad : \quad V_{sm_1}^2 = \frac{\mu_m}{r_{m_1}}$$

$$1 - \epsilon_m^2 = \left(\frac{V_{m_1}}{V_{sm_1}}\right)^2\left[2 - \left(\frac{V_{m_1}}{V_{sm_1}}\right)^2\right]\cos^2\gamma_{m_1} \qquad \text{(A-10b)}$$

the periselenium altitude and range angle (θ_{mp}) from the point of entry into the volume of influence to periselenium can be determined.

With the total range angle from the entry point to the leaving point on the volume of influence being defined as θ_{mc} (not yet determined), Eq (A-10) can be used to determine V_{m_2}, γ_{m_2} and r_{m_2}. The time of flight through the volume of influence can be determined from:

$$t_{(\theta)} = \left(\frac{C}{\epsilon_m^2 - 1}\right)\left\{\tan\gamma_m - \frac{1}{\sqrt{\epsilon_m^2 - 1}}\tanh^{-1}\left(\frac{\sqrt{\epsilon_m^2 - 1}\,\sin\theta_m}{\epsilon_m + \cos\theta_m}\right)\right\}$$

Where:
$$C = \left(\frac{r_{m_1}}{V_{sm_1}}\right)\left(\frac{V_{m_1}}{V_{sm_1}}\right)^3 \cos^3\gamma_{m_1}$$

(A-11)

$$\tanh^{-1}\left(\frac{\sqrt{\epsilon_m^2 - 1}\,\sin\theta_m}{\epsilon_m + \cos\theta_m}\right) = \frac{1}{2}\ln\left[\frac{\epsilon_m + \cos\theta_m + \sqrt{\epsilon_m^2 - 1}\,\sin\theta_m}{\epsilon_m + \cos\theta_m - \sqrt{\epsilon_m^2 - 1}\,\sin\theta_m}\right]$$

Where the time from entry to periselenium is obtained using $\theta_m = \theta_{m_p}$ and $\gamma_m = -\gamma_{m_1}$, and the time from periselenium to exit is obtained using $\theta_m = (\theta_{m_c} - \theta_{m_p})$ and $\gamma_m = \gamma_{m_2}$. The total time of flight through the volume of influence (t_{m_c}) is the sum of the two.

An axis transformation from the earth-centered axes (x_e, y_e, z_e) to a moon-centered axis system (x_m, y_m, z_m) whose x_m, y_m axes lie in the plane of flight around the moon and travel with the moon during the time (t_{m_c}) must be made before the vehicle position relative to x_e, y_e, z_e axes at the exit position can be determined.

Using the cosine matrices:

$$\begin{vmatrix} l_1 & m_1 & n_1 \\ l_2 & m_2 & n_2 \\ l_3 & m_3 & n_3 \end{vmatrix} \begin{Bmatrix} x_c \\ y_e \\ z_e \end{Bmatrix} = \begin{Bmatrix} x_m \\ y_m \\ z_m \end{Bmatrix}$$

and (A-12)

$$\begin{vmatrix} \lambda_1 & \mu_1 & \nu_1 \\ \lambda_2 & \mu_2 & \nu_2 \\ \lambda_3 & \mu_3 & \nu_3 \end{vmatrix} \begin{Bmatrix} x_m \\ y_m \\ z_m \end{Bmatrix} = \begin{Bmatrix} x_e \\ y_e \\ z_e \end{Bmatrix}$$

$$l_1 = \lambda_1 = \cos\eta_1 \cos\eta_2 \qquad m_1 = \lambda_2 = \sin\eta_1 \cos\eta_2$$

$$l_2 = \mu_1 = -\sin\eta_1 \qquad m_2 = \mu_2 = \cos\eta_1 \qquad \text{(A-13)}$$

$$l_3 = \nu_1 = \cos\eta_1 \sin\eta_2 \qquad m_3 = \nu_2 = \sin\eta_1 \sin\eta_2$$

$$n_1 = \lambda_3 = -\sin\eta_2$$

$$n_2 = \mu_3 = 0$$

$$n_3 = \nu_3 = \cos\eta_2$$

Axis Transformation Geometry

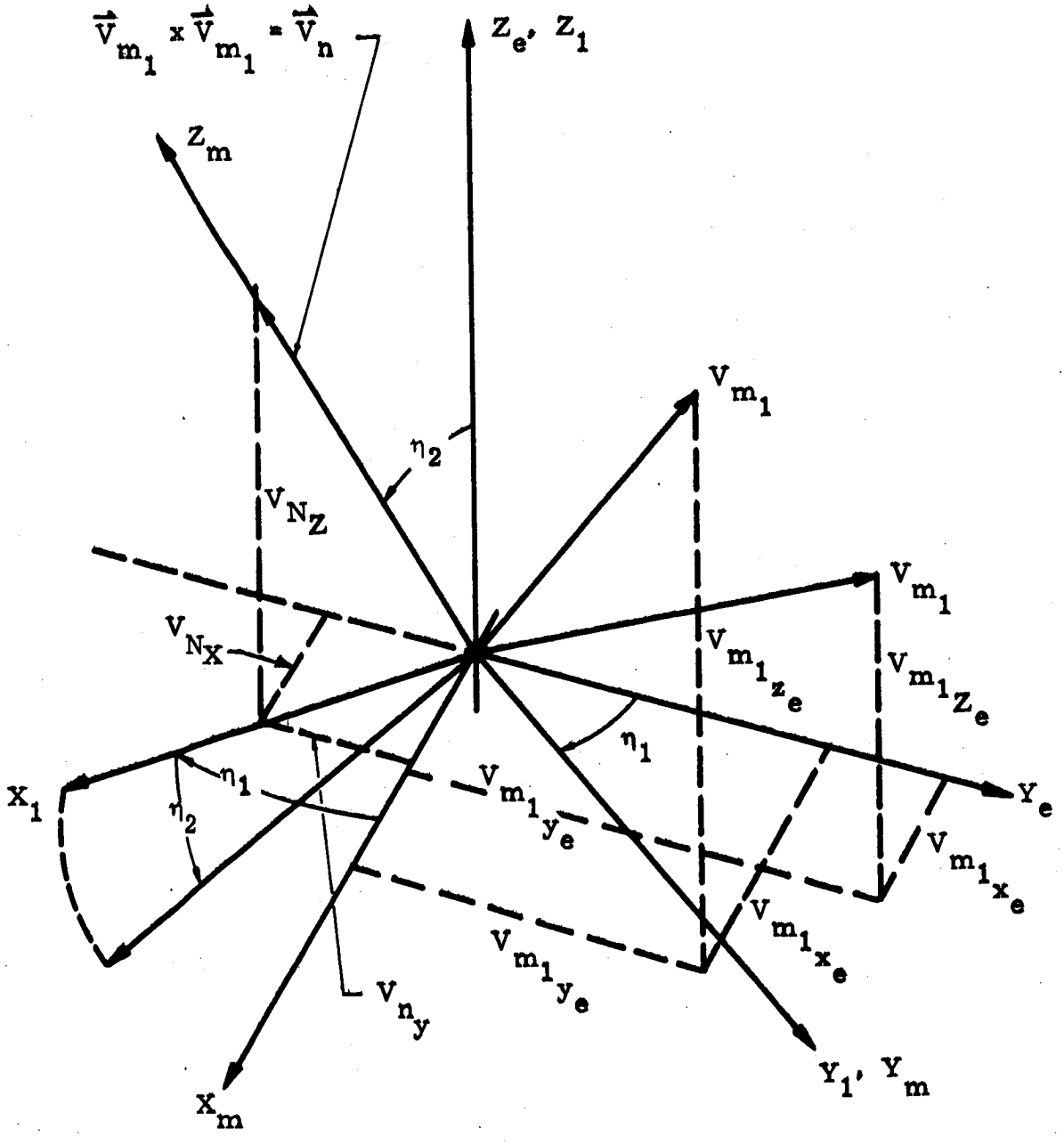

First Rotation: η_1 deg about Z_e-axis. (Note: Negative rotation is shown).

Second Rotation: η_2 deg about Y_1- axis.

$$\vec{V}_{m_1} \times \vec{r}_{m_1} = V_N \vec{1}_N = (V_{m_1 y_e} r_{m_1 z_e} - V_{m_1 z_e} r_{m_1 y_e})\vec{i} +$$
$$+ (V_{m_1 z_e} r_{m_1 x_e} - V_{m_1 x_e} r_{m_1 z_e})\vec{j} +$$
$$+ (V_{m_1 x_e} r_{m_1 y_e} - V_{m_1 y_e} r_{m_1 x_e})\vec{k}$$

where $\vec{i}$, $\vec{j}$ & $\vec{k}$ are unit vectors in the x_e, y_e & z_e directions.

$$V_{N_x} = (V_{m_1 y_e} r_{m_1 z_e} - V_{m_1 z_e} r_{m_1 y_e})$$

$$V_{N_y} = (V_{m_1 z_e} r_{m_1 x_e} - V_{m_1 x_e} r_{m_1 z_e})$$

$$V_{N_z} = (V_{m_1 x_e} r_{m_1 y_e} - V_{m_1 y_e} r_{m_1 x_e})$$

$$\therefore \cos \eta_1 = \frac{V_{N_x}}{\sqrt{V_{N_x}^2 + V_{N_y}^2}} \qquad \cos \eta_2 = \frac{V_{N_z}}{V_N}$$

$$\sin \eta_1 = \frac{V_{N_y}}{\sqrt{V_{N_x}^2 + V_{N_y}^2}} \qquad \sin \eta_2 = \frac{\sqrt{V_{N_x}^2 + V_{N_y}^2}}{V_N}$$

Then, in the moon axis systems

$$r_{m_1 x_m} = r_{m_1 x_e} l_1 + r_{m_1 y_e} m_1 + r_{m_1 z_e} n_1$$

$$r_{m_1 y_m} = r_{m_1 x_e} l_2 + r_{m_1 y_e} m_2 + r_{m_1 z_e} n_2 \qquad \text{(A-14)}$$

$$r_{m_1 z_m} = r_{m_1 x_e} l_3 + r_{m_1 y_e} m_3 + r_{m_1 z_e} n_3$$

$$
\begin{aligned}
V_{m_1 x_m} &= V_{m_1 x_e}\, l_1 + V_{m_1 y_e}\, m_1 + V_{m_1 z_e}\, n_1 \\
V_{m_1 y_m} &= V_{m_1 x_e}\, l_2 + V_{m_1 y_e}\, m_2 + V_{m_1 z_e}\, n_2 \\
V_{m_1 z_m} &= V_{m_1 x_e}\, l_3 + V_{m_1 z_e}\, m_3 + V_{m_1 z_e}\, n_3
\end{aligned}
\qquad \text{(A-15)}
$$

It is important to know if the vehicle passed behind the moon or in front of it. The angle ρ_m is defined as the angle in the x_m, y_m plane between the r_{m_1}, vector and the x_m-axis.

$$
\rho_m = \tan^{-1}\left(\frac{r_{m_1 y_m}}{r_{m_1 x_m}}\right) \qquad \text{(A-16)}
$$

then:

$$
V_{m_1 x_m} \cos(90^\circ - \rho_m) - V_{m_1 y_m} \sin(90 - \rho_m) \begin{cases} > 0 & \text{CASE I} \\ < 0 & \text{CASE II} \end{cases} \qquad \text{(A-17)}
$$

Case I: Vehicle passes behind moon.
Case II: Vehicle passes in front of moon.

The exit position and velocity, as a function of θ_{m_c}, become:

Case I:

$$
\begin{aligned}
r_{m_2 x_m} &= r_{m_2} \cos(\theta_{m_c} - \rho_m) \\
r_{m_2 y_m} &= -r_{m_2} \sin(\theta_{m_c} - \rho_m) \\
r_{m_2 z_m} &= 0
\end{aligned}
\qquad \text{(A-18)}
$$

$$V_{m_{2x_m}} = -V_{m_2} \sin\left[(\theta_{m_c} - \rho_m) - \gamma_{m_2}\right]$$
$$V_{m_{2y_m}} = -V_{m_2} \cos\left[(\theta_{m_c} - \rho_m) - \gamma_{m_2}\right] \qquad \text{(A-19)}$$

Case II:

$$r_{m_{2x_m}} = r_{m_2} \cos(\theta_{m_c} + \rho_m)$$
$$r_{m_{2y_m}} = r_{m_2} \sin(\theta_{m_c} + \rho_m) \qquad \text{(A-20)}$$

$$V_{m_{2x_m}} = -V_{m_2} \sin\left[(\theta_{m_c} + \rho_m) - \gamma_{m_2}\right]$$
$$V_{m_{2y_m}} = V_{m_2} \cos\left[(\theta_{m_c} + \rho_m) - \gamma_{m_2}\right] \qquad \text{(A-21)}$$

Depending upon the case

$$r_{m_{2x_e}} = r_{m_{2x_m}} \lambda_1 + r_{m_{2y_m}} \mu_1$$
$$r_{m_{2y_e}} = r_{m_{2x_m}} \lambda_2 + r_{m_{2y_m}} \mu_2 \qquad \text{(A-22)}$$
$$r_{m_{2z_e}} = r_{m_{2x_m}} \lambda_3 + r_{m_{2y_m}} \mu_3$$

} Components of r_{m_2} and V_{m_2} in the earth-centered axis system (x_e, y_e, z_e)

$$V_{m_{2x_e}} = V_{m_{2x_m}} \lambda_1 + V_{m_{2y_m}} \mu_1$$
$$V_{m_{2y_e}} = V_{m_{2x_m}} \lambda_2 + V_{m_{2y_m}} \mu_2 \qquad \text{(A-23)}$$
$$V_{m_{2z_e}} = V_{m_{2x_m}} \lambda_3 + V_{m_{2z_m}} \mu_3$$

$$
\begin{aligned}
r_{e_{z_{x_e}}} &= R_M \cos(\omega_o + \dot{\omega} t_{m_c}) + r_{m_{z_{x_e}}} \\
r_{e_{z_{y_e}}} &= R_m \sin(\omega_o + \dot{\omega} t_{m_c}) + r_{m_{z_{y_e}}} \\
r_{e_{z_{z_e}}} &= r_{m_{z_{z_e}}}
\end{aligned}
\qquad \text{(A-24)}
$$

$$
r_{e_z} = \sqrt{r_{e_{z_{x_e}}}^2 + r_{e_{z_{y_e}}}^2 + r_{e_{z_{z_e}}}^2} \qquad \text{(A-25)}
$$

$$
\begin{aligned}
V_{e_{z_{x_e}}} &= -\dot{\omega} R_M \sin(\omega_o + \dot{\omega} t_{m_c}) + V_{m_{z_{x_e}}} \\
V_{e_{z_{y_e}}} &= \dot{\omega} R_M \cos(\omega_o + \dot{\omega} t_{m_c}) + V_{m_{z_{y_e}}} \\
V_{c_{z_{z_e}}} &= V_{m_{z_{z_e}}}
\end{aligned}
\qquad \text{(A-26)}
$$

$$
V_{e_z} = \sqrt{V_{e_{z_{x_e}}}^2 + V_{e_{z_{y_e}}}^2 + V_{e_{z_{z_e}}}^2} \qquad \text{(A-27)}
$$

With r_{e_z} and r_{m_z} determined as a function of θ_{m_c}, ($\frac{r_{m_z}}{r_{e_z}}$) can be compared to the constant k to obtain the required θ_{m_c} to satisfy the required conditions at exit from the volume of influence.

1. Direction of Return Orbit

The calculations defining the direction of the return orbit will be clarified by using the following expressions:

defining:

$$N_{ex} = V_{e2ye} r_{e2ze} - V_{e2ze} r_{e2ye}$$

$$N_{ey} = V_{e2ze} r_{e2xe} - V_{e2xe} r_{e2ze}$$

$$N_{ey} = V_{e2xe} r_{e2ye} - V_{e2ye} r_{e2xe}$$

then:

$$\sin \omega_f = \frac{N_{ex}}{\sqrt{N_{ex}^2 + N_{ey}^2}}$$

$$\cos \omega_f = \frac{-N_{ey}}{\sqrt{N_{ex}^2 + N_{ey}^2}}$$

} quadrant of w_f determined from these two equations

$$\tan i_{V_{TE}} = \frac{\sqrt{N_{ex}^2 + N_{ey}^2}}{N_{ez}}$$

If $(-N_{ey})$ is positive, multiply $i_{V_{TE}}$ by minus one.

If $(-N_{ey})$ is negative:

$$\omega_f = \omega_{f\,CALC.} - 180^\circ$$

Then the direction of the return orbit will be:

Retrograde from north	$i_{V_{TE}}$	in first quadrant
Direct from north	$i_{V_{TE}}$	in second quadrant
Direct from south	$i_{V_{TE}}$	in third quadrant
Retrograde from south	$i_{V_{TE}}$	in fourth quadrant

also, with:

$$\tilde{r}_{\xi} = \tilde{r}_{e_{2x_e}} \cos\omega_f + \tilde{r}_{e_{2y_e}} \sin\omega_f$$

$$\tilde{r}_{\eta} = -\tilde{r}_{e_{2x_e}} \sin\omega_f \cos i_{V_{TE}} + \tilde{r}_{e_{2y_e}} \cos\omega_f \cos i_{V_{TE}} - \tilde{r}_{e_{2z_e}} \sin i_{V_{TE}}$$

$$\cos\alpha_{e_2} = \left(\frac{\tilde{r}_{\xi}}{\tilde{r}_{e_2}}\right)$$

$$\sin\alpha_{e_2} = \left(\frac{-\tilde{r}_{\eta}}{\tilde{r}_{e_2}}\right)$$

Quadrant determined from these two quantities

$$\theta_{o2} = \theta_2 + \alpha_{e_2} - 180^\circ$$

2. Latitude-Longitude Calculation

The following sketch introduces the new quantities which define the moon position relative to the equatorial plane and the latitude and longitude.

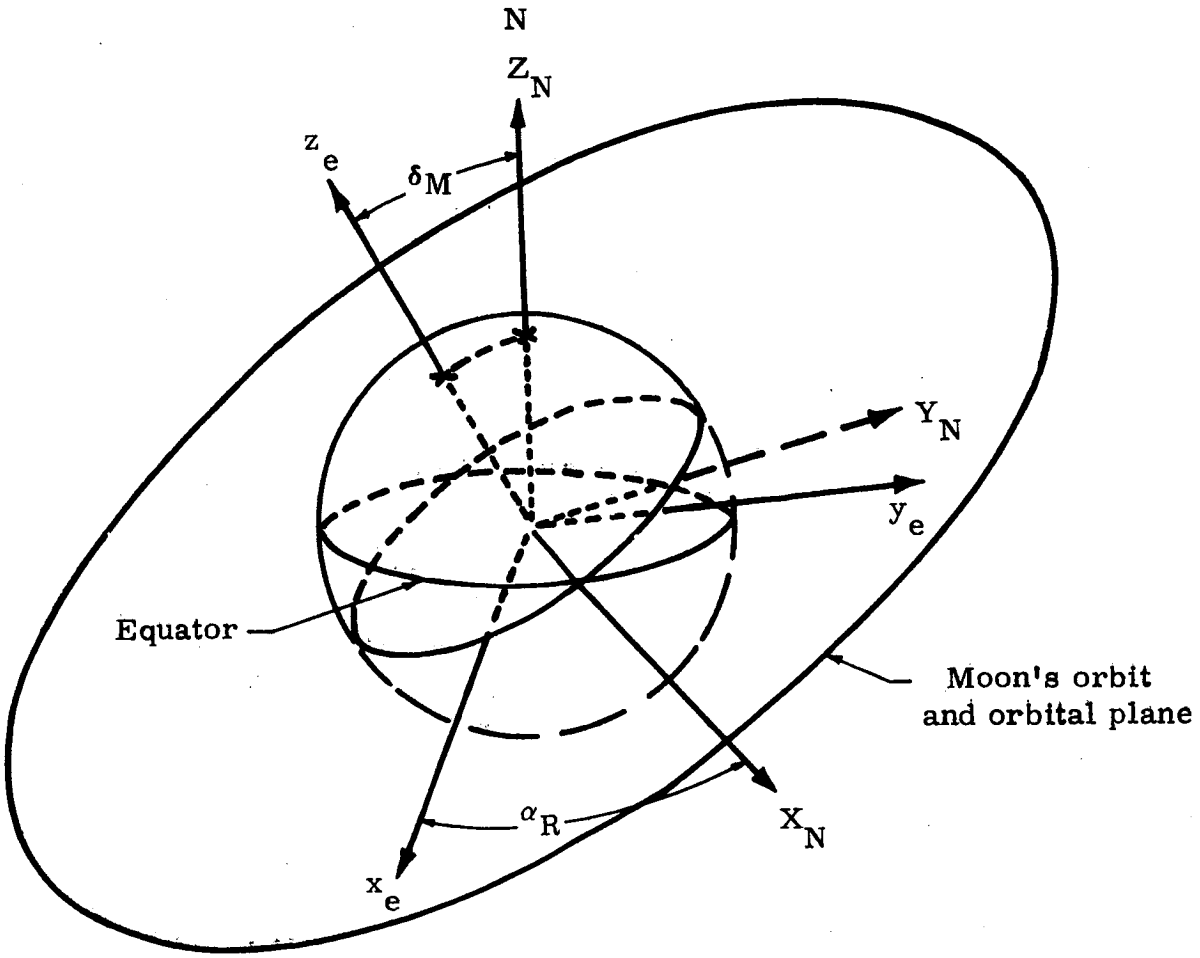

The X_e, Y_e, Z_e axis system is the same one used in previous calculations, with X_e, Y_e in the moon's orbital plane and Z_e normal to it. The X_N, Y_N axes lie in the equatorial plane with X_N along the intersection of the equatorial plane and the moon's orbital plane. The Z_N axis is along the true North direction, perpendicular to the equatorial plane.

CONFIDENTIAL

The cosine matrix relating the two axis systems is:

$$\begin{vmatrix} L_1 & M_1 & N_1 \\ L_2 & M_2 & N_2 \\ L_3 & M_3 & N_3 \end{vmatrix} \begin{Bmatrix} x_e \\ y_e \\ z_e \end{Bmatrix} = \begin{Bmatrix} x_N \\ y_N \\ z_N \end{Bmatrix}$$

where:

$L_1 = \cos x_R$ $\qquad$ $M_1 = \sin x_R$

$L_2 = -\sin x_R \cos \delta_M$ $\qquad$ $M_2 = \cos x_R \cos \delta_M$

$L_3 = \sin x_R \sin \delta_M$ $\qquad$ $M_3 = -\cos x_R \sin \delta_M$

$N_1 = 0$

$N_2 = \sin \delta_M$

$N_3 = \cos \delta_M$

The latitude and longitude of the injection point can be found with the following equations:

Available data: $h_0, V_{01}, \gamma_{01}, \theta_1', \theta_{01}, i_{V_{TE}}$

and $r_{01} = R_e + h_0$ $\qquad$ (R_0 = earth radius)

then:

$$V_{01_{x_e}} = V_{01} \sin (\theta_1' - \theta_{01} - \gamma_{01})$$

$$V_{01_{y_e}} = -V_{01} \cos (\theta_1' - \theta_{01} - \gamma_{01}) \cos i_{V_{TE}}$$

$$V_{01_{z_e}} = V_{01} \cos (\theta_1' - \theta_{01} - \gamma_{01}) \sin i_{V_{TE}}$$

CONFIDENTIAL

$$r_{01_{x_e}} = -r_{01} \cos(\theta_1' - \theta_{01})$$

$$r_{01_{y_e}} = -r_{01} \sin(\theta_1' - \theta_{01}) \cos i_{V_{TL}}$$

$$r_{01_{z_e}} = r_{01} \sin(\theta_1' - \theta_{01}) \sin i_{V_{TL}}$$

Using the cosine matrix:

$$X_{IN} = r_{01_{x_e}} L_1 + r_{01_{y_e}} M_1$$

$$Y_{IN} = r_{01_{x_e}} L_2 + r_{01_{y_e}} M_2 + r_{01_{z_e}} N_2$$

$$Z_{IN} = r_{01_{x_e}} L_3 + r_{01_{y_e}} M_3 + r_{01_{z_e}} N_3$$

and

$$\dot{X}_{IN} = V_{01_{x_e}} L_1 + V_{01_{y_e}} M_1$$

$$\dot{Y}_{IN} = V_{01_{x_e}} L_2 + V_{01_{y_e}} M_2 + V_{01_{z_e}} N_2$$

$$\dot{Z}_{IN} = V_{01_{x_e}} L_3 + V_{01_{y_e}} M_3 + V_{01_{z_e}} N_3$$

defining:

$$P_{1_{X_N}} = \dot{Y}_{IN} Z_{IN} - \dot{Z}_{IN} Y_{IN}$$

$$P_{1_{Y_N}} = \dot{Z}_{IN} X_{IN} - \dot{X}_{IN} Z_{IN}$$

$$P_{1_{Z_N}} = \dot{X}_{IN} Y_{IN} - \dot{Y}_{IN} X_{IN}$$

The inclination between the translunar plane and the equatorial plane (azimuth) will be:

$$\tan i_{EQ_{TL}} = \frac{\sqrt{P_{1_{X_N}}^2 + P_{1_{Y_N}}^2}}{P_{1_{Z_N}}}$$

The latitude of the injection point is:

$$\tan \lambda_{TL} = \frac{Z_{IN}}{\sqrt{X_{IN}^2 + Y_{IN}^2}}$$

1st or 4th quadrant

The longitude of the injection point, relative to the X_N-axis, is:

$$\sin \Phi_{TL} = \frac{Y_{IN}}{\sqrt{X_{IN}^2 + Y_{IN}^2}}$$

$$\cos \Phi_{TL} = \frac{X_{IN}}{\sqrt{X_{IN}^2 + Y_{IN}^2}}$$

Quadrant determined by these two quantities

The latitude and longitude of the return perigee point can be found with the following equations:

Available data: h_{PE}, V_{02}, θ_{02}, ω_f, iv_{TE}, t_{TOT}, $\dot{\Omega}_E$

where: $\dot{\Omega}_E$ = earth rotation velocity (rad/sec)

and: $r_{02} = R_0 + h_{PE}$

then:

with $r_{02_\xi} = - r_{02} \cos \theta_{02}$

$r_{02_\eta} = + r_{02} \sin \theta_{02}$

$r_{02_{xe}} = r_{02_\xi} \cos \omega_f - r_{02_\eta} \sin \omega_f \cos iv_{TE}$

$r_{02_{ye}} = r_{02_\xi} \sin \omega_f + r_{02_\eta} \cos \omega_f \cos iv_{TE}$

$r_{02_{ze}} = - r_{02_\eta} \sin iv_{TE}$

and

$$V_{o2_\xi} = V_{o2} \sin\theta_{o2}$$
$$V_{o2_\eta} = V_{o2} \cos\theta_{o2}$$

$$V_{o2_{x_e}} = V_{o2_\xi} \cos\omega_f - V_{o2_\eta} \sin\omega_f \cos\iota_{V_{TE}}$$
$$V_{o2_{y_e}} = V_{o2_\xi} \sin\omega_f + V_{o2_\eta} \cos\omega_f \cos\iota_{V_{TE}}$$
$$V_{o2_{z_e}} = -V_{o2_\eta} \sin\iota_{V_{TE}}$$

The cosine matrix is used, as in the injection point case, to obtain:

$$X_{2N} = \tilde{r}_{o2_{x_e}} L_1 + \tilde{r}_{o2_{y_e}} M_1$$
$$Y_{2N} = \tilde{r}_{o2_{x_e}} L_2 + \tilde{r}_{o2_{y_e}} M_2 + \tilde{r}_{o2_{z_e}} N_2$$
$$Z_{2N} = \tilde{r}_{o2_{x_e}} L_3 + \tilde{r}_{o2_{y_e}} M_3 + \tilde{r}_{o2_{z_e}} N_3$$

and

$$\dot{X}_{2N} = V_{o2_{x_e}} L_1 + V_{o2_{y_e}} M_1$$
$$\dot{Y}_{2N} = V_{o2_{x_e}} L_2 + V_{o2_{y_e}} M_2 + V_{o2_{z_e}} N_2$$
$$\dot{Z}_{2N} = V_{o2_{x_e}} L_3 + V_{o2_{y_e}} M_3 + V_{o2_{z_e}} N_3$$

defining:

$$P_{2_{X_N}} = \dot{Y}_{2N} Z_{2N} - \dot{Z}_{2N} Y_{2N}$$
$$P_{2_{Y_N}} = \dot{Z}_{2N} X_{2N} - \dot{X}_{2N} Z_{2N}$$
$$P_{2_{Z_N}} = \dot{X}_{2N} Y_{2N} - \dot{Y}_{2N} X_{2N}$$

The inclination to the equatorial plane will be:

$$\tan \iota_{EQ_{TE}} = \frac{\sqrt{P_{2X_N}^2 + P_{2Y_N}^2}}{P_{2Z_N}}$$

1st or 2nd quadrant

The latitude of the return perigee point is:

$$\tan \lambda_{TE} = \frac{Z_{2N}}{\sqrt{X_{2N}^2 + Y_{2N}^2}}$$

1st or 4th quadrant

To obtain the longitude of the return perigee point, the rotation of the earth during the time of flight must be taken into account.

Thus:

$$\sin \phi'_{TE} = \frac{Y_{2N}}{\sqrt{X_{2N}^2 + Y_{2N}^2}}$$

$$\cos \phi'_{TE} = \frac{X_{2N}}{\sqrt{X_{2N}^2 + Y_{2N}^2}}$$

Quadrant determined from these two quantities

and, also:

$$\sin \Delta\phi = \sin (\dot{\Omega}_E t_{TOT.})$$

$$\cos \Delta\phi = \cos (\dot{\Omega}_E t_{TOT.})$$

Quadrant determined from these two quantities

then:

$$\phi_{TE} = \phi'_{TE} - \Delta\phi$$

The addition of the following equations to the general lunar trajectory program will reduce the final output data to actual longitudes and latitudes for trajectories which leave Cape Canaveral.

Equations to determine true longitude of the injection point, return vacuum perigee point and the intersection of the return trajectory with the return base latitude.

The following calculations are performed for each α_R.

ϕ_{LL} True longitude of launch point

λ_{LL} True latitude of launch point

λ_b True latitude of return base

Step 1 Range from launch point to injection point

ρ = Range in degrees

R = Range in naut mi

where R = ρ (60.107792) naut mi

ρ_1 = Range angle from launch point to equator

ρ_2 = Range angle from injection point to equator

$$\sin \rho_1 = \frac{\sin \lambda_{LL}}{\sin i_{EQ_{TE}}}$$

$$\sin \rho_2 = \frac{\sin \lambda_{T_h}}{\sin i_{EQ_{TE}}}$$

Note: if $|\sin \rho| > 1.0$, go on to next α_R

Test: If $\dot{Z}_{IN}$ is positive (+) (or zero)

$$(\rho_{TOT})_{TL} = 180^\circ + \rho_1 + \rho_2$$

If $\dot{Z}_{IN}$ is negative (–)

$$(\rho_{TOT})_{TL} = \rho_1 - \rho_2 \qquad \lambda_{TL} = (-)$$

$$(\rho_{TOT})_{TL} = \rho_1 - \rho_2 + 360^\circ \qquad \lambda_{TL} = (+)$$

The above calculations result in a single range angle, ρ .

Step 2 Earth rotation during time from launch point to injection point and time in parking orbit

$$\Delta\phi_{E.R.} = 1.02289 + .061636(\rho_{TOT})_{TL} \qquad \text{deg.}$$

Parking orbit (coast range)

$$\rho_{PARK} = (\rho_{TOT})_{TL} - 35.952$$

Step 3 True longitude of injection point

ϕ = Δ Longitude: launch point to equator

ϕ_2 = Δ Longitude: injection point to equator

$$\sin\phi_1 = \frac{\tan\lambda_{cc}}{-\tan i_{EQ_{TL}}} \qquad \sin\phi_2 = \frac{\tan\lambda_{TL}}{-\tan i_{EQ_{TL}}}$$

Test: If $\dot{Z}_{IN}$ is positive (+) or zero

$$(\Delta\phi_{TOT})_{TL} = 180^\circ + \phi_1 + \phi_2$$

If $\dot{Z}_{IN}$ is negative (–)

$$(\Delta\phi_{TOT})_{TL} = \phi_1 - \phi_2 \qquad \lambda_{TL} = (-)$$

or

$$(\Delta\phi_{TOT})_{TL} = \phi_1 - \phi_2 + 360^\circ \qquad \lambda_{TL} = (+)$$

The true longitude of the injection point will be:

$$(\phi_T)_{TL} = \phi_{CC} + (\Delta\phi_{TOT})_{TL} - (\Delta\phi_{CR})_{TL}$$

Step 4 True longitude of return vacuum perigee:

$$\Delta\phi_{CCR} = (\phi_T)_{TL} - \phi_{TL}$$

$$(\phi_T)_{TE} = \phi_{TE} + \Delta\phi_{CCR}$$

Step 5 Range to return base at latitude λ_b

Two ranges are required.

ρ_3 = Range angle from λ_b to equator (deg)

ρ_4 = Range angle from λ_{TE} to equator (deg)

$$\sin \rho_3 = \frac{\sin \lambda_b}{\sin i_{EQ_{TL}}}$$

$$\sin \rho_4 = \frac{\sin \lambda_{TE}}{\sin i_{EQ_{TE}}}$$

Note: If $|\sin \rho_3| > 1.0$, print out results from Steps 1 through 4 and go to next α_R.

Test: If Z_{IN} is positive (+) or zero

$$(\rho_{TOT})_{TL_1} = \rho_3 - \rho_4$$

$$(\rho_{TOT})_{TE_2} = 180^\circ - \rho_3 - \rho_4$$

If Z_{IN} is negative (-)

$$(\rho_{TOT})_{TE_1} = 180^\circ + \rho_3 + \rho_4$$

and

$$(\rho_{TOT})_{TE_2} = 360^\circ - \rho_3 + \rho_4$$

The results of this step are two range angles.

Step 6 Earth rotation during flight time from perigee to return base.

$$(\Delta\phi_{ER})_{TE_1} = .627 + .065338\,(\rho_{TOT})_{TE_1}$$

and

$$(\Delta\phi_{ER})_{TE_2} = .627 + .065338\,(\rho_{TOT})_{TE_2}$$

Step 7 True longitude of return base.

ϕ_3 = Δ Longitude : λ_b to equator

ϕ_4 = Δ Longitude : λ_{TE} to equator

$$\sin\phi_3 = \frac{\tan\lambda_b}{\tan i_{EQ_{TE}}} \qquad \sin\phi_4 = \frac{\tan\lambda_{TE}}{\tan i_{EQ_{TE}}}$$

Test: If $\dot{Z}_{IN}$ is positive (+) or zero

$$(\Delta\phi_{TOT})_{TE_1} = \phi_3 - \phi_4$$

$$(\Delta\phi_{TOT})_{TE_2} = 180^\circ - \phi_3 - \phi_4$$

If $\dot{Z}_{IN}$ is negative (-)

$$(\Delta\phi_{TOT})_{TE_1} = \phi_3 + \phi_4 + 180^\circ$$

$$(\Delta\phi_{TOT})_{TE_2} = 360^\circ - \phi_3 + \phi_4$$

The true longitude of the return base will be

$$(\phi_T)_{b_1} = (\phi_T)_{TE} + (\Delta\phi_{TOT})_{TE_1} - (\Delta\phi_{ER})_{TE_1}$$

and

$$(\phi_T)_{b_2} = (\phi_T)_{TE} + (\Delta\phi_{TOT})_{TE_2} - (\Delta\phi_{ER})_{TE_2}$$

3. Determine Characteristics of Lunar Orbit

From the program, the following data is available:

$r_{m_1 x_e}$	$r_{m_2 x_e}$	t_{m_p}
$r_{m_1 y_e}$	$r_{m_2 y_e}$	t_{m_c}
$r_{m_1 z_e}$	$r_{m_2 z_e}$	θ_{m_p}, θ_{m_c}

Then, defining:

$$\vec{r}_{m_1} \times \vec{r}_{m_2} = M_r \vec{1}_N = (r_{m_1} r_{m_2} \sin\theta_{m_c}) \vec{1}_N$$
$$= M_{r_{x_e}} \vec{i} + M_{r_{y_e}} \vec{j} + M_{r_{z_e}} \vec{k}$$

where

$$M_{r_{x_e}} = r_{m_1 y_e} r_{m_2 z_e} - r_{m_1 z_e} r_{m_2 y_e}$$
$$M_{r_{y_e}} = r_{m_1 z_e} r_{m_2 x_e} - r_{m_1 x_e} r_{m_2 z_e}$$
$$M_{r_{z_e}} = r_{m_1 x_e} r_{m_2 y_e} - r_{m_1 y_e} r_{m_2 x_e}$$

$$\tan i_M = \frac{\sqrt{M_{r_{x_e}}^2 + M_{r_{y_e}}^2}}{M_{r_{z_e}}}$$ 1st or 2nd quadrant

$$\tan \phi_{\bar{e}} = \frac{M_{r_{x_e}}}{-M_{r_{y_e}}}$$ Quadrant from num.-den. values

$$\cos\beta_M = \frac{r_{m_1 x_e} \cos\phi_{\bar{e}} + r_{m_1 y_e} \sin\phi_{\bar{e}}}{r_{m_1}}$$

$$\gamma = \theta_{m_p} - \beta_M$$

The ΔV required to go into lunar orbit will be:

$$\Delta V = V_{P_L} - V_{S_L}$$

where:

$$\left(\frac{V_{P_L}}{V_{S_L}}\right) = \sqrt{1 + \epsilon_m}$$

R_L = Radius of moon

$$V_{S_L} = \sqrt{\frac{\mu_m}{R_L + h_{P_L}}}$$

The moon position can be obtained from:

$$\omega_p = \omega_0 + \dot{\omega} t_{mp}$$

APPENDIX B

THE MOTION OF A SATELLITE OF THE MOON

Some of the more important features of the motion of a satellite of the moon are analyzed. Account is taken of the earth's perturbing field and the moon's triaxiality, but only near-circular satellite orbits are considered.

The equations of motion, taken directly from Ref. 1, are expressed in a simpler form and some specific results are deduced.

The differential equations of motion were integrated approximately to obtain the average rate of precession of the nodes (about the lunar spin axis) and the variation of the orbital inclination. The variation of the eccentricity was not investigated since it is of minor importance for orbits of low eccentricity.

1. Nodal Precession

The nodal precession rate is given approximately by:

$$\omega_p = F(\rho) \cdot \cos\beta_o = \left[1.7\,\rho^{-7/2} + .021\,\rho^{3/2}\right] \cos\beta_o$$

where nodal precession rate (in degrees per day) relative to a non-rotating reference frame = ω_p

β_o = "mean" orbital inclination (neglecting slight oscillation);

ρ = radius of orbit in units of the moon's radius.

Fig III-30 shows plots of ω_p vs. ρ for several values of β_o . As the orbit altitude increases, the function $F(\rho)$ first falls off sharply due to the rapid decrease of the triaxial perturbation field with altitude; it reaches a minimum at an altitude of about 1900 stat mi, then starts to slowly increase because of the earth's perturbing field.

The factor $\cos\beta_o$ shows that the precession rate is zero for polar orbits, and increases to a maximum for equatorial orbits.

2. Orbital Inclination Angle

The inclination angle undergoes a periodic variation of small amplitude. The amplitude is given very roughly by the following formula:

$$\Delta\beta = \pm G(\rho) \sin\beta_0 \approx \pm .40\left[\rho^{-7/2} + .73\rho^{3/2}\right]\sin\beta_0$$

Where $\Delta\beta$ = amplitude of periodic variation of the inclination angle β, in degrees;

β_0 = "mean" orbital inclination angle;

ρ = radius of satellite orbit in units of the moon's radius.

As the altitude ρ increases, the function $G(\rho)$ first decreases, reaching a minimum at an altitude of about 800 miles, then increases again. For $\beta_0 \approx 90°$ (polar orbits) and for very low altitudes, $\Delta\beta$ is about 0.45^o. At an altitude of 1000 mi, it is about 0.2^o. At an altitude of 8000 mi, it increases to about 1.5^o.

The factor $\sin\beta_0$ shows that $\Delta\beta$ is zero for equatorial orbits and increases to a maximum for polar orbits.

3. The Differential Equations of Motion

Brief description of analysis in Ref B-1. The equations of motion are written in a moon-centered, rotating coordinate system; the x and y axes lie in the moon's equatorial plane, with the x-axis always pointing toward the earth, and the z-axis is directed along the moon's spin axis. The moon is considered to be a triaxial ellipsoid, and its potential is approximated by an expansion in spherical harmonics up to the second order. The perturbing field of the earth is first written exactly, and then approximated on the assumption that the ratio of the orbit radius to the earth-moon distance is very small. The earth's perturbing field is shown to be comparable in magnitude to the perturbing field due to the lunar triaxiality. The perturbing field of the sun is shown to be about 1/200 that of the earth, and is therefore neglected.

With these approximations, the equations of motion of a lunar satellite are then written in Lagrangian form, using as coordinates the quantities:

α = longitude of the node = angle between the x-axis of the rotating frame and the ascending node;

β = orbital inclination angle;

$$h = \sqrt{\mu \ell}$$

where

μ = lunar gravitational constant, and

ℓ = semi-latus rectum of orbit;

ψ = angle measured in the orbit plane from the ascending node to the satellite;

ϵ = eccentricity;

ω = argument of pericenter (angle in orbit plane from ascending node to pericenter).

The differential equations of motion thus obtained are quite complicated. To simplify them, Ref. B-1 transforms the independent variable from time to the angular variable ψ, and applies the averaging process of Kryloff-Bogoliuboff to the resulting equations. This averaging process has the effect of smoothing the equations of motion, so that their solutions will exhibit the correct long-period variations, but will be stripped of most of the complicated, rapid fluctuations of the true solutions. The averaged equations of motion are presented in Ref. B-1 as Eq. (13). From these equations, Ref. B-1 derives an integral of the motion.

Presentation of the smoothed equations of motion. The averaged equations of motion for the variables α, β and h are reproduced below, together with the integral of the motion:

$$\frac{d\alpha}{d\psi} = \frac{\Omega h^3}{\mu^2} - \left(\frac{\mu^2 R^2}{h^4}\right)\cos\beta\left(J - K\cos 2\alpha + \frac{3M_E h^{10}\sin^2\alpha}{2M_M \mu^5 R^2 D^3}\right)$$

$$\frac{d\beta}{d\psi} = \left(\frac{\mu^2 R^2}{h^4}\right)\left(K + \frac{3M_E h^{10}}{4M_M \mu^5 R^2 D^3}\right)\sin 2\alpha \sin\beta$$

$$\frac{dh}{d\psi} = 0$$

Smoothed Equations of Motion

$$-\left(\frac{2\Omega h^7}{\mu^4 R^2}\right)\cos\beta + \left(J - K\cos 2\alpha + \frac{3M_E h^{10}\sin^2\alpha}{2M_M \mu^5 R^2 D^3}\right)\sin^2\beta = \text{CONST.}$$

Integral of the Motion

Ω = angular speed of the moon in its orbital motion about the earth.

μ = gravitational constant of the moon.

R = radius of the moon (equatorial, in the direction of the moon's orbit).

J, K = dimensionless constants associated with the triaxiality of the moon ("mechanical ellipticities").

M_E = mass of the earth.

M_M = mass of the moon.

D = earth-moon distance (assumed fixed).

4. Improved Form of the Equations of Motion

The equations given above are in a somewhat clumsy form for our purposes. To simplify them, we do the following things:

(1) Change the independent variable from ψ back to t, by the approximate transformation:

$$\frac{d}{d\psi} = \frac{1}{\omega}\frac{d}{dt}$$

where

$\omega = \sqrt{\frac{\mu}{r^3}}$

ω = angular speed of satellite in its near-circular orbit.

This transformation, in which ω is treated as a constant, will be approximately valid for orbits of small eccentricity; for we can then write:

$$\psi \approx \psi_0 + \omega t$$

$$\frac{d\psi}{dt} \approx \omega$$

$$\frac{d}{dt} = \frac{d}{d\psi} \cdot \frac{d\psi}{dt} \cong \omega \frac{d}{d\psi}$$

(2) Express h in terms of r :

Strictly, $h^2 = \mu r\left[1 + \epsilon \cos(\psi - \omega)\right]$

But $\frac{dh}{d\psi} = 0$, and therefore $\frac{dh}{dt} = \frac{dh}{d\psi} \cdot \frac{d\psi}{dt} = 0$

Since h is a constant, then, there is no harm in approximating it by setting $\epsilon = 0$:

$h^2 = \mu r$ (where the slight variation of μ is neglected)

(3) Simplify the notation:

(a) Define the following basic, nondimensional parameters:

$$\rho \equiv \frac{r}{R}$$

$$f_M \equiv \frac{M_E}{M_M}$$

$$f_d \equiv D/R$$

$$\ell \equiv \Omega P_0 \qquad \text{where} \qquad P_0 = \frac{2\pi}{\sqrt{\mu/R^3}}$$

P_0 = period of a circular orbit at surface of moon

(b) Further define:

$$a \equiv \frac{2\pi}{\rho^{7/2}}$$

$$b \equiv \left(\frac{3}{4}\right)\left(\frac{f_m}{f_d^3}\right)\rho^5$$

Upon doing the above three things, we obtain the equations of motion for α and β, and the integral of the motion, in the following simple form:

$$\dot{\alpha} = \frac{\ell}{P_o} - \frac{a}{P_o}\left[(b+J) - (b+K)\cos 2\alpha\right]\cos\beta \qquad \text{(B-1)}$$

$$\dot{\beta} = \frac{a}{P_o}(b+K)\sin 2\alpha \sin\beta \qquad \text{(B-2)}$$

$$2\frac{b}{a}\cos\beta + \left[(b+J) - (b+K)\cos 2\alpha\right]\sin^2\beta = C \quad (\text{CONST.}) \qquad \text{(B-3)}$$

5. Approximate Solutions of the Equations of Motion

Solution for α. In order to solve the equations of motion for α, we must eliminate β from Eq.(B-1); perhaps the best way to do this is to solve Eq.(B-3) for $\cos\beta$ and substitute the resulting expression into (B-1). This yields:

$$\dot{\alpha} = \pm \frac{1}{P_o}\left[\ell^2 + a^2(A - B\cos 2\alpha)(A - B\cos 2\alpha - C)\right]^{1/2}$$

where: $A = b + J$, $B = b + K$

This equation contains only α . But as it stands, it is not in a very convenient or simple form. To put it into a form in which it can be conveniently examined for possible simplifications, we proceed as follows:

(1) Square the equation to eliminate the radical.

(2) Substitute the values of the constants ℓ, a, b, C and in terms of the basic parameters Ω, P_o, f_m, f_d, ρ, α_o and β_o (where the last two are the values of α and β at $t = 0$)

(3) Collect together like powers of ρ

(4) List the numerical values of the basic parameters, examine the numerical magnitude of all terms in the equation and drop out all neglible terms.

In carrying out step (2), the value of C is obtained by setting $\beta = \beta_o$ and $\alpha = \alpha_o$ in Eq (B-3). The result is:

$$C = \frac{3}{2}\left(\frac{f_m}{f_d^3}\right)\left(\sin^2\beta_o \sin^2\alpha_o\right)\rho^5 + \left(\frac{\Omega P_o}{\pi}\right)\left(\cos\beta_o\right)\rho^{7/2} + \\ + \left(J - K\cos 2\alpha_o\right)\sin^2\beta_o$$

After carrying out steps (1), (2) and (3), we obtain the equation:

$$\dot{\alpha}^2 = \Omega^2 + \left(\frac{4\pi^2}{P_o^2}\right)\left[\left(\frac{27}{32}\right)\left(\frac{f_m^2}{f_d^6}\right)\left(1 - \frac{4}{3}\sin^2\beta_o \sin^2\alpha_o\right)\rho^3 - \left(\frac{3}{4\pi}\right)\left(\frac{f_m}{f_d^3}\right)\left(\Omega P_o\right)\left(\cos\beta_o\right)\rho^{3/2} + \right.$$
$$+ \left(\frac{3}{4}\right)\left(\frac{f_m}{f_d^3}\right)\left\{\left(2J+K\right)\left(1 - \sin^2\alpha_o \sin^2\beta_o\right) + \left(-J + K\cos^2\alpha_o\right)\sin^2\beta_o\right\}\rho^{-2} -$$
$$- \left(\frac{1}{\pi}\right)\left(\Omega P_o\right)J\left(\cos\beta_o\right)\rho^{-7/2} + \left\{\frac{1}{2}K^2 + J^2\cos^2\beta_o + KJ\sin^2\beta_o\cos 2\alpha_o\right\}\rho^{-7}\Big] +$$
$$+ \left(\frac{4\pi^2}{P_o^2}\right)\left[\frac{9}{8}\left(\frac{f_m^2}{f_d^4}\right)\left(1 - \sin^2\beta_o \sin^2\alpha_o\right)\rho^3 - \left(\frac{3}{4\pi}\right)\left(\frac{f_m}{f_d^3}\right)\left(\Omega P_o\right)\left(\cos\beta_o\right)\rho^{3/2} + \right.$$
$$+ \left(\frac{3}{4}\right)\left(\frac{f_m}{f_d^3}\right)\left\{2\left(J+K\right) - 3K\sin^2\alpha_o \sin^2\beta_o - \left(J - K\cos^2\alpha_o\right)\sin^2\beta_o\right\}\rho^{-2} -$$
$$- \left(\frac{1}{\pi}\right)\left(\Omega P_o\right)K\left(\cos\beta_o\right)\rho^{-7/2} + \left\{JK + JK\cos^2\beta_o + K^2\sin^2\beta_o\cos 2\alpha_o\right\}\rho^{-7}\Big] +$$
$$+ \left(\frac{4\pi^2}{P_o^2}\right)\left[\frac{9}{32}\left(\frac{f_m^2}{f_d^4}\right)\rho^3 + \left(\frac{3}{4}\right)K\left(\frac{f_m}{f_d^3}\right)\rho^{-2} + \left(\frac{1}{2}\right)K^2\rho^{-7}\right]\cos 4\alpha$$

To carry out step (4) we list the numerical values of the parameters:

$\Omega = 8.73 \times 10^{-3}$ rad/hr

$P_e = 1.81$ hr

$f_m = 81.3$

$f_d = 240$

$J = 3.4 \times 10^{-4}$

$K = 3.5 \times 10^{-5}$

Upon substituting these values into the above equation we obtain:

$$\dot{\alpha}^2 = 7.6 \times 10^{-5} + \left\{(3.5 - 4.7 \sin^2\beta_e \sin^2\alpha_e) 10^{-10} \rho^3 - \right.$$

$$-(2.7 \cos\beta_e) 10^{-7} \rho^{3/2} + \left[3.8 - (1.8 + 3.8 \sin^2\alpha_e - .19 \cos^2\alpha_e)(\sin^2\beta_e)\right] \times$$

$$\times (10^{-6}) \rho^{-2} - (2.1 \cos\beta_e) 10^{-5} \rho^{-7/2} + \left[1.4 \cos^2\beta_e + \right.$$

$$\left. + .14 \sin^2\beta_e \cos 2\alpha_e + .0074\right](10^{-6}) \rho^{-7} +$$

+ A second harmonic whose amplitude is about equal to the constant term "[ ]" above,

+ A negligible fourth harmonic.

Since the primary Ω^2 term is much larger than either the constant term "[ ]" or the second harmonic term for the range of interest of ρ (probably about 1→4), we can neglect the second harmonic (and also the fourth harmonic) thus the part of the formula written out above is a good approximation as it stands.

Furthermore, we can neglect most of the terms in the above formula; for the probable range of interest of ρ (about 1→4), all terms except the second and fourth can be neglected. Retaining only these terms, then, we can write (reverting to the literal formula):

$$\dot{\alpha}^2 \cong \Omega^2 + \left(\frac{4\pi^2}{P_o}\right)\left\{-\left(\frac{3}{4}\right)\left(\frac{\rho_m}{\rho_d}\right)(\Omega P_o)(\cos\beta_o)\rho^{-3/2} - \right.$$

$$\left. -\left(\frac{1}{\pi}\right)(\Omega P_o)J(\cos\beta_o)\rho^{-7/2}\right\}$$

This completes step (4). However, we can simplify this equation even further by the following device: write the equation in the form:

$$\dot{\alpha}^2 = \Omega^2 + T = \Omega^2\left(1 + \frac{T}{\Omega^2}\right)$$

$$\dot{\alpha} = -\Omega\left(1 + \frac{T}{\Omega^2}\right)^{1/2} = -\Omega\left(1 + \frac{1}{2}\frac{T}{\Omega^2} - \frac{1}{8}\frac{T^2}{\Omega^4} + \cdots\cdots\right)$$

$$\dot{\alpha} \cong -\Omega\left(1 + \frac{1}{2}\frac{T}{\Omega^2}\right)$$

Since the succeeding terms of the series are negligible. (The minus sign was chosen to make the sense of rotation correct.)

If we now define α_I as the longitude of the node relative to the x-axis of a nonrotating reference frame, then:

$$\omega_p \equiv \dot{\alpha}_I = \dot{\alpha} + \Omega$$

$$\dot{\alpha}_I \cong -\frac{1}{2}\frac{T}{\Omega}$$

If we now replace the symbol T by the quantity for which it stands and change the units to degrees per day, we obtain finally:

$$\omega_p \cong -\left(1.7\rho^{-1/2} + 0.021\rho^{3/2}\right)\cos\beta_o$$

This last equation should be a good approximation to the nodal precession rate; it holds for all inclination angles, and for orbital altitudes from zero out to at least 10,000 mi.

Fig III-30 gives ω_p as a function of β_o and ρ, as calculated from the above equation.

(NOTE: In the above derivation there appears to be some confusion as to the sign of ω_p. This stems from the fact that, in Ref. B-1, the moon's angular rate Ω (about the earth) is written as $-\Omega$; thus Ω is a negative quantity, since the angular rate must be positive to be in accord with the usual sign conventions. Thus, on the previous page, the quantity T is actually positive, but everywhere else that Ω appears it may be taken to be positive (the square root of Ω^2 is considered positive, and the Ω appearing in the definition of α_I is positive, in accordance with the usual sign convention for rotation). Thus, in the formula for α_I, T is positive and Ω is also positive; therefore ω_p is negative, as it must be.)

Solution for β. There are several ways in which we could attempt to solve the equations of motion Eq (B-2) for ; three possible ways are listed below.

Method 1:

In Eq (B-2) do the following: (1) substitute for α the solution found in the previous section; (2) set $\beta = \beta_o + \Delta\beta$; assume $\Delta\beta$ is very small, and write $\sin\beta = \sin(\beta_o + \Delta\beta) = \sin\beta_o\cos\Delta\beta + \cos\beta_o\sin\Delta\beta \cong \sin\beta_o + \Delta\beta\cos\beta_o$. Solve the resulting differential equation for $\Delta\beta$.

Method 2:

In this method also we substitute the solution found above for α into Eq (B-2). However, we now make no assumptions about the smallness of $\Delta\beta$. Equation (B-2) is solved directly for β. Although the solution is more complicated than that derived by Method 1, it is easy to obtain and is easily simplified. Since it is only slightly more trouble than Method 1, and since it has the virtue of exhibiting the solution as an oscillation of small amplitude without any prior assumptions, we will use this method.

Method 3:

Solve Eq (B-3) for $\sin 2\alpha$, and substitute this value into Eq (B-2). The resulting equation is considerably more complicated than those of Methods 1 and 2.

Using Method 2, Eq (B-2) can be integrated as it stands:

$$\beta = \left(\frac{a}{P_o}\right)(b+K)\sin 2\alpha \sin\beta$$

$$\frac{d\beta}{\sin\beta} = \left(\frac{a}{P_o}\right)(b+K)\sin 2\alpha \, dt$$

$$\ln \tan \tfrac{1}{2}\beta = \left(\frac{a}{P_o}\right)(b+K)\int \sin 2\alpha \, dt + C_1$$

(C_1 = Constant of Integration)

To evaluate the integral we must use the solution for α found in the previous section; there we found that:

$$\dot{\alpha} = \dot{\alpha}_I - \Omega \equiv \omega_p - \Omega$$

CONFIDENTIAL

And ω_p was given as a function of ρ and β_o. Integrating this equation gives:

$$\alpha = (\omega_p - \Omega)t + C_2 \qquad t=0,\ \alpha = \alpha_o$$
$$\therefore\ C_2 = \alpha_o$$

$$\alpha = -(\Omega - \omega_p)t + \alpha_o$$

We therefore have:

$$\int \sin 2\alpha\, dt = \int \sin 2[-(\Omega-\omega_p)t + \alpha_o]\, dt$$
$$= \frac{1}{2(\Omega-\omega_p)} \cos 2[-(\Omega-\omega_p)t + \alpha_o]$$
$$= \frac{1}{2(\Omega-\omega_p)} \cos 2[(\Omega-\omega_p)t - \alpha_o]$$

Placing this expression in the equation for β, and introducing the notation

$$\delta = \frac{a(b+K)}{2P_c(\Omega-\omega_p)}, \qquad \omega \equiv \Omega - \omega_p$$

we obtain:

$$\ln \tan \tfrac{1}{2}\beta = \delta \cos 2(\omega t - \alpha_o) + C_1$$

To evaluate C_1, we note that when $t=0, \beta = \beta_o$. Therefore,

$$C_1 = \ln \tan \tfrac{1}{2}\beta_o - \delta \cos 2\alpha_o$$

Using this value for C_1, and solving the equation for β, we readily obtain:

CONFIDENTIAL

$$\beta = 2\tan^{-1}\left\{(\tan\tfrac{1}{2}\beta_0)e^{-\delta\cos 2\alpha_0}\, e^{\delta\cos(2\omega t - 2\alpha_0)}\right\}$$

Evidently, β varies periodically between the limits

$$\beta_{MAX.} = 2\tan^{-1}\left\{(\tan\tfrac{1}{2}\beta_0)\, e^{\delta(1-\cos 2\alpha_0)}\right\}$$

$$\beta_{MIN} = 2\tan^{-1}\left\{\tan\tfrac{1}{2}\beta_0\, e^{-\delta(1+\cos 2\alpha_0)}\right\}$$

Therefore we can expand β in a Fourrier series in t . This is probably most easily done by first expanding β in a Taylor series in the small parameter δ out to the second order, and then rearranging the resulting expression into a series of harmonics of $\cos 2\omega t$. To prove that δ is small, we evaluate it numerically:

$$\delta = \frac{\pi\left[\left(\frac{3}{4}\right)\left(\frac{f_m}{f_j^3}\right) + \frac{K}{\rho^5}\right]\rho^{3/2}}{P_0(\Omega - \omega_p)}$$

ω_p can be neglected since: $\omega_p \leq \frac{1}{10}\Omega$

$$\delta \cong (0.088 + \frac{0.70}{\rho^5})(10^{-2})\rho^{3/2} \approx 10^{-2} \qquad (\text{for } \rho \leq 9)$$

The Taylor expansion of β out to the second order in δ is:

$$\beta = \beta_0 + 2(\sin\tfrac{1}{2}\beta_0\cos\tfrac{1}{2}\beta_0)\left[\cos(2\omega t - 2\alpha_0) - \cos 2\alpha_0\right]\delta +$$
$$+ (\sin\tfrac{1}{2}\beta_0\cos^3\tfrac{1}{2}\beta_0)\left[\cos(2\omega t - 2\alpha_0) - \cos 2\alpha_0\right]^2\delta^2 +$$
$$+ \ldots\ldots .$$

Upon rearranging this into a series of multiples of $\cos(2\omega t - 2\alpha_0)$, we obtain:

$$\beta \cong \left[\beta_c - \delta \cos 2\alpha_0 \sin\beta_0 + \tfrac{1}{2}\delta^2\left(\tfrac{1}{2} + \cos^2 2\alpha_0\right)\sin\beta_c \cos^2\tfrac{1}{2}\beta_c\right] +$$

$$+ \left[\delta \sin\beta_0 - \delta^2 \cos 2\alpha_0 \sin\beta_0 \cos^2\tfrac{1}{2}\beta_c\right]\cos(2\omega t - 2\alpha_0) +$$

$$+ \left[\left(\tfrac{1}{4}\right)\delta^2 \sin\beta_0 \cos^2\tfrac{1}{2}\beta_0\right]\cos(4\omega t - 4\alpha_0)$$

The second harmonic term, being of the order of δ^2, is about two orders of magnitude below the first harmonic and may thus be safely dropped; dropping also the other terms of order δ^2, we obtain:

$$\beta \cong \beta_0 - \delta \cos 2\alpha_0 \sin\beta_0 + \delta \sin\beta_0 \cos(2\omega t - 2\alpha_0)$$

From this it is seen that β oscillates between the limits

$$\beta_{MAX} = \beta_c + \delta(1 - \cos 2\alpha_0)\sin\beta_0$$

$$\beta_{MIN} = \beta_0 - \delta(1 + \cos 2\alpha_0)\sin\beta_c$$

These limits are functions of α_0; but the amplitude of the oscillation,

$$\Delta\beta \equiv \tfrac{1}{2}(\beta_{MAX} - \beta_{MIN}) = \delta \sin\beta_0$$

does not depend on α_0.

To get a reasonably accurate yet simple formula for $\Delta\beta$, we use the approximation given above for δ

$$\delta \approx \left(0.70\rho^{-7/2} + 0.088\rho^{3/2}\right)10^{-2}$$

This, multiplied by $\sin\beta_o$, gives $\Delta\beta$ in radians. Converting to degrees, we have:

$$\Delta\beta \approx 0.40\left(\rho^{-7/2} + 0.13\rho^{3/2}\right)\sin\beta_o \qquad \text{(Deg.)}$$

This formula should be accurate to at least within 20%. Although it is approximate, it has the virtue of exhibiting quite clearly the behavior of $\Delta\beta$ as a function of ρ and β

6. Reference

B-1. Harry Lass and Carleton B. Solloway, "Motion of a Satellite of the Moon," ARS Journal, Vol. 31, No. 2, Feb. 1961, pp. 220-222.

APPENDIX C

VOLUME OF INFLUENCE TO INTEGRATED TRAJECTORY

The "volume of influence" technique, being an approximation of a fairly complex physical model, was not expected to give close to exact answers. Investigation has shown that trends exhibited by the technique are quite accurate for conditions near the earth or moon, however, and can be used with considerable accuracy considering the sensitivity of the answers to the input variables.

The volume of influence technique has been programmed on an IBM 7090 computer. The principal inputs are injection point altitude and flight path angle, translunar orbital plane inclination, desired periselenium altitude and desired transearth trajectory perigee. The computer solves this problem and returns a pair of trajectories. These two trajectories are one returning from the north and another returning from the south, both at approximately the same inclination to the moon's orbital plane. Further inputs include the inclination of the moon's orbital plane to the equatorial plane, position of periselenium measured from the descending node, latitude and longitude of the launch point, and latitude of the return base. The computer gives the true latitude and longitude of the injection point and return trajectory vacuum perigee and the true longitude of the first two intersections of the return trajectory extended beyond perigee to the return base latitude (where it exists). The inclination of the translunar and transearth trajectory to the equatorial plane, range angle in parking orbit, and range to return base latitude is also given. These solutions to the pair of trajectories take approximately 36 sec. Other output includes flight times, inclination and orientation of the lunar orbit phase of the trajectory and periselenium positions.

The technique used to obtain an integrated trajectory is presented below.

(1) Pick the trajectory to be obtained.

(2) Determine volume of influence injection point position, moon position at injection and injection velocity.

(3) Use inputs directly in integrated trajectory program. The results obtained from Step (3) are usually too low at the moon (200 to 300 naut mi) and too high at earth (600 to 1, 000 naut mi).

(4) The integrated trajectory is rerun with the injection velocity (or moon lead angle) increased 0. 1 to 0. 6 fps. This will bring the perigee altitude to $\pm$500, 000 ft and increase periselenium altitude approximately 50 to 100 naut mi.

(5) The output of the second integrated trajectory is introduced into the volume of influence program, with matches on periselenium altitude, perigee, and transearth trajectory inclination.

(6) The injection velocity, position, and moon lead angle from Step 5 are compared to the results of Step 2. The increments are added to the last set of integrated trajectory inputs and the process is repeated. (Steps 3 to 6)

The data shown for the eight trajectories compared in Tables 1 through 4 and 10 through 13 show a rapid convergence.

Since the volume of influence technique is used only for the first guess for injection conditions and then only for increments, the technique shows promise for correcting, at least partially, the effects of sun and earth oblateness. The major forces acting on the vehicle are still the earth and moon, and the technique accurately corrects variations in periselenium and perigee altitude.

APPENDIX D

OPTIMUM TRAJECTORY PROGRAM

During the Apollo study program, it became apparent that improved techniques would be required in any future design effort of vehicles which enter at superorbital velocities. These techniques would be required to answer such questions as:

(1) What is the maximum possible re-entry heat load to a particular point on the re-entry vehicle?

(2) What is the maximum longitudinal and lateral range angle of attack and bank angle program assuming certain maximum altitude or minimum dynamic pressure limitations?

(3) What is the effect of changing the design limits of crew on load factor tolerance, considering both magnitude and duration?

(4) What is the minimum heat load trajectory from given re-entry conditions to a specified landing site?

To answer these questions and many similar ones which must be known to design the re-entry vehicle, an "optimum trajectory" digital program is being prepared. Its aim is to develop a method for determining and studying the re-entry trajectory, i. e., the angle of attack time history which minimizes or maximizes the heat input to a particular point on the vehicle while simultaneously satisfying the following requirements:

(1) The acceleration levels must be maintained within specified endurance limits.

(2) The re-entry trajectory must terminate at a specified location on the surface of the earth.

(3) The re-entry trajectory must be capable of being restrained from skipping beyond a specified altitude.

(4) If it is necessary to assure aerodynamic control of the vehicle throughout the re-entry, a dynamic pressure endurance limit must also be provided.

For the initial phase of the study, a two-dimensional optimum trajectory technique has been formulated and is presently being programmed at Martin for calculation on the IBM 7090. A secondary goal of the study is to refine and, if possible, simplify the digital program to determine the optimum re-entry

trajectory with the least use of computer time and equipment, thus enabling feasible onboard computation with the vehicle's airborne computer.

Several methods for trajectory optimization were initially considered, namely, the indirect method of variational calculus (the Mayer problem); direct variational methods; dynamic programming techniques and approximate optimization methods. Because of the high accuracy needed in a short computation time, a direct variational method similar to those of Refs. D-1 and D-2 was deemed most feasible for application to the problem.

A discussion of the methods presently being programmed is given in the following sections.

1. Derivation of Method

The equations of motion which determine the trajectory, the equation representing the heat transferred to the vehicle and the equations which constrain the accelerations, altitude and dynamic pressure can be represented by the following system of non-linear differential equations

$$\frac{dyi}{dt} = fi \ (y, \alpha, t) \quad i = 1, 2, \ldots n \tag{D-1}$$

Let $\bar{y}_i$ (t) be values of the dependent variables which satisfy the constraining (D-1) for a specified driving function $\bar{\alpha}$ (t). The values of $\bar{y}_i$ (t) and $\bar{\alpha}$ (t) represent the nominal trajectory which in general is nonoptimum. Let y_i(t) and and α (t) be neighboring values related to the nominal values as follows

$$\begin{aligned} y_i \ (t) &= \bar{y}_i \ (t) + \delta y_i \ (t) \\ \alpha(t) &= \bar{\alpha}(t) + \delta \alpha(t) \end{aligned} \tag{D-2}$$

where y_i (t) and $\delta \alpha$(t) are small perturbations about the nominal trajectory. Performing a Taylor Expansion about the nominal we see that if second order terms are neglected the small perturbations are related by the following equation

$$\frac{d}{dt} (\delta y_i) = \sum_{j=1}^{n} \frac{\partial f_i}{\partial y_i} \quad y_j + \frac{\partial f_i}{\partial \alpha} \delta \alpha \qquad i = 1, 2, \ldots n \tag{D-3}$$

Equation (D-3), a system of linear differential equations with variable coefficients, is more amenable to mathematical analysis than the nonlinear Eq (D-1). The values of the variable coefficients in Eq (D-3) are known along the nominal trajectory.

Consider the homogeneous part of Eq (D-3) written in matrix notation as follows

$$\dot{\delta y} = A\,\delta y \tag{D-4}$$

where δy is an n-element column matrix and A is an nxn matrix of coefficients. Let δY be a fundamental solution to Eq (D-4), then

$$\dot{\delta Y} = A\,\delta Y \tag{D-5}$$

and

$$\dot{\delta Y}\,\delta Y^{-1} = A \tag{D-6}$$

also

$$\delta Y^{-1}\delta Y = I \tag{D-7}$$

where I is the identity matrix. Differentiating gives

$$\delta Y^{-1}\dot{\delta Y} - \dot{\delta Y}^{-1}\,\delta Y = 0$$

or

$$\dot{\delta Y}^{-1} = -\delta Y^{-1}\dot{\delta Y}\,\delta Y^{-1} \tag{D-8}$$

Substituting Eq (D-6) into Eq (D-8) gives

$$\dot{\delta Y}^{-1} = -\delta Y^{-1}A \tag{D-9}$$

Transposing both sides

$$\dot{\delta Y}^{*-1} = -A^{*}\,\delta Y^{*-1} \tag{D-10}$$

Therefore δY^{*-1} is the fundamental solution to the homogeneous linear system

$$\dot{\lambda} = -A^{*}\lambda \tag{D-11}$$

Equations (D-11) are adjoint to (D-14), the two having their fundamental solutions related by

$$\Lambda = \delta Y^{*-1} \tag{D-12}$$

Rewriting the adjoint system in summation notation we get

$$\frac{d\lambda_i}{dt} = \sum_{j=1}^{n} \frac{\partial f_j}{\partial y_i} \lambda_j \qquad \text{(D-13)}$$

Next multiply the small perturbation Eq (D-3) by λ_i, the adjoint Eq (D-13) by δy_i and add

$$\lambda_i \frac{d}{dt}(\delta y_i) + \delta y_i \frac{d}{dt}(\lambda_i) = \sum_{j=1}^{n} \frac{\partial f_i}{\partial y_j} \delta y_j \lambda_i - \sum_{j=1}^{n} \frac{\partial f_j}{\partial y_i} \delta y_i \lambda_j + \frac{\partial f_i}{\partial \alpha} d\delta\alpha \delta y_i \qquad \text{(D-14)}$$

Summing on i yields

$$\sum_{i=1}^{n} \frac{d}{dt}(\lambda_i \delta y_i) = \sum_{i=1}^{n} \sum_{j=1}^{n} \frac{\partial f_i}{\partial y_j} \delta y_j \lambda_i - \sum_{i=1}^{n} \sum_{j=1}^{n} \frac{\partial f_j}{\partial y_i} \delta y_i \lambda_j + \sum_{i=1}^{n} \frac{\partial f_i}{\partial \alpha} \delta\alpha \delta y_i \qquad \text{(D-15)}$$

The second and third terms in Eq (D-15) are equal but of opposite sign and therefore cancel each other. Integrating the remaining terms from $t = t_o$ to $t = T$, the initial and final time of the nominal trajectory we obtain

$$\left[\sum_{i=1}^{n} \lambda_i \delta y_i \right]_{t_o}^{T} = \int_{t_o}^{T} \lambda_\alpha \delta x \, dt \qquad \text{(D-16)}$$

where

$$\lambda_\alpha = \sum_{i=1}^{n} \frac{\partial f_i}{\partial \alpha} \delta y_i \qquad \text{(D-17)}$$

Equation (D-16) is a one-dimensional form of Green's Theorem. The method employed in the preceding development is identical with those of Refs. D-1, D-2 and D-3.

In Eq (D-16), the upper limit of integration or "stopping condition" on the problem is assumed to be the final time, T. Frequently stopping conditions other than final time are desired, for which case we can write

$$dy_i = \delta y_i + \dot{y}_i dT \qquad \text{(D-18)}$$

for small changes, dT, in final time. Substituting Eq (D-18) into (D-16) and replacing y_i by f_i gives

$$\left[\sum_{i=1}^{n} \lambda_i dy_i\right]_T = \left[\sum_{i=1}^{n} \lambda_i f_i\right]_T dT + \int_{\tau_o}^{T} \lambda_\alpha \delta\alpha \, dt + \left[\sum_{i=1}^{n} \lambda_i \delta y_i\right]_{t_o} \qquad \text{(D-19)}$$

The usefulness of Eqs (D-17) and (D-19) in determining the correction, $\delta\alpha(t)$, to be applied to the nominal value of the driving function will become apparent in the following paragraphs.

2. Application of Method

Applying the equations discussed above to the optimum re-entry problem, we have for the constraint Eq (D-1), the following system of differential equations.

$$\dot{V} = f_v \qquad \text{where} \qquad f_v = -g \sin\gamma - \frac{D(h, V, \alpha)}{m} \qquad \text{(D-20)}$$

$$\dot{\gamma} = f_\gamma \quad : \quad f_\gamma = \frac{V\cos\gamma}{R+h} - \frac{g\cos\gamma}{V} + \frac{L(h,V,\alpha)}{mV} \tag{D-21}$$

$$\dot{x} = f_x \quad : \quad f_x = \frac{R}{R+h} V\cos\gamma \tag{D-22}$$

$$\dot{h} = f_h \quad : \quad f_h = V\sin\gamma \tag{D-23}$$

$$\dot{Q} = f_q \quad f_q = C_1 \rho^{1/2} V^{3.15} G_{AVG} A(\alpha) + H(h,V) R_n B(\alpha) \tag{D-24}$$

$$\dot{\psi} = f_\psi \quad f_\psi = \frac{1}{\tau_\beta} \tag{D-25}$$

$$\dot{\phi} = f_\phi \quad f_\phi = \frac{1}{\tau_h} \tag{D-26}$$

$$\dot{\theta} = f_\theta \quad f_\theta = \frac{1}{\tau_g} \tag{D-27}$$

Equations (D-20) and (D-21) are the dynamic equations of motion for a non-thrusting, constant mass vehicle about a spherical, non-rotating earth. Equations (D-22) and (D-23) are the kinematic equations of motion. Equation (D-24) is the heat transfer equation. In the first term on the right $C_1 \rho^{1/2} V^{3.15} G_{avg}$ is the stagnation point convective heat transfer at zero angle-of-attack. In the second term on the right H (h, V) R_n is the heat radiated to the stagnation point at zero angle of attack. The functions A (α) and B (α) represent the ratios of the respective heating terms at angle-of-attack to their values at zero angle-of-attack. The constraint Eq (D-25), (D-26) and (D 27) represent the acceleration, altitude and dynamic pressure endurance limits, respectively. The quantities τ_a, τ_h and τ_q are the maximum endurance times at which the vehicle can operate at the instantaneous value of acceleration, (a), altitude, (h), and dynamic pressure (q), respectively. The values of τ_a τ_h and τ_q versus a, h and q will be inputs to the program. By imposing final boundary conditions that ψ_f, ϕ_f and θ_f be less than or equal to unity, we require that at no time during re-entry does the vehicle operate at an a, h or q for a period of time which exceeds the maximum specified by the endurance limits.

The system of equations adjoint to the small perturbation equations given previously by Eq (D-13) is:

$$\dot{\lambda}_V = g_{VV}\lambda_V + g_{V\gamma}\lambda_\gamma + g_{Vx}\lambda_x + g_{Vh}\lambda_h + g_{V\alpha}\lambda_\alpha + g_{V\psi}\lambda_\psi + g_{V\theta}\lambda_\theta \qquad \text{(D-28)}$$

$$\dot{\lambda}_\gamma = g_{\gamma V}\lambda_V + g_{\gamma\gamma}\lambda_\gamma + g_{\gamma x}\lambda_x + g_{\gamma h}\lambda_h \qquad \text{(D-29)}$$

$$\dot{\lambda}_x = 0 \qquad \text{(D-30)}$$

$$\dot{\lambda}_h = g_{hV}\lambda_V + g_{h\gamma}\lambda_\gamma + g_{hx}\lambda_x + g_{h\alpha}\lambda_\alpha + g_{h\psi}\lambda_\psi + g_{h\phi}\lambda_\phi + g_{h\theta}\lambda_\theta \qquad \text{(D-31)}$$

$$\dot{\lambda}_\alpha = 0 \qquad \text{(D-32)}$$

$$\dot{\lambda}_\psi = 0 \tag{D-33}$$

$$\dot{\lambda}_\phi = 0 \tag{D-34}$$

$$\dot{\lambda}_\theta = 0 \tag{D-35}$$

where

$$g_{VV} = \frac{2D}{mV}$$

$$g_{V\gamma} = -\frac{\cos\gamma}{R+h} - \frac{L}{mV^2} - g\frac{\cos\gamma}{V^2}$$

$$g_{Vx} = -\frac{R\cos\gamma}{R+h}$$

$$g_{Vh} = -\sin\gamma$$

$$g_{V\alpha} = -3.15\, C_1 \rho^{1/2} V^{2.15} G_{AVG} A(\alpha) - \frac{\partial H}{JV} B(\alpha)$$

$$g_{V\tau} = -\frac{2\partial}{V}\frac{d}{d\partial}\left(\frac{1}{T_\partial}\right)$$

$$g_{Vq} = -\frac{2q}{V}\frac{d}{dq}\left(\frac{1}{T_q}\right)$$

$$g_{\gamma V} = g\cos\gamma$$

$$g_{\gamma\gamma} = \frac{V\sin\gamma}{R+h} - \frac{g\cos\gamma}{V}$$

$$g_{\gamma x} = \frac{RV\sin\gamma}{R+h} \tag{D-36}$$

$$
\begin{aligned}
g_{rh} &= -V\cos\gamma \\
g_{hv} &= -\frac{2g\sin\gamma}{R+h} + \frac{D}{\rho m}\frac{d\rho}{dh} \\
g_{h\gamma} &= \frac{V\cos\gamma}{(R+h)^2} - \frac{L}{\rho m V}\frac{d\rho}{dh} - \frac{2g\cos\gamma}{V(R+h)} \\
g_{hx} &= \frac{RV\cos\gamma}{(R+h)^2} \\
g_{hq} &= -\frac{1}{2}C_1\rho^{\frac{1}{2}}V^{3.15}G_{nvs}\frac{d\rho}{dh}A(\alpha) - \frac{\partial H_e}{\partial h}B(\alpha) \\
g_{h\psi} &= -\frac{a}{\rho}\frac{d\rho}{dh}\frac{d}{da}\left(\frac{1}{r_a}\right) \\
g_{h\phi} &= -\frac{d}{dh}\left(\frac{1}{r_h}\right) \\
g_{h\theta} &= -\frac{q}{\rho}\frac{d\rho}{dh}\frac{d}{dq}\left(\frac{1}{r_q}\right)
\end{aligned}
\qquad \text{(D-36)}
$$

The equation for λ_α corresponding to Eq (D-17) is

$$
\lambda_\alpha^{(i)} = g_{\alpha V}\lambda_V^{(i)} + g_{\alpha\gamma}\lambda_\gamma^{(i)} + g_{\alpha\psi}\lambda_\psi^{(i)} + g_{\alpha Q}\lambda_Q^{(i)} \qquad \text{(D-37)}
$$

where

$$g_{\alpha v} = -\frac{D}{C_D m}\frac{dC_D}{d\alpha}$$

$$g_{\alpha \gamma} = \frac{D}{C_D m V}\frac{dC}{d\alpha}$$

$$g_{\alpha \psi} = \frac{D\left(\frac{C_L}{C_D}\frac{dC_L}{d\alpha} + \frac{dC_D}{d\alpha}\right)}{\sqrt{C_L^2 + C_D^2}} \qquad \text{(D-38)}$$

$$g_{\alpha Q} = \frac{dA}{d\alpha} C_1 \rho^{1/2} V^{3.15} G_{AVS} + \frac{dB}{d\alpha} H(h,v) R_N$$

3. Methods of Solution

Having developed the necessary equations and presented their counterparts for the optimum re-entry problem, we now proceed to determine the desired correction $\delta\alpha(t)$ to the driving function. First, we recognize that the quantity which we are minimizing, Q_f, is dependent on the re-entry trajectory. The re-entry trajectory, in turn, is dependent upon the driving function $\alpha(t)$ assuming initial conditions are specified. Therefore, Q_f is dependent on the function $\alpha(t)$. By the method of steepest descent the correction to $\alpha(t)$ is determined by

$$\delta\alpha = -K \, \text{grad} \, Q_f \qquad \text{(D-39)}$$

where

$$\text{grad.} \, Q_f = \frac{\partial Q}{\partial \alpha} \qquad \text{(D-40)}$$

Thus, we wish to determine, $\frac{\partial Q}{\partial \alpha}$, the influence function which tells how a small change in α affects Q_f.

By defining

$$\lambda_i^{(Q)}(T) = \left[\frac{\partial Q}{\partial y_i}\right]_T \tag{D-41}$$

where y_i are the problem variables, then

$$\left[\sum_{i=1}^{n} \lambda_i^{(Q)} dy_i\right]_T = \left[\frac{\partial Q}{\partial y_1} dy_1 + \frac{\partial Q}{\partial y_2} dy_2 + \cdots\cdots + \frac{\partial Q}{\partial y_n} dy_N\right]_T = \left[dQ\right]_T \tag{D-42}$$

and Equation (D-19) can be written for this case

$$[dQ]_T = J_Q\, dT + \int_{t_o}^{T} \lambda_\alpha^{(Q)} \delta\alpha\, dt + \left[\sum_{i=1}^{n} \lambda_i^{(Q)} \delta y_i\right]_{t_o} \tag{D-43}$$

where

$$J_Q = \left[\sum_{i=1}^{n} \lambda_i^{(Q)} f_i\right]_T \tag{D-44}$$

Note that $\lambda_\alpha^{(Q)}$ in Eq (D-43) is the influence function desired in Eq (D-40). There, we can write

$$\delta\alpha = -K \lambda_\alpha^{(Q)} \tag{D-45}$$

for the desired correction. The values of $\lambda_\alpha^{(Q)}$ in Eq (D-45) are determined from Eq (D-37) where the λ_i in Eq (D-37) are solutions to the adjoint system Eqs (D-28) to (D-35) with boundary conditions given by Eq (D-41). Since the boundary conditions are given at final time, T, the adjoint equations are integrated backwards.

Equation (D-45) does not assure satisfaction of other problem requirements, namely specified range and final boundary conditions ψ, ϕ and θ. To simultaneously satisfy these requirements additional influence functions can be generated which tell how small changes in α affect their respective values.

For instance define

$$\lambda_i^{(h)}(T) = \left[\frac{\partial h}{\partial y_i}\right]_T \tag{D-46}$$

then Eq (D-19) becomes

$$[dh]_T = J_n\, dT + \int \lambda_\alpha^{(h)} \delta\alpha\, dt + \left[\Sigma \lambda_i^{(h)} \delta y_i\right]_{t_0} \tag{D-47}$$

Similarly let

$$\lambda_i^{(x)}(T) = \left[\frac{\partial x}{\partial y_i}\right]_T \tag{D-48}$$

then

$$[dx]_T = J_x\, dt + \int \lambda_\alpha^{(x)} \delta\alpha\, dt + \left[\Sigma \lambda_i^{(x)} \delta y_i\right]_{t_0} \tag{D-49}$$

$$\lambda_i^{(\psi)}(T) = \left[\frac{\partial \psi}{\partial y_i}\right]_T \tag{D-50}$$

then

$$[d\psi]_T = J_\psi\, dT + \int \lambda_\alpha^{(\psi)} \delta\alpha\, dt + \left[\Sigma \lambda_i^{(\psi)} \delta y_i\right]_{t_0} \tag{D-51}$$

$$\lambda_i^{(\phi)}(T) = \left[\frac{\partial \phi}{\partial y_i}\right]_T \tag{D-52}$$

then

$$[d\phi]_T = J_\phi dT + \int \lambda_\alpha^{(\phi)} dt + \left[\Sigma \lambda_i^{(\phi)} \delta y_i\right]_{t_o} \qquad \text{(D-53)}$$

$$\lambda_i^{(\theta)}(T) = \left[\frac{\partial \theta}{\partial y_i}\right]_T \qquad \text{(D-54)}$$

then

$$[d\theta]_T = J_\theta dT + \int \lambda_\alpha^{(\theta)} \delta\alpha\, dt + \left[\Sigma \lambda_i^{(\theta)} \delta y_i\right]_{t_o} \qquad \text{(D-55)}$$

The ultimate goal is to determine $\delta\alpha$ which simultaneously minimizes Q_f and causes $(dh)_T$, $(dx)_T$, $(d\psi)_T$, $(d\phi)_T$ and $(d\theta)_T$ to vanish. Since initial conditions for the re-entry problem are specified, the last term in Eqs (D-43), (D-47), (D-49), (D-51), (D-53) and (D-55) is zero. If we extend our steepest descent form for $\delta\alpha$ to include the other boundary requirements, we have

$$\delta\alpha = K_Q \lambda_\alpha^{(Q)} + K_x \lambda_\alpha^{(x)} + K_\psi \lambda_\alpha^{(\psi)} + K_\phi \lambda_\alpha^{(\phi)} + K_\theta \lambda_\alpha^{(\theta)} \qquad \text{(D-56)}$$

where K_p, $K_x \ldots K_\theta$ are unknown step sizes to be determined. Substituting (D-56) into (D-43), (D-47), (D-49), (D-51), (D-53) and (D-55), we obtain the following abbreviated system

$$\begin{bmatrix} dT \\ K_Q \\ K_x \\ K_\psi \\ K_\phi \\ K_\theta \end{bmatrix} = [A]^{-1} \begin{bmatrix} dh_f \\ dQ_f \\ dx_f \\ d\psi_f \\ d\phi_f \\ d\theta_f \end{bmatrix} \text{ where } [A] = \begin{bmatrix} J_h & I_{Qh} & I_{xh} & I_{\psi h} & I_{\phi h} & I_{\theta h} \\ J_Q & I_{QQ} & I_{xQ} & I_{\psi Q} & I_{\phi Q} & I_{\theta Q} \\ J_x & I_{Qx} & I_{xx} & I_{\psi x} & I_{\phi x} & I_{\theta x} \\ J_\psi & I_{Q\psi} & I_{x\psi} & I_{\psi\psi} & I_{\phi\psi} & I_{\theta\psi} \\ J_\phi & I_{Q\phi} & I_{x\phi} & I_{\psi\phi} & I_{\phi\phi} & I_{\theta\psi} \\ J_\theta & I_{Q\theta} & I_{x\theta} & I_{\psi\theta} & I_{\phi\theta} & I_{\theta\theta} \end{bmatrix} \qquad \text{(D-57)}$$

where

$$\mathcal{J}_\beta = \left[\sum_{i=1}^{n} \lambda_i^{(\beta)} f_i\right]_T \qquad \text{(D-58)}$$

and

$$I_{\beta\delta} = \int_{t_o}^{T} \lambda_\alpha^{(\beta)} \lambda_\alpha^{(\delta)} \, dt \qquad \text{(D-59)}$$

From Eq (D-57) values of dT, $K_Q \ldots K_\theta$ are determined which, in conjunction with the λ_α's yield the correction $\delta\alpha$ to be applied to the nominal driving function α (t). The corrected driving function is then used to determine a new nominal trajectory and the procedure is repeated until the optimum trajectory is determined. At the optimum, the value of $\lambda_\alpha^{(Q)}$ (t) goes to zero.

When numerically integrating the constraint equations on a computer, the stopping condition is normally altitude, i. e., when a specified altitude is reached the integration stops. Therefore, $[\,dh\,]_f$ in Eq (D-47) vanishes. Solving (D-47) for dT gives

$$dT = \frac{1}{\mathcal{J}_h} \int_{t_o}^{T} \lambda_\alpha^{(h)} \delta\alpha \, dt \qquad \text{(D-60)}$$

Substituting Eq (D-60) into (D-43), (D-49), (D-51), (D-53) and (D-55) we can reduce the order by one. The resulting equations after simplification are

$$[dQ]_T = \int_{t_o}^{T} \lambda_\alpha^{(Q,h)} \delta\alpha \, dt + \left[\sum_{i=1}^{n} \lambda_i^{(Q,h)} \delta y_i\right]_{t_o} \qquad \text{(D-61)}$$

$$[dx]_T = \int_{t_o}^{T} \lambda_\alpha^{(x,h)} \delta\alpha \, dt + \left[\sum_{i=1}^{n} \lambda_i^{(x,h)} \delta y_i\right]_{t_o} \qquad \text{(D-62)}$$

$$[d\psi]_T = \int_{t_o}^{T} \lambda_\alpha^{(\psi,h)} \delta\alpha \, dt + \left[\sum_{i=1}^{n} \lambda_i^{(\psi,h)} \delta y_i\right]_{t_o} \qquad \text{(D-63)}$$

$$[d\phi]_T = \int_{t_o}^{T} \lambda_\alpha^{(\phi,h)} \delta\alpha\, dt + \left[\sum_{i=1}^{n} \lambda_i^{(\phi,h)} \delta y_i\right]_{t_o} \qquad \text{(D-64)}$$

$$[d\theta]_T = \int_{t_o}^{T} \lambda_\alpha^{(\theta,h)} \delta\alpha\, dt + \left[\sum_{i=1}^{n} \lambda_i^{(\theta,h)} \delta y_i\right]_{t_o} \qquad \text{(D-65)}$$

where

$$\lambda_i^{(\beta,h)}(T) = \left[\frac{\partial\beta}{\partial y_i} - \frac{J_\beta}{J_h}\frac{\partial h}{\partial y_i}\right]_{t=T} \qquad \text{(D-66)}$$

and

$$J_\beta = \left[\sum_{i=1}^{n} \lambda_i^{(\beta)} f_i\right]_T = \left[\sum_{i=1}^{n} \frac{\partial\beta}{\partial y_i} f_i\right]_T \qquad \text{(D-67)}$$

The λ_α's in Eq (D-61) to (D-65) correspond to solutions of the adjoint system, λ i, obtained for the boundary conditions given by Eq (D-66). Substituting Eq (D-56) into (D-61) to (D-65) yields the following for $K_Q \cdots K_\theta$.

$$\begin{bmatrix} K_Q \\ K_x \\ K_\psi \\ K_\phi \\ K_\theta \end{bmatrix} = [A]^{-1} \begin{bmatrix} dQ \\ dx \\ d\psi \\ d\phi \\ d\theta \end{bmatrix} \quad \text{where } [A] = \begin{bmatrix} I_{QQ} & I_{Qx} & I_{Q\psi} & I_{Q\phi} & I_{Q\theta} \\ I_{xQ} & I_{xx} & I_{x\psi} & I_{x\phi} & I_{x\theta} \\ I_{\psi Q} & I_{\psi x} & I_{\psi\psi} & I_{\psi\phi} & I_{\psi\theta} \\ I_{\phi Q} & I_{\phi x} & I_{\psi\psi} & I_{\phi\phi} & I_{\phi\theta} \\ I_{\theta Q} & I_{\theta x} & I_{\theta\psi} & I_{\theta\phi} & I_{\theta\theta} \end{bmatrix} \qquad \text{(D-68)}$$

where

$$I_{\beta\delta} = \int_{t_o}^{T} \lambda_\alpha^{(\beta,h)} \lambda_\alpha^{(\delta,h)} dt \qquad \text{(D-69)}$$

Thus, by defining λ_i (T) by Eq (D-66), we need only determine five sets of solutions to the adjoint equations.

Since the ultimate goal of the method is to determine the function α(t) which minimizes Q_f and causes dx_f, $d\psi_f$, $d\phi_f$ and $d\theta_f$ to vanish we will next define a scalar function to be

$$F = W_1 Q_f^2 + W_2 dx_f^2 + W_3 d\psi_f^2 + W_4 d\phi_f^2 + W_5 d\theta_f^2 \qquad \text{(D-70)}$$

Where W_1 W_2 ... W_5 are arbitrary constant weighting functions selected to suit the needs of the problem. Minimizing Q_f and causing dx_f, $d\psi_f$, $d\phi_f$ and $d\theta_f$ to vanish is tantamount to minimizing F.

Therefore, let us define

$$\lambda_i^{(F)}(T) = \left[\frac{\partial F}{\partial y_i}\right]_T \qquad \text{(D-71)}$$

then Eq (D-19) becomes

$$[dF]_T = J_F dT + \int_{t_o}^{T} \lambda_\alpha^{(F)} \delta\alpha \, dt \qquad \text{(D-72)}$$

where

$$J_F = \left[\sum_{i=1}^{n} \lambda_i^{(F)} f_i\right]_T \qquad \text{(D-73)}$$

Once again the initial conditions on the problem variables are assumed known and their influence is eliminated from Eq (D-72).

Let us also define

$$-\lambda_i^{(h)}(T) = \left[\frac{\partial h}{\partial y_i}\right]_T \tag{D-74}$$

so that

$$[dh]_T = 0 = J_h\, dT + \int_{t_o}^{T} \lambda_\alpha^{(h)}\, \delta\alpha\, dt \tag{D-75}$$

Solving Eq (D-75) for dT and substituting the results into Eq (D-72) gives

$$[dF]_T = \int_{t_o}^{T} \lambda_\alpha^{(F,h)}\, \delta\alpha\, dt \tag{D-76}$$

where

$$\lambda_i^{(F,h)}(T) = \left[\lambda_i^{(F)} - \frac{J_F}{J_h}\lambda_i^{(h)}\right]_T = \left[\frac{\partial F}{\partial y_i} - \frac{J_F}{J_h}\frac{\partial h}{\partial y_i}\right]_T \tag{D-77}$$

Letting

$$\delta\alpha = K\,\lambda_\alpha^{(F,h)} \tag{D-78}$$

and substituting Eq (D-78) into (D-76) we obtain for K

$$K = \frac{[dF]_T}{\int_{t_o}^{T} \lambda_\alpha^{(F,h)}\, \lambda_\alpha^{(F,h)}\, dt} \tag{D-79}$$

The boundary conditions for the single set of solutions to the adjoint equations are given by Eq (D-77). The optimum solution is obtained by initially specifying desired changes in $(dF)_T$ and obtaining the corrections corresponding to these specified changes. After several iterations a curve can be fit to $(F)_T$ and the value of $(dF)_T$ selected so as to cause $(F)_T$ to be minimum.

4. Nomenclature

A	Abbreviation of matrix in Eq (D-68)
a	Acceleration, $g's$
C_1	Coefficient in heating Eq (D-24) $\cong \dfrac{17600}{R_N \rho_o^{1/2} V_c^{3.15}}$
C_2	Lift coefficient, L/qS
C_D	Drag coefficient, D/qS
D	Aerodynamic drag, lb
f_i	Abbreviation in constraint Eq (D-1)
F	Abbreviation of quantity given by Eq (D-70)
g	Acceleration of gravity at altitude
g_o	Acceleration of gravity at sea level
g_{ij}	Coefficients in adjoint Eq (D-28) to (D-35) $= \dfrac{2f_j}{2y_i}$
G_{avg}	Parameter in heating Eq (D-10) to account for wall temperature variations.
h	Altitude, ft
H(h V)	Gas cap radiation term in heating Eq (D-24)
$I_{\beta\delta}$	Abbreviation of integral given by Eq (D-59)
J	Abbreviation defined in Eq (D-58)
L	Lift, lb
m	Vehicle mass, slugs
Q	Heat transfer, Btu/ft^2
q	Dynamic pressure, $1/2\ \rho V^2$

R	Mean earth radius = 2.09029×10^7 ft
R_N	Body nose radius, ft
T	Time at termination of flight
t	Time
t_o	Time at initiation of flight
V	Velocity relative to earth's surface
x	Range along earth's surface
y_i	Abbreviation of dependent variables in Eq (D-1)
α	Angle of attack
β	Dummy index in Eq (D-58) and (D-59)
γ	Flight path angle, positive up from local horizon in Eq (D-20) to (D-27)
θ	Parameter introduced in Eq (D-27)
λ	Adjoint variables Eq (D-13) (influence coefficients)
ρ	Atmospheric density
ϕ	Parameter introduced by Eq (D-26)
ψ	Parameter introduced by Eq (D-25)
V_C	Circular satellite velocity, $\sqrt{gR}$ = 26,000 fps

References

D-1 Bryson, A. E., Denham, W. F., Carroll, F. J. and Mikami, K., "Determination of the Lift or Drag Program that Minimized Re-Entry Heating with Acceleration or Range Constraints Using a Steepest Descent Computation Procedure," Institude of the Aeronautical Sciences Paper 61-6, 1961.

D-2 Kelley, H. J., "Gradient Theory of Optinial Flight Paths," American Rocket Society Preprint 1230-60, 1960.

D-3 Goodman, T. R. and Lance, G. N.; "The Numerical Integration of Two-Point Boundary Value Problems," Mathematical Tables and Other Aids to Computation, Vol. 10, No. 54, April 1956.

THE FINAL REPORT of The Martin Company's Apollo design feasibility study comprises the following publications:

System and Operation	ER 12001
Support	ER 12002
Trajectory Analysis	ER 12003
Configuration	ER 12004
Aerodynamics	ER 12017
Mechanical Systems	ER 12005
Aerodynamic Heating	ER 12006
Guidance and Control	ER 12007
Life Sciences	ER 12008
Onboard Propulsion	ER 12009
Structures and Materials	ER 12010
Instrumentation and Communications	ER 12011
Space Environment Factors	ER 12018
Test Program	ER 12012
Fabrication and Quality Assurance	ER 12013
Program Management	ER 12014
Business Plan	ER 12015
Preliminary Specifications	ER 12016